May 1992 Research Report UMCEE 92-4

BEHAVIOR OF 3-D STEEL MOMENT FRAME STRUCTURES UNDER THE INFLUENCE OF BI-DIRECTIONAL GROUND EXCITATION

Jodi Firmansjah
Robert D. Hanson

Department of Civil Engineering
The University of Michigan
College of Engineering
Ann Arbor, MI 48109-2125

engl
UMR 0462

ABSTRACT

BEHAVIOR OF 3-D STEEL MOMENT FRAME STRUCTURES UNDER THE INFLUENCE OF BI-DIRECTIONAL GROUND EXCITATION

by

Jodi Firmansjah

and

Robert D. Hanson

This report presents an investigation of nonlinear response of three dimensional steel moment frame structures under the influence of bidirectional ground excitation of different intensities and characteristics. The study is comprised of three topics: first, development of analytical model of three dimensional beam column, second, investigation of three-dimensional symmetrical and asymmetrical steel moment frame structures subjected to unidirectional and bidirectional ground excitations, and third, investigation of dynamic instability of three-dimensional symmetrical steel moment frame structures subjected to bidirectional ground excitations and large column axial loads.

The development of a three dimensional beam column element analytical model uses a prismatic fiber model under finite displacements. The model includes material nonlinearity due to plasticity with strain hardening under monotonic or cyclic loading, and geometric nonlinearity due to large deflections and rotation.

The torsional behavior of three-dimensional symmetrical and asymmetrical steel moment frame structures subjected to unidirectional and bidirectional ground excitations with different intensities was studied by comparing bidirectional earthquake

response with combinations of single directional responses, for both doubly symmetric as well as for torsionally sensitive building configurations. Results indicate that torsional response of the initially symmetric structure was not important and that the nonlinear response remained primarily translational. Inelastic torsional response of the torsionally sensitive building was smaller than that predicted from elastic response results. Torsional motion was less significant for increased ground motion intensities.

The presence of large axial column loads affects the load-displacement hysteresis curves when the story drifts are large. Nonlinear static analysis shows that the inverted triangular floor force profile can be used as a lower bound to actual earthquake response ultimate capacity. Large drift and yielding in the columns of a story under combined biaxial bending and axial force can induce frame instability and collapse of the entire structure. Structures with a weak story and limited structural redundancy should be avoided for seismic resistance.

ACKNOWLEDGEMENTS

The author would like to express his deepest gratitude to Dr.Robert D. Hanson, Professor of Civil Engineering, for introducing me to the field of earthquake engineering, for his guidance and encouragement throughout the doctoral program, and his painstaking editing in preparation of this report. It has been a real pleasure and privilege to work with him. Appreciation is also extended to members of the dissertation committee, Professors Subhash C. Goel, Movses J. Kaljian and Wei H. Yang, for reviewing the report and offering helpful suggestions and comments.

I also take this opportunity to convey my thanks and gratitude to my friends: Oday Hassan, Marwan El-Bkaily, Hae-In Kim, Ahmad Itani, Khaled Soubra, and all the rest of my friends, who enhance the meaning of care, generosity and true friendship.

I also wish to express my special thanks to my parents, my brothers, my father and mother in-law for their love, support and encouragement.

For reasons that I cannot describe, I am most of all indebted to my wife. Without her encouragement and understanding, I would not have been able to finish my Ph.D. study by now.

TABLE OF CONTENTS

LIST OF FIGURES

Figure

LIST OF TABLES

LIST OF NOTATIONS

Notation

M	mass matrix
C	damping matrix
	factor depending on natural period of the structure and soil type
K	elastic stiffness matrix
K_T	tangential stiffness matrix
	incremental stiffness matrix of beam-column element
K_G	geometric stiffness matrix
	incremental initial stress matrix of beam-column element
$\Delta R_{E,i}$	increment of external load for current step
$R_{I,i}$	static internal resisting load vector at step i
$X_i, \dot{X}_i, \ddot{X}_i$	displacement, velocity and acceleration at step i
ΔX	increment in displacement
K_T^*	effective stiffness matrix
ΔR_i^*	effective load vector
$\alpha_m, \beta_o, \beta_T$	damping proportionality constants
α	HHT integration constant or Euler angle
β, γ	Euler angles
Δt	time step

	ΔR_m	the midstep error vector
	R_U	unbalanced load vector
	u, v, w	displacement components in the element x, y, z-axes
	φ	torsional rotation at cross section center of rigidity
	$[D_e]$	elastic stress-strain matrix
	$[D_{ep}]$	elastic-plastic stress-strain matrix
	$\{\underline{n}\}$	dimensionless unit vector normal to the yield surface
	E_{pi}	plastic moduli between yield surfaces i and $i+1$
	σ_{yi}	yield stress of yield surfacs i
	σ	normal stress
	τ	shear stress
	E_t	tangent modulus
	E_p	plastic modulus
	$\Delta\varepsilon_e$	elastic strain increment
	$\Delta\varepsilon_p$	plastic strain increment
	σ_{vi}	virgin state yield stress of yield surface i
	σ_{si}	saturated state yield stress of yield surface i
	w	weighting factor
	E_{pvi}	virgin state plastic modulus of yield surface i
E_{ps}	E_{psi}	saturated state plastic modulus of yield surface i
$\underline{\alpha_i}$	$\underline{\alpha_i}$	vector of yield surface i origin
$\underline{d}$	$\underline{d}$	element nodal displacements
$\underline{p}$	$\underline{p}$	element nodal forces
$[R]$	$[R]$	element rotation matrix

$\underline{e}_{xm}, \underline{e}_{ym}, \underline{e}_{zm}$	unit vector in the x, y, z-directions of element axes
$\underline{e}_{jp}$	unit vector in the element $x-y$ plane
n_{tf}	no. of integration point on top flange
n_{bf}	no. of integration point on bottom flange
n_w	no. of integration point on web
E_{Ti}	tangential modulus at integration point i
G_{Ti}	shear modulus at integration point i
f_i	section properties calculation weight function
ε^0_{xx}	initial strain due to the fixed-end moment
σ^0_{xx}	initial stress due to the fixed-end moment
$[R_e]$	end eccentricity transformation matrix
u_m, v_m, θ_m	'master' or C.M. horizontal translations and rotation
u_i, v_i, θ_i	'slave' horizontal translations and rotation
$[R_m]$	rigid diaphragm transformation matrix
$[R_t], [R_d], [R_a]$	large displacement transformation matrices
u_1, v_1 and w_1	element relative displacement in the original coordinate system
$\Delta\sigma^l$	linear stress increments
$\Delta\sigma^n$	nonlinear stress increments
μ_i	event factor which is required to produce the next 'event'
σ_y	yield stress
E	young's modulus of elasticity
G	shear modulus of elasticity
h_n	the building height in feet above the base
T	the natural period of the structure

R_w	response modification
S	soil condition factor
Z	seismic zone factor
I	importance factor
W	total dead load of the structure
A_x	UBC accidental torsion amplification factor

CHAPTER 1

INTRODUCTION

1.1 Introductory Remarks

During its lifetime, a highrise building will always be subjected to static loading, and sometimes to dynamic loading. Dynamic loading acting on highrise buildings may result from several different sources, such as rotating machinery in the building, tornado wind, earthquake, etc. The type of dynamic loading which is most troublesome to a structural engineer undoubtedly is that produced by earthquakes. This is due to the major difficulty of prediciting the character and intensity of earthquakes that might occur during the lifetime of a building structure, and from the terrible consequences of major earthquakes in a heavily populated areas. For many years, a height limit for highrise structures built in regions of high seismicity was imposed by building codes. Highrise buildings are unavoidable in highly populated regions due to increasing urban property cost.

At the same time, modern building construction economics have reduced lateral force resisting redundancy in highrise buildings. To reduce dead loads, it is common to replace concrete exterior walls by curtain walls, and to use lighweight interior walls. As a result, there is little uncalculated secondary strength. The structural frame is required to carry the entire seismic loading. Since it is economically unrealistic to

design a structure so it remains elastic during a major earthquake, limited inelastic deformation is allowed to occur. Moreover, the structural engineer needs to account for the fact that 10 or 100-story buildings near the same site will respond differently to an earthquake, as will reinforced concrete and steel buildings or rectangular and irregular, L-shaped buildings. Clearly, complex algorithms are required to predict, analyze and simulate the response of structures subjected to strong ground motion.

During the last two decades, much research has been done in the area of inelastic analysis and design of the structure. A considerable amount of knowledge about the behavior of structures in the inelastic range has been obtained, leading to some changes in design philosophy for highrise structure built in regions of high seismicity. One design philosophy has emerged in which highrise buildings should be designed so that their elements remain elastic during small earthquakes that can be expected to occur more than once in their lifetime. They should be able to resist minor earthquakes without damages. Moreover, they should be able to undergo 'limited plastic deformation' under moderate earthquakes without structural damage, but with some nonstructural damage. Finally, they should be able to survive 'large plastic deformation' under major earthquakes without collapse. The buildings should be ductile enough to ensure that the structure can dissipate the earthquake input energy and avoid failure. Design within the framework of this philosophy requires a detailed investigation of the nonlinear behavior of structures under large dynamic loading. The safety of the structure can be increased and in many instances their cost can be reduced if the inelastic behavior can be predicted quite accurately.

Nonlinear behavior of structures under dynamic loading has been a topic of interest for many years, and has been subjected to considerable amount of research throughout the past two decades. Work in this area has proceeded basically along

two main lines:

1. In depth study of inelastic dynamic behavior of single degree-of-freedom systems. This area of study increased our understanding of the effects of gravity load, softening stiffness and hysteretic energy dissipation on the dynamic response and ductility requirements of simple sytems. Various mathematical models to represent restoring-force characteristic have been used. Penzien [1], and Veletsos and Newmark [2] used a bilinear model. Jennings [3] used a Ramberg-Osgood model, including as particular cases elastic and elasto-plastic models.

2. Studies on inelastic dynamic behavior of multi-degree-of-freedom systems. This area of study increased our understanding of the effects of member stiffness degradation and instability on the load-carrying capacity and the behavior of structures. Various experimental and analytical studies have been done on the the inelastic behavior of the structural elements, and the results of these studies have been used to predict the overall nonlinear behavior of structures under dynamic loading. With the advent of high speed digital computers and the advancement of computational methods for analysis, several computer programs capable of predicting the inelastic behavior of structures have been developed. Therefore a detailed response of structure can be obtained.

The investigation of deterioration processes and member instability on the carrying capacity of the structure can be only done if the material and geometrical nonlinearities are taken into account in the problem formulation. Various analytical models to represent these nonlinearities have been proposed. Depending on the degree of complexity, these analytical model fall into two basic categories: the simple

model, where one is most interested in the overall behavior of the element, and the elaborate model, where one is most interested in the local nonlinearity and local behavior of the element.

In the elaborate model, a structural member can be subdivided into a series of finite elements over the volume of the member. The cross section geometry and material properties of each finite element are defined and an analysis of the complete system is performed. The advantages of finite element techiques are:

1. They are applicable to many types of problems, and

2. Only element geometry and material properties need to be defined.

However, this approach is computationally expensive. Moreover, given a large number of degrees-of-freedom in each member, and large storage requirements to keep the ever changing element properties, this approach is impractical for the nonlinear dynamic analysis of large structures; therefore, the simple model is preferable for building response studies.

In the simple model, the members of framed structures are modeled depending on the type of load they carry. Members of frame structures are identified by different names depending upon their function and their loading condition. The main parts of a basic structural frame are the brace element, the beam element and the beam column element. The brace element is a member in which the axial load, compression or tension, is dominant. The beam element is a member in which the bending moment is dominant. And the beam-column element is a member in which the axial load and the bending moment are equally dominant. Even though the simple model may not be able to represent local nonlinearity, such as local buckling, cross-section deformation etc., material and geometrical nonlinearity can be considered in the

element formulation. Some experimental and analytical studies have been carried out in the past on the inelastic behavior of structural elements. Using this studies, several computer programs capable of predicting the inelastic behavior of structural elements have been proposed and applied. Kanaan and Powell [4], [5] developed DRAIN-2D, a general computer program for inelastic dynamic and elastic static analysis of plane frame structures. Tang [6] developed DRAIN-2DM, an extended version of DRAIN-2D, which includes all modifications and additions made at the University of Michigan. Unlike DRAIN-2D, this version has the capability to do incremental inelastic static analysis of frame structure. Oughourlian and Powell [7] developed ANSR-III, a general computer program for inelastic dynamic and static analyses of three-dimensional structures. A large number of element types is available in these programs. They have been developed based on theoretical considerations, experimental results, or a mixture of both; and they all have been formulated using the simple model approach. In these programs, each nodal point has three or six degrees of freedom, as in typical plane or space frame analyses.

The beam-column element is an important part of a building structure. When a frame structure is subjected to a horizontal load, the total story shear is either carried entirely by the column element, or carried by the combination of the column and brace elements. Moreover, all compression members should be treated as beam-column elements since they have an unavoidable bending moments along the member due to the eccentricity of axial forces.

In designing a structure in a seismic region, it is generally desireable to provide strong columns which ensure prior flexural yielding of the beams. The reasons for this choice are the following :

1. Yielding in the columns, particularly under combined bending and axial forces

may quickly lead to frame instability and collapse of the entire building.

2. In a weak-column structure, plastic deformation usually is concentrated at one story level. Consequently, large ductility factors are required for these columns.

3. In both shear and flexural failure, column stiffness degradation is greater than for beams due to the presence of large axial forces in the column.

The inelastic behavior of building structures subjected to major earthquakes principally depends on the behavior of their beam-column elements. The predicition reliability of the structures' overall behavior depends in large part on the accuracy of predicting the inelastic behavior of their beam column element. An ideal model for the beam-column element is one having the capability of properly describing the restoring-force characteristics, and which accounts for the damage and loss of load carrying capacity or the increase in maximum strength due to the extension of the compressive strain into the strain-hardening range as observed during cyclic loadings. The most useful models for beam-column elements are those which are practical and efficient for the computer analysis of complete structures. Various simple models have been developed for treating material and geometrical nonlinearities in the beam-column element, and these models fall into two basic categories: the distributed and the lumped models. Mallet and Marcal [8], Yang and Saigal [9], Cichon [10], Holzer and Somers [11], Kang and Scordelis [12], Sundaramoorthy and Murray [13] and others used the distributed model for their beam-column element; and Kanaan and Powell [4], Jain and Goel [14], Kassimali [15], Ueda and Akamatsu [16], Inoue and Ogawa [17], Chen and Powell [18] and others used the lumped model for their beam-column element.

In three-dimensional frame structures, the multi-dimensional motion of an earth-

quakes has its greatest effect on column loading. These columns are subjected to biaxial bending from combined longitudinal, transverse and torsional motion of the structure, with added axial loads due to building overturning moments. It is well known that the bending strength in any particular direction is decreased by the simultaneous moment along another axis.

The lateral and torsional motions are coupled in three-dimensional frame structures subjected to earthquake ground motion if the floor center of mass do not coincide with the floor center rigidity. A transient state of torsional coupling can be excited during the inelastic response of an initially symmetric structures subjected to bidirectional ground excitation. The torsional motion develops when one element yields and the others remain elastic, creating eccentricity.

For elastic systems, the earthquake response of buildings with eccentric center of mass and rigidity have been the subject of many studies [23-32]. For this system, the controlling parameters have been identified. They are the uncoupled lateral frequency, uncoupled torsional to lateral frequency ratio and the system eccentricity. Shepherd and Donald [27] studied the seismic response of torsionally unbalanced building and found that quite severe torsional oscillation is likely to occur and the behavior of building in low intensity earthquakes is likely to be generally unsatisfactory for building having small eccentricity and similar translational and torsional periods. Kan and Chopra [31] stated that the effects of torsional coupling for an elastic system depend strongly on the uncoupled torsional to lateral frequency ratio. For systems with smaller values of system eccentricity ratio, this effect is most pronounced when structure's torsional period is the same as the translational period.

Even though the influence of these parameters on the response of the elastic system have been evaluated, results of linear response are not applicable directly to

calculation of the design forces for building because they are usually designed to deform significantly beyond yield limit during moderate to very intense earthquake motion. For inelastic systems, the earthquake response of buildings with eccentric center of mass and rigidity have been the subject of many studies [33-46] where most of the studies have been concerned with one story models. Historically, the study of inelastic torsional response of asymmetric structures to strong earthquakes has been an area where contradictory conclusions have been reached by various researchers because inelastic responses are often model and ground motion specific. While only a few system parameters are needed to completely define an elastic eccentric system, much more detailed specifications of the structural model, such as the location and force-deformation charateristics of the resisting elements are needed for the inelastic system. Therefore, it is possible to have the same overall elastic response but different inelastic response. Kan and Chopra [33], using a single element model, found that torsional coupling generally affects maximum deformation in inelastic systems to a lesser degree than in the corresponding elastic systems, because after initial yielding the system has a tendency to yield further primarily in translation and behaves more and more like an inelastic single degree of freedom system, responding primarily in translation. In another study, using a two element mass eccentric model, Irvine and Kountouris [34] reported results generally confirming this conclusion. It was shown that ductility demands in the resisting elements are insensitive to the system eccentricity and the uncoupled torsional to lateral frequency ratio. Furthermore, the ductility demand on the worst loaded frame was shown to be rarely more than 30 percent greater than the ductility demand in a similar symmetric plan structure. Syamal and Pekau [35] studied the inelastic behavior of eccentric one story structure subjected to sinusoidal ground excitation where the structural resisting elements

are assumed to exhibit bilinear hysteretic behavior. Their results indicate the absence of amplified response when torsional and translational frequencies are close, in contrast to the response of elastic system. However, Tso and Sadek [36], using a three element model, showed that significant rotational motion is involved at the instant when the peak ductility demand is reached. They also illustrated that an increase of over 100 percent in ductility demand is not uncommon for inelastic system with large eccentricity when compared with the response of the systems with small eccentricity. Using the same structural model, Bozorgnia and Tso [37] found that the effect of asymmetry is most pronounced for stiff structures with low yield strength. Exceptionally large ductility demand can be expected on eccentric stiff structures with low yield strength when exposed to ground motion with large and long duration acceleration peaks. Edge displacements, which are affected more by plan-asymmetry than the ductility demand, can be more sensitive to the uncoupled torsional to lateral frequency ratio, and that the lateral displacement at the center of mass is not sensitive to the system eccentricity. Erdik [38], based on the response of four and sixteen element mass eccentric model concluded that for small eccentricities the torsionally coupled system behaves more and more like an inelastic single degree of freedom system, responding in translation after initial yielding. A recent study by Goel and Chopra [43] found that the inelastic response of systems is influenced significantly by the contribution to the torsional stiffness from the resisting elements perpendicular to the direction of ground motion. The effects of torsional coupling are larger in systems without such elements than in systems with these perpendicular elements. More specifically, torsional coupling decreases the lateral deformation to a greater degree and increases the torsional deformation, the element deformations and the maximum ductility demands to a greater degree in system without the per-

pendicular element. It is concluded that the conclusion from Tso and Sadek [36], and Bozorgnia and Tso [37], which are neglecting the contribution from the perpendicular element, are generally not applicable to most actual buildings which invariably include resisting elements in the two lateral directions to provide resistance to both horizontal components of ground motion.

Unlike the one story building, limited research has been carried out on the inelastic torsional behavior of multi story structures. Vignoli and Berti [45] studied the behavior of four story square steel tower subjected to two horizontal components of ground motion. It is found that the results were not quantitatively influenced by different values used for the eccentricity between center of mass and center of rigidity. However, a recent study by Sedarat and Bertero [46] found that real nonlinear torsional response of structures may be significantly underestimated by a linear elastic dynamic analysis, especially for large values of static eccentricity ratio and intensity ground motion.

Several studies have been made on the importance of the P-Δ effect on dynamic response of inelastic systems [47-51]. In the study by Goel [47], it was found that for relatively small axial loads, the gravity effect on inelastic response was insignificant. Jennings and Husid [48] studied the effect of gravity load on the collapse of simple yielding structures, in which artificially generated earthquakes were used as the excitation force. It was found that gravity load increases the amount of plastic drift significantly over that found when gravity is neglected. Large values of plastic drift lead to collapse. Sun [51] studied the gravity effect on the dynamic instability of inelastic systems. It is concluded that the gravity effect becomes significant in the case of water tower type of structures or structures which support heavy weight near their tops and that error will occur when ignoring the gravity effect in analysis.

1.2 Objective and Scope

Research on improving the analytical model of the beam-column element will be conducted in three phases:

Phase I : Modification of ANSR-III

Phase II : Developing beam-column element subroutines for ANSR-III

Phase III : Verification and Numerical Analysis

First, the main program of ANSR-III will be verified and modified to increase its capabilities to solve nonlinear problem of frame structures in static or dynamic cases.

Second, new beam-column element subroutines will be developed and implemented in ANSR-III.

Third, verification of this beam column element will be conducting by comparing the computer results and the experimental results. Furthermore, by using this element, some numerical analysis of three dimensional steel moment frame structures will be conducted.

1.3 Outline of Thesis

In Chapter 2, the analytical method used to study the nonlinear behavior of three-dimensional steel moment frame structures subjected to multi-component earthquakes of different intensities is discussed. The extensions and modifications of the ANSR-III program is presented.

In Chapter 3, a brief review of the existing model for beam-column element is made. Their developmental basis, applicabilities and limitations are examined.

In Chapter 4, analytical model of three-dimensional beam-column element was

developed and used to predict the inelastic response of three-dimensional building structure for this research is discussed. Model based on theoretical consideration to represent beam-column element in three dimensional analysis are proposed. This model uses a two-node beam-column element where the tranverse and axial displacements are approximated by cubic and linear interpolations. The torsional rotation will be approximated by linear interpolation. Material nonlinearity is considered, and a combination of kinematic and isotropic hardening is used to modelling the strain hardening and the Bauschinger effects for arbitrary cyclic loading. Geometrical nonlinearity is considered by including the second order terms in the Green-Lagrange strain formula. Large deformation is considered by using the Update Lagrangian formulation in describing the motion of the element. To obtain the element stiffness matrix, the Gauss Quadrature formula is used for numerical integration over the volume of the element. Their applicabilities and limitations are examined by comparing the computer results with the experimental results which were available for model evaluation.

In Chapter 5, the results of nonlinear response analyses of three-dimensional symmetrical and asymmetrical steel moment frame structures subjected to unidirectional and bidirectional ground excitations of different intensities will be presented. The earthquake impact upon irregularly shaped building, as they tend to experience more pronounced twisting than do regularly shaped building will be studied and will be compared with linear dynamic analysis response. The effects of ground motion coupling on the ultimate capacity of different types of multi-story buildings are observed by studying the base shear, story displacement, story drift, column ductility demand and the relationship between column forces and their associated deformations in relation to the ground input excitation.

In Chapter 6, the results of nonlinear response analyses of three-dimensional symmetrical steel moment frame structures subjected bidirectional ground excitations will be presented. The effects of ground motion intensity, duration, frequency content and column axial load on the ultimate capacity of symmetrical multi-story buildings are observed by studying the base shear, story shear, overturning moment, floor displacement, story drift, column ductility demand and the relationship between column forces and their associated deformations in relation to the ground input excitation.

The conclusions are summarized in Chapter 7.

CHAPTER 2

COMPUTATIONAL ASPECTS OF NONLINEAR ANALYSIS

2.1 Introduction

In recent years a variety of problems involving nonlinear structural behavior have been presented to structural engineers and several types of nonlinear behavior have been identified. A number of numerical solution schemes have been developed or proposed, but no single scheme has been found to be suitable for all types of nonlinear behavior. In this chapter, the computational schemes used in the original ANSR-III [7] program are summarized.

2.2 Equation of Motions

At time t_i, the damped equation of motion for a multi degree of freedom system is

$$M\ddot{X}_i + C\dot{X}_i + K_{T,i}X_i = R_{E,i} \tag{2.1}$$

Similarly, at time $t_{i+1} = t_i + \Delta t$, the equation of motion become

$$M\left(\ddot{X}_i + \Delta\ddot{X}_i\right) + C\left(\dot{X}_i + \Delta\dot{X}_i\right) + K_T\left(X_i + \Delta X_i\right) = R_{E,i+1} \tag{2.2}$$

Substraction of equation 2.1 from equation 2.2 produces the incremental equation of motion as

$$M\Delta\ddot{X}_i + C\Delta\dot{X}_i + K_T\Delta X_i = \Delta R_{E,i} \tag{2.3}$$

where

$$\begin{aligned}
M &= \text{mass matrix} \\
C &= \text{damping matrix} \\
K_T &= \text{tangential stiffness matrix} \\
\Delta R_{E,i} &= \text{increment of external load for current step} \\
&= R_{E,i+1} - \left[R_{I,i} + M\ddot{X}_i + C\dot{X}_i\right] \\
R_{I,i} &= \text{static internal resisting load vector at step } i \\
&= R_{I,i-1} + K_{T,i}\Delta X_i \\
X_i, \dot{X}_i, \ddot{X}_i &= \text{displacement, velocity and acceleration at step } i \\
\Delta X &= \text{increment in displacement}
\end{aligned}$$

In many structural dynamics applications, only lowest mode response is of interest. For these cases the use of implicit unconditionally stable algorithms is generally preferred over conditionally stable algorithms because conditionally stable algorithms require the size of the time step employed be inversely proportional to the highest frequency of the system. In practice this is a severe limitation as accuracy in the lower modes can be attained with time steps which are very large compared with the period of the highest mode. For unconditionally stable algorithms a time step may be selected independent of stability consideration and thus result in a substantial saving of computational effort.

In addition to being unconditionally stable, when only low mode response is of interest, it is often advantageous for an algorithm to posses some form of numerical dissipation to damp out any spurious participation of the higher modes. Examples

of algorithms commonly used in structural dynamics which posses these properties are Houbolt's method [52], the Wilson-θ method [53], the Newmark family of methods [54] and Hilber-Hughes-Taylor (HHT) method [55]. In the ANSR-III, there are three options available to solve the incremental equations of motion 2.3. They are the Newmark average acceleration method, HHT method and Hibbitt's modification of the HHT method [56].

2.3 Newmark Average Acceleration Method

The average acceleration method has been one of the most popular and effective implicit algorithm for the transient analysis of linear systems in structural dynamics. It exactly conserves total energy for undamped system and it is conditionally stable, i.e. solution does not depend upon the size of time step employed. In this method, the incremental velocities at the end of time step Δt can be obtained by using a trapezoidal rule as follows

$$\Delta \dot{X}_i = \frac{1}{2}\left(\ddot{X}_i + \ddot{X}_{i+1}\right)\Delta t = \ddot{X}_i \Delta t + \frac{1}{2}\Delta \ddot{X}_i\, \Delta t \tag{2.4}$$

Similarly, the incremental displacements at the end of the step become

$$\Delta X_i = \frac{1}{2}\left(\dot{X}_i + \dot{X}_{i+1}\right)\Delta t = \dot{X}_i \Delta t + \frac{1}{2}\Delta \dot{X}_i\, \Delta t \tag{2.5}$$

Substitution of equation 2.4 into equation 2.5 yields

$$\Delta X_i = \dot{X}_i \Delta t + \frac{1}{2}\ddot{X}_i\,(\Delta t)^2 + \frac{1}{4}\Delta \ddot{X}_i\,(\Delta t)^2 \tag{2.6}$$

Solving for the incremental accelerations in equation 2.6 gives

$$\Delta \ddot{X}_i = \frac{4}{(\Delta t)^2}\Delta X_i - \frac{4}{\Delta t}\dot{X}_i - 2\,\ddot{X}_i \tag{2.7}$$

Substituting this expression into equation 2.4 produces

$$\Delta \dot{X}_i = \frac{2}{\Delta t}\Delta X_i - 2\dot{X}_i \tag{2.8}$$

where Δt is the time step. With these relationships, an incremental equilibrium can be written as

$$\left[\frac{4}{(\Delta t)^2}M + \frac{2}{\Delta t}C + K_T\right]\Delta X_i = \Delta R_{E,i} + M\left[2\ddot{X}_i + \frac{4}{\Delta t}\dot{X}_i\right] + 2C\dot{X}_i \tag{2.9}$$

or

$$K_T^* \Delta X_i = \Delta R_i^* \tag{2.10}$$

where

K_T^* = effective stiffness matrix

ΔR_i^* = effective load vector

If mass and stiffness proportional damping are used, then

$$C = \alpha_m M + \beta_o K_o + \beta_T K_T \tag{2.11}$$

where α_m, β_o, β_T are proportionality constants. The effective stiffness matrix and effective load vector are

$$K_T^* = \left[\frac{4}{(\Delta t)^2} + \frac{2\alpha_m}{\Delta t}\right]M + \frac{2}{\Delta t}\beta_o K_o + \left[1 + \frac{2}{\Delta t}\beta_T\right]K_T \tag{2.12}$$

and

$$\Delta R^* = R_{E,i+1} - R_{I,i} + M\ddot{X}_i + \left[\frac{4}{\Delta t} + \alpha_m\right]M\dot{X}_i + [\beta_o K_o + \beta_T K_T]\dot{X}_i \tag{2.13}$$

Hence, there are three main steps for dynamic analysis

1. Form the effective stiffness matrix

$$K_T^* = \frac{4}{(\Delta t)^2}M + \frac{2}{\Delta t}C + K_T$$

2. Form the effective load vector

$$\Delta R^* = \Delta R_{E,i} + M\left[2\ddot{X}_i + \frac{4}{\Delta t}\dot{X}_i\right] + 2C\dot{X}_i$$

3. Perform equilibrium check by calculating the equilibrium error

$$R_U = R_{E,i+1} - \left[R_{I,i+1} + M\ddot{X}_{i+1} + C\dot{X}_{i+1}\right]$$

where

$\dot{X}_{i+1}, \ddot{X}_{i+1}$ = velocity and acceleration at end of step

$R_{E,i+1}$ = external load vector at end of step

$R_{I,i+1}$ = static internal resisting load vector at end of step

2.4 Hilber-Hughes-Taylor (HHT) Method

The HHT methods adds numerical damping by solving the following modified equilibrium equation :

$$\left[\frac{4}{(\Delta t)^2}M + \frac{2}{\Delta t}C + (1+\alpha)K_T\right]\Delta X_i = \Delta R_{E,i} + M\left[2\ddot{X}_i + \frac{4}{\Delta t}\dot{X}_i\right] + 2C\dot{X}_i \qquad (2.14)$$

where

$\alpha =$ HHT integration constant $(-\frac{1}{3} \leq \alpha \leq 0)$

If mass and stiffness proportional damping are used, then K_T^* should be modified as follows

$$K_T^* = \left[\frac{4}{(\Delta t)^2} + \frac{2\alpha_m}{\Delta t}\right]M + \frac{2}{\Delta t}\beta_o K_o + \left[1 + \frac{2}{\Delta t}\beta_T + \alpha\right]K_T \qquad (2.15)$$

For dynamic analysis using the HHT method, there are two modifications from the Newmark method as follows

1. Form the effective stiffness matrix

$$K_T^* = \frac{4}{(\Delta t)^2} M + \frac{2}{\Delta t} C + (1+\alpha) K_T$$

2. Perform equilibrium check by calculating the equilibrium error

$$R_U = R_{E,i+1} - \left[R_{I,i+1} + M\ddot{X}_{i+1} + C\dot{X}_{i+1} \right] - \alpha \left(R_{I,i+1} - R_{I,i} \right)$$

where $\alpha \left(R_{I,i+1} - R_{I,i} \right)$ is a correction which must be applied because true equilibrium is not satisfied.

2.5 Hibbitt's Modification of the HHT Method

Hibbitt and Karlsson [56] further modified the HHT equilibrium to the form

$$\begin{aligned} \left[\frac{4}{(\Delta t)^2} M + \frac{2}{\Delta t} C + (1+\alpha) K_T \right] \Delta X_i &= (1+\alpha) \Delta R_{E,i} \\ &+ M \left[2\ddot{X}_i + \frac{4}{\Delta t} \dot{X}_i \right] + 2C\dot{X}_i \end{aligned} \tag{2.16}$$

If mass and stiffness proportional damping are used, then K_T^* is given by the equation 2.15 and ΔR^* should be modified as follows

$$\begin{aligned} \Delta R^* &= (1+\alpha) R_{E,i+1} - \alpha R_{E,i} - R_{I,i} + M\ddot{X}_i \\ &+ \left[\frac{4}{\Delta t} + \alpha_m \right] M\dot{X}_i + \left[\beta_o K_o + \beta_T K_T \right] \dot{X}_i \end{aligned} \tag{2.17}$$

This scheme requires two modifications from the HHT method as follows

1. Form the effective load vector

$$\Delta R^* = (1+\alpha) \Delta R_{E,i} + M \left[2\ddot{X}_i + \frac{4}{\Delta t} \dot{X}_i \right] + 2C\dot{X}_i$$

2. Perform equilibrium check by calculating the equilibrium error

$$\begin{aligned} R_U &= R_{E,i+1} - \left[R_{I,i+1} + M\ddot{X}_{i+1} + C\dot{X}_{i+1} \right] \\ &- \alpha \left(\Delta R_{E,i} \right) - \alpha \left(R_{I,i+1} - R_{I,i} \right) \end{aligned}$$

where $\alpha(\Delta R_{E,i}) - \alpha(R_{I,i+1} - R_{I,i})$ is a correction which must be applied because true equilibrium is not satisfied.

2.6 Time Step Control in Dynamics Analysis

2.6.1 Midstep Error for Linear Dynamics Analysis

Hibbitt and Karlsson [56] have proposed a criteria for the selection of the time step, Δt. This criterion assumes that if the equilibrium error, ΔR_m, at the middle of any step is small, then overall equilibrium errors will also be small and the time step is acceptable. The midstep error can be calculated as follows

$$\Delta R_m = \frac{\Delta t}{8} K \Delta \dot{X} \tag{2.18}$$

where

K = elastic stiffness matrix

$\Delta \dot{X}$ = increment in nodal velocities

Δt = time step

Within each step, a test is made to check whether the time step is too large for acceptable accuracy. This is done by comparing a norm of the midstep error with an upper tolerance. If the tolerance is exceeded, the time step Δt is reduced by a user specified factor (usually 0.5). If the error is smaller than the lower tolerance for two consecutive steps, then the time step Δt is increased by a second-factor (usually 2). This algorithm thus controls the equilibrium error by automatically adjusting the time step.

2.6.2 Midstep Error for Nonlinear Dynamics Analysis

For a nonlinear problem, exact equilibrium is never, in general, satisfied at the end of a step or within a step. Nevertheless, equation 2.20 can still be used to estimate the midstep error, provided that it is recognized that the stiffness may change within the step. If the stiffness does not change, the tangent stiffness matrix must be used when calculating the midstep error. In the ANSR-III program, the midstep error for nonlinear dynamics is calculated as follows

$$\Delta R_m = \frac{\Delta t}{8} K_T \Delta \dot{X} = \frac{\Delta t}{8} K_T \left(-2\dot{X}_i + \frac{2}{\Delta t} \Delta X \right) \tag{2.19}$$

With the event-to-event solution strategy, if any event occur within a step, the midstep error, ΔR_m, is weighted by the governing event factor and accumulated over the entire step in the following manner

$$\Delta R_m = \sum_i \alpha_i K_{Ti} \Delta \dot{X}_i \tag{2.20}$$

where i = substep number. The midstep error calculation are performed at the element level and ΔR_m is assembled from the element contribution. If the maximum norm of ΔR_m exceeds a user specified tolerance, the time step is reduce. If the norm is less than a lower tolerance for two consecutive steps, the time step is increased.

2.7 Event-to-event Strategy

The event-to-event solution strategy for nonlinear analysis provides means of controlling the equilibrium error. To apply the event-to-event solution strategy, an event factor must be calculated for each element, and the minimum factor chosen to determine a scaling factor for the displacement increment, ΔX, for the step. An event could also be defined in terms of nodal displacement limits. Any significant event occuring within any element determines a substep. The tangent stiffness is modified

in each substep, hence, the solution closely follows the exact response. If the exact response of the structure is piecewise linear and if no overshoot of the exact event is allowed, the solution will follow the exact load-deflection curve and no equilibrium unbalance will result. In general, however, the response is not linear between well-defined events. In this case, the solution does not follow the exact response, with the result that there is an unbalanced load, R_U, at the end of the step, This unbalanced load will be small if the events are well chosen. The main disadvantage of using the event-to-event solution strategy is the need for calculation of events factors. However, the strategy has the advantage that it follows the true equilibrium path more closely, and hence, tends to be more stable because the unbalance load is small. It prevents the associated numerical shock, which can occur when the loading force suddenly change because of the large unbalance load.

2.7.1 Event-to-event Strategy with Variable Time Step

The flow diagram in figure 2.1 illustrates the logic followed by the event-to-event strategy with time step control. The major operations are as follows for each time step

1. Begin with the state at the beginning of the step

2. Set up the load vector ΔR^*

3. Increment the substep counter ($NSUB$) and check against the maximum allowable number of substeps ($MAXSUB$). If $MAXSUB$ is exceeded, reduce the time step (DT) by the factor $CRED$, reform the stiffness matrix, and repeat from step (1).

4. Solved the equilibrium equation:

$$K_T^* X = \Delta R^*$$

5. Compute the velocity increment $\Delta \dot{X}$

6. Calculate the event factors and retain the minimum factor ($FACTOR$)

7. Calculate the midstep error and assemble R_m

8. Compare the maximum norm of R_m againts the upper tolerance ($TOLUP$). If tolerance is exceeded, repeat from step (3).

9. Check the maximum norm of R_m againts the lower tolerance ($TOLOW$). If tolerance is exceeded, set the counter $LOTOL$ to one.

10. Check if $FACTOR = 1$. If so, the step is complete and the displacements, velocoties and accelerations must be updated. If not, scale the displacements vector ΔX by $FACTOR$.

11. Perform state determination

12. If the step is complete, check $LOTOL$. If $LOTOL$ is zero, increase the time step indicator ($INCDT$) by one, and check if $INCDT$ is equal to two. If so, increase time step DT by the factor $CINC$ and reset $INCDT$ to zero, reform K_T^* and continue from step (1).

13. If the step is incomplete, modify K_T^*, compute the remaining proportion of the load vector by scaling ΔR^* by $(1 - FACTOR)$, then continue from step (3)

2.8 Imposed Displacement

The equilibrium equations to be solved at frequent intervals during the analysis are

$$K_T^* X = \Delta R^* \tag{2.21}$$

For dynamic analysis, K_T^* and ΔR^* are effective matrices containing inertia and damping forces. If all terms in ΔX are initially unknown, the equation solving operation is straight forward. In some cases, however, certain terms in ΔX are specified. Such imposed displacement can be accounted for during the equation solving. This is done by skipping over the columns and rows of the corresponding equation during the decomposition of the stiffness matrix K_T^* and subtracting from ΔR^* the inner products of the matrix containing the symmetric part of the skipped columns or rows and the vector containing the imposed displacements. The back-substitution to compute the displacements is then done also by skipping over the equation corresponding to imposed displacements

The procedure is as follows. Let equation number i and j correspond to imposed displacements. The equations could be rearranged and the matrix partitioned as

$$K_T^* = \begin{bmatrix} \cdots & \cdots & \cdots & \cdots & \cdots \\ \cdots & k_{ii} & \cdots & k_{ij} & \cdots \\ \cdots & \cdots & \cdots & \cdots & \cdots \\ \cdots & k_{ji} & \cdots & k_{jj} & \cdots \\ \cdots & \cdots & \cdots & \cdots & \cdots \end{bmatrix} \rightarrow \begin{bmatrix} A & B \\ C & D \end{bmatrix} \tag{2.22}$$

the equations to be solved can thus be expressed as

$$\begin{bmatrix} A & B \\ C & D \end{bmatrix} \begin{Bmatrix} X_{ud} \\ X_{id} \end{Bmatrix} = \begin{Bmatrix} P_{ud} \\ P_{id} \end{Bmatrix} \tag{2.23}$$

or

$$A X_{ud} = P_{ud} - B X_{id} \tag{2.24}$$

and

$$P_{id} = C\,X_{ud} + D\,X_{id} \tag{2.25}$$

where

A, B, C, D = submatrices of K_T^*

X_{ud} = unknown displacements

X_{id} = imposed displacements

P_{ud} = load vector corresponding to unknown displacements

P_{id} = load vector corresponding to imposed displacements

2.9 Program Expansion

In this study, ANSR-III has been extended and modified. The main extensions include : Element Type 7, an element to model the three dimensional beam-column element, was developed and added to the element subroutine library; and calculation of additional output values such as story shear, overturning moment at each story, story displacement and floor inertia force was introduced. In the original version, the joint displacements can only be ouput in the same file as member forces and deformations. This makes it difficult to read the data to plot the floor response, especially in the case where the output is large. The story shear forces are calculated from the forces acting at floor levels, and the story drifts are calculated from floor displacements. The user is required to specify the number of stories and the height of the stories. Arbitrary three dimensional frame structures can be modelled by giving an indicator for each floor. The main modifications include : calculation of absolute input energy has been added, where the absolute energy equation [57] has been implemented. Unlike the original ANSR-III, where the member load/stress due to member loads must be calculated separately, the program was modified to include

the effect of element Fixed End Moment on the response of the structure. For this purpose, the main program was modified, by adding a one dimensional array R_F to represent the fixed end loads. The fixed end moment calculations are performed at the element level and R_F is assembled from the element contribution. In the distributed model, unlike the lumped model, the initial stress and the initial strain at the integration points due to fixed end forces must be given, because the new state can only be determined if the initial state has been given.

CHAPTER 3

REVIEW OF BEAM-COLUMN ELEMENT

The nonlinear behavior of beam-column elements has been a topic of interest for many years, and has been subjected to considerable research throughout the past decade. Various simple models have been developed for treating material and geometrical nonlinearities in the beam column element. Most of the work in this area have proceeded basically along two directions: the distribution and the lumped models.

In the distributed model, plastification is distributed over the volume of the element. In this model, the member cross section is divided into a number of small areas (fibers). Each area is assumed to be uniaxially stressed and to have behavior governed by the hysteresis stress-strain characteristic of the material it simulates. Generally, a variational formulation is used to express the total stiffness matrix, and then the elements of the stiffness matrix are obtained by using numerical integration. Mallet and Marcal [8], Yang and Saigal [9], Cichon [10], Holzer and Somers [11], Kang and Scordelis [12], Sundaramoorthy and Murray [13] and others used this approach for their beam-column element.

In the lumped model, it is assumed that inelastic behavior is defined for the cross-section as a whole, not for individual fibers. Force-deformation relationship for

the cross-section must be specified, each governed by the cross-section dimensions and the hysteretic force-deformation charateristic of the member material. Models of this type tend to be more difficult to establish and less accurate than fiber models. In this model, plastification is assumed to occur at a generalized plastic hinge at the end of the element, while the remainder of the element remain elastic. Yielding of an element section may be attained when the combination of member end forces exceeds a certain empirical yield function. After yielding, some models used a certain flow rule, similar to Pandtl flow rule, to find the relationship between the incremental member end forces and the end plastic deformations. The total member stiffness is then obtained by combining this relationship with the stiffness matrix of the elastic part of the element. Kanaan and Powell [4], Jain and Goel [14], Kassimali [15], Ueda and Akamatsu [16], Inoue and Ogawa [17], Chen and Powell [18] and others used this approach for their beam column element.

3.1 Lumped Model

Clough [19] was the first one to develop an analytical model to represent the inelastic behavior of 2-D beam elements. In this model, he introduced dual component systems; a fully elastic component to represent strain hardening and an elasto-plastic component to represent yielding. Plastic hinges were assumed to occur at the end of the elasto-plastic component only, so the effect of spreading of yielding was neglected. A plastic hinge was inserted at the end of the elasto-plastic component when the bending moment at the end exceeded the specified plastic moment capacity of the beam element. This plastic hinge vanishs upon unloading. During the response, the stiffness of the elasto-plastic component depends on the status of the plastic hinge. The total element stiffness matrix is the cummulation stiffness matrix of the

elastic and elasto-plastic components. Small deformation theory was used to obtain the stiffness matrix for both components.

Kanaan and Powell [4] used the modification of the Clough beam element for their beam column element. The reduction of section plastic moment capacity in presence of an axial force was introduced by using an interaction formula. However, the effects of spreading of yielding, geometrical nonlinearity, the variation of the axial stiffness with progressive yielding, the membrane flexure coupling, the increase in maximum strength during cyclic loading due to the compressive strain extended into the strain hardening range and the stiffness degradation were neglected in their formulation. This model seems be reasonable for analysis where the member axial load is small and for predicting the behavior of structures where member buckling is not dominant. This model was implemented as element type 2 in DRAIN-2D.

Jain and Goel [14] developed an analytical model to represent the inelastic behavior of 2-D bracing elements. The effect of spreading of yielding, geometrical nonlinearity and the variation of axial stiffness with progressive yielding are approximated by using six segment hysteresis loops. Their model has the ability to follow axial force-deformation hysteretic loops, and experimental results have been used to formulate this loop. This model has two buckling loads, one for the first cycle and the other for subsequent cycles; and also incorporates a feature to account for the observed growth in the member during buckling and straightening. This model has been implemented as element type 9 in DRAIN-2D.

Jain and Goel [14] developed an analytical model to represent the behavior of 2-D beam-column elements by combining the features of their brace element and the Kanaan beam column element. Similar to Kanaan and Powell, the reduction of section plastic moment capacity in presence of axial force is introduced by an

interaction formula. This model was implemented as element type 10 in DRAIN-2D.

Kassimali [15] developed a simple model to represent the inelastic behavior of beam-column elements. The AISC interaction formula was used to introduce the presence of an axial force for the reduction in section plastic moment capacity. A plastic hinge is assumed to occur at the end of the element, while the remainder of the element remains elastic. To account for the geometrical nonlinearity, a slope deflection equation with a stability function is adopted, and the change in member chord length and flexural bowing are considered for the elastic portion of the elements. The formulae presented by Saafan [20] are used for this stability function and flexural bowing. Plastic hinge reversal is not allowed, so this type of element can only be used for monotonic static nonlinear analysis.

Ueda and Akamatsu [16] developed a simple lumped model to represent the inelastic behavior of beam-column element. In their model, only material nonlinearity is considered, and the yielding of an element section may be attained when the combination of the element forces exceeds a certain empirical yield function. After yielding, a plastic hinge will be inserted at the end of the element, while the remainder of the element remains elastic. At the plastic hinge, Von-Mises flow rule has been used to relate the incremental member end forces and the end plastic deformations. The total member stiffness is then obtained by combining this relationship with the stiffness matrix of the elastic part of the element.

Inoue and Ogawa [17] developed a simple lumped model to represent the inelastic behavior of beam-column elements. In their model, material and geometric nonlinearities are considered. The flow rule of Von-Mises and Ziegler's modification of Prager's rule of kinematic hardening have been used to relate the incremental member end forces and the end plastic deformations. Similar to Ueda and Akamatsu,

the yielding of element section may be attained when the combination of the member end forces exceeds a certain empirical yield function. After yielding, a plastic hinge will be inserted at the end of the element, while the remainder of the element remains elastic. Similar to Kassimali, to account for the geometrical nonlinearity, a slope deflection equation with a stability function is adopted, and the changes in member chord length and flexural bowing are considered for the elastic portion of the element. The formulas presented by Saafan [20] are used for this stability function and flexural bowing. The total member stiffness is obtained by combining this relationship with the stiffness matrix of the elastic part of the element.

Chen and Powell [18] developed a lumped beam column element model, where it is assume that inelastic behavior is concentrated in plastic hinges at the element ends and the part of the element between the hinges is assumed remain linearly elastic. In this model, inelastic interaction between bending moments, torque and axial force has been considered by means of four dimensional yield interaction surfaces and a flow-rule type of plasticity theory. A kinematic hardening rule is assumed for post-yield behavior. Even though models of this type are more efficient computationally, they tend to be more difficult and less accurate than the fiber model.

3.2 Distributed Model

Mallet and Marcal [8] developed a simple distributed model to represent the inelastic behavior of beam column elements. In describing the motion of the elements, the Update-Lagrangian formulation is used where element length and direction will be updated for each load increment. Their model uses a two-node beam column element where the axial and transverse displacements are approximated by linear and cubic polynomials. Material nonlinearity is taken into account, gemetric nonlinearity

is considered by including the second order terms in the Green-Lagrange strain formula, and a linear curvature is used in the problem formulation. Three alternative methods have been used to obtain the total stiffness matrix: the potential energy method, the direct method and the linear incremental method. In their model, there are three terms contributing to the total stiffness matrix: the conventional small deflection theory stiffness matrix K_o, and the geometric stiffness matrices N_1 and N_2. The geometric stiffness matrix N_1 depends on the initial stress and is indirectly a linear function of member end deformations. This matrix serves to couple the membrane and flexure actions. This coupling affects the mutual degradation of the initial membrane and flexure stiffness, leading to buckling in critical conditions. On the other hand, under tensile forces, the element initial membrane and flexure stiffness will increase. The second order stiffness matrix N_2 depends on the initial stress and indirectly a quadratic function of member end deformations. This matrix is essential for the accurate prediction of behavior in the presence of significant nonlinearity. No post-buckling solution can exist in its absence. The formulation using the potential energy method and the direct method produces a set of nonlinear simultaneous equations. Generally, iterative methods will be used to solve these simultaneous equations. In the incremental method, member and deformations are assumed as a combination of known quantities from previous loading increment and unknown incremental quantities for current loading increment, leading to a set of linear simultaneous equations.

Yang and Saigal [9] developed a simple distributed model to represent the inelastic behavior of 2-D beam-column elements. In describing the motion of the elements, the Update-Lagrangian formulation is used where element length and direction were updated for each load increment. Their model used a two-node beam column element

where the axial and transverse displacements are approximated by linear and cubic polynomials. Material nonlinearity is taken into account, geometric nonlinearity is approximated by adding a simplified form of the geometric stiffness matrix, and a linear curvature is used in the problem formulation. The Gauss Quadrature formula is used for numerical integration over the volume of the element to obtain element stiffness matrix.

Cichon [10] developed a simple distributed model to represent the inelastic behavior of 2-D beam-column elements. In describing the motion of the elements, the Lagrangian formulation was used. A two-node beam column element was used where both the axial and transverse displacements are approximated by cubic polynomial. As a result, this model needs four degrees-of-freedom for each joint which is not suited for implementation in a conventional computer program such as DRAIN-2D. Material nonlinearity is taken into account, geometric nonlinearity is considered by using the complete form of the Green-Lagrange strain formula, and a second order curvature is used in the problem formulation. The incremental variational principle is used to obtain the total stiffness matrix, leading to a set of linear simultaneous equations. To obtain the element stiffness matrix, the Gauss Quadrature formula is used for numerical integration over the volume of the element.

Holzer and Somers [11] developed a simple distributed model to represent the inelastic behavior of 2-D beam-column elements. In describing the motion of the elements, the Lagrangian formulation was used. A three-node beam column element has been used where the axial and transverse displacements were approximated by quadratic and cubic polynomials. Material nonlinearity is taken into account, geometric nonlinearity is considered by using an incomplete form of the Green-Lagrange strain formula, and a linear curvature is used in the problem formulation. The po-

tential energy method is used to obtain the total stiffness matrix, leading to a set of nonlinear simultaneous equations in terms of member end deformations. To obtain the element stiffness matrix, the Gauss Quadrature formula was used for numerical integration over the volume of the element. The formidable numerical analysis problem posed by the nonlinear simultaneous equations was circumvented by using a minimization approach.

Kang and Scordelis [12] developed a distributed model to represent the inelastic behavior of 2-D beam-column elements. In describing the motion of the elements, the Update-Lagrangian formulation was used where element length and direction were updated for each load increment. Their model used a two-node beam column element where the axial and transverse displacements were approximated by linear and cubic polynomials. Material nonlinearity is taken into account, geometric nonlinearity is considered by using an incomplete form of the Green-Lagrange strain formula, and a linear curvature is used in the problem formulation. To obtain the element of stiffness matrix, the three-point Gauss Quadrature formula was used for numerical integration over the volume of element.

It can be seen that various beam-column elements have been proposed. Because of the versatile nature of the fiber model, it seems desirable to develop a fiber model for nonlinear beam-column elements, so that frames with arbitrary geometry, complex loading and boundary conditions can be treated straightforwardly. In the following section, the formulation of the fiber model beam-column element used in this study will be presented.

CHAPTER 4

ANALYTICAL MODEL FOR 3-D BEAM-COLUMN ELEMENT

4.1 Introduction

In this chapter, a beam column element for three-dimensional analysis based on a fiber model is proposed. This model is a two-node beam-column element where the transverse and axial displacements at any point within the element are approximated by a polynomial of third order and first order, respectively. The torsional rotation is approximated by using a polynomial of first order. Material nonlinearity is considered, and a combination of kinematic and isotropic hardening is used to model the strain hardening and the Bauschinger effects. The basic Mroz kinematic hardening theory is implemented numerically and combined with an isotropic hardening rule to extend its modelling capabilities for arbitrary cyclic behavior. Geometrical nonlinearity is considered by including the second order terms in the Green-Lagrange strain formula. Large deformation is considered by using the Updated Lagrangian in describing the motion of the element.

In the Updated Lagrangian formulation, the equilibrium equations for the entire structure are set up and solved in the global coordinate system (X, Y, Z) which is fixed in space. However, element properties are described in the moving coordinate

system (x, y, z) which is defined by a beam axis joining the two ends of each element and a vector formed from one end of the element to a pointer node specified by the user. By applying the incremental principle of virtual work at time $t + \Delta t$, and by neglecting some higher order terms, the incremental equilibrium equations at time $t + \Delta t$ can be obtained and solved.

It is economical in the design of steel structural members to minimize member total weight or to maximize the load carrying capacity of steel members by using thin-walled sections instead of solid sections. Steel structural members usually possess thin-walled cross sectional shapes whose thicknesses are much smaller than the other cross-sectional dimensions. Although it is true that these members are a three dimensional continua, it is tedious and cumbersome in analysis to treat them as three dimensional problems. In three dimensional continuum, any arbitrary displacement is permited as long as strain continuity is satisfied. Displacements and strains which satisfy a given strain-displacement relationship is referred to as a kinematic field. Solid or thin-walled beam elements, however, have some constraints among their displacements. Hence their kinematic fields are limited to a partial space, and it is possible to treat these members as a one dimensional problem, where only one coordinate is independent. Generally, the x-axis taken along the member axis is used as the element independent coordinate.

If the material and geometrical nonlinearity are considered in the problem formulation, it is neccesary to state the problem in the incremental form. To formulate a fiber model of a thin-walled beam-column element, equations describing the behavior of three-dimensional beam-column element are needed. They can generally be divided into two major categories:

1. strain-displacement relationship or kinematics equation, and

2. stress-strain relationship or constitutive equation

The first is purely geometrical and the second depends only on the material properties of the continuum.

4.2 Incremental Strain Displacement Relationship

Based on the second order kinematical field formulated by Nishino [68], the strain-displacement relationship measured from the centroid of the cross-section can be expressed as

$$\begin{aligned}\Delta\varepsilon_{xx} &= \Delta u' - y\Delta v'' - z\Delta w'' + \frac{1}{2}\left[(\Delta v')^2 + (\Delta w')^2\right] \\ &+ \frac{1}{2}\left(y^2+z^2\right)(\Delta\varphi')^2 - y\Delta w''\Delta\varphi + z\Delta v''\Delta\varphi \qquad (4.1)\\ \Delta\varepsilon^l_{xs} &= (y-z)\,\Delta\varphi' \qquad (4.2)\end{aligned}$$

where

$$\begin{aligned}u, v, w &= \text{displacement components in the } x, y, z\text{-axes}\\ \varphi &= \text{torsional rotation at cross section center of rigidity}\end{aligned}$$

Then, the normal incremental strain-displacement relationship can generally be divided into two parts which are linearly and quadratically dependent on the displacement increments as follows

$$\Delta\varepsilon_{xx} = \Delta\varepsilon^l_{xx} + \Delta\varepsilon^n_{xx} \qquad (4.3)$$

where

$$\begin{aligned}\Delta\varepsilon^l_{xx} &= \Delta u' - y\Delta v'' - z\Delta w''\\ \Delta\varepsilon^n_{xx} &= \frac{1}{2}\left[(\Delta v')^2 + (\Delta w')^2\right] + \frac{1}{2}\left(y^2+z^2\right)(\Delta\varphi')^2 - y\Delta w''\Delta\varphi + z\Delta v''\Delta\varphi\end{aligned}$$

4.3 Incremental Stress-Strain Relationship

4.3.1 Normal Stress Relationship

The incremental stress-strain in the plastic state can be expressed explicitly in the following form

$$\{\Delta\underline{\sigma}\} = [D_{ep}]\{\Delta\underline{\varepsilon}\} \tag{4.4}$$

where

$$[D_{ep}] = [D_e] - \frac{(\{\underline{n}\}[D_e])^T([D_e]\{\underline{n}\})}{\{\underline{n}\}^T[D_e]\{\underline{n}\} + E_{pi}} \tag{4.5}$$

and

$[D_e]$ = elastic stress-strain matrix

$\{\underline{n}\}$ = dimensionless unit vector normal to the current yield surface i

E_{pi} = plastic moduli between yield surfaces i and $i+1$

The Von-Mises yield function for a biaxial state of stress in $\sigma - \tau$ space is given by

$$f(\underline{\sigma}) = \sigma^2 + 3\tau^2 - \sigma_y^2 \tag{4.6}$$

the normal vector this yield function is

$$\underline{v} = 2\begin{Bmatrix} \sigma \\ 3\tau \end{Bmatrix} \tag{4.7}$$

then, the unit vector $\underline{n}$ normal to the yield surface can be expressed as

$$\underline{n} = \frac{\underline{v}}{(\underline{v}^T\underline{v})^{\frac{1}{2}}} \tag{4.8}$$

$$= \frac{1}{(\sigma^2 + 9\tau^2)}\begin{Bmatrix} \sigma \\ 3\tau \end{Bmatrix} \tag{4.9}$$

The elastic constitutive matrix for a biaxial state of stress in $\sigma - \tau$ space is given by

$$[D_e] = \begin{bmatrix} E & 0 \\ 0 & G \end{bmatrix} \tag{4.10}$$

Substituting equations 4.8 and 4.10 into equation 4.5, the plastic stress-strain matrix can be expressed as

$$[D_{ep}] = \begin{bmatrix} E & 0 \\ 0 & G \end{bmatrix} - \frac{1}{E\sigma^2 + 9G\tau^2 + E_p(\sigma^2 + 9G\tau^2)} \begin{bmatrix} E^2\sigma^2 & 3E\sigma G\tau \\ 3E\sigma G\tau & 9G^2\tau^2 \end{bmatrix} \tag{4.11}$$

This incremental stress-strain can be used to obtain a solution of the deformation problem in a biaxial state of stress. However, the beam-column element being developed in this study uses only a single line of integration points at the middle of each plate of the cross-section. Consequently, the torsional shear stress τ of this integration point will always have zero value. If one assumes that the material behaves elasto-plastically, only normal stress flows at the plastic state and the torsional shear stress remains zero. Consequently, the plastic shear modulus will always have the same value as the elastic shear modulus G, regardless of the state of stress. It will be assumed that the shear stress-strain relationship is proportional to the normal stress-strain relationship. Hence,

$$\Delta\sigma = \frac{E_p}{E + E_p} E\,\Delta\varepsilon_{xx} = E_T\,\Delta\varepsilon_{xx} \tag{4.12}$$

$$\Delta\tau = \frac{E_p}{E + E_p} G\,\Delta\varepsilon_{sx} = G_T\,\Delta\varepsilon_{sx} \tag{4.13}$$

4.3.2 Tangent Modulus E_t and Plastic Modulus E_p Relationship

It was shown in Section 4.3.1 that the plastic stress-strain matrices $[D_{ep}]$ are defined in terms of the plastic modulus E_p. In this section, the relationship between the tangent modulus E_t and the plastic modulus E_p will be presented. It will be

assumed that a strain increment $\Delta\varepsilon$ consists of two parts: the elastic strain increment $\Delta\varepsilon_e$ and the plastic strain increment $\Delta\varepsilon_p$ such as

$$\Delta\varepsilon = \Delta\varepsilon_e + \Delta\varepsilon_p \tag{4.14}$$

The stress increment $\Delta\sigma$ is related to the strain increment $\Delta\varepsilon$ by

$$\Delta\sigma = E_t \Delta\varepsilon \tag{4.15}$$

where E_t is the tangent modulus whose value changes during plastic deformation. The plastic strain increment $\Delta\varepsilon_p$ and the stress increment $\Delta\sigma$ are related by

$$\Delta\sigma = E_p \Delta\varepsilon_p \tag{4.16}$$

For the elastic strain increment $\Delta\varepsilon_e$, we have the usual relationship

$$\Delta\sigma = E_e \Delta\varepsilon_e \tag{4.17}$$

Substituting equations 4.15, 4.16, and 4.17 into equation 4.14, the relationship between any tangent modulus E_t and the corresponding plastic modulus E_p can be expressed as

$$\frac{1}{E_t} = \frac{1}{E_e} + \frac{1}{E_p} \tag{4.18}$$

Hence

$$E_t = \frac{E_e E_p}{E_e + E_p} \tag{4.19}$$

or

$$E_p = \frac{E_e E_t}{E_e - E_t} \tag{4.20}$$

4.3.3 Hardening Rule

In order to obtain a solution to a deformation problem, it is necessary to idealize the material stress-strain relationship. Various constitutive models have been proposed and these models fall into two basic models: non-hardening model and hardening model.

In the non-hardening model, it is assumed that material behaves as an elastic-perfectly plastic material. The plastic flow occurs as soon as the stress reaches the yield stress. In this model, it is assumed that the yield function remains unchanged during loading after the material yielding.

In the hardening model, it is assumed that the stress-strain curve continues to rise after yielding, although the slope gradually decreasing and falls to zero when failure occurs. For a strain hardening material, the yield function changes progressively. The hardening rule defines how this function changes. Several hardening rules have been proposed in the past and these include the classical isotropic hardening theory of Hill [67], the kinematic hardening theory of Prager, the series and parallel formulations of Iwan [63], the constant plastic moduli of Mroz [61], [62], and the parallel material models of Dafalias-Popov [64] and Peterson-Popov [65],[66]. In the study by Mosaddad and Powell [58], it was concluded that the Mroz model is the most flexible and a suitable model for numerical implementation. Based on this model, they developed an extended model suitable for arbitrary cyclic model which includes rate-dependent behavior. This extended model has been implemented for axi-symmetric, plane-strain, plane stress and plate elements in the ANSR-III program.

The hardening rule originally proposed by Mroz basically is a kinematic hardening model. This model corresponds to the translation of the yield surface without changes in size and shape and the general stress-strain behavior is approximated by a series

of yield surfaces with constant hardening moduli. Each yield surface is represented by two constants, yield stress σ_{yi} and plastic modulus E_{pi}. In uniaxial tension, the stress-strain relationships for the Mroz model are approximated by a multilinear curves as shown in figure 4.1. Accordingly, the uniaxial stress-strain relationship can be represented by an elastic spring and a rigid-plastic hardening spring as shown in figure 4.2.

Kinematic model is generally incorrect in predicting the material behavior under cyclic loading. This model predicts a steady state cyclic behavior for constant cyclic strain, whereas for actual materials, steady state hysteresis loops are reached only after a period of transition. The nature and duration of this transition varies for different materials and may depend on variety of parameters, including loading path, temperature, manufacturing process, etc. On the other hand, isotropic model predicts elastic shakedown under cyclic loading, which is grossly incorrect. The actual material behavior under cyclic loading generally can be represented by two limiting states, the virgin state and the saturated state, figure 4.3. The virgin state represents the strength and hardening properties of the material for the first half cycle of loading. The saturated state represents the strength and hardening properties of the material when it reaches steady state cyclic behavior. As plastic strain accumulates, the properties of material migrates from the virgin state toward the saturated state.

To account for cyclic behavior, the concept of constant hardening model of Mroz is extended to a variable field model proposed by Mosaddad and Powell [58]. In their model, the transition from the virgin state to the fully saturated state is controlled by a weighting function, which is based on the accumulated plastic strain. Typical stress-strain curves for the virgin and saturated state, together with a typical weight function are shown in figure 4.4. During the transition, the value of σ_{yi} is assumed

to be

$$\sigma_{yi} = w\,\sigma_{vi} + (1 - w)\,\sigma_{si} \tag{4.21}$$

where

σ_{vi} = virgin state yield stress of yield surface i

σ_{si} = saturated state yield stress of yield surface i

w = weighting factor, which is a function of the effective plastic strain ε_p

The plastic modulus E_{pi} during the transition can be determined according to the following equation

$$E_{pi} = w\,E_{pvi} + (1 - w)\,E_{psi} \tag{4.22}$$

where

E_{pvi} = virgin state plastic modulus of yield surface i

$$= \frac{\sigma_{vj} - \sigma_{vi}}{\varepsilon_{pj} - \varepsilon_{pi}}$$

E_{psi} = saturated state plastic modulus of yield surface i

$$= \frac{\sigma_{sj} - \sigma_{si}}{\varepsilon_{sj} - \varepsilon_{si}}$$

$j = i + 1$

4.3.4 State Determination and Updating Procedure

Figure 4.5 shows two successive yield surfaces, i and j in the $\sigma - \tau$ plane. Both surfaces have moved from their initial positions, due to prior plastic straining.

The yield surface origins are located by vectors $\underline{\alpha}_i$ and $\underline{\alpha}_j$, respectively. The current state of stress is $\underline{\sigma}$ on the yield surface i. The stress increment is $\Delta\underline{\sigma}$, moving from the yield surface i toward yield surface j. The hardening rule proposed by

Mroz requires that these surfaces never overlap. This means that they must have a common tangent or normal at the point of contact. It is also desirable that the point of contact be the current stress point as shown in figure 4.6(a), rather than some other point as shown in figure 4.6(b). If the situation in figure 4.6(b) is permitted, two hardening rules must be formulated, the first one governing the behavior before the yield surfaces make contact, and the second one governing the behavior after the yield surfaces make contact. The situation could become particularly complicated if several yield surfaces were in contact, as shown in figure 4.6(c). If, on the other hand, the yield surfaces are constrained to move so that the current stress point is also a contact point, only one hardening rule needs to be formulated, and multi-surface contacts will always be shown as in figure 4.6(d).

A stress point $\underline{\sigma}'$ on yield surface j that satisfies these conditions can be determined by simple geometry as follows

$$\frac{\underline{\sigma} - \underline{\alpha}_i}{\sigma_{yi}} = \frac{\underline{\sigma}' - \underline{\alpha}_j}{\sigma_{yj}} \tag{4.23}$$

In which σ_{yi} and σ_{yj} are the uniaxial yield stresses for surfaces i and j, respectively. Hence,

$$\underline{\sigma}' = \underline{\alpha}_j + \frac{\sigma_{yj}}{\sigma_{yi}} \{\underline{\sigma} - \underline{\alpha}_i\} \tag{4.24}$$

The instantaneous translation of yield surface i can be assumed parallel to $\underline{\sigma}' - \underline{\sigma}$, that is

$$d\underline{\alpha}_i = \{\underline{\sigma}' - \underline{\sigma}\}\, d\mu \tag{4.25}$$

in which $d\mu$ is a scalar multiplier.

The multiplier $d\mu$ can be obtained from the requirement that the stress point must remain on the surface i. Accordingly

$$df_i = 0 = \underline{n}_i^T . d\{\underline{\sigma} - \underline{\alpha}_i\} \tag{4.26}$$

By substituting equation 4.25 into equation 4.26, the multiplier $d\mu$ can be expressed as

$$d\mu = \frac{\underline{n}_i^T . d\underline{\sigma}}{\underline{n}_i^T . \{\underline{\sigma}' - \underline{\sigma}\}} \tag{4.27}$$

Then,

$$d\underline{\alpha}_i = \frac{\underline{n}_i^T . d\underline{\sigma}}{\underline{n}_i^T . \{\underline{\sigma}' - \underline{\sigma}\}} \{\underline{\sigma}' - \underline{\sigma}\} \tag{4.28}$$

For each subincrement in the state determination computation, the center of the current yield surface is first translated according to the equation 4.28. The size of the current and all other surfaces are then updated according to equation 4.24.

Updating of the surfaces $f_{i+1}, f_{i+2}, \ldots, f_n$ involves only expansion or contraction of the yield surface without translation of its center. However, surfaces $f_1, f_2, \ldots, f_i$ which pass through the current stress point $\underline{\sigma}$ must be kept tangent to each other at $\underline{\sigma}$, and hence, must be translated and expanded (or contracted), such that they remain tangent to each other at $\underline{\sigma}$. This constraint requires that the centers of these surfaces, as well as their size, be adjusted. The new center coordinates of the surface f_i, for example, can be determined by simple geometry as follow

$$\underline{\alpha}'_k = \underline{\alpha}_k + \left(1 - \frac{\sigma'_{yk}}{\sigma_{yk}}\right) \{\underline{\sigma} - \underline{\alpha}_i\} \quad \text{k=1,2,}\ldots, i-1 \tag{4.29}$$

in which α'_k locates the updated center of the surface f_k; σ_{yk} and σ'_{yk} are the uniaxial yield stresses of the surface k before and after updating, where

$$\sigma'_{yk} = w\,\sigma_{vk} + (1-w)\,\sigma_{sk}$$

4.3.5 Updating Options

The Mroz theory requires that the yield surfaces which are currently engaged by the stress point be updated continuously at the end of every inelastic subincrement.

With the continuous updating option, the hardening modulus field is updated at the end of every inelastic subincrement of the state determination process, figure 4.7(b). With this option, the multilinear nature of the stress-strain is no longer preserved, and the material stiffness matrix changes continuously within the subincrement.

Computationally, however, it is not necessary to move all yield surfaces. Instead, the state can be obtained more efficiently by translating only the current yield surface. That is, if, for example, yield surface f_1 through f_i are engaged by the current stress point, only surface f_i needs to be translated towards f_{i+1}, as long as loading continues along the same path. If loading continues until yield surface f_{i+1} is reached, the surface f_i can also be left alone, and only the motion of the surface f_{i+1} needs to be monitored. The configuration of the yield surfaces following this procedure is shown in figure 4.7(c). With this procedure, it is necessary to restore the material memory, by translating the surfaces f_1 through f_i to their final position as shown in figure 4.7(d) when unloading occurs. The new coordinates of the surfaces f_1 through f_{i-1} can be determined according to

$$\underline{\alpha}'_k = \underline{\alpha}_i + \left(1 - \frac{\sigma'_{yk}}{\sigma'_{yi}}\right)\{\underline{\sigma} - \underline{\alpha}_i\} \quad \text{k=1,2,...,} i \tag{4.30}$$

With the discontinuous updating option, the hardening modulus field is updated only when unloading occurs, and otherwise kept constant along each loading path. For most practical applications, the material cyclic behavior can be modelled with sufficient accuracy using this option. It has the advantage of being more efficient computationally, and of preserving the multi-linear nature of the stress-strain relationship. This is particularly advantageous for the event-to-event strategies that have been implemented in the ANSR-III program, because fewer events are detected, and hence, fewer stiffness matrix reformulations are needed.

4.3.6 Unloading Criteria

It was shown in the previous section that the constitutive equation is completely different in elastic and plastic state. Unlike monotonic loading, material will experience elastic unloading during cyclic loading. Hence, loading and unloading criteria are needed to distinguish between plastic loading and elastic unloading state. Several criteria have been proposed in the past. In this study, plastic loading is defined to be continued loading if the elastic stress increment $\Delta\sigma$ has a positive values corresponding to a specified strain increment. Hence, plastic loading occurs if the following criteria is satisfied

$$\underline{n}_i^T . [D_e] \{\Delta\underline{\varepsilon}\} > 0 \tag{4.31}$$

and elastic unloading occurs if the following criteria is satisfied

$$\underline{n}_i^T . [D_e] \{\Delta\underline{\varepsilon}\} < 0 \tag{4.32}$$

4.4 Incremental Element Stiffness Matrix

4.4.1 Basic Equations

An incremental form of the stiffness matrix for the finite element solution of the beam-column element will be formulated in this section. To identify the unknown joint displacements that completely define the displacement response of the model, a two-node beam column element will be used. Its two end nodes i and j are numbered as shown in figure 4.8. At each node, there are three nodal translations and rotations in the element x, y, z axes. Thus, the corresponding nodal displacements at nodes i and j are

$$\underline{d} = \{d_1\ d_2\ d_3\ d_4\ d_5\ d_6\ d_7\ d_8\ d_9\ d_{10}\ d_{11}\ d_{12}\}^T$$

or

$$\underline{d} = \{\underline{d}_u \; \underline{d}_v \; \underline{d}_w \; \underline{d}_t\}^T$$

where

$$\underline{d}_u = \left\{ d_1 \quad d_7 \right\}^T$$

$$\underline{d}_v = \left\{ d_2 \quad d_6 \quad d_8 \quad d_{12} \right\}^T$$

$$\underline{d}_w = \left\{ d_3 \quad d_5 \quad d_9 \quad d_{11} \right\}^T$$

$$\underline{d}_t = \left\{ d_4 \quad d_{10} \right\}^T$$

and the corresponding generalized nodal forces at nodes i and j are

$$\underline{p} = \{p_1 \; p_2 \; p_3 \; p_4 \; p_5 \; p_6 \; p_7 \; p_8 \; p_9 \; p_{10} \; p_{11} \; p_{12}\}^T$$

or

$$\underline{p} = \left\{\underline{p}_u \; \underline{p}_v \; \underline{p}_w \; \underline{p}_t\right\}^T$$

where

$$\underline{p}_u = \left\{ p_1 \quad p_7 \right\}^T$$

$$\underline{p}_v = \left\{ p_2 \quad p_6 \quad p_8 \quad p_{12} \right\}^T$$

$$\underline{p}_w = \left\{ p_3 \quad p_5 \quad p_9 \quad p_{11} \right\}^T$$

$$\underline{p}_t = \left\{ p_4 \quad p_{10} \right\}^T$$

As mentioned before, the strain-displacement relationship measured from the centroid of the cross-section can be decomposed into two parts, which are linearly and quadratically dependent on the displacement increment as follows

$$\Delta\varepsilon^l_{xx} = \Delta u' - y\Delta v'' - z\Delta w''$$

$$\Delta\varepsilon^n_{xx} = \frac{1}{2}\left[(\Delta v')^2 + (\Delta w')^2\right] + \frac{1}{2}\left(y^2 + z^2\right)(\Delta\varphi')^2 - y\Delta w''\Delta\varphi + z\Delta v''\Delta\varphi$$

$$\Delta\varepsilon^l_{xs} = (y - z)\,\Delta\varphi'$$

In order to get the stiffness matrix of the element, the continuous field of u, v, w and φ are approximated by a polynomial of first and third order as follows

$$\Delta u = [BU]\{\Delta \underline{d}_u\} \tag{4.33}$$

$$\Delta v = [BV]\{\Delta \underline{d}_v\} \tag{4.34}$$

$$\Delta w = [BW]\{\Delta \underline{d}_w\} \tag{4.35}$$

$$\Delta \varphi = [BT]\{\Delta \underline{d}_t\} \tag{4.36}$$

where

$$[BU] = \begin{bmatrix} N_1 & N_2 \end{bmatrix} \tag{4.37}$$

$$[BV] = \begin{bmatrix} N_3 & N_4 & N_5 & -N_6 \end{bmatrix} \tag{4.38}$$

$$[BW] = \begin{bmatrix} N_3 & -N_4 & N_5 & N_6 \end{bmatrix} \tag{4.39}$$

$$[BT] = \begin{bmatrix} N_1 & N_2 \end{bmatrix} \tag{4.40}$$

$$N_1 = \frac{x}{L} \tag{4.41}$$

$$N_2 = \left(1 - \frac{x}{L}\right) \tag{4.42}$$

$$N_3 = \left(1 - 3\frac{x^2}{L^2} + 2\frac{x^3}{L^3}\right) \tag{4.43}$$

$$N_4 = \left(x - 2\frac{x^2}{L} + \frac{x^3}{L^2}\right) \tag{4.44}$$

$$N_5 = \left(3\frac{x^2}{L^2} - 2\frac{x^3}{L^3}\right) \tag{4.45}$$

$$N_6 = \left(\frac{x^2}{L} - \frac{x^3}{L^2}\right) \tag{4.46}$$

and

$$\{\Delta \underline{d}_u\} = \begin{Bmatrix} \Delta d_1 & \Delta d_7 \end{Bmatrix}^T \tag{4.47}$$

$$\{\Delta \underline{d}_v\} = \begin{Bmatrix} \Delta d_2 & \Delta d_6 & \Delta d_8 & \Delta d_{12} \end{Bmatrix}^T \tag{4.48}$$

$$\{\Delta \underline{d}_w\} = \begin{Bmatrix} \Delta d_3 & \Delta d_5 & \Delta d_9 & \Delta d_{11} \end{Bmatrix}^T \tag{4.49}$$

$$\{\Delta \underline{d}_t\} = \left\{ \Delta d_4 \quad \Delta d_{10} \right\}^T \tag{4.50}$$

Using the constitutive equtions developed in Section 4.3.1, the incremental stress-strain in the linearized form can be expressed as

$$\Delta\sigma = E_T \left(\Delta u' - y\Delta v'' - z\Delta w''\right) \tag{4.51}$$

$$\Delta\tau = G_T \left(y - z\right) \Delta\varphi' \tag{4.52}$$

The incremental variational principle as given by Washizu [69] will be used to obtain the basic equation for a linear incremental problem of the beam-column element. Following Washizu, the Internal Virtual Work for an individual element at configuration $t + \Delta t$ has the following form

$$INT = \int_{V_{t+\Delta t}} \underline{\sigma}_{t+\Delta t} \delta\Delta\underline{\varepsilon}\, dV = \int_{V_{t+\Delta t}} \left(\underline{\sigma}_t + \Delta\underline{\sigma}\right) \delta\Delta\underline{\varepsilon}\, dV \tag{4.53}$$

and the External Virtual Work at the configuration $t+\Delta t$ is assumed to be calculated for the conservative forces and moments concentrated at the nodes only, so

$$EXT = \delta\Delta\underline{d}^T \Delta\underline{p} \tag{4.54}$$

where the integral in the first integrand of equation 4.53 is extended over the volume of the element at the configuration $t + \Delta t$.

4.4.2 Incremental Element Stiffness Matrix in Local Coordinate System

The basic equations for an individual element formulated in the section 4.4.1 can be utilized to obtain the incremental of the element stiffness matrix in the local coordinate system. Substituting equations 4.33, 4.37 and 4.47 into equation 4.53, the following result can be obtained

$$INT = \delta\Delta\underline{d}^T \left[SM\right] \Delta\underline{d} \tag{4.55}$$

where

$$SM = \text{element stiffness matrix in local coordinate system}$$

$$= [K_T + K_G]$$

In this equation, $[K_T]$ is the incremental linear stiffness matrix of beam-column element in the local coordinate system, and $[K_G]$ is the incremental initial stress matrix of beam-column element in the local coordinate system, where

$$[K_T] = \int_{V_t} \begin{Bmatrix} [BU']^T & -y\,[BV'']^T & -z\,[BW'']^T & [O] \\ [O] & [O] & [O] & (y-z)\,[BT']^T \end{Bmatrix} \begin{bmatrix} E_T & 0 \\ 0 & G_T \end{bmatrix} \begin{Bmatrix} [BU'] & [O] \\ -y\,[BV''] & [O] \\ -z\,[BW''] & [O] \\ [O] & (y-z)\,[BT'] \end{Bmatrix} dV \qquad (4.56)$$

or

$$[K_T] = \begin{bmatrix} K_{11} & K_{12} & K_{13} & O \\ K_{21} & K_{22} & K_{23} & O \\ K_{31} & K_{32} & K_{33} & O \\ O & O & O & K_{44} \end{bmatrix} \qquad (4.57)$$

and the incremental initial stress matrix is

$$[K_G] = \int_{V_t} \sigma_t \begin{Bmatrix} [O] & [BV']^T & [BW']^T & (y^2+z^2)\,[BT']^T \end{Bmatrix} [I] \begin{Bmatrix} [O] \\ [BV'] \\ [BW'] \\ [BT'] \end{Bmatrix} dV$$

$$+ \int_{V_t} \sigma_t \begin{Bmatrix} [O] \\ z\,[BV'']^T \\ -y\,[BW'']^T \\ [O] \end{Bmatrix} \begin{Bmatrix} [O] & [O] & [O] & [BT'] \end{Bmatrix} dV$$

$$+ \int_{V_t} \sigma_t \begin{Bmatrix} [O] \\ [O] \\ [O] \\ [BT']^T \end{Bmatrix} \begin{Bmatrix} [O] & z\,[BV''] & -y\,[BW''] & [O] \end{Bmatrix} dV$$

or

$$[K_G] = \begin{bmatrix} O & O & O & O \\ O & G_{22} & O & G_{24} \\ O & O & G_{33} & G_{34} \\ O & G_{42} & G_{43} & G_{44} \end{bmatrix} \tag{4.58}$$

The element of $[K_T]$ can be expressed as

$$\begin{aligned}
K_{11} &= \int_{V_t} E_T\,[BU']^T\,[BU']\,dV = \int_L EA_x\,[BU']^T\,[BU']\,dx \\
K_{12} &= -\int_{V_t} yE_T\,[BU']^T\,[BV'']\,dV = -\int_L ES_z\,[BU']^T\,[BV'']\,dx \\
K_{13} &= -\int_{V_t} zE_T\,[BU']^T\,[BW'']\,dV = -\int_L ES_y\,[BU']^T\,[BW'']\,dx \\
K_{22} &= \int_{V_t} y^2E_T\,[BV'']^T\,[BV'']\,dV = \int_L EI_{zz}\,[BV'']^T\,[BV'']\,dx \\
K_{23} &= \int_{V_t} yzE_T\,[BV'']^T\,[BW'']\,dV = \int_L EI_{yz}\,[BV'']^T\,[BW'']\,dx \\
K_{33} &= \int_{V_t} z^2E_T\,[BW'']^T\,[BW'']\,dV = \int_L EI_{yy}\,[BW'']^T\,[BW'']\,dx \\
K_{44} &= \int_{V_t} (y-z)^2\,G_T\,[BT']^T\,[BT']\,dV = \int_L GJ\,[BT']^T\,[BT']\,dx
\end{aligned}$$

where the element section properties of are defined as

$$EA_x = \int_A E_T\,dA$$

$$
\begin{aligned}
ES_z &= \int_A y E_T \, dA \\
ES_y &= \int_A z E_T \, dA \\
EI_{yy} &= \int_A z^2 E_T \, dA \\
EI_{zz} &= \int_A y^2 E_T \, dA \\
EI_{yz} &= \int_A yz E_T \, dA \\
GJ &= \int_A (y-z)^2 G_T \, dA
\end{aligned}
\tag{4.59}
$$

The element of $[K_G]$ can be expressed as

$$
\begin{aligned}
G_{22} &= \int_{V_t} \sigma_t [BV']^T [BV'] \, dV = \int_L P_x [BV']^T [BV'] \, dx \\
G_{24} &= \int_{V_t} z\sigma_t [BV'']^T [BT] \, dV = \int_L M_y [BV'']^T [BT] \, dx \\
G_{33} &= \int_{V_t} \sigma_t [BW']^T [BW'] \, dV = \int_L P_x [BW']^T [BW'] \, dx \\
G_{34} &= -\int_{V_t} y\sigma_t [BW'']^T [BT] \, dV = -\int_L M_z [BW'']^T [BT] \, dx \\
G_{44} &= \int_{V_t} \left(y^2 + z^2\right) \sigma_t [BT']^T [BT'] \, dV = \int_L M_t [BT']^T [BT'] \, dx
\end{aligned}
$$

where the element geometrix internal forces are defined as

$$
\begin{aligned}
P_x &= \int_A \sigma_t \, dA \\
M_y &= \int_A z\sigma_t \, dA \\
M_z &= \int_A y\sigma_t \, dA \\
M_t &= \int_A \left(y^2 + z^2\right) \sigma_t \, dA
\end{aligned}
$$

4.4.3 Incremental Element Stiffness Matrix in Global Coordinate System

In the global coordinate system, the increment of corresponding nodal displacements and forces of the beam-column element at nodes i and j are

$$
\Delta \underline{D} = \left\{ \begin{array}{cccc} \Delta D_1 & \Delta D_2 & \cdots & \Delta D_{12} \end{array} \right\}
$$

$$\Delta \underline{P} = \left\{ \Delta P_1 \quad \Delta P_2 \quad \cdots \quad \Delta P_{12} \right\}$$

The nodal displacement increment $\Delta \underline{D}$ and $\Delta \underline{d}$ are related one another by the transformation matrix as follows

$$\Delta \underline{D} = [T]\, \Delta \underline{d}$$

where

$$[T] = \begin{bmatrix} [R] & O & O & O \\ O & [R] & O & O \\ O & O & [R] & O \\ O & O & O & [R] \end{bmatrix}$$

$[R]$ = rotation matrix

Then

$$[SM]\, [T]\, \Delta \underline{D} = [T]\, \Delta \underline{P}$$

Premultiplying with $[T]^{-1}$,

$$[T]^{-1}\, [SM]\, [T]\, \Delta \underline{D} = \Delta \underline{P}$$

or

$$[S]\, \Delta \underline{D} = \Delta \underline{P}$$

where

$$[S] = [T]^{-1}\, [SM]\, [T] \tag{4.60}$$

Using equation 4.60, the incremental equilbrium for the total structure is assembled in the global coordinate system from the contribution of all elements.

4.4.4 Rotation Matrix R

In the calculation of element stiffness matrix in the global system, a rotation matrix $[R]$ that relates the displacements measured in the element and global coordinate systems is needed. There are various ways in which element three-dimensional local coordinate systems may be defined. In this study, in order to define completely the position of the element in space, in addition to the element nodal coordinates, the orientation of the element cross sectional local axes can be found by using an auxiliary node k, figure 4.9, that together with nodes i and j define the plane containing the element $x-y$ plane. The location of node k most not lie along the x-axis of the element. Once this plane is known, the unit vector of the z-axis is obtained by imposing the condition of orthogonality to the $x-y$ plane.

In vector algebra, a plane can be uniquely define by two intersecting vectors. A cross product of these vectors yield a third vector which is perpendicular to this plane. By using these facts, the orientation of a particular element with respect to the global axes can be defined by two unit vectors $\underline{e}_{xm}$ and $\underline{e}_{jp}$, where

$\underline{e}_{xm}$ = unit vector in the x-direction of element axes

$\underline{e}_{jp}$ = unit vector in the element $x-y$ plane

Suppose the coordinates of i and j-ends of the elements are (x_i, y_i, z_i) and (x_j, y_j, z_j), respectively. Then

$$\underline{e}_{xm} = \frac{1}{\sqrt{a_x^2 + a_y^2 + a_z^2}} \begin{Bmatrix} a_x \\ a_y \\ a_z \end{Bmatrix}$$

where

$$a_x = x_j - x_i$$

$$a_y = y_j - y_i$$

$$a_z = z_j - z_i$$

Unit vector $\underline{e}_{jp}$ can be defined by using the element j-end coordinate and pointer node k coordinate (x_k, y_k, z_k). Then

$$\underline{e}_{jp} = \frac{1}{\sqrt{d_x^2 + d_y^2 + d_z^2}} \begin{Bmatrix} d_x \\ d_y \\ d_z \end{Bmatrix}$$

where

$$d_x = x_k - x_j$$

$$d_y = y_k - y_j$$

$$d_z = z_k - z_j$$

The orientation matrix $[R]$ can be expressed as

$$[R] = \begin{Bmatrix} \underline{e}_{xm}^T \\ \underline{e}_{ym}^T \\ \underline{e}_{zm}^T \end{Bmatrix}$$

where

$$\underline{e}_{zm} = \underline{e}_{zm} \times \underline{e}_{jp}$$

$$\underline{e}_{ym} = \underline{e}_{zm} \times \underline{e}_{xm}$$

4.4.5 Section Properties Calculation

Section properties EA_x, ES_y, ES_z, EI_{yy}, EI_{yz}, EI_{zz}, and GJ, are required in the formulation of the element stiffness matrix $[K_T]$, and their values can be determined according to equation 4.59. Let figure 4.10 represent a WF section with its centroid

at C. Then, the element section properties can be approximated by the following equations

$$
\begin{aligned}
EA_x &= \int_A E_T\, dA \\
&= \frac{1}{n_{tf}} b_{tf} t_{tf} \sum_{i=1}^{n_{tf}} f_i E_{Ti} + \frac{1}{n_{bf}} b_{bf} t_{bf} \sum_{i=1}^{n_{bf}} f_i E_{Ti} + \frac{1}{n_w} b_w t_w \sum_{i=1}^{n_w} f_i E_{Ti} \\
ES_z &= \int_A y E_T\, dA \\
&= \frac{1}{n_{tf}} b_{tf} t_{tf} y_{tf} \sum_{i=1}^{n_{tf}} f_i E_{Ti} + \frac{1}{n_{bf}} b_{bf} t_{bf} y_{bf} \sum_{i=1}^{n_{bf}} f_i E_{Ti} + \frac{1}{n_w} b_w t_w \sum_{i=1}^{n_w} f_i y_i E_{Ti} \\
ES_y &= \int_A z E_T\, dA \\
&= \frac{1}{n_{tf}} b_{tf} t_{tf} \sum_{i=1}^{n_{tf}} f_i z_i E_{Ti} + \frac{1}{n_{bf}} b_{bf} t_{bf} \sum_{i=1}^{n_{bf}} f_i z_i E_{Ti} \\
EI_{yy} &= \int_A z^2 E_T\, dA \\
&= \frac{1}{n_{tf}} b_{tf} t_{tf} \sum_{i=1}^{n_{tf}} f_i z_i^2 E_{Ti} + \frac{1}{n_{bf}} b_{bf} t_{bf} \sum_{i=1}^{n_{bf}} f_i z_i^2 E_{Ti} + \frac{1}{12} \frac{1}{n_w} b_w t_w^3 \sum_{i=1}^{n_w} f_i E_{Ti} \\
EI_{zz} &= \int_A y^2 E_T\, dA \\
&= \frac{1}{n_{tf}} b_{tf} t_{tf} \left[\frac{1}{12} t_{tf}^2 + y_{tf}^2 \right] \sum_{i=1}^{n_{tf}} f_i E_{Ti} + \frac{1}{n_{bf}} b_{bf} t_{bf} \left[\frac{1}{12} t_{bf}^2 + y_{bf}^2 \right] \sum_{i=1}^{n_{bf}} f_i E_{Ti} \\
&+ \frac{1}{n_w} b_w t_w \sum_{i=1}^{n_w} f_i y_i^2 E_{Ti} \\
EI_{yz} &= \int_A yz E_T\, dA \\
&= \frac{1}{n_{tf}} b_{tf} t_{tf} y_{tf} \sum_{i=1}^{n_{tf}} f_i z_i E_{Ti} + \frac{1}{n_{bf}} b_{bf} t_{bf} y_{bf} \sum_{i=1}^{n_{bf}} f_i z_i E_{Ti} \\
GJ &= \int_A (y - z)^2 G_T\, dA \\
&= \frac{1}{3} \left[\frac{1}{n_{tf}} b_{tf} t_{tf}^3 \sum_{i=1}^{n_{tf}} f_i G_{Ti} + \frac{1}{n_{bf}} b_{bf} t_{bf}^3 \sum_{i=1}^{n_{bf}} f_i G_{Ti} + \frac{1}{n_w} b_w t_w^3 \sum_{i=1}^{n_w} f_i G_{Ti} \right]
\end{aligned}
$$

where

n_{tf} = no. of integration point on top flange

n_{bf} = no. of integration point on bottom flange

n_w = no. of integration point on web

E_{Ti} = tangential modulus at integration point i

G_{Ti} = shear modulus at integration point i

f_i = weight function

4.4.6 Geomatrix Internal Forces Calculation

Geomatrix internal forces P_x, M_y, M_z and M_t, are required in the formulation of the element geometric matrix $[K_T]$. Let figure 4.10 represent a WF section with its centroid at C. Then, the element geometric internal forces can be approximated by the following equations

$$
\begin{aligned}
P_x &= \int_A \sigma_t \, dA \\
&= \frac{1}{n_{tf}} b_{tf} t_{tf} \sum_{i=1}^{n_{tf}} f_i \sigma_i + \frac{1}{n_{bf}} b_{bf} t_{bf} \sum_{i=1}^{n_{bf}} f_i \sigma_i + \frac{1}{n_w} b_w t_w \sum_{i=1}^{n_w} f_i \sigma_i \\
M_y &= \int_A z \sigma_t \, dA \\
&= \frac{1}{n_{tf}} b_{tf} t_{tf} \sum_{i=1}^{n_{tf}} f_i z_i \sigma_i + \frac{1}{n_{bf}} b_{bf} t_{bf} \sum_{i=1}^{n_{bf}} f_i z_i \sigma_i \\
M_z &= \int_A y \sigma_t \, dA \\
&= \frac{1}{n_{tf}} b_{tf} t_{tf} y_{tf} \sum_{i=1}^{n_{tf}} f_i \sigma_i + \frac{1}{n_{bf}} b_{bf} t_{bf} y_{bf} \sum_{i=1}^{n_{bf}} f_i \sigma_i + \frac{1}{n_w} b_w t_w \sum_{i=1}^{n_w} f_i y_i \sigma_i \\
M_t &= \int_A \left(y^2 + z^2\right) \sigma_t \, dA \\
&= \frac{1}{n_{tf}} b_{tf} t_{tf} \left[\frac{1}{12} t_{tf}^2 + y_{tf}^2\right] \sum_{i=1}^{n_{tf}} f_i \sigma_i + \frac{1}{n_{bf}} b_{bf} t_{bf} \left[\frac{1}{12} t_{bf}^2 + y_{bf}^2\right] \sum_{i=1}^{n_{bf}} f_i \sigma_i \\
&+ \frac{1}{n_w} b_w t_w \sum_{i=1}^{n_w} f_i y_i^2 \sigma_i + \frac{1}{n_{tf}} b_{tf} t_{tf} \sum_{i=1}^{n_{tf}} f_i z_i^2 \sigma_i + \frac{1}{n_{bf}} b_{bf} t_{bf} \sum_{i=1}^{n_{bf}} f_i z_i^2 \sigma_i \\
&+ \frac{1}{12} \frac{1}{n_w} b_w t_w^3 \sum_{i=1}^{n_w} f_i \sigma_i
\end{aligned}
$$

4.4.7 Internal Forces Calculation

The internal forces for an individual element at the configuration $t + \Delta t$ has the form

$$\{F\} = \int_{V_{t+\Delta t}} \begin{Bmatrix} [BU']^T \sigma_{t+\Delta t} \\ -y\,[BV'']^T \sigma_{t+\Delta t} \\ -z\,[BW'']^T \sigma_{t+\Delta t} \\ (y-z)\,[BT']^T \tau_{t+\Delta t} \end{Bmatrix} dV = \int_0^L \begin{Bmatrix} F_u\,[BU']^T \\ F_v\,[BV'']^T \\ F_w\,[BW'']^T \\ F_t\,[BT']^T \end{Bmatrix} dx \quad (4.61)$$

Let figure 4.10 represent a WF section with its centroid at C. Then, the element internal forces may be approximated by the following equations

$$\begin{aligned} F_u &= P_x \\ F_v &= M_z \\ F_w &= M_y \\ F_t &= \int_A (y-z)\,\tau_{t+\Delta t}\,dA \\ &= \frac{1}{3}\left[\frac{1}{n_{tf}} b_{tf} t_{tf}^2 \sum_{i=1}^{n_{tf}} f_i \tau_i + \frac{1}{n_{bf}} b_{bf} t_{bf}^2 \sum_{i=1}^{n_{bf}} f_i \tau_i + \frac{1}{n_w} b_w t_w^2 \sum_{i=1}^{n_w} f_i \tau_i\right] \end{aligned}$$

4.5 Fixed End Moment and Initial Stress

Unlike the original ANSR-III or ADYNA, where the member load/stress due to member loads must be calculated separately, in this program, ANSR-IIIM, one can include the effect of element Fixed End Moment on the response of the structure. However, only uniform load can be accomodated by this element at this time.

The loads acting on the member are taken into account by calculating the fixed-end action that they produce. These fixed actions then be transformed into

1. equivalent joint loads and combined with actual joint loads on the structure, and

2. initial stresses at every integration point in the element.

4.5.1 Equivalent Joint Load

The fixed-end action $\{F\}$ in the member axes due to uniform load in $x-y$ and $x-z$ planes, figure 4.11, can be expressed as follows

$$\{\underline{F}\} = \begin{Bmatrix} \underline{p}_a \\ \underline{p}_v \\ \underline{p}_w \end{Bmatrix} \tag{4.62}$$

where

$$\underline{p}_a = \begin{Bmatrix} 0 \\ 0 \end{Bmatrix} \tag{4.63}$$

$$\underline{p}_v = \frac{w_y L}{2} \begin{Bmatrix} 1 \\ \frac{L}{6} \\ 1 \\ -\frac{L}{6} \end{Bmatrix} \tag{4.64}$$

$$\underline{p}_w = \frac{w_z L}{2} \begin{Bmatrix} 1 \\ -\frac{L}{6} \\ 1 \\ \frac{L}{6} \end{Bmatrix} \tag{4.65}$$

(4.66)

then, the equivalent load vector $\{A_e\}$ in the global coordinate system can be calculated as

$$\{A_e\} = [R]^T \{\underline{F}\} \tag{4.67}$$

4.5.2 Initial Stress due to Member Load

If the fixed-end action due to member load has been calculated, it can be used to calculate the initial strain in the member. In this section, a technique that requires the inversion of the element stiffness will be described.

Suppose the member fixed-end action due to uniform load w_y and w_z can be expressed as follows

$$\{\underline{m}_v\} = \begin{Bmatrix} m_6 \\ m_{12} \end{Bmatrix} \tag{4.68}$$

$$\{\underline{m}_w\} = \begin{Bmatrix} m_5 \\ m_{11} \end{Bmatrix} \tag{4.69}$$

then, the member end rotation due to these actions can be calculated as follows

$$\begin{Bmatrix} \theta_6 \\ \theta_{12} \end{Bmatrix} = \begin{bmatrix} k_{6,6} & k_{6,12} \\ k_{12,6} & k_{12,12} \end{bmatrix}^{-1} \begin{Bmatrix} m_6 \\ m_{12} \end{Bmatrix} \tag{4.70}$$

$$\begin{Bmatrix} \theta_5 \\ \theta_{11} \end{Bmatrix} = \begin{bmatrix} k_{5,5} & k_{5,11} \\ k_{11,5} & k_{11,11} \end{bmatrix}^{-1} \begin{Bmatrix} m_5 \\ m_{11} \end{Bmatrix} \tag{4.71}$$

$$\tag{4.72}$$

Hence, the initial strain due to the fixed-end moment can be expressed as

$$\varepsilon^0_{xx} = -y\,[BV'']\begin{Bmatrix} \theta_6 \\ \theta_{12} \end{Bmatrix} - z\,[BW'']\begin{Bmatrix} \theta_5 \\ \theta_{11} \end{Bmatrix} \tag{4.73}$$

The the initial stress due to the fixed-end moment is

$$\sigma^0_{xx} = E\,\varepsilon^0_{xx} \tag{4.74}$$

$$= -E\left[y\,[BV'']\begin{Bmatrix} \theta_6 \\ \theta_{12} \end{Bmatrix} + z\,[BW'']\begin{Bmatrix} \theta_5 \\ \theta_{11} \end{Bmatrix}\right] \tag{4.75}$$

4.6 Member End Eccentricity

All structural members have finite dimension. In many structures, the dimensions of the members are large and can have significant effect on the stiffness of the structure. An analysis based upon a centerline to centerline dimensions, in general, overestimate the deflections. Moreover, plastic hinges in frames or frame-shearwall structures normally will form at the faces of the joints, rather than at the theoretical joint centerlines. This effect can be approximated by postulating rigid, infinitely strong connecting links between the centerline nodes and the element ends, as shown in figure 4.12.

The displacement transformation relating increments of nodal displacements $\Delta\underline{n}$ to increments of displacement at the element ends $\Delta\underline{d}$ can be expressed as

$$\Delta\underline{d} = [R_e]\,\Delta\underline{n} \tag{4.76}$$

where

$$[R_e] = \begin{bmatrix} [T_{pi}] & [0] \\ [0] & [T_{pj}] \end{bmatrix} \tag{4.77}$$

$$[T_{pi}] = \begin{bmatrix} [I_3] & -[C_{pi}] \\ [0] & [I_3] \end{bmatrix} \tag{4.78}$$

$$[T_{pj}] = \begin{bmatrix} [I_3] & -[C_{qj}] \\ [0] & [I_3] \end{bmatrix} \tag{4.79}$$

and

$$[C_{pi}] = \begin{bmatrix} 0 & -z_i & y_i \\ z_i & 0 & -x_i \\ -y_i & x_i & 0 \end{bmatrix} \tag{4.80}$$

$$[C_{qj}] = \begin{bmatrix} 0 & -z_j & y_j \\ z_j & 0 & -x_j \\ -y_j & x_j & 0 \end{bmatrix} \tag{4.81}$$

The transformation matrix $[R_e]$ can be used to modify the element stiffness matrix $[S]$ and the increment of the element end-forces $\{\Delta P\}$ in the global axes to allow for end eccentricity effects as follows

$$[S]^* = [R_e]^T [S] [R_e] \tag{4.82}$$

$$= [R_e]^T [R]^T [SM] [R] [R_e] \tag{4.83}$$

$$\{\Delta P\}^* = [R_e]^T [R]^T \{\Delta P\} \tag{4.84}$$

$$\{\Delta \underline{d}\}^* = [R_e] \{\Delta \underline{n}\} \tag{4.85}$$

and

$$\left\{\underline{F}_p\right\}^* = \begin{Bmatrix} \{\Delta \underline{F}_{vi}\} \\ \{\Delta \underline{F}_{\theta i}\} + [C_{pi}] \{\Delta \underline{F}_{vi}\} \end{Bmatrix} \tag{4.86}$$

$$\left\{\underline{F}_q\right\}^* = \begin{Bmatrix} \left\{\Delta \underline{F}_{vj}\right\} \\ \left\{\Delta \underline{F}_{\theta j}\right\} + [C_{qj}] \left\{\Delta \underline{F}_{vj}\right\} \end{Bmatrix} \tag{4.87}$$

(4.88)

$$\{\Delta \underline{d}_i\}^* = \begin{Bmatrix} \{\Delta \underline{n}_{vi}\} - [C_{pi}] \{\Delta \underline{n}_{\theta i}\} \\ \{\Delta \underline{n}_{\theta i}\} \end{Bmatrix} \tag{4.89}$$

$$\left\{\Delta \underline{d}_j\right\}^* = \begin{Bmatrix} \left\{\Delta \underline{n}_{vj}\right\} - [C_{qj}] \left\{\Delta \underline{n}_{\theta j}\right\} \\ \left\{\Delta \underline{n}_{\theta j}\right\} \end{Bmatrix} \tag{4.90}$$

where

$[SM]$ = the element incremental stiffness matrix in the local axis

$\{\Delta \underline{F}\}$ = the increment of element end forces

4.7 Rigid Floor Diaphgram

A frequently made assumption in the analysis of tall buildings is that each floor diaphragm is rigid in its own plane. Allowance has been made for rigid floor diaphragm by means of a 'slaving' feature. This slaving feature has been incorporated at the element level because ANSR-III cannot account for slaving at the nodal level. To introduce the rigid floor assumption, a 'master' node at the center of mass of each floor may be specified, as shown in figure 4.13.

Because each horizontal lamina is taken to be rigid in its own plane, all points at that level are constrained to displace in a rigid body pattern. Accordingly, each master node at each story level has three degrees of freedom as shown in this figure, which are the movement of the diaphgram horizontally and rotationally as a rigid body, two horizontal translations u_m and v_m, and one rotation about the vertical axis θ_m. Therefore, the mass matrix required for dynamic analysis will be diagonal matrix, thus simplifying the solution procedure.

Each end of a beam-column element in the structure has a full set of six degrees of freedom. If the i-end of the beam-column element is connected to a diaphragm at a certain floor level, then the element's two horizontal translation u_{xi} and u_{yi} and the element rotation about z-axis or vertical axis θ_{zi} become slave to the corresponding degrees of freedom of floor master node at that level, as shown in figure 4.13. However, the rest of element's degrees of freedom, vertical translation u_{zi} and rotations about two orthogonal axes θ_{xi} and θ_{yi}, are not affected by the rigid diaphragm assumption and become local degrees of freedom. The element's slave displacements can be expressed in term of its master displacements. Therefore, the element stiffness matrix must be formulated partly in terms of master degrees of freedom and partly in

terms of local degrees of freedom. Accordingly, the corresponding coefficients of the element stiffness matrix must be modified to account for the slaving. The resulting element stiffness matrix is assembled in terms of three master degrees of freedom plus three local degrees of freedom at each node.

The displacement transformation relating the displacement increment of the master node $\{\Delta \underline{d}_m\}$ to the displacement increment of its slave $\{\Delta \underline{d}_s\}$ can be expressed as

$$\{\Delta \underline{d}_s\} = [R_m]\{\Delta \underline{d}_m\} \tag{4.91}$$

where

$$[R_m] = \begin{bmatrix} [T_i] & [0] \\ [0] & [T_j] \end{bmatrix} \tag{4.92}$$

$$\{\Delta \underline{d}_m\} = \begin{Bmatrix} \Delta \underline{d}_{mi} \\ \Delta \underline{d}_{mj} \end{Bmatrix} \tag{4.93}$$

and

$$[T_i] = \begin{bmatrix} 1 & 0 & 0 & 0 & 0 & -y_i \\ 0 & 1 & 0 & 0 & 0 & x_i \\ 0 & 0 & 1 & 0 & 0 & 0 \\ 0 & 0 & 0 & 1 & 0 & 0 \\ 0 & 0 & 0 & 0 & 1 & 0 \\ 0 & 0 & 0 & 0 & 0 & 1 \end{bmatrix} \tag{4.94}$$

and

$$\{\Delta \underline{d}_i\} = \begin{Bmatrix} \Delta d_1 & \Delta d_2 & \Delta d_3 & \Delta d_4 & \Delta d_5 & \Delta d_6 \end{Bmatrix}^T \tag{4.95}$$

$$\{\Delta \underline{d}_j\} = \begin{Bmatrix} \Delta d_7 & \Delta d_8 & \Delta d_9 & \Delta d_{10} & \Delta d_{11} & \Delta d_{12} \end{Bmatrix}^T \tag{4.96}$$

Similarly, the force transformation relating the force increment of the master node $\{\Delta \underline{R}_m\}$ to the force increment of its slave $\{\Delta \underline{R}_s\}$ can be expressed as

$$\begin{Bmatrix} \Delta \underline{R}_{mi} \\ \Delta \underline{R}_{mj} \end{Bmatrix} = \begin{bmatrix} [T_i] & [0] \\ [0] & [T_j] \end{bmatrix}^T \begin{Bmatrix} \Delta \underline{R}_{si} \\ \Delta \underline{R}_{sj} \end{Bmatrix} \tag{4.97}$$

The relationship between the slave element end force increment and its deformation increment can be expressed as

$$\begin{Bmatrix} \Delta \underline{R}_{si} \\ \Delta \underline{R}_{sj} \end{Bmatrix} = \begin{bmatrix} [k_{ii}] & [k_{ij}] \\ [k_{ji}] & [k_{jj}] \end{bmatrix} \begin{Bmatrix} \Delta \underline{d}_{si} \\ \Delta \underline{d}_{sj} \end{Bmatrix} \tag{4.98}$$

Hence, the relationship between the master element end force increment and its deformation increment can be expressed as

$$\begin{Bmatrix} \Delta \underline{R}_{mi} \\ \Delta \underline{R}_{mj} \end{Bmatrix} = \begin{bmatrix} [T_i] & [0] \\ [0] & [T_j] \end{bmatrix}^T \begin{bmatrix} [k_{ii}] & [k_{ij}] \\ [k_{ji}] & [k_{jj}] \end{bmatrix} \begin{bmatrix} [T_i] & [0] \\ [0] & [T_j] \end{bmatrix} \begin{Bmatrix} \Delta \underline{d}_{mi} \\ \Delta \underline{d}_{mj} \end{Bmatrix} \tag{4.99}$$

4.8 Large Displacement Analysis

In the Update Lagrangian formulation, a transformation matrix $[R_t]$ that relates displacements measured in the current configuration to the displacement measured in the original configuration is needed. Various transformation models have been used, the most notably are the formulation by Belytschko and Hsieh [70], Nishino [68], and Bathe and Bolourchi [71].

In this study, the transformation matrix based on the average rotations of the element axes as proposed by Bathe and Bolourchi [71] will be used. The transformation matrix $[R_t]$ is evaluated using the Euler angles α, β and γ, which describes the motion of the element relative to its original configuration. These angles are shown in figures 4.14 and 4.15. In order to arrive at the current configuration, the motion of the element can be decomposed into two successive steps. The first step

is the motion of the element axes from configuration (x_1, y_1, z_1) coordinate system to (x_2, y_2', z_2') coordinate system, as shown in figure 4.14. The displacement in the (x_2, y_2', z_2') system can be related to the displacement in the (x_1, y_1, z_1) system by the transformation matrix $[R_d]$, where the components of matrix $[R_d]$ are the direction cosines of the axes (x_2, y_2', z_2') with respect to (x_1, y_1, z_1). These components are

$$[R_d] = \begin{bmatrix} cos\alpha\, cos\beta & sin\beta & sin\alpha\, cos\beta \\ -cos\alpha\, sin\beta & cos\beta & -sin\alpha\, sin\beta \\ -sin\alpha & 0 & cos\alpha\, cos \end{bmatrix} \tag{4.100}$$

The angle α represents the rotation about the negative y_1 axis.

$$cos\alpha = \frac{L_0 + u_1}{\overline{IJ_1}}$$

where L_0 is the original length of the beam and

$$\overline{IJ_1} = \sqrt{(L_0 + u_1)^2 + (w_1)^2}$$

The angle β represents the rotation about the positive z_2 axis.

$$sin\beta = \frac{v_1}{L_1}$$

where

$$L_1 = \sqrt{\left(\overline{IJ_1}\right)^2 + (v_1)^2}.$$

The relative displacement u_1, v_1, and w_1 between the two ends of the element measured in the original coordinate system can be evaluated as follows

$$\begin{Bmatrix} u_1 \\ v_1 \\ w_1 \end{Bmatrix} = [R] \begin{Bmatrix} d_7 - d_1 \\ d_8 - d_2 \\ d_9 - d_3 \end{Bmatrix}$$

where $\underline{d}$ are the current element nodal displacements measured in the global coordinate system, and $[R]$ is the transformation matrix that transform the global nodal point displacement to the original element local axes.

The second step is the rotation through an angle γ about the positive x_2 axis, causing the y_2' and y_2 axes to coincide, figure 4.15. The displacement in the (x_2, y_2, z_2) system can be related to the displacement in the (x_2, y_2', z_2') system by the transformation matrix $[R_a]$, where the components of matrix $[R_a]$ are the direction cosines of the axes (x_2, y_2, z_2) with respect to (x_2, y_2', z_2'). These components are

$$[R_a] = \begin{bmatrix} 1 & 0 & 0 \\ 0 & cos\gamma_t & sin\gamma_t \\ 0 & -sin\gamma_t & cos\gamma_t \end{bmatrix} \tag{4.101}$$

The angle γ is the rigid body rotation of the beam about the x_2 axis in the current configuration. This angle is calculated using

$$\Delta\gamma = \frac{1}{2}(\Delta d_4 + \Delta d_{10})$$

$$\gamma_t = \gamma_{t-1} + \Delta\gamma$$

where

$\Delta d_4, \Delta d_{10}$ = the increment of torsional rotation at i and j ends.

The components of matrix $[R_t]$ are then constructed from the multiplication of matrices $[R_a]$ and $[R_d]$, as follows

$$[R_t] = [R_a]\,[R_d]$$

4.9 State Determination

For the beam-column element developed in this study, the nonlinear stress-strain relationship can be represented by a maximum five piece-wise linear curve. Each change of slope corresponds to yielding at a new point or unloading at a previously yielded point and will be termed an 'event'. In general, several events may occur within a single time step for any integration point during loading or unloading, as shown in figure 4.16.

Within any time step, nodal deformation increments are computed, and hence strain increments of each integration point of each element. It is necessary to compute the stress increments corresponding to these deformation increments, because the new state of element forces can only be determined if the stress state of the integration point has been determined. This calculation may be termed as the 'state determination' phase. The linearization for the time step is based on the state of the integration point at the beginning of the step. The computed behavior would be correct if no events occurred within the time step, and the stress follows the dashed line shown in figure 4.17. This linear stress increment is indicated as $\Delta\sigma^l$ in this figure.

The dynamic analysis in ANSR-III permits two options to solve the equations of motion. A solution strategy using event-to-event with the automatic time step selection or a solution strategy where the event calculations are omitted. In the second option, no iteration is performed within a time step. Any unbalanced forces at the end of the step are eliminated by applying correcting forces in the next time step.

To apply the event-to-event solution strategy, an event factor must be calculated

for each element, and the minimum factor chosen is used to determine a scaling factor for the displacement increment, ΔX, for the step. Any significant event occuring within any element determines a substep and the tangent stiffness is modified in each substep.

In case the event calculations are omitted, several events may occur within a single time step and the computed member deformation and stress increments will not be correct, because they are computed by assuming linear behavior within the time step. However, it is reasonable to assume that the same deformation increments would be obtained during the time step, because the time step is small. Hence, nonlinear stress increments $\Delta\sigma^n$ may be computed, as indicated in figure 4.18. A general procedure for computing the nonlinear stress increments without event calculation is as follows

1. Let $\Delta\underline{d}$ be the computed element deformation increment for the time step. Then, the strain increments for each integration point can be calculated as

$$\Delta\varepsilon = [BU']\{\Delta\underline{d}_u\} - y[BV'']\{\Delta\underline{d}_v\} - z[BW'']\{\Delta\underline{d}_w\}$$

2. Suppose that the k^{th} integration point is in state i. Let $\Delta\sigma^n$ be the nonlinear stress increment for point k, which is to be computed. The stress increment $\Delta\sigma^n$ will be calculated from the sum of one or more subincrements $\mu_1\Delta\sigma_1$, $\mu_2\Delta\sigma_2$, etc. as indicated in figure 4.18. Hence,

$$\Delta\sigma^n = \mu_1\Delta\sigma_1 + \mu_2\Delta\sigma_2 + \cdots + \Delta\sigma_{i+n}$$

3. Let

$$\Delta\varepsilon_i = \Delta\varepsilon$$

Then for the current status of the element, determine the stress increment $\Delta\sigma_i$, corresponding to $\Delta\varepsilon_i$

$$\Delta\sigma_i = E_i \Delta\varepsilon_i$$

4. Determine μ_i, the proportion of this stress increment which is required to produce the next 'event'. Two types of 'event' will usually be possible, namely unloading and yielding. A test should first be made for unloading. Unloading occurs if

$$\text{sign}(\sigma_t) \times E\Delta\varepsilon_i < 0$$

where σ_t is the stress at previous time step.

5. If unloading occurs, the following procedure will be followed, which depends upon the material hardening model.

a. Kinematic Hardening

- adjust the center coordinates α_j for yield surface j, according to the following equation

$$\alpha_k = \alpha_i + \left(1 - \frac{\sigma_{yk}}{\sigma_{yi}}\right)\{\sigma_i - \alpha_i\} \quad \text{k=1,2,...,} i-1$$

- calculate the stress at the end state.

$$\sigma_{t+\Delta t} = \sigma_t + E\Delta\varepsilon_i$$

b. Combined Hardening with Discontinuous Updating

- calculate the weight function w for the current total plastic strain ε_{pk}, figure 4.19, as follows

$$w = w_i + \frac{w_j - w_i}{\varepsilon_j - \varepsilon_i}(\varepsilon_{pk} - \varepsilon_i) \quad j = i+1$$

- adjust the yield point stress σ'_{yk} and the tangent plastic moduli field E_{pk} for yield surface k, according to equation

$$\begin{aligned} \sigma'_{yk} &= w\,\sigma_{vk} + (1-w)\,\sigma_{sk} \\ E_{pk} &= w\,E_{pvk} + (1-w)\,E_{psk} \end{aligned} \qquad \text{k=1,2,...,} n$$

- adjust the center coordinates α_i' for yield surface i, according to the following equation

$$\alpha_i' = \frac{\sigma_{yi}'}{\sigma_{yi}}\alpha_i + \left(1 - \frac{\sigma_{yi}'}{\sigma_{yi}}\right)\sigma_i$$

- check overlapping of yield surface i and $j = i + 1$. A test should be made for overlapping. Overlapping occurs if surface j is contracting instead of expanding. Hence, if

  $\sigma_{yj}' < \sigma_{yj}$ then overlapping occurs.

  In case of overlapping, the center of yield surface j will be modified according to the following equation

$$\alpha_j = \alpha_j' + \left(1 - \frac{\sigma_{yj}'}{\sigma_{yj}}\right)(\sigma_i - \alpha_i')$$

- adjust the center coordinates α_k for yield surface k, according to the following equation

$$\alpha_k = \alpha_i' + \left(1 - \frac{\sigma_{yk}'}{\sigma_{yi}'}\right)(\sigma_i - \alpha_i) \quad \text{k=1,2,...,} i-1$$

c. Combined Hardening with Continuous Updating

- calculate the weight function α for the current total plastic strain ε_{pk} as follows

$$w = w_i + \frac{w_j - w_i}{\varepsilon_j - \varepsilon_i}(\varepsilon_{pk} - \varepsilon_i) \quad j = i + 1$$

- adjust the yield point stress σ_{yj} and the tangent plastic moduli field E_{pj} for yield surface j, according to equation

$$\begin{aligned} \sigma_{yk}' &= w\,\sigma_{vk} + (1-w)\,\sigma_{sk} \\ E_{pk} &= w\,E_{pvk} + (1-w)\,E_{psk} \end{aligned} \qquad \text{k=1,2,...,} i+1$$

- check overlapping of yield surface i and $j = i + 1$. A test should be made for overlapping. Overlapping occurs if surface j is contracting instead of expanding. Hence, if

$\sigma'_{yj} < \sigma_{yj}$ then overlapping occurs.

In case of overlapping, the center of yield surface j will be modified according to the following equation

$$\alpha_j = \alpha'_j + \left(1 - \frac{\sigma'_{yj}}{\sigma_{yj}}\right)(\sigma_i - \alpha'_i)$$

- adjust the center coordinates α_k for yield surface k, according to the following equation

$$\alpha_k = \alpha'_i + \left(1 - \frac{\sigma'_{yk}}{\sigma'_{yi}}\right)(\sigma_i - \alpha_i) \quad \text{k=1,2,...,} i$$

6. If loading occurs, the following procedure will be followed

a. Determine μ_i, the proportion of $\Delta\sigma_i$ which is required to produce the next 'event', according to the following equation

$$\mu_i = \frac{\sigma_{i+1} - \sigma_i}{\Delta\sigma_i}$$

If μ_i exceeds one, no further 'event' occurs within this time step, and the value of $\mu_i = 1$ is used. If this value is less than one, an 'event' occurs within this time step.

b. Add $\mu_i \Delta\sigma_i$ to $\Delta\sigma$ and make appropriate changes in the center of yield surface i

$$\sigma'_i = \sigma_i + \mu_i \Delta\sigma_i$$

$$\alpha'_i = \alpha_i + \mu_i \Delta(\sigma_{i+1} - \sigma_i)$$

c. Based on new α'_i, scale the current stress vector σ'_i, so it lies on yield surface i.

$$\sigma''_{yi} = \alpha'_i + \sigma'_{yi}$$

d. For the continuous updating model, follow the previous procedure as in step 5.c

7. If μ_i is less than one, reduce $\Delta\varepsilon_i$ to $(1-\mu_i)\,\Delta\varepsilon_i$, and repeat from step 2. Ultimately, μ_i when equals one the calculation of the nonlinear stress increment is complete.

4.10 Results and Evaluation

The biaxial beam-column element described in section 4.4 has been implemented in the computer program ANSR-IIIM and has been applied to several problems. In this section, the results of the analysis will be reported for two cases in which experimental results were available for model evaluation. It should be noted that the column was loaded uniaxially in these experiments. No experimental data are available for biaxially loaded steel column. Even though experimental data are available for full cyclic loading, comparison between the numerical and experimental results are not reported. The experimental data was too limited to establish the weight function necessary to model the transition from the virgin state to the fully saturated state. If kinematic hardening assumption is used, it resulted in different strength for the subsequent cycles in comparison to the experimental result. More analytical and experimental studies are needed to establish the appropriate weight function for columns subjected to cyclic loading.

4.10.1 Van Kuren and Galambos Experiments

Monotonic tests on full-scale wide-flange beam-columns were conducted by Van Kuren and Galambos [21] to study the strength and deformation behavior in the inelastic range. In the experimental test, a predetermined axial force of $0.158P_y$ was first applied to the member. This axial force was kept constant while end moments were applied by hydraulic jacks through lever arms monotonically. The beam section

used was 4WF13 with yield stress $\sigma_y = 35$ ksi and Young's modulus $E = 29.4$ ksi. In the numerical study, it was assumed that the member strength is based on bare steel strength of elasto-plastic material. The geometric configurations and section properties used are shown in figure 4.20. Figure 4.21 compares the normalized moment and beam end rotation of the numerical and experimental results. It can be seen that the results obtained from the numerical computation compare favorably with the experimental result.

4.10.2 Popov Subassemblages Experiments

Cyclic tests on subassemblages of beams and columns were conducted by Popov et.al. [22] to study the strength and deformation behavior of columns in the inelastic range. The geometric configuration of the subassemblages are shown in figure 4.22. The beam size, yield stress and Young's modulus are $W12 \times 31$, $\sigma_y = 32.5$ ksi and $E = 29$ ksi, respectively, and the column size, yield stress and Young's modulus are $W4 \times 48$, $\sigma_y = 38.0$ ksi, and $E = 29$ ksi, respectively. The beam length, L, is 160 in., and the column height, h, is 80 in. The gravity load P, G_1 and G_2 shown in this figure, representing the effects of dead and reduced live loads at the working load level were applied first. In the experimental test, the axial load at the lower column was kept at $0.80P_y$ throughout the test. In the experiment, a full cycle could not be completed. The column was deformed into a pronounced C-shape, causing instability, and the test had to be discontinued because the axial force in the column could not be maintained. In the numerical study, it was assumed that the member strength is based on bare member strength with kinematic hardening steel with 5% strain hardening. Figure 4.23 compares the relationship between the horizontal force H and horizontal displacement Δ. It can be seen that there is some difference

between the result obtained from the numerical computation and the result from the experimental. The model does not account for the stiffness and strength degradation due to the presence of very high axial load, so that it tends to overestimate both the strength and the amount of energy dissipation. However, the difference is not large and the element is able to model post-buckling strength loss and the increase in the maximum horizontal force load during unloading. It should be noted that the effect of residual stress has not been included in the numerical computation.

CHAPTER 5

BEHAVIOR OF 3-D MOMENT FRAMES STEEL STRUCTURES UNDER THE INFLUENCE OF BI-DIRECTIONAL GROUND EXCITATION

In this chapter, the results of nonlinear response analyses of three-dimensional symmetrical and asymmetrical steel moment frame structures subjected to unidirectional and bidirectional ground excitations of different intensities are presented. The effects of ground motion coupling on the ultimate capacity of different types of multi-story buildings are observed by studying the base shear, story displacement, story drift, column ductility demand and the relationship between column internal forces and their associated deformations in relation to the ground input excitation.

The base shear and story shear vary continuously with time, however, the envelopes of maximum base shear and story shear are used for comparison with the design values. Moreover, the correlation between base shear and ground velocity time histories give an indication of resonance that develops during the inelastic response of the structure. This resonance occurs when the dominant frequency of the ground motion is approximately the same as the effective frequency of the structure.

Similar to the base shear response, the story displacements vary continously with time. However, the envelopes of maximum lateral displacements were used to evalu-

ate the importance of the P-Δ effect and the necessary amount of building separation. These results provide information on the effect of ground motion coupling and increased ground acceleration on the structural response. The interstory displacement gives an indication of the possible damage to structural and non-structural components.

In this study, the ductility ratio is defined as the ratio of maximum end rotation to the yield rotation of the member with equal end rotations and no joint translation. The member ductilities are compared for a structure subjected to bidirectional ground excitation and to a similar structure subjected to unidirectional excitation.

The column shear force and column drift hysteresis curves provide a record of inelastic behavior under dynamic loading. It also gives information on the column strength and energy dissipation charateristics when the structure is subjected to uni and bidirectional earthquake excitations.

5.1 Symmetrical Structure

When an initially symmetric three dimensional steel moment frame structure is subjected to bidirectional ground excitation, a transient state of torsional coupling can be excited during its inelastic response. The torsional motion develops when one element yields and the others remain elastic, creating an eccentricity. In this study, the structural response due to bidirectional excitation will be compared with the response due to unidirectional excitation.

5.1.1 Design of Steel Frame Structure

A five story, rectangular building with single bay moment-resistant steel frames to provide resistance for both earthquake and gravity loads is used. The web of all the

columns is parallel to the X-axis of the structure. Typical floor plan and elevation of the frames are shown in figure 5.1 in which the dimensions are center-line to center-line. The moment frame span length is 24 ft and the typical story height is 12 ft. Gravity loads used in the design are uniform dead loads of 80 psf and uniform live loads of 20 psf for the roof, and uniform dead loads of 100 psf and uniform live loads of 50 psf for the typical floor. The total dead weight of the building is 403 kips.

Design lateral forces were taken to be the earthquake forces as specified by the 1988 UBC [75]. The earthquake design forces were determined using the estimated building period T, given by the formula.

$$T = 0.035(h_n)^{\frac{3}{4}} \tag{5.1}$$

where h_n is the building height in feet above the base.

The design base shear along each of the principal directions of the structure is calculated from the following formula :

$$V = \frac{ZIC}{R_w} \times W = C_s \times W \tag{5.2}$$

and

$$C = \frac{1.25S}{T^{2/3}} \tag{5.3}$$

The factors selected for use in these formulae are:

$Z = 0.4$ (for a building in zone No. 4)

$I = 1.0$ (importance factor)

$S = 1.0$ (soil condition factor)

$R_w = 12$ (Steel Special Moment Resisting Frames)

$W = 403$ kips (total dead load of the building)

Using formula 5.1, the estimated building period is 0.75 second, the base shear coefficient C_s is calculated to be

$$C_s = 0.05$$

and the base shear force V_{base} becomes

$$V_{base} = .05 \times \mathrm{W} = 20.2 \text{ kips.}$$

The total shear force is distributed over the height of the building according to the UBC formulae (12-6), (12-7), and (12-8) of Section 2312 (e). The lateral force distribution to the floor levels is given in Table 5.1

A set of preliminary member sizes was selected based on an approximate analysis. Using these preliminary member sizes a conventional static analysis was performed using the ETABS computer program. A bidirectional combination of loads with 100 percent in one direction plus 30 percent in the transverse direction was used and the more severe load condition for each element was used in the design. The adequacy of the member sizes was checked with both the provisions of the AISC Specification [74] and 1988 UBC. The member sizes were modified as necessary to satisfy the design provisions. Effective length factor K was assumed to be 1.0 for the column design and column sizes were held constant for two-story heights to represent current building practice. The resulting member sizes are shown in figure 5.1.

The calculated periods of vibration of the first three modes of the final structure are 1.05, 0.90 and 0.55 seconds respectively. The first two modes correspond to the translational modes in the Y and X-directions, respectively, and the third mode corresponds to the torsional mode. The modal contributions of the first translational mode in the X and Y-directions to the base shear are 0.80 and 0.82. Based on UBC-Spectra, their values are 16 and 17 kips, respectively.

The largest story drifts due to the code design lateral forces in the X and Y-

directions occur at 3rd and 2nd stories respectively, and the maximum values are 0.17 and 0.24 inches, which are 0.0012 and 0.0017 times story heights. This shows that the 3rd and 2nd stories are the most flexible.

5.1.2 Earthquake Record

A representative set of ground excitations is needed to obtain a good estimate of expected maximum responses with limited number of nonlinear analyses. A previous study by Derecho, Freskakis and Fintel [72] has shown the importance of knowing the frequency characteristics of a given input motion. Near maximum response to an earthquake excitation can be expected if the dominant ground motion frequency components occur in the same frequency range as the dominant effective frequency of the structure. For this reason, the dynamic excitation used for this study was the North-South component of the 1978 Miyagi-Ken-Oki earthquake. An earthquake of larger magnitude was approximated by increasing the peak acceleration of the record to 0.5 g. To study the effect of ground motion intensity, a peak acceleration of 0.75 g was also used.

Elastic acceleration and velocity response spectra for Miyagi ground motion with peak acceleration 0.5 g are shown in figure 5.2. The largest values in these spectra are located near a period of 0.9 second. It is well known that the peak values in the velocity spectrum reflect the concentration of input energy at or near the same periods. As mentioned before, the building translational fundamental periods are 0.90 and 1.05 seconds. It can be seen from these spectra that these structural periods are approximately the same as the dominant periods of the input ground motion. Thus, it is expected that for this building, this record will give a maximum response. The modal contributions of the first translational mode in the X and Y-directions to

the base shear based on Miyagi-Spectra with zero damping are 1228 and 902 kips, respectively.

5.1.3 Loading Cases

In order to evaluate the effects of bidirectional ground motion on the maximum responses in comparison to unidirectional ground motion, the behavior of the structure is studied for three loading cases as follows :

X+Y : three dimensional analysis where the structure was subjected to two correlated horizontal components of Miyagi N-S record in the X and Y-directions.

X : three dimensional analysis where the structure was subjected to horizontal components of Miyagi N-S record in the X-directions.

Y : three dimensional analysis where the structure was subjected to horizontal components of Miyagi N-S record in the Y-directions.

5.1.3.1 Assumptions

The mathematical model of the building is based on the following assumptions :

(1) The floor diaphgrams are assumed to be completely rigid in their own plane. Therefore, the rigid body deformation of each floor can be represented by two horizontal translations and one torsional rotation. Furthermore, it is assumed that there is no composite action between the girder and the floor diaphragm. Hence, all flexural resistance normal to the floor is provided by the girders.

(2) The mass of the structure is assumed to be lumped at each floor at the center of mass (C.M). The rotatory mass moment of inertia is assumed to be zero in the analysis.

(3) Each nodal point has six degrees of freedom, a vertical translation, two horizontal translations and three rotations. However, due to assumptions (1) above, the two horizontal translations and the rotation about vertical axis are transformed to the corresponding lateral and torsional degrees of freedom at the floor master node. The vertical translation and the remaining two rotations are retained as local degrees of freedom.

(4) The reduction in the frame stiffness due to column axial load and change in geometry is considered by using a geometrical stiffness matrix which includes the P-Δ effect. An iterative procedure is used to include the change in axial load due to lateral displacements.

(5) The member strength is based on bare member strength with kinematic hardening steel which has a yield strength of 36 ksi and 5% strain hardening.

(6) Because the effect of viscous damping is not of central importance in this study, it is assumed that the building has zero damping.

(7) It is assumed that the computed and actual values of stiffness, the yield strengths, the amount and distributions dead load and live load masses are as specified. Also, the ground motion does not have a rotational component about the vertical axis. Thus it is assumed that accidental eccentricity is zero.

5.1.4 Method of Analysis

The response of the system to the selected ground motion is determined by solving the equation of motion by a numerical, step-by-step integration procedure. The time scale is discretized into equal intervals of 0.001 second. Within each time interval, the tangent and the geometric stiffness matrix of the structure is assumed to

remain constant. For the time interval in which the stiffness of any resisting elements changes, the tangent and the geometric stiffness matrix are re-evaluated and the force unbalance created by the numerical procedure is reduced to an acceptably small value by an event-to-event solution procedure. In order to obtain a check on the accuracy of the numerical solution, the energy balance calculation has been performed. The kinetic energy, elastic-plastic work, viscous damping work and external work are computed at the end of each step. This provides an estimate of the work done by the unbalanced forces, with the aim of providing information on the reliability and the accuracy of the solution. The event-to-event solution strategy has been used for the purpose of controlling equilibrium error. Any significant event occuring within the element such as yielding, overshooting, unloading, etc., determines the need for a substep. The tangent stiffness is modified in each substep, and hence the solution closely follows the exact response. If the exact solution is piecewise linear and no overshoot of the exact event is allowed, the solution will follow the exact load-deflection curve and no unbalance force will result. In general, however, it is impossible to use a no overshoot option, since this option can lead to solution instability (looping). This results in an unbalanced force at the end of the step. However, this unbalanced forces is small if the time step is well chosen. In the case that the unbalanced force is larger than a specified tolerance, the current step will be repeated where the time step will be reduced by half. If the unbalanced forces is less than the specified tolerance, any error at the end of the time step can in most cases be eliminated by adjusting the nodal accelerations to satisfy equilibrium. Alternatively, the option is available to apply an equilibrium correction in the following time step if the structure has zero mass.

5.1.5 Discussion of the Results

The nonlinear dynamic responses of the structure for the 0.5 g Miyagi-Ken-Oki earthquake record are presented below.

5.1.5.1 Story Shears, Floor Forces and Absolute Input Energies

The envelopes of maximum story shear developed in the principal directions of the structure are shown in figure 5.3 and given in Tables 5.2 and 5.3. It can be seen that the largest response correspond to unidirectional cases X and Y. However, there are only small differences between the three cases. The maximum base shear in the X-direction corresponding to cases X+Y and X are 303 kips and 314 kips, respectively. Considering the effective seismic mass to be from the total dead weight, these base shears are approximately 0.75 of the dead load. It can be seen that these base shears are approximately 15 times the design base shear specified by the UBC, about 0.05 of the dead load. The maximum base shear in the Y-direction corresponding to cases X+Y and Y are 224 kips and 236 kips, respectively. These are approximately 0.60 of the dead load and approximately 12 times the design base shear specified by the UBC. In terms of the first mode modal contribution, the base shears in the X-direction corresponding to cases X+Y and X are approximately 18 times of UBC spectral values, and 0.26 times of Miyagi spectral values. The base shears in the Y-direction corresponding to cases X+Y and Y are approximately 14 times of UBC spectral values, and 0.26 times of Miyagi spectral values. It is interesting to note that even though the fundamental periods in the two principal directions of the structure are approximately the same, the maximum base shear developed in these directions are significantly different.

Figure 5.4 shows the input ground velocity and the base-shear time history re-

sponses developed in the principal directions of the structure. The ground velocity of the record is characterized by five distinct velocity pulses. The fourth pulse is the largest having a maximum amplitude of 28.31 inch/second at $T = 10.778$ seconds of the record. It is noted that input ground velocity pulses are accompanied by peaks in the base shear response. Because the absolute energy input, shown in figure 5.5 was computed by integrating the product of the structure base shear and the ground velocity input, energy input pulses occur in concurrence with the input ground velocity pulses. The absolute energy input to the building in the Y-direction is smaller than in the X-direction because the base shear developed in the Y-direction is smaller than in the X-direction. The error in the energy balance, that is the ratio of the difference between the total input energy and the total output energy to the total input energy, are -0.0015, -0.0004 and -0.0008. These ratios correspond to cases X+Y, X and Y, respectively.

Figure 5.6 shows the envelopes of maximum floor force. It can be seen that the floor force distributions are different from the UBC force distribution. Moreover, the maximum force developed at the roof of the structure is less than at the next lowest floor. UBC suggests that the magnitude of this force be increased by adding a concentrated load at the top of the structure to account for higher mode effects. It should be noted that the vertical distribution of forces will affect the internal forces developed in the resisting elements of the structure.

By comparing the maximum response due to uni and bidirectional earthquake excitations, it was observed that the base shears corresponding to unidirectional excitation are larger than those corresponding to bidirectional excitation. Similar observations are found for the absolute input energy, but are mixed for the floor forces.

5.1.5.2 Floor Displacement

Figure 5.7 shows the envelope of maximum floor displacement of the center of mass (C.M) developed in the principal directions of the structure. The numerical values for the C.M maximum displacement are given in Tables 5.4 and 5.5. It can be seen that in general the largest response for all floors corresponds to case X+Y. However, maximum story displacement envelopes must be viewed with caution. Figure 5.8 shows a comparison of the 3rd and 4th floor C.M displacement time history response in the Y-direction of the structure corresponding to cases X+Y and Y. These figures show some differences in the response, even though the difference in the maximum response is small.

The floor response time histories for C.M displacement, floor torsional rotation and edge displacement in the X-direction corresponding to case X+Y is shown in figure 5.9. It can be seen that the maximum response for the 1st floors occurred at approximately 10.7 seconds into the excitation and it occurred prior to the maximum response of the 2nd, 3rd, 4th and 5th floors, which occurred at approximately 15.4 seconds into the excitation. Except for the first floor, the maximum response started at the 5th floor and followed by the 4th, 3rd, and 2nd floors, respectively. This figure shows that the structure vibrates about a displaced equilibrium position after approximately 15 seconds into the excitation.

5.1.5.3 Torsional Response

The envelopes of the torsional rotation about the center of mass due to case X+Y is shown in figure 5.10. Even though the structure is initially symmetric, the torsional motion was excited during the inelastic response. The torsional mode develops when one element yields while the others remains elastic, therefore creating

an instantaneous eccentricity. Figure 5.9 shows that torsional mode started at approximately 3 second into the excitation, which was the time when the structure started to experience large displacements in its principal directions.

The torsional response will increase or decrease column line displacements depending on the distance between the column line and the C.M and the phase of the torsional and translational vibrations. It can be seen from figure 5.11 that the maximum ratio of edge to C.M displacements due to this torsion is less than 1.02. This implies that the torsional response for the initially symmetric structure is not important, that is the response is primarily in translation for this type of structure.

5.1.5.4 Story Drift

Figure 5.12 shows envelopes of C.M maximum story drift in the principal directions of the structure. The numerical values of this response are tabulated in Tables 5.4 and 5.5. All the responses show a concentration of large relative displacement at the 2nd story of the structure, which is the most flexible for this structure. It can be seen that bidirectional case produce larger story drift at the lower part of the structure and smaller drift at the upper part of the structure. This response can be explained by the fact that bidirectional loading increase the column axial load at the lower part of the structure significantly in comparison to unidirectional loading, figure 5.13. Consequently, for the lower part of the structure, bidirectional loading reduced the effective story stiffness. The hysteresis loops for bidirectional loading are larger than for unidirectional loading, as will be shown in Section 5.1.5.5.

The largest story drifts which correspond to bidirectional case X+Y are 4.3 and 5.8 inches, which are approximately 0.03 and 0.04 times story height. For unidirectional case X, the largest story drift occurs at the 3rd story with a maximum value

of 4.2 inch, approximately 0.03 times story height, and for unidirectional case Y, the largest story drift occurs at the 2nd story with a maximum value of 5.1 inch, approximately 0.035 times story height.

It is interesting to note that when the base shear corresponding to bidirectional excitation is smaller than for unidirectional excitation, the story displacements and story drifts for bidirectional excitation are larger than for unidirectional excitation. This implies that biaxial moments reduce the effective column stiffness.

5.1.5.5 Column Rotation and Ductility

The envelopes of maximum column rotation and column ductility ratio are shown in figures 5.14 and 5.15. The numerical values for column ductility ratio are tabulated in Tables 5.2 and 5.3. It is not surprising to see that the largest column rotations and column ductility ratios correspond to the bidirectional case X+Y, because this case produced the largest floor displacements.

The maximum ductility ratios of the structure corresponding to bidirectional case X+Y are 7.3 and 9.3 in the X and Y-directions, respectively, and the maximum ductility ratios corresponding to unidirectional case X and Y are 7.2 and 7.9, respectively. These are large column ductility ratios, but it should be remembered that these response calculations assume zero damping. From the acceleration spectra of Miyagi record shown in figure 5.2, it can be seen that 5% damping will reduce the elastic response to about 60% of the zero damped response at a 1.0 second period. It also was assumed that the ground motion in both the principal directions are in phase. This implies that the maximum excitation occurs at the same time in each directions of the structure, which is a very conservative assumption.

The effect of gravity load, ground motion direction and torsional response on the

column maximum ductility ratio can be determined from figures 5.16 and 5.17. Unidirectional loading combined with rotational response will result in different ductility ratios for columns located on opposite sides of the center of mass, while bidirectional loading will result in different ductility ratios for each column. By comparing the response envelopes due to uni and bidirectional earthquake excitations, one can observe that the maximum column ductility ratios are larger for bidirectional excitation than for unidirectional excitation in the lower stories of the frame.

Figure 5.18 compare the column shear force versus story drift hysteresis curves for columns 16 and 20, which are located at the 2nd and 1st stories respectively. It can be seen that bidirectional flexural loading beyond yield resulted in a small decrease in column yield strength and an increase in lateral deformation in comparison to similar member during unidirectional loading.

5.1.6 Effect of Ground Acceleration Magnitude

The nonlinear dynamic response of the structure subjected to the Miyagi-Ken-Oki earthquake record at 0.75 g is compared to the response at 0.5 g and presented below.

5.1.6.1 Story Shears, Floor Forces and Absolute Input Energies

The envelopes of maximum story shear developed in the principal directions of the structure are compared in figure 5.19 and their numerical values are given in Tables 5.2 and 5.3. Similar to the 0.5 g Miyagi responses, the largest 0.75 g responses correspond to the unidirectional cases X and Y. However, the difference between the responses for the three cases is not large. The maximum base shear in the X-direction corresponding to bidirectional and unidirectional cases X+Y and X are 324 kips and

343 kips, respectively, which are approximately 0.80 of the dead load. These base shears are approximately 16 times larger than the design base shear. The maximum base shear in the Y-direction corresponding to bidirectional and unidirectional cases X+Y and Y are 230 kips and 237 kips, which are approximately 0.60 of the dead load. These base shears are 12 times larger than the design base shear. In terms of the first mode modal contribution, the base shears in the X-direction corresponding to cases X+Y and X are approximately 20 times of UBC spectral values, and 0.26 times of Miyagi spectral values. The base shears in the Y-direction corresponding to cases X+Y and Y are approximately 14 times of UBC spectral values, and 0.26 times of Miyagi spectral values. It should be noted that a fifty percent increase in the magnitude of the ground motion acceleration resulted in very small increases in the maximum story shears. This implies that the dynamic ultimate of the structure had been nearly achieved with the 0.5 g input ground motion.

The ratio of the difference between the total input energy and the total output energy to the total input energy, are -0.0028, -0.0003 and -0.0006. These ratios correspond to cases X+Y, X and Y, respectively.

5.1.6.2 Floor Displacement

Figure 5.20 compares the envelopes of maximum displacement of the C.M in the X and Y-directions and their numerical values are given in Tables 5.4 and 5.5. It can be seen that the largest response for all floors corresponds to the bidirectional case X+Y. As mentioned before, bidirectional loading reduces the effective story stiffness. A fifty percent increase in the ground motion acceleration for bidirectional ground excitation produced a doubling of the floor displacement in the X-direction and a tripling in the Y-direction. The displacement response of the 5th floor C.M

in the Y-direction for bidirectional and unidirectional loading are compared in figure 5.21. For the 0.75 g ground motion, the shift in equilibrium position started at approximately 3 seconds into the excitation. A notable feature of this response is the large shift in the equilibrium position around 10 seconds of the excitation. The structure vibrated about a displaced equilibrium position which continously drifted from the zero position.

5.1.6.3 Torsional Response

The envelopes for rotation at the C.M due to the bidirectional case X+Y are shown in figure 5.22. It can be seen that a fifty percent increase in the ground motion acceleration produced approximately a tenfold increase in the maximum floor rotation. The effect of this torsional response on the edge displacement is shown in figure 5.23. The ratio of maximum edge to maximum C.M displacements due to rotation is approximately 1.08. As described before, this torsional response in the initially symmetric structure is not very important, that is, the response remains primarily translational.

5.1.6.4 Story Drift

Envelopes of the maximum story drift of the C.M in the principal directions of the structure are compared in figure 5.24 and their numerical values are given in Tables 5.4 and 5.5. It can be seen that the maximum story drift occurs at the 2nd story for the bidirectional case X+Y with values of 8.9 and 18.8 inches, in the X and Y-directions, respectively. These are approximately 0.06 and 0.13 times story height. For unidirectional case X, the largest story drift of 5.8 inch occurs at the 3rd story, which is approximately 0.04 times story height, and for unidirectional case Y, the

largest story drift of 9.6 inch occurs at the 2nd story, which is approximately 0.07 times the story height.

Under the increased ground motion there is a dramatic increase in the story drift, specially the story drift corresponding to bidirectional excitation. It is interesting to note that for the increased ground motion, the story shear values remain practically the same while the story displacements increase severely. The hysteresis loops for bidirectional case are larger than for unidirectional cases, which implies a reduced effective story stiffness under bidirectional loading.

5.1.6.5 Column Ductility Ratio

The envelopes of the maximum column ductility ratio are compared in figure 5.25. It can be seen that the maximum ductility ratios in the principal directions of the structure for bidirectional case X+Y are 17.0 and 25.9. A fifty percent increase in the ground motion acceleration produced a dramatic increase in column maximum ductility ratios for the bidirectional ground excitation and columns of first three story of the structure. It is unlikely that the column will be able to achieve these large ductility values before failure. However, it should be mentioned that these response calculations assume zero damping. It also was assumed that the ground motion in both the principal directions are in phase. This implies that the maximum excitation occurs at the same time in each directions of the structure, which is a very conservative assumption.

Figure 5.26 shows the column shear force versus story drift hysteresis curves for column 20, which is located at the 1st story. Similar to previous loading response, it can be seen that bidirectional flexural loading beyond yield resulted in a small reduction in column yield strength and an increase in lateral deformation in comparison to

similar member loaded unidirectionally. The drift caused by bidirectional excitation also can be seen on this plot, especially for the weak axis (Y) of the column.

5.2 Asymmetrical Structure

The purpose of this analysis is to study the effect of bi-directional ground excitation on the response of a torsionally sensitive building configuration. It is well known that both translational and torsional motion are induced by earthquakes in asymmetrical structures. Under strong shaking, many of the resisting elements will be inelastic and it is expected that element inelastic action will affect the lateral-torsional response of the system. In this study, the effect of inelastic action on the structural response to bidirectional excitation is compared to the response to unidirectional excitation for an asymmetric structure designed in accordance with the 1988 UBC.

5.2.1 Design of Steel Frame Structure

The frame selected for this study is a five story, L-shape moment-resistant steel frame. Typical floor plan is shown in figure 5.27. The dimensions shown in this figure are center-line to center-line dimensions. The bays are 24 ft by 24 ft and the typical story height is 12 ft. Gravity loads used in the design include uniform dead loads of 80 psf and uniform live loads of 20 psf for the roof, and uniform dead loads of 100 psf and uniform live loads of 50 psf for the typical floor. Only the dead loads are used for the lateral inertia force. The total dead weight was 1210 kips.

The earthquake design forces were determined using the 1988 UBC and the estimated building period T given by the formula 5.1. The design base shear in each of the principal direction are calculated using formulae 5.2 and 5.3. The coefficients

are:

$Z = 0.4$ (for a building in zone No. 4)

$I = 1.0$ (importance factor)

$S = 1.0$ (soil condition factor)

$R_w = 12$ (Steel Special Moment Resisting Frames)

$W = 1210$ kips (total dead load of the building)

Using formula 5.1, the estimated building period is 0.75 second which results in the base shear coefficient C_s of 0.05 and a minimum base shear force V_{base} of $.05 \times W = 60.5$ kips. The corresponding lateral force distribution to the floor levels is summarized in Table 5.6.

Bidirectional combinations of loads with 100 percent in one direction plus 30 percent in the transverse direction were used. The effects of torsional irregularity were accounted by increasing the accidental torsion at each level by an amplification factor A_x, determined from the following formula

$$A_x = \left[\frac{\delta_{max}}{1.2\delta_{avg}}\right]^2 \tag{5.4}$$

where

δ_{max} = the maximum displacement at level x

δ_{avg} = the average of the displacements at the extreme points of the structure at level x

A set of preliminary member sizes was selected based on an approximate analysis. Using these preliminary member sizes a conventional static analysis was performed using the ETABS computer program.

The more severe loading for each element was considered in the member design, and the adequacy of the member sizes was checked to be in accordance with the

provisions of both the AISC Specification and 1988 UBC. The member sizes were modified as necessary to satisfy these design provisions. Effective length factor K was assumed to be 1.0 for columns and column sizes were held constant for two-story heights to represent current building practice. To simplified the input data, with the exception of internal columns, the size of the columns located at every exterior corner of the structure were made the same size. The resulting member sizes are shown in figure 5.27.

The periods of vibration of the first three modes are 1.46, 1.19 and 1.18 seconds. The first corresponds to the torsional mode, and the last two correspond to the translational modes in the X and Y-directions respectively. The modal contributions of the first translational mode in the X and Y-directions to the base shear are 0.75. Based on UBC-Spectra, their values are 45 kips.

The largest story drift caused by the design lateral forces in the X and Y-directions occurs at 2nd and 3rd floors, respectively. These maximum story drift values are 0.37 and 0.32 inches, which are 0.0026 and 0.0022 times story heights. This shows that the 3rd and 2nd stories are the most flexible. The 1988 UBC story drift limitation for the building less than 65 feet in height is 0.005 or $0.04/R_w$ times the story height. For this building, the second limitation is 0.0033.

5.2.2 Earthquake Record

Like the symmetrical structure, the dynamic excitation used for this study was the North-South component of the 1978 Miyagi-Ken-Oki earthquake. A higher magnitude earthquake was approximated by increasing the peak acceleration of the record to 0.5 g, and to study the effect of ground motion intensity, a peak acceleration 0.75 g was used.

The acceleration and velocity response spectra for Miyagi ground motion with peak acceleration 0.5 g are shown in figures 5.2. As mentioned before, the fundamental translational periods are 1.18 and 1.19 seconds. It can be seen that the translational periods are near the dominant period of the input ground motion. The modal contributions of the first translational mode in the X and Y-directions to the base shear based on Miyagi-Spectra with zero damping are 2487 kips.

The behavior of the structure is studied for six loading cases as follows :

X+Y : three dimensional analysis where the structure was subjected to two correlated horizontal components of Miyagi N-S record in the X and Y-directions.

X-Y : similar to case X+Y, except the algebraic sign of the acceleration in the Y-direction was reversed.

X : three dimensional analysis where the structure was subjected to one horizontal component of Miyagi N-S record in the X-direction.

Y : three dimensional analysis where the structure was subjected to one horizontal component of Miyagi N-S record in the Y-direction.

2DX : two dimensional analysis where the structure was subjected to the horizontal component of Miyagi N-S record in the X-direction.

2DY : two dimensional analysis where the structure was subjected to the horizontal component of Miyagi N-S record in the Y-direction.

5.2.3 Assumptions

The mathematical model of the structure uses the same assumptions as used for the symmetrical building described in Section 5.1.3.1.

5.2.4 Method of Analysis

The same method of analysis was used here as was used for the symmetrical building described in Section 5.1.4.

5.2.5 Discussion of the Results

The nonlinear dynamic response of the structure is reported in terms of story shear, floor force, floor displacement, story drift, column ductility ratio and energy. The results from the study are presented and discussed in the following.

5.2.5.1 Story Shears, Floor Forces and Absolute Input Energies

The envelopes of maximum story shear in the principal directions of the structure are shown in figure 5.28 and their values are given in Tables 5.7, 5.8, 5.9, and 5.10. It can be seen that the largest responses correspond to the two dimensional analysis cases 2DX and 2DY. There is not much difference between the response at all floor levels for cases X and 2DX. A similar observation can be made for the responses correspond to cases Y and 2DY, and the responses correspond to cases X+Y and X-Y. However, there is a considerable difference between the base shear values corresponding to bidirectional cases in comparison to unidirectional cases.

The maximum base shears corresponding to cases X and 2DX are 599 and 620 kips, respectively. Assuming the effective weight to be the total dead weight as would be done in design, these base shears are approximately 0.50 of the effective weight. It can be seen these base shears are approximately 10 times larger than the design base shear, which was 0.05 times the effective weight. The maximum base shear corresponding to cases Y and 2DY are 588 kips and 607 kips, respectively which also are approximately 0.50 of the effective weight. Similar to the response in the

X-direction, these base shears are approximately 10 times larger than the design base shear specified by the UBC. In terms of the first mode modal contribution, the base shears in the X-direction are approximately 14 times of UBC spectral values, and 0.25 times of Miyagi spectral values, and the base shears in the Y-direction are approximately 14 times of UBC spectral values, and 0.26 times of Miyagi spectral values.

Because the structure has plan eccentricity, shear is developed in the frames perpendicular to the earthquake excitation direction. These orthogonal base shears corresponding to cases X and Y are 131 kips and 126 kips, respectively which are approximately 0.10 of the effective weight. These base shears are approximately 7 times the design base shear which was 0.015 W.

Figure 5.29 shows the input ground velocity and the base-shear time history responses. The ground velocity of the record is characterized by five distinct velocity pulses having a maximum amplitude of 28.31 inch/second. Similar to the symmetrical building response, the input ground velocity pulses are accompanied by peaks in the base shear response. In general, the maximum base shear for all cases occurred approximately at the same time. Moreover, the base shear time history is in phase with the input ground velocity, and there is little variation in the base shear magnitude during the response. This is not surprising, since the fundamental period of the structure are almost the same as the dominant period of the record and the motion is large enough to cause significant yielding. This results in the increasing trend in the absolute input energy as shown in figure 5.30. Rapid increases in energy input occur at approximately the same time as the ground velocity pulses. The absolute energy input in the Y-direction is practically the same as in the X-direction, since the base shear in the X-direction is practically the same as in the Y-direction. As might

be expected because the 2D cases had the largest base shear, the two dimensional analyses resulted in the largest absolute input energy. The ratio of the difference between the total input energy and the total output energy to the total input energy, are -0.0040, -0.0035, -0.0003, -0.0004, -0.0001 and -0.0001. These ratio correspond to cases X+Y, X-Y, X, Y, 2DX, 2DY, respectively.

Figure 5.31 shows the envelopes of maximum floor forces. Similar to the response of symmetrical building, the floor force distributions are quite different than the UBC force distribution. The envelopes of story force are closer to a uniform distribution than the inverted triangular distribution suggested by UBC.

5.2.5.2 Floor Displacement

Figure 5.32 shows the C.M maximum displacement envelope in the principal directions of the structure and these values are given in Tables 5.11, 5.12, 5.13, and 5.14. It can be seen that the largest response for the first two floors corresponds to case X+Y, and the largest response for the top three floors corresponds to cases X and Y. In general, the C.M maximum displacements from three dimensional analysis with unidirectional excitation are practically the same as the corresponding two dimensional analysis. There is a considerable difference in the response corresponding to cases X+Y and X-Y, particularly in the top three floor responses. It is interesting to note that in general, the smallest responses correspond to the three dimensional case X-Y.

5.2.5.3 Torsional Response

The envelopes of rotation about the C.M are shown in figure 5.33. This figure reveals that the floor rotation is sensitive to the sign of horizontal ground excitation,

and the phase of the ground excitations can amplify or deamplify the torsional motion. The largest rotations for all floor levels correspond to case X-Y, followed by cases Y, X and X+Y. As mentioned before, this rotation may increase or decrease the column line displacements or edge displacements, depending on the distance to the C.M and the sign of the rotation. It can be seen in figure 5.34 that the largest ratio of edge maximum to C.M maximum displacements of approximately 1.4 corresponds to case X-Y. Elastic response results show that the largest ratio is approximately 1.6 for the same load case, figure 5.35. The major difference between the inelastic and elastic responses is the smaller torsional contribution to the edge displacement in the inelastic response. The decrease is nearly linear along the height of the structure. As will be shown in section 5.2.5.5, a large first story drift will change the torsional mode during inelastic response.

It is interesting to compare the response corresponding to bidirectional cases X+Y and X-Y. As mentioned before, these cases produced practically the same maximum base shear. However, there is a considerable difference for the floor displacement response, where the smallest response correspond to case X-Y. The discrepancy in the response can be explained by comparing their torsional response. It can be seen that there is a considerable difference for the floor torsional response, where the smallest response correspond to case X+Y. This implies that in case X+Y, most of the story shear was used to produce the translational motion, while in case X-Y, the story shear was used to produce both translational and torsional motions.

5.2.5.4 Edge Displacement

Figure 5.36 shows the envelopes of maximum edge displacement. By comparing the C.M and edge displacement responses corresponding to cases X and 2DX,

and cases Y and 2DY, it is seen that two and three dimensional analyses produce approximately the same C.M response, but because of torsional motion, the three dimensional analysis produces larger edge response.

In general the largest edge displacements in each principal direction of the building correspond to cases X and Y. This not surprising since these cases produce the largest C.M maximum displacement. However, it is interesting to note that even though the base shear corresponding to bidirectional loading is smaller than that for unidirectional loading, the largest maximum edge displacement for the 1st floor corresponds to bidirectional case X-Y. As mentioned before, case X-Y produces the smallest C.M displacement. However, the additional translational edge displacement due to rotation is large enough to produce the largest first floor edge displacement.

Figure 5.37 shows the maximum edge displacement corresponding to case X+Y. It can be seen that the center of rotation is located in the fourth quadrant. It is noted that the largest edge displacement in the X-direction occurred at column line C, which is located at the stiff side of the structure and the maximum displacement in the Y-direction occurred at column line I, which is located at the weak side of the structure. The largest ratio of maximum displacement of weak and stiff sides of the the structure in the X-direction is approximately 0.89. In the Y-direction, this ratio is approximately 1.13. This implies that the stiff side of the structure in the X-direction experienced more inelastic action than the weak side. This ratio for other floors is the smaller than the first floor, because the torsional contribution to the edge displacement is smaller. The decrease is nearly linear along the height of the structure. The shifting in the equilibrium can be seen in this figure, where the maximum displacements in the positive side of the structure in both directions are larger than in the negative side. As mentioned before, this case produced the

smalllest torsional response. This resulted in nearly linear envelope of maximum edge displacement. Moreover, figure 5.38 shows that the maximum response started at the 1st floor followed by the 2nd, 3rd, 4th and 5th floors, respectively.

Figure 5.39 shows the maximum edge displacement corresponding to bidirectional case X-Y. It can be seen that the center of rotation is located in the first quadrant, and the largest edge displacement in the X and Y-directions occurred at column lines A and I, which are located at the weak side of the structure. It is noted that there is a large difference in the maximum response between the stiff and the weak edge of the structure. In the X-direction, the largest ratio of stiff to weak edge maximum displacement of approximately 1.58 occurred at the 1st floor, and in the Y-direction, this ratio was approximately 1.61 which occurred at the 1st floor. As mentioned before, this load case produced the largest torsional response. This resulted in the smaller translational response of the interior column lines B and II in comparison to the exterior column lines. Similar to case X+Y, the torsional contribution to the edge displacement is smaller for the other floors than the for the first floor, and the decrease is nearly linear along the height of the structure. The shifting in floor rotation is noticeable on all floors, as shown in figure 5.40. The maximum response started at the 1st floor followed by the 2nd, 3rd, 4th and 5th floors, respectively. Furthermore, the torsional vibration is not in phase with the translational vibration.

Figure 5.41 shows the edge maximum displacement corresponding to case X. It can be seen that the centers of rotation are located in the first quadrant and the largest edge displacement in the X-direction occurred at column line A, which is located at the weak side of the structure. In the X-direction, the largest ratio of weak to stiff edge maximum displacement is approximately 1.31 which occurs at the 1st floor. As might be expected, this ratio is smaller than the X-Y case and

larger than the X+Y case, because the maximum torsional response for this case falls somewhere between the maximum torsional response of cases X-Y and X+Y. Similar to previous cases, the maximum response started at the first floor followed by the 2nd, 3rd, 4th and 5th floors, respectively, figure 5.42. Observations for case Y are similar to those for case X.

5.2.5.5 Story Drift

Figure 5.43 shows envelopes of C.M maximum story drift in the principal directions of the structure and their numerical values are given Tables 5.11, 5.12, 5.13, and 5.14. It can be seen that the largest story drift corresponds to bidirectional case X+Y and all the responses show a concentration of large relative displacement at the 2nd story of the structure, which is the most flexible for this structure.

The largest story drift in the principal directions of the structure correspond to bidirectional case X+Y and are 5.17 and 5.22 inches, which are approximately 0.036 of story height. As might be expected, the C.M story drift from three dimensional analyses with unidirectional excitation is practically the same as its corresponding two dimensional analyses. It is interesting to note that even though the base shear corresponding to bidirectional case X+Y is smaller than for unidirectional cases, the C.M story drift for bidirectional case X+Y is larger than for unidirectional cases. This implies that biaxial moments reduce the effective column stiffness.

Figure 5.44 shows the comparison of maximum edge story drift in the X and Y-direction of the structure. It is not surprising to see that in general, the largest drift correspond to unidirectional cases X and Y, since these cases produce the largest C.M displacement. Similar to story displacement response, the largest maximum story drift for the 1st floor correspond to bidirectional case X-Y.

Figures 5.45 and 5.46 show the maximum story drift corresponding to elastic and inelastic analyses for bidirectional case X+Y. Both analyses produced the largest story drift at the 2nd story and the maximum story drift in the X and Y-directions correspond to the inelastic analysis are 5.41 and 5.57 inches, respectively, which are approximately 0.038 of story height. The major difference between the inelastic and elastic responses is the much smaller story drift and drift dispersion for the inelastic response. In the X-direction, the maximum story drift for all floor levels occurred at column line C, which is located at the the stiff side of the structure, and in the Y-direction the maximum story drift occurred at column line I, which is located at the weak side of the structure. As mentioned before, in the the inelastic response the contribution of torsional rotation on the edge displacement decreases along the height of the structure. This is reflected in the decrease of edge drift dispersion along the height of the structure. For the top two floors, there are practically no difference between column line maximum drift. It is noted that the story displacement and story drift response have a similar pattern for all floor levels, that the maximum response occurs at the stiff and the weak sides of the X and Y-directions respectively.

Figures 5.47 and 5.48 show the maximum story drift corresponding to elastic and inelastic analyses for bidirectional case X-Y. Both analyses produced the largest story drift at the 2nd story and the maximum story drift in the X and Y-directions correspond to the inelastic analysis are 5.75 and 5.77 inches, respectively, which are approximately 0.04 of story height. The major difference between the inelastic and elastic responses is much smaller story drift and drift dispersion in the inelastic response and the shift of maximum story drift from the weak to the stiff side of the structure for the top two stories. In the X-direction, the maximum story drift for the first three stories occurred at column line A, which is located at the the weak

side of the building, and for the top two stories, the maximum story drift shifted to column line C, which is located at the the stiff side of the building. Similar to the response in the X-direction, the maximum story drift in the Y-direction for the first three stories occurred at column line I, which is located at the the weak side of the building, and for the top two stories, it shifted to column line III, which is located at the stiff side of the building.

The shift in the story drift at the upper stories can be explained by observing torsional motions at the 1st and 4th floors of the structure, as shown in figure 5.40. It can be seen that in the inelastic response, the 1st floor has different torsional response than the 4th floor. This difference can be explained by observing the envelope of edge maximum drift shown in figure 5.48. It can be seen that there are some substantial difference in the maximum story drift between column located at the weak and the stiff sides of the structure, especially for columns of the first three story. Torsional response amplify the story drift due to translational motion at one side of the structure, and deamplify the story drift at the opposite side. Consequently, one side of the structure was excited into the inelastic range more heavily than the opposite side. However, for the the top two stories, columns located at both sides of the structure were excited to approximately the same inelastic range.

Figure 5.49 show the maximum story drift corresponding to elastic and inelastic analyses for unidirectional case X. Both analyses produced the largest story drift at the 2nd story. The maximum story drift in the X direction corresponds to the inelastic analysis is 5.78 inch, which are approximately 0.04 of story height. Similar to the case X-Y response, the major difference between the inelastic and elastic responses is the much smaller story drift and drift dispersion in the inelastic response and the shift of maximum story drift from the weak to the stiff side of the building for

the top two stories. In the X-axis, the maximum story drift for the first three stories occurred at column line A, which is located at the the weak side of the building, and for the top two stories, the maximum story drift shifted to column line C, which is located at the stiff side of the building. As might be expected, the story drift dispersion is smaller in comparison to case X-Y, and larger in comparison to case X+Y, because the maximum torsional response for this case falls somewhere between the maximum torsional response of cases X-Y and X+Y. Similar observation can be made for case Y.

Figure 5.50 shows the comparison between the ductility ratio of column 8 corresponding to case X and 2DX. This column is located at the stiff side of the building. It can be seen that the ductility ratio for the top two stories corresponding to case X is larger than case 2DX because of the shifting in the story drift. However, the difference in the response is small.

5.2.5.6 Column Rotation and Ductility Ratio

The envelopes of maximum column rotation and column ductility ratio are shown in figures 5.51 and 5.52, and their numerical values are given in Tables 5.15, 5.16, 5.17, and 5.18. It can be seen that the largest column rotation and ductility ratio are corresponding to cases X and Y. It should be noted that even though in case X and Y the structure was subjected to unidirectional excitation, shear is developed in the frames perpendicular to the earthquake excitation direction, because the structure has plan eccentricity. This implies that frames were subjected to bidirectional loading.

Similar to story drift response, the largest column rotation and ductility ratio for the 1st story corresponds to bidirectional case X-Y. The maximum ductility ratio

in the principal directions of the structure corresponding to bidirectional case X-Y are 8.71 and 8.41, respectively, and the maximum ductility ratio corresponding to unidirectional cases X and Y are 8.55 and 8.21, respectively. While these are large values, it should be remembered that these response calculations assume zero damping. From the elastic acceleration spectra of Miyagi record shown in figure 5.2, it can be seen that 5% damping will reduce the elastic response to about 60% of the zero damped response at a 1.0 second period. It also was assumed that the ground motion in both the principal directions are in phase. This implies that the maximum excitation occurs at the same time in each directions of the structure, which is a very conservative assumption.

Figures 5.53 and 5.54 compare column shear force versus story drift hysteresis curves for columns 25 and 32, which are located at the second story. It can be seen that biaxial flexural loading beyond yield level resulted in a decrease in the column yield strength. In the Y-direction, columns 25 and 32 are located at the weak and the stiff sides of the structure. It is noted that for column 25, bidirectional loading resulted in small decrease in the column yield strength and an increase in lateral deformation in comparison to similar member loaded uniaxially. The hysteresis loops for columns subjected to bidirectional earthquake loading are larger than similar members subjected to unidirectional earthquake loading. Of particular interest is the comparison between the weak and stiff side response corresponding to bidirectional case X-Y which produced the largest torsional response. As mentioned before, the torsional rotations amplify and deamplify the drift in the weak and the stiff sides respectively. For column 25 and 32, this is reflected in column shear force hysteresis loop in the Y-direction. As can be seen, column 25 experienced more inelastic deformation than column 32. The hysteresis loops for column 25 are larger than for

column 32.

5.2.6 Effect of Ground Acceleration Magnitude

5.2.6.1 Story Shear, Floor Force and Absolute Input Energies

The envelopes of maximum story shear in the principal directions of the building are shown in figure 5.55 and their numerical values are given in Tables 5.7, 5.8, 5.9, 5.10. Similar to 0.5 g Miyagi responses, the largest response corresponds to two dimensional cases 2DX and 2DY. However, the difference between the response corresponding to cases X and 2DX is not large. Similar observation can be made for the response corresponding to cases Y and 2DY, and the response corresponding to cases X+Y and X-Y. The maximum base shear in the X-direction corresponds to cases X and 2DX are 679 kips and 693 kips, respectively, which are approximately 0.55 of the effective weight. These base shears are approximately 11 times larger than the design base shear. The maximum base shear in the Y-direction corresponds to cases Y and 2DY are 670 kips and 699 kips, respectively, which are approximately 0.55 of the effective weight. Similar to the response in the X-direction, these base shears are approximately 11 times larger than the design base shear. In terms of the first mode modal contribution, the base shears in the X-direction are approximately 14 times of UBC spectral values, and 0.25 times of Miyagi spectral values, and the base shears in the Y-direction are approximately 14 times of UBC spectral values, and 0.26 times of Miyagi spectral values. By comparing these values with those for 0.5 g input, figure 5.28, it can be noted that a fifty percent increase in the magnitude of the ground acceleration resulted in a very small increase in the maximum story shear.

The orthogonal base shears corresponding to cases X and Y under the increased

ground motion are 100 kips and 107 kips respectively, which are approximately 0.09 of the effective weight. These base shears are approximately 6 times larger than the design base shear. It can be seen that a fifty percent increase in the magnitude of ground motion acceleration resulted in small increases in the maximum base shear and a reduction in the orthogonal base shear. This reduction implies that under the increased ground motion, the torsional response is less significant.

Figure 5.56 shows the input ground velocity and the base-shear time history responses. Similar to 0.5 g Miyagi responses, the maximum base shear for all cases occurred approximately at the same time. However, they occurred earlier in comparison to the 0.5 g response. It can be seen that a fifty percent increase in the magnitude of ground motion acceleration resulted in almost hundred percent increase in the energy input to the structure, as shown in figure 5.57. The ratio of the difference between the total input energy and the total output energy to the total input energy, are -0.0054, -0.0050, -0.0002, -0.0004, -0.0001 and -0.0001. These ratio correspond to cases X+Y, X-Y, X, Y, 2DX, 2DY, respectively.

Figure 5.58 shows the envelopes of maximum floor force. Similar to 0.5 g Miyagi responses, the envelopes of floor force are closer to a uniform distribution rather than the inverted triangular suggested by UBC.

5.2.6.2 Floor Displacement

Figure 5.59 shows the envelopes of maximum displacement of the C.M in the principal directions of the structure, and their numerical values are given in Tables 5.15, 5.16, 5.17, and 5.18. Unlike the 0.5 g Miyagi response, it can be seen that the largest response corresponds to bidirectional cases X+Y and X-Y. The largest increase occurred for bidirectional case X-Y. For this case, a fifty percent increase in

the ground motion acceleration produced approximately an eighty percent increase of the floor displacement in the X and Y-directions.

5.2.6.3 Torsional Response

The envelopes of C.M torsional rotation due to the increased ground motion is shown in figure 5.60. When comparing figure 5.33 with figure 5.60 it can be seen that a fifty percent increase in the ground motion acceleration resulted in practically no increase in the maximum torsional rotation for cases X and Y. For case X-Y, the increased ground motion resulted in a small increase in the maximum torsional rotation. The major difference between the 0.5 g and 0.75 g Miyagi response is the smaller maximum torsional response for case X+Y under the increased ground motion. This implies that under increased ground motion the torsional response becomes less significant. This explains the reduction in orthogonal base-shear and the large increase in the maximum displacement of the C.M for case X-Y under the increased ground motion.

5.2.6.4 Edge Displacement

By figure 5.61 shows the envelopes of the maximum edge displacement for cases X+Y, X-Y, X and Y under the increased ground motion. Unlike the 0.5 g Miyagi response, bidirectional case X-Y produced the largest rather than the smallest edge displacements. This increased ground motion case produced the largest C.M maximum displacement and the largest torsional rotation. It should be noted that the maximum story displacement corresponding to the bidirectional case is larger than those corresponding to unidirectional cases, even though the base shear correspond to bidirectional case is smaller than those correspond to unidirectional cases.

Figure 5.62 shows the first floor time history responses corresponding to case X+Y due to the increased ground motion. The major difference between this response and the one corresponding to 0.5 g Miyagi is that the maximum displacement occurred at the negative side of both principal directions and they occurred earlier during the earthquake. Similar observations can be obtained for other cases.

5.2.6.5 Story Drift

Figure 5.63 shows envelopes of maximum story drift of the C.M in the principal directions of the structure, and their numerical values are given in Tables 5.11, 5.12, .13, 5.14. Unlike the 0.5 g Miyagi response, the largest response corresponds to idirectional case X-Y. Similar to floor displacement response, the smallest responses orrespond to the two dimensional analysis response cases 2DX and 2DY. It should e noted that the differences in response corresponding to cases X+Y and X-Y are mall. Similar observation can be made for the responses corresponding to cases X nd 2DX, and the responses corresponding to cases Y and 2DY. The major difference between these responses and that corresponding to 0.5 g Miyagi is that there is a marked increase in the C.M drift of the 2nd and the 3rd stories, which are the most flexible, for the bidirectional cases X+Y and X-Y.

Figure 5.64 shows the comparison of edge maximum story drift in X and Y-directions of the structure. All the responses show a concentration of large relatively displacement at the 2nd story of the structure. It can be seen that under the increased ground motion there is a dramatic increase in the story drift, specially the story drift corresponding to bidirectional case X-Y. It is interesting to note that for the increased ground motion, there are very small increases in the story shear values while the story displacements increase severely.

Figure 5.65 shows that the maximum story drift corresponding to bidirectional case X+Y occurred at the 2nd story with values of 7.5 and 7.6 inches in the X and Y-directions, respectively. These are approximately 0.05 of the story height. It can be seen that there is a considerable increase in the story drift under the increased ground motion. The major difference between this response and the one corresponding to 0.5 g Miyagi is that there is a smaller story drift dispersion under the increased ground motion. Similar observations can be made for cases X and Y.

Figure 5.66 shows the maximum story drift in the principal directions of the structure correspond to case X-Y under the increased ground motion. The largest story drift occurred at the 2nd story and the maximum story drift in the X and Y-directions are 9.0 and 9.1 inches, respectively, which are approximately 0.06 of the story height. There is a shift in maximum drift response from the weak side into the stiff side of the structure similar to that seen for the 0.5 g Miyagi response.

5.2.6.6 Column Ductility Ratio

The effects of increased ground motion on the maximum column ductility ratio are shown in figure 5.67. The numerical values are given in Tables 5.15, 5.16, 5.17, 5.18. Unlike the 0.5 g Miyagi response, the largest responses correspond to bidirectional case X-Y. It is noted that there is a dramatic increase in the first story column response for this case. The maximum ductility ratio in the X and Y-direction corresponding to bidirectional case X-Y are 14.8 and 15.0, respectively and the maximum ductility ratio in the X and Y-directions correspond to unidirectional cases X and Y are 9.8 and 9.5, respectively.

It is unlikely that the column members will be able to achieve these large ductility values before failure. However, it should be mentioned that these response

calculations assume zero damping. From the elastic acceleration spectra of Miyagi record shown in figure 5.2, it can be seen that 5% damping will reduce the elastic response to about 60% of the zero damped response at a 1.2 second period. It also was assumed that the ground motion in both the principal directions are in phase. This implies that the maximum excitation occurs at the same time in each directions of the structure, which is a very conservative assumption.

Figures 5.68 and 5.69 compares the column shear force versus story drift hysteresis curves for columns 25 and 32, which are located at the 2nd story. Similar to those corresponding to 0.5 g Miyagi, it can be seen that bidirectional flexural loading beyond yield resulted in a small decrease in column yield strength and an increase in lateral deformation in comparison to similar members subjected to unidirectional earthquake loading.

CHAPTER 6

BEHAVIOR OF SYMMETRIC 3-D MOMENT FRAMES STEEL STRUCTURES UNDER THE INFLUENCE OF BI-DIRECTIONAL GROUND EXCITATION AND LARGE COLUMN AXIAL LOAD

In this chapter, the results of nonlinear response analyses of three-dimensional symmetrical steel moment frame structures subjected to large column axial loads and bidirectional ground excitations of different intensities and characteristics are presented. The effects of ground motion intensity, duration, frequency content and column axial load on the ultimate capacity of symmetrical multi-story buildings are observed by studying the base shear, story shear, overturning moment, floor displacement, story drift, column ductility demand and the relationship between column forces and their associated deformations in relation to the ground input excitation.

The base shear, story shear and overturning moment vary continuously with time, however, the maximum base shear, story shear and overturning moment time history responses are used to compare the effects of axial load and earthquake characteristics on the ultimate capacity of the structure.

Similar to the base shear response, the floor displacements vary continously with

time. The envelopes of maximum lateral displacements were used to evaluate the importance of the P-Δ effect and the required amount of building separation. These results provide information on the effects of axial load, ground motion coupling, intensity, duration and frequency content on the structural response. The inter-story displacement gives an indication of the possible damage to structural and non-structural components.

In this study, the ductility ratio is defined as the ratio of maximum end rotation to the yield rotation of the member with equal end rotations and no joint translation. The member ductilities are compared for a structure subjected to different levels of initial axial column loads and different earthquake ground motions. The column shear force-drift hysteresis curves provide a record of inelastic behavior under dynamic loading. They also give information on the column strength and energy dissipation charateristics.

6.1 Design of Steel Frame Structure

A five story, rectangular building with single bay moment-resistant steel frames as described in Section 5.1 was used. The intensity of initial column axial load was amplified to three, four, five and six-tenths of its yield value in compression at every story to evaluate the effects of vertical load on the ultimate capacity of the structure. To study the seismic performance of structure with a weak story, additional calculations were made where the column axial load was initially amplified to six-tenth of its yield value in compression only for columns located at the 3rd story. The structure was subjected to correlated horizontal components of 0.50 g Miyagi N-S record in the X and Y-directions simultaneously.

6.2 Earthquake Record

Three recorded earthquake ground motions which have different intensity, duration and frequency content were selected to study the effects of column axial load on the behavior of three dimensional steel moment frame structures. They were the 1978 Miyagi-Ken-Oki earthquake (N-S component), 1940 El Centro earthquake (N-S and E-W components) and 1985 Mexico City SCT earthquake (N-S and E-W components). The ground acceleration time histories of these three earthquakes are shown in figures 6.1 to 6.3 and their elastic acceleration spectra are shown in figures 5.2, 6.4 and 6.5. For the Miyagi record, an earthquake of larger magnitude was approximated by increasing the peak acceleration of the record to 0.5 g. To study the effect of ground motion intensity, a peak acceleration of 0.75 g was also used. For the El Centro record, an earthquake of larger magnitude was approximated by increasing the peak acceleration of the record twice as large as its original value to 0.68 g. To reduce computing time, only the first ten seconds of the record was used. For the Mexico City SCT record, the original peak acceleration was used because this record was considered to be particularly severe and it is a peaking accelerogram at period 2 seconds, as shown in figure 6.5. An earthquake spectra can be classified as either a broad band or a peaking spectra. A broad range ascending accelerogram spectra has a spectrum which increases with increasing period within the period range of interest, and a peaking accelerogram spectra has a spectrum exhibiting dominant frequencies over a well defined period range. It is anticipated that the presence of large axial column loads will increase the effective period of the structure substantially during inelastic response. A previous study by Derecho, Freskakis and Fintel [72] has shown that when extensive yielding significantly changes the effective period of the struc-

ture, a broad band accelerogram earthquake is likely to produce more severe response than peaking accelerogram earthquake of the same intensity and duration. On the other hand, when minor yielding results in no significant increase in the effective period, peaking accelerogram earthquake will likely produce more severe response. To reduce computing time, only the twenty three second segment of the record was used. The full record of the 1978 Miyagi, 1940 El Centro and 1985 Mexico SCT earthquakes are 40, 53 and 180 seconds, respectively.

It can be seen that the maximum spectral values of each earthquake occur at different periods. The maximum spectral acceleration for the Miyagi earthquake is located near a period of 0.9 second and this earthquake can be classified as a broad band descending earthquake within the period range 0.9 to 2 second. The spectra of the N-S component of 1940 El Centro earthquake has peak values at periods less than 1 second and the spectra of the E-W component has peak values at periods between 0.3 and 1.2 seconds. The N-S component can be classified as descending earthquake within the period range 1 to 2 seconds and the E-W component can be classified as peaking earthquake within the period range 1 to 1.2 seconds. The spectra of the N-S and E-W components of 1985 Mexico City SCT earthquake have a peak values at period of 2 seconds. As mentioned in Section 5.1, the building elastic translational fundamental periods are 0.90 and 1.05 seconds. These structural periods are approximately the same as the dominant period of the Miyagi earthquake. Thus, it is expected that for this building the amplified Miyagi earthquake record will give the maximum response.

6.3 Loading Cases

The behavior of the structure for the three recorded earthquakes will be discussed in the following section.

6.3.1 1978 Miyagi-Ken-Oki Earthquake

(a) 0.50 g 1978 Miyagi-Ken-Oki Earthquake

0.3PY50 : three dimensional analysis where the structure was subjected to two correlated horizontal components of 0.50 g Miyagi N-S record in the X and Y-directions, and column axial force at every story is initially amplified to three-tenths of its yield value in compression.

0.4PY50 : similar to case 0.3PY50, except column axial force at every story is initially amplified to four-tenths of its yield value in compression.

0.5PY50 : similar to case 0.3PY50, except column axial force at every story is initially amplified to five-tenths of its yield value in compression.

0.6PY50 : similar to case 0.3PY50, except column axial force at every story is initially amplified to six-tenths of its yield value in compression.

(b) 0.75 g 1978 Miyagi-Ken-Oki Earthquake

0.3PY75 : three dimensional analysis where the structure was subjected to two correlated horizontal components of 0.75 g Miyagi N-S record in the X and Y-directions, and column axial force at every story is amplified to three-tenths of its yield value in compression.

0.4PY75 : similar to case 0.3PY75, except column axial force at every story is initially amplified to four-tenths of its yield value in compression.

0.5PY75 : similar to case 0.3PY75, except column axial force at every story is initially amplified to five-tenths of its yield value in compression.

0.6PY75 : similar to case 0.3PY75, except column axial force at every story is initially amplified to six-tenths of its yield value in compression.

(c) Soft Story structure subjected to 0.50 g 1978 Miyagi-Ken-Oki Earthquake

0.6PYSS : three dimensional analysis where the structure was subjected to two correlated horizontal components of 0.50 g Miyagi N-S record in the X and Y-directions, and every column axial force at 3rd story is amplified to six-tenths of its yield value in compression.

6.3.2 1985 Mexico City SCT Earthquake

0.3PYMX : three dimensional analysis where the structure was subjected to 1985 Mexico City SCT earthquake and the column axial force at every story is initially amplified to three-tenths of its yield value in compression. The E-W component of this earthquake, which produces the largest spectral values, is applied in the X-direction and the N-S component is applied in the Y-direction.

0.6PYMX : similar to case 0.3PYMX, except column axial force at every story is initially amplified to six-tenths of its yield value in compression.

6.3.3 1940 El Centro Earthquake

0.6PYEL : three dimensional analysis where the structure was subjected to 1940 El Centro earthquake and the column axial force at every story is initially amplified to six-tenths of its yield value in compression. The N-S component

of this earthquake, which produces the largest spectral values, is applied in the X-direction and the E-W component is applied in the Y-direction.

6.4 Assumptions

The mathematical model of the building uses the same assumptions as used for the symmetrical building described in Sectio 5.1.3.1. As mentioned before, the intensity of column axial load is amplified to three, four, five and six-tenths of its yield value in compression. However, the mass of the structure is assumed constant for every loading case.

6.5 Method of Analysis

The same method of analysis was used here as was used for the symmetrical building described in Section 5.1.4.

6.6 Discussion of the Results

6.6.1 Results for the 0.50 g Miyagi Earthquake Record

The nonlinear dynamic responses of the structure are reported in terms of the base shear, story shear, overturning moment, floor displacement, story drift, column ductility demand and the relationship between column forces and their associated deformations in relation to the ground input excitation. The results from the study are presented below.

6.6.1.1 Story Shears, Floor Forces and Absolute Input Energies

The envelopes of maximum story shear developed in the principal axes of the structure are shown in figure 6.6 and summarized in Tables 6.1 and 6.2. It can be

seen that the largest shear forces correspond to case 0.3PY50. The maximum base shear in the X-direction corresponding to cases 0.3PY50, 0.4PY50, 0.5PY50 and 0.6PY50 are 303, 284, 257 and 213 kips, respectively, and the maximum base shear in the Y-direction are 224, 212, 196 and 163 kips, respectively. Even though the fundamental periods in the two principal directions of the structure are approximately the same, the maximum base shear values developed in these directions are significantly different. The smaller maximum response in the Y-direction follows from the fact that the structure has a smaller story yield shear in the Y-direction.

Figure 6.7 shows the input ground velocity and the base-shear time history responses in the principal directions of the structure. In can be seen that the base shear time history is correlated with the input ground velocity, and there is little variation in the maximum base shear during the response. This is not surprising, because the fundamental periods of the structure are almost the same as the dominant period of the earthquake record and the ground motion is large enough to cause significant yielding. It should be noted that the responses for cases 0.5PY50 and 0.6PY50 stop at approximately 15.5 and 8 seconds of the excitation. As will be shown in Section 6.6.1.6, structural instability occurred for these cases at these times. It should be mentioned that the maximum base shear reported for these cases occurred before structure instability started.

In order to study the effect of different floor force distributions on the ultimate capacity of the structure, nonlinear static analyses were conducted by monotonically applying three lateral force profiles until the structural strength was reached. The first profile has the dynamic floor force profile which was recorded at the time of maximum base shear, figure 6.8. The second set has a uniform profile and the third set has an inverted triangular profile similar to the UBC design distribution. For

this study, the structure was modeled as two-dimensional planar frame. The total base shear in the principal directions of the structure from the 0.5PY50 and 0.6PY50 cases versus the roof displacement correspond to the dynamic, uniform and inverted triangular floor force profiles are shown in figures 6.9 and 6.10. It can be seen that the smallest ultimate base shear corresponds to the inverted triangular profile. Because this profile produces the largest overturning moments for the same base shear value the resulting column axial force reduce the column yield capacities.

Figure 6.11 shows the overturning moment time history in the principal directions of the structure corresponding to case 0.5PY50. The largest overturning moment in X and Y-directions are 155,000 and 130,000 kip-in., respectively, both of which occurred approximately at 15.5 seconds of the excitation and which corresponds to the time structural instability started. Similar results were seen for the response corresponding to case 0.6PY50, figure 6.12, where the largest overturning moment in X and Y-directions are 137,000 and 124,000 kip-in., respectively, which occurred at approximately 7.8 seconds of the excitation.

The ultimate strength of the structure depends, among other things, the ratio of column axial loads to their yield values in compression and the distribution of floor forces along the height of the structure. Nonlinear static monotonic analysis shows that the calculated structure seismic resistance ultimate capacity based on the inverted triangular floor force profile is a lower bound to the actual earthquake response capacity.

The absolute energy input time history in the principal directions of the structure are given in figure 6.13. It can be seen that the largest input energies correspond to case 0.3PY50. The maximum absolute energy input in the X-direction corresponding to cases 0.3PY50, 0.4PY50, 0.5PY50 and 0.6PY50 are 16,800, 15,700, 13,500 and

4,800 kip-in, respectively, and the maximum absolute energy input in the Y-direction are 7,900, 7,700, 7,000 and 4,000 kip-in, respectively. Because the absolute energy input was computed by integrating the product of the structure base shear and the ground velocity input, energy input pulses occur in concurrence with the input ground velocity pulses. It is noted that the absolute energy input is accumulates gradually during the response because the base shear time history is in phase with the input ground velocity. The absolute energy input to the building in the Y-direction is smaller than in the X-direction because the base shear developed in the Y-direction is smaller than in the X-direction. The error in the energy balance, that is the difference between the total input energy and the total output energy divided by the total input energy, are -0.0015, -0.0016, -0.0019 and -0.0019. These ratios correspond to cases 0.3PY50, 0.4PY50, 0.5PY50 and 0.6PY50, respectively.

The envelopes of maximum floor forces are given in figure 6.14. It can be seen that the envelopes of maximum floor force are closer to uniform distribution than an inverted triangular distribution.

By comparing the maximum responses, it was observed that the base shears corresponding to frames with smaller column axial force are larger than those corresponding to frames with larger column axial force. This is true also for absolute input energies and floor forces.

6.6.1.2 Column Axial Force

The envelope of maximum column axial loads and its ratio to their yield values in pure compression are given in figure 6.15. As might be expected, the largest ratio occurs at the first story for all cases and the largest ratio of $0.83P_y$ corresponds to case 0.6PY50, an increase of about $0.23P_y$. It is noted there are only small

differences in the relative increase in column axial load between these cases. This is not suprising, because even though the columns of these frames were initially loaded to different intensities of axial load, all frames used the same beam sections and the motion was large enough to cause significant beam yielding. Moreover, the maximum overturning moments in principal directions occurred at approximately the same time. The increase in column axial load decreases along the height of the structure, and the decrease is nearly linear.

6.6.1.3 Floor Displacement

The envelope of maximum floor displacements in the principal directions of the structure is shown in figure 6.16 and their numerical values are summarized in Tables 6.7 and 6.8. It can be seen that very large displacements occur in the Y-direction corresponding to cases 0.5PY50 and 0.6PY50. However, the maximum floor displacements in the X-direction for case 0.5PY50 and case 0.6PY50 must be viewed with caution because of the Y-direction collapse. Figure 6.17 shows a comparison of the floor C.M displacement time history response in the X-direction of the structure for all cases.

The floor response time histories for C.M displacement in the Y-direction corresponding to all case is shown in figure 6.18. Unlike the response in the X-direction, the presence of large axial load in the column clearly shows structural instability. The single bay unbraced steel frames structure has limited structural redundancy and the unstable response occurred when initial column axial load was larger than four-tenths of the yield value in compression. It can be noted that the larger initial column axial loads produce earlier structural instability. Structural instability corresponding to cases 0.5PY50 and 0.6PY50 occurred approximately 15.5 and 8

seconds into the excitation, respectively. The unstable response will be explained by comparing the column shear force hysteresis curves in Section 6.6.1.6. Even though the frame instability did not occur when the column initial axial load was less than or equal to four-tenths of its yield value in compression, the structure vibrated about a displaced equilibrium position. As might be expected, the shift in equilibrium position in the Y-direction is larger than in the X-direction.

6.6.1.4 Torsional Response

The envelopes of the torsional rotation about the center of mass corresponding to all cases are shown in figure 6.19. The maximum torsional rotation for cases 0.5PY50 and 0.6PY50 must be viewed with caution because of the Y-direction collapse. It can be seen that case 0.4PY50 produce larger response at the first two floors than the response correspond to case 0.3PY50. However, the difference between the responses for these cases is small.

The torsional response will increase or decrease column line displacements depending on the distance between the column line and the C.M and the phase of the torsional and translational vibrations. It can be seen from figure 6.20 that the maximum ratio of edge to C.M displacements due to this torsion is less than 1.05 correspond to case 0.4PY50. This implies that the torsional response for the initially symmetric structure is not important, that is the response is primarily in translation for this type of structure.

6.6.1.5 Story Drift

Figure 6.21 shows envelopes of maximum story drift in the principal directions of the structure. The numerical values of this response are tabulated in Tables 6.9

and 6.10. All responses show a concentration of large relative displacement at the 2nd story of the structure, which is the most flexible for this structure. It can be seen that case 0.5PY50 produced larger story drifts at all stories. As will be shown in Section 6.6.1.6, the negative slope of the shear force hysteresis curve for this case initiated at larger story drift than case 0.6PY50.

The smaller base shear values and larger story displacements and story drifts for frames with larger initial axial loads implies that the increased of axial loads reduces the effective column stiffness.

6.6.1.6 Column Ductility Ratio

The envelope of maximum column ductility ratio is shown in figure 6.22 and their values are given in Tables 6.11 and 6.12. It can be seen that extensive yielding occurred in the structure, particularly in the Y-direction. It is not surprising to see that the largest column ductility ratios correspond to cases 0.5PY50 and 0.6PY50 because unstable response occurred for these cases.

Figures 6.23 and 6.24 present the column shear force versus story drift hysteresis curves for columns 16 and 20, which are located at the 2nd and 1st stories respectively. It can be seen that the large column axial loads reduce column yield strength and increase lateral deformation, or induce unstable response when the story drift is large, for the weak axis (Y) of the column. This shows the importance of column axial load on restoring force capabilities in multistory buildings. The negative slope of the hysteresis curves in the Y-direction for cases 0.5PY50 and 0.6PY50 should be noted. This negative slope started at at larger story drift values for case 0.5PY50 than for case 0.6PY50.

6.6.2 Effect of Ground Acceleration Intensity

The nonlinear dynamic response of the structure subjected to the Miyagi-Ken-Oki earthquake record at 0.75 g is compared to similar responses at 0.5 g below.

6.6.2.1 Story Shears, Floor Forces and Absolute Input Energies

The envelopes of maximum story shear developed in the principal directions of the structure are shown in figure 6.25 and their numerical values are given in Tables 6.1 and 6.2. Similar to the 0.5 g Miyagi responses, the largest shear force correspond to case 0.3PY75. The maximum base shear in the X-direction corresponding to cases 0.3PY75, 0.4PY75, 0.5PY75 and 0.6PY75 are 325, 319, 229 and 207 kips, respectively, and the maximum base shear values in the Y-direction are 230, 223 192 and 148 kips, respectively. It should be noted that a fifty percent increase in the ground motion acceleration resulted in a very small increases in the maximum story shears. This implies that the ultimate capacity of the structures had been nearly achieved with the 0.5 g input ground motion.

The ratio of the difference between the total input energy and the total output energy to the total input energy, are -0.0028, -0.0029, -0.0030 and -0.0026. These ratios correspond to cases 0.3PY75, 0.4PY75, 0.5PY75 and 0.6PY75, respectively.

6.6.2.2 Column Axial Force

Figure 6.26 shows the envelope of maximum column axial load and its ratio to their yield values in compression. As might be expected, the largest ratio occurs at the first story for all cases and the largest ratio corresponding to case 0.6PY75 is $0.84P_y$, an increase about $0.24P_y$. Similar to 0.5 g Miyagi response, there are only small differences in the increase of column axial loads between all cases. The increase

in column axial load decreases nearly linearly along the height of the structure. It should be noted that a fifty percent increase in the ground motion acceleration resulted in practically no increase in the maximum column axial forces.

6.6.2.3 Floor Displacement

Figure 6.27 shows the envelopes of maximum displacement in the X and Y-directions and their values are given in Tables 6.7 and 6.8. It can be seen that very large displacements occur in the Y-direction corresponding to cases 0.4PY75, 0.5PY75 and 0.6PY75. The major difference between the 0.5 g and 0.75g Miyagi responses is that the structural instability occurs in the Y-direction for case 0.4PY75 in addition to cases 0.5PY75 and 0.6PY75, figure 6.28. Moreover, unstable response corresponding to cases 0.5PY75 and 0.6PY75 occur earlier in comparison to cases 0.5PY50 and 0.6PY50. For case 0.3PY75, a fifty percent increase in ground motion acceleration produced a doubling of the floor displacement in the X-direction and a tripling in the Y-direction.

6.6.2.4 Story Drift

Envelopes of the maximum story drift in the principal directions of the structure are given in figure 6.29 and their numerical values are given in Tables 6.9 and 6.10. Similar to 0.5 g Miyagi response, it can be seen that the maximum story drift occurs at the 2nd story for all cases. It is interesting to note that for the increased ground motion, the story shear values remained practically the same while the story displacements increase severely. In particular, the response corresponding to case 0.3PY75 has a large increase.

6.6.2.5 Column Ductility Ratio

The envelopes of the maximum column ductility ratio are shown in figure 6.30 and their values are given in Tables 6.11 and 6.12. It can be seen that extensive yielding occurred in the structure, particularly in the Y-direction. It is not surprising to see that the largest column ductility ratio corresponds to cases 0.4PY75, 0.5PY75 and 0.6PY75, because the structure experienced large story drifts for these cases. It is noted that the maximum ductility ratios in the principal directions of the structure for case 0.3PY75 are 15.0 and 25.9. For this case, a fifty percent increase in the ground motion acceleration produced a dramatic increase in maximum column ductility ratios. It is unlikely that the columns would be able to achieve these large ductility values before failure.

Figures 6.31 and 6.32 show the column shear force versus story drift hysteresis curves for columns 16 and 20, which are located at the 2nd and 1st floor. Similar to 0.5g Miyagi response, the large axial loads reduce column yield strength and increase lateral deformation, or induce unstable response when the story drift is large, particularly for the weak axis (Y) of the column. Note the negative slope of the hysteresis curves in the Y-direction for case 0.4PY75, 0.5PY75 and 0.6PY75.

6.6.3 Results of Soft Story Structure Subjected to 0.50 g Miyagi Earthquake

6.6.3.1 Story Shears, Floor Forces and Absolute Input Energies

The envelopes of maximum story shear in the principal axes of the structure corresponding to cases 0.6PYSS and 0.6PY50 are shown in figure 6.33 and their values are given in Tables 6.1 and 6.2. The maximum base shear in the X and Y-

directions corresponding to case 0.6PYSS are 300 and 221 kips, respectively, which are larger than the maximum base shear corresponding to case 0.6PY50.

Figure 6.34 shows the input ground velocity and the base-shear time history responses in the principal directions of the structure. It can be seen that the base shear time history is in phase with the input ground velocity. It is noted that the response corresponding to case 0.6PYSS stopped at approximately 12 seconds of the excitation and the maximum base shear occurred before the structure instability started. Figure 6.35 shows the overturning moment time histories in the principal directions of the structure corresponding to case 0.6PYSS. The largest overturning moment in Y-direction which occurred at approximately 12 seconds in the 3rd story is 92,400 kip-in.

Figure 6.36 shows the absolute energy input time history in the principal directions of the structure. It can be seen that the maximum absolute energy input in the X and Y-directions are 12,000 and 6,300 kip-in, respectively. These are larger than the maximum absolute energy input correspond to case 0.6PY50 because the base shear corresponding to case 0.6PYSS is larger than for case 0.6PY50 and the earthquake duration corresponding to case 0.6PYSS is longer than for case 0.6PY50. Similar to case 0.6PY50, it is noted that the absolute energy input accumulates gradually during the response. The ratio of the difference between the total input energy and the total output energy to the total input energy correspond to case 0.6PYSS is -0.0010.

6.6.3.2 Floor Displacement

Figure 6.37 shows the envelopes of maximum floor displacement in the principal directions of the structure and their numerical values are given in Tables 6.7 and 6.8.

It can be seen that very large displacements occur at the 3rd floor the Y-direction correspond to case 0.6PYSS. This is not surprising because the initial column axial load for the 3rd story was increased to six-tenths of its yield value in compression. It will be shown in Section 6.6.3.5 that the presence of large column axial load induces structural instability in the Y-direction at this story. Figures 6.38 and 6.39 show the 3rd and 4th floor C.M displacement time history response in the X and Y-directions of the structure corresponding to case 0.6PYSS. These figures show that structural instability occurred in the Y-direction at approximately 12 seconds into the excitation.

6.6.3.3 Torsional Response

The envelopes of the torsional rotation about the center of mass are shown in figure 6.40. As might be expected, there is a significant difference in the response between the upper and lower parts of the structure corresponding to case 0.6PYSS because structural instability occurred at the 3rd story. Consequently, the 3rd floor was excited into the inelastic range more heavily than the other floors.

6.6.3.4 Story Drift

Figure 6.41 shows envelopes of maximum story drift in the principal directions of the structure. The numerical values of this response are tabulated in Tables 6.9 and 6.10. It can be seen that the response corresponding to case 0.6PYSS shows a concentration of large relative displacement at the 3rd story of the structure. Figure 6.42 shows the 2nd and 3rd floor story drift time histories in the Y-direction. It is noted that the story drift corresponding to case 0.6PYSS vibrates about a displaced equilibrium position after at approximately 8 seconds and the structural instability

occurred at the 3rd story at approximately 12 seconds.

6.6.3.5 Column Ductility Ratio

The envelopes of maximum column ductility ratio are shown in figure 6.43 and their values are given in Tables 6.11 and 6.12. It is not surprising to see that the largest column ductility ratios correspond to case 0.6PYSS and occurred at the 3rd story in the Y-direction because unstable response occurred at this story.

Figures 6.44 and 6.45 illustrate the column shear force versus story drift hysteresis curves corresponding to case 0.6PYSS for columns 12 and 16, which are located at the 3rd and 2nd story, respectively. Similar to the 0.6PY50 response, large column axial load induced unstable response when story drift is large. It is noted that the negative slope of the hysteresis curve increase as the story drift increases in the weak axis (Y) of the column 12.

6.6.4 Results for the Mexico Earthquake Record

6.6.4.1 Story Shears, Floor Forces and Absolute Input Energies

The envelopes of maximum story shear developed in the principal axes of the structure are shown in figure 6.46 and given in Tables 6.1 and 6.2. It can be seen that the largest story shear in X-direction corresponds to case 0.3PYMX and the largest story shear in Y-direction corresponds to case 0.6PYMX. The maximum base shear in the X-direction corresponding to cases 0.3PYMX and 0.6PYMX are 105 and 88 kips, respectively, and the maximum base shear in the Y-direction are 74 and 111 kips, respectively. It is noted that the maximum base shear in the principal directions of structure are mixed. As mentioned before, the building translational period in the X and Y-direction are 0.9 and 1.05 seconds and the E-W component of

this earthquake record was applied in the X-direction and the N-S component was applied in the Y-direction. As will be shown in Section 6.6.4.6, this earthquake was not large enough to cause significant yielding, case 0.3PYMX produced nearly linear response and case 0.6PYMX produced small yielding. Consequently, the change in the effective period of the structure corresponding to case 0.3PYMX is smaller than for case 0.6PYMX. Moreover, the change in period in the Y-direction is larger than the change in period in the X-direction, because Y-direction yields more. The larger maximum response in the X-direction corresponding to case 0.3PYMX follows from the fact that the E-W component spectra is descending at periods slightly larger than 1.0 second. The spectrum decreases with increasing period within the range of 1.0 to 1.10 seconds with the spectral values of 0.34 g to 0.24 g. The smaller maximum response in the Y-direction corresponding to case 0.3PYMX follows from the fact that the N-S component spectra is ascending at periods slightly larger than 1.0 second. The spectrum increase with increasing period within the range of 1.0 to 1.10 seconds with the spectral values of 0.18 g to 0.26 g.

Figure 6.47 shows the input ground velocity and the base-shear time histories in the principal directions of the structure. In can be seen that the input ground velocity in the X and Y-directions are almost a harmonic function with a period of 2 seconds and the base shear response in the X and Y-directions have periods approximately equal to 1 second. This portion of the E-W component ground velocity is characterized by eleven distinct velocity pulses. The ninth pulse is the largest having a maximum amplitude of 33.35 inch/second at $T = 17.349$ seconds of the record, which is larger than the maximum ground velocity corresponding to the 0.5 Miyagi earthquake. This portion of the N-S component ground velocity is characterized by eleven distinct velocity pulses. The ninth pulse is the largest having

a maximum amplitude of 21.42 inch/second at $T = 13.590$ seconds of the record, which is smaller than the maximum ground velocity corresponding to the 0.5 Miyagi earthquake. Unlike the Miyagi response, the input ground velocity pulses are not always accompanied by peaks in the base shear response.

Figure 6.48 shows the absolute energy input time histories in the principal directions of the structure. It can be seen that the largest energies in the X and Y-directions correspond to cases 0.3PYMX and 0.6PYMX, respectively. The maximum absolute energy input in the X-direction corresponding to cases 0.3PYMX and 0.6PYMX are 820 and 620 kip-in, respectively, and the maximum absolute energy input in the Y-direction are 290 and 520 kip-in, respectively. It should be noted that these maximum responses for the Mexico earthquake are much smaller than the maximum energies for a similar structure subjected to 0.5 g Miyagi earthquake. The smaller maximum response correspond to the Mexico earthquake follows from the fact that the Mexico record has smaller velocity spectra in comparison to 0.5 g Miyagi record. The error in the energy balance are -0.0010 and -0.0005. These ratios correspond to cases 0.3PYMX and 0.6PYMX respectively.

Figure 6.49 shows the envelopes of maximum floor forces. It can be seen that the maximum floor forces follows the story shear pattern, where the maximum response in the X-direction corresponds to case 0.3PYMX and the maximum response in the Y-direction corresponds to case 0.6PYMX. It is noted that the floor force distributions are similar to the UBC design force distribution.

By comparing the maximum responses corresponding to cases 0.3PYMX and 0.6PYMX, it was observed that the maximum responses are mixed for base shear, absolute input energy and floor force because the input ground motion in the X and Y-directions have different spectral characteristics within the period range of

interest.

6.6.4.2 Column Axial Force

Figure 6.50 shows the envelope of maximum column axial loads and their ratio to yield load. As might be expected, the largest ratio occurs at the first story for all cases and the largest ratio which corresponds to case 0.6PYMX is $0.69P_y$, an increase about $0.09P_y$. There are only small differences in the amount of increase of columns axial load between cases 0.3PYMX and 0.6PYMX. The increase in column axial load decreases along the height of the structure nearly linearly.

6.6.4.3 Floor Displacement

Figure 6.51 shows the envelope of maximum floor displacements in the principal directions of the structure and their numerical values are given in Tables 6.7 and 6.8. Similar to story shear response, it can be seen that the largest response in X-direction corresponds to case 0.3PYMX and the largest response in Y-direction corresponds to case 0.6PYMX. The maximum floor displacements in the X-direction corresponding to cases 0.3PYMX and 0.6PYMX are 3.72 and 3.34 inches, respectively, and the maximum floor displacements in the Y-direction are 3.80 and 7.02 inches, respectively. Unlike Miyagi response, structural instability does not occur even though the column initial axial load was amplified to six-tenths of its yield value in compression, because the Mexico earthquake at these structural period is not strong enough to cause significant yielding.

The floor response time histories for C.M displacement, floor torsional rotation and edge displacement in the X-direction corresponding to case 0.6PYMX are shown in figure 6.52. It can be seen that the maximum response for the 1st floors occurred

at approximately 17.9 seconds into the excitation. The maximum response started at the 1st floor and followed by the 2nd, 3rd, 4th and 5th floors, respectively.

6.6.4.4 Torsional Response

The envelopes of the rotation about the center of mass corresponding to cases 0.3PYMX and 0.6PYMX are shown in figure 6.53. It can be seen that a doubling of the initial column axial force resulted in approximately a three fold increase in the maximum floor rotation. However, the maximum floor rotation is very small.

6.6.4.5 Story Drift

Figure 6.54 shows envelopes of maximum story drift in the principal directions of the structure. The numerical values of this response are tabulated in Tables 6.9 and 6.10. It can be seen that the largest relative displacement occurred at the second story of the structure, which is the most flexible for this structure. It is noted that the story drift response has a pattern similar to the maximum floor force response, where the maximum response in the X-direction corresponds to case 0.3PYMX and the maximum response in the Y-direction corresponds to case 0.6PYMX. The largest story drifts in the X-direction which correspond to cases 0.3PYMX and 0.6PYMX are 0.94 and 0.87 inches, respectively, or approximately 0.007 and 0.006 times the story height. The largest story drifts in the Y-direction are 1.00 and 2.01 inches, respectively, or approximately 0.007 and 0.014 times the story height.

6.6.4.6 Column Ductility Ratio

The envelope of maximum column ductility ratio is shown in figure 6.55 and their values are given in Tables 6.11 and 6.12. Similar to story drift response, the

maximum column ductilities in the X-direction corresponds to case 0.3PYMX and the maximum ductilities in the Y-direction corresponds to case 0.6PYMX. The largest ductility ratios in the X-direction which correspond to cases 0.3PYMX and 0.6PYMX are 1.5 and 1.4, respectively, and the largest ductility ratios in the Y-direction are 1.4 and 2.8.

Figures 6.56, 6.57 and 6.58 show the column shear force versus story drift hysteresis curves for columns 20, 16 and 12, which are located at the 1st, 2nd and 3rd stories, respectively. It can be seen that Mexico record at these structural response periods is not large enough to cause significant yielding for this structure. Case 0.3PYMX had nearly linear response and case 0.6PYMX had amounts of small yielding. It is noted that large axial column loads increase lateral deformation, especially in the weak axis (Y) direction of the column.

6.6.5 Results for the 0.68 g El Centro Earthquake Record

In the previous study by Wu and Hanson [73], various ground motion intensity indices were introduced and normalized to the N-S component of 1940 El Centro earthquake. Using peak ground acceleration as a scaling factor, it was found that the Miyagi record should be scaled down by a factor of 0.84. Because the Miyagi used in this study was amplified to 0.5 g, for the El Centro record, an earthquake of larger magnitude was approximated by increasing the peak acceleration of the record twice as large as its original value to 0.68 g.

The nonlinear dynamic responses of the structure are reported in terms of the base shear, story shear, overturning moment, floor displacement, story drift, column ductility demand and the relationship between column forces and their associated deformations in relation to the ground input excitation. The results from the study

are presented below.

6.6.5.1 Story Shears, Floor Forces and Absolute Input Energies

The envelopes of maximum story shear developed in the principal axes of the structure are shown in figure 6.59 and given in Tables 6.1 and 6.2. The maximum base shear in the X and Y-directions corresponding to cases 0.6PYEL are 258 and 167 kips, respectively, which are larger than the maximum base shear correspond to case 0.6PY50. The larger the maximum story shears correspond to the El Centro earthquake follows from the fact that the increase in column axial loads correspond to case 0.6PYEL is smaller in comparison to case 0.6PY50, as shown in figure 6.60. Moreover, the maximum base shears in the X and Y-directions corresponding to case 0.6PYEL occur at different times. However, the difference between the maximum base shear for these cases is not large, particularly the maximum base shear in the Y-direction.

Figure 6.61 shows the input ground velocity and the base-shear time history responses in the principal directions of the structure. It is noted that the input ground velocities of the El Centro earthquake are irregular in comparison to the input ground velocity corresponds to the Miyagi and Mexico earthquake records. It can be seen that the base shear time history is not in phase with the input ground velocity, and there is substantial variation in the base shear magnitude during the response, particularly the base shear in the X-direction. The N-S component ground velocity is characterized by five distinct velocity pulses. The second pulse is the largest having a maximum value of 30.19 inch/second at $T = 2.173$ seconds of the record. The E-W component ground velocity is characterized by four distinct velocity pulses. The second pulse is the largest having a maximum value of 38.24 inch/second

at $T = 2.143$ seconds. Both of these are larger than the maximum ground velocity of the 0.5 g Miyagi earthquake. Unlike the responses to the Miyagi earthquake, the input ground velocity pulses are not always accompanied by peaks in the base shear response.

Figure 6.62 shows the absolute energy input time history in the principal directions of the structure. Input energy pulses occur in concurrence with the input ground velocity pulses. The maximum absolute input energies in the X and Y-directions corresponding to case 0.6PYEL are 2,947 and 2,100 kip-in, respectively. They are smaller than the 0.5 g Miyagi earthquake input energies even though the maximum base shear and the maximum input ground velocities for the El Centro earthquake are larger than 0.5 g Miyagi earthquake. The smaller maximum absolute energy input corresponding to the El Centro earthquake results from the uncoupling of base shear and the input ground velocities. The absolute energy input to the building in the Y-direction is smaller than in the X-direction because the base shear in the Y-direction is smaller than in the X-direction. The error in the energy balance is -0.0009.

Figure 6.63 shows the overturning moment time histories in the principal directions of the structure corresponding to case 0.6PYEL. The largest overturning moments in X and Y-directions are 121,000 and 97,200 kip-in., respectively, which occurred at approximately 4.37 and 9.01 seconds. The maximum overturning moment is smaller for case 0.6PYEL than for case 0.6PY50.

Figure 6.64 shows the envelopes of maximum floor forces. It can be seen that the maximum floor force distributions are closer to uniform distribution than the inverted triangular UBC design force distribution.

By comparing these maximum responses corresponding to El Centro and Miyagi

earthquake excitations, it was observed that the component of base shears and the input ground velocities in the X and Y-directions corresponding to El Centro excitation are larger than those corresponding to Miyagi excitation. However, the absolute energies input are smaller.

6.6.5.2 Column Axial Force

Figure 6.65 shows the envelope of maximum column axial loads and their yield ratio values. As might be expected, the largest yield ratio occurs in the first story for all cases and the value corresponding to case 0.6PYEL is $0.76P_y$, an increase about $0.16P_y$. It is interesting to note that even though the maximum base shear corresponding to case 0.6PYEL is larger than for case 0.6PY50, the maximum column axial load corresponding to case 0.6PYEL is smaller because the maximum base shears in the X and Y-directions occur at different times. Also there is substantial variations in the base shear magnitude throughout the response in the principal directions of the structure. The increase in column axial load decreases nearly linearly along the height of the structure.

6.6.5.3 Floor Displacement

Figure 6.66 shows the envelope of maximum floor displacements in the principal directions of the structure and their numerical values are given in Tables 6.7 and 6.8. The maximum floor displacements in the X and Y-directions which correspond to case 0.6PYEL are 9.8 and 11.3 inches, respectively. Structural instability does not occur even though the column initial axial load was amplified to six-tenths of its compression yield value, because the overturning moment correspond to case 0.6PYEL not large enough to significantly increase the column axial loads.

The floor response time histories for C.M displacement, floor torsional rotation and edge displacement in the Y-direction corresponding to case 0.6PYEL are shown in figure 6.67. It can be seen that the torsional contribution to the edge displacement is very small and the response primarily in translation. This figure shows that the structure begins vibrating about a displaced equilibrium position at approximately 2.5 seconds. However, the shift in equilibrium position is smaller than for a similar structure subjected to 0.5 g Miyagi. Similar observations can be made for responses in the X-direction.

6.6.5.4 Story Drift

Figure 6.68 shows envelopes of maximum story drift in the principal directions of the structure. The numerical values are tabulated in Tables 6.9 and 6.10. A large relative displacement occurs at the 2nd story of the structure, which is the most flexible for this structure. The largest story drifts in the X and Y-directions corresponding to case 0.6PYEL are 2.6 and 3.4 inches, respectively, which are approximately 0.018 and 0.024 times the story height. It is interesting to note that even though the maximum base shears corresponding to case 0.6PYEL is larger than for case 0.6PY50, their floor displacements and story drifts are smaller.

6.6.5.5 Column Ductility Ratio

The envelopes of maximum column ductility ratio are shown in figure 6.69 and their values are given in Tables 6.11 and 6.12. The largest ductility ratios in the X and Y-directions which correspond to case 0.6PYEL are 4.6 and 5.7, respectively. These are smaller than for case 0.6PY50.

Figure 6.70 shows the column shear force versus story drift hysteresis curves for

column 16, which is located at the 2nd story. It can be seen that El Centro record does not induce unstable response even though the column initial axial load was amplified to six-tenths of its yield value and the maximum peak ground acceleration was amplified to 0.68 g.

CHAPTER 7

SUMMARY AND CONCLUSIONS

7.1 Summary of Torsional Behavior of Three-Dimensional Steel Moment Frame Structures Subjected to Unidirectional and Bidirectional Ground Excitations

This study examined the seismic response of special moment-resistant steel frames, which were proportioned in accordance with the 1988 UBC. The objective of this study was to compare inelastic earthquake responses to unidirectional and bidirectional earthquake ground motion for a doubly symmetric building configuration as well as for a torsionally sensitive building configuration. The dynamic excitation used for this study was an amplified North-South component of the 1978 Miyagi-Ken-Oki earthquake. The effect of ground intensity was studied by increasing the peak acceleration to 0.75 g.

In order to evaluate the structure behavior, the floor diaphgrams of the five story symmetrical and L-shape structures were assumed to be completely rigid in their own plane and the mass of the structure was assumed to be lumped at the center of mass at each floor. Only the horizontal translational and torsional masses were included in the analyses. The reduction in frame stiffness due to column axial load and change in geometry was incorporated by using a geometrical stiffness matrix which includes the P-Δ effect. Moreover, it was assumed that the member strength is based on bare

member strength, and that the steel material has kinematic hardening with yield strength of 36 ksi and 5% strain hardening. It was assumed that the structure has zero damping and no accidental eccentricity.

The response of the system to the selected ground motion was determined by solving the equations of motion by a numerical, step-by-step integration procedure. The time scale was discretized into equal intervals of 0.001 second and the event-to-event solution strategy was used to control the equilibrium errors. Any significant event occuring within the element such as yielding, overshooting, unloading, etc., was used to determine the need for a substep. The tangent stiffness was modified in each substep, and hence the force unbalance created by the numerical procedure was reduced to a small value. In the case that the largest unbalance load was larger than a specified tolerance, the current step was repeated with a time step reduced by half. If the unbalance load was less than the tolerance, any error at the end of the time step was eliminated by adjusting the nodal accelerations to satisfy equilibrium, or an equilibrium correction in the following time step was applied if the structure had zero mass associated with that equilibrium term. The largest ratio of the difference between the total input energy and the total output energy to the total input energy was -0.0054. This ratio came from the L-shape building response when subjected to bidirectional case X+Y for 0.75 g Miyagi earthquake input.

The effects of ground motion coupling on the ultimate capacity of these buildings are observed by studying the base shear, story displacement, story drift, column ductility demand and the relationship between column internal forces and their associated deformations in relation to the ground input excitation.

The results are presented in Sections 5.1 and 5.2, and observations base on these results are strictly applicable only to the structures and the earthquake records used

in this study. However, it is expected that many of the response characteristic seen in this study will be applicable to other structures and other ground motions.

7.2 Summary of Dynamic Instabilities of Three-Dimensional Symmetrical Steel Moment Frame Structures Subjected to Large Column Axial Loads and Bidirectional Ground Excitations

This study examined the seismic response of special moment-resistant steel frames which were subjected to large column axial loads and bidirectional ground motions with different characteristics. The objective was to compare the effects of different bidirectional earthquake characteristics on the dynamic structural stability of a doubly symmetric building configuration at initial axial column loads of three, four, five and six-tenths of their yield values. Three recorded earthquake ground motions having different intensities, duration and frequency content were selected to study the three dimensional steel moment frame structure behavior. The selected accelerogram were the 1978 Miyagi-Ken-Oki earthquake (N-S component used in each direction) amplified to 0.5 g, the 1940 El Centro earthquake (N-S and E-W components) amplified by a factor of two and 1985 Mexico City SCT earthquake (N-S and E-W components). The effect of increased ground motion intensity was studied using a 0.75 g Miyagi earthquake.

The floor diaphgrams of the five story symmetrical structure were assumed to be completely rigid in their own plane and the mass of the structure was assumed to be lumped at the center of mass at each floor so that only two horizontal and one torsional mass per floor were included in the analyses. The effect of column axial load and change in geometry on frame stiffness was incorporated by using a geometrical stiffness matrix which included the P-Δ effect. Moreover, it was assumed that

member strength was based on bare member strength, and that the steel material has kinematic hardening with yield strength of 36 ksi and 5% strain hardening. It was assumed that the structure had zero damping and no accidental eccentricity.

The response of the system to the selected ground motions was determined by solving the equations of motion by a numerical, step-by-step integration procedure. The time scale was discretized into equal intervals of 0.001 second and an event-to-event solution strategy was used to control the equilibrium errors. Any significant event occuring within an element such as yielding, overshooting, unloading, etc., was used to determine the need for a substep. The tangent stiffness was modified in each substep, and the force unbalance created by the numerical procedure was reduced to a small value. In the case that the largest unbalance load was larger than a specified tolerance, the current step was repeated with a time step reduced by half. If the unbalance load was less than the tolerance, any error at the end of the time step was eliminated by adjusting the nodal accelerations to satisfy equilibrium, or an equilibrium correction in the following time step was applied if the structure had zero mass associated with that equilibrium term. The largest ratio of the difference between the total input energy and the total output energy to the total input energy was -0.0030. This ratio came from the building subjected to case 0.6PY75 for 0.75 g Miyagi earthquake input.

The effects of ground motion intensity, duration, frequency content and column axial load on the ultimate capacity of symmetrical multi-story building were observed by studying the base shear, story shear, overturning moment, floor displacement, story drift, column ductility demand and the relationship between column internal forces and their associated deformations in relation to the ground input excitation.

The results are presented in Sections 6.6.1, 6.6.2, 6.6.3, 6.6.4 and 6.6.5, and

observations based on these results are strictly applicable only to the structure and the earthquake records used in this study. However, it is expected that many of the response characteristics seen in this study will be applicable to other structures and other ground motions.

7.3 Conclusions of Torsional Behavior of Three-Dimensional Steel Moment Frame Structures Subjected to Unidirectional and Bidirectional Ground Excitations

The following conclusions can be made with respect to the nonlinear response of doubly symmetric and torsionally sensitive buildings subjected to uni and bidirectional loading.

(1) The component of base shear in the principal direction of the structure which correspond to unidirectional excitation is larger than that of bidirectional excitation. This is true also for floor forces and absolute input energies.

(2) A fifty percent increase in the the ground motion peak acceleration resulted in almost a hundred percent increase in the energy input to the structure, but a small increase in the maximum base shear or floor forces.

(3) The torsional response developed in the initially symmetric structure was not important. The nonlinear response remained primarily translational. In the torsionaly sensitive building, the phasing of the ground excitations can amplify or deamplify the torsional motion. In certain cases, the response is primarily translational motion, while in other cases, the response gives translational and torsional motions.

(4) The inelastic torsional response is smaller than that which would be predicted from elastic response results for the torsionally sensitive building. The major

difference between the inelastic and elastic responses is the smaller torsional contribution to the edge displacement in the inelastic response. The decrease in torsional response increases nearly linearly along the height of the structure.

(5) Under the increased ground motion from 0.5 g to 0.75 g peak ground acceleration, the torsional motion was less significant in affecting the structure lateral-torsional reponse. This is reflected in the reduction of the orthogonal base shear and no increase or a reduction in the maximum torsional rotation. From this observation, it can be concluded that the torsional motion is less significant in affecting the structure lateral-torsional response of a weaker structure in comparison to a stronger structure.

(6) The hysteresis loops for columns subjected to bidirectional earthquake inputs are larger than that for unidirectional inputs, which implies a reduced effective story stiffness under bidirectional loading. This behavior is dramatically shown for the increased ground motion.

(7) A large increases in column deformation capabilities are needed for bidirectional earthquake input in comparison with unidirectional input. This was illustrated by the larger column rotations and ductility ratios for the bidirectional input response.

(8) Bidirectional input resulted in a reduced column strength in comparison with unidirectional input. In member terms, this is reflected by smaller biaxial column yield strengths. In global terms, this is reflected by smaller base shear capacities.

(9) For the inelastic response, uneven distribution of nonlinearity along the plan and height of the building changes the torsional motion. These changes in torsional response produce results different than expected from corresponding elastic response results. The maximum story drift shifts from the soft side of the building to the stiff side.

7.4 Conclusions of Dynamic Instabilities of Three-Dimensional Symmetrical Steel Moment Frame Structures Subjected to Large Column Axial Loads and Bidirectional Ground Excitations

The following conclusions can be made with respect to the nonlinear response of doubly symmetric buildings subjected to bidirectional loading and large axial column loads.

(1) The presence of large axial column loads affect their load-displacement hysteresis curves. When the story drifts are large the instability appears in the hysteretic behavior and this induces the unstable feature of a structure. The larger initial column axial loads produce earlier structural instability.

(2) The dynamic ultimate strength of the structure depends on the column axial load yield ratio in compression and the distribution of floor forces along the height of the structure. Nonlinear static analysis shows that the calculated structure ultimate capacity based on the inverted triangular floor force profile is a lower bound to actual earthquake response capacity.

(3) The torsional response developed in the initially symmetric structure with large axial loads was not important. The nonlinear response remained primarily translational.

(4) A large increases in column deformation capabilities are needed for structure subjected to bidirectional earthquakes and large column axial loads. This was illustrated by the large column ductility ratio demands.

(5) The hysteresis loops for columns with higher axial loads are larger than that for smaller axial loads. This implies that a reduced effective story stiffness will occur when large axial loads exist. This is reflected in larger floor displacements and story drifts, and smaller base shear values.

(6) Structures with a weak story and limited structural redundancy should be avoided for seismic resistance. In these structures, plastic deformation is concentrated at a particular story level. Large drift and yielding in the columns of this story under combined biaxial bending and axial force induce frame instability and collapse of the entire structure.

7.5 Future Studies

As a result of this initial investigation, several additional studies are suggested for future work. Briefly these are :

(1) It was assumed that the structures had zero damping. This assumption resulted in a relatively high ductility ratios for the columns in the lower stories of the structure during bidirectional ground excitation. It is recommended that damping be included in future investigations.

(2) This study showed that moment-resistant structures subjected to large bidirectional ground motions produced high column ductility demands. It would be valuable to study dual framing systems for similar ground motion conditions. It is expected that a combination of braced-frame and moment-resistant frame

structures would reduce the effect of biaxial flexural loading on the column yield strength and deformation. Moreover, braced frames can increase the torsional rigidity of the structure.

(3) The dynamic excitation used for study of torsional behavior of three-dimensional steel moment frame structures was the North-South component of the 1978 Miyagi-Ken-Oki earthquake, which is an impulse type ground motion. Moreover, it was assumed that the ground excitations acting in both principal directions of the structure were in phase, which implies that the maximum excitation occurs at the same time in each direction of the structure. Response to other strong motion earthquake records should be studied.

(4) It was assumed that the steel was kinematic hardening material. It would be interesting to see the response corresponding to isotropic hardening or a combination of kinematic and isotropic hardening material under similar conditions. The option for isotropic or combination of kinematic and isotropic hardening material has been implemented in the current program.

(5) It was assumed that the structures had zero accidental eccentricity. The effect of accidental eccentricity should be investigated.

(6) Structure with nonuniform vertical stiffness distribution should be investigated.

(7) The structure used for this study was five story steel moment frame structures. Taller structures should be investigated.

Table 5.1: Lateral force distribution for symmetrical structure

Floor No.	Floor Weight (kips)	Lateral Force (kips)
5	57.6	5.95
4	86.4	5.69
3	86.4	4.26
2	86.4	2.84
1	86.4	1.42

Table 5.2: Maximum Story Shear, Floor Force and Column Ductility Ratio of Five Story Symmetrical Structure (X-direction : 0.50 g and 0.75 g Miyagi)

Load case	Story No.	Story Shear (kips)		Floor Force (kips)		Column Ductility	
		0.50 g	0.75 g	0.50 g	0.75 g	0.50 g	0.75 g
(X+Y)	5	89.4	87.7	89.4	87.7	4.28	2.93
	4	163.6	174.7	122.9	119.2	6.20	5.06
	3	215.8	234.0	105.2	104.8	7.33	7.88
	2	256.3	270.4	93.2	107.3	7.33	8.96
	1	302.9	324.7	88.3	75.9	5.84	5.16
(X)	5	90.2	97.1	90.2	97.1	4.95	6.53
	4	177.6	184.8	141.0	147.0	6.41	8.96
	3	245.8	246.6	112.0	128.7	7.18	10.25
	2	259.2	269.2	100.4	127.7	7.18	10.25
	1	313.7	343.9	91.7	110.0	5.27	8.66

Table 5.3: Maximum Story Shear, Floor Force and Column Ductility Ratio of Five Story Symmetrical Structure (Y-direction : 0.50 g and 0.75 g Miyagi)

Load case	Story No.	Story Shear (kips)		Floor Force (kips)		Column Ductility	
		0.50 g	0.75 g	0.50 g	0.75 g	0.50 g	0.75 g
(X+Y)	5	69.3	82.7	69.3	82.7	3.25	4.40
	4	120.1	129.1	84.8	92.2	4.70	9.82
	3	152.6	171.5	77.0	103.6	7.27	23.37
	2	186.5	220.3	82.3	89.5	8.79	24.49
	1	223.7	230.3	67.5	79.5	9.29	25.88
(Y)	5	63.2	71.5	63.2	71.5	3.79	5.69
	4	139.2	159.2	96.0	105.2	5.52	11.44
	3	175.9	180.9	84.3	97.5	7.92	16.95
	2	199.2	216.9	74.6	87.3	7.92	16.95
	1	235.9	237.2	61.2	77.8	7.38	10.83

Table 5.4: Maximum Floor Displacement and Story Drift of Five Story Symmetrical Structure (X-direction : 0.50 g and 0.75 g Miyagi)

Load case	Story No.	Floor Disp. (in.)		Story Drift (in.)	
		0.50 g	0.75 g	0.50 g	0.75 g
(X+Y)	5	16.44	30.95	2.06	2.93
	4	14.36	28.33	3.47	5.06
	3	10.94	23.32	4.28	7.88
	2	6.75	15.15	4.24	8.96
	1	2.64	5.55	2.60	5.16
(X)	5	15.64	23.10	2.50	3.21
	4	13.52	19.89	3.70	4.89
	3	10.03	15.00	4.26	5.89
	2	5.85	9.14	3.88	5.75
	1	1.99	3.39	1.99	3.39

Table 5.5: Maximum Floor Displacement and Story Drift of Five Story Symmetrical Structure (Y-direction : 0.50 g and 0.75 g Miyagi)

Load case	Story No.	Floor Disp. (in.)		Story Drift (in.)	
		0.50 g	0.75 g	0.50 g	0.75 g
(X+Y)	5	16.87	50.69	1.61	2.13
	4	16.16	48.59	2.80	5.36
	3	14.06	43.23	4.04	12.40
	2	10.18	31.26	5.78	18.81
	1	4.42	12.09	4.34	11.71
(Y)	5	17.61	31.00	1.76	2.67
	4	16.01	29.04	3.32	6.22
	3	12.85	23.58	4.75	9.55
	2	8.33	14.02	5.16	9.66
	1	3.19	4.40	3.19	4.40

Table 5.6: Lateral force distribution for asymmetrical structure

Floor No.	Floor Weight (kips)	Lateral Force (kips)
5	172.8	17.84
4	259.2	17.06
3	259.2	12.79
2	259.2	8.53
1	259.2	4.26

Table 5.7: Maximum Story Shear, Floor Force and Column Ductility Ratio of Five Story L-shape Structure (X-direction : bidirectional excitation, 0.50 g and 0.75 g Miyagi)

Load	Story	Story Shear (kips)		Floor Force (kips)		Column Ductility	
case	No.	0.50 g	0.75 g	0.50 g	0.75 g	0.50 g	0.75 g
	5	198.8	239.0	198.8	239.0	3.66	4.81
	4	307.4	351.2	196.4	224.0	5.68	9.96
(X+Y)	3	396.6	437.1	211.9	229.3	8.49	13.17
	2	484.3	504.7	205.3	236.8	8.49	13.17
	1	531.0	593.0	176.5	196.6	8.25	12.76
	5	183.3	204.3	183.3	204.3	3.79	5.35
	4	308.2	347.9	184.5	226.9	6.27	10.09
(X-Y)	3	408.8	442.4	179.7	209.5	8.27	13.38
	2	473.1	496.1	185.4	212.4	8.51	14.72
	1	526.4	591.5	146.8	180.5	8.71	14.79

Table 5.8: Maximum Story Shear, Floor Force and Column Ductility Ratio of Five Story L-shape Structure (X-direction : unidirectional excitation, 0.50 g and 0.75 g Miyagi)

Load	Story	Story Shear (kips)		Floor Force (kips)		Column Ductility	
case	No.	0.50 g	0.75 g	0.50 g	0.75 g	0.50 g	0.75 g
	5	203.8	231.9	203.8	231.9	4.66	6.34
	4	370.5	394.0	236.1	272.1	7.29	10.18
(X)	3	447.1	500.9	202.0	234.4	9.99	11.34
	2	554.1	587.5	182.3	242.4	9.99	11.34
	1	599.2	679.1	142.2	242.1	8.55	10.06
	5	226.2	244.6	226.2	244.6	4.62	6.10
	4	395.7	407.4	240.5	278.7	6.92	10.10
(2DX)	3	469.7	535.3	194.6	287.4	8.81	11.27
	2	570.2	618.3	193.2	277.0	8.81	11.27
	1	620.4	693.6	152.7	260.4	7.85	9.87

Table 5.9: Maximum Story Shear, Floor Force and Column Ductility Ratio of Five Story L-shape Structure (Y-direction : bidirectional excitation, 0.50 g and 0.75 g Miyagi)

Load	Story	Story Shear (kips)		Floor Force (kips)		Column Ductility	
case	No.	0.50 g	0.75 g	0.50 g	0.75 g	0.50 g	0.75 g
	5	197.8	228.3	197.8	228.3	3.63	4.77
	4	306.6	358.3	191.9	229.3	5.70	9.73
(X+Y)	3	397.2	436.8	188.0	220.9	8.64	12.69
	2	480.5	505.3	181.6	213.8	8.64	12.69
	1	534.5	593.5	151.0	182.9	8.45	12.26
	5	171.1	197.7	171.1	197.7	3.80	5.18
	4	302.7	337.1	190.7	219.2	6.05	10.14
(X-Y)	3	417.2	443.7	172.2	201.7	8.18	12.77
	2	476.0	499.0	179.9	192.3	8.37	14.91
	1	524.5	578.0	153.2	172.2	8.41	14.98

Table 5.10: Maximum Story Shear, Floor Force and Column Ductility Ratio of Five Story L-shape Structure (Y-direction : unidirectional excitation, 0.50 g and 0.75 g Miyagi)

Load case	Story No.	Story Shear (kips)		Floor Force (kips)		Column Ductility	
		0.50 g	0.75 g	0.50 g	0.75 g	0.50 g	0.75 g
(Y)	5	196.7	236.4	196.7	236.4	4.58	6.35
	4	369.1	387.3	239.6	269.6	7.14	10.00
	3	444.4	506.4	216.9	225.5	9.48	11.22
	2	541.9	580.6	167.6	251.0	9.48	11.22
	1	588.3	669.8	151.1	216.1	8.21	10.76
(2DY)	5	222.1	241.7	222.2	241.7	4.73	6.24
	4	395.7	415.2	243.7	290.5	6.97	10.11
	3	477.3	530.7	195.6	270.1	9.33	10.90
	2	561.5	616.9	198.3	272.1	9.33	10.90
	1	607.6	699.0	170.2	265.9	8.11	9.52

Table 5.11: Maximum C.M Displacement and C.M Story Drift of Five Story L-shape Structure (X-direction : bidirectional excitation, 0.50 g and 0.75 g Miyagi)

Load case	Story No.	C.M. Displ. (in.)		C.M. Drift (in.)	
		0.50 g	0.75 g	0.50 g	0.75 g
(X+Y)	5	16.44	24.67	1.82	2.15
	4	15.27	22.82	3.04	5.09
	3	12.81	18.23	4.42	7.05
	2	8.52	12.61	5.17	7.31
	1	3.43	5.36	3.43	5.36
(X-Y)	5	14.48	25.52	1.63	2.26
	4	13.29	23.66	3.05	5.23
	3	10.88	18.89	3.81	7.17
	2	7.33	12.07	4.57	7.54
	1	2.99	5.22	2.99	5.22

Table 5.12: Maximum C.M Displacement and C.M Story Drift of Five Story L-shape Structure (X-direction : unidirectional excitation, 0.50 g and 0.75 g Miyagi)

Load case	Story No.	C.M. Displ. (in.)		C.M. Drift (in.)	
		0.50 g	0.75 g	0.50 g	0.75 g
(X)	5	17.98	22.67	2.16	2.89
	4	16.34	20.27	3.68	5.36
	3	13.01	15.28	4.90	6.45
	2	8.20	9.81	5.17	5.90
	1	3.06	4.01	3.06	4.01
(2DX)	5	17.92	22.35	2.34	2.89
	4	16.30	19.90	3.66	5.29
	3	13.05	15.59	4.86	6.40
	2	8.28	9.95	5.17	6.15
	1	3.10	3.81	3.10	3.81

Table 5.13: Maximum C.M Displacement and C.M Story Drift of Five Story L-shape Structure (Y-direction : bidirectional excitation, 0.50 g and 0.75 g Miyagi)

Load case	Story No.	C.M. Displ. (in.)		C.M. Drift (in.)	
		0.50 g	0.75 g	0.50 g	0.75 g
(X+Y)	5	16.50	24.68	1.83	2.20
	4	15.37	22.73	3.06	5.16
	3	12.92	18.10	4.47	7.04
	2	8.60	12.60	5.22	7.24
	1	3.47	5.38	3.47	5.38
(X-Y)	5	14.35	25.54	1.67	2.21
	4	13.19	23.73	3.14	5.20
	3	10.86	18.92	3.82	7.20
	2	7.32	12.35	4.54	7.56
	1	3.01	5.33	3.01	5.33

Table 5.14: Maximum C.M Displacement and C.M Story Drift of Five Story L-shape Structure (Y-direction : unidirectional excitation, 0.50 g and 0.75 g Miyagi)

Load case	Story No.	C.M. Displ. (in.)		C.M. Drift (in.)	
		0.50 g	0.75 g	0.50 g	0.75 g
(Y)	5	18.24	22.43	2.15	2.97
	4	16.51	20.09	3.71	5.27
	3	13.01	15.25	4.98	6.38
	2	8.08	9.81	5.16	5.91
	1	2.97	4.00	2.97	4.00
(2DY)	5	17.80	22.63	2.28	2.95
	4	16.19	20.14	3.64	5.37
	3	12.94	15.50	4.81	6.43
	2	8.22	9.88	5.14	6.12
	1	3.09	3.76	3.09	3.76

Table 5.15: Maximum Floor Displacement and Story Drift of Five Story L-shape Structure (X-direction : bidirectional excitation, 0.50 g and 0.75 g Miyagi)

Load case	Story No.	Floor Displ. (in.)		Story Drift (in.)	
		0.50 g	0.75 g	0.50 g	0.75 g
(X+Y)	5	17.01	24.86	1.87	2.19
	4	15.86	22.94	3.06	5.19
	3	13.38	18.81	4.56	7.09
	2	8.96	13.18	5.41	7.53
	1	3.62	5.67	3.62	5.67
(X-Y)	5	16.83	26.14	2.05	2.73
	4	16.13	24.73	3.20	5.31
	3	14.05	21.95	4.39	7.45
	2	9.83	16.22	5.76	9.01
	1	4.14	7.24	4.14	7.24

Table 5.16: Maximum Floor Displacement and Story Drift of Five Story L-shape Structure (X-direction : unidirectional excitation, 0.50 g and 0.75 g Miyagi)

Load case	Story No.	Floor Displ. (in.)		Story Drift (in.)	
		0.50 g	0.75 g	0.50 g	0.75 g
(X)	5	19.61	23.36	2.29	2.98
	4	18.05	20.83	3.74	5.38
	3	14.59	16.49	5.30	6.48
	2	9.35	11.12	5.78	6.51
	1	3.58	4.64	3.58	4.64
(2DX)	5	17.92	22.35	2.34	2.89
	4	16.30	19.90	3.66	5.29
	3	13.05	15.59	4.86	6.40
	2	8.28	9.95	5.17	6.15
	1	3.10	3.81	3.10	3.81

Table 5.17: Maximum Floor Displacement and Story Drift of Five Story L-shape Structure (Y-direction : bidirectional excitation, 0.50 g and 0.75 g Miyagi)

Load case	Story No.	Floor Displ. (in.)		Story Drift (in.)	
		0.50 g	0.75 g	0.50 g	0.75 g
(X+Y)	5	17.33	24.94	1.86	2.28
	4	16.22	22.91	3.08	5.31
	3	13.75	18.95	4.66	7.10
	2	9.23	13.41	5.57	7.61
	1	3.74	5.81	3.74	5.81
(X-Y)	5	16.79	26.16	2.06	2.60
	4	16.12	24.82	3.26	5.28
	3	14.07	22.22	4.42	7.49
	2	9.84	16.52	5.77	9.16
	1	4.16	7.38	4.16	7.38

Table 5.18: Maximum Floor Displacement and Story Drift of Five Story L-shape Structure (Y-direction : unidirectional excitation, 0.50 g and 0.75 g Miyagi)

Load case	Story No.	Floor Displ. (in.)		Story Drift (in.)	
		0.50 g	0.75 g	0.50 g	0.75 g
(Y)	5	20.87	23.40	2.36	3.05
	4	19.28	21.02	3.91	5.33
	3	15.62	17.53	5.62	6.47
	2	10.02	11.95	6.20	6.98
	1	3.82	5.00	3.82	5.00
(2DY)	5	17.80	22.63	2.28	2.95
	4	16.19	20.14	3.64	5.37
	3	12.94	15.50	4.81	6.43
	2	8.22	9.88	5.14	6.12
	1	3.09	3.76	3.09	3.76

Table 6.1: Maximum Story Shear : X-direction

Load case	Story No.	Miyagi 0.50 g	Miyagi 0.75 g	Soft Story 0.50 g	Mexico 0.18 g	El Centro 0.68 g
	5	89.4	87.7		21.7	
	4	163.6	174.7		53.9	
0.3 P_y	3	215.8	233.9		76.6	
	2	256.3	270.4		92.9	
	1	302.9	324.7		105.2	
	5	85.4	76.1			
	4	160.3	150.1			
0.4 P_y	3	206.7	210.3			
	2	243.5	255.1			
	1	283.8	319.2			
	5	81.8	68.7			
	4	160.9	143.6			
0.5 P_y	3	199.7	192.6			
	2	232.3	218.5			
	1	256.7	229.3			
	5	56.2	60.5	82.4	15.0	77.0
	4	120.3	137.7	164.2	36.5	135.2
0.6 P_y	3	162.3	180.0	213.7	56.2	163.9
	2	190.9	198.3	258.1	73.5	196.7
	1	213.0	207.3	299.8	88.3	257.8

Table 6.2: Maximum Story Shear : Y-direction

Load case	Story No.	Miyagi 0.50 g	Miyagi 0.75 g	Soft Story 0.50 g	Mexico 0.18 g	El Centro 0.68 g
	5	69.3	82.7		16.7	
	4	120.1	129.1		40.9	
0.3 P_y	3	152.6	177.8		56.0	
	2	186.5	220.3		66.2	
	1	223.7	230.3		74.0	
	5	62.4	67.4			
	4	115.3	122.3			
0.4 P_y	3	139.1	171.5			
	2	175.3	210.1			
	1	211.5	223.3			
	5	60.1	58.1			
	4	101.0	111.8			
0.5 P_y	3	142.7	125.9			
	2	172.6	157.4			
	1	195.8	191.5			
	5	43.4	49.0	67.4	20.0	55.6
	4	96.0	103.9	129.0	51.8	95.8
0.6 P_y	3	113.1	117.9	161.8	77.7	108.5
	2	126.8	135.9	182.8	98.2	131.8
	1	162.9	148.2	220.1	111.0	166.8

Table 6.3: Maximum Floor Force : X-direction

Load case	Story No.	Miyagi 0.50 g	Miyagi 0.75 g	Soft Story 0.50 g	Mexico 0.18 g	El Centro 0.68 g
	5	89.4	87.7		21.7	
	4	122.9	119.2		34.2	
0.3 P_y	3	105.2	104.7		26.9	
	2	93.2	107.3		24.1	
	1	88.3	75.9		18.7	
	5	85.4	76.1			
	4	117.6	106.4			
0.4 P_y	3	98.9	99.1			
	2	85.4	88.5			
	1	85.6	86.5			
	5	81.8	68.7			
	4	108.0	98.9			
0.5 P_y	3	100.4	99.7			
	2	88.5	79.4			
	1	64.0	82.4			
	5	56.2	60.5	82.4	15.0	77.0
	4	74.7	85.5	110.7	24.1	108.4
0.6 P_y	3	67.3	76.9	108.7	21.5	102.4
	2	56.6	58.2	95.1	18.8	97.5
	1	44.4	56.3	76.6	16.6	83.3

Table 6.4: Maximum Floor Force : Y-direction

Load case	Story No.	Miyagi 0.50 g	Miyagi 0.75 g	Soft Story 0.50 g	Mexico 0.18 g	El Centro 0.68 g
	5	69.3	82.7		16.7	
	4	84.8	92.2		25.8	
0.3 P_y	3	77.0	103.6		21.2	
	2	82.3	89.5		18.4	
	1	67.5	79.5		14.1	
	5	62.4	67.4			
	4	83.4	74.7			
0.4 P_y	3	69.9	98.0			
	2	77.6	65.2			
	1	66.0	73.7			
	5	60.1	58.1			
	4	75.3	76.5			
0.5 P_y	3	74.6	59.2			
	2	66.7	64.8			
	1	59.5	61.5			
	5	43.4	50.3	67.4	20.0	55.6
	4	63.9	62.8	88.0	32.3	68.2
0.6 P_y	3	53.9	83.3	92.9	28.5	59.0
	2	56.0	71.5	82.3	23.9	59.4
	1	43.2	59.4	77.1	16.8	57.0

Table 6.5: Maximum Column Axial Force

Load case	Story No.	Miyagi 0.50 g	Miyagi 0.75 g	Soft Story 0.50 g	Mexico 0.18 g	El Centro 0.68 g
	5	346.0	349.1		323.7	
	4	397.3	403.4		340.8	
0.3 P_y	3	585.9	600.6		476.0	
	2	674.5	708.3		510.3	
	1	810.4	859.6		582.0	
	5	451.3	450.0			
	4	502.6	501.6			
0.4 P_y	3	723.4	734.5			
	2	817.6	838.1			
	1	968.4	998.8			
	5	557.1	553.7			
	4	609.4	600.8			
0.5 P_y	3	874.8	857.6			
	2	980.3	953.8			
	1	1157.0	1111.0			
	5	657.2	659.2	50.0	637.7	653.4
	4	705.6	709.0	136.6	655.3	692.2
0.6 P_y	3	1002.0	1007.0	1000.0	898.0	960.6
	2	1100.0	1109.0	391.6	939.3	1027.0
	1	1276.0	1293.0	505.7	1062.0	1164.0

Table 6.6: Maximum Column Axial Force Ratio

Load case	Story No.	Miyagi 0.50 g	Miyagi 0.75 g	Soft Story 0.50 g	Mexico 0.18 g	El Centro 0.68 g
	5	0.33	0.33		0.31	
	4	0.38	0.39		0.33	
0.3 P_y	3	0.42	0.43		0.34	
	2	0.48	0.51		0.37	
	1	0.53	0.56		0.38	
	5	0.43	0.43			
	4	0.48	0.48			
0.4 P_y	3	0.52	0.53			
	2	0.59	0.60			
	1	0.63	0.65			

Table 6.6: Maximum Column Axial Force Ratio (Continue)

Load case	Story No.	Miyagi 0.50 g	Miyagi 0.75 g	Soft Story 0.50 g	Mexico 0.18 g	El Centro 0.68 g
	5	0.53	0.53			
	4	0.58	0.57			
0.5 P_y	3	0.63	0.61			
	2	0.70	0.68			
	1	0.75	0.72			
	5	0.63	0.63	0.05	0.61	0.62
	4	0.67	0.68	0.13	0.63	0.66
0.6 P_y	3	0.72	0.72	0.72	0.64	0.69
	2	0.79	0.79	0.28	0.67	0.74
	1	0.83	0.84	0.33	0.69	0.76

Table 6.7: Maximum Floor Displacement : X-direction

Load case	Story No.	Miyagi 0.50 g	Miyagi 0.75 g	Soft Story 0.50 g	Mexico 0.18 g	El Centro 0.68 g
	5	16.44	30.95		3.73	
	4	14.36	28.33		3.17	
0.3 P_y	3	10.94	23.32		2.35	
	2	6.75	15.15		1.42	
	1	2.64	5.55		0.49	
	5	16.77	23.31			
	4	14.64	21.72			
0.4 P_y	3	11.12	18.80			
	2	6.76	12.66			
	1	2.63	4.58			
	5	27.60	17.90			
	4	25.46	16.83			
0.5 P_y	3	21.50	15.01			
	2	14.41	11.30			
	1	4.77	4.71			
	5	14.87	26.76	18.40	3.35	9.82
	4	13.43	25.36	16.85	2.88	8.43
0.6 P_y	3	11.07	22.44	13.84	2.20	6.51
	2	7.06	15.29	7.20	1.36	4.14
	1	2.31	3.52	2.76	0.49	1.58

Table 6.8: Maximum Floor Displacement : Y-direction

Load case	Story No.	Miyagi 0.50 g	Miyagi 0.75 g	Soft Story 0.50 g	Mexico 0.18 g	El Centro 0.68 g
	5	16.87	50.69		3.80	
	4	16.16	48.59		3.33	
0.3 P_y	3	14.06	43.23		2.51	
	2	10.18	31.26		1.58	
	1	4.42	12.09		0.58	
	5	17.68	61.57			
	4	16.47	61.11			
0.4 P_y	3	14.00	58.42			
	2	9.68	43.53			
	1	3.92	15.06			
	5	60.16	60.19			
	4	59.87	59.70			
0.5 P_y	3	58.63	58.00			
	2	46.88	46.27			
	1	15.12	15.08			
	5	59.56	60.40	59.18	7.02	11.35
	4	60.18	61.35	60.94	6.27	10.43
0.6 P_y	3	60.13	61.32	58.63	4.95	8.81
	2	46.26	46.83	8.53	3.23	6.36
	1	8.16	8.27	3.18	1.22	3.01

Table 6.9: Maximum Story Drift : X-direction

Load case	Story No.	Miyagi 0.50 g	Miyagi 0.75 g	Soft Story 0.50 g	Mexico 0.18 g	El Centro 0.68 g
	5	2.07	3.03		0.57	
	4	3.47	5.12		0.82	
0.3 P_y	3	4.31	8.21		0.94	
	2	4.25	9.61		0.93	
	1	2.64	5.55		0.49	
	5	2.26	2.11			
	4	3.60	3.48			
0.4 P_y	3	4.47	5.88			
	2	4.32	7.78			
	1	2.63	4.58			
	5	2.70	2.15			
	4	4.76	3.11			
0.5 P_y	3	7.62	4.49			
	2	9.86	6.79			
	1	4.77	4.71			
	5	1.96	2.56	1.93	0.47	1.96
	4	2.95	4.10	3.10	0.69	2.49
0.6 P_y	3	4.06	6.64	8.77	0.84	2.64
	2	4.85	9.74	4.44	0.87	2.59
	1	2.31	3.52	2.76	0.49	1.58

Table 6.10: Maximum Story Drift : Y-direction

Load case	Story No.	Miyagi 0.50 g	Miyagi 0.75 g	Soft Story 0.50 g	Mexico 0.18 g	El Centro 0.68 g
	5	1.62	2.16		0.47	
	4	2.80	5.40		0.81	
0.3 P_y	3	4.07	12.68		0.93	
	2	5.79	19.20		1.00	
	1	4.42	12.09		0.58	
	5	1.82	1.75			
	4	2.96	3.64			
0.4 P_y	3	4.43	11.37			
	2	5.85	22.70			
	1	3.92	13.70			
	5	1.74	1.52			
	4	3.14	2.84			
0.5 P_y	3	14.13	11.28			
	2	25.76	30.03			
	1	9.90	15.08			
	5	1.73	1.87	1.39	0.80	1.79
	4	3.09	3.32	3.62	1.37	3.01
0.6 P_y	3	12.46	12.07	30.24	1.74	2.76
	2	20.00	27.05	5.57	2.01	3.37
	1	8.16	8.25	3.18	1.22	3.01

Table 6.11: Maximum Column Ductility Ratio : X-direction

Load case	Story No.	Miyagi 0.50 g	Miyagi 0.75 g	Soft Story 0.50 g	Mexico 0.18 g	El Centro 0.68 g
	5	4.28	5.87		1.17	
	4	6.20	9.71		1.40	
0.3 P_y	3	7.33	15.20		1.58	
	2	7.33	15.20		1.58	
	1	5.84	12.68		1.34	
	5	4.55	4.15			
	4	6.58	6.75			
0.4 P_y	3	7.68	12.23			
	2	7.68	12.23			
	1	6.14	10.01			

Table 6.11: Maximum Column Ductility Ratio : X-direction (Continue)

Load case	Story No.	Miyagi 0.50 g	Miyagi 0.75 g	Soft Story 0.50 g	Mexico 0.18 g	El Centro 0.68 g
	5	5.46	4.24			
	4	9.35	5.95			
0.5 P_y	3	14.05	8.53			
	2	14.05	9.38			
	1	10.94	9.43			
	5	4.03	5.18	3.86	1.00	3.65
	4	5.12	8.18	6.50	1.23	4.25
0.6 P_y	3	7.97	14.31	8.00	1.46	4.63
	2	7.97	14.31	8.00	1.46	4.63
	1	5.22	8.23	6.33	1.30	4.06

Table 6.12: Maximum Column Ductility Ratio : Y-direction

Load case	Story No.	Miyagi 0.50 g	Miyagi 0.75 g	Soft Story 0.50 g	Mexico 0.18 g	El Centro 0.68 g
	5	3.25	4.40		1.12	
	4	4.70	9.82		1.28	
0.3 P_y	3	7.27	23.37		1.45	
	2	8.79	24.49		1.45	
	1	9.29	25.88		1.44	
	5	3.44	3.66			
	4	4.79	6.72			
0.4 P_y	3	8.25	31.35			
	2	8.29	31.43			
	1	8.76	33.21			

Table 6.12: Maximum Column Ductility Ratio : Y-direction (Continue)

Load case	Story No.	Miyagi 0.50 g	Miyagi 0.75 g	Soft Story 0.50 g	Mexico 0.18 g	El Centro 0.68 g
	5	3.54	3.10			
	4	5.44	5.63			
0.5 P_y	3	29.01	27.04			
	2	32.86	32.40			
	1	34.72	34.23			
	5	3.61	3.66	3.48	1.75	3.70
	4	5.62	5.32	35.04	2.19	4.14
0.6 P_y	3	35.51	35.13	35.31	2.77	4.53
	2	35.51	35.13	24.16	2.77	5.45
	1	22.05	21.10	6.12	2.81	5.76

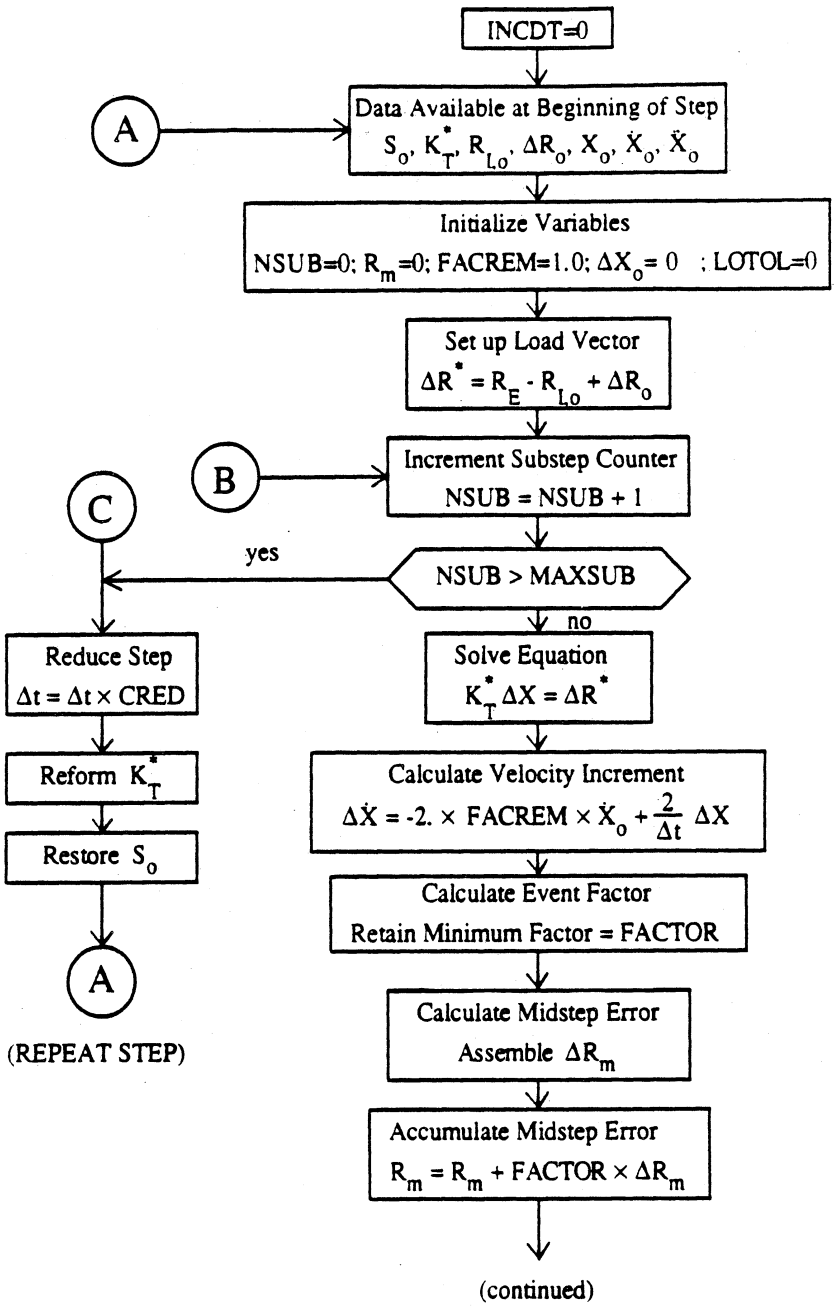

Figure 2.1: Flow-Chart for Event-to-Event Dynamic Analysis

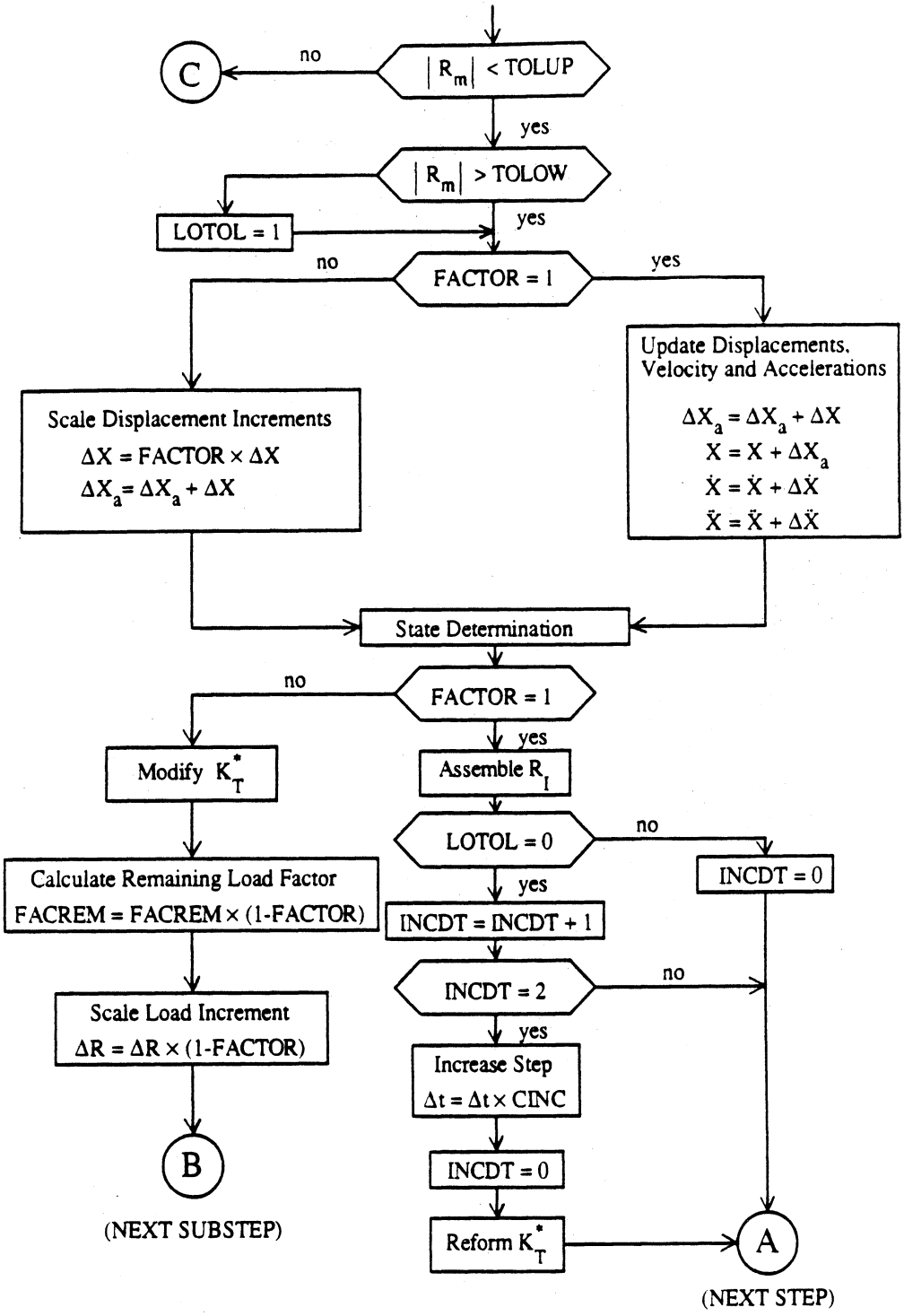

Figure 2.1: Flow-Chart for Event-to-Event Dynamic Analysis (Continue)

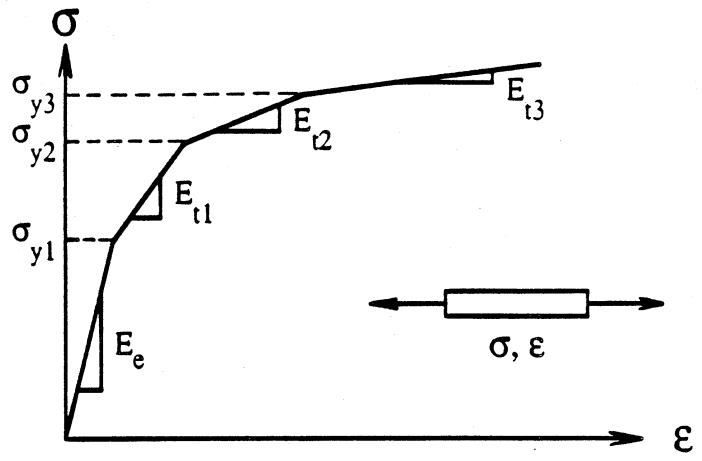

Figure 4.1: Multilinear Stress-Strain Relationship

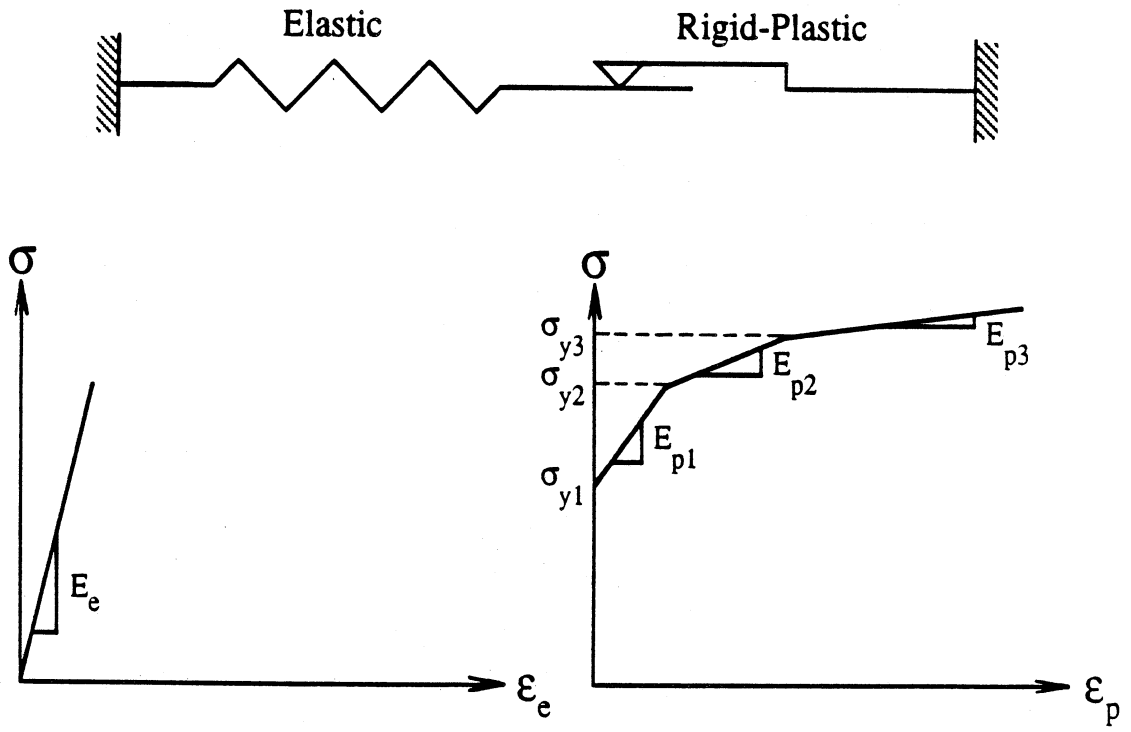

Figure 4.2: Elastic Spring and Rigid-Plastic Hardening Spring

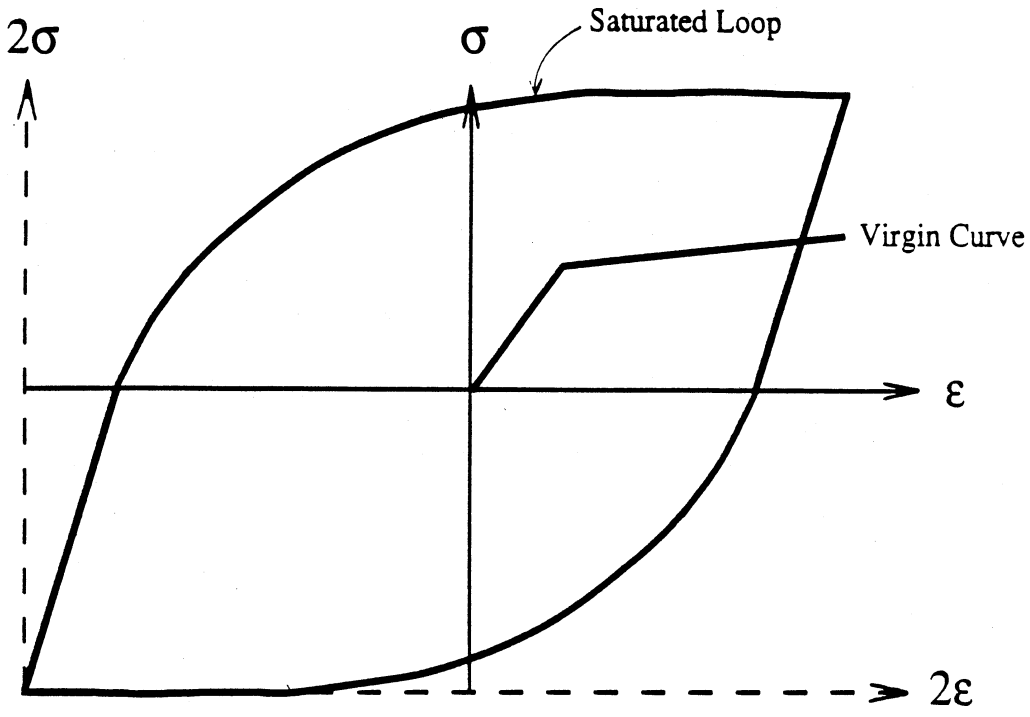

Figure 4.3: Saturated and Virgin Curve

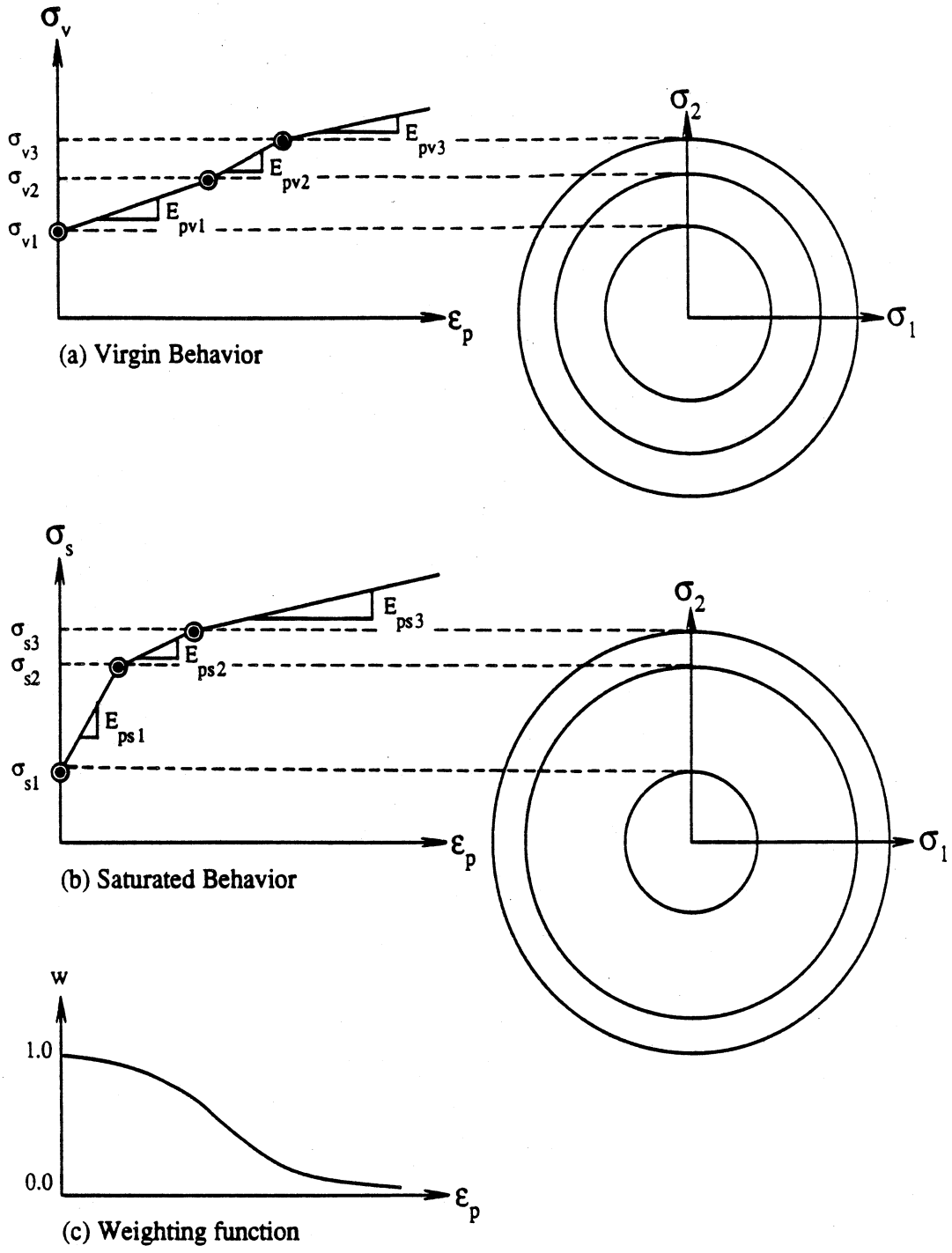

Figure 4.4: Typical Stress-Strain Curves for Extended Mroz Model

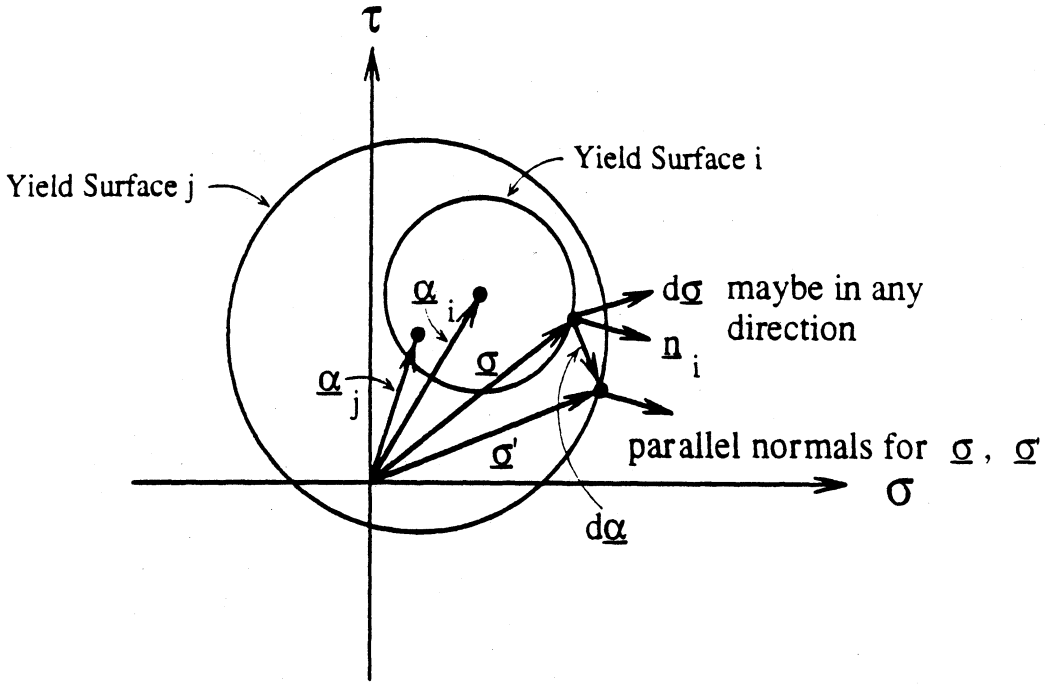

Figure 4.5: Direction of Yield Surface Translation

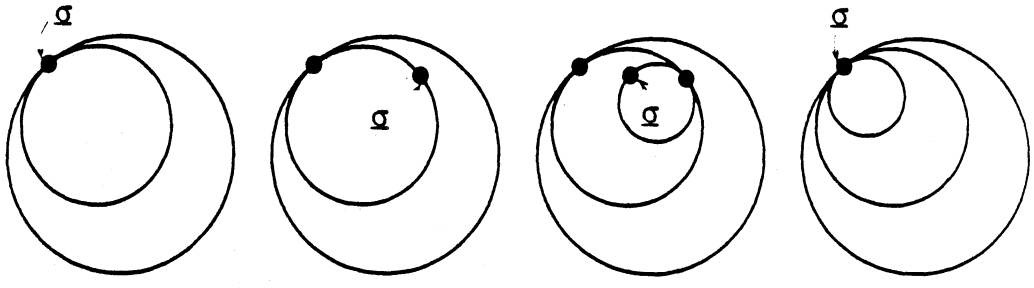

Figure 4.6: Multi-Surface Contact

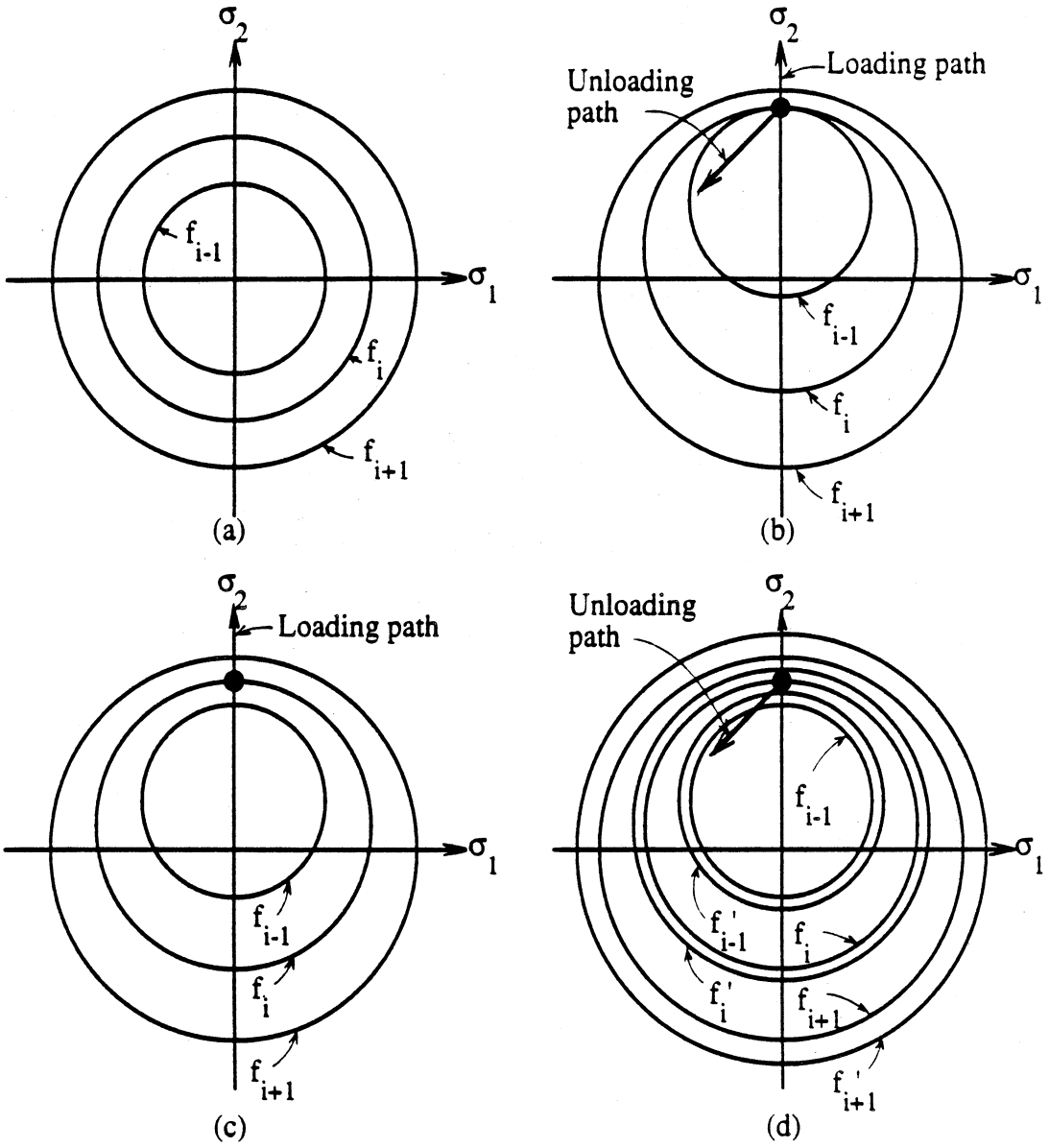

Figure 4.7: Updating Procedures

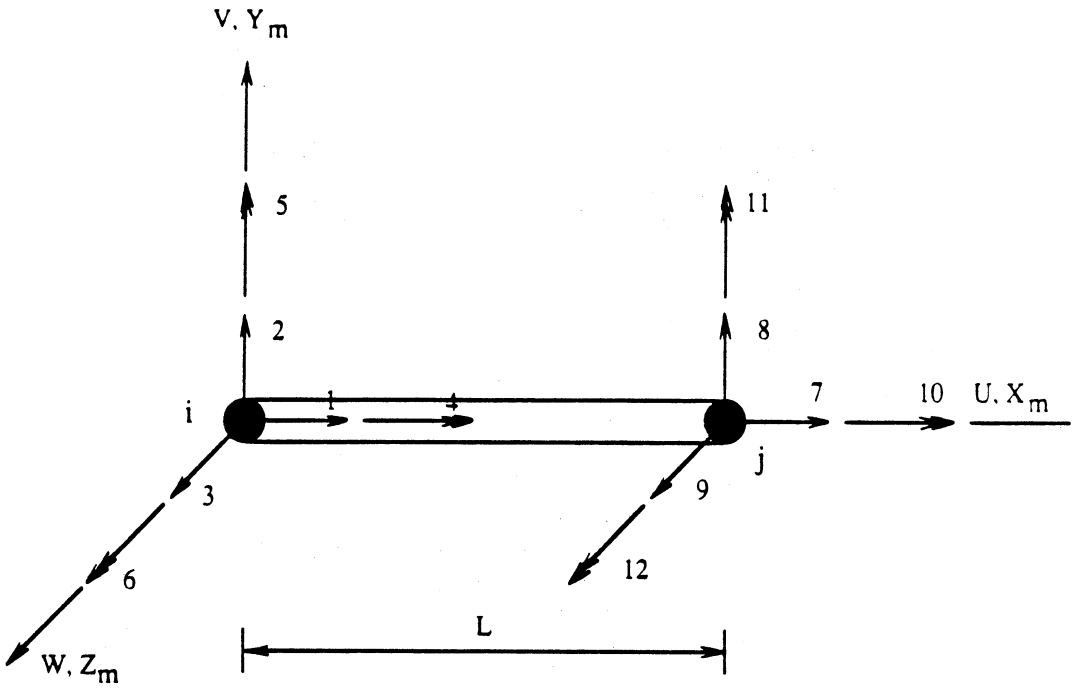

Figure 4.8: Degree of Freedom of Beam-Column Element

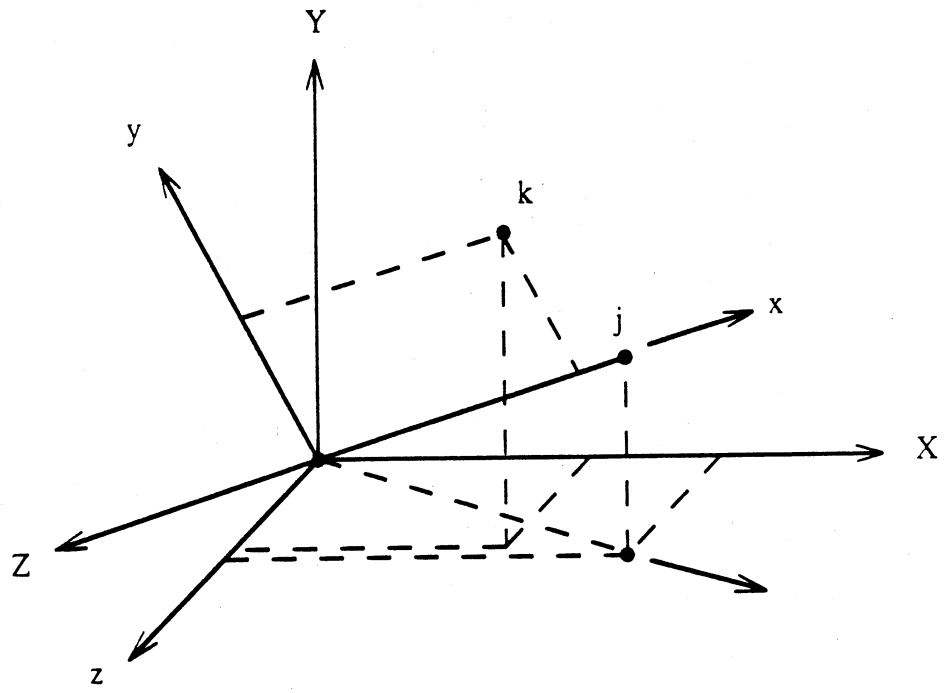

Figure 4.9: Rotation of Axes for a Space Frame Member

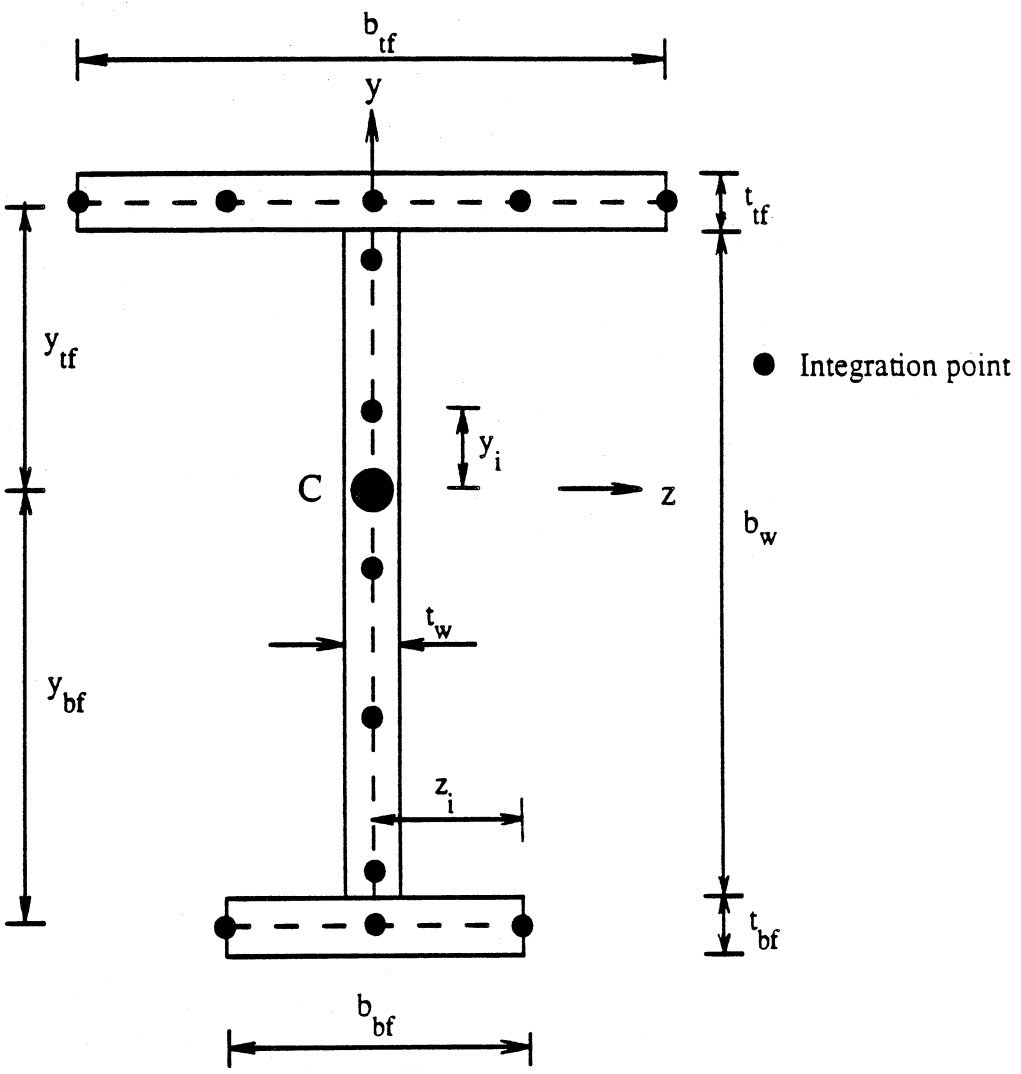

Figure 4.10: WF Section Geometrics

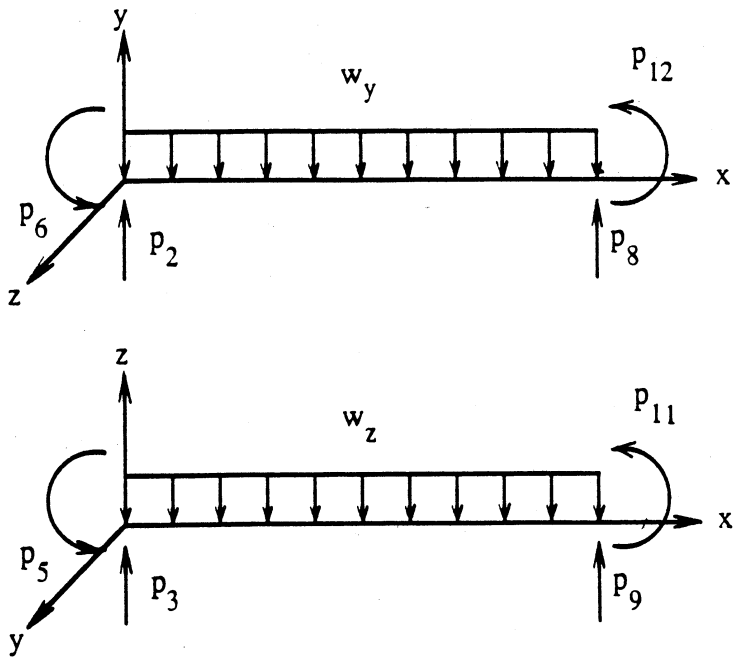

Figure 4.11: Fixed End Action in Member Axes

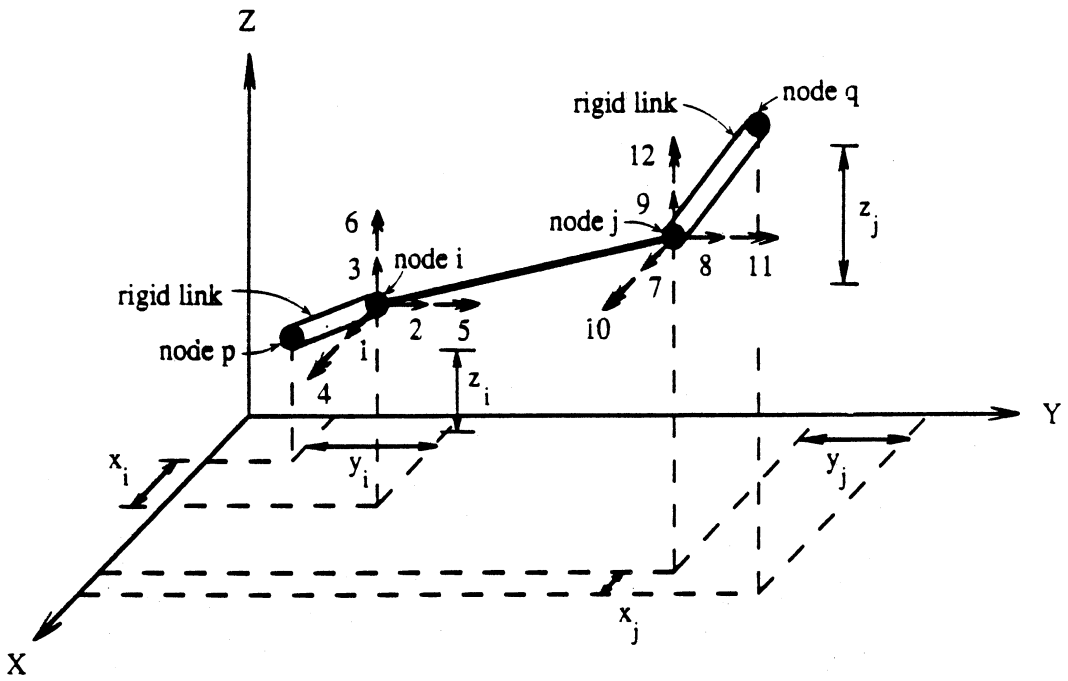

Figure 4.12: Element End Eccentricity

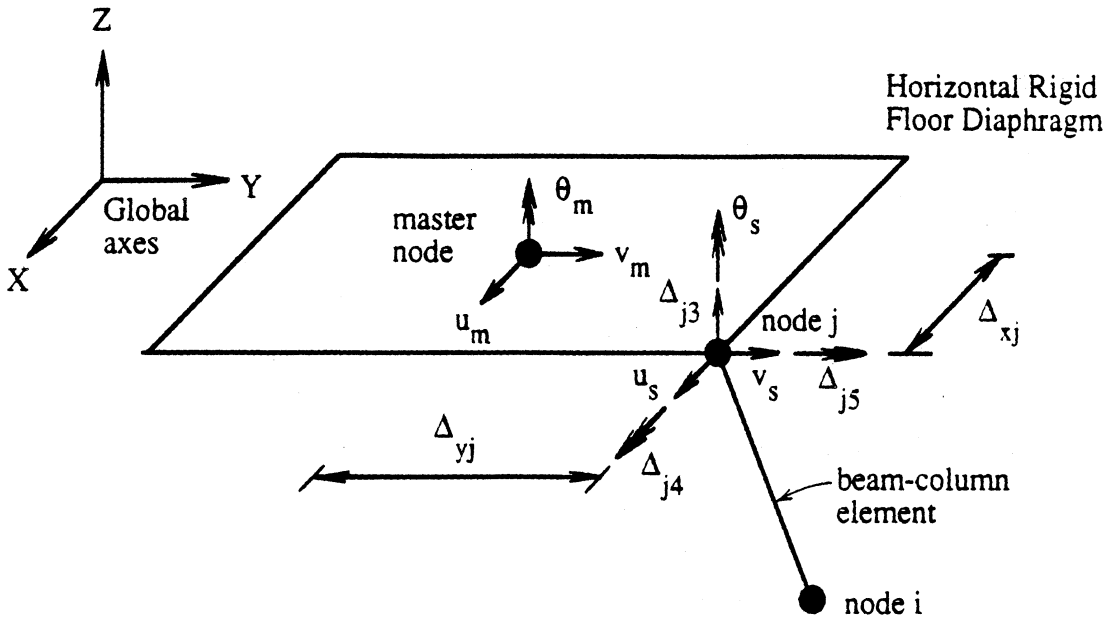

Figure 4.13: Rigid Floor Diaphgram

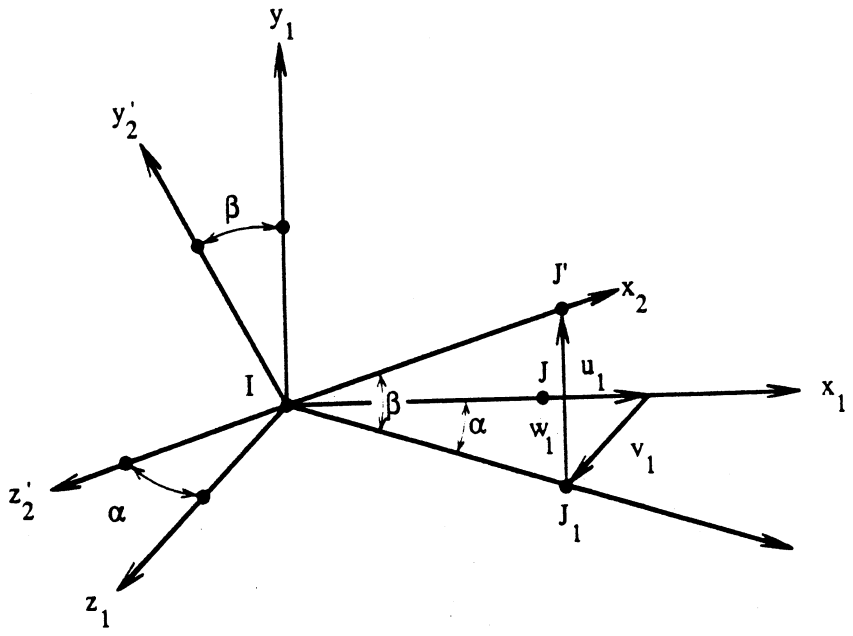

Figure 4.14: Rotation of Coordinate Axes from (x_1, y_1, z_1) to (x_2, y_2', z_2')

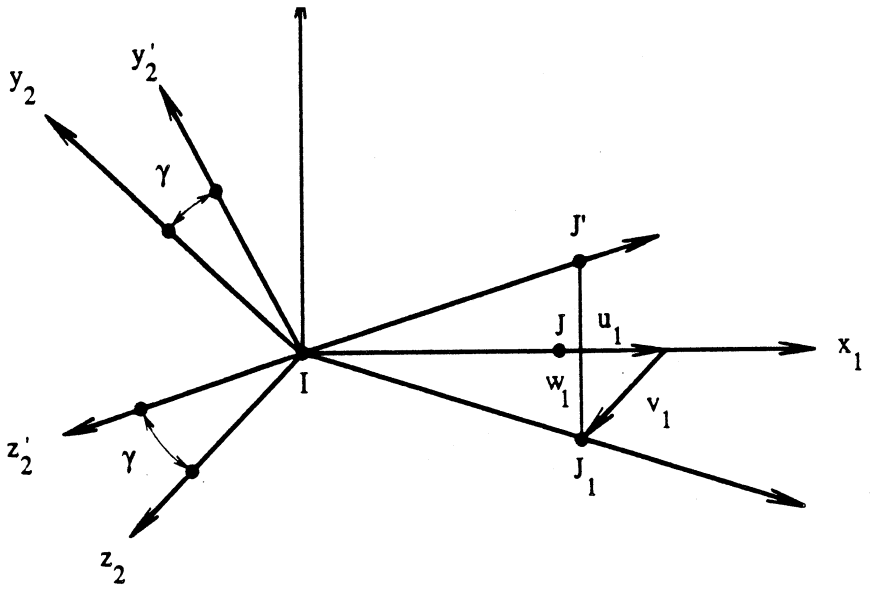

Figure 4.15: Rotation of Coordinate Axes from (x_2, y_2', z_2') to (x_2, y_2, z_2)

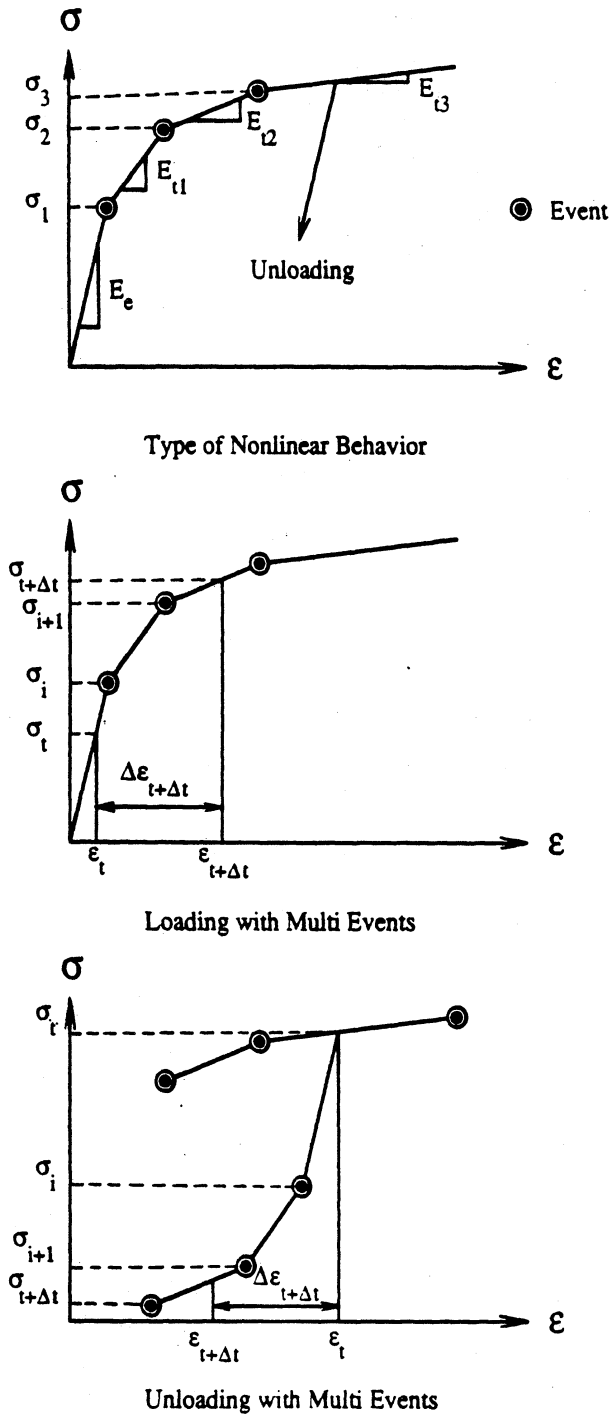

Figure 4.16: Loading and Unloading with Multi Events

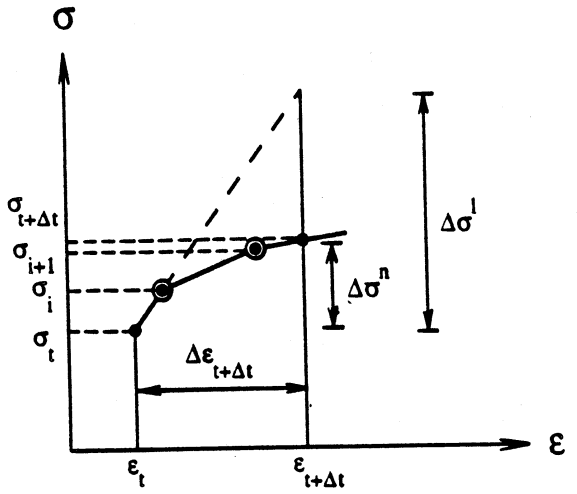

Figure 4.17: Linear and Nonlinear Stress Increments

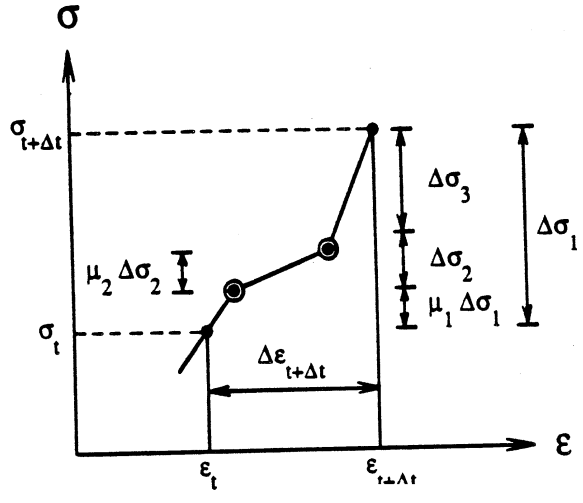

Figure 4.18: Computation of Stress Increment

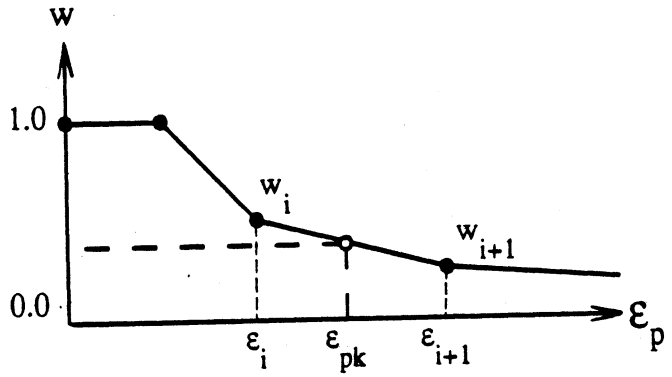

Figure 4.19: Multilinear Weighting Function

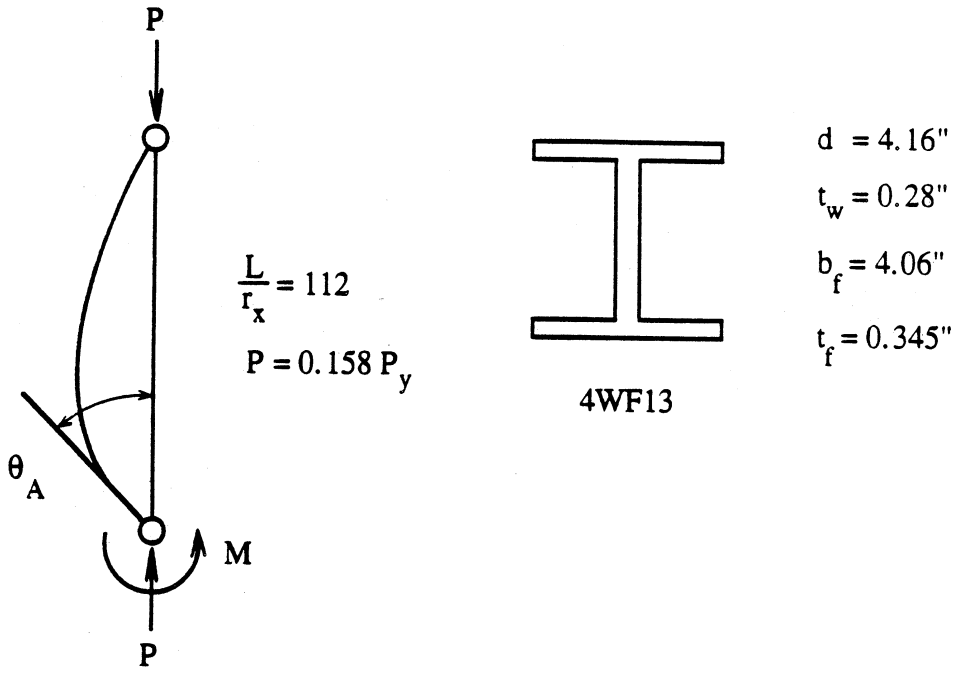

Figure 4.20: Geometric Configuration and Section Property of Van Kuren and Galambos Test

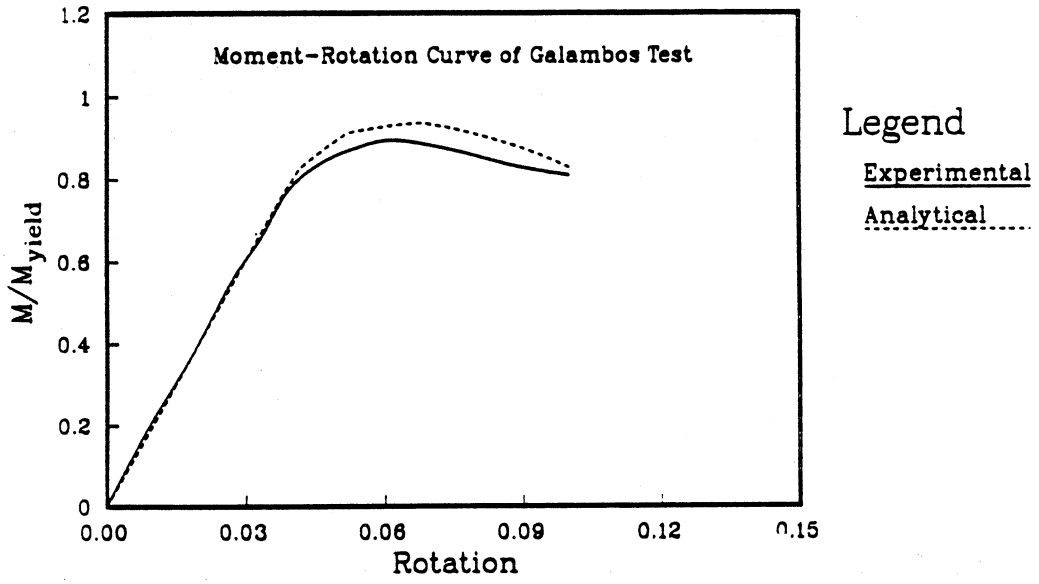

Figure 4.21: Numerical and Experimental Results of Galambos Test

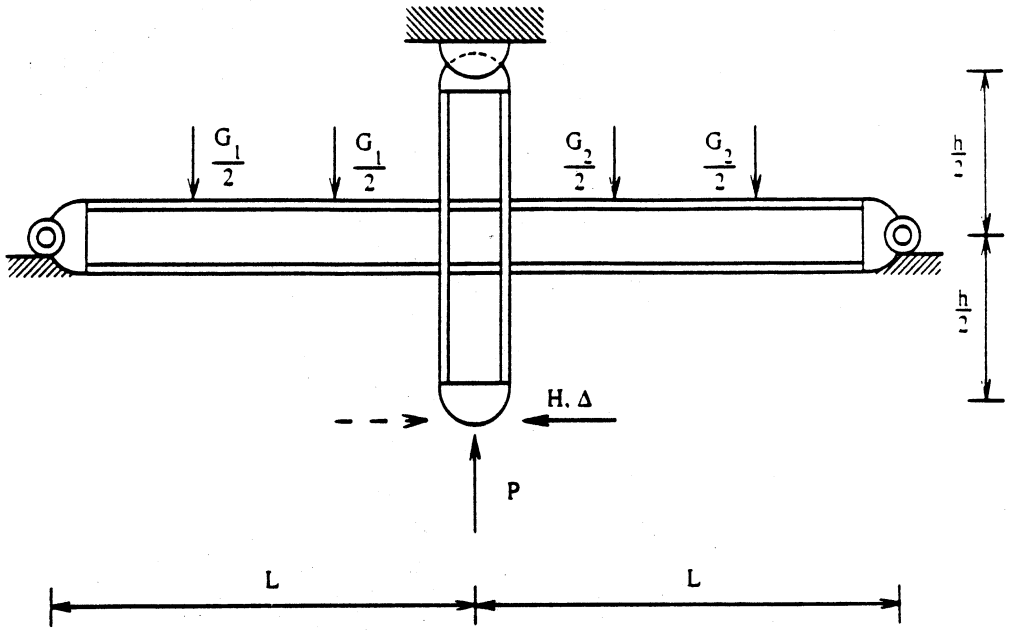

Figure 4.22: Geometric Configuration of Popov Subassemblages

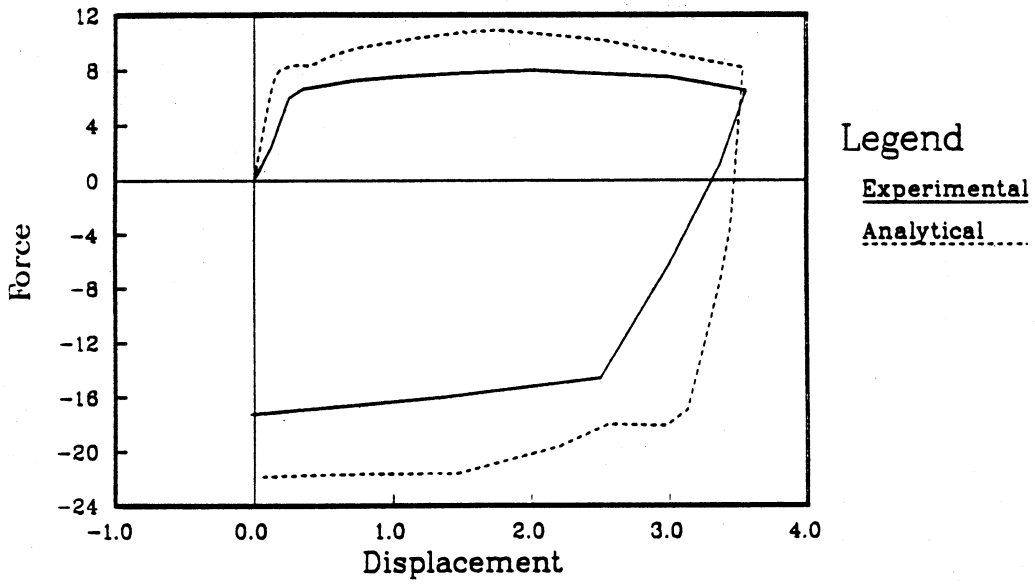

Figure 4.23: Numerical and Experimental Results of Popov Test

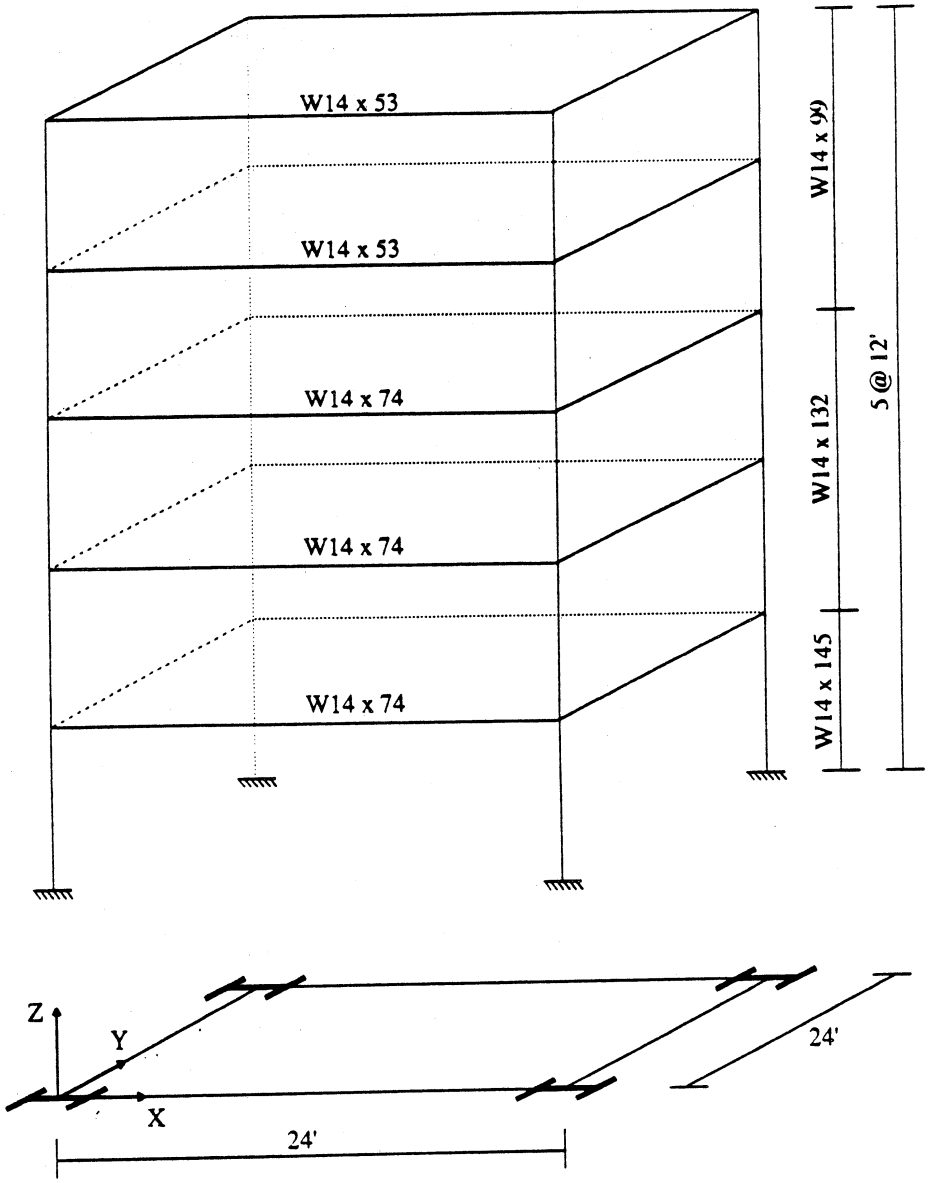

Figure 5.1: Plane View of Five Story Symmetric Building

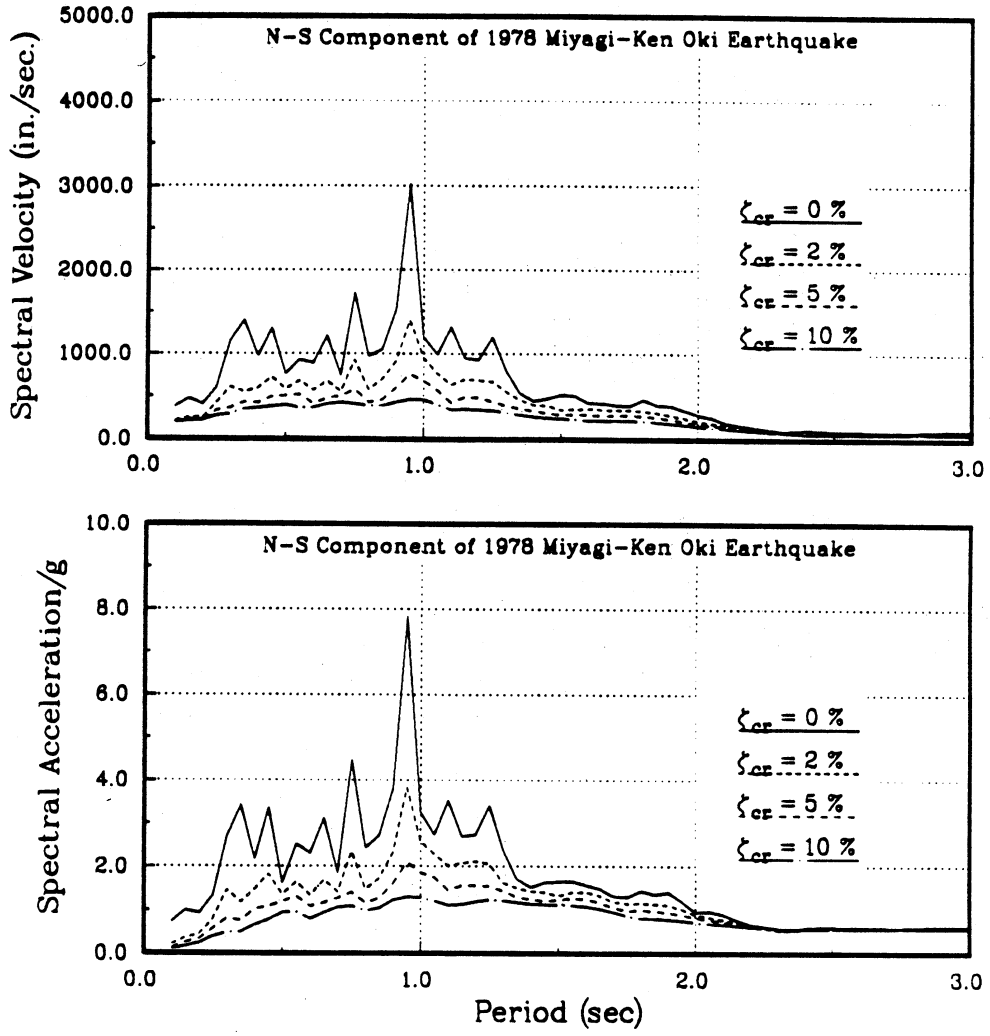

Figure 5.2: N-S Component Velocity and Acceleration Spectra of Modified 1978 Miyagi-Ken-Oki Earthquake (0.5 g)

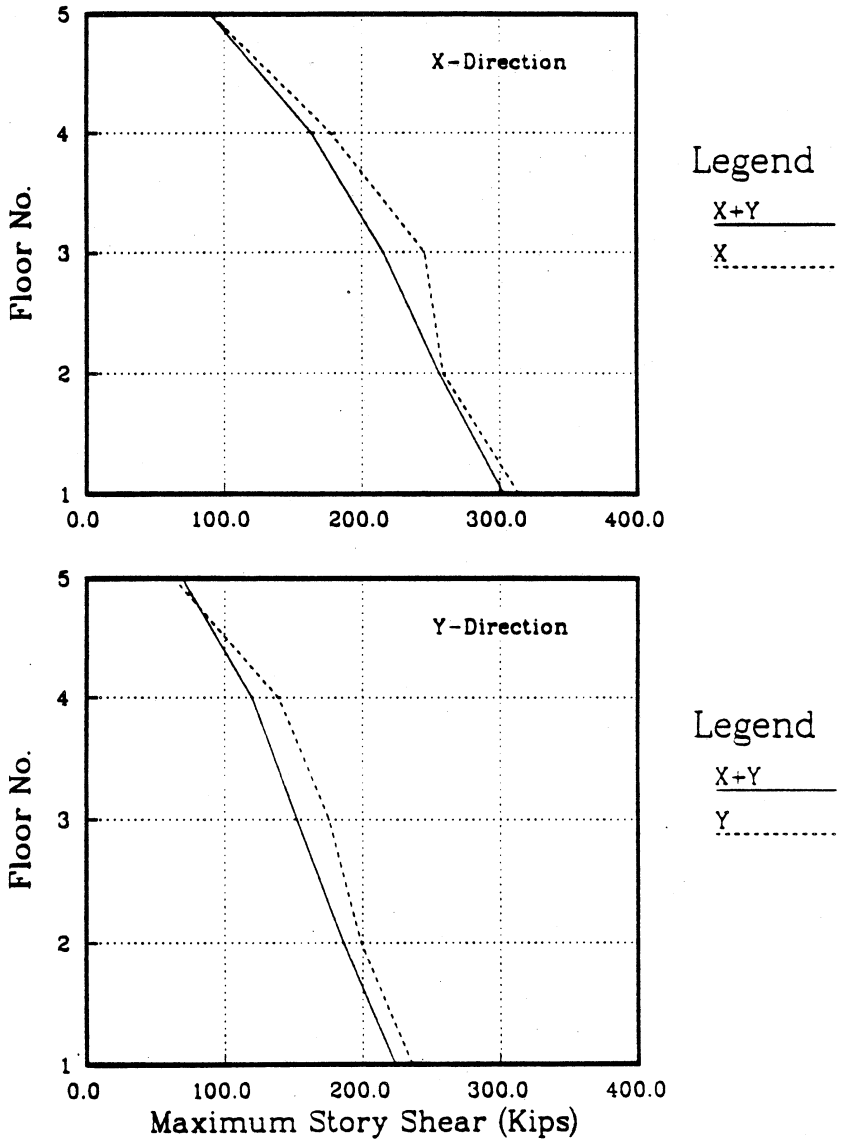

Figure 5.3: Comparison of Maximum Story Shear of Five Story Symmetrical Building Subjected to 0.5 g 1978 Miyagi-Ken-Oki Earthquake

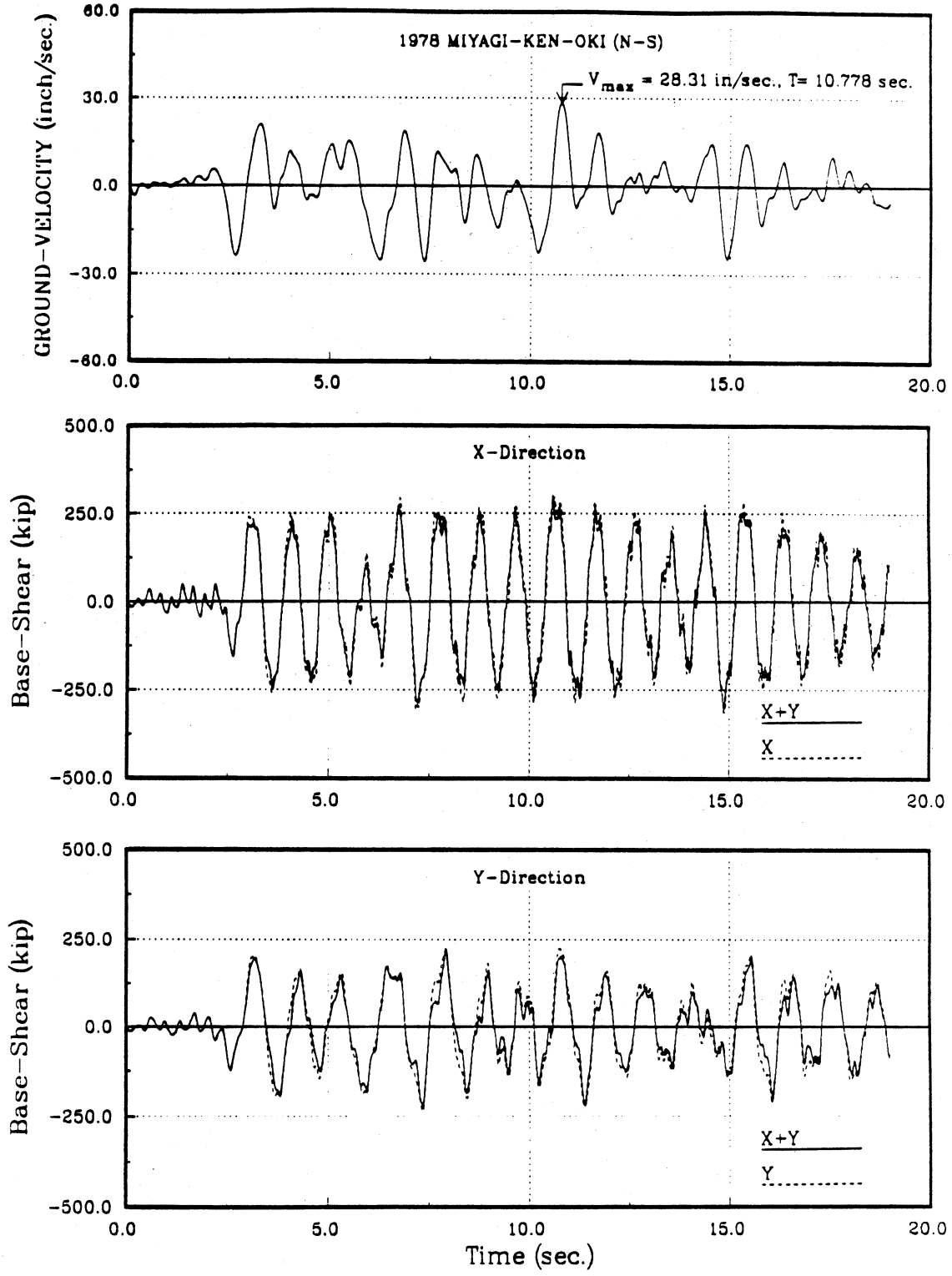

Figure 5.4: Input Ground Velocity and Base Shear Time History in the Principal Directions of Five Story Symmetrical Building Subjected to 0.5 g 1978 Miyagi-Ken-Oki Earthquake

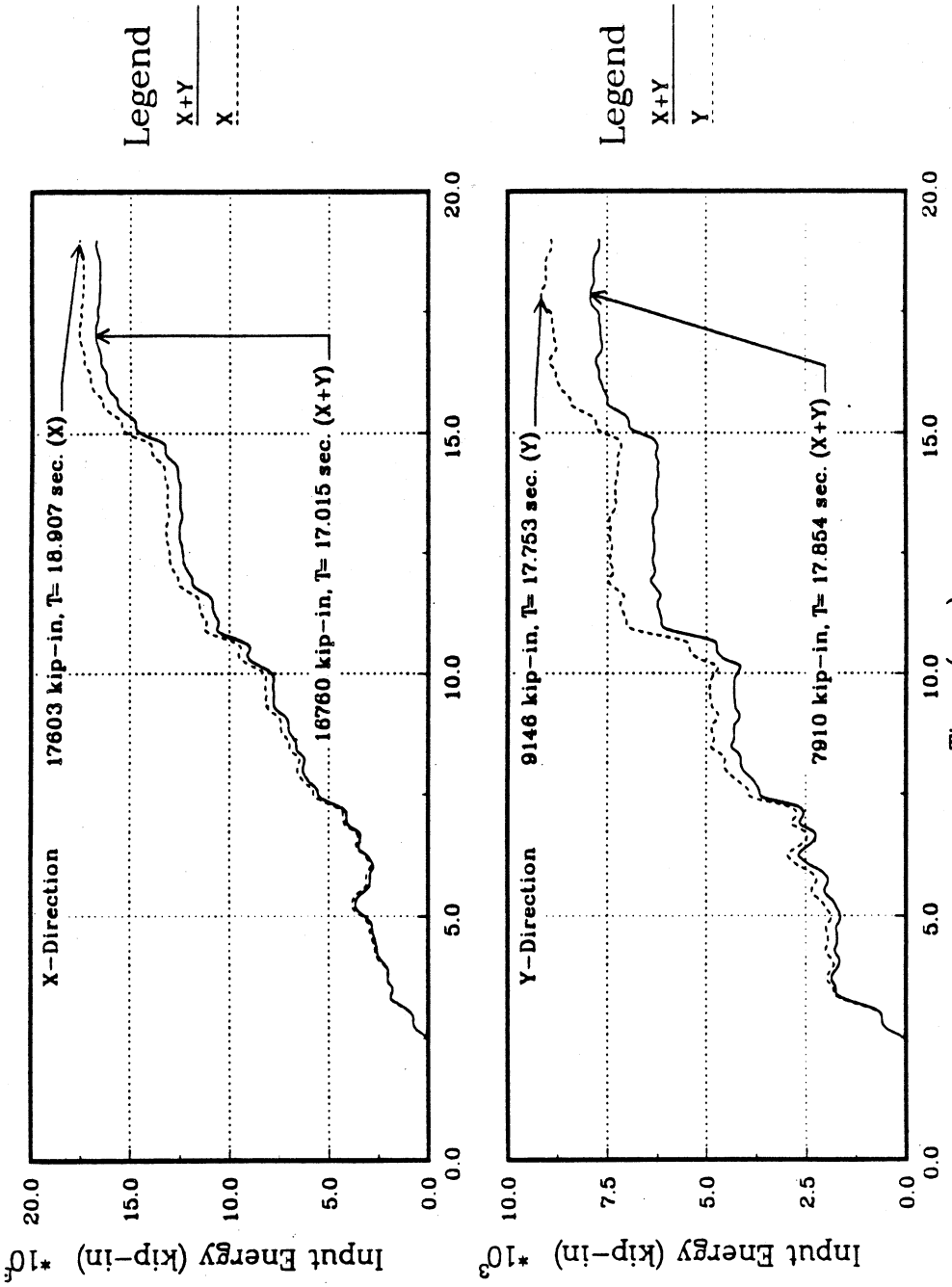

Figure 5.5: Absolute Input Energy Time History in the Principal Directions of Five Story Symmetrical Building Subjected to 0.5 g 1978 Miyagi-Ken-Oki Earthquake

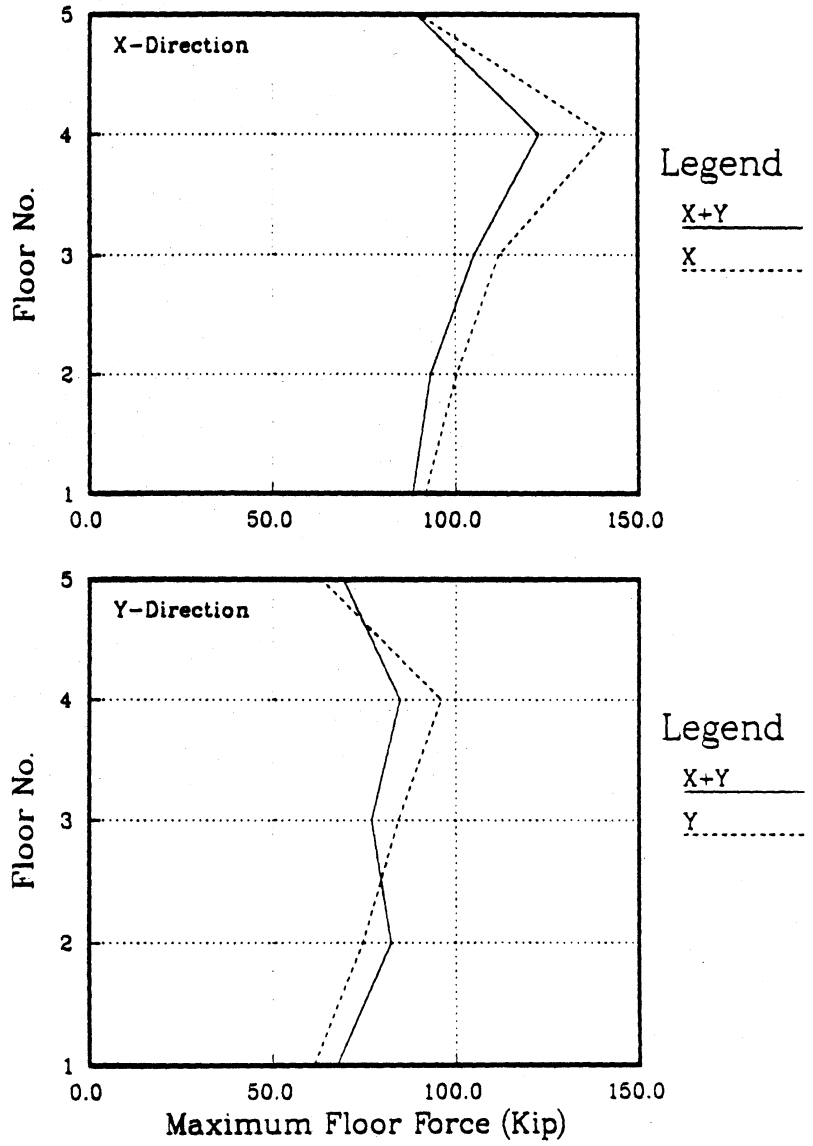

Figure 5.6: Comparison of Maximum Floor Force of Five Story Symmetrical Building Subjected to 0.5 g 1978 Miyagi-Ken-Oki Earthquake

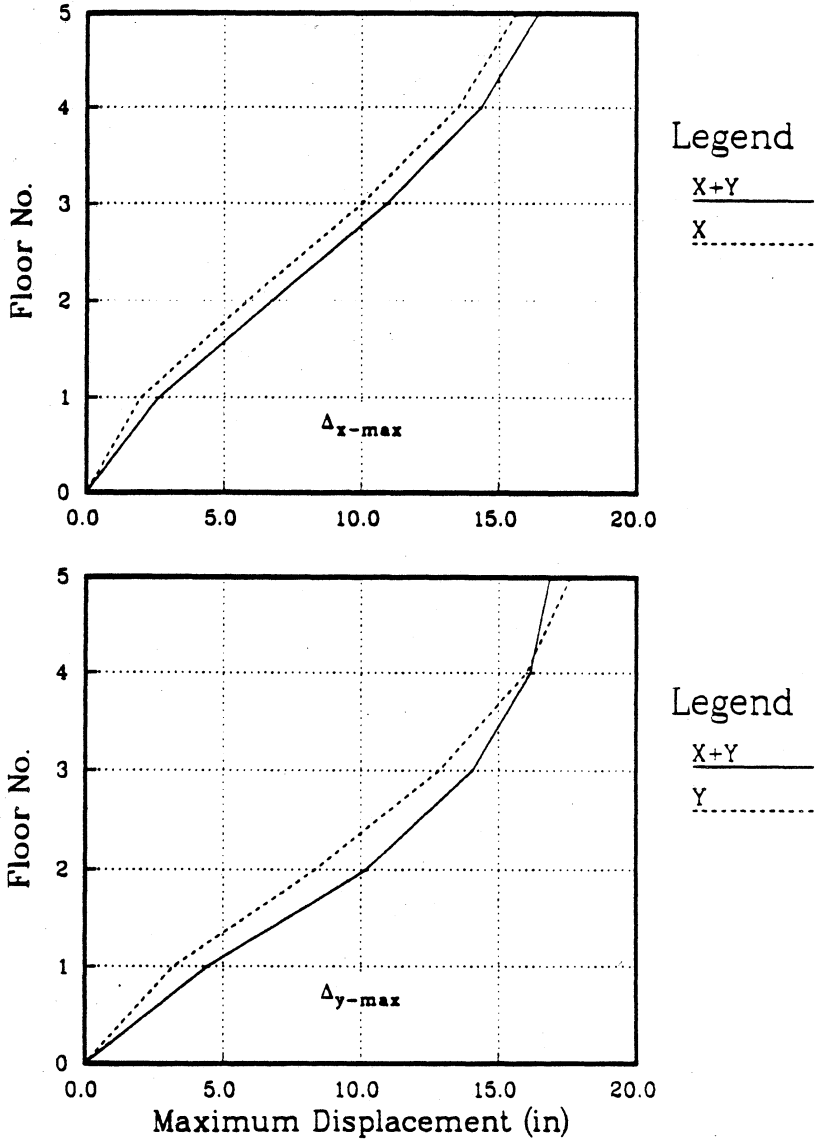

Figure 5.7: Comparison of C.M. Maximum Displacement of Five Story Symmetrical Building Subjected to 0.5 g 1978 Miyagi-Ken-Oki Earthquake

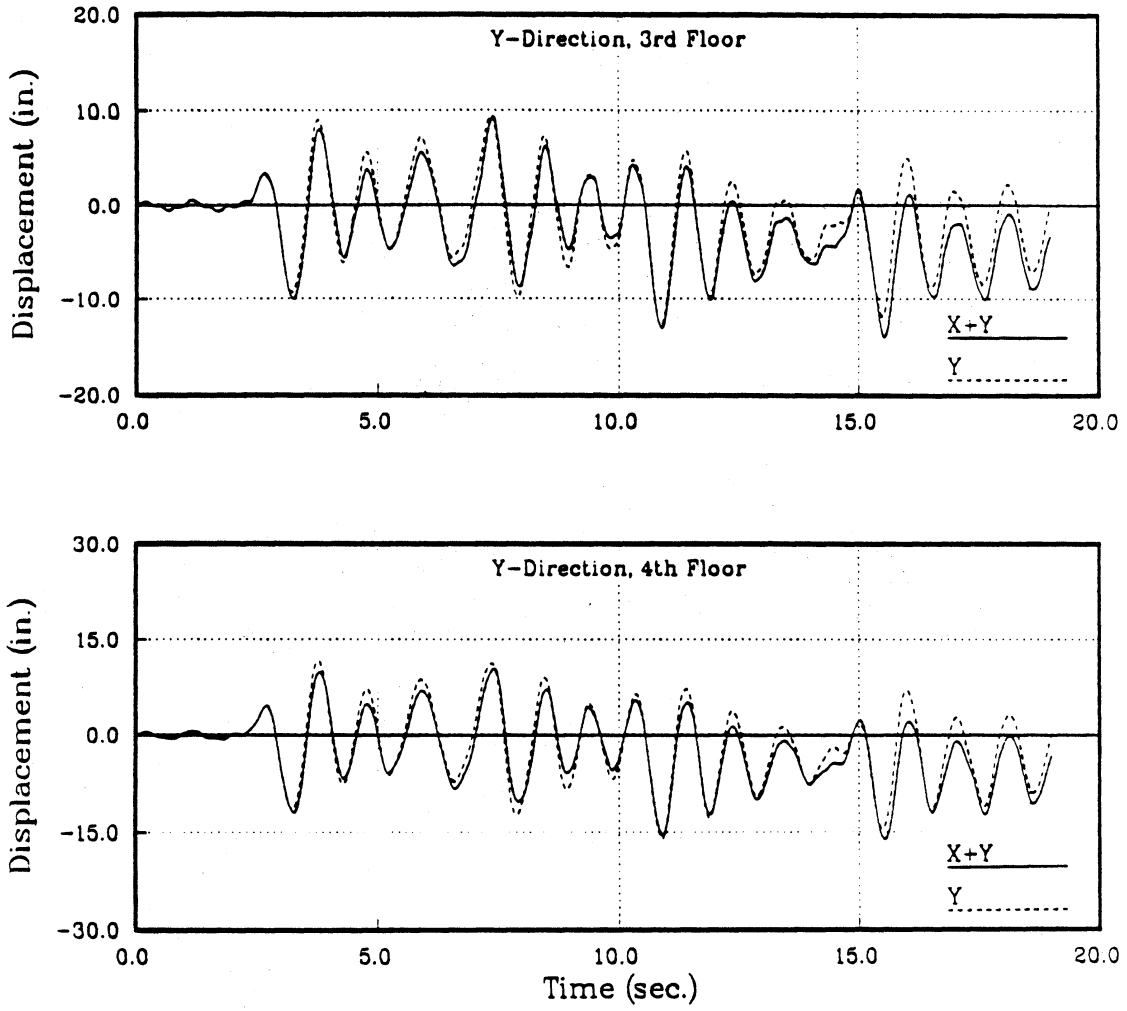

Figure 5.8: 3rd and 4th Floor Center of Mass Displacement Time History Response in the Y-direction of Five Story Symmetrical Building Subjected to 0.5 g 1978 Miyagi-Ken-Oki Earthquake

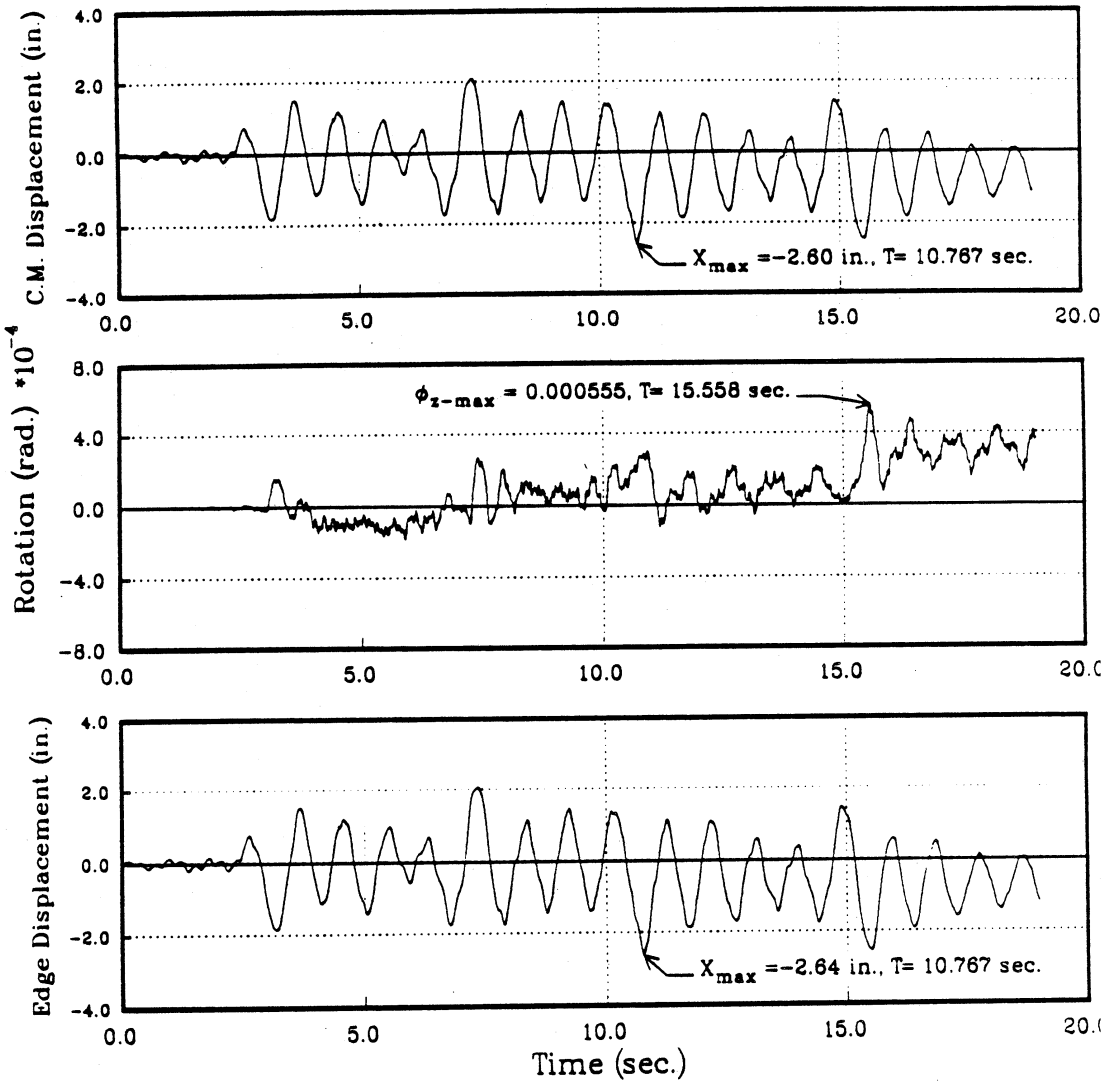

Figure 5.9: (a)1st Floor Center of Mass Displacement and Rotation, Edge Displacement Time History of Five Story Symmetrical Building Subjected to 0.5 g 1978 Miyagi-Ken-Oki Earthquake : X-Direction

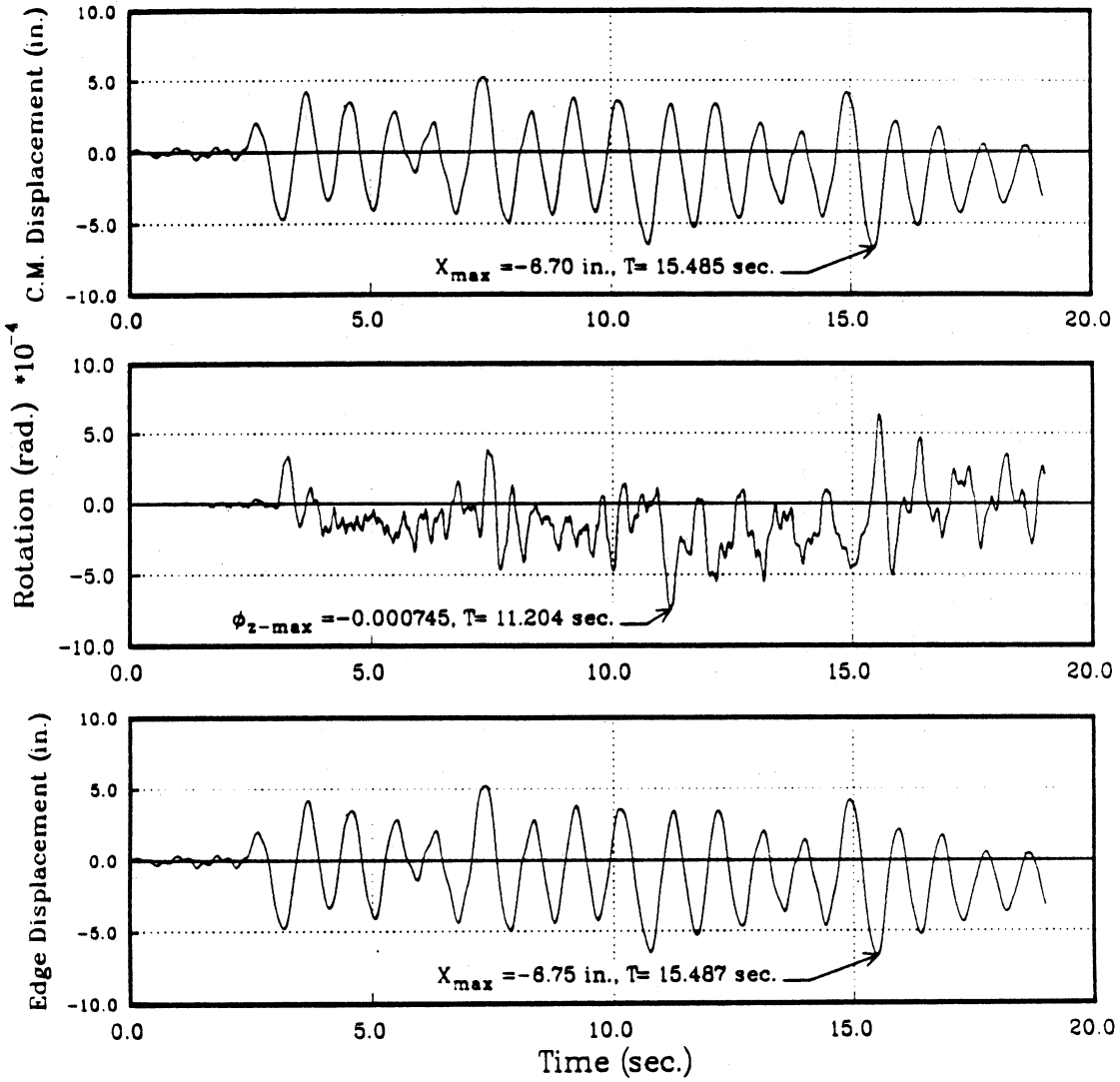

Figure 5.9: (b)2nd Floor Center of Mass Displacement and Rotation, Edge Displacement Time History of Five Story Symmetrical Building Subjected to 0.5 g 1978 Miyagi-Ken-Oki Earthquake : X-Direction (Continue)

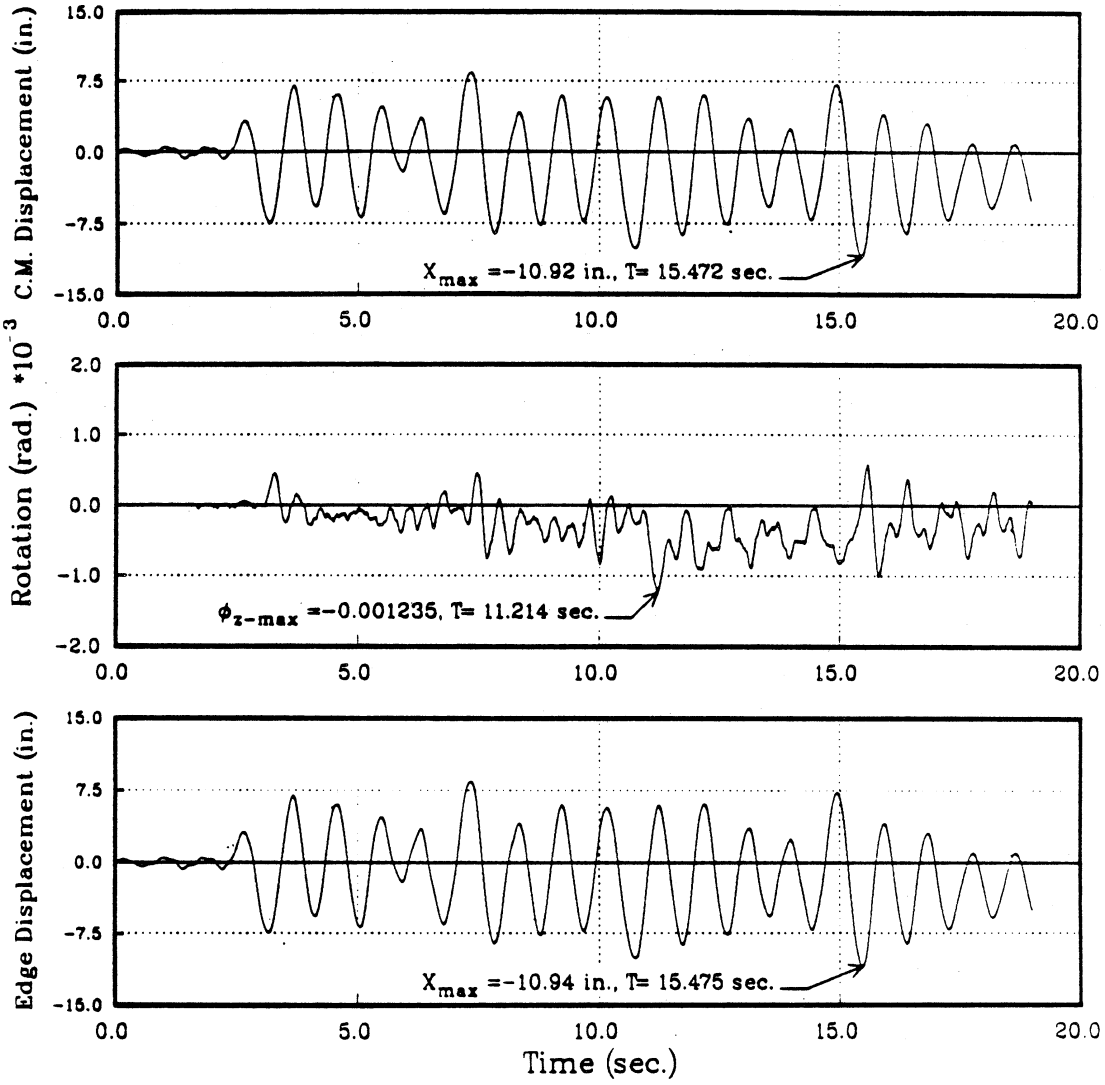

Figure 5.9: (c)3rd Floor Center of Mass Displacement and Rotation, Edge Displacement Time History of Five Story Symmetrical Building Subjected to 0.5 g 1978 Miyagi-Ken-Oki Earthquake : X-Direction (Continue)

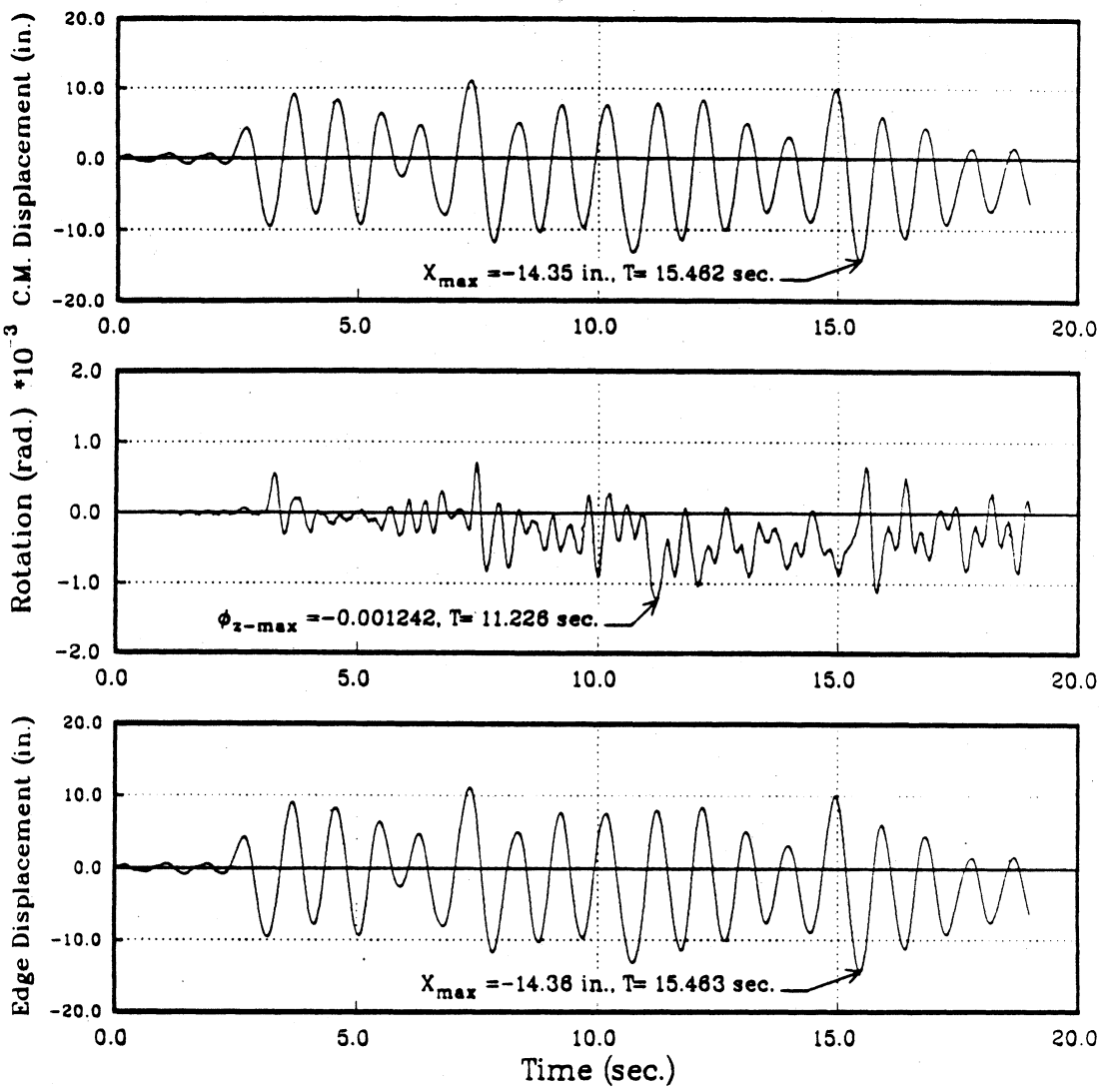

Figure 5.9: (d)4th Floor Center of Mass Displacement and Rotation, Edge Displacement Time History of Five Story Symmetrical Building Subjected to 0.5 g 1978 Miyagi-Ken-Oki Earthquake : X-Direction (Continue)

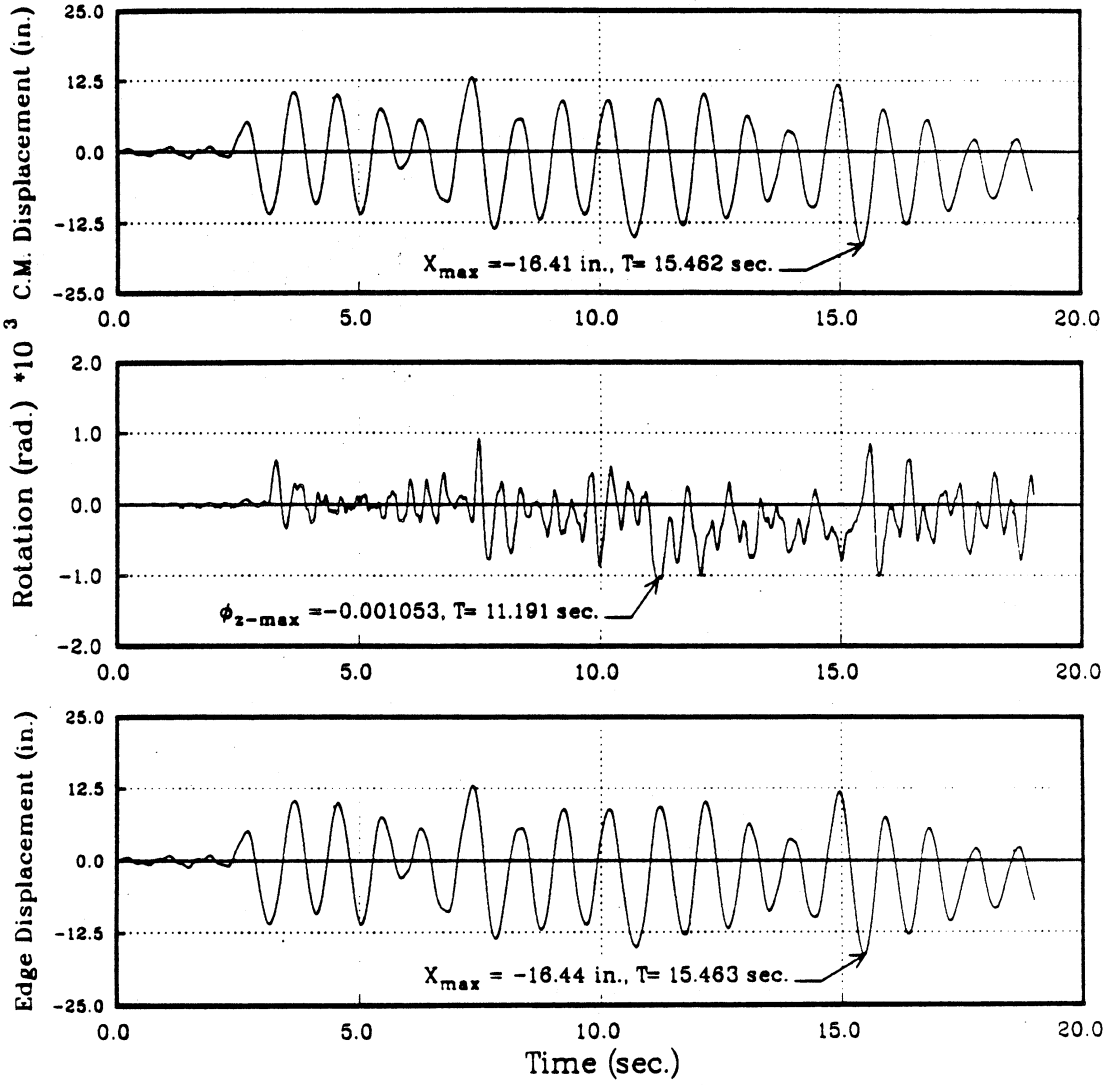

Figure 5.9: (e)5th Floor Center of Mass Displacement and Rotation, Edge Displacement Time History of Five Story Symmetrical Building Subjected to 0.5 g 1978 Miyagi-Ken-Oki Earthquake : X-Direction (Continue)

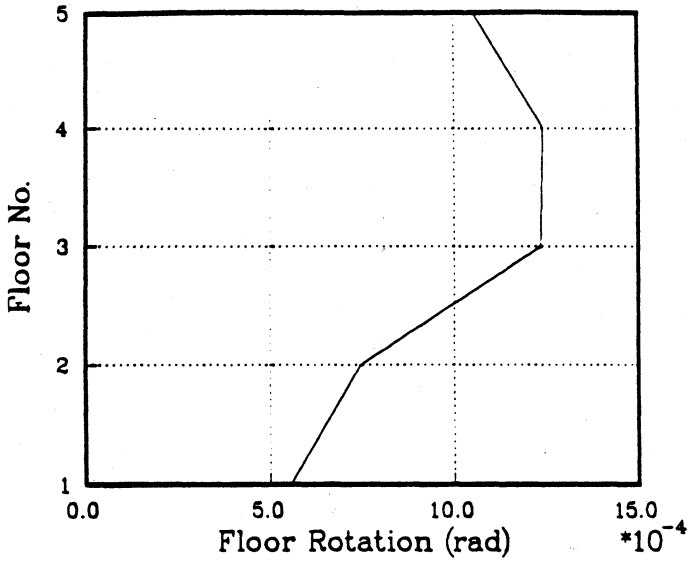

Figure 5.10: Envelope of Center of Mass Rotation of Five Story Symmetrical Building Subjected to 0.5 g 1978 Miyagi-Ken-Oki Earthquake

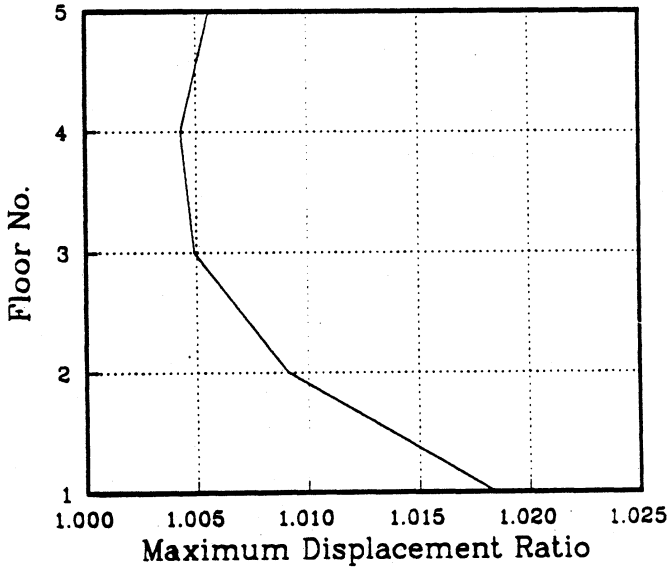

Figure 5.11: Maximum Ratio of Edge to Center of Mass Floor Displacement of Five Story Symmetrical Building Subjected to 0.5 g 1978 Miyagi-Ken-Oki Earthquake

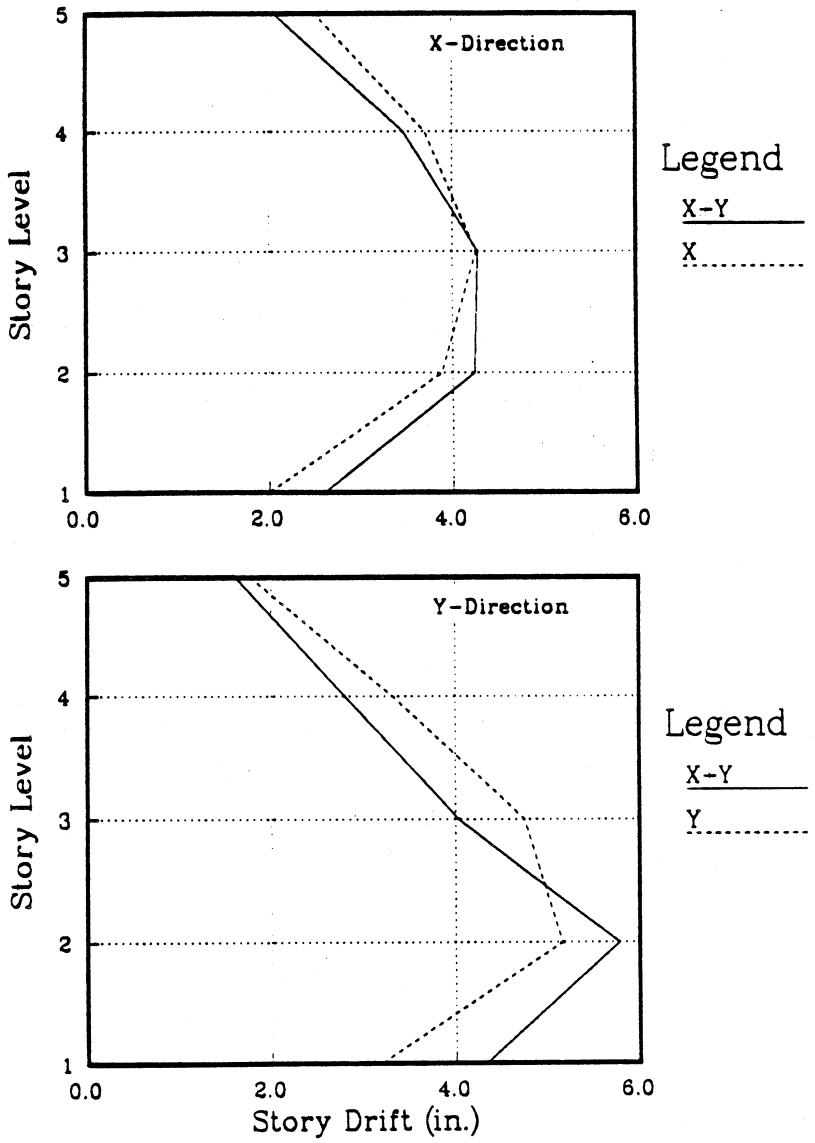

Figure 5.12: Comparison of Center of Mass Maximum Story Drift of Five Story Symmetrical Building Subjected to 0.5 g 1978 Miyagi-Ken-Oki Earthquake

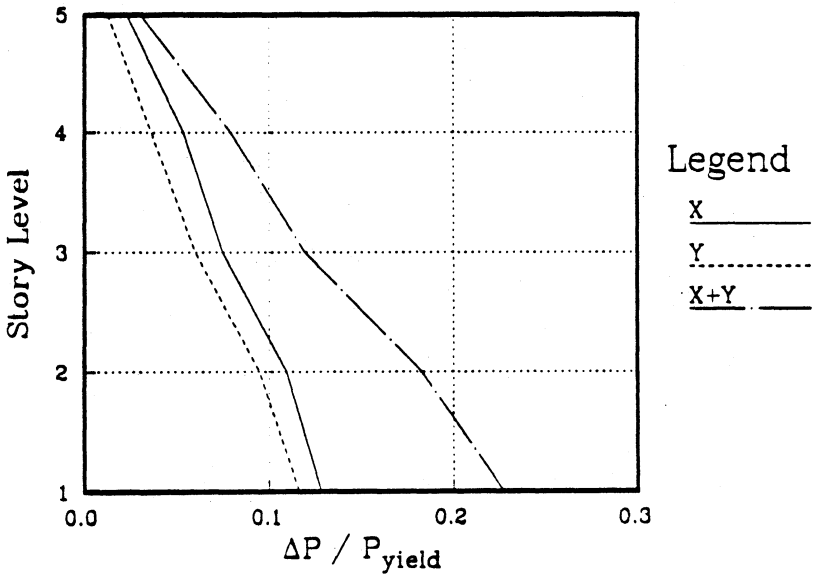

Figure 5.13: Comparison of Column Axial Force Increase : Cases X, Y and X+Y

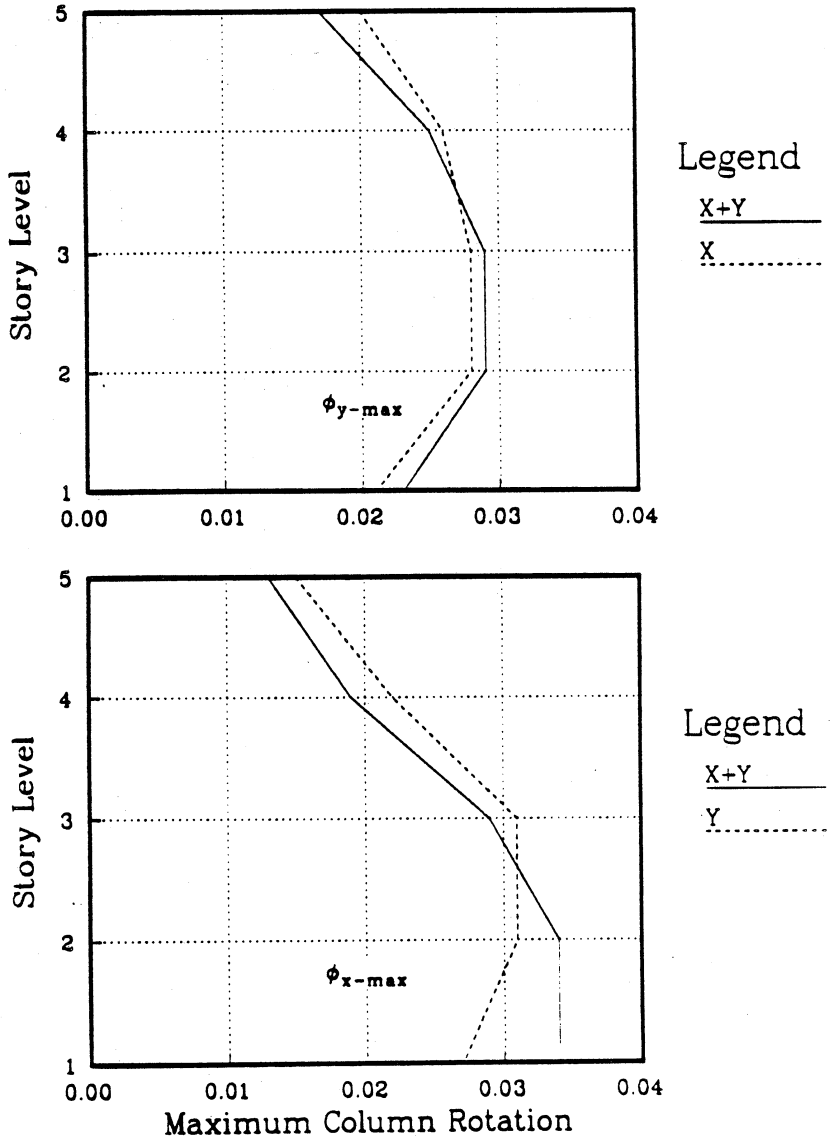

Figure 5.14: Envelope of Maximum Column Rotation of Five Story Symmetrical Building Subjected to 0.5 g 1978 Miyagi-Ken-Oki Earthquake

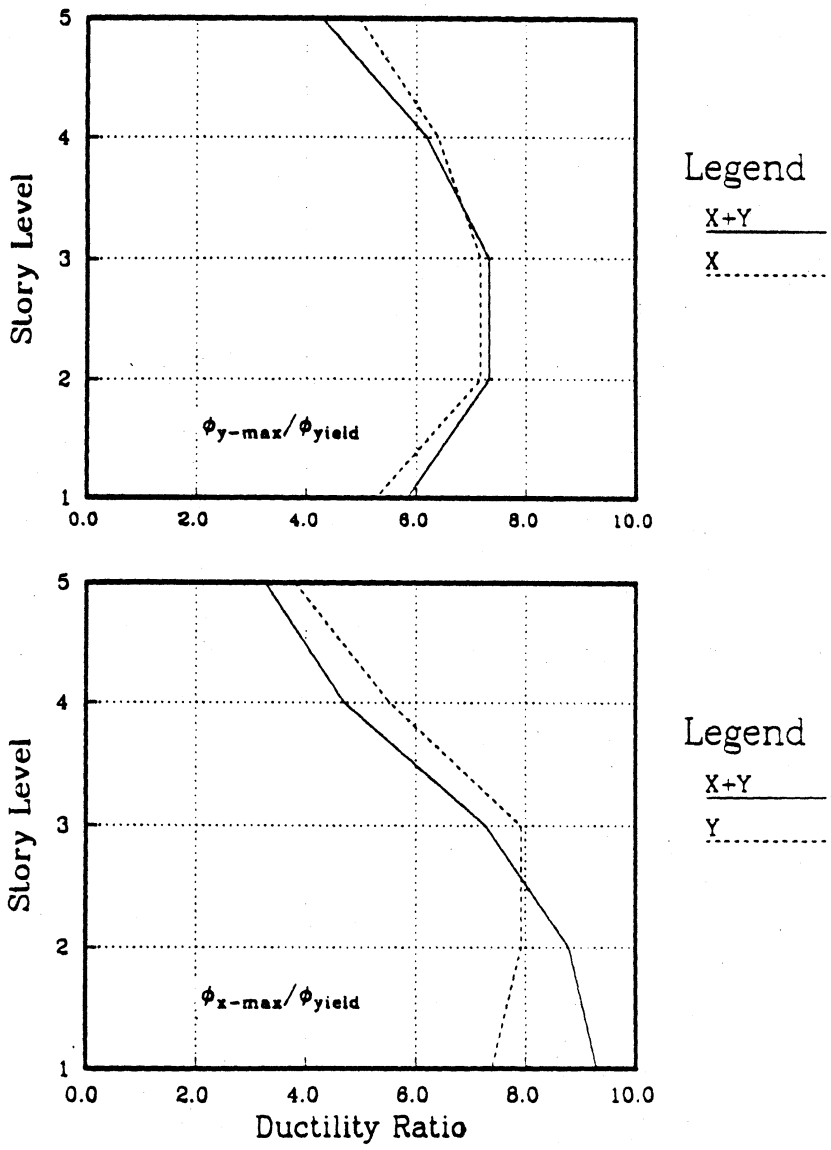

Figure 5.15: Envelope of Maximum Column Ductility Ratio of Five Story Symmetrical Building Subjected to 0.5 g 1978 Miyagi-Ken-Oki Earthquake

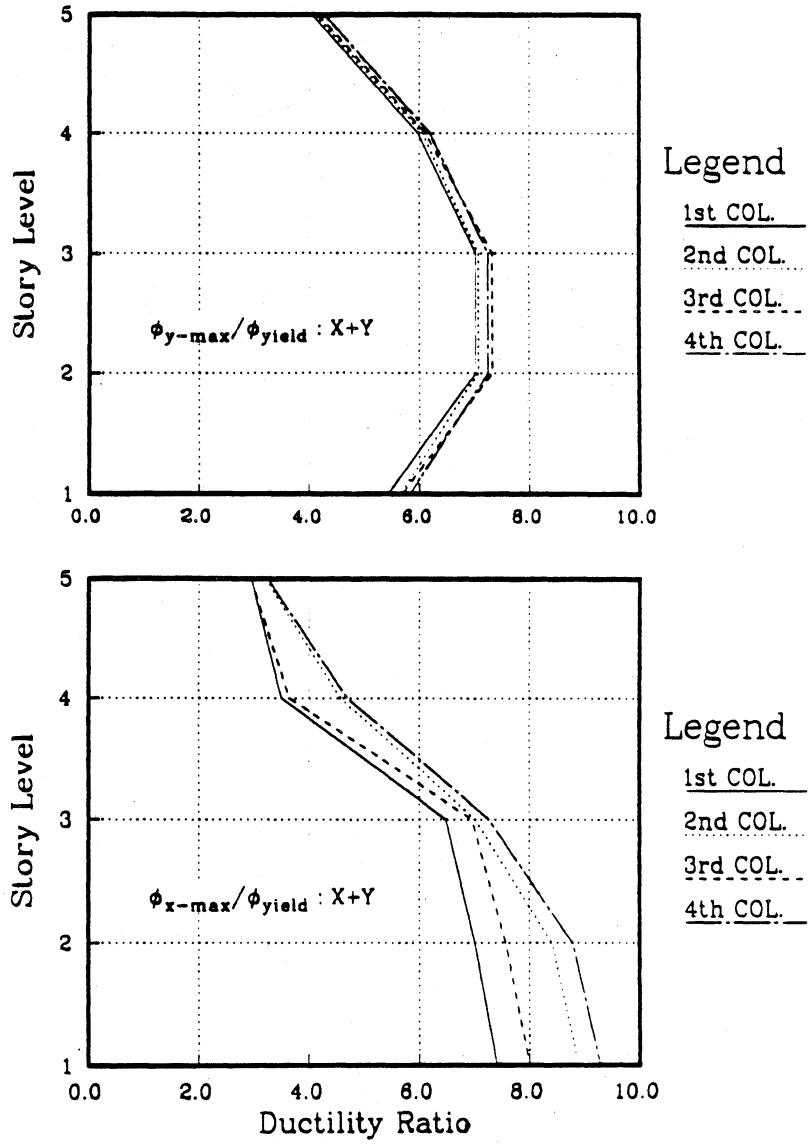

Figure 5.16: Envelope of Maximum Column Ductility Ratio of Five Story Symmetrical Building Subjected to 0.5 g 1978 Miyagi-Ken-Oki Earthquake : Case X+Y

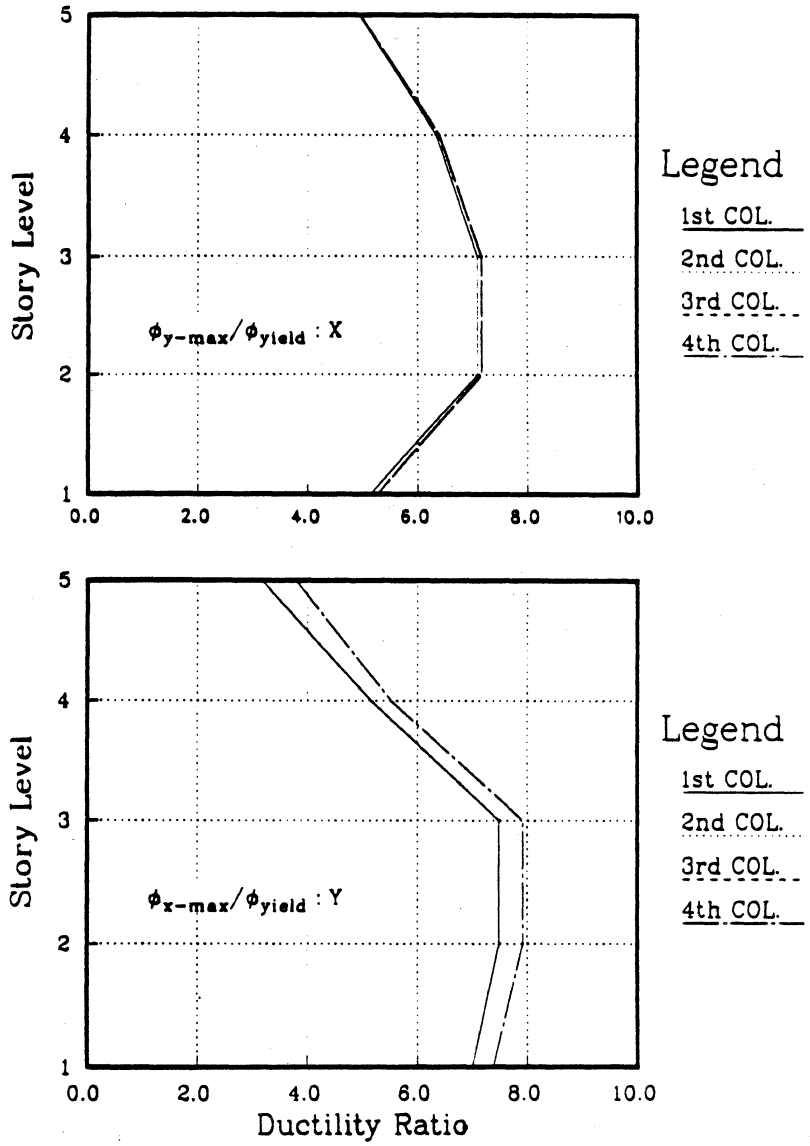

Figure 5.17: Envelope of Maximum Column Ductility Ratio of Five Story Symmetrical Building Subjected to 0.5 g 1978 Miyagi-Ken-Oki Earthquake : Cases X and Y

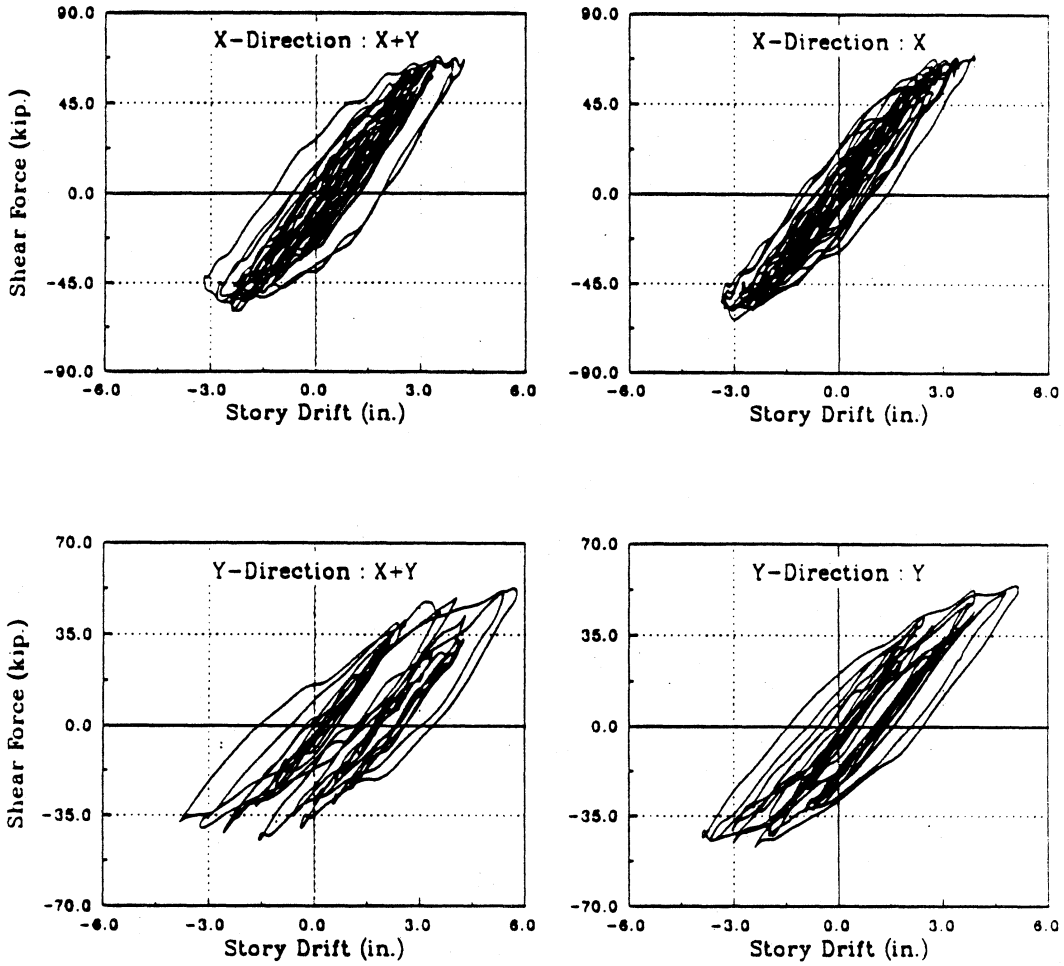

Figure 5.18: (a)Shear Force Hysteresis of Column 16 of Five Story Symmetrical Building Subjected to 0.5 g 1978 Miyagi-Ken-Oki Earthquake : 2nd Story

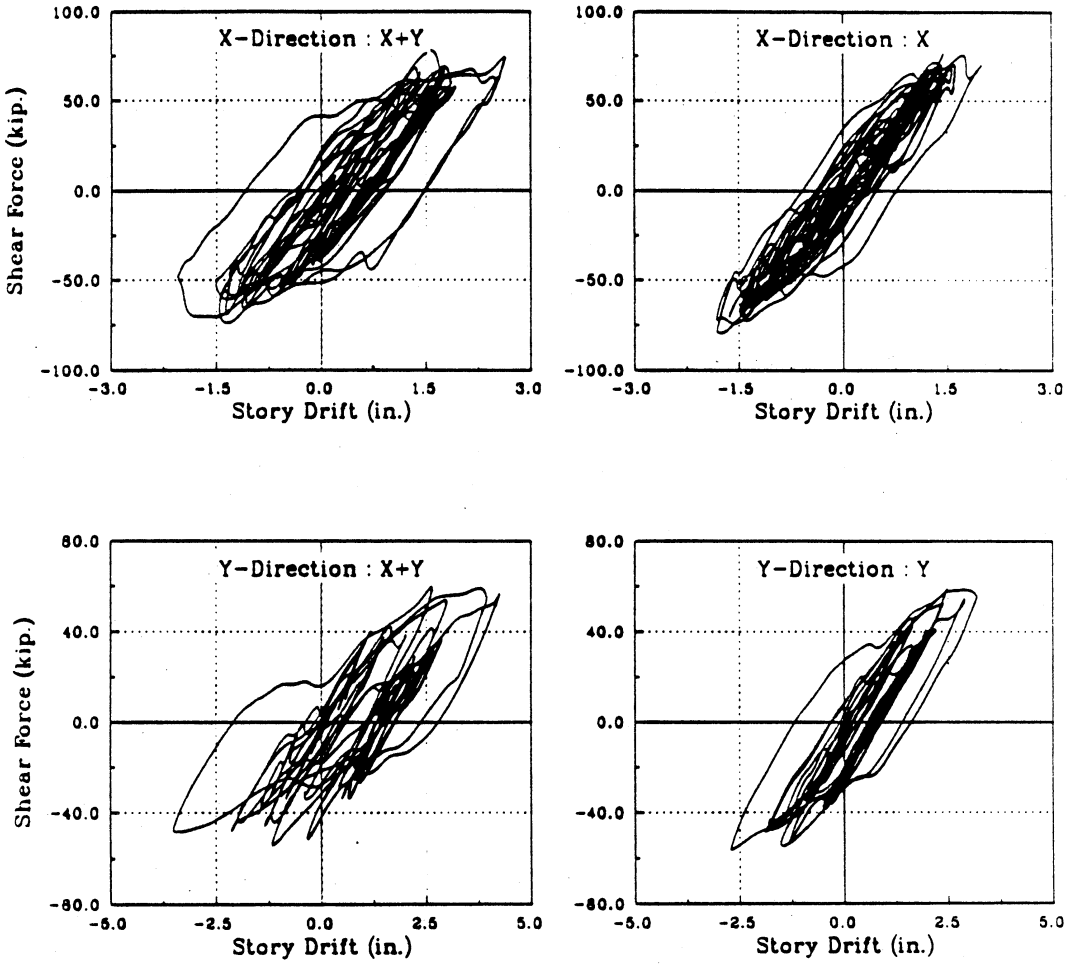

Figure 5.18: (b)Shear Force Hysteresis of Column 20 of Five Story Symmetrical Building Subjected to 0.5 g 1978 Miyagi-Ken-Oki Earthquake : 1st Story (Continue)

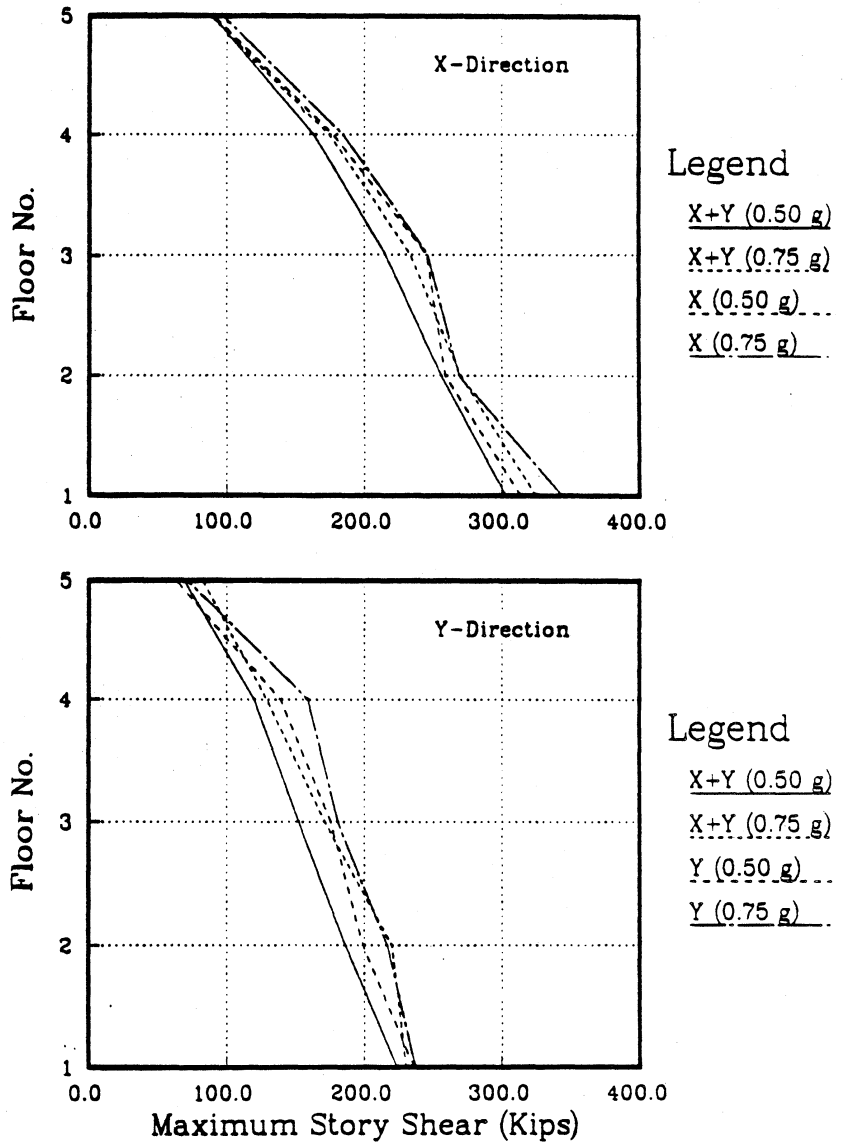

Figure 5.19: Comparison of Maximum Story Shear of Five Story Symmetrical Building Subjected to 0.50 g and 0.75 g 1978 Miyagi-Ken-Oki Earthquake

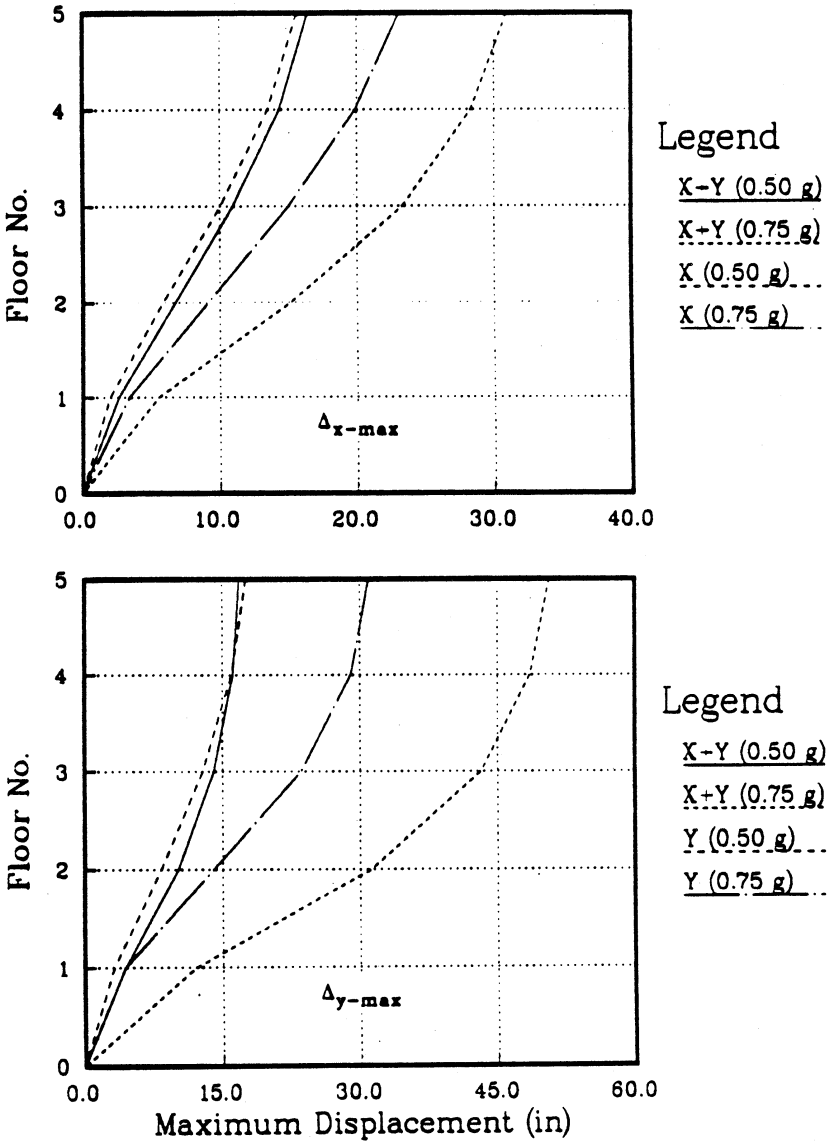

Figure 5.20: Comparison of C.M. Maximum Displacement of Five Story Symmetrical Building Subjected to 0.5 g and 0.75 g 1978 Miyagi-Ken-Oki Earthquake

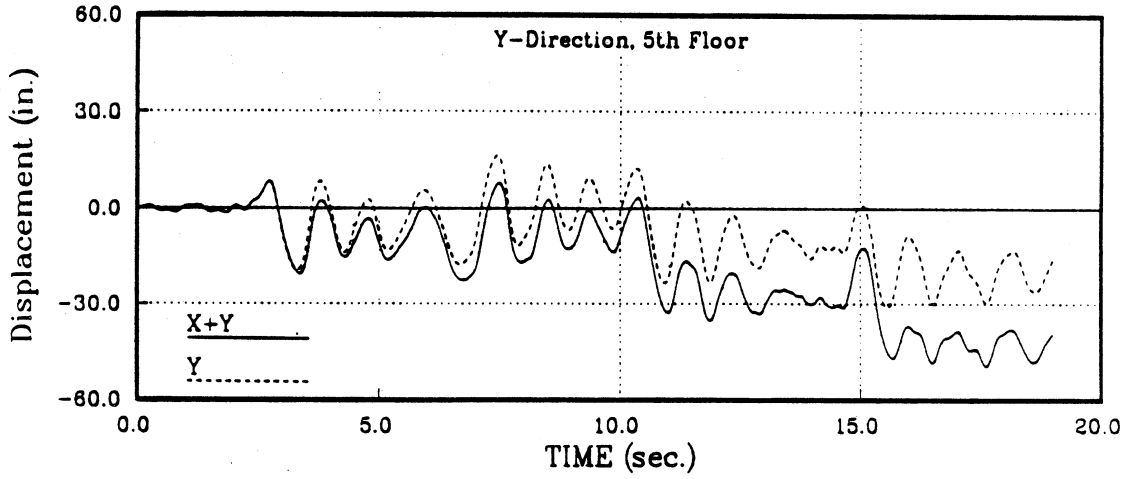

Figure 5.21: 5th Floor Center of Mass Displacement and Rotation, Edge Displacement Time History of Five Story Symmetrical Building Subjected to 0.75 g 1978 Miyagi-Ken-Oki Earthquake

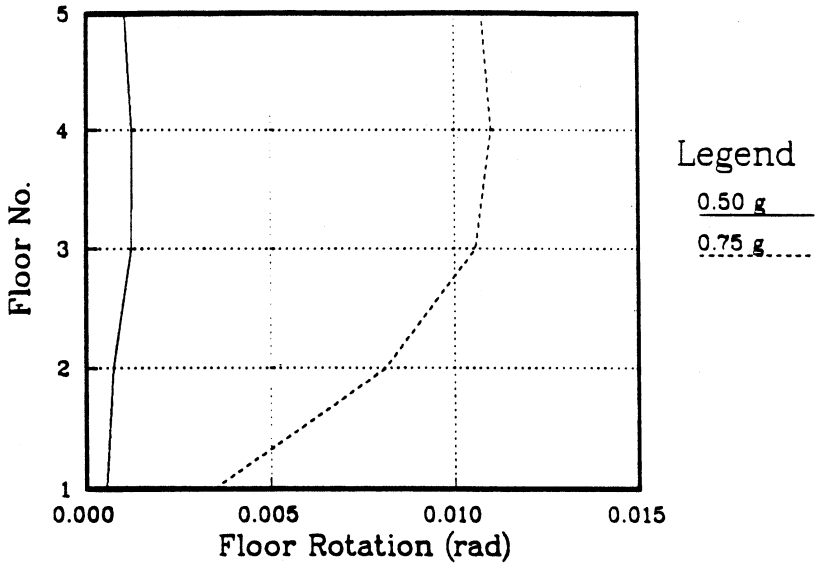

Figure 5.22: Envelope of Center of Mass Rotation of Five Story Symmetrical Building Subjected to 0.5 g and 0.75 g 1978 Miyagi-Ken-Oki Earthquake

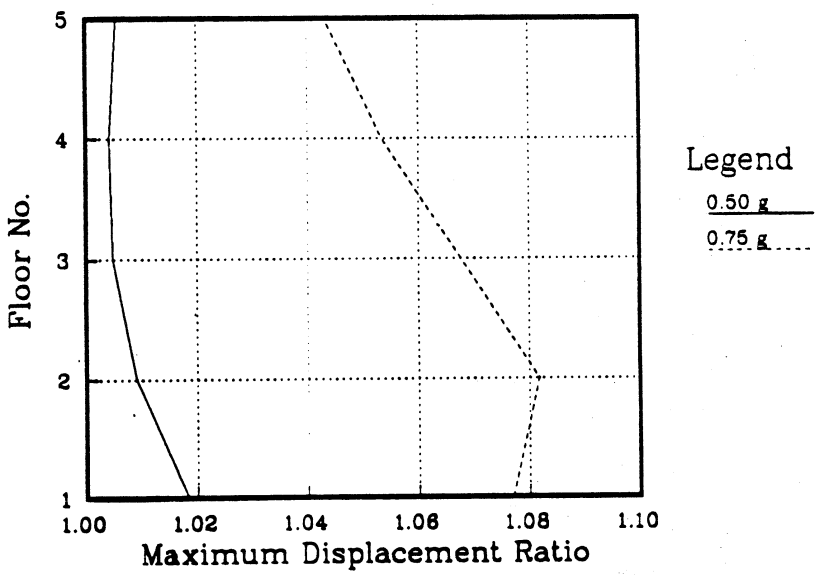

Figure 5.23: Maximum Ratio of Edge to Center of Mass Floor Displacement of Five Story Symmetrical Building Subjected to 0.5 g and 0.75 g 1978 Miyagi-Ken-Oki Earthquake

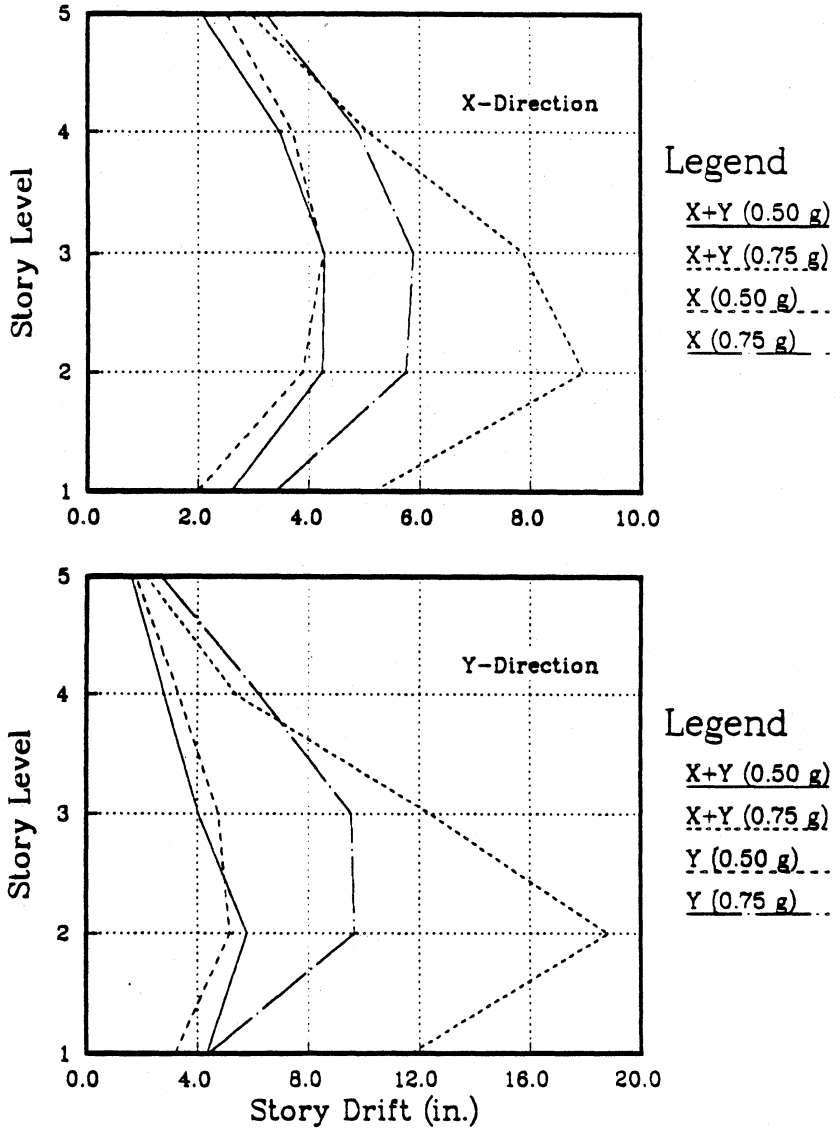

Figure 5.24: Comparison of Center of Mass Maximum Story Drift of Five Story Symmetrical Building Subjected to 0.5 g and 0.75 g 1978 Miyagi-Ken-Oki Earthquake

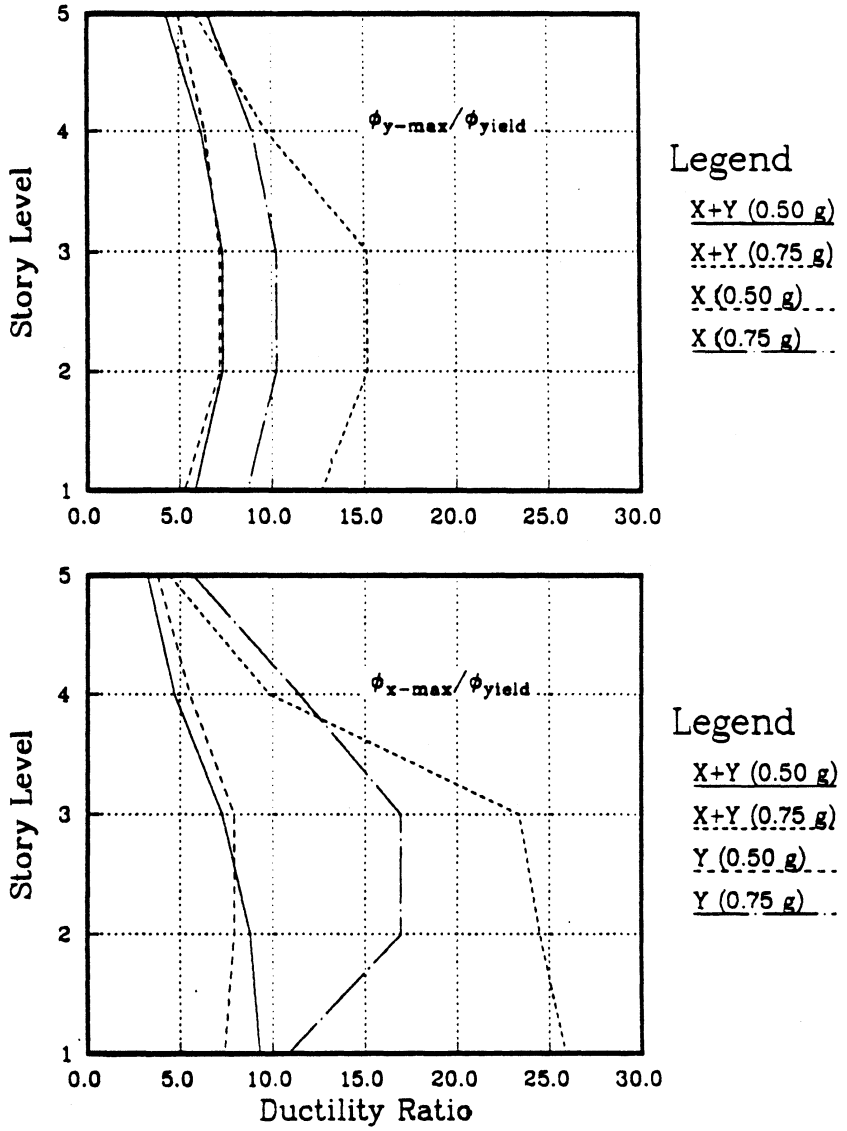

Figure 5.25: Envelope of Maximum Column Ductility Ratio of Five Story Symmetrical Building Subjected to 0.5 g and 0.75 g 1978 Miyagi-Ken-Oki Earthquake

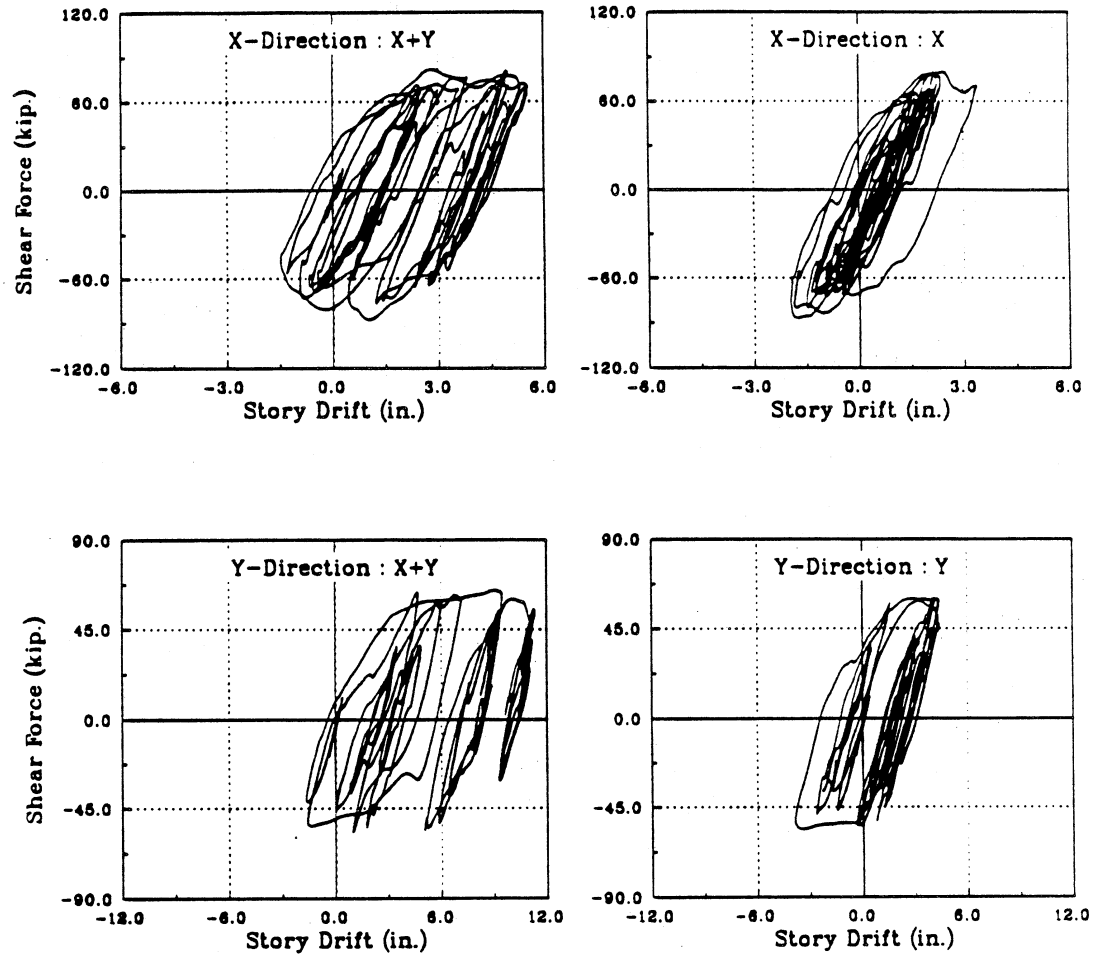

Figure 5.26: Shear Force Hysteresis of Column 16 of Five Story Symmetrical Building Subjected to 0.75 g 1978 Miyagi-Ken-Oki Earthquake : 1st Story

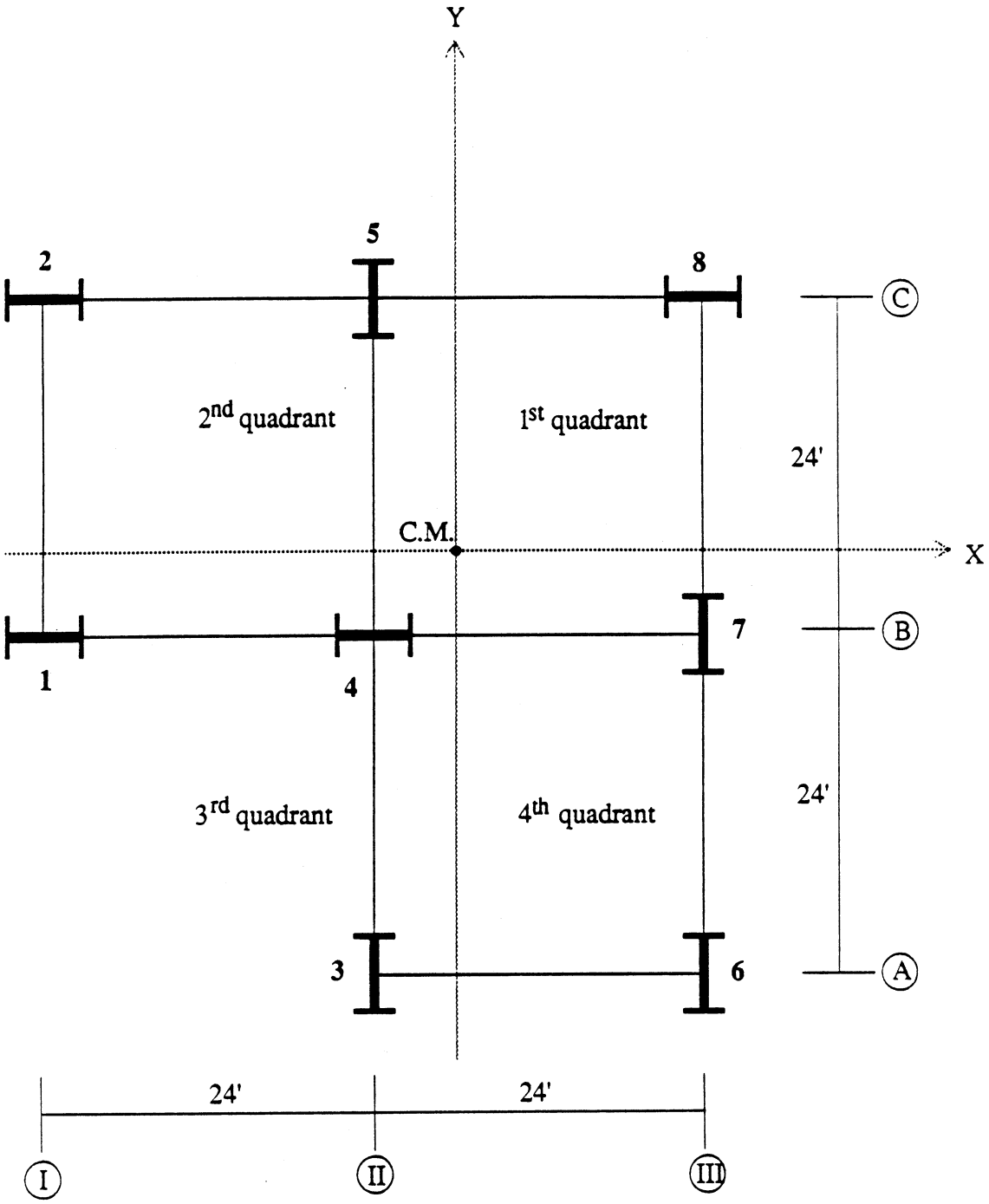

PLAN VIEW

Figure 5.27: (a)Floor Plan, Column Line and Quadrant numbering of Five Story L-Shape Moment Resistant Steel Frame

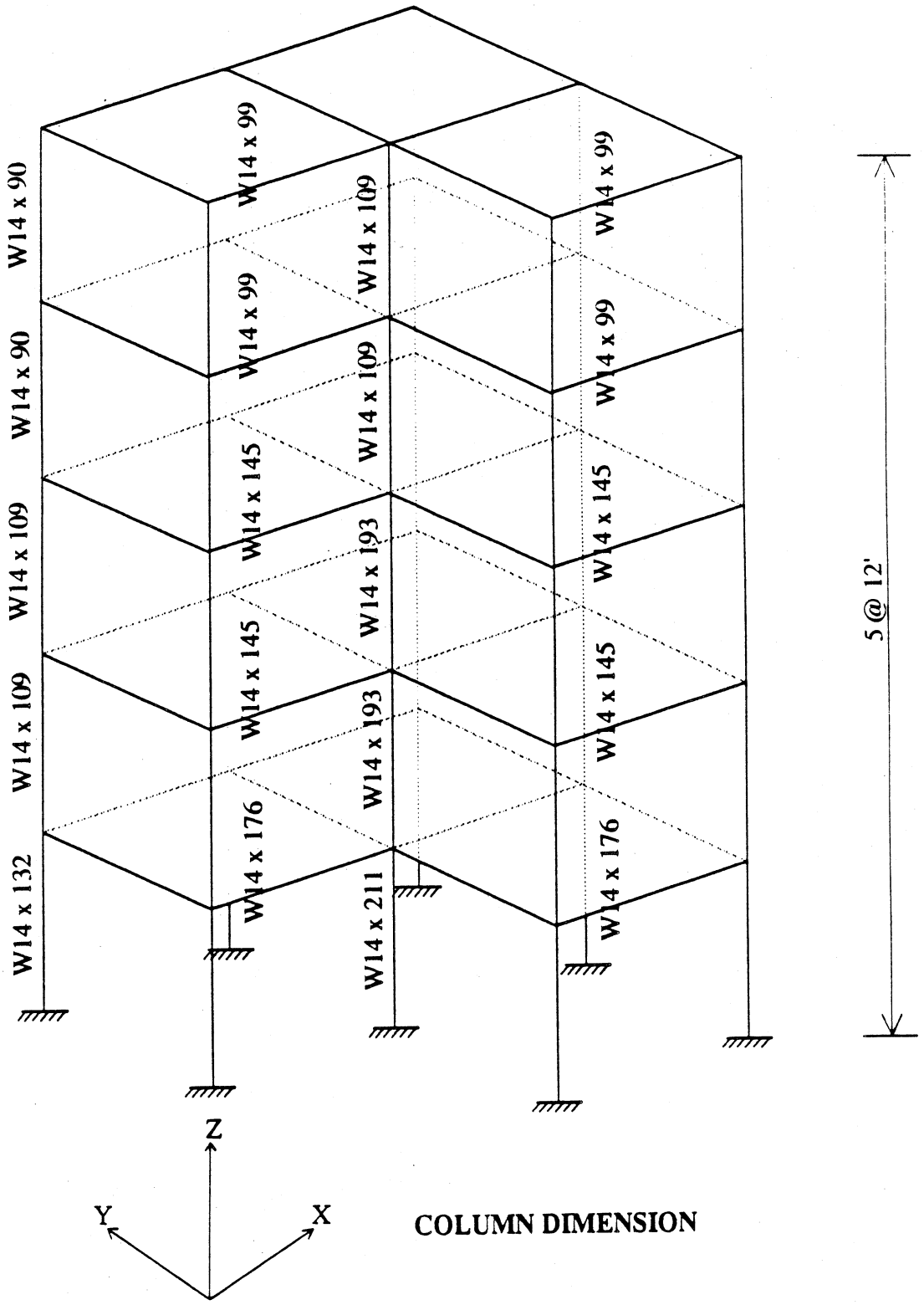

Figure 5.27: (b)Column Dimension of Five Story L-Shape Moment Resistant Steel Frame (Continue)

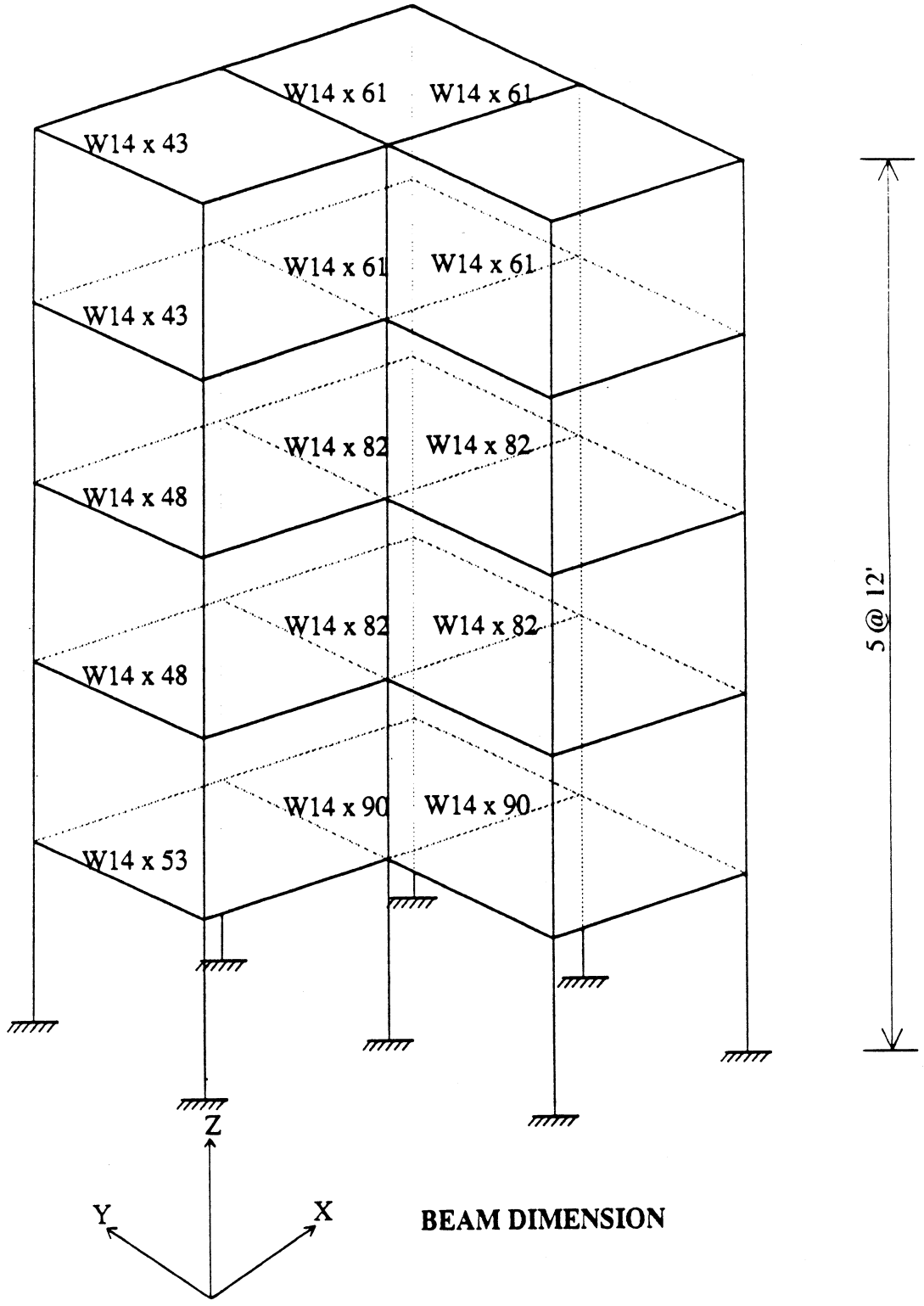

Figure 5.27: (c)Beam Dimension of Five Story L-Shape Moment Resistant Steel Frame (Continue)

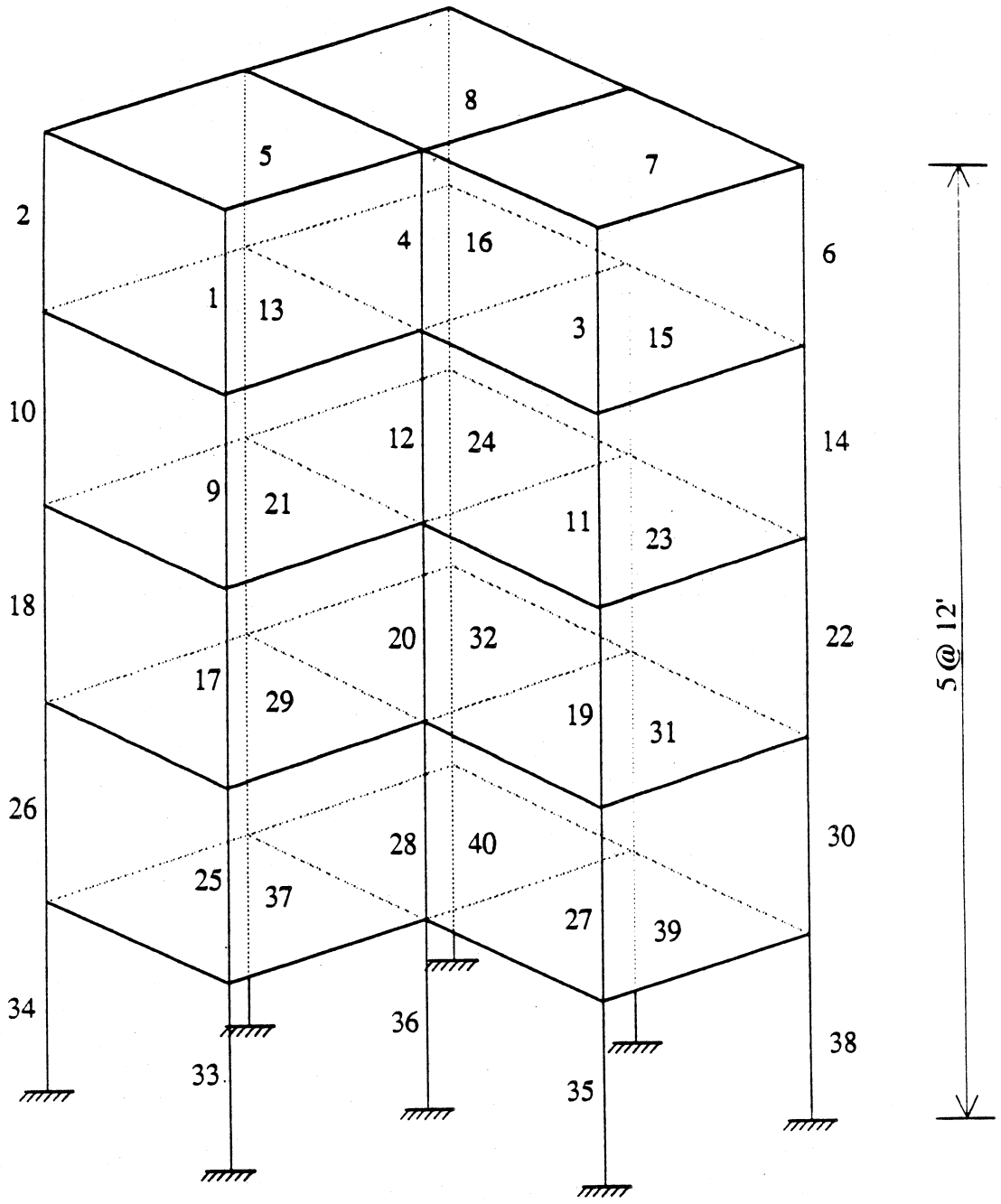

Figure 5.27: (d)Column Numbering of Five Story L-Shape Moment Resistant Steel Frame (Continue)

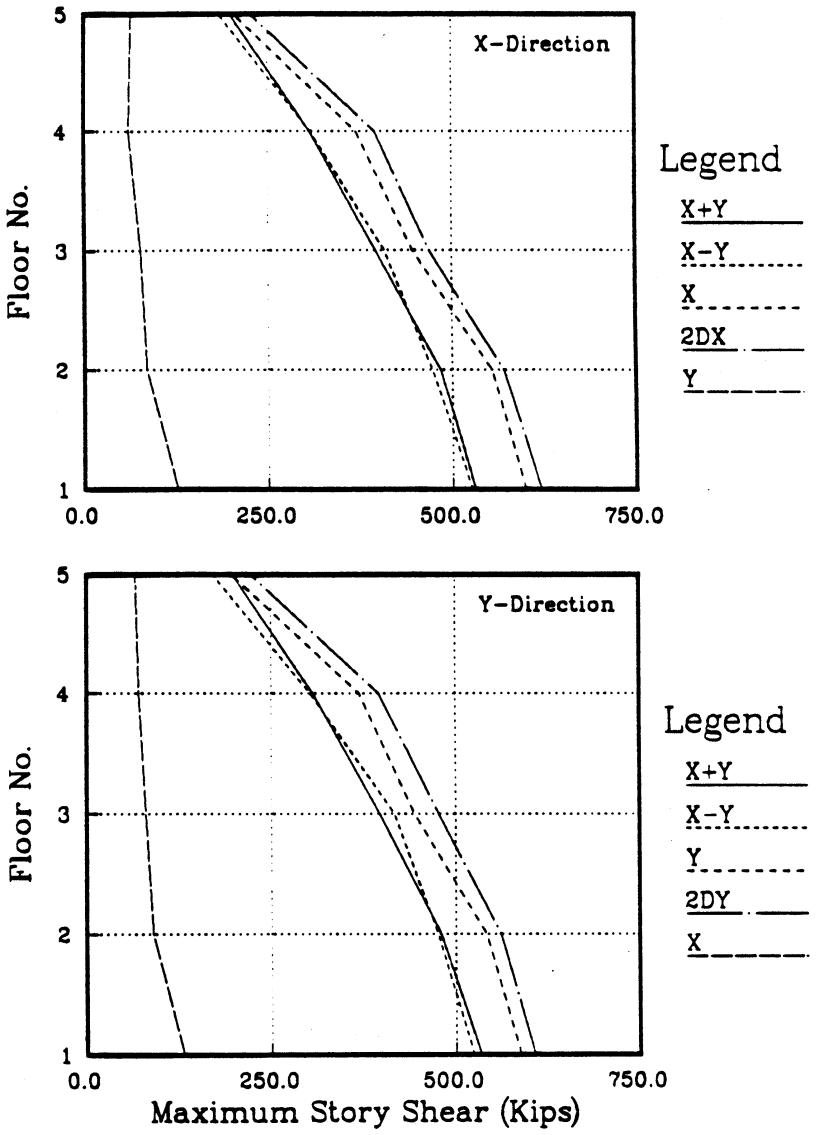

Figure 5.28: Comparison of Maximum Story Shear of Five Story L-Shape Building Subjected to 0.5 g 1978 Miyagi-Ken-Oki Earthquake

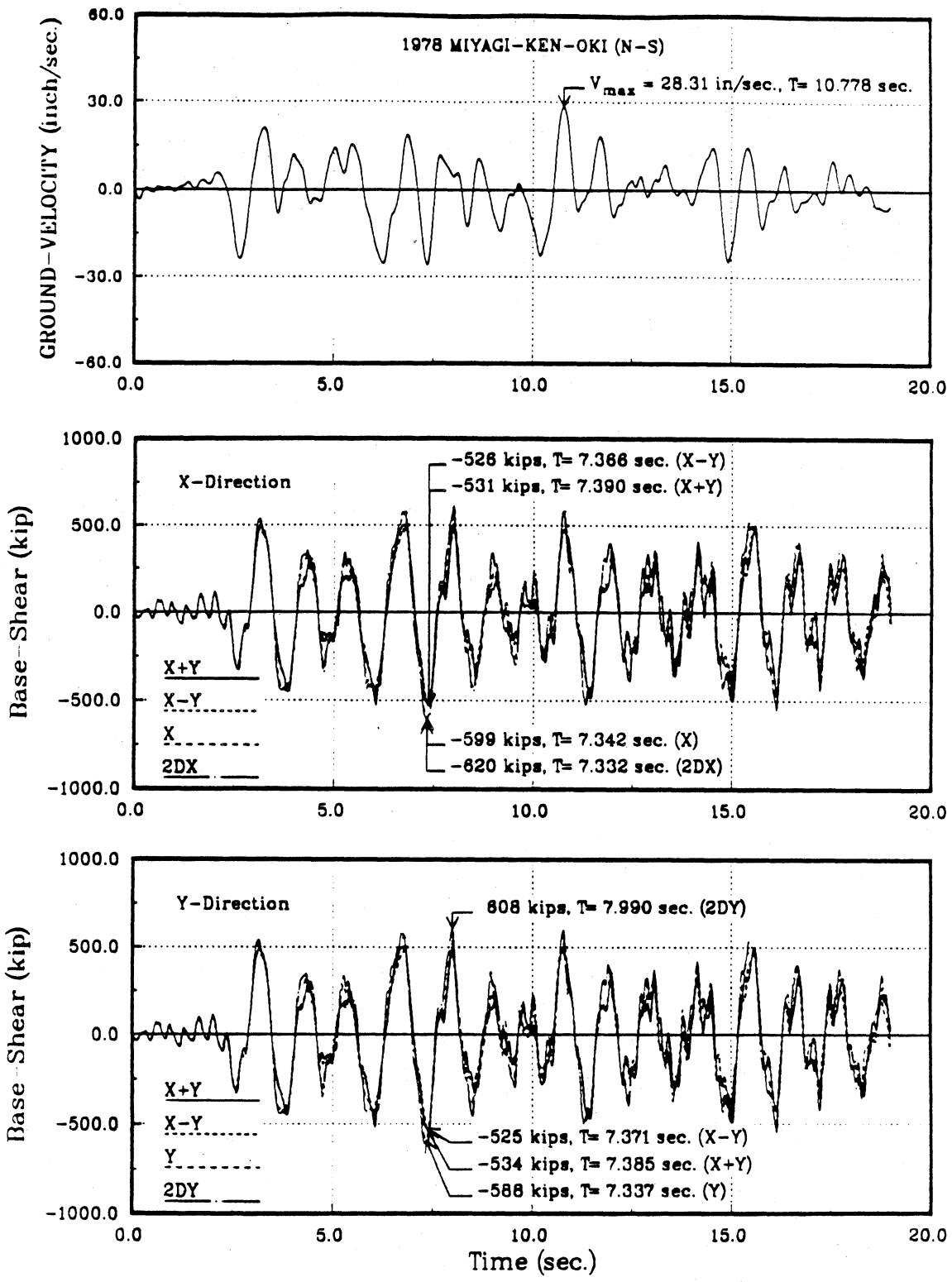

Figure 5.29: Input Ground Velocity and Base Shear Time History in the Principal Directions of Five Story L-Shape Building Subjected to 0.5 g 1978 Miyagi-Ken-Oki Earthquake

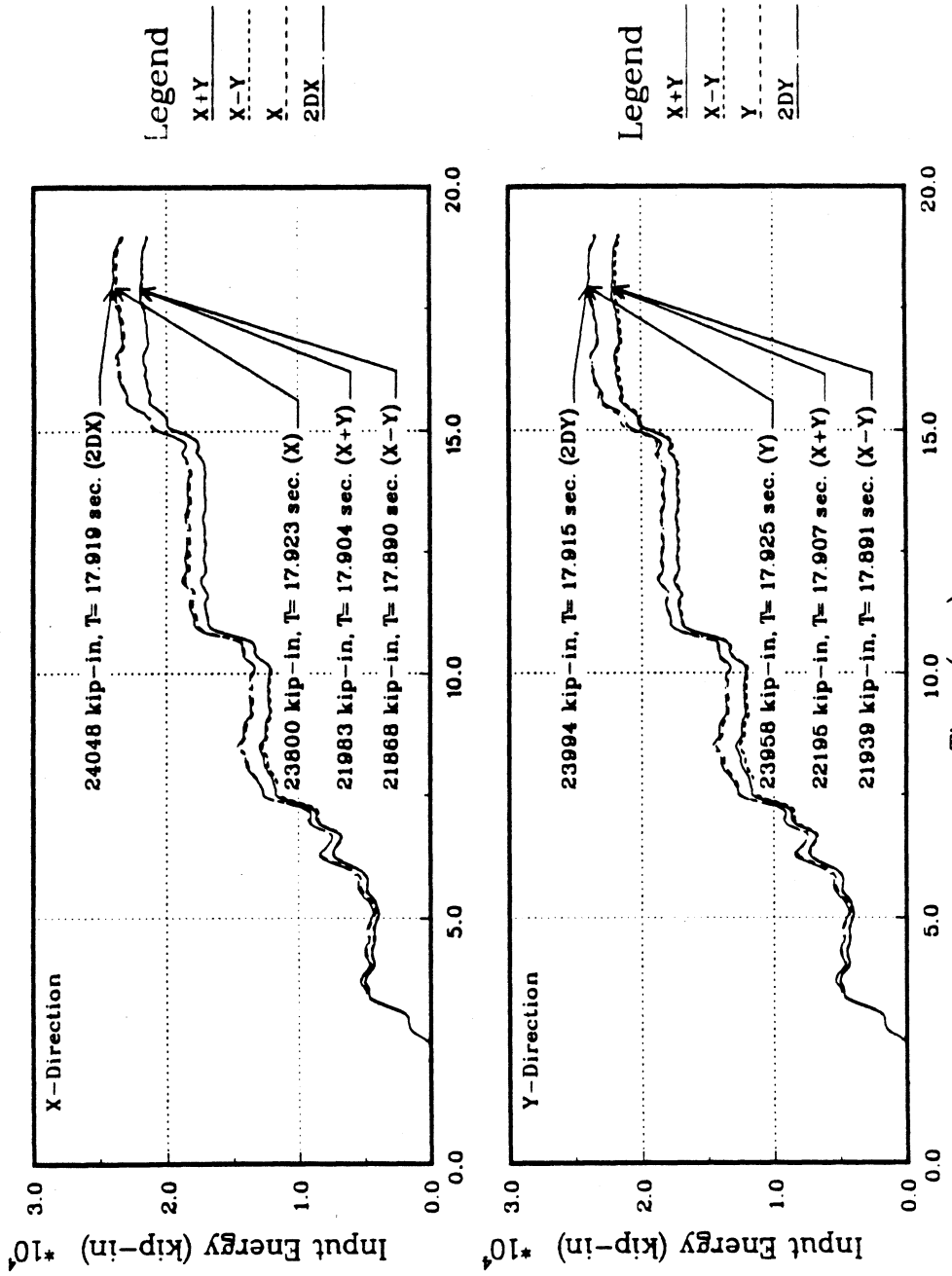

Figure 5.30: Absolute Input Energy Time History in the Principal Directions of Five Story L-Shape Building Subjected to 0.5 g 1978 Miyagi-Ken-Oki Earthquake

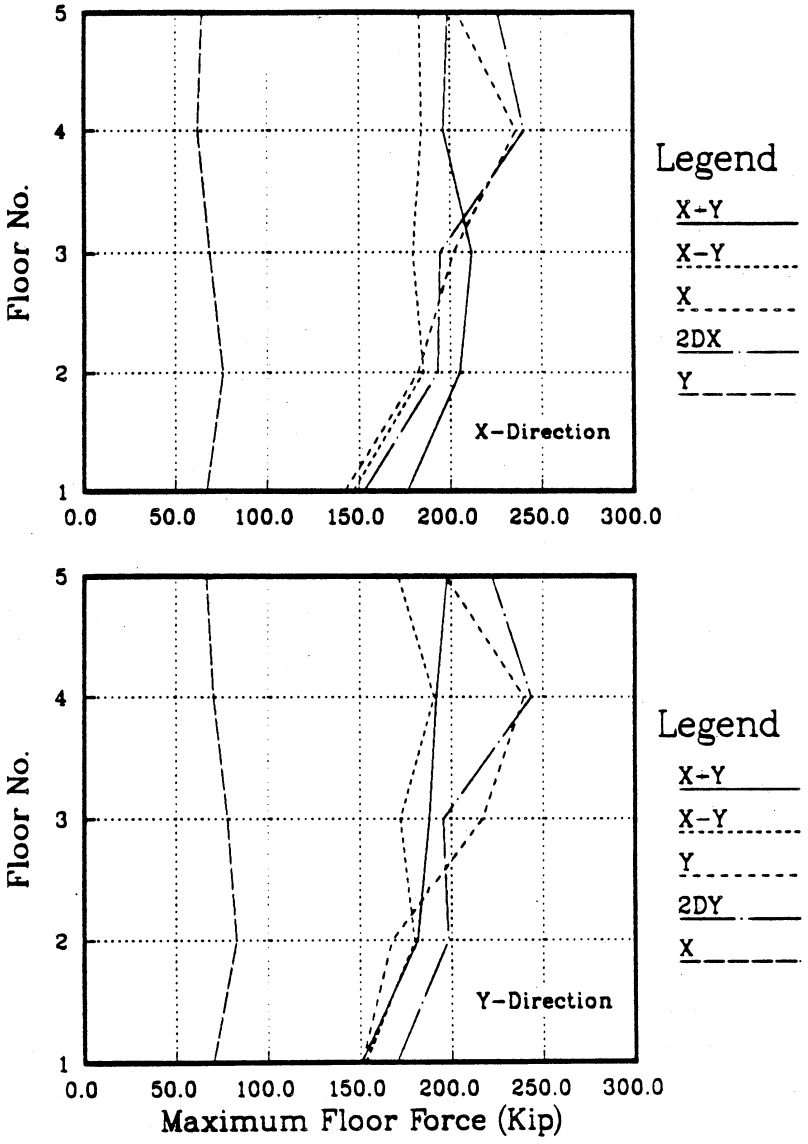

Figure 5.31: Comparison of Maximum Floor Force of Five Story L-Shape Building Subjected to 0.5 g 1978 Miyagi-Ken-Oki Earthquake

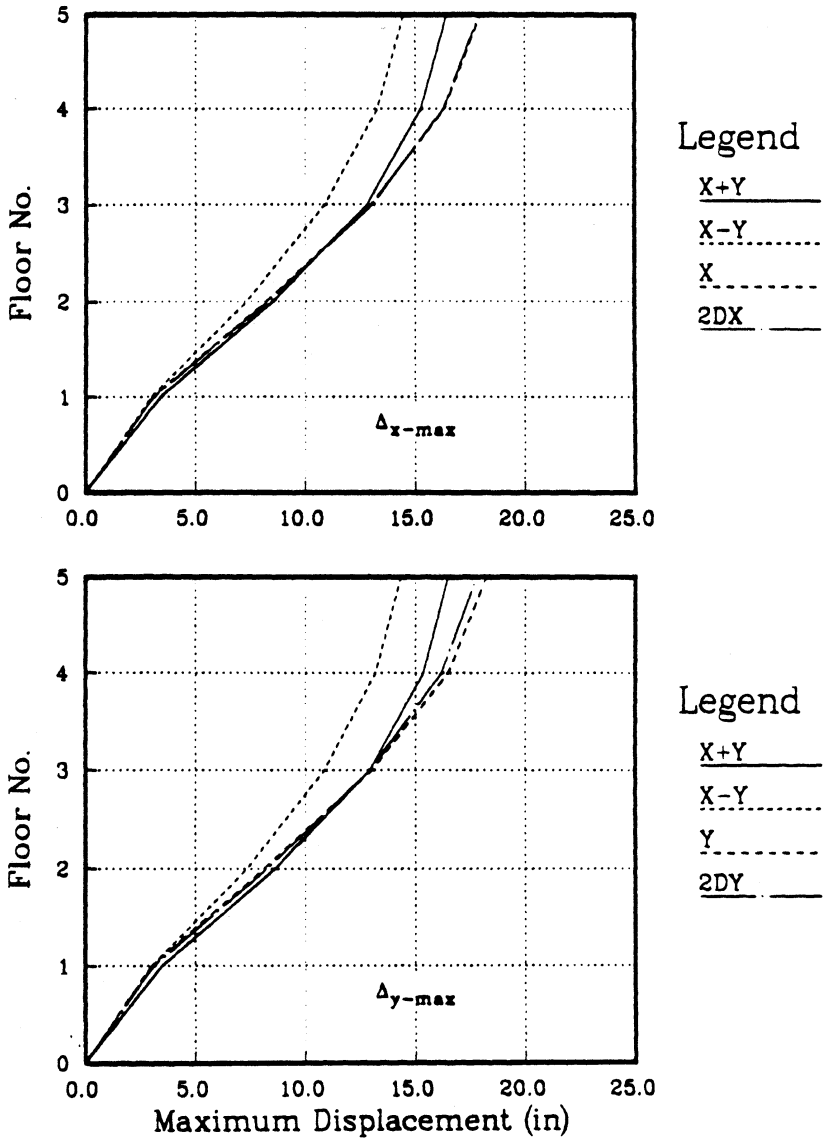

Figure 5.32: Comparison of C.M. Maximum Displacement of Five Story L-Shape Building Subjected to 0.5 g 1978 Miyagi-Ken-Oki Earthquake

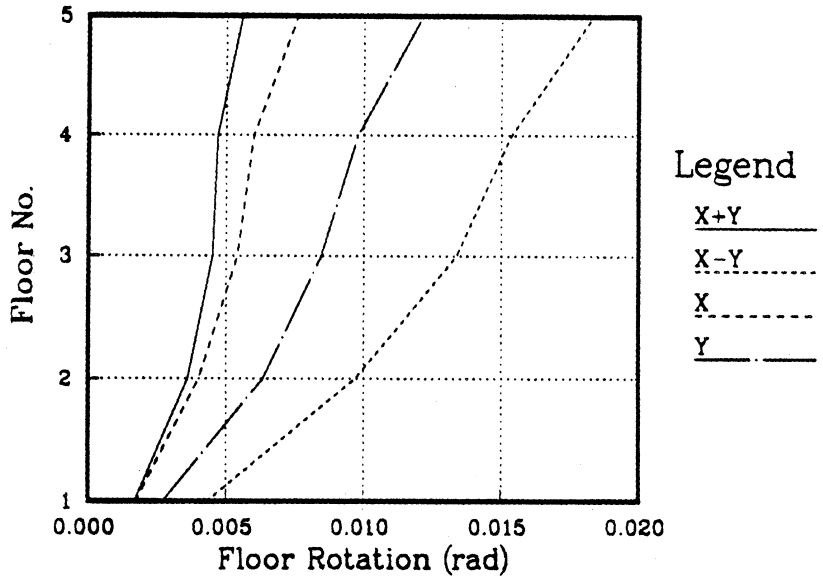

Figure 5.33: Envelope of Center of Mass Rotation of Five Story L-Shape Building Subjected to 0.5 g 1978 Miyagi-Ken-Oki Earthquake

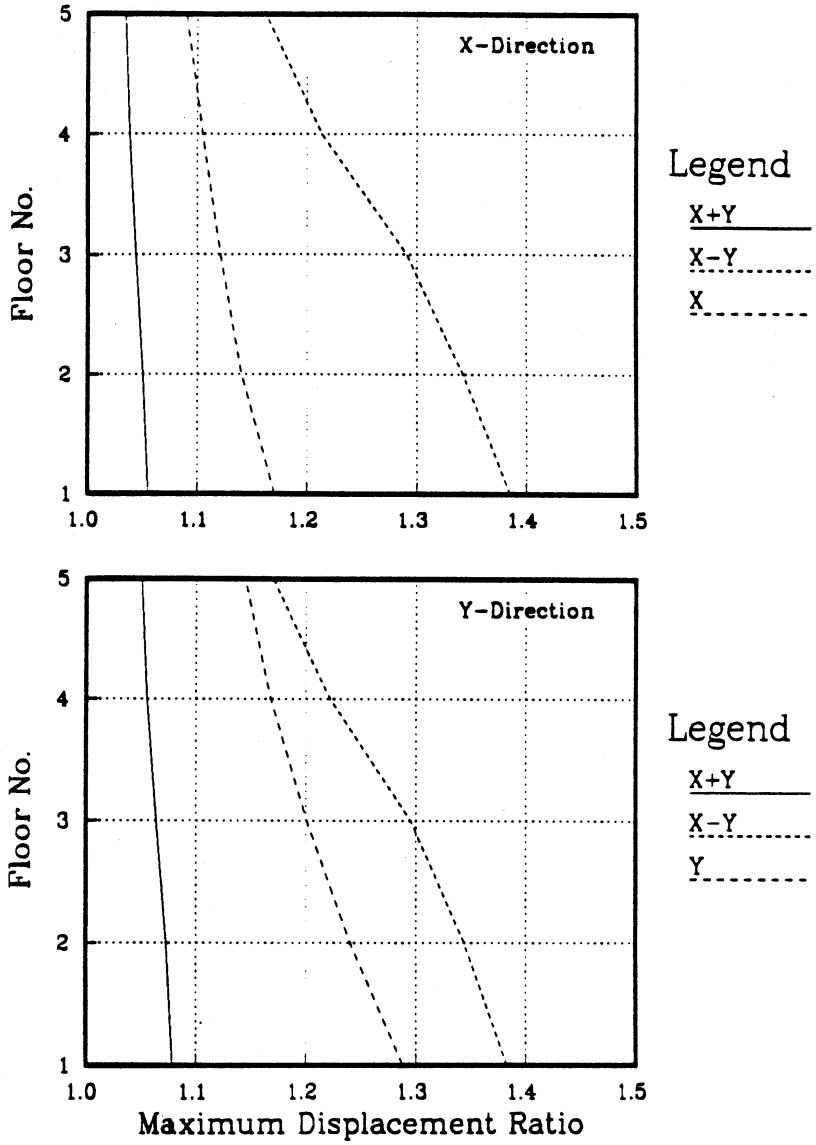

Figure 5.34: Maximum Ratio of Edge to Center of Mass Floor Displacement of Five Story L-Shape Building Subjected to 0.5 g 1978 Miyagi-Ken-Oki Earthquake : Inelastic

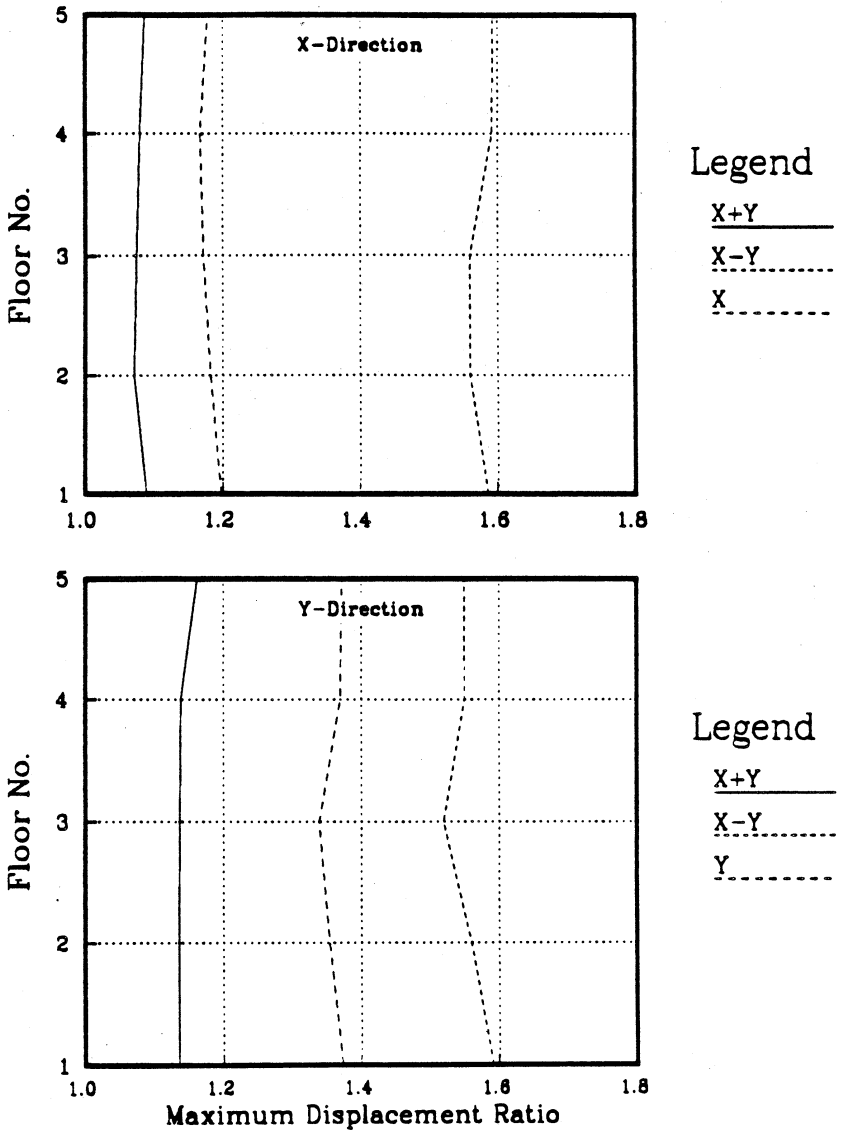

Figure 5.35: Maximum Ratio of Edge to Center of Mass Floor Displacement of Five Story L-Shape Building Subjected to 0.5 g 1978 Miyagi-Ken-Oki Earthquake : Elastic

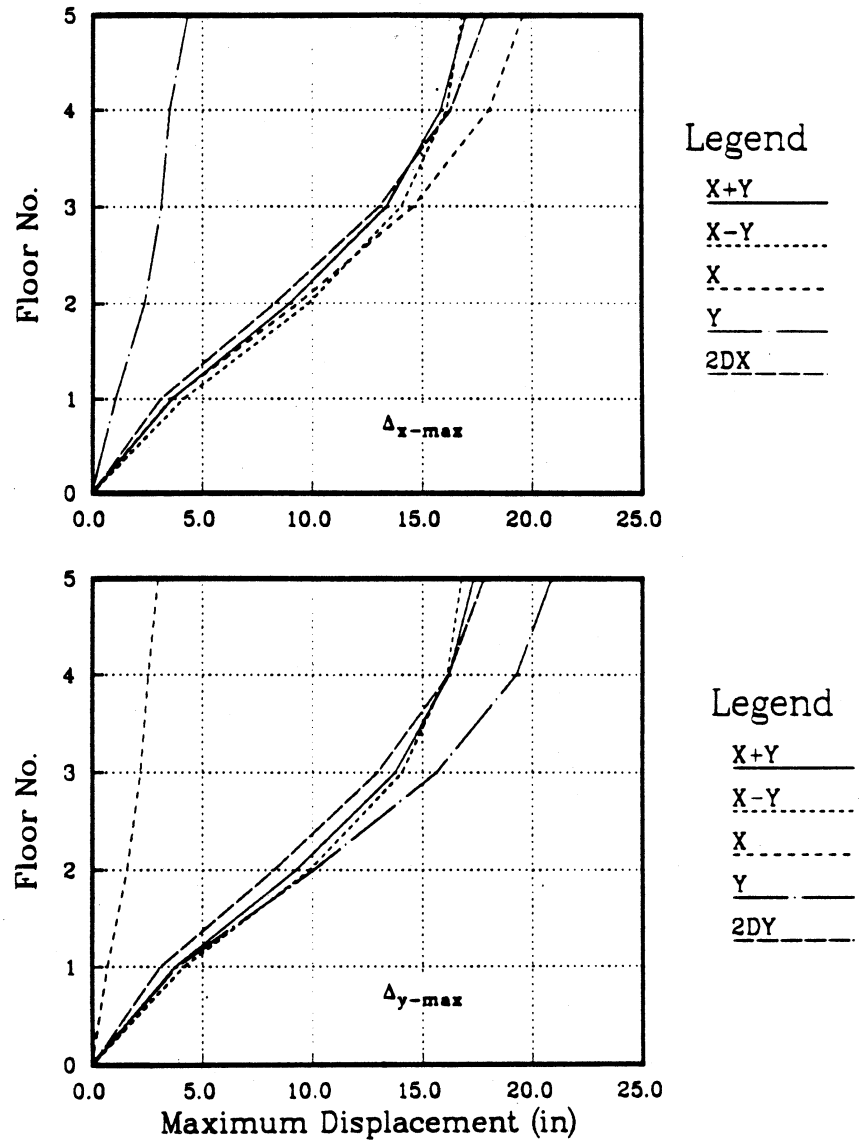

Figure 5.36: Comparison of Maximum Displacement of Five Story L-Shape Building Subjected to 0.5 g 1978 Miyagi-Ken-Oki Earthquake

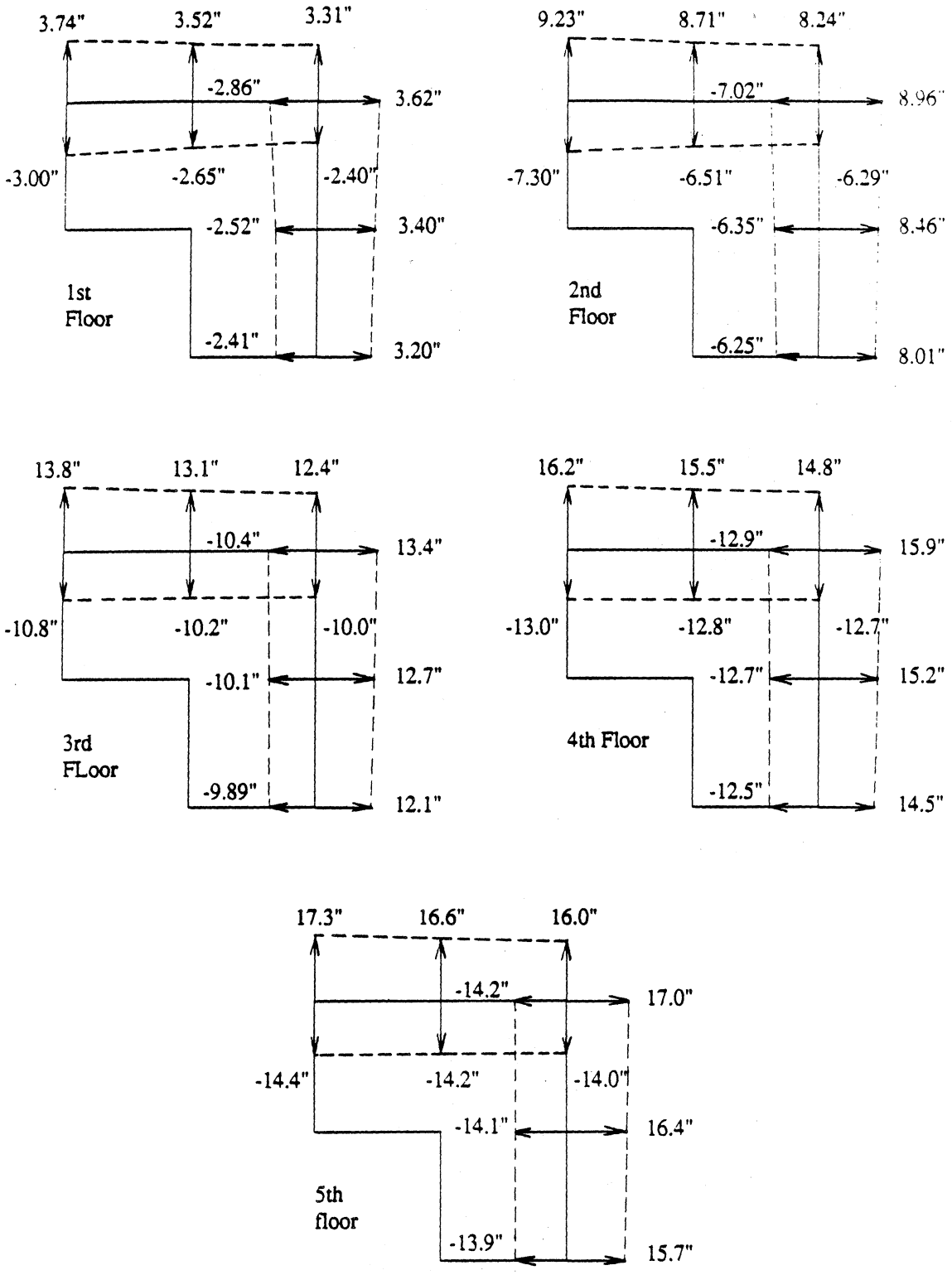

Figure 5.37: Envelopes of Maximum Edge Displacement of Five Story L-Shape Building Subjected to 0.5 g 1978 Miyagi-Ken-Oki Earthquake : Case X+Y

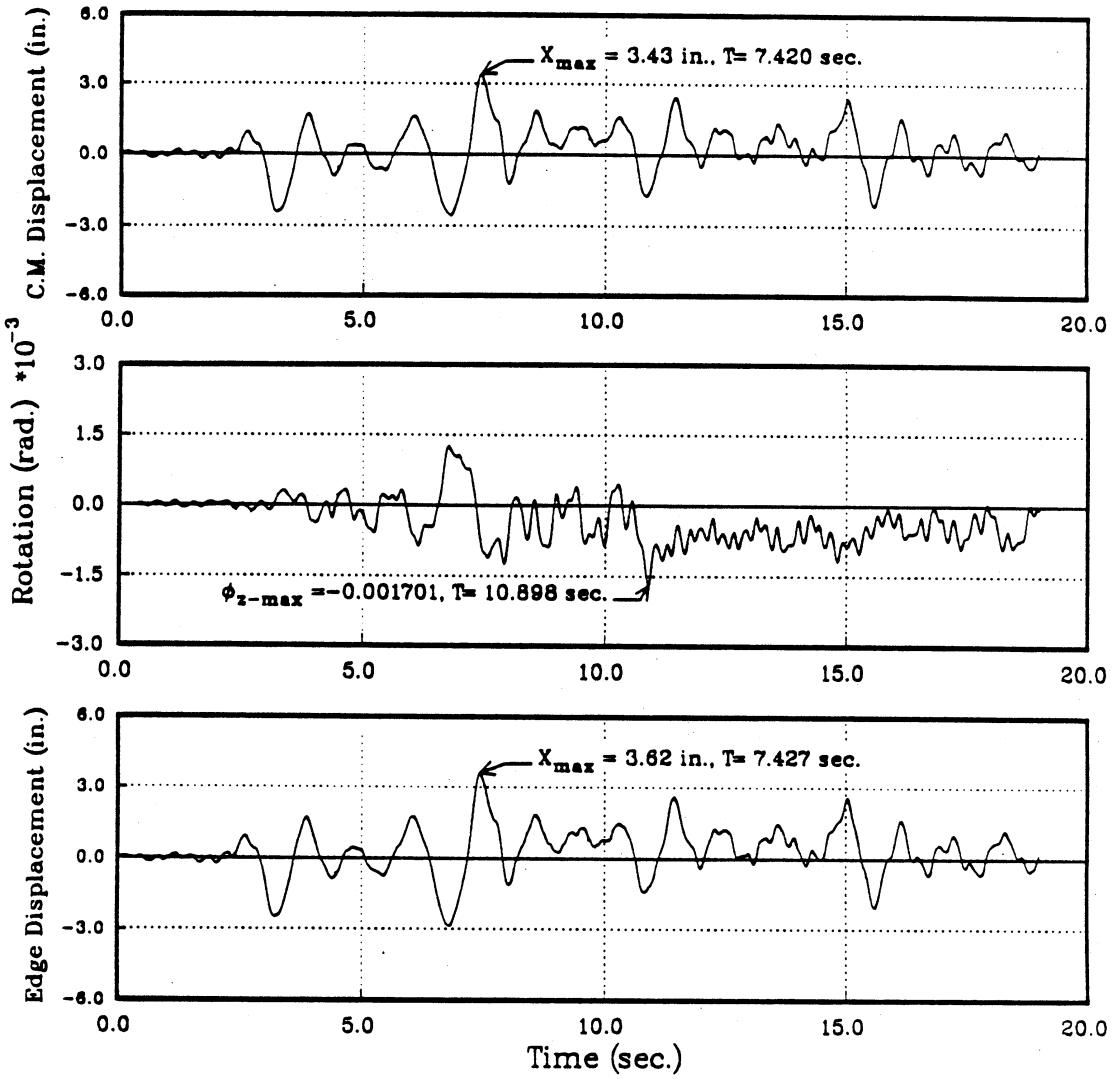

Figure 5.38: (a)1st Floor Center of Mass Displacement and Rotation, Edge Displacement Time History of Five Story L-Shape Building Subjected to 0.5 g 1978 Miyagi-Ken-Oki Earthquake : Case X+Y

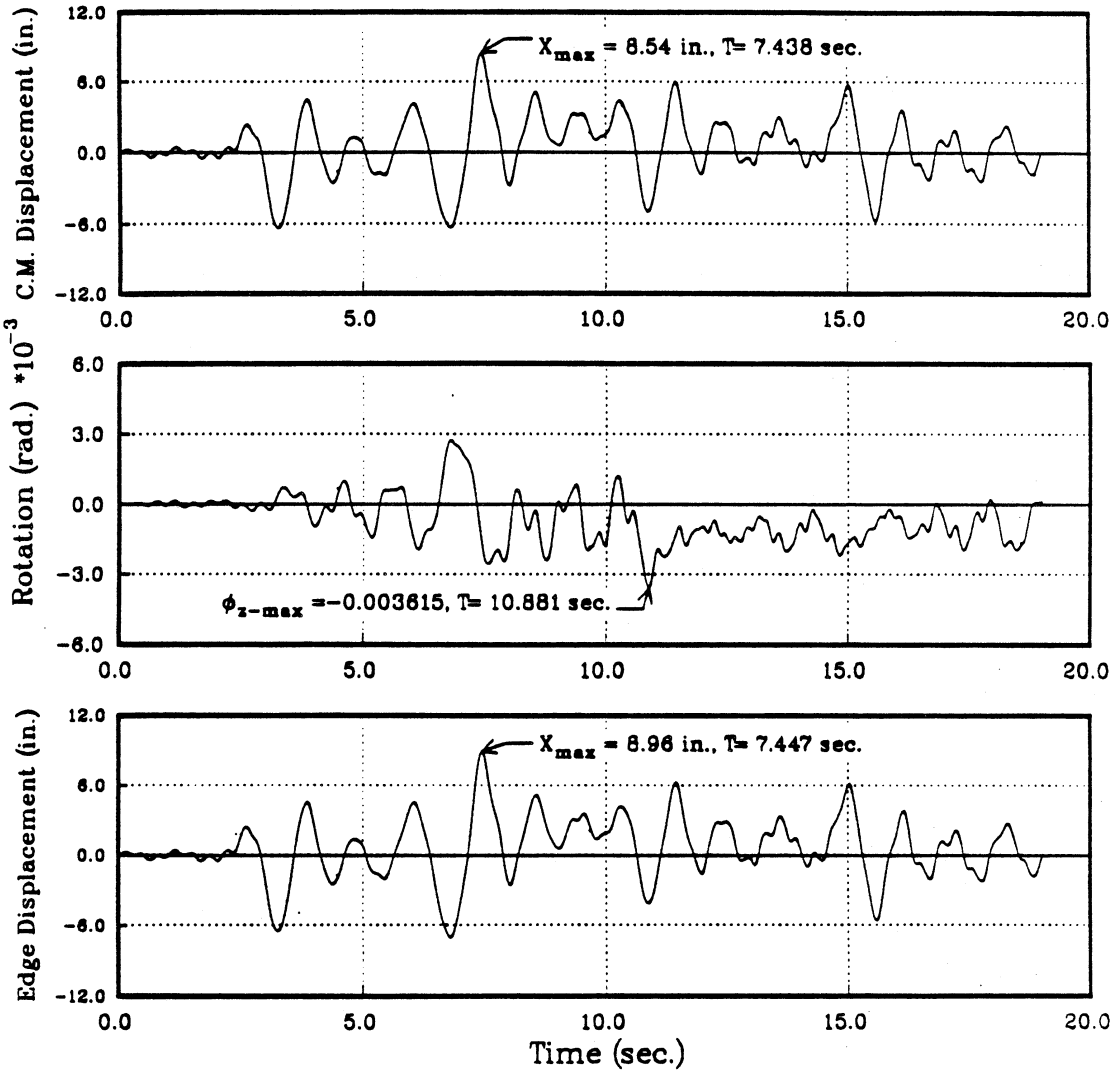

Figure 5.38: (b)2nd Floor Center of Mass Displacement and Rotation, Edge Displacement Time History of Five Story L-Shape Building Subjected to 0.5 g 1978 Miyagi-Ken-Oki Earthquake : Case X+Y (Continue)

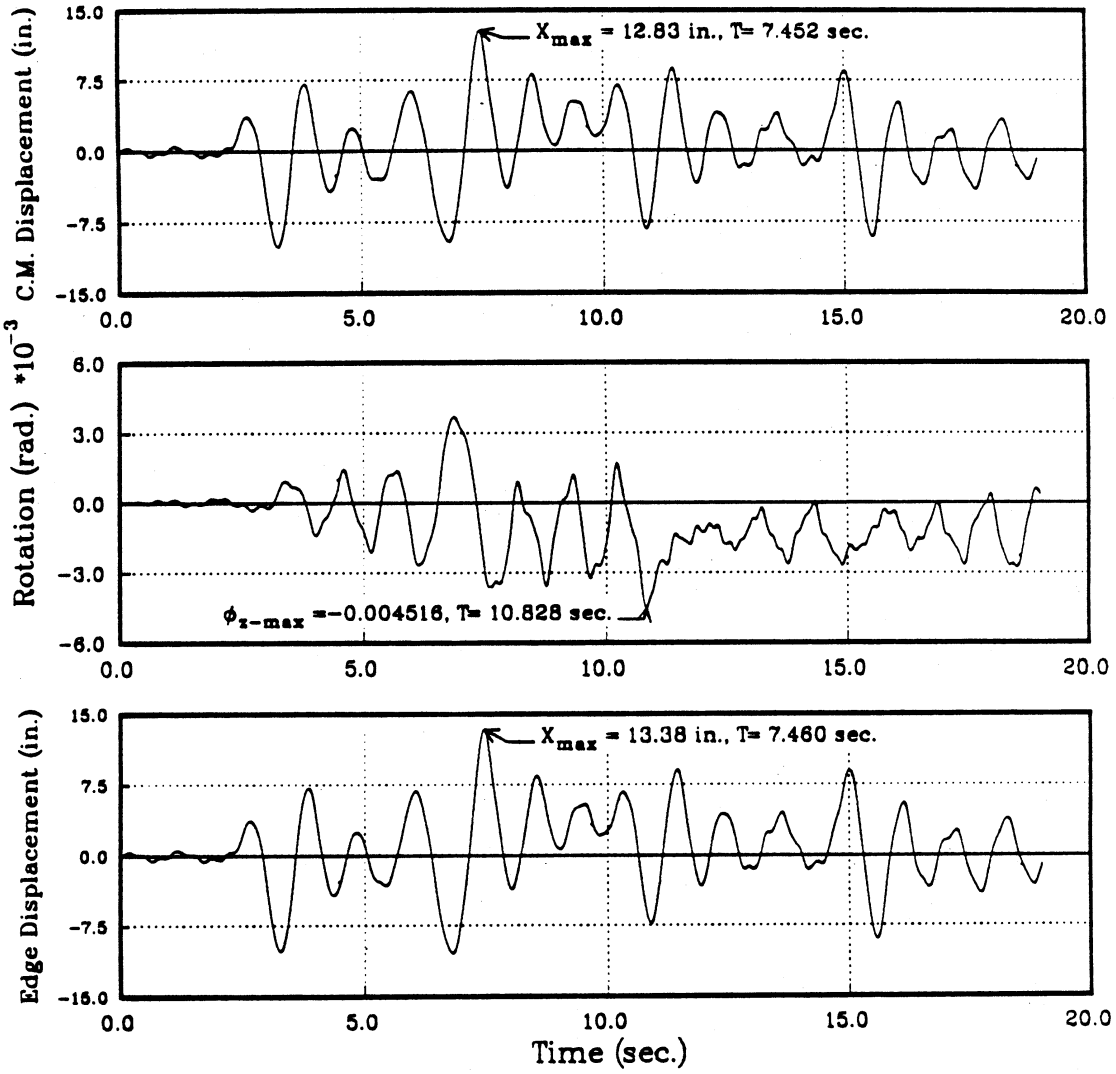

Figure 5.38: (c)3rd Floor Center of Mass Displacement and Rotation, Edge Displacement Time History of Five Story L-Shape Building Subjected to 0.5 g 1978 Miyagi-Ken-Oki Earthquake : Case X+Y (Continue)

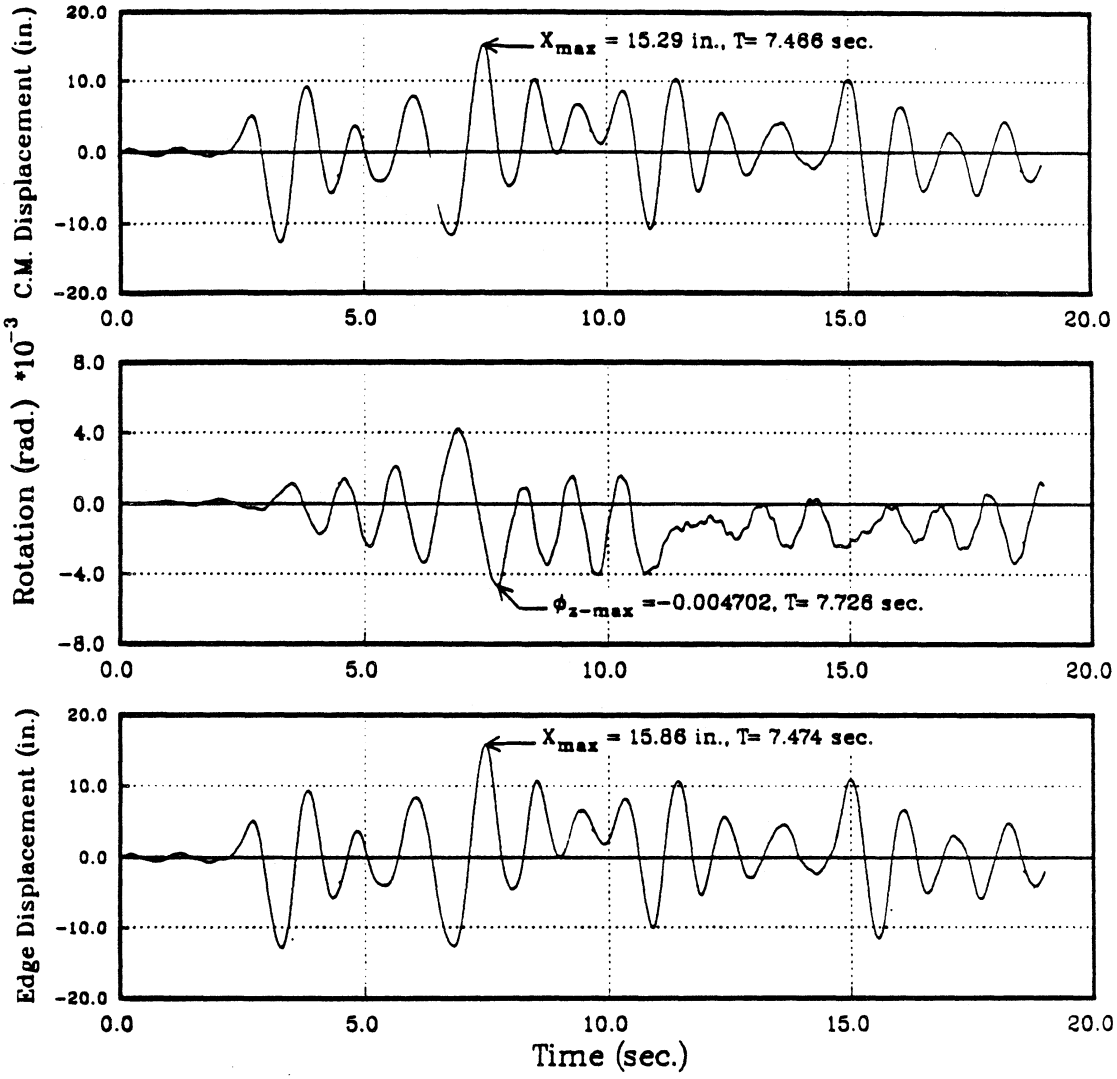

Figure 5.38: (d)4th Floor Center of Mass Displacement and Rotation, Edge Displacement Time History of Five Story L-Shape Building Subjected to 0.5 g 1978 Miyagi-Ken-Oki Earthquake : Case X+Y (Continue)

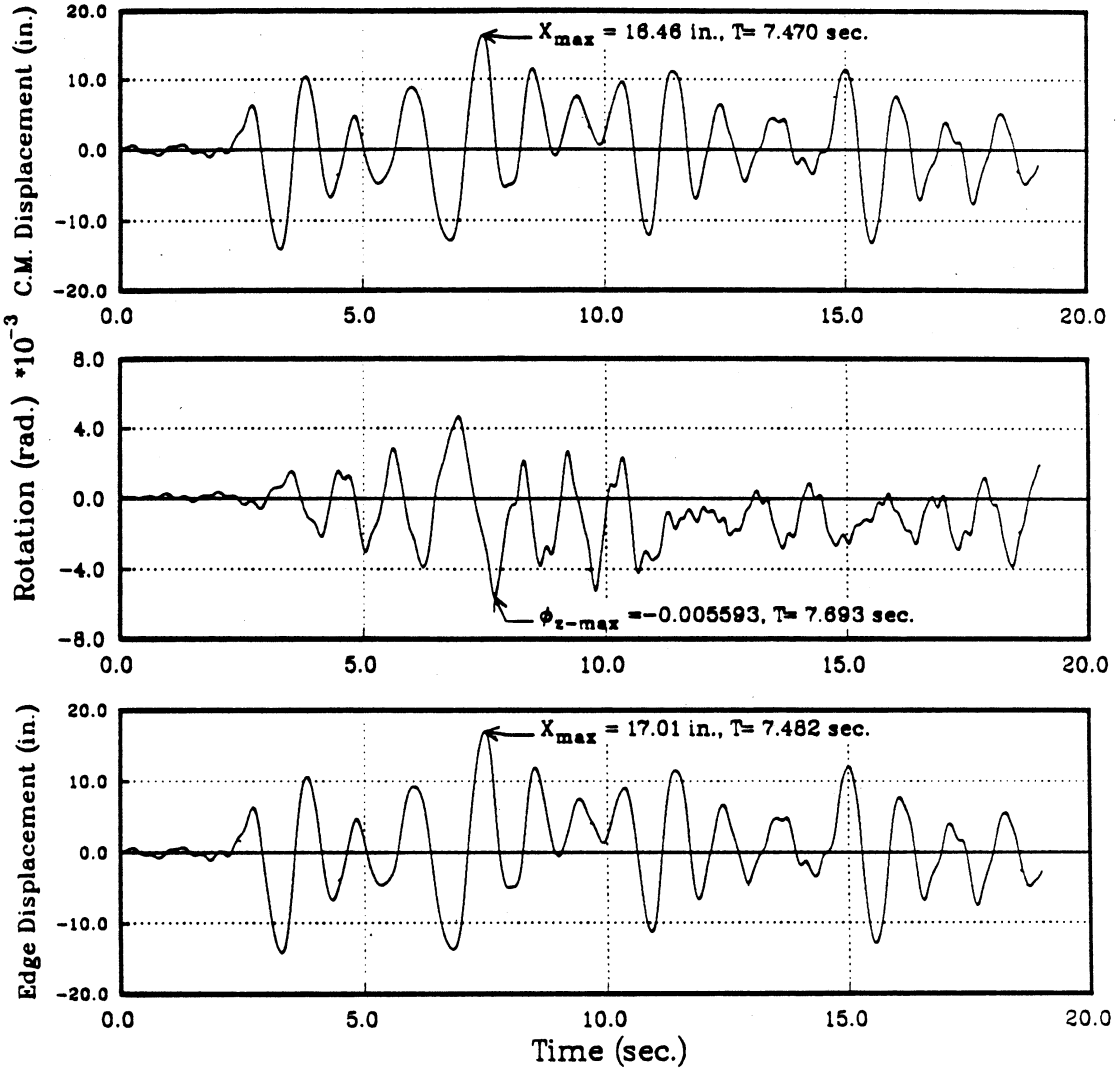

Figure 5.38: (e)5th Floor Center of Mass Displacement and Rotation, Edge Displacement Time History of Five Story L-Shape Building Subjected to 0.5 g 1978 Miyagi-Ken-Oki Earthquake : Case X+Y (Continue)

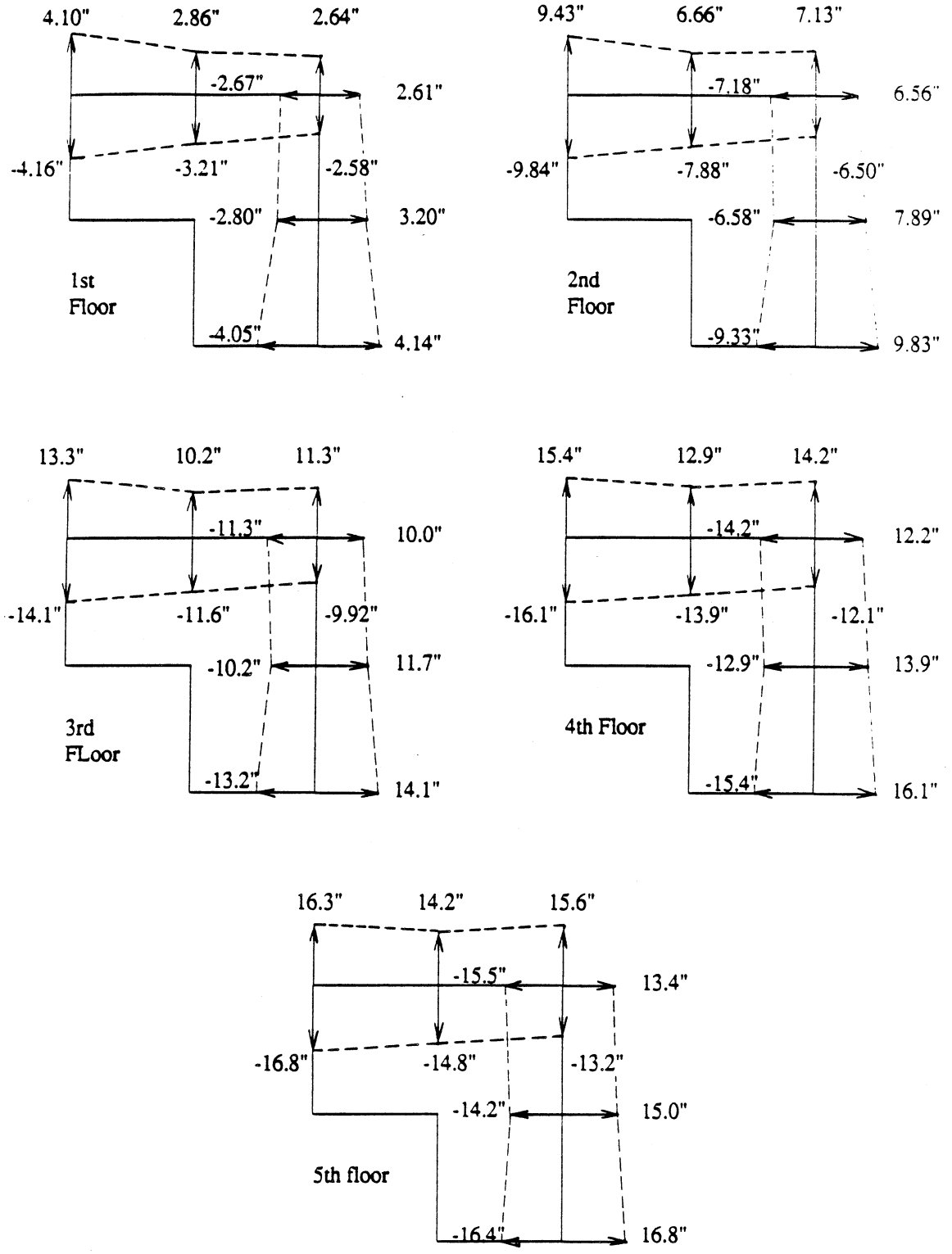

Figure 5.39: Envelopes of Maximum Edge Displacement of Five Story L-Shape Building Subjected to 0.5 g 1978 Miyagi-Ken-Oki Earthquake : Case X-Y

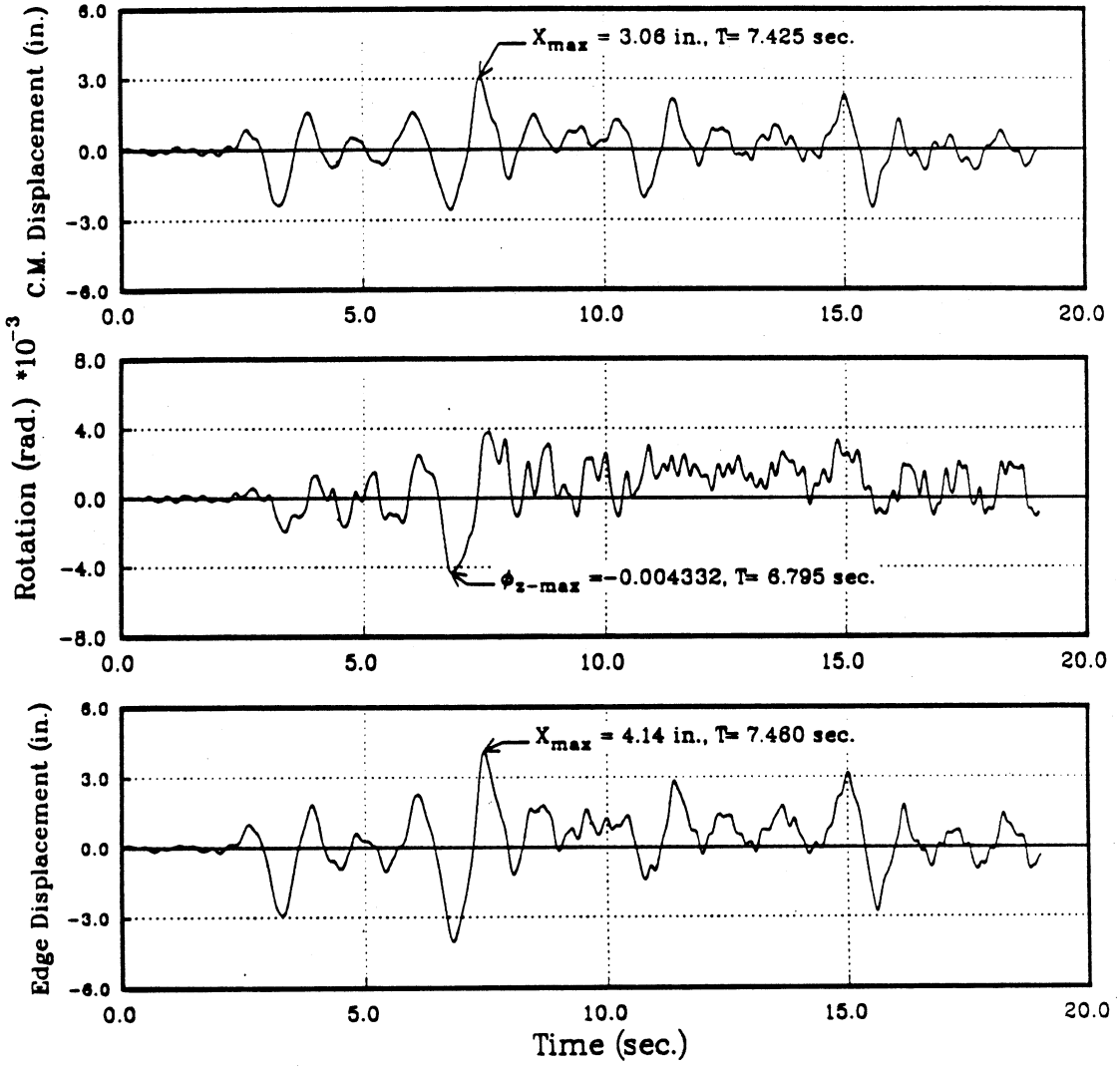

Figure 5.40: (a)1st Floor Center of Mass Displacement and Rotation, Edge Displacement Time History of Five Story L-Shape Building Subjected to 0.5 g 1978 Miyagi-Ken-Oki Earthquake : Case X-Y

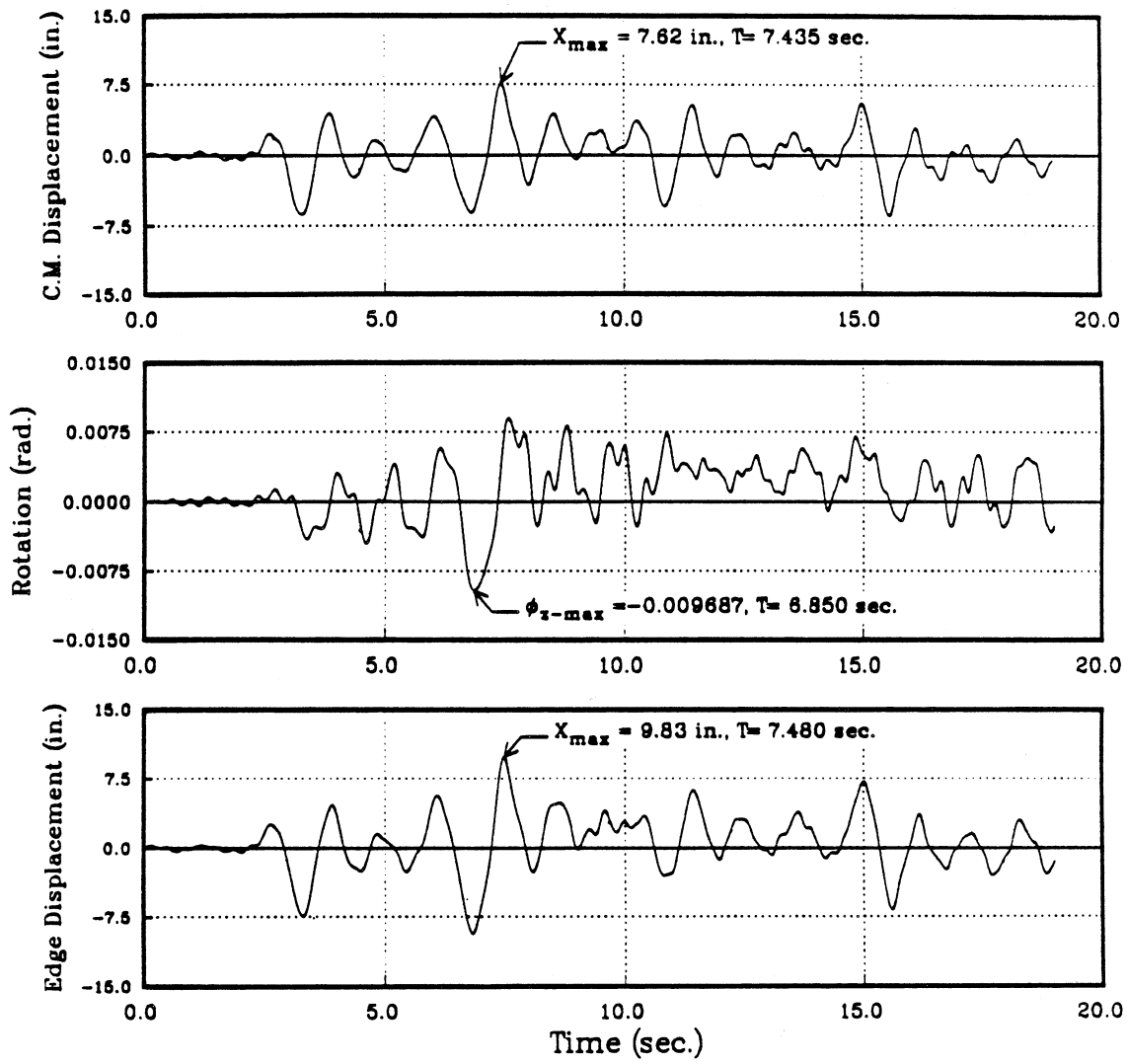

Figure 5.40: (b)2nd Floor Center of Mass Displacement and Rotation, Edge Displacement Time History of Five Story L-Shape Building Subjected to 0.5 g 1978 Miyagi-Ken-Oki Earthquake : Case X-Y (Continue)

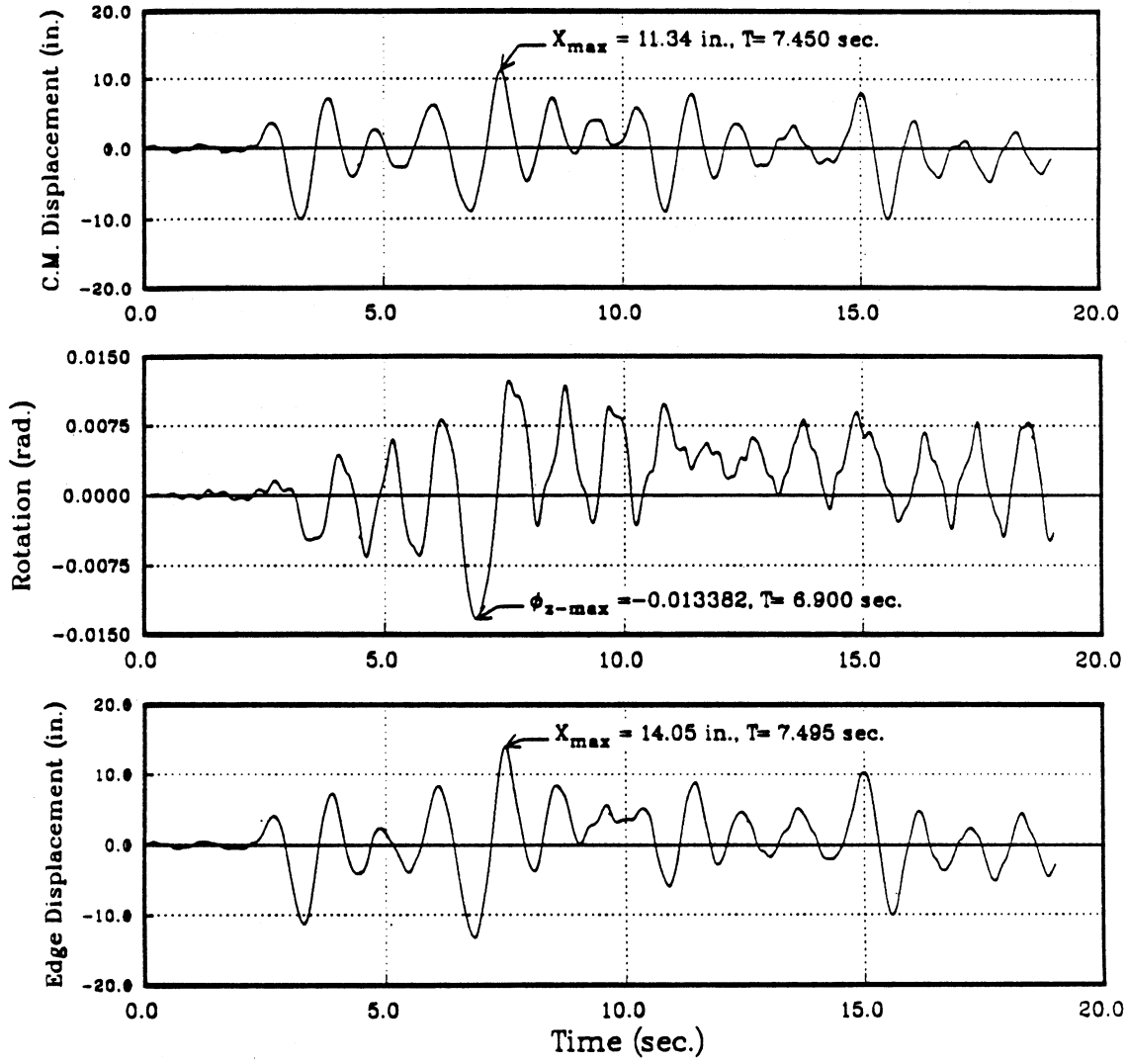

Figure 5.40: (c)3rd Floor Center of Mass Displacement and Rotation, Edge Displacement Time History of Five Story L-Shape Building Subjected to 0.5 g 1978 Miyagi-Ken-Oki Earthquake : Case X-Y (Continue)

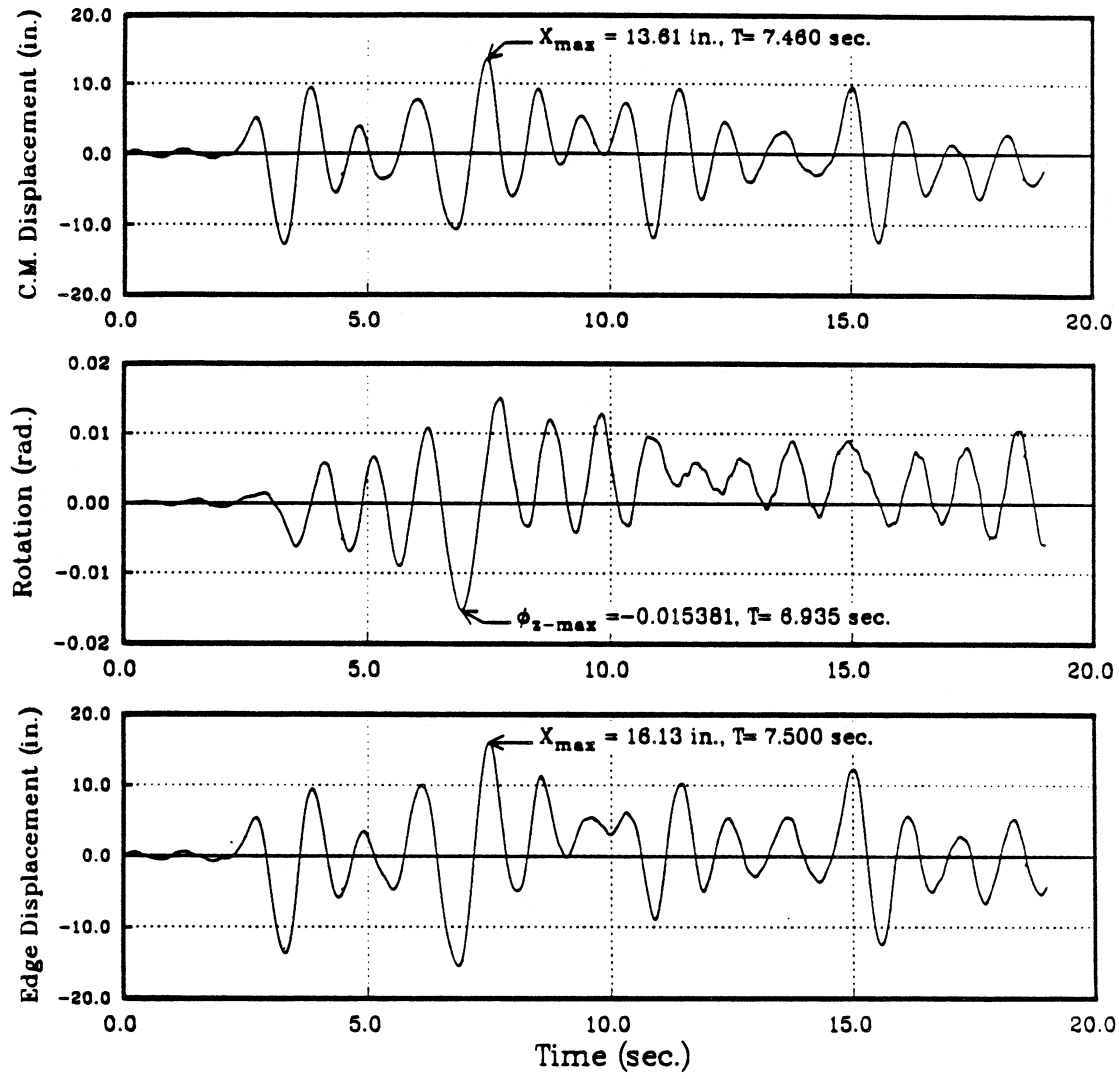

Figure 5.40: (d)4th Floor Center of Mass Displacement and Rotation, Edge Displacement Time History of Five Story L-Shape Building Subjected to 0.5 g 1978 Miyagi-Ken-Oki Earthquake : Case X-Y (Continue)

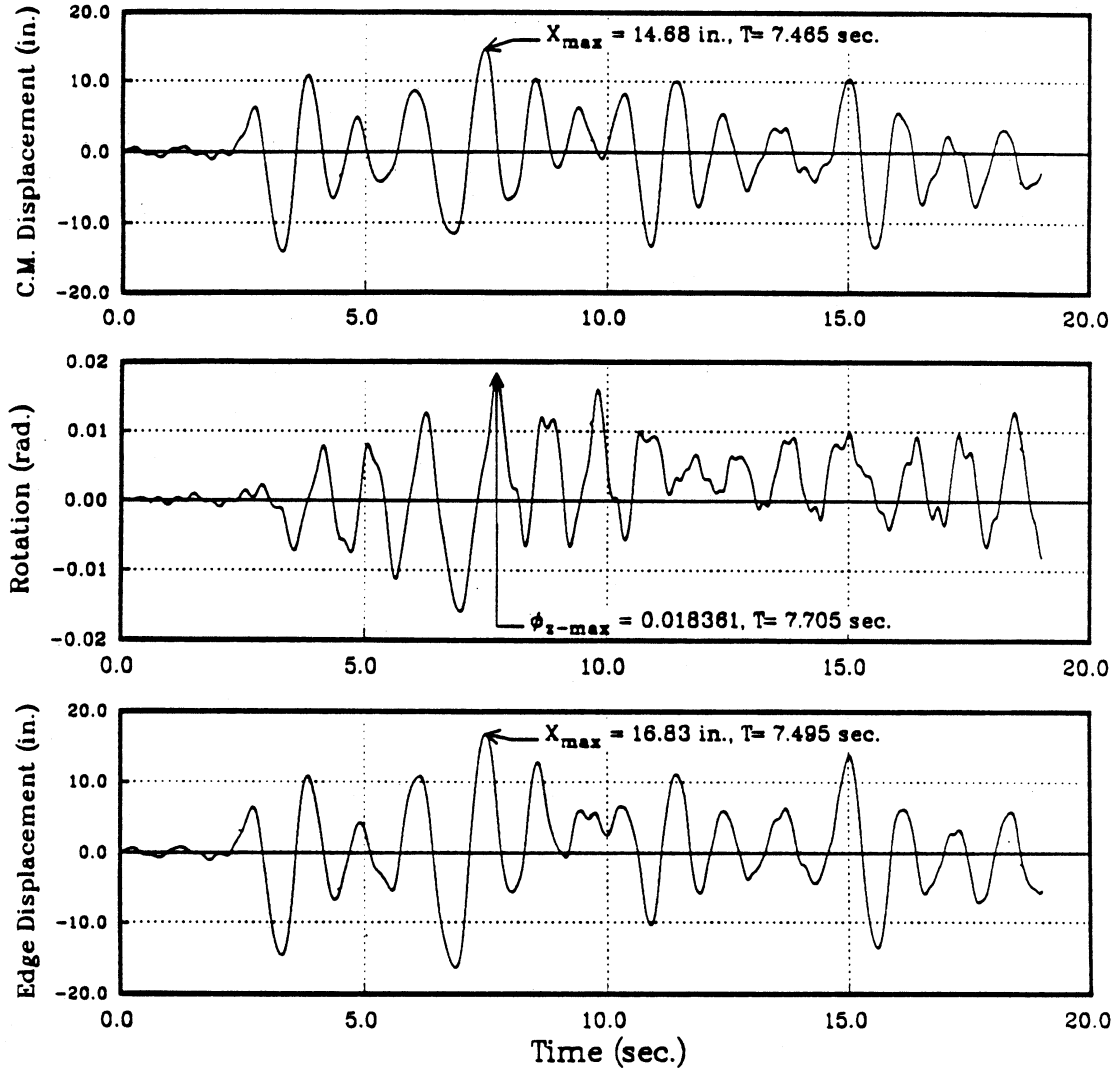

Figure 5.40: (e)5th Floor Center of Mass Displacement and Rotation, Edge Displacement Time History of Five Story L-Shape Building Subjected to 0.5 g 1978 Miyagi-Ken-Oki Earthquake : Case X-Y (Continue)

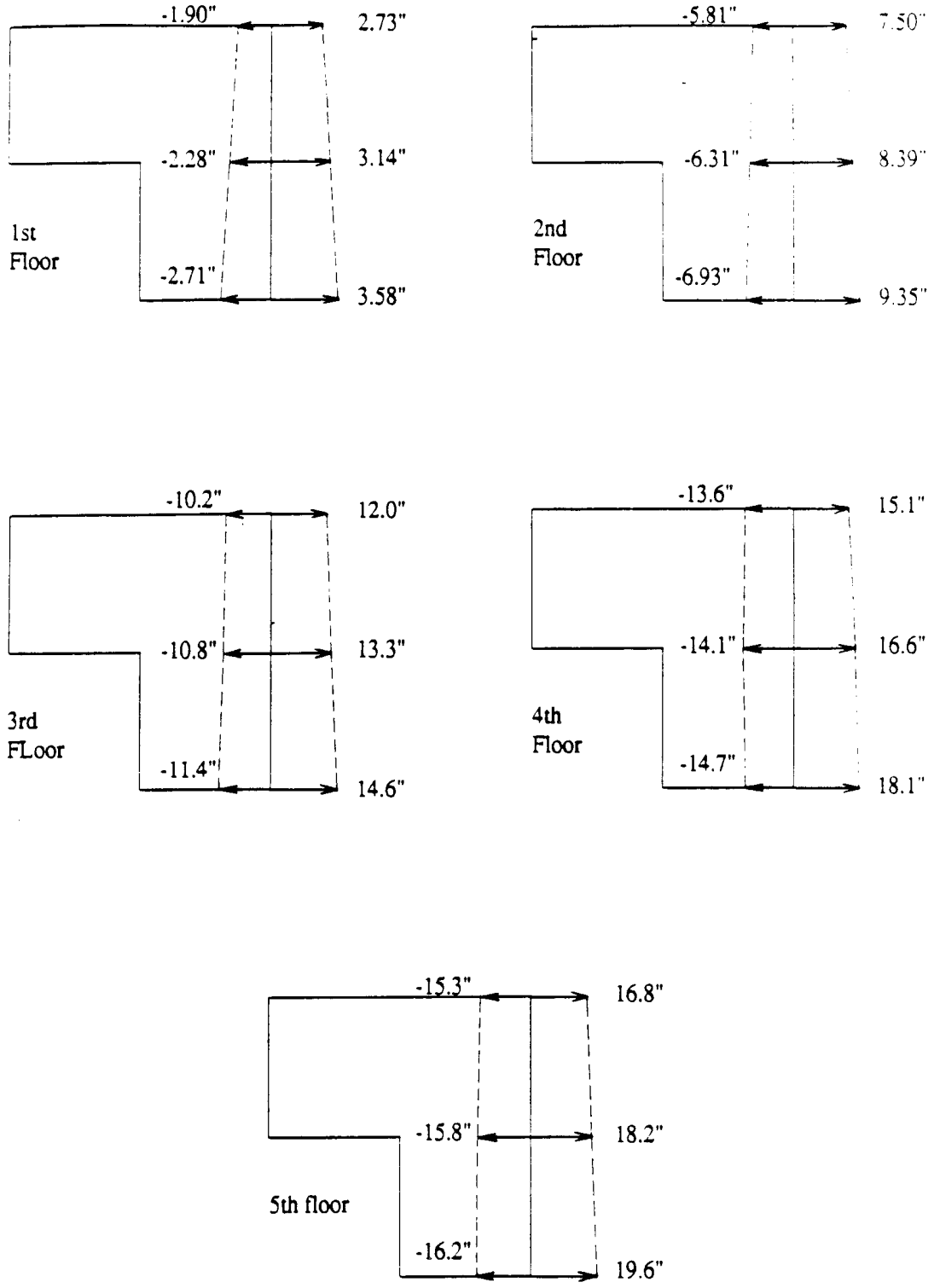

Figure 5.41: Envelopes of Maximum Edge Displacement of Five Story L-Shape Building Subjected to 0.5 g 1978 Miyagi-Ken-Oki Earthquake : Case X

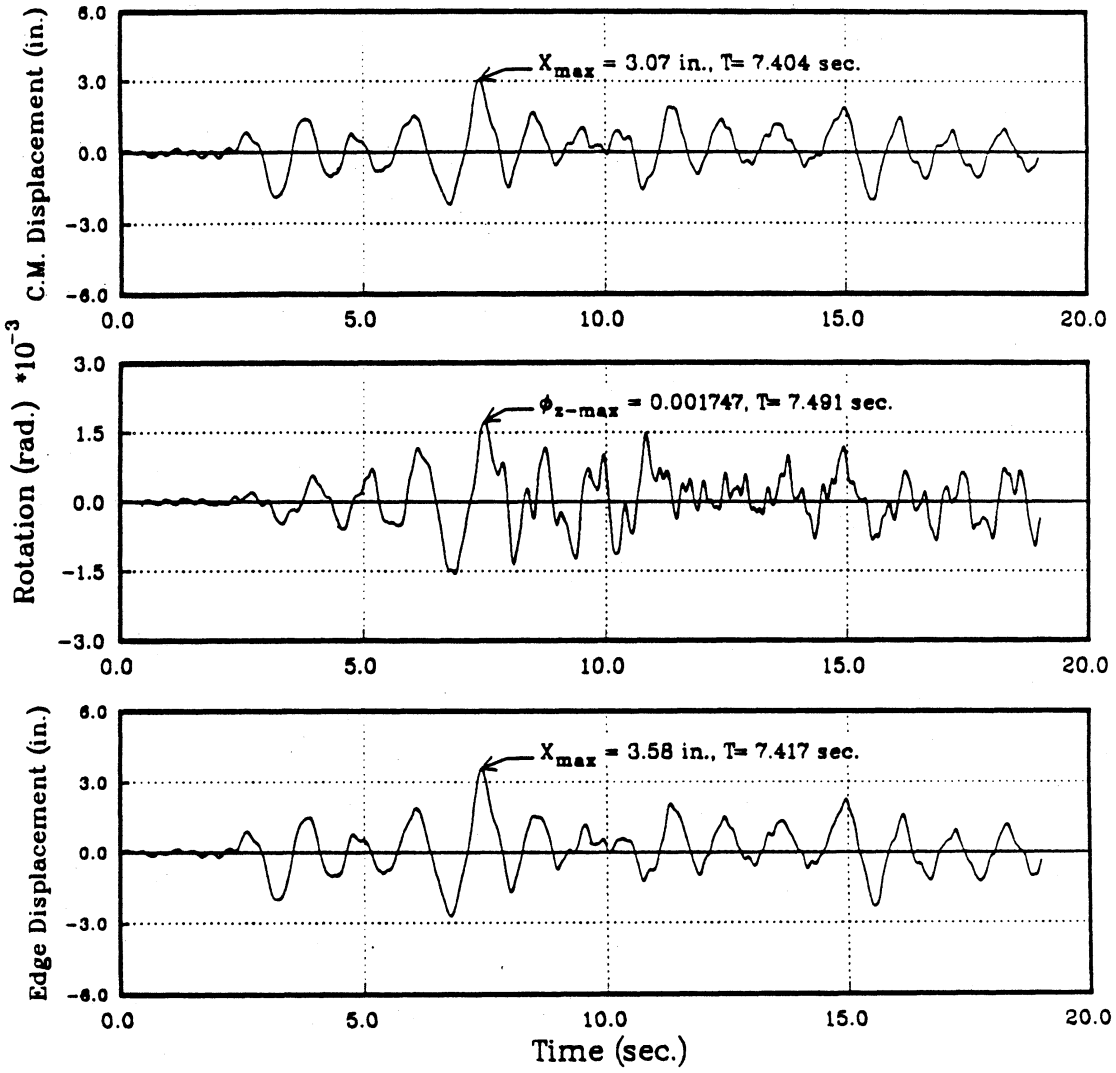

Figure 5.42: (a)1st Floor Center of Mass Displacement and Rotation, Edge Displacement Time History of Five Story L-Shape Building Subjected to 0.5 g 1978 Miyagi-Ken-Oki Earthquake : Case X

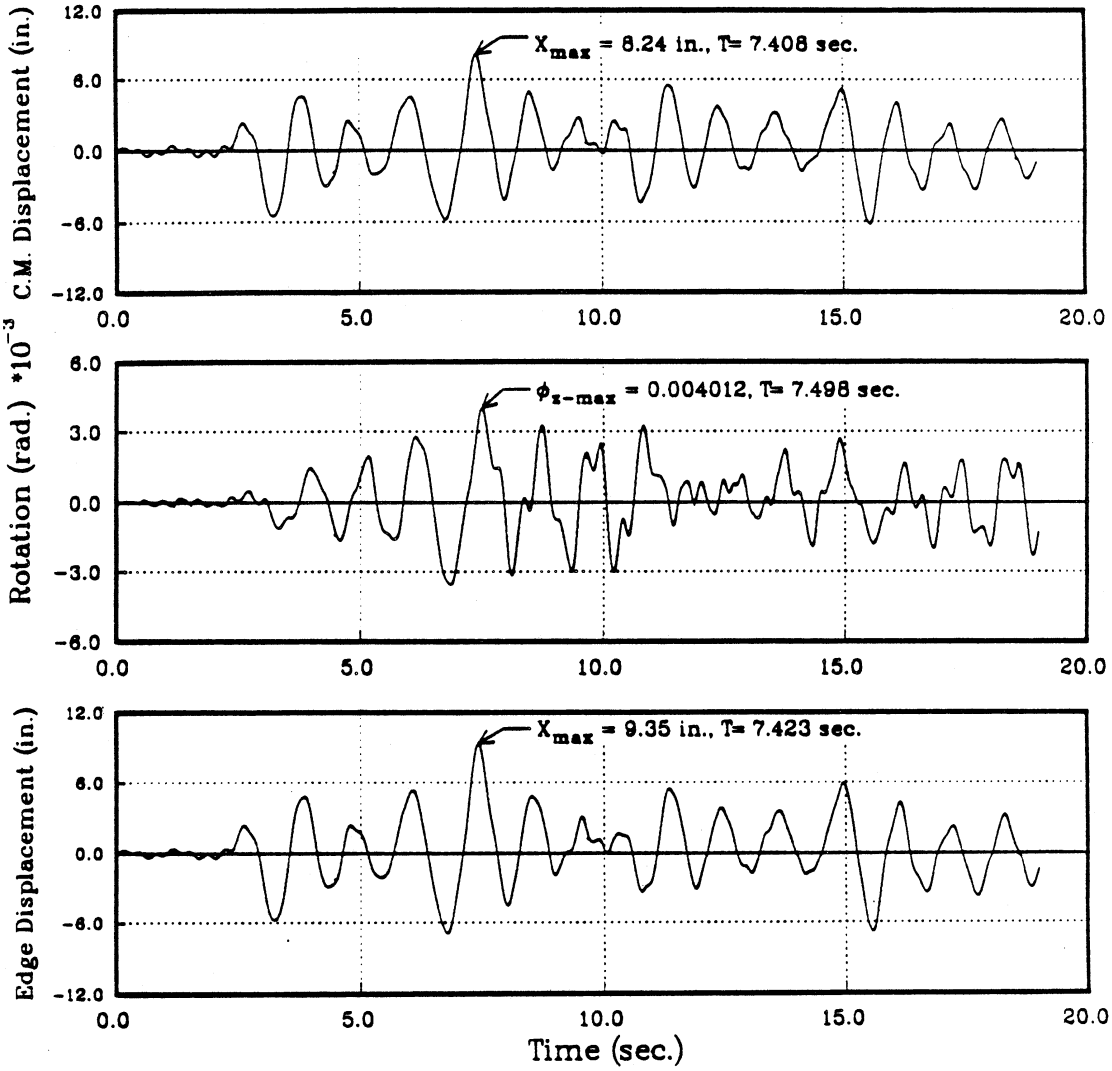

Figure 5.42: (b)2nd Floor Center of Mass Displacement and Rotation, Edge Displacement Time History of Five Story L-Shape Building Subjected to 0.5 g 1978 Miyagi-Ken-Oki Earthquake : Case X (Continue)

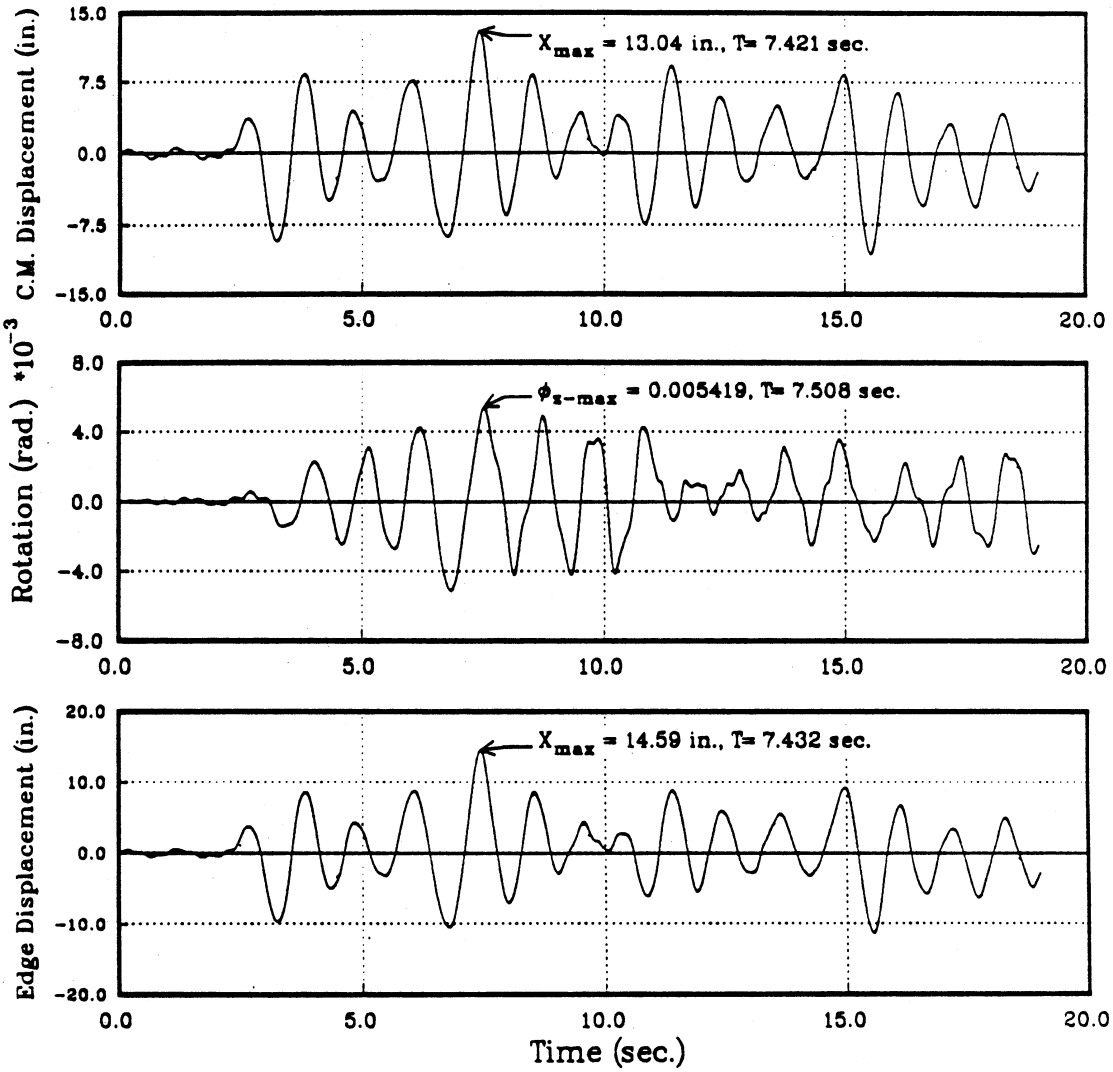

Figure 5.42: (c)3rd Floor Center of Mass Displacement and Rotation, Edge Displacement Time History of Five Story L-Shape Building Subjected to 0.5 g 1978 Miyagi-Ken-Oki Earthquake : Case X (Continue)

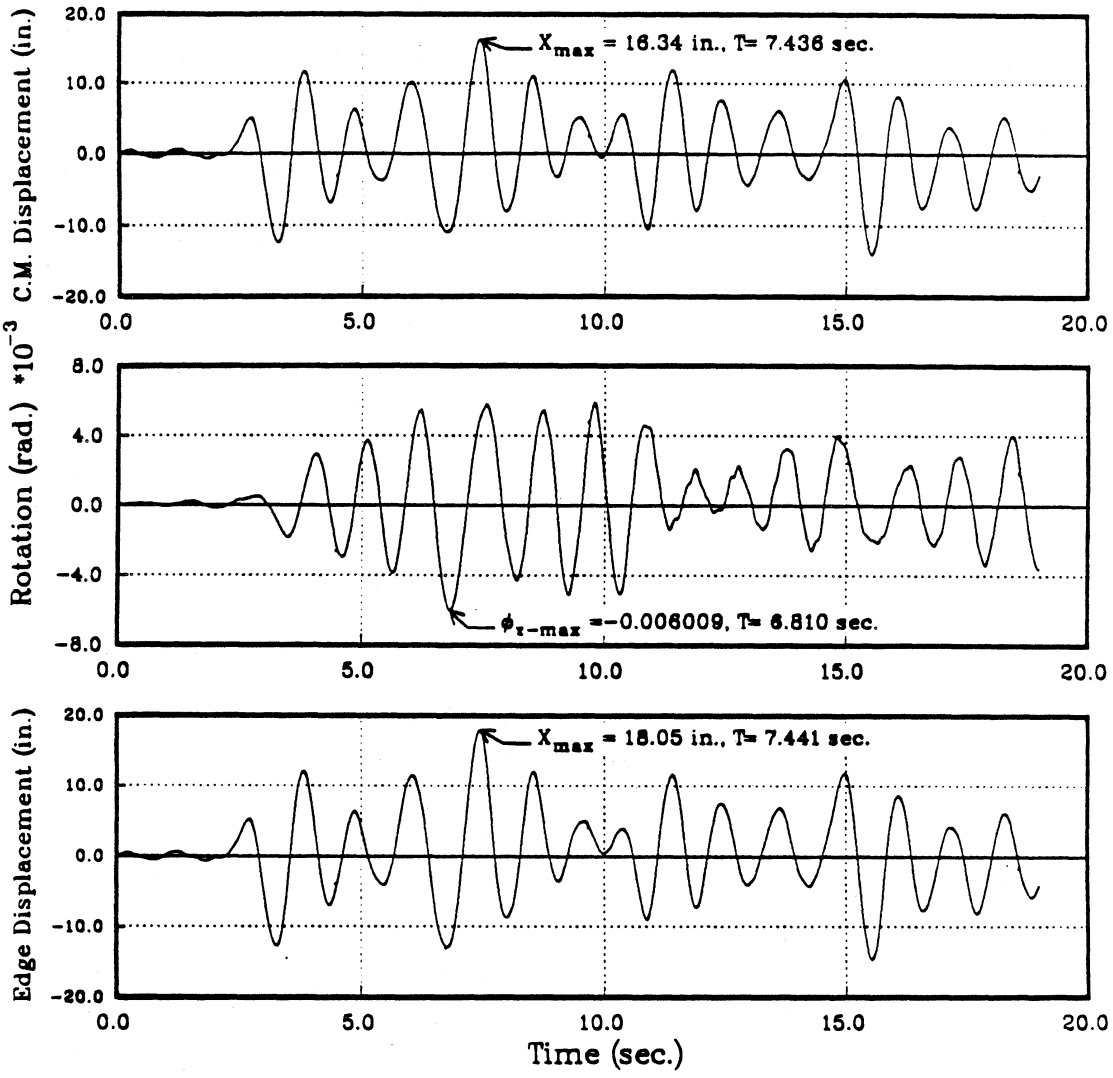

Figure 5.42: (d)4th Floor Center of Mass Displacement and Rotation, Edge Displacement Time History of Five Story L-Shape Building Subjected to 0.5 g 1978 Miyagi-Ken-Oki Earthquake : Case X (Continue)

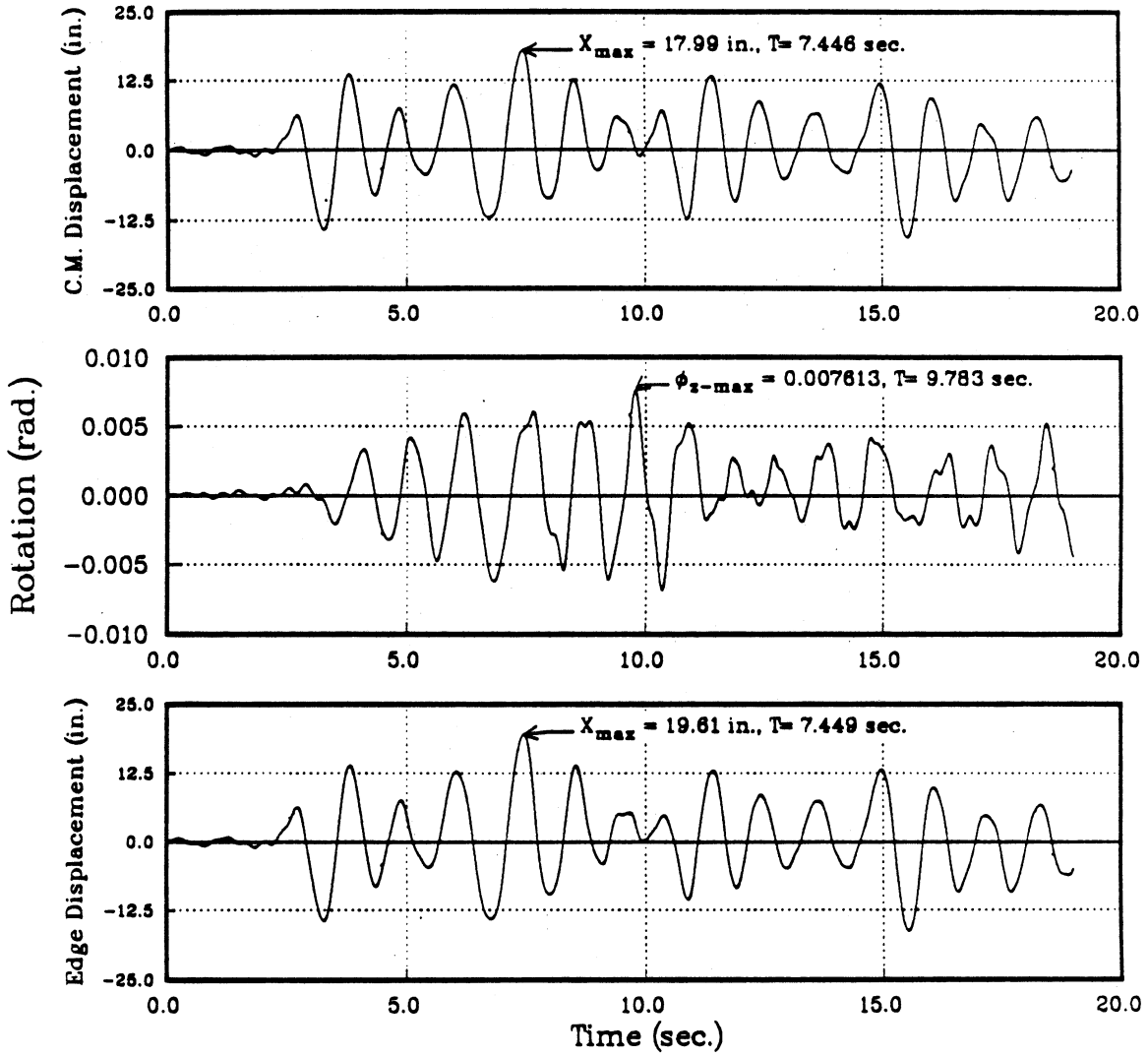

Figure 5.42: (e)5th Floor Center of Mass Displacement and Rotation, Edge Displacement Time History of Five Story L-Shape Building Subjected to 0.5 g 1978 Miyagi-Ken-Oki Earthquake : Case X (Continue)

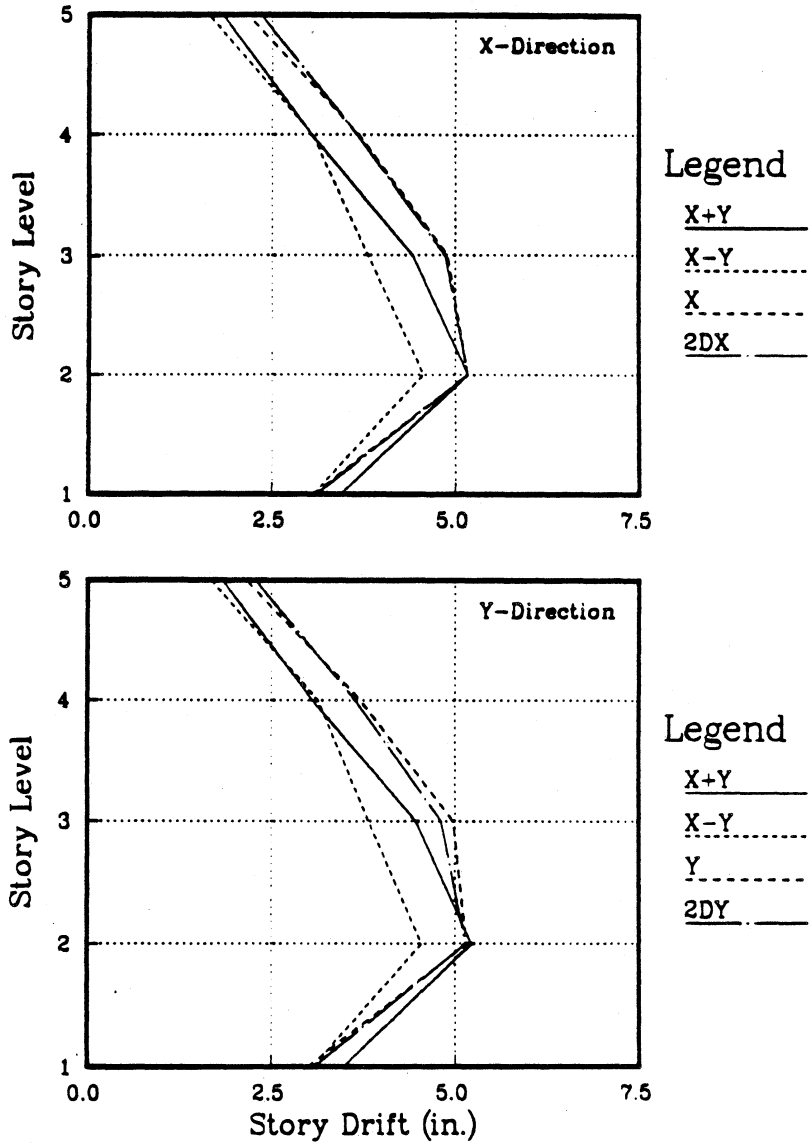

Figure 5.43: Comparison of Center of Mass Maximum Story Drift of Five Story L-Shape Building Subjected to 0.5 g 1978 Miyagi-Ken-Oki Earthquake

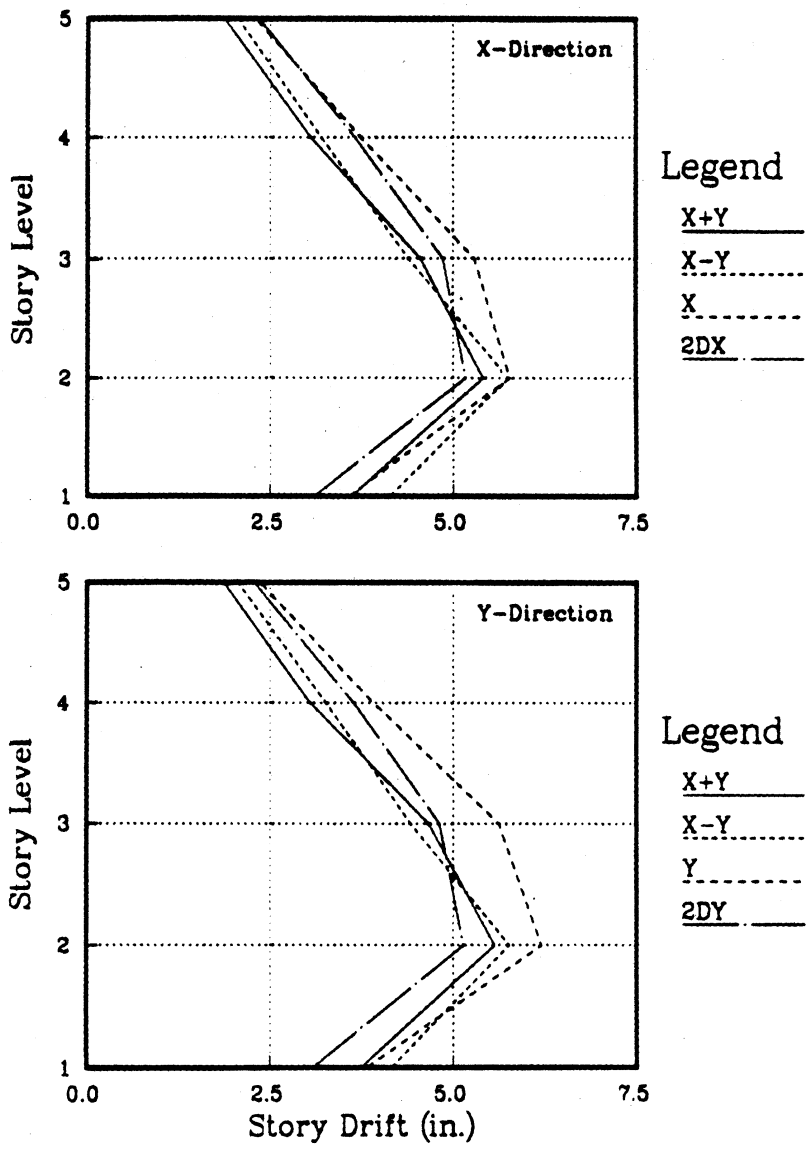

Figure 5.44: Comparison of Maximum Story Drift of Five Story L-Shape Building Subjected to 0.5 g 1978 Miyagi-Ken-Oki Earthquake

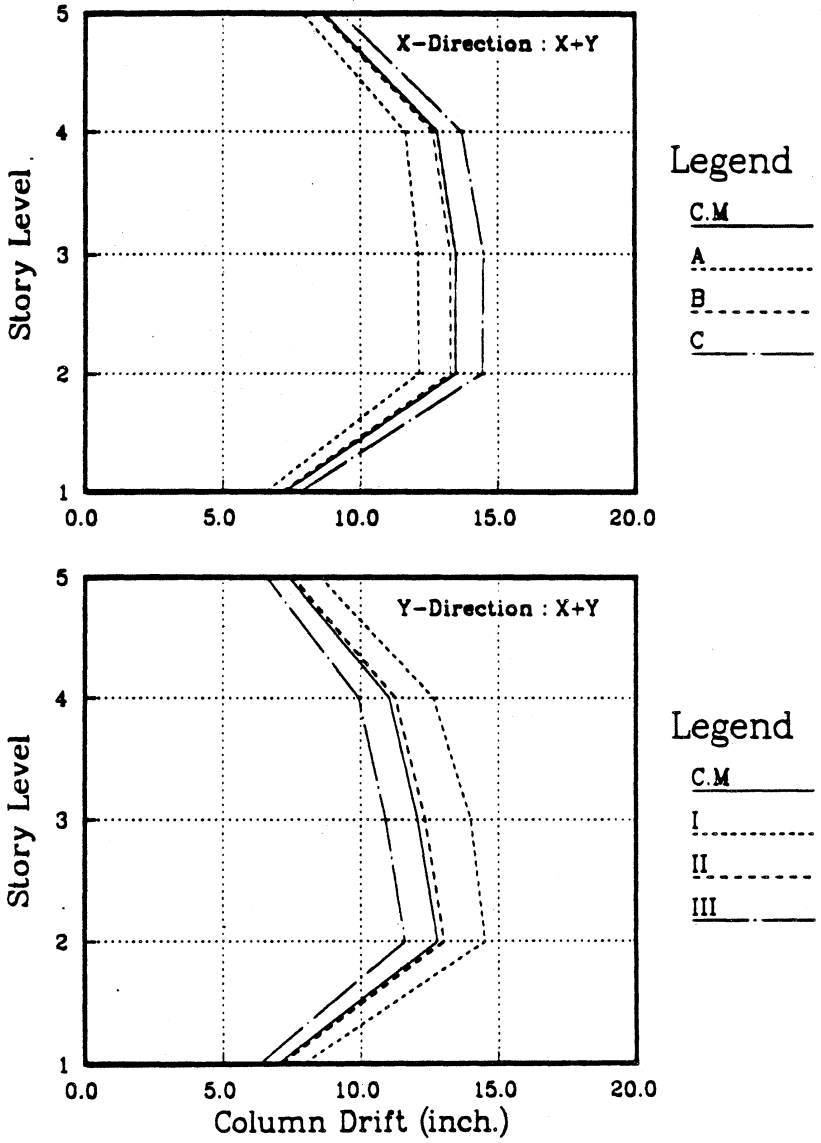

Figure 5.45: Envelopes of C.M. and Edge Story Drift of Five Story L-Shape Building Subjected to 0.5 g 1978 Miyagi-Ken-Oki Earthquake : Case X+Y, Elastic

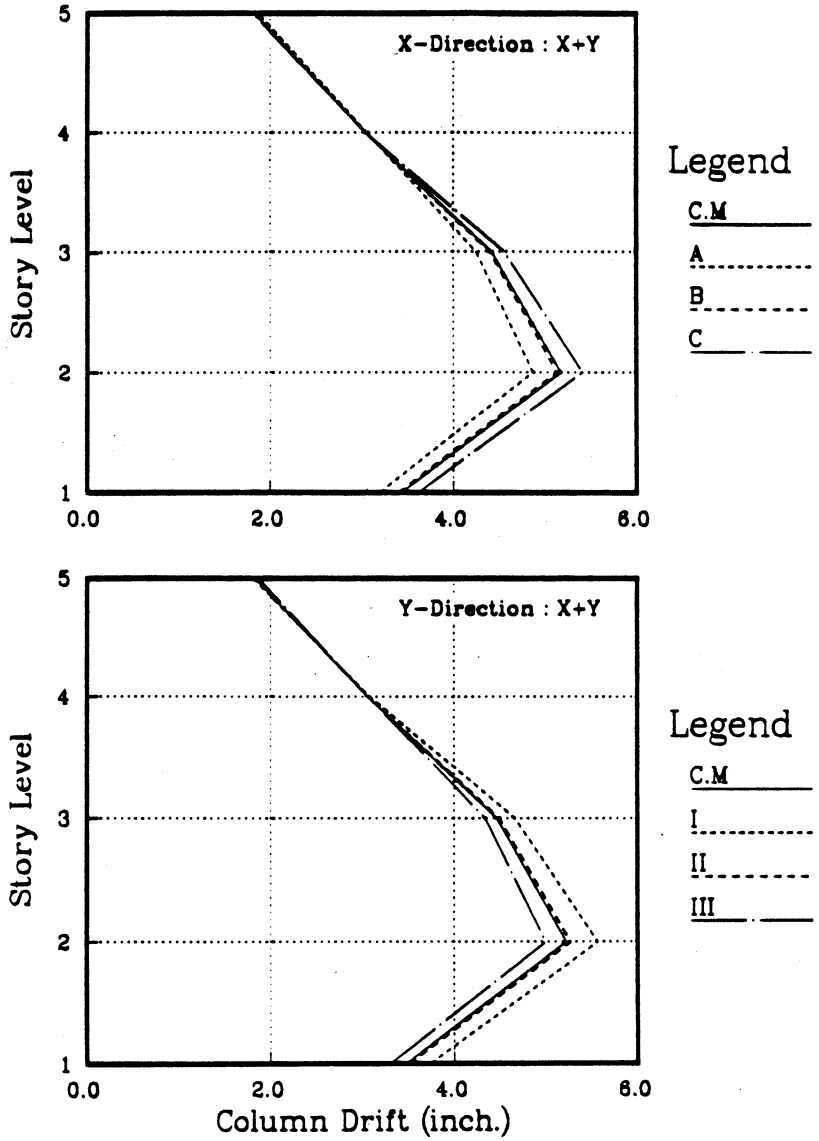

F Figure 5.46: Envelopes of C.M. and Edge Story Drift of Five Story L-Shape Building Subjected to 0.5 g 1978 Miyagi-Ken-Oki Earthquake : Case X+Y, Inelastic

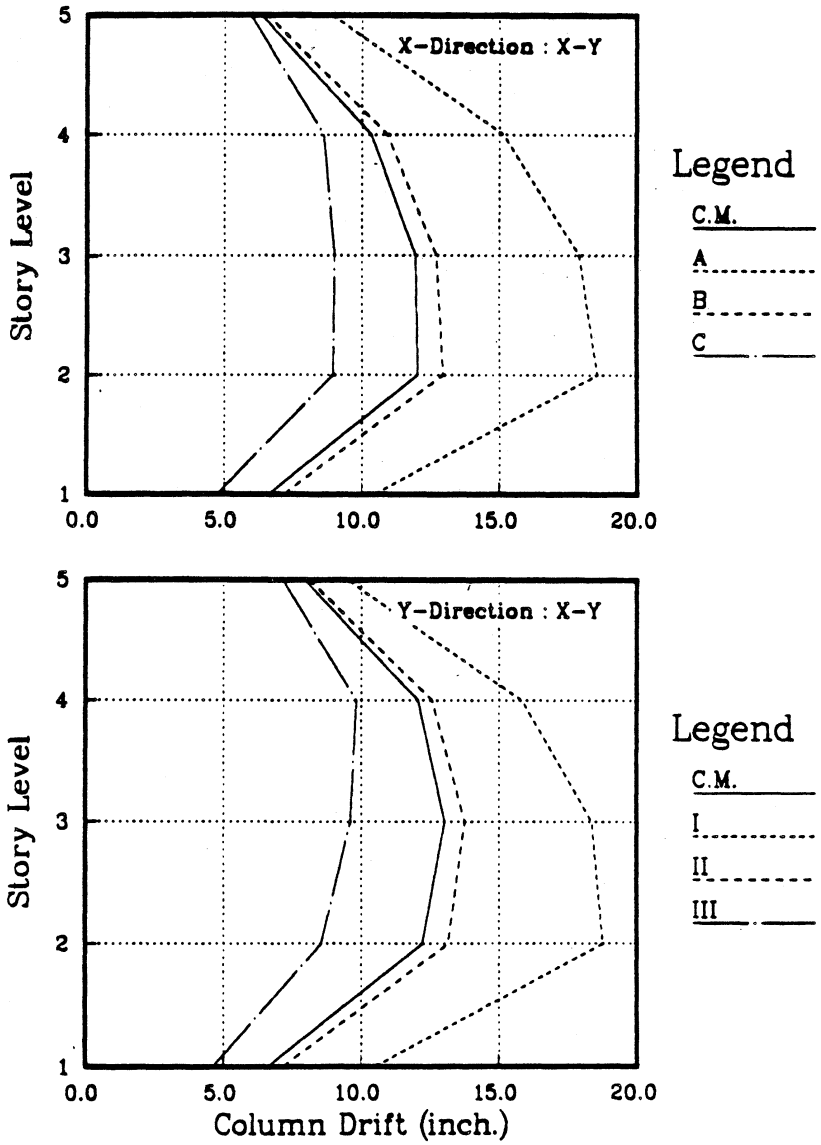

Figure 5.47: Envelopes of C.M. and Edge Story Drift of Five Story L-Shape Building Subjected to 0.5 g 1978 Miyagi-Ken-Oki Earthquake : Case X-Y, Elastic

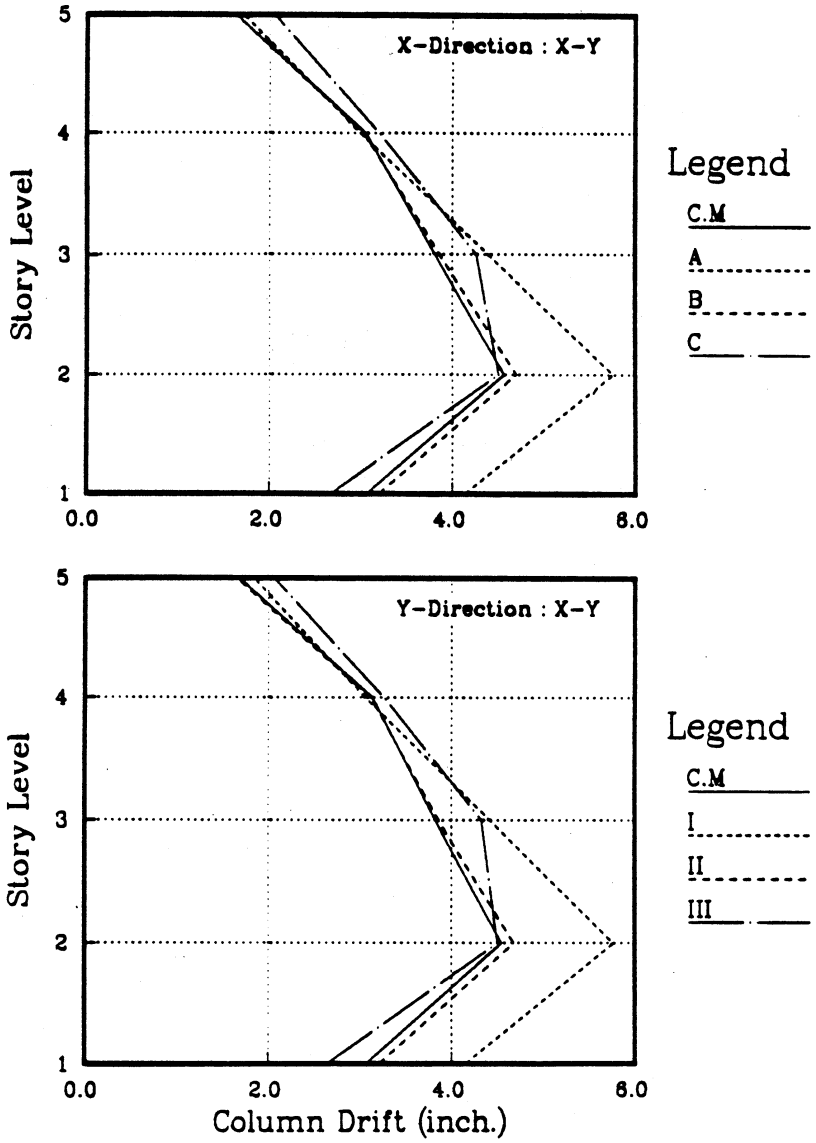

Figure 5.48: Envelopes of C.M. and Edge Story Drift of Five Story L-Shape Building Subjected to 0.5 g 1978 Miyagi-Ken-Oki Earthquake : Case X-Y, Inelastic

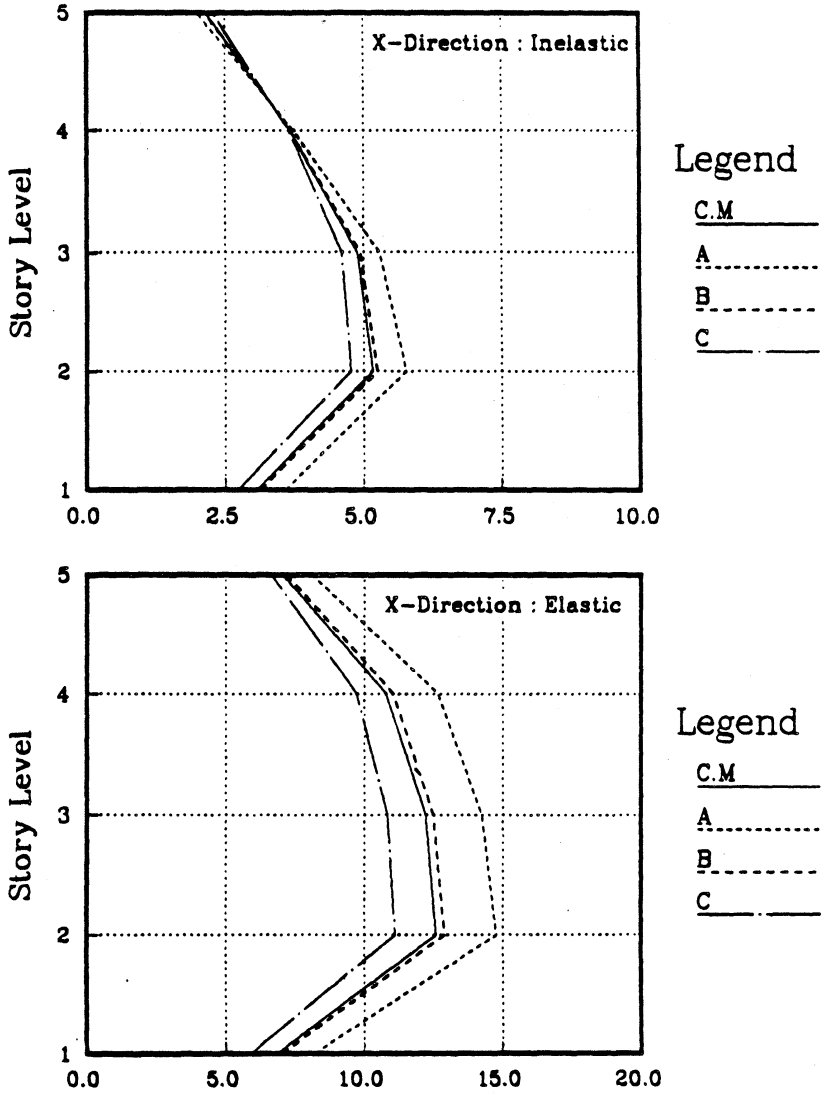

Figure 5.49: Envelopes of C.M. and Edge Story Drift of Five Story L-Shape Building Subjected to 0.5 g 1978 Miyagi-Ken-Oki Earthquake : Case X, Elastic and Inelastic

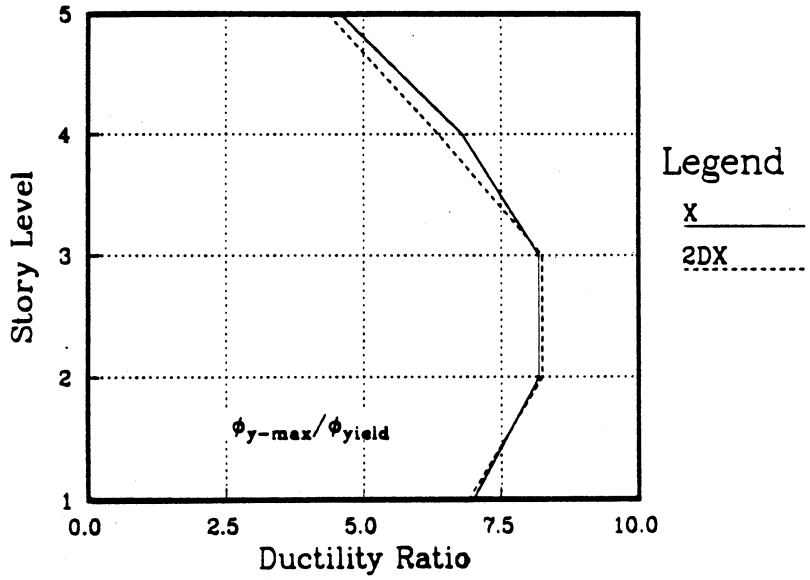

Figure 5.50: Comparison of Column 8 Ductility Ratio of Five Story L-Shape Building Subjected to 0.5 g 1978 Miyagi-Ken-Oki Earthquake : Case X and 2DX

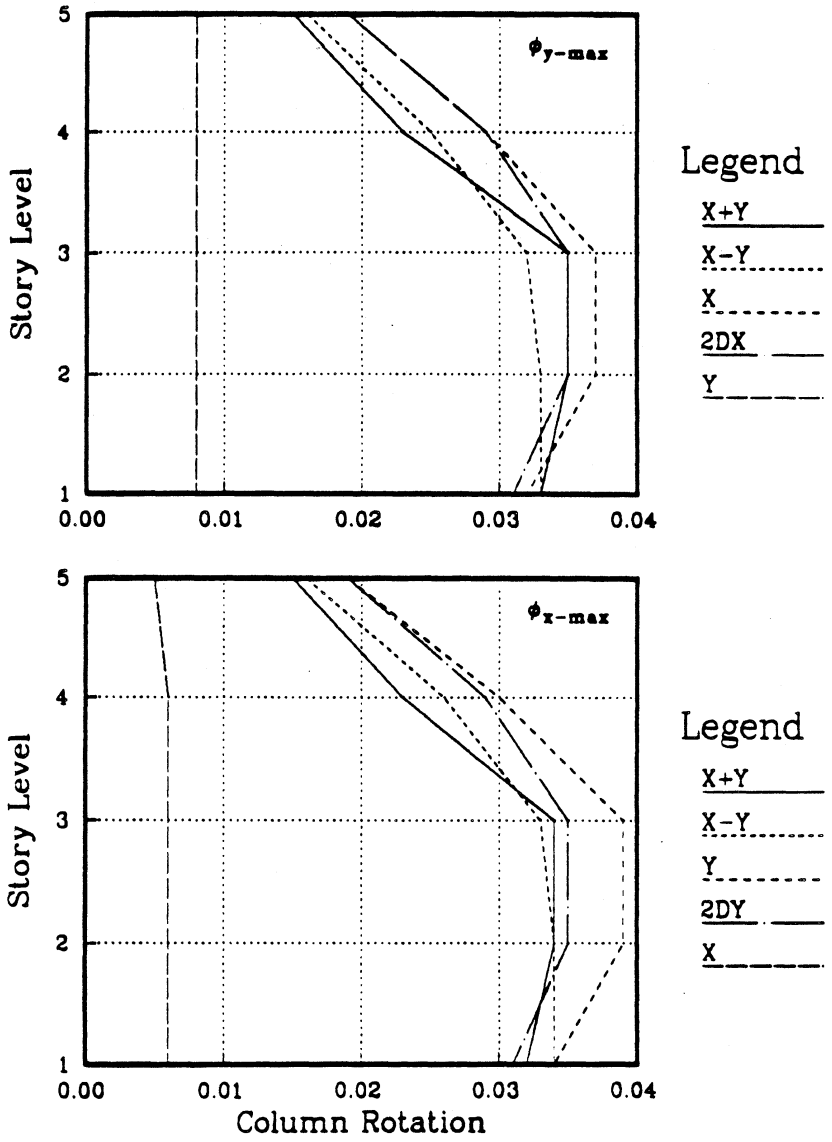

Figure 5.51: Envelope of Maximum Column Rotation of Five Story L-Shape Building Subjected to 0.5 g 1978 Miyagi-Ken-Oki Earthquake

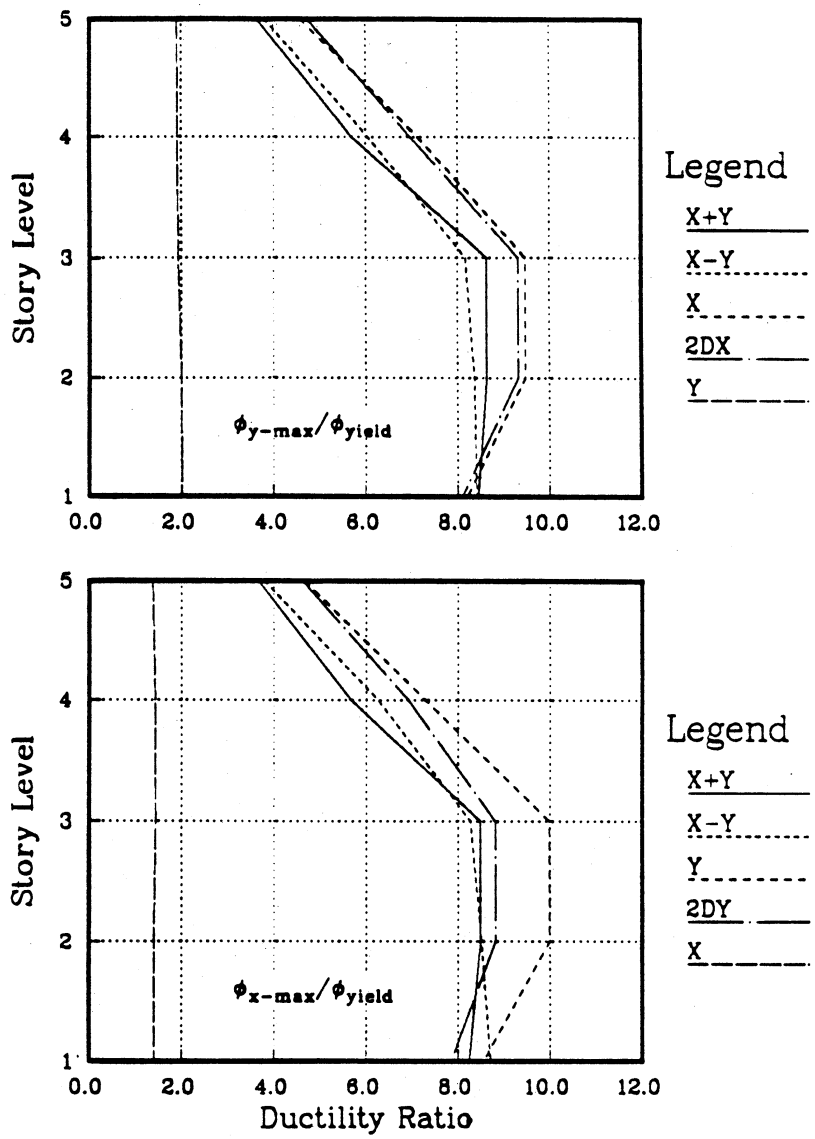

Figure 5.5 5.52: Envelope of Maximum Column Ductility Ratio of Five Story L-Shape Building Subjected to 0.5 g 1978 Miyagi-Ken-Oki Earthquake

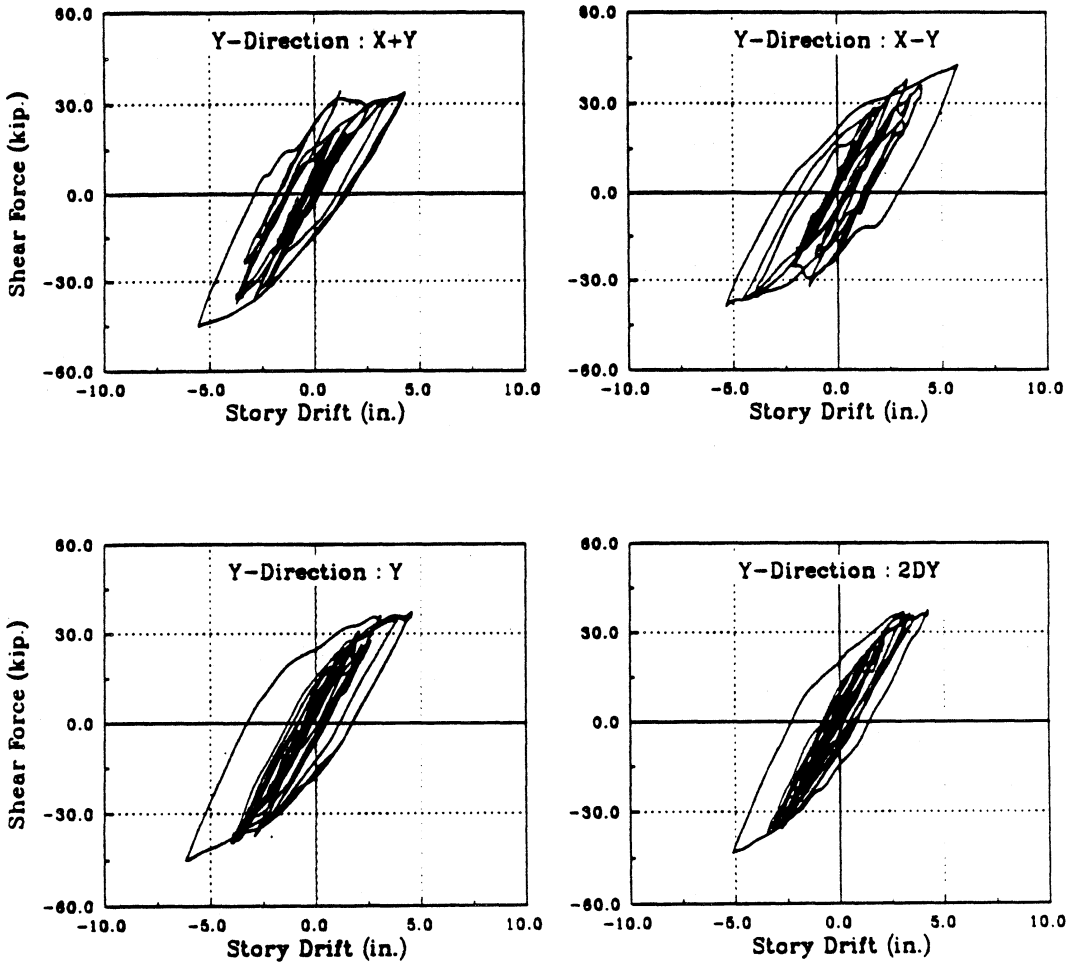

Figure 5.53: (a)Column 25 Shear Force Hysteresis of Five Story L-Shape Building Subjected to 0.5 g 1978 Miyagi-Ken-Oki Earthquake : Y-Direction, Weak Side, 2nd Story

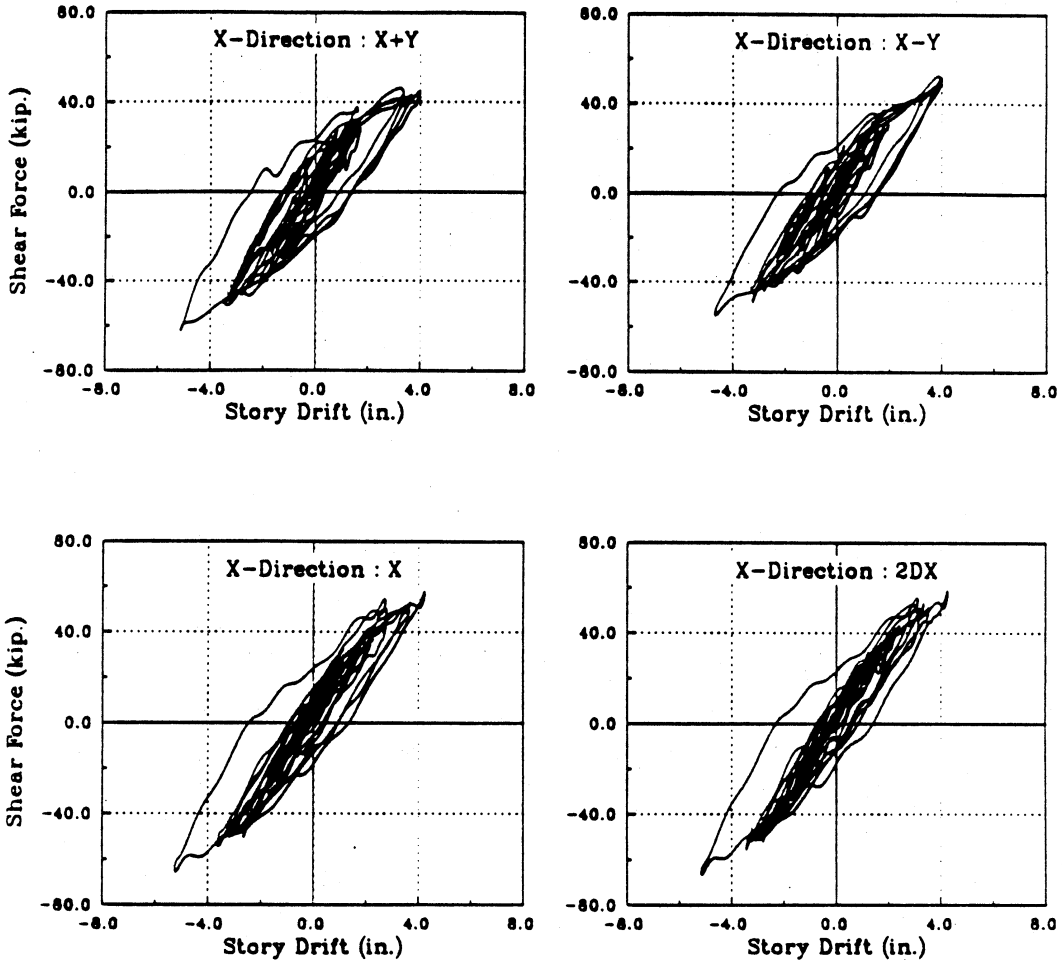

Figure 5.53: (b)Column 25 Shear Force Hysteresis of Five Story L-Shape Building Subjected to 0.5 g 1978 Miyagi-Ken-Oki Earthquake : X-Direction, Interior Col., 2nd Story (Continue)

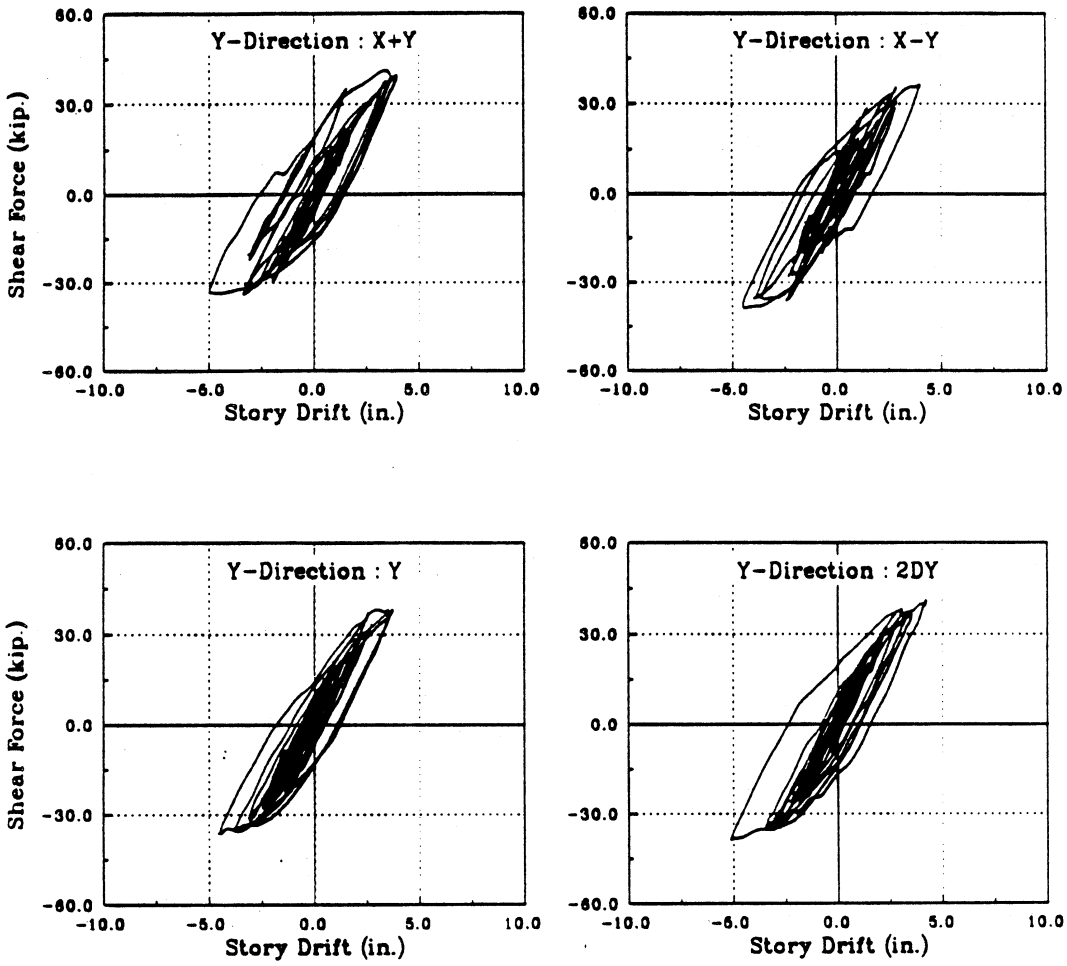

Figure 5.54: (a)Column 32 Shear Force Hysteresis of Five Story L-Shape Building Subjected to 0.5 g 1978 Miyagi-Ken-Oki Earthquake : Y-Direction, Stiff Side, 2nd Story

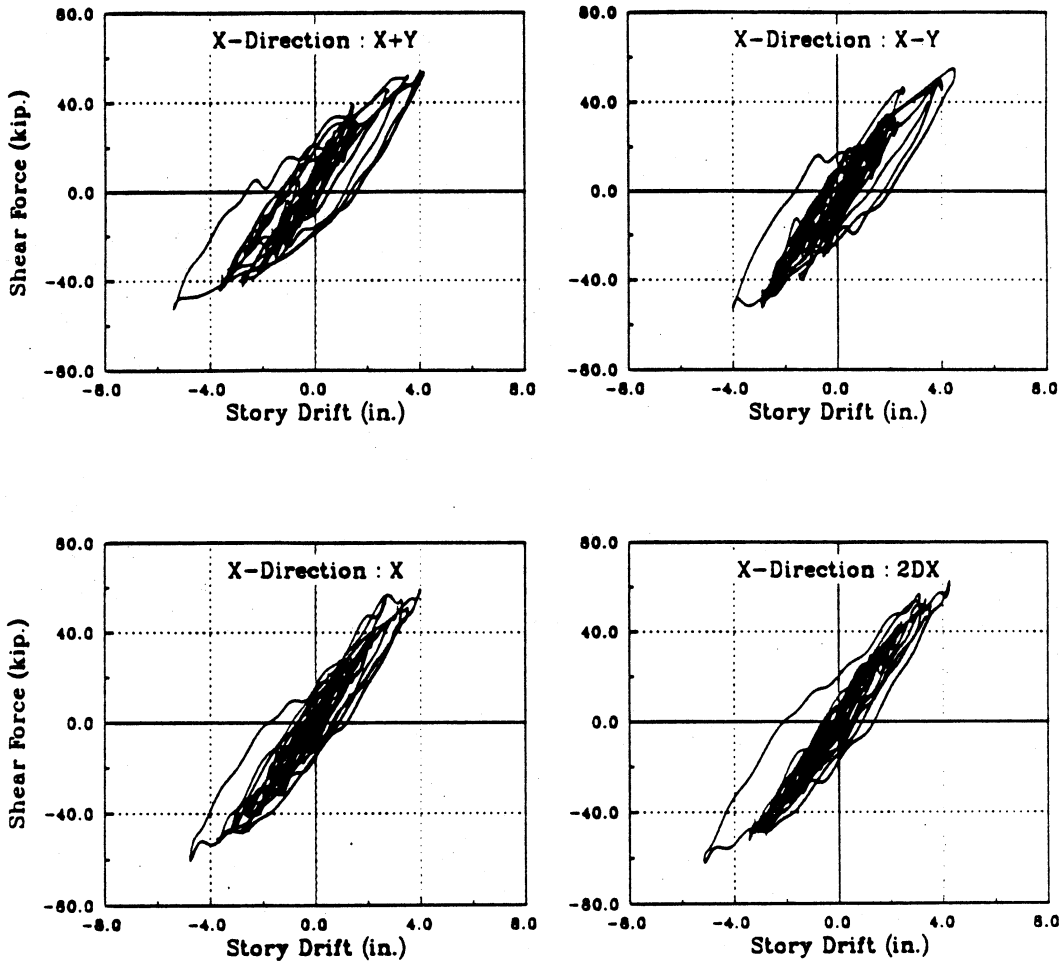

Figure 5.54: (b)Column 32 Shear Force Hysteresis of Five Story L-Shape Building Subjected to 0.5 g 1978 Miyagi-Ken-Oki Earthquake : X-Direction, Stiff Side, 2nd Story (Continue)

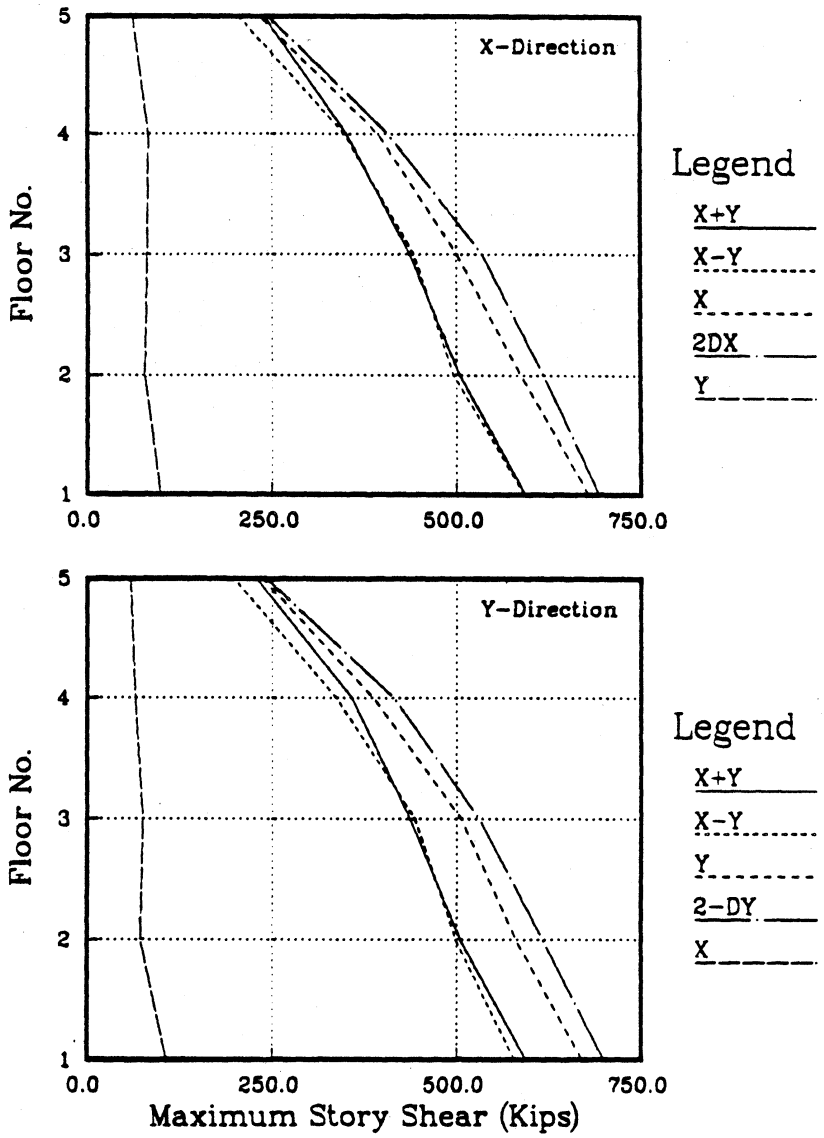

Figure 5.55: Comparison of Maximum Story Shear of Five Story L-Shape Building Subjected to 0.75 g 1978 Miyagi-Ken-Oki Earthquake

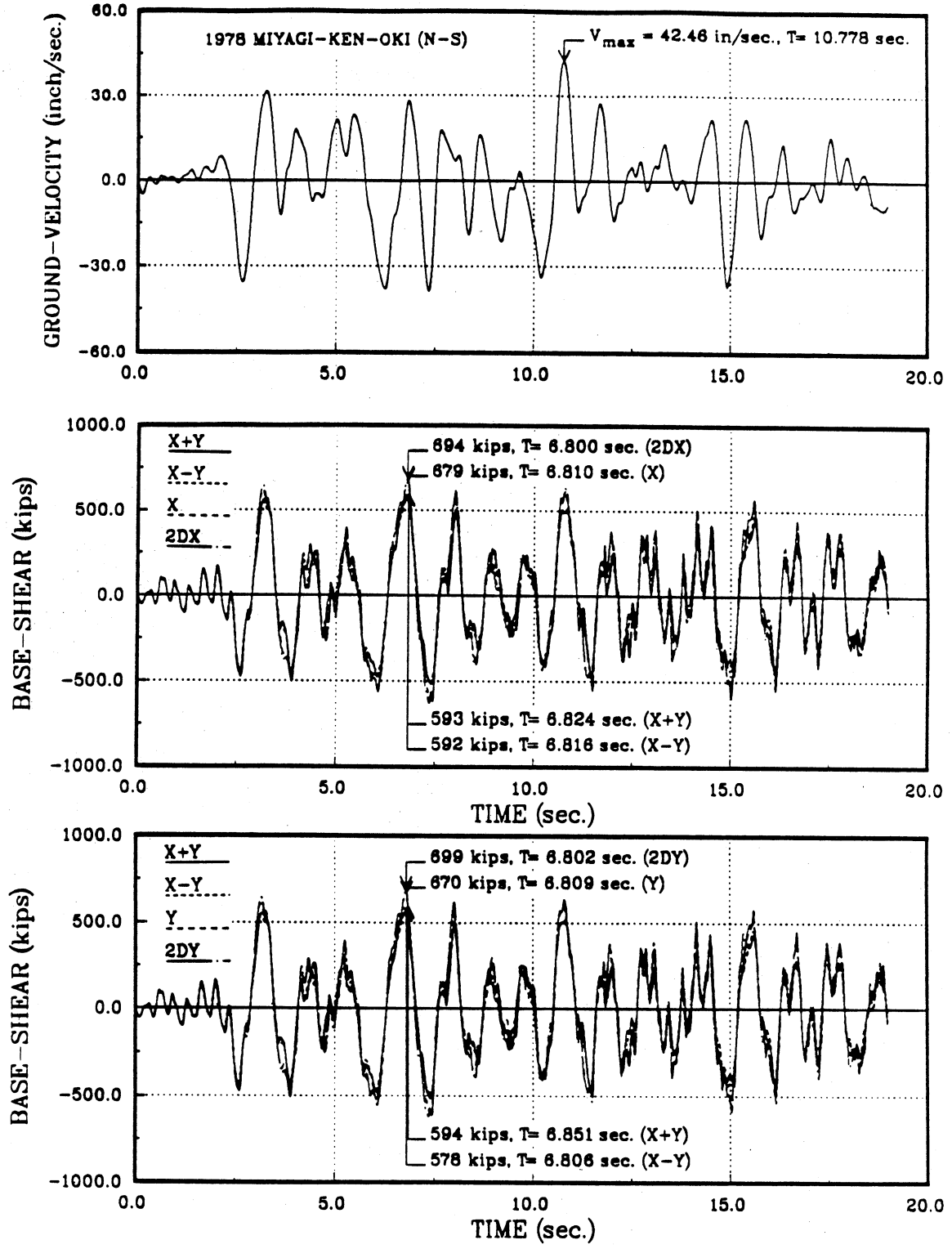

Figure 5.56: Input Ground Velocity and Base Shear Time History in the Principal Directions of Five Story L-Shape Building Subjected to 0.75 g 1978 Miyagi-Ken-Oki Earthquake

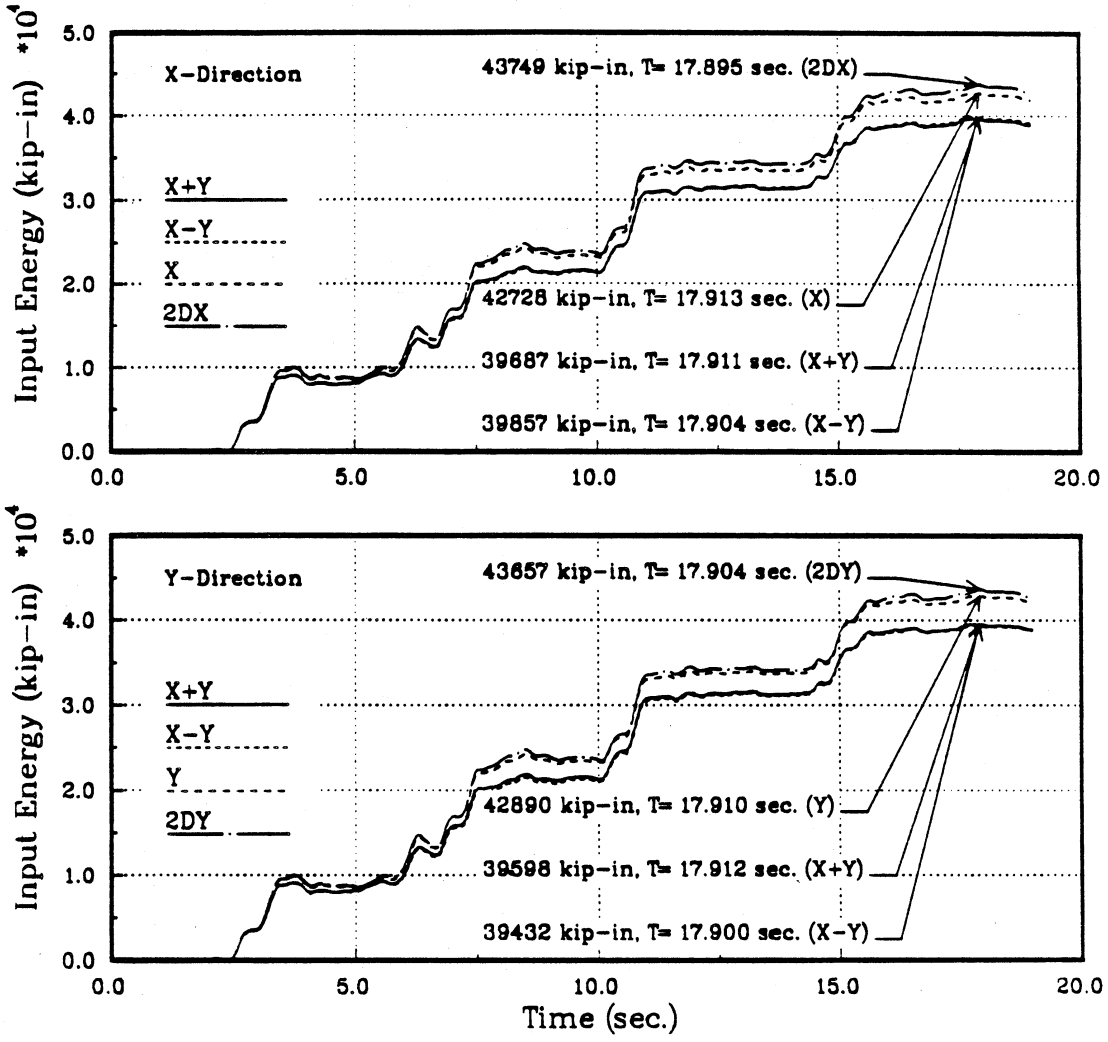

Figure 5.57: Absolute Input Energy Time History in the Principal Directions of Five Story L-Shape Building Subjected to 0.75 g 1978 Miyagi-Ken-Oki Earthquake

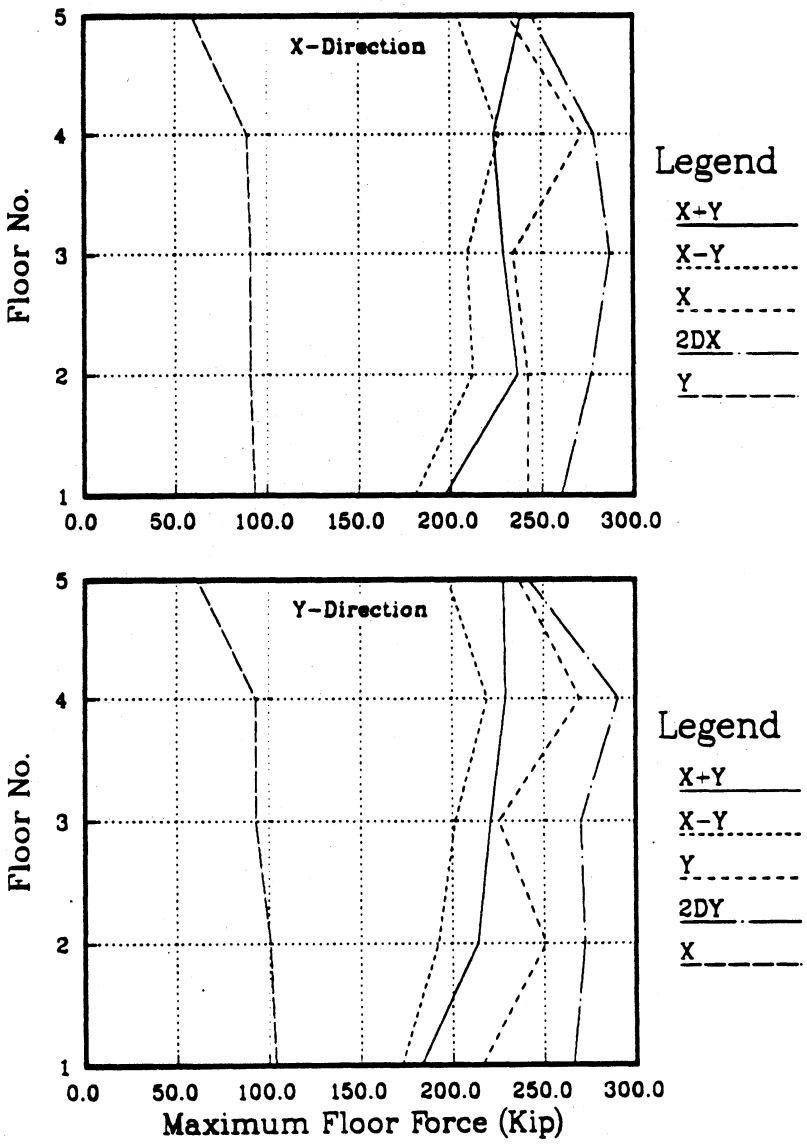

Figu gure 5.58: Comparison of Maximum Floor Force of Five Story L-Shape Buildin Subjected to 0.75 g 1978 Miyagi-Ken-Oki Earthquake

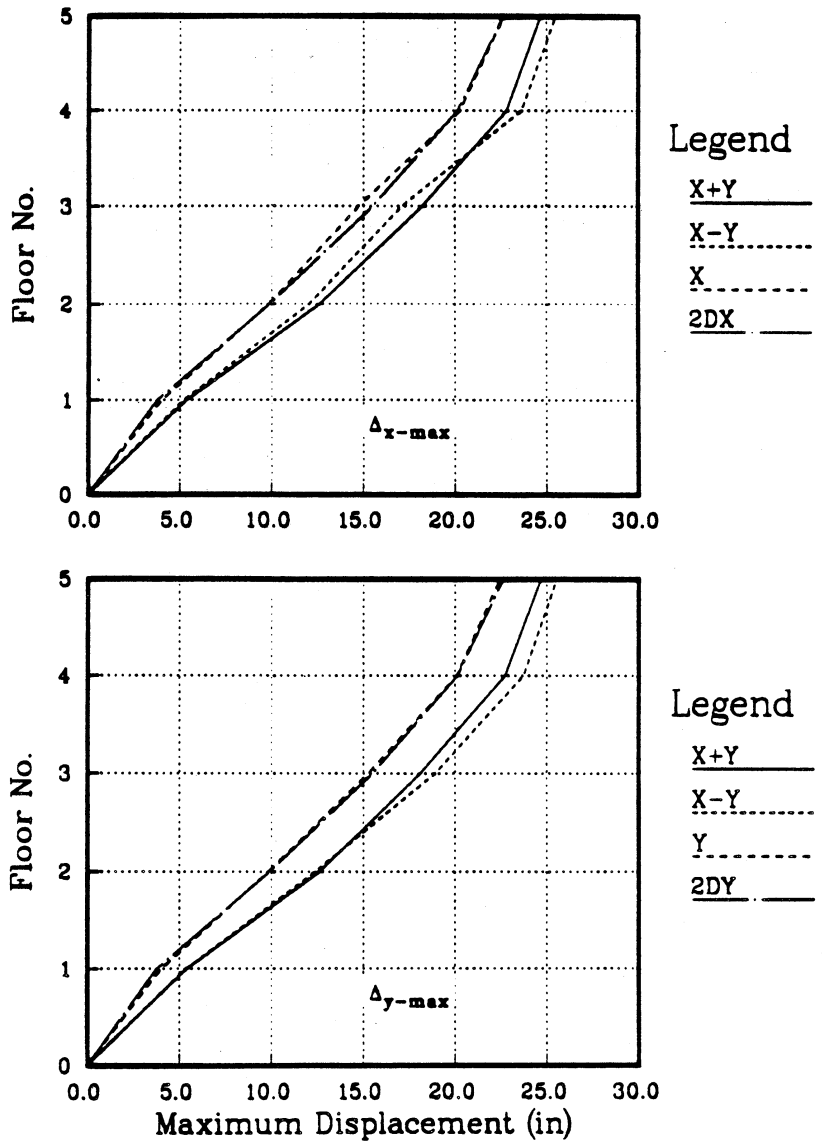

Figure 5.59: Comparison of C.M. Maximum Displacement of Five Story L-Shape Building Subjected to 0.75 g 1978 Miyagi-Ken-Oki Earthquake

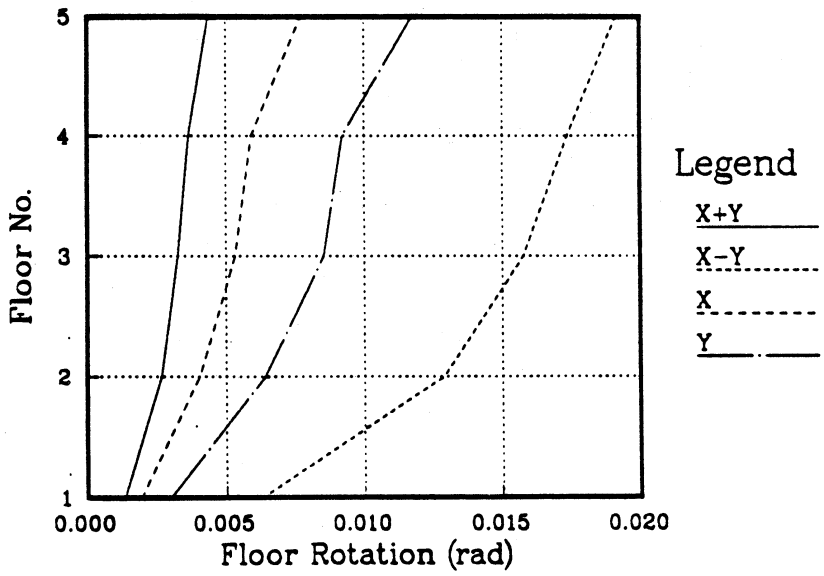

ɟure 5.60: Envelope of Center of Mass Rotation of Five Story L-Shape Buildingling Subjected to 0.75 g 1978 Miyagi-Ken-Oki Earthquake

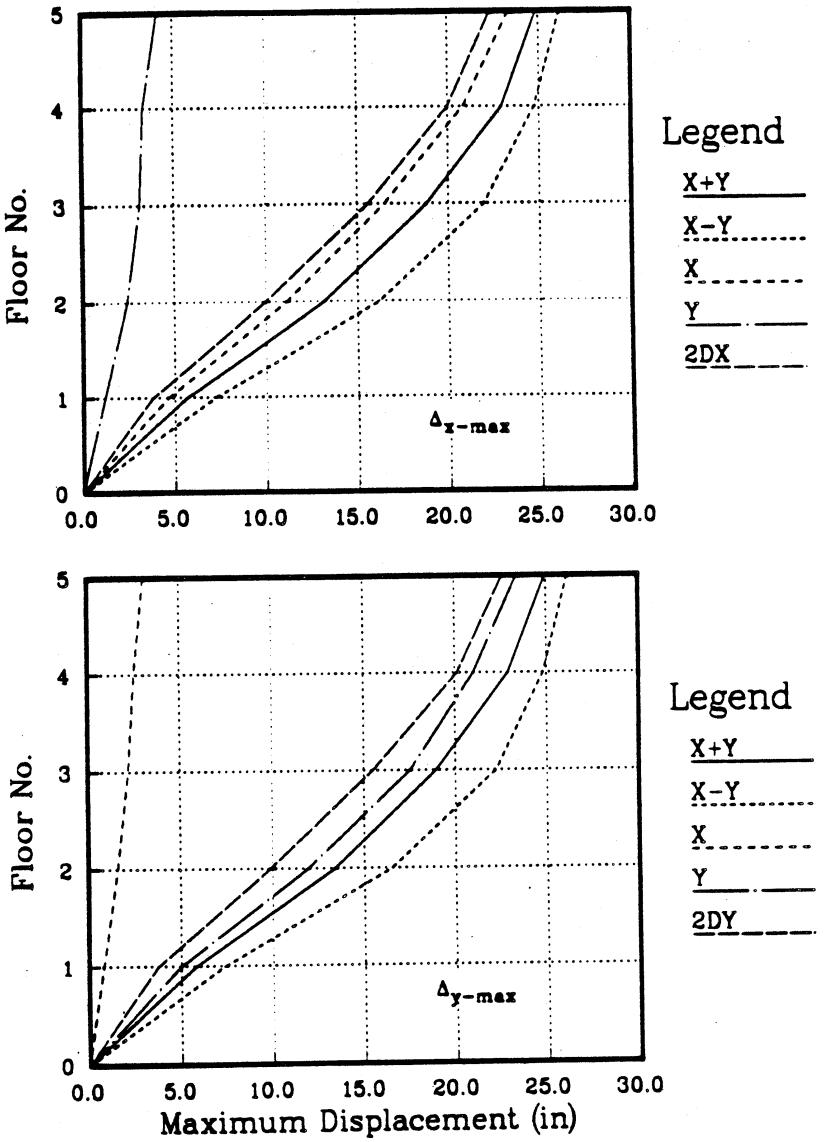

Figure 5.61: Comparison of Maximum Displacement of Five Story L-Shape Building Subjected to 0.75 g 1978 Miyagi-Ken-Oki Earthquake

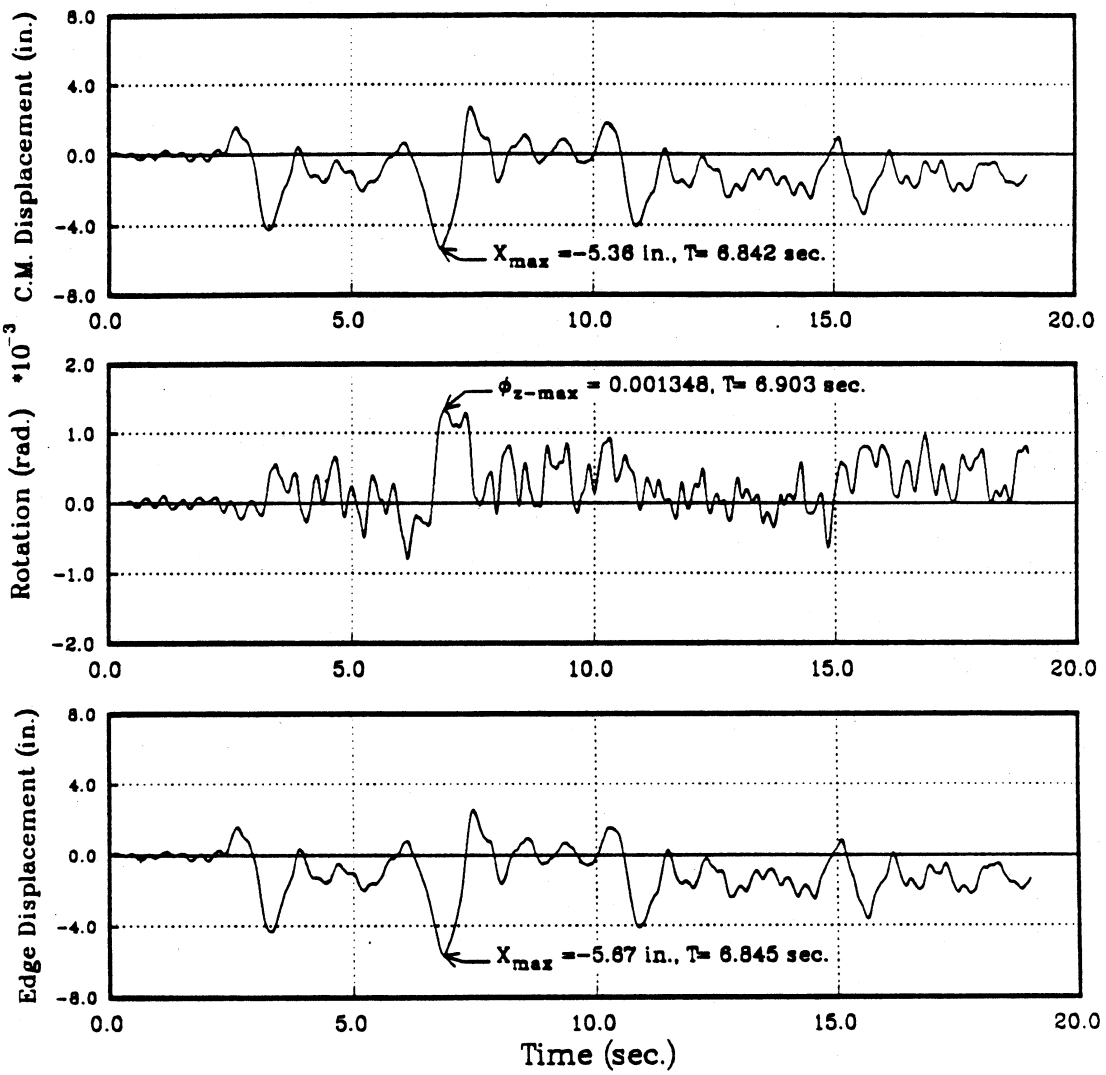

Figure 5.62: 1st Floor Center of Mass Displacement and Rotation, Edge Displacement Time History of Five Story L-Shape Building Subjected to 0.75 g 1978 Miyagi-Ken-Oki Earthquake : Case X+Y

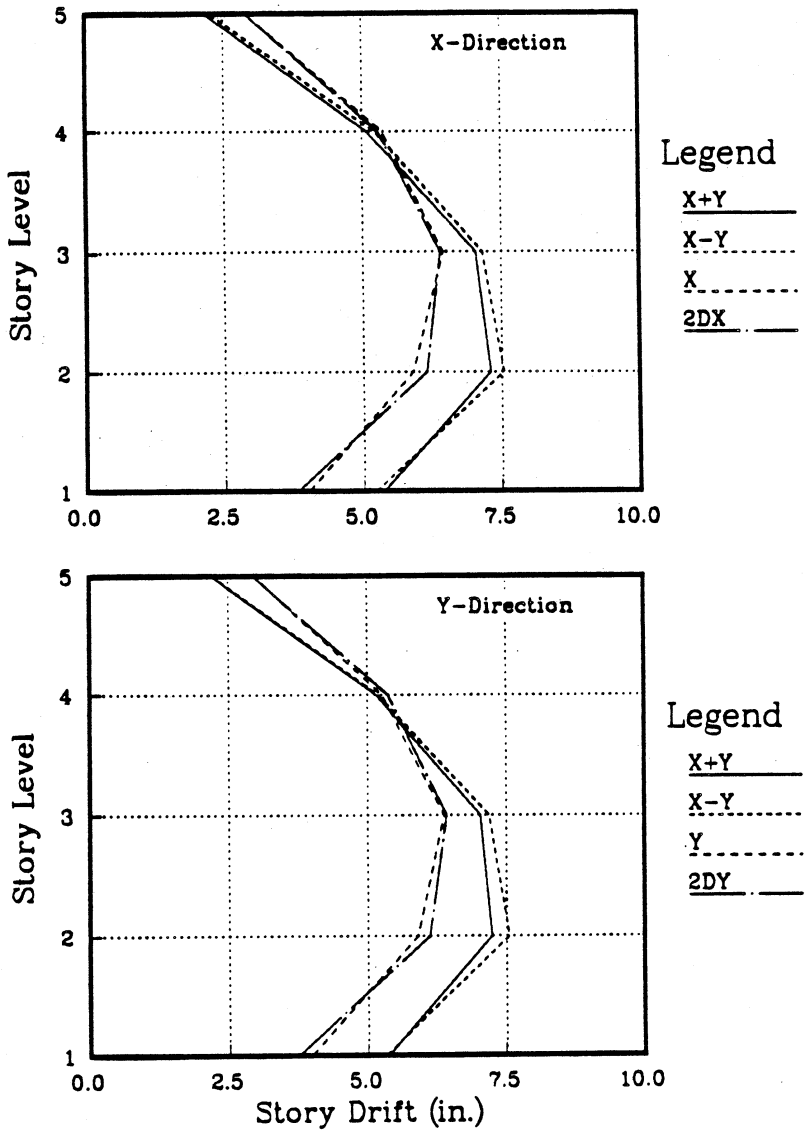

Figure 5.63: Comparison of Center of Mass Maximum Story Drift of Five Story L-Shape Building Subjected to 0.75 g 1978 Miyagi-Ken-Oki Earthquake

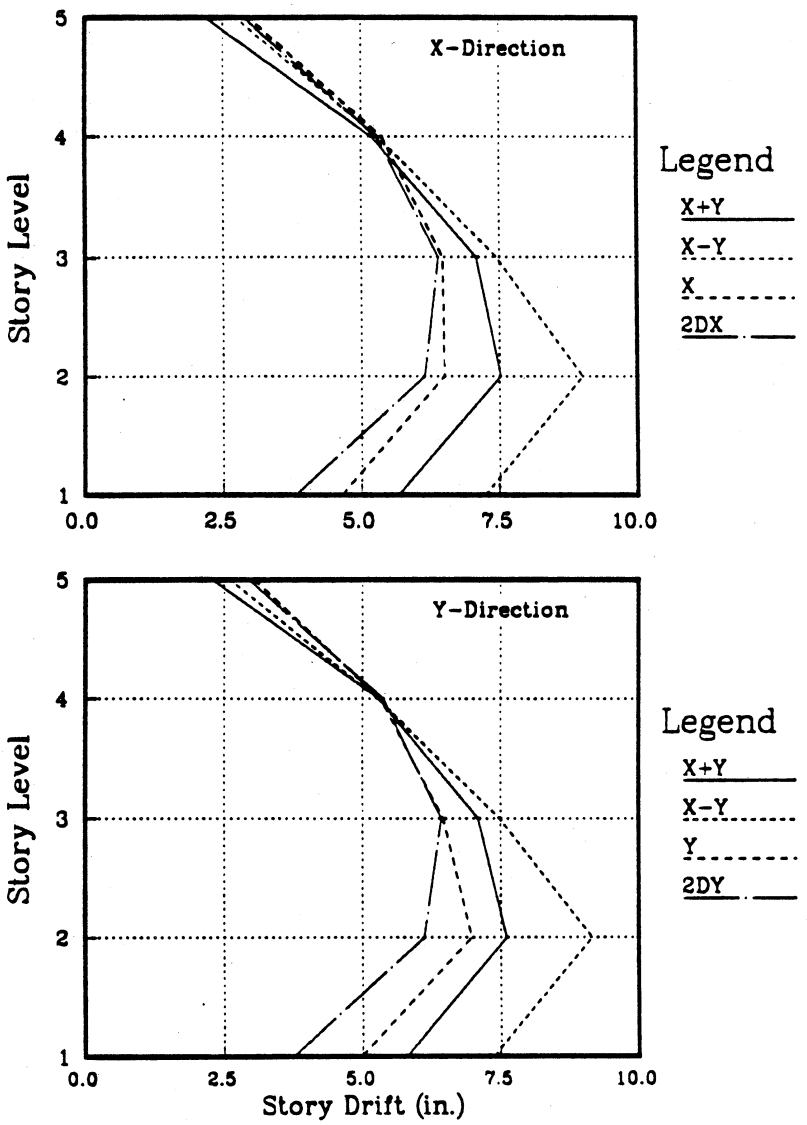

Figure 5.64: Comparison of Maximum Story Drift of Five Story L-Shape Building Subjected to 0.75 g 1978 Miyagi-Ken-Oki Earthquake

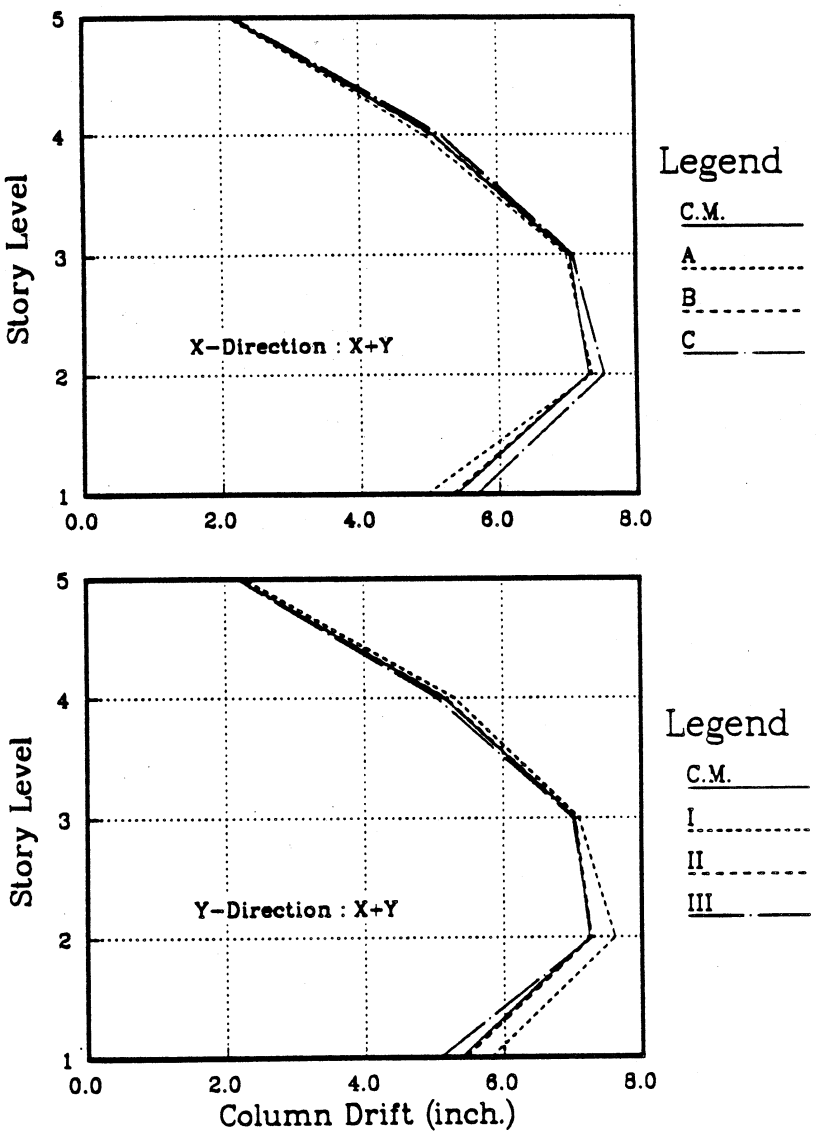

Figure 5.65: Envelopes of C.M. and Edge Story Drift of Five Story L-Shape Building Subjected to 0.75 g 1978 Miyagi-Ken-Oki Earthquake : Case X+Y, Inelastic

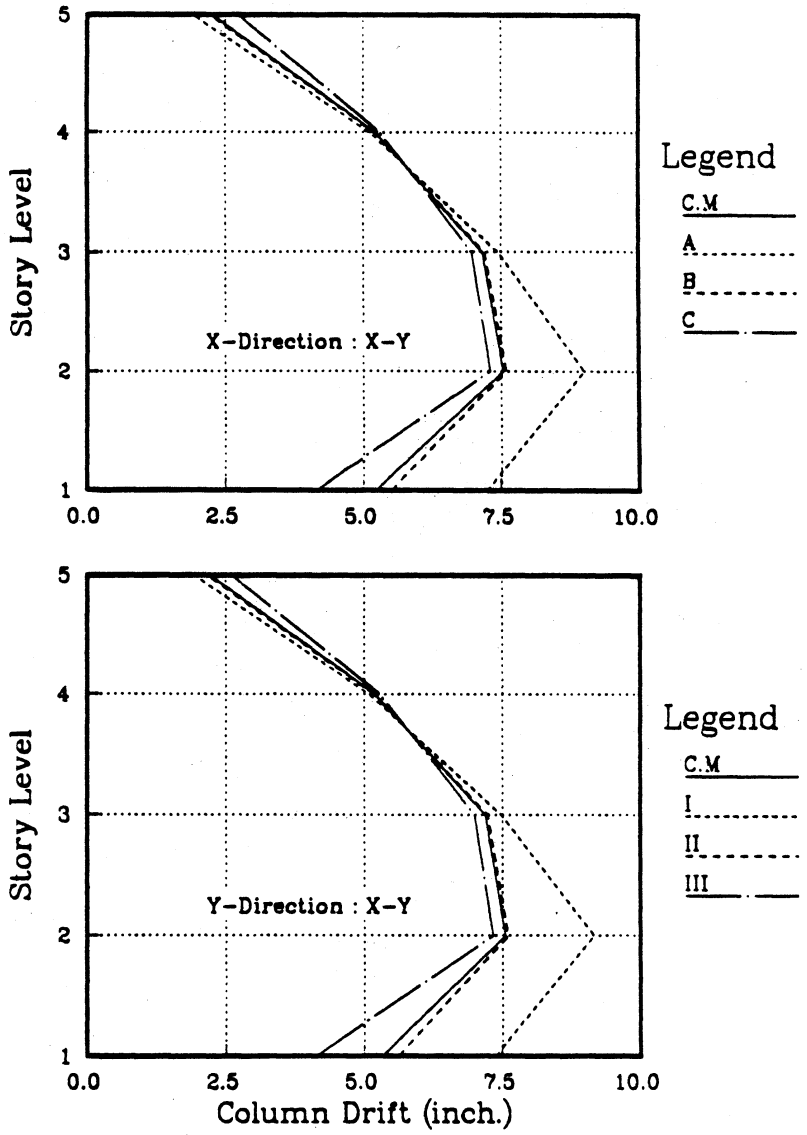

Fig Figure 5.66: Envelopes of C.M. and Edge Story Drift of Five Story L-Shape Building Subjected to 0.75 g 1978 Miyagi-Ken-Oki Earthquake : Case X-Inelastic

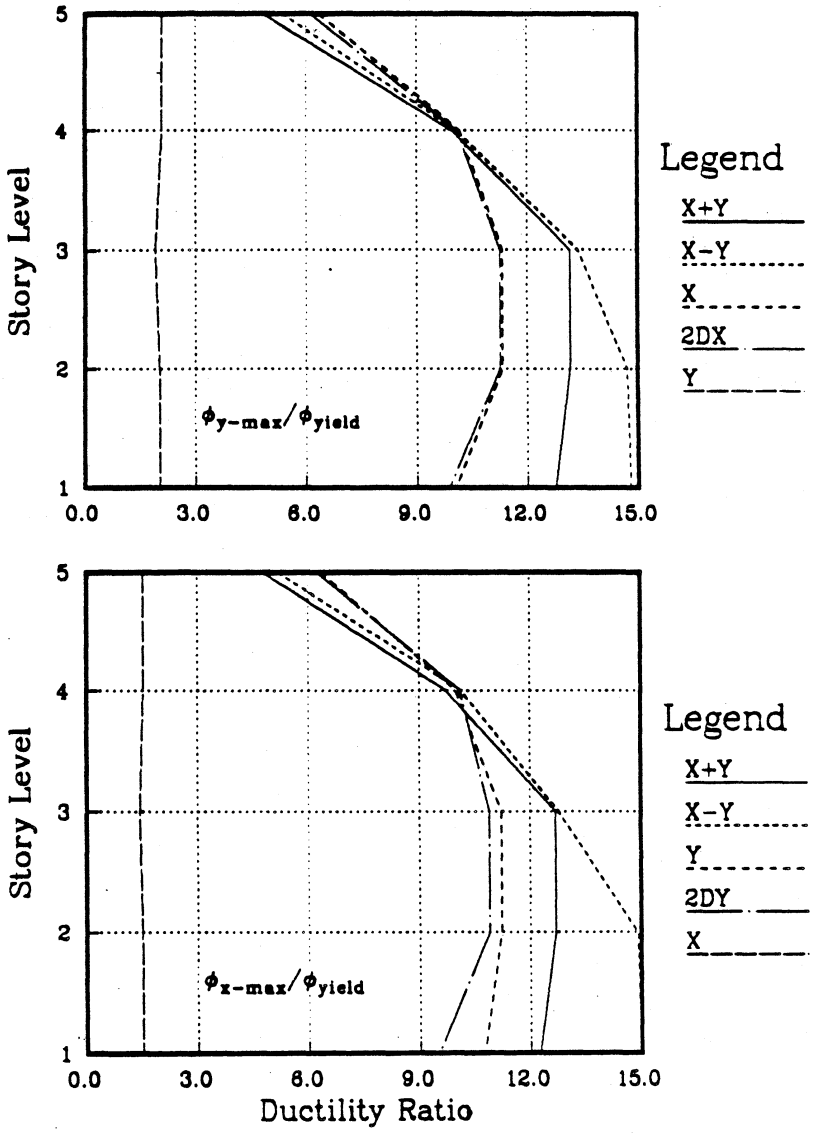

Figure 5.67: Envelope of Maximum Column Ductility Ratio of Five Story L-Shape Building Subjected to 0.75 g 1978 Miyagi-Ken-Oki Earthquake

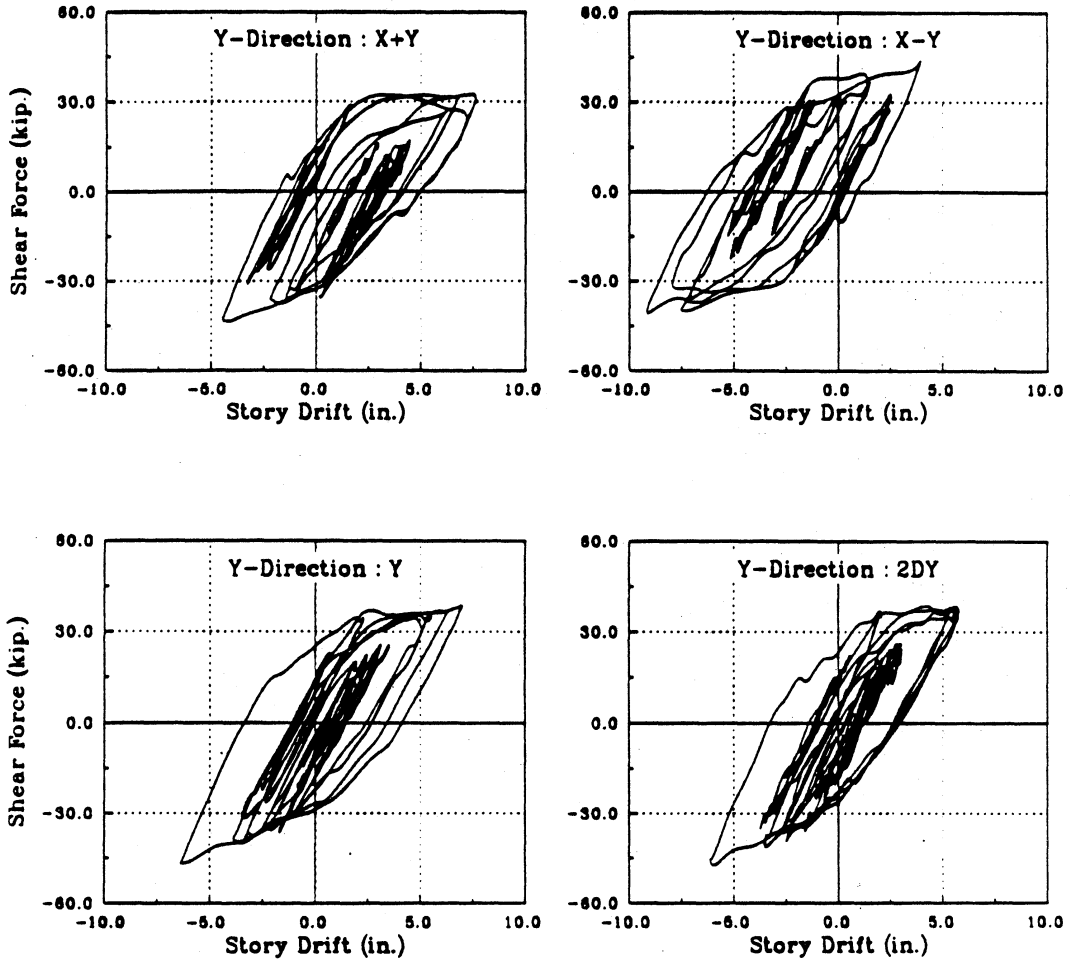

Figure 5.68: (a)Column 25 Shear Force Hysteresis of Five Story L-Shape Building Subjected to 0.75 g 1978 Miyagi-Ken-Oki Earthquake : Y-Direction, Weak Side, 2nd Story

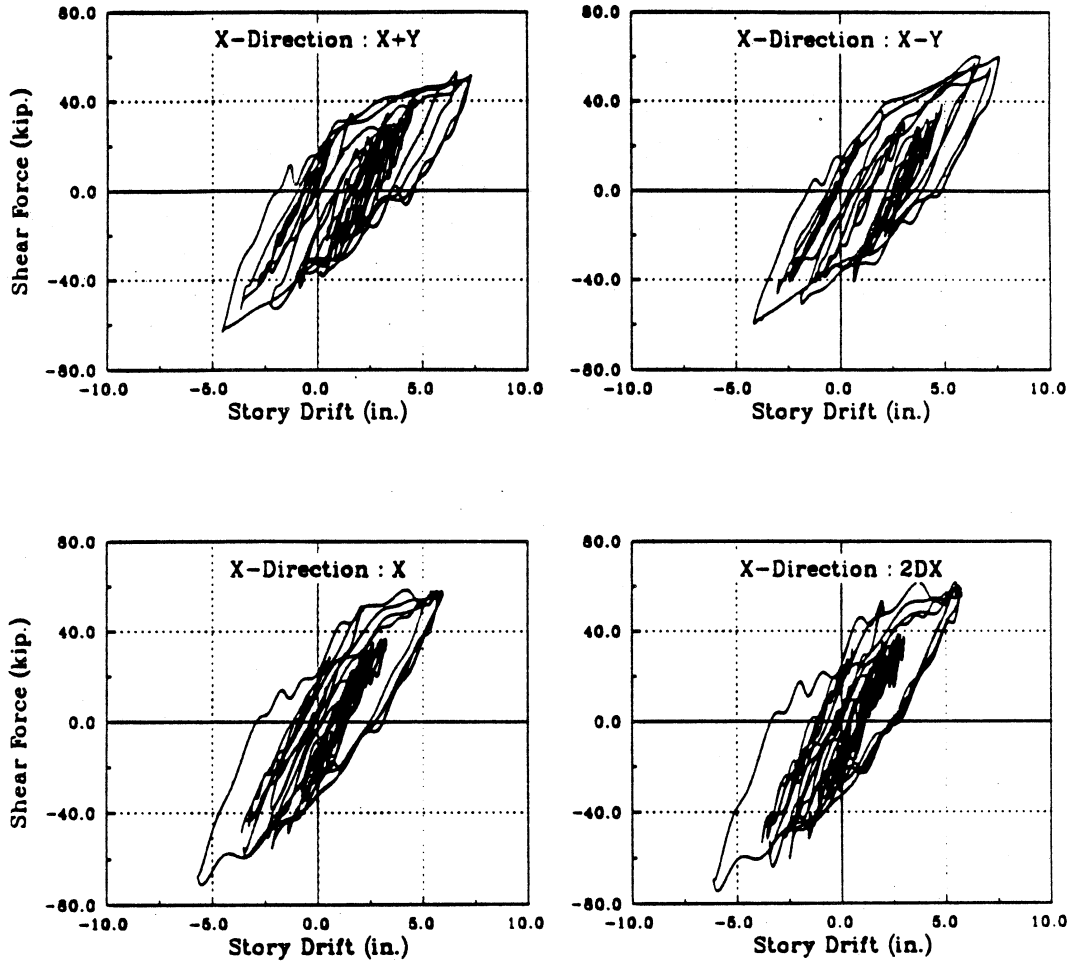

Figure 5.68: (b)Column 25 Shear Force Hysteresis of Five Story L-Shape Building Subjected to 0.75 g 1978 Miyagi-Ken-Oki Earthquake : X-Direction, Interior Col., 2nd Story (Continue)

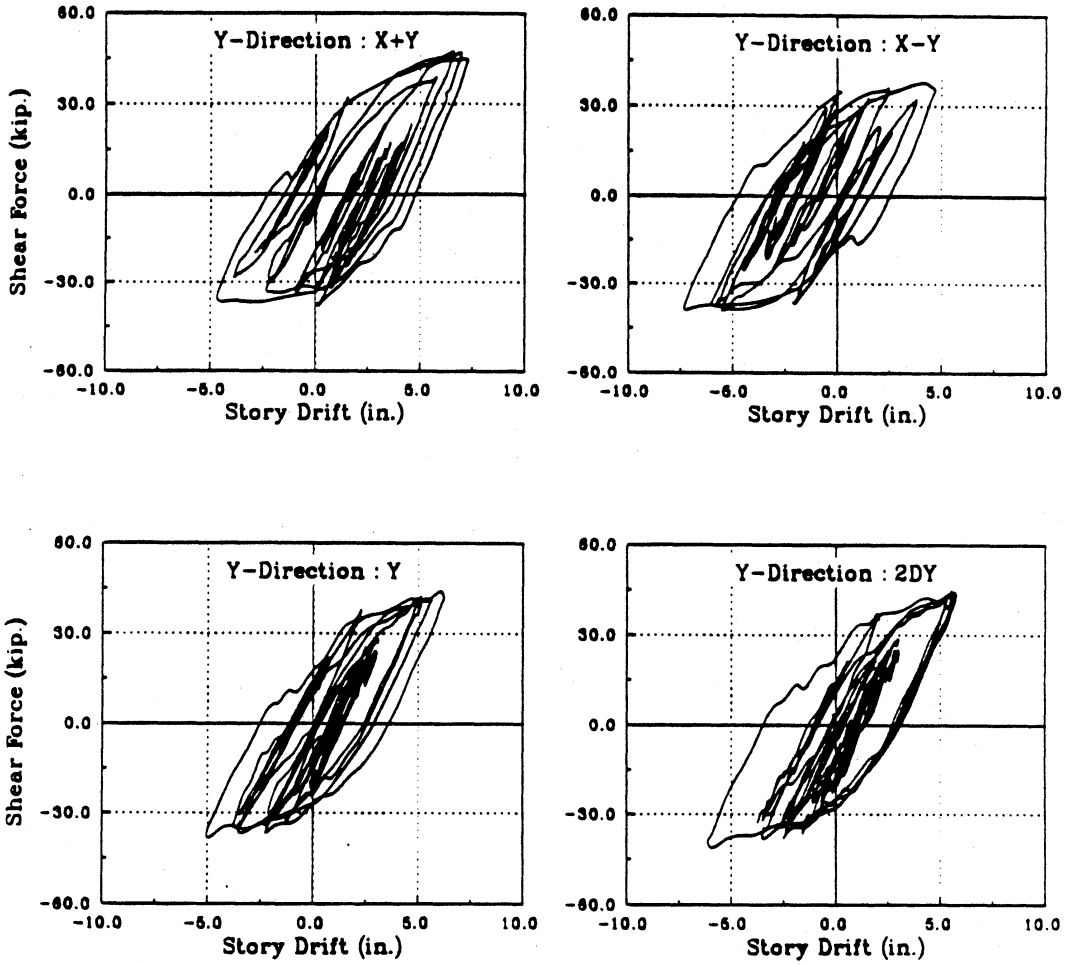

Figure 5.69: (a)Column 32 Shear Force Hysteresis of Five Story L-Shape Building Subjected to 0.75 g 1978 Miyagi-Ken-Oki Earthquake : Y-Direction, Stiff Side, 2nd Story

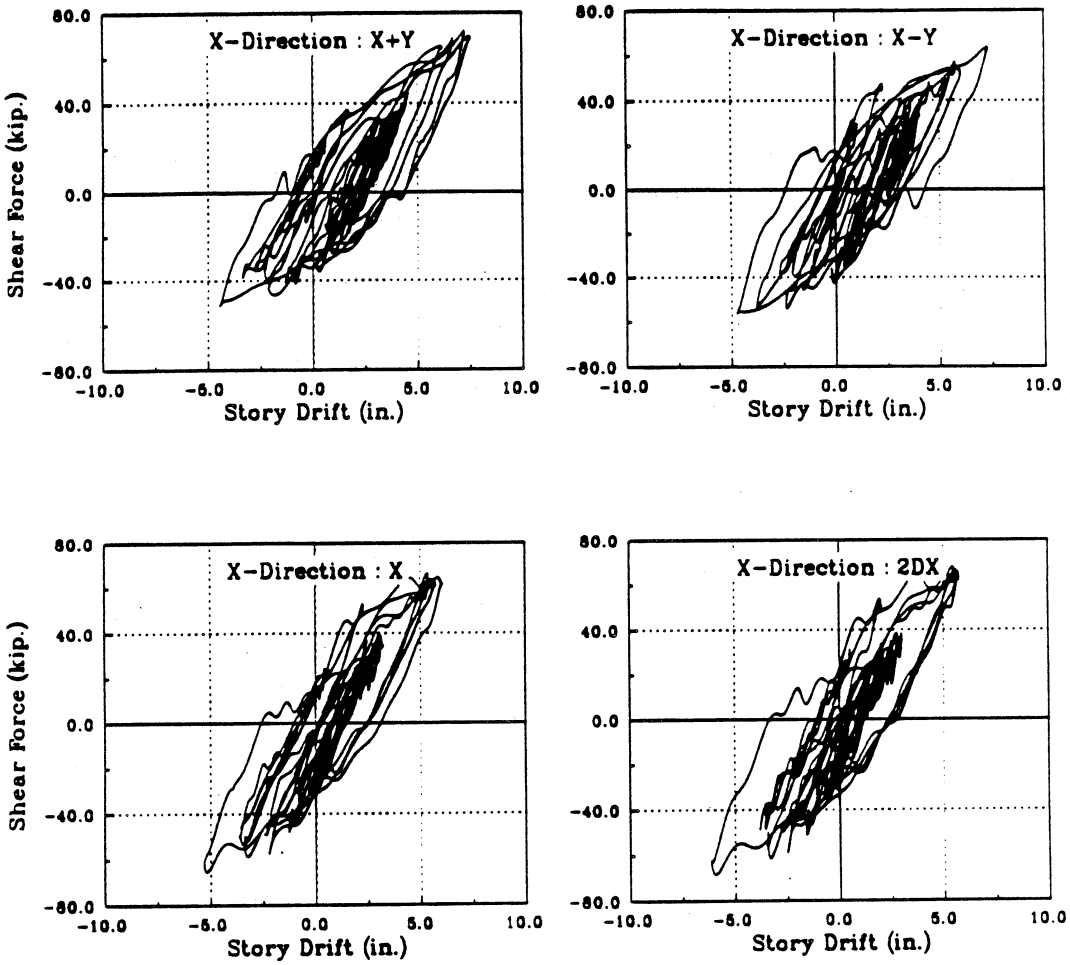

Figure 5.69: (b)Column 32 Shear Force Hysteresis of Five Story L-Shape Building Subjected to 0.75 g 1978 Miyagi-Ken-Oki Earthquake : X-Direction, Stiff Side, 2nd Story (Continue)

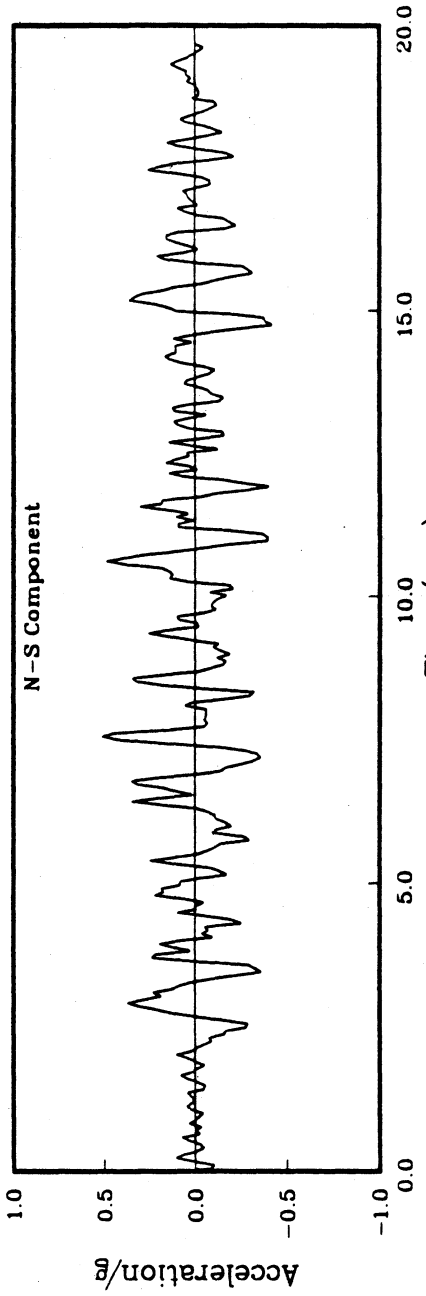

Figure 6.1: 1978 Miyagi-Ken-Oki Earthquake Record (0.5 g)

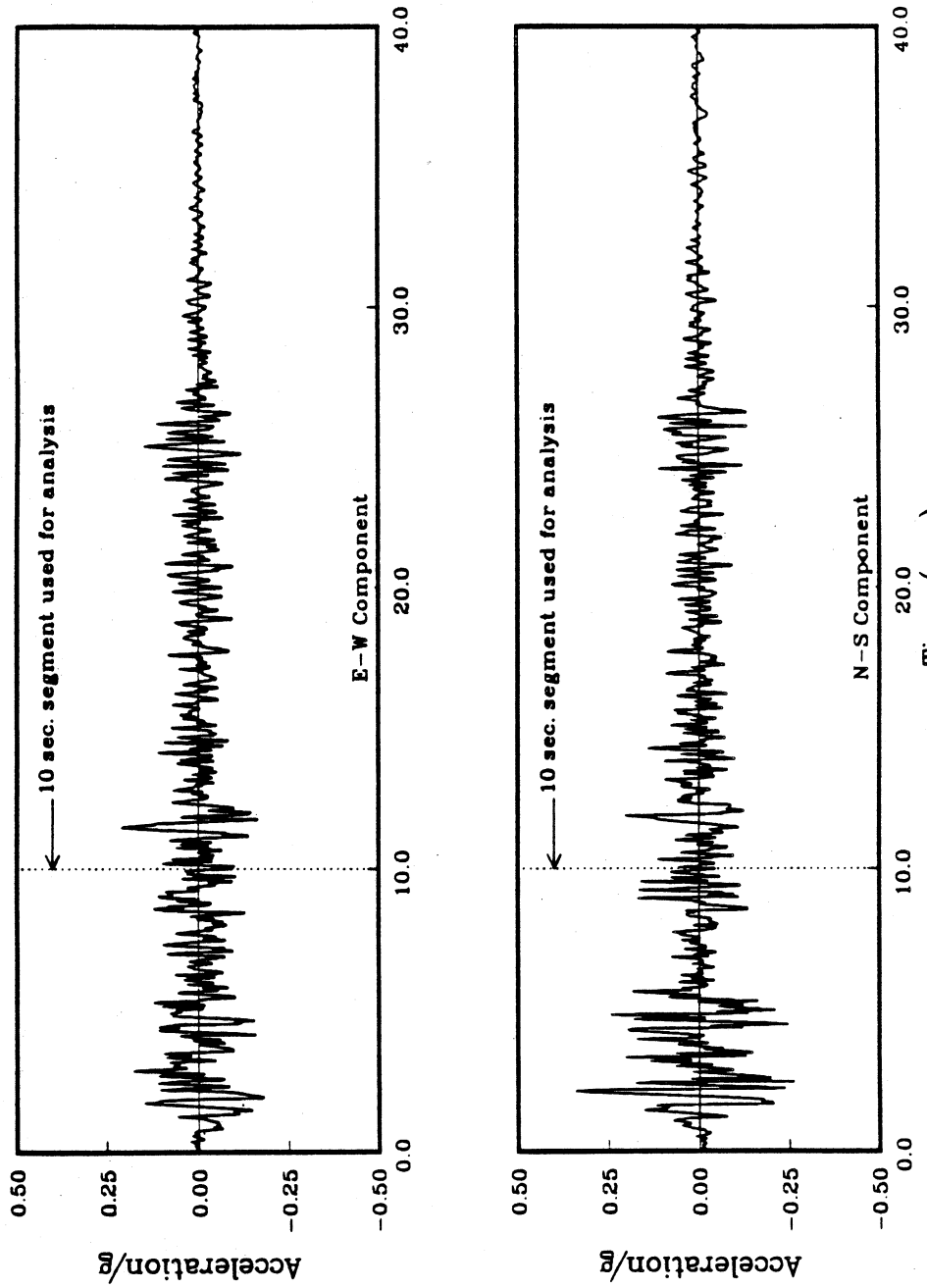

Figure 6.2: 1940 El Centro Earthquake Record

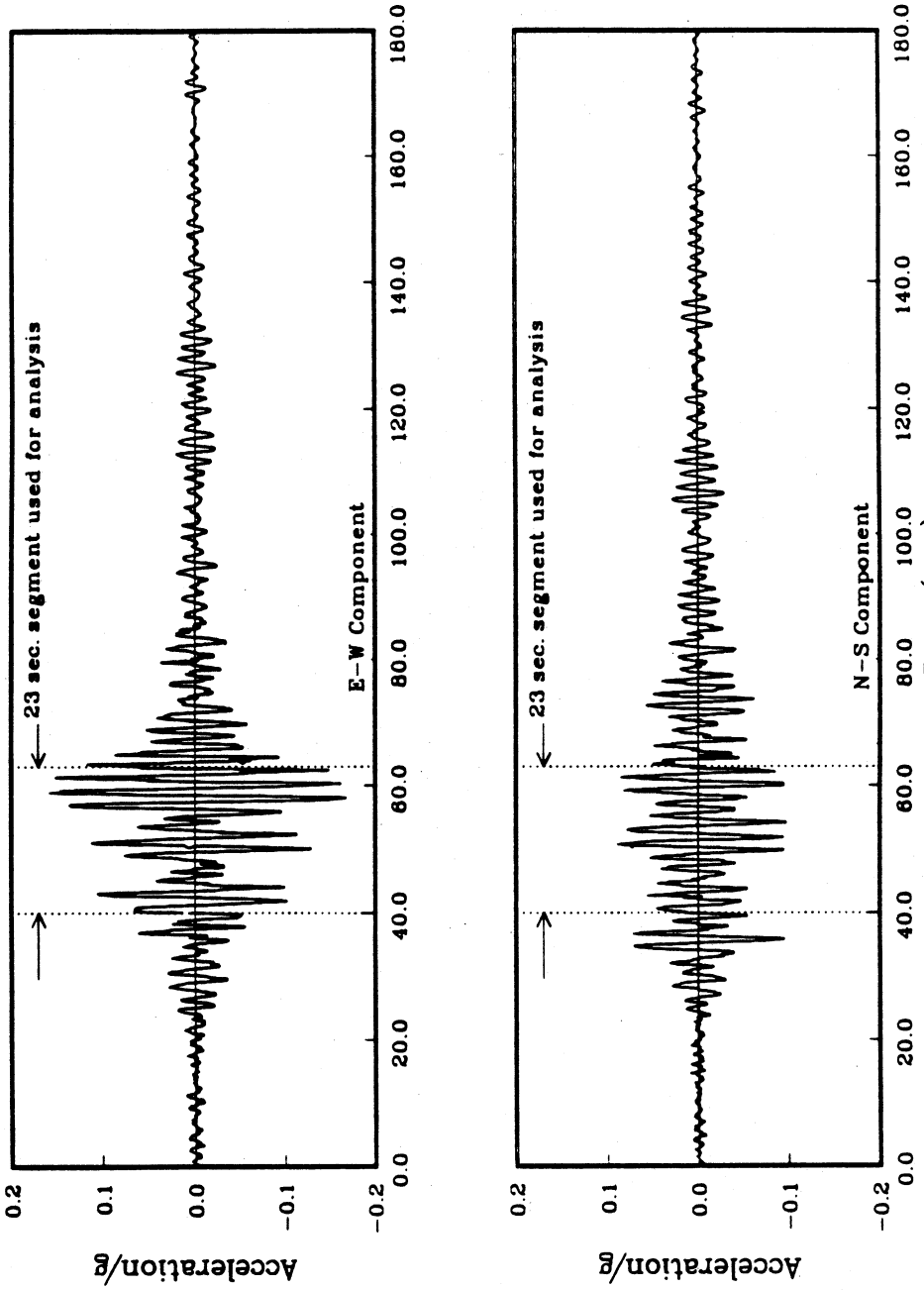

Figure 6.3: 1985 Mexico SCT Earthquake Record

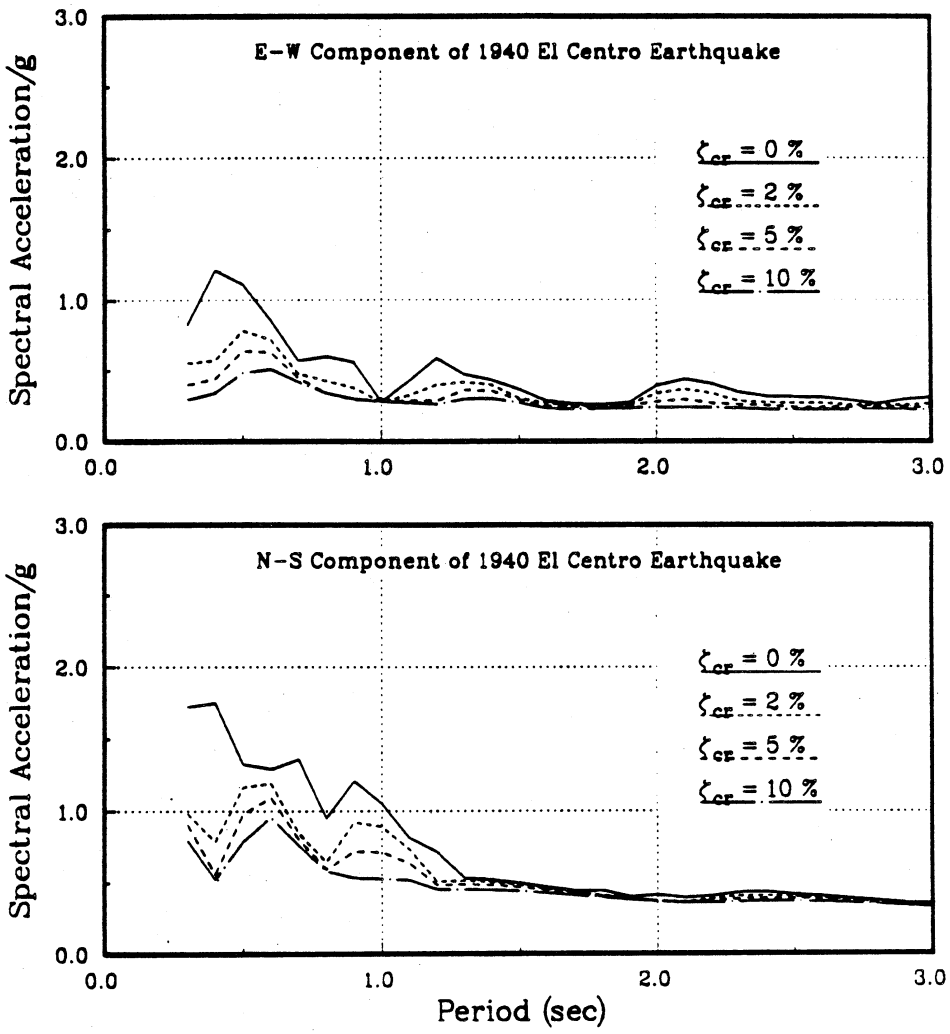

Figure 6.4: E-W and N-S Components Acceleration Spectra of 1940 El Centro Earthquake (0.68 g)

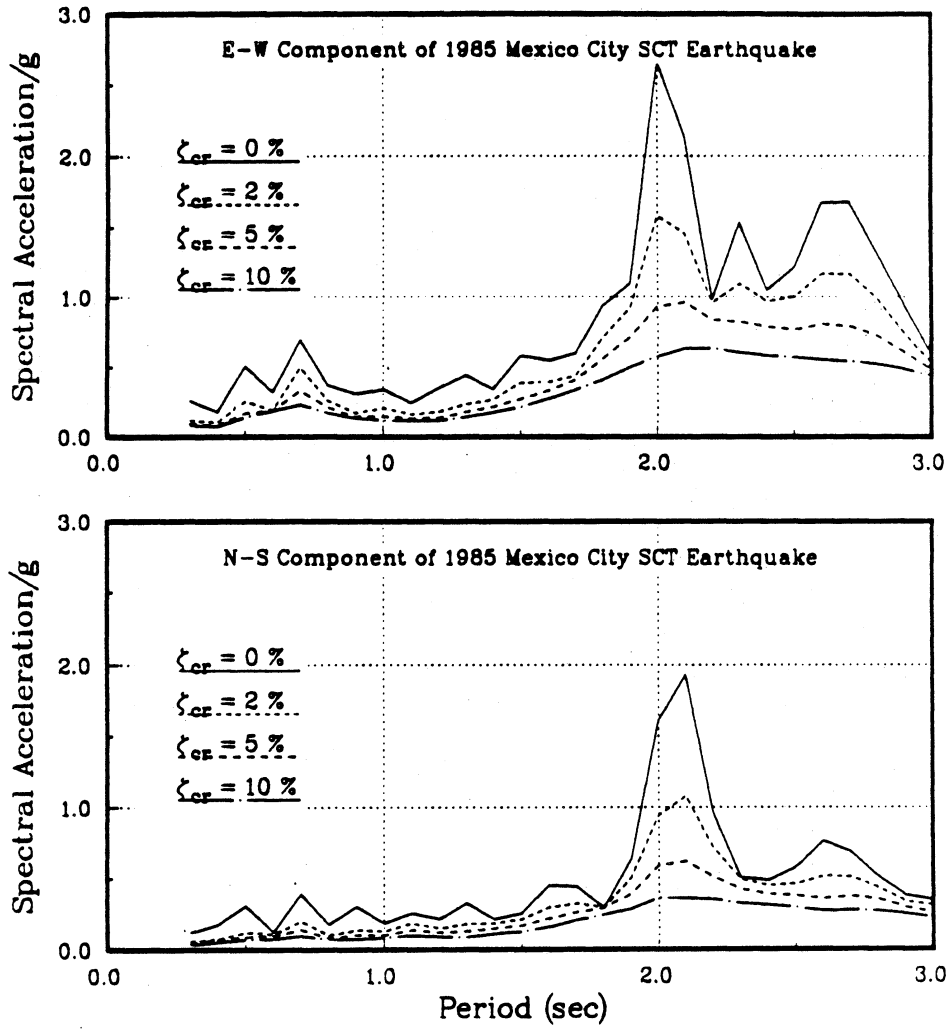

Fig

Figure 6.5: E-W and N-S Components Acceleration Spectra of 1985 Mexico SCT Earthquake

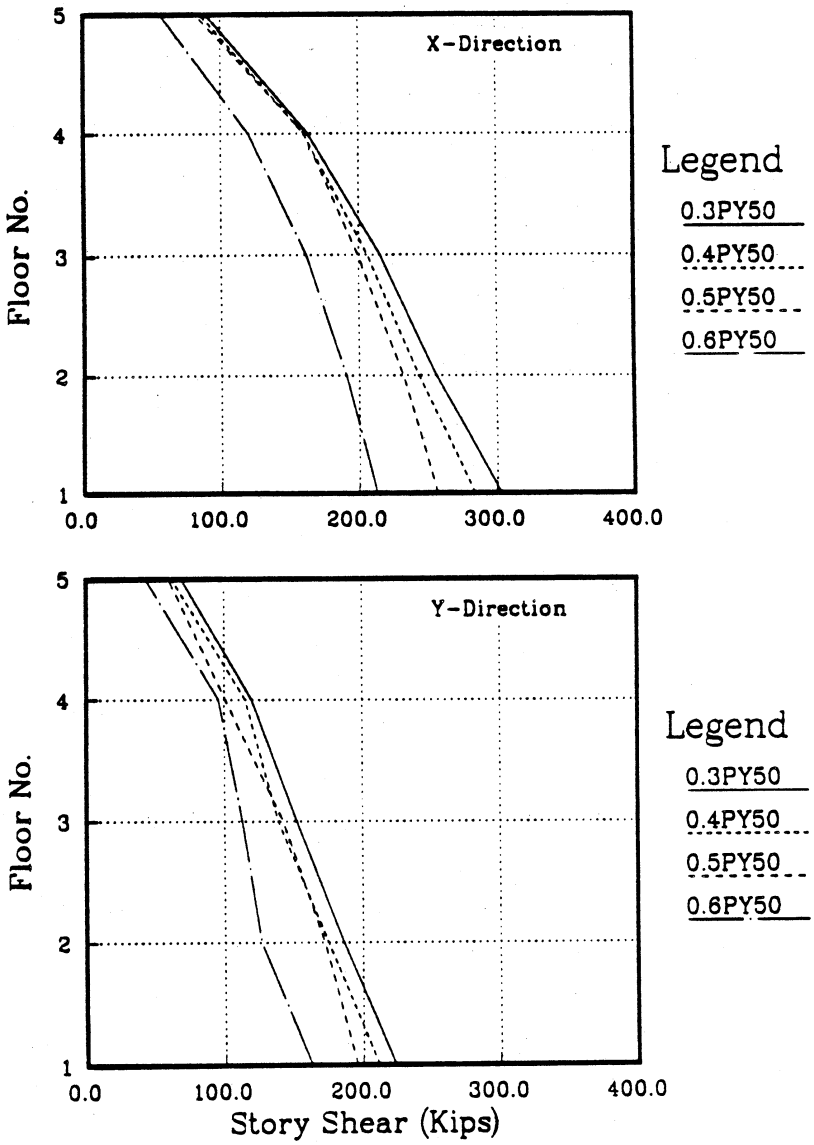

Figure 6.6: Comparison of Maximum Story Shear of Five Story Symmetrical Building Subjected to 0.5 g 1978 Miyagi-Ken-Oki Earthquake

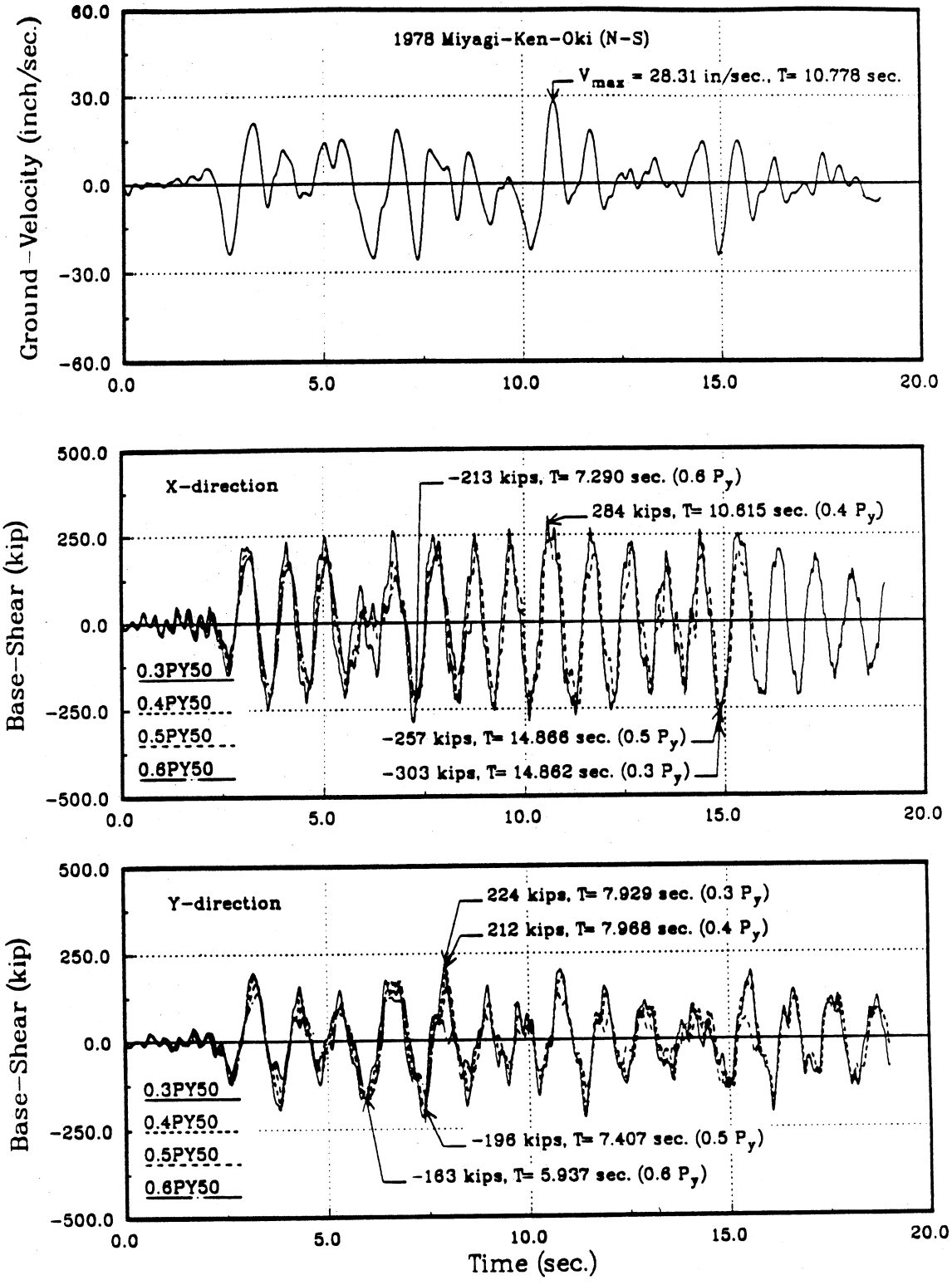

Figure 6.7: Input Ground Velocity and Base Shear Time History in the Principal Directions of Five Story Symmetrical Building Subjected to 0.5 g 1978 Miyagi-Ken-Oki Earthquake

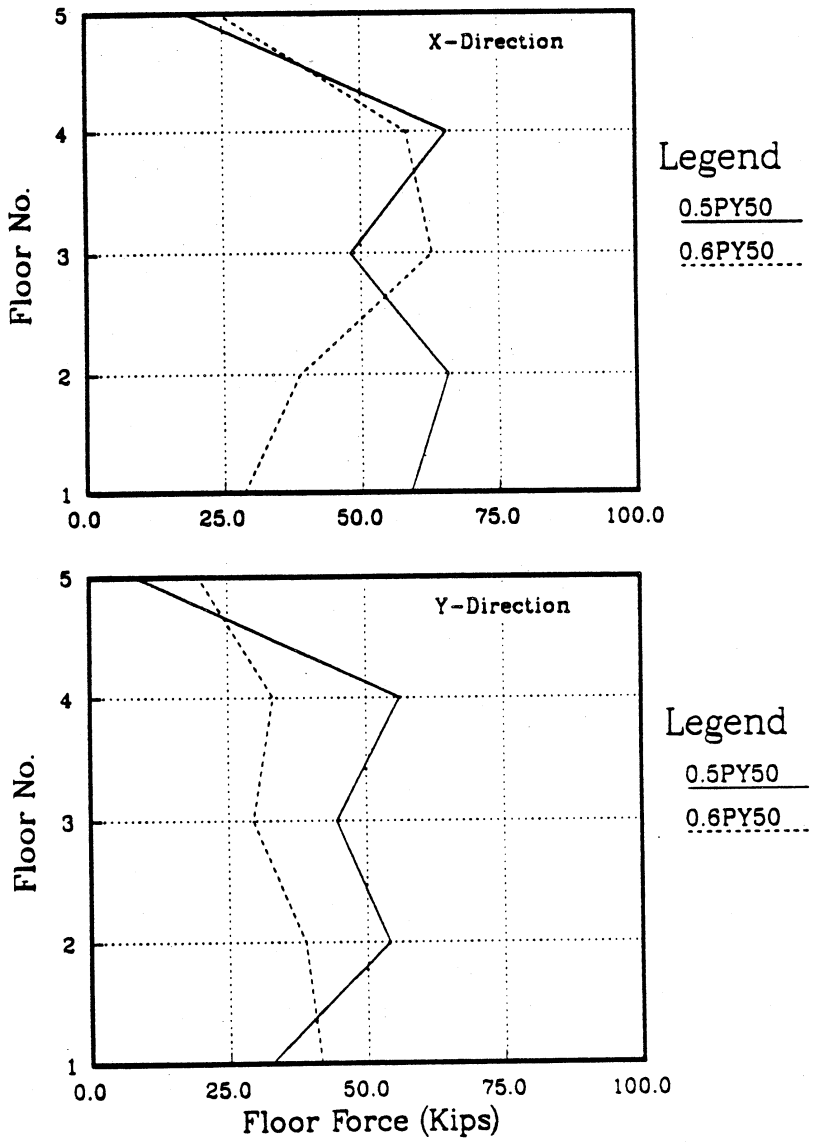

Figure 6.8: Comparison of Floor Force at Base Shear Maximum of Five Story Symmetrical Building Subjected to 0.5 g 1978 Miyagi-Ken-Oki Earthquake

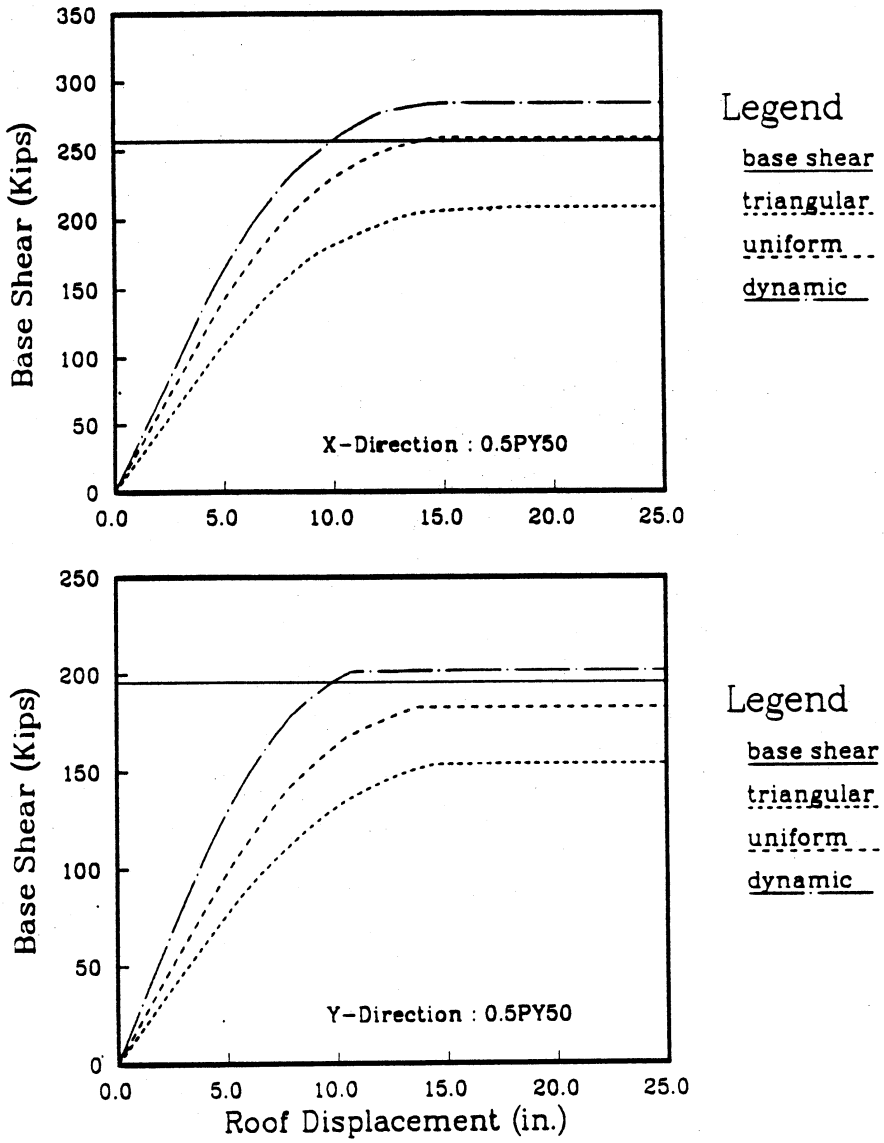

Figure 6.9: Comparison of Static Monotonic Strength of Five Story Symmetrical Building and the Maximum Base Shear : Case 0.5PY50

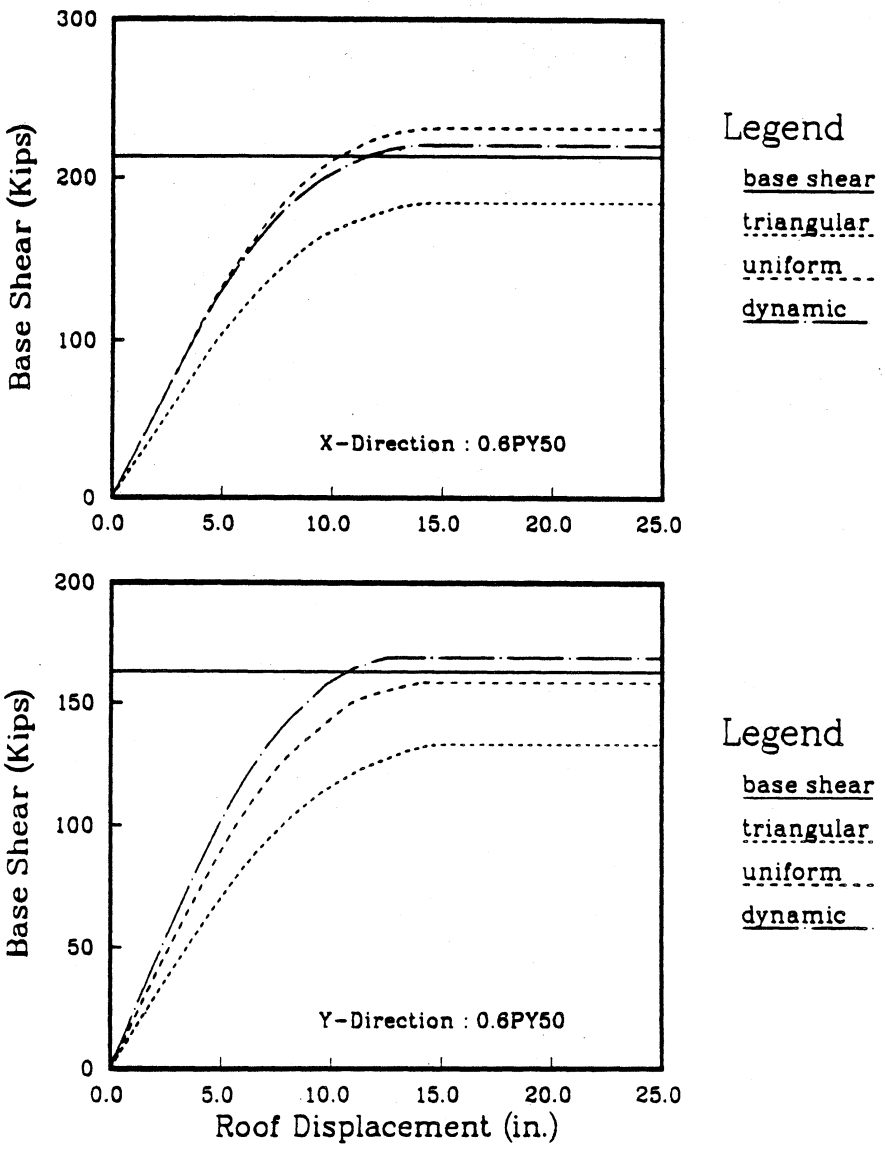

Figure 6.10: Comparison of Static Monotonic Strength of Five Story Symmetrical Building and the Maximum Base Shear : Case 0.6PY50

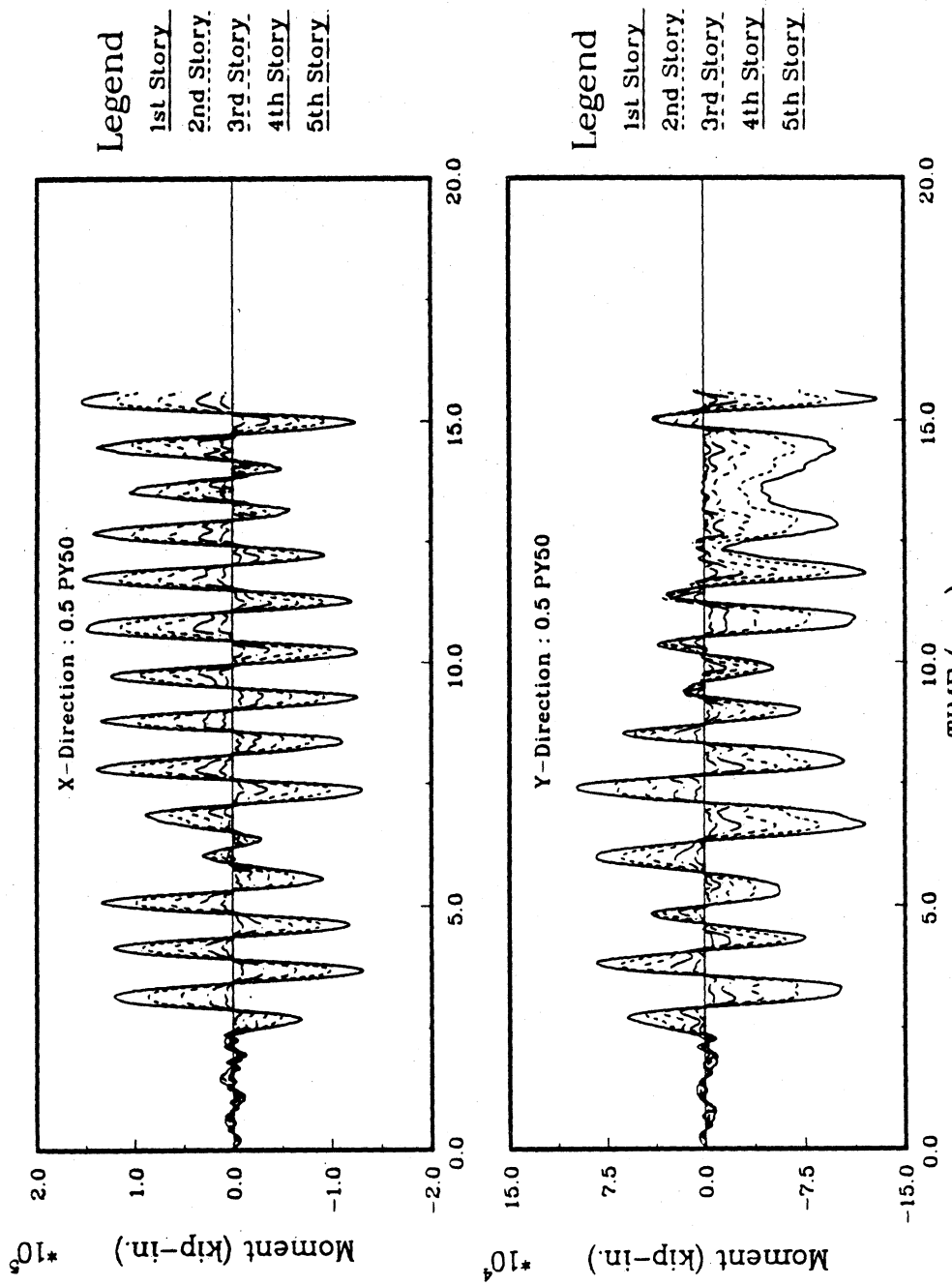

Figure 6.11: Overturning Moment Time History of Five Story Symmetrical Building Subjected to 0.5 g 1978 Miyagi-Ken-Oki Earthquake : Case 0.5PY50

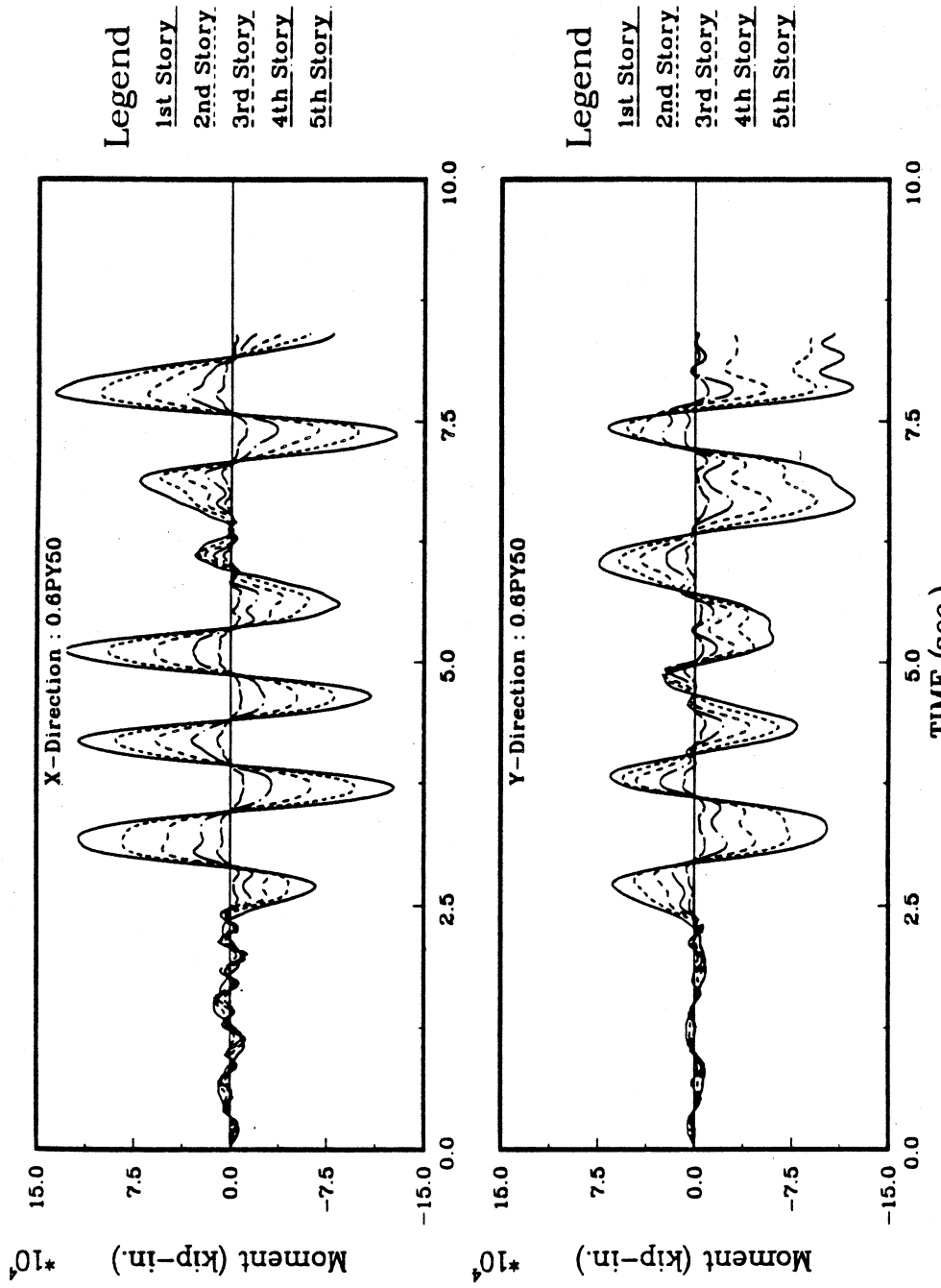

Figure 6.12: Overturning Moment Time History of Five Story Symmetrical Building Subjected to 0.5 g 1978 Miyagi-Ken-Oki Earthquake : Case 0.6PY50

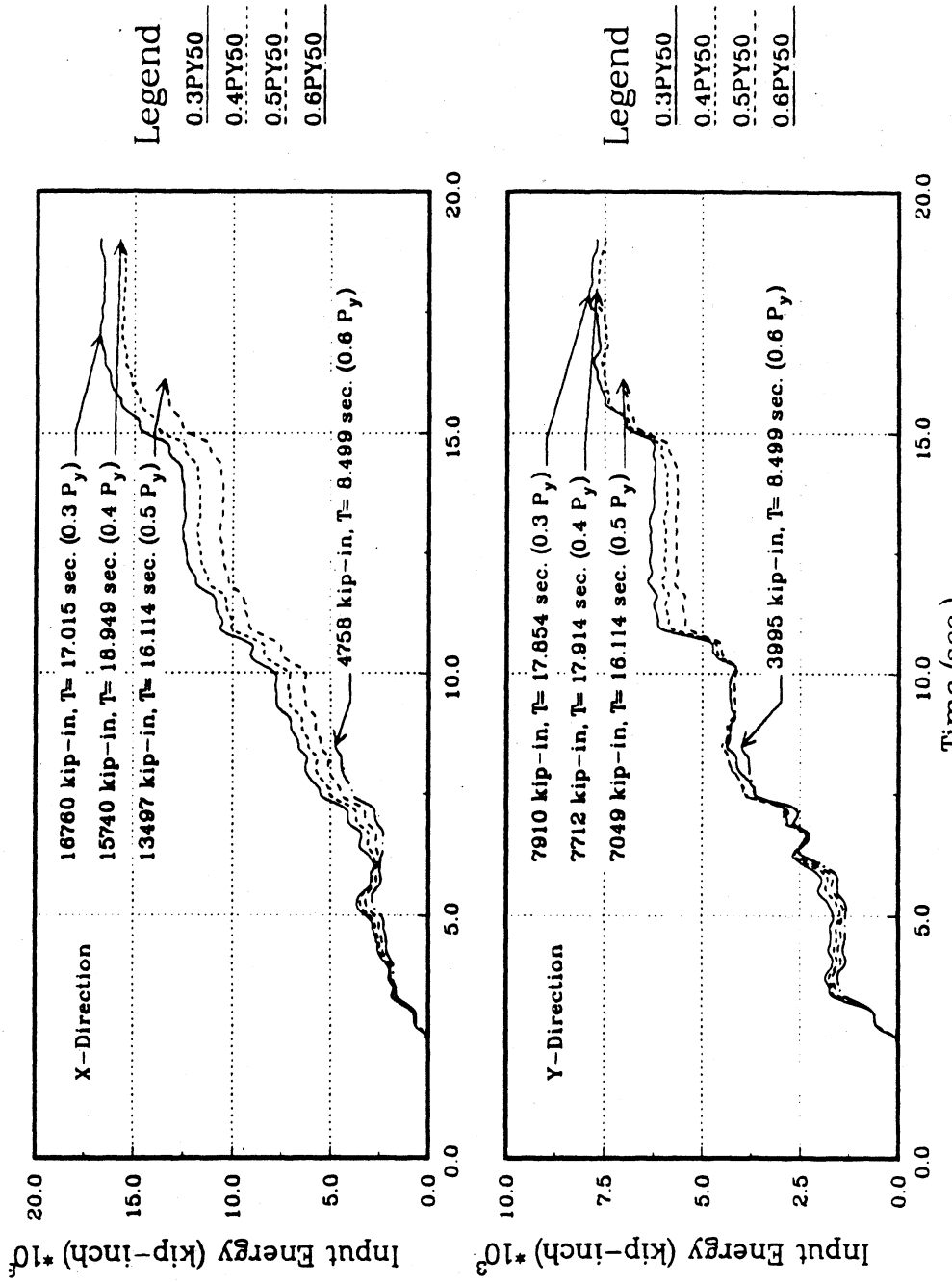

Figure 6.13: Absolute Input Energy Time History in the Principal Directions of Five Story Symmetrical Building Subjected to 0.5 g 1978 Miyagi-Ken-Oki Earthquake

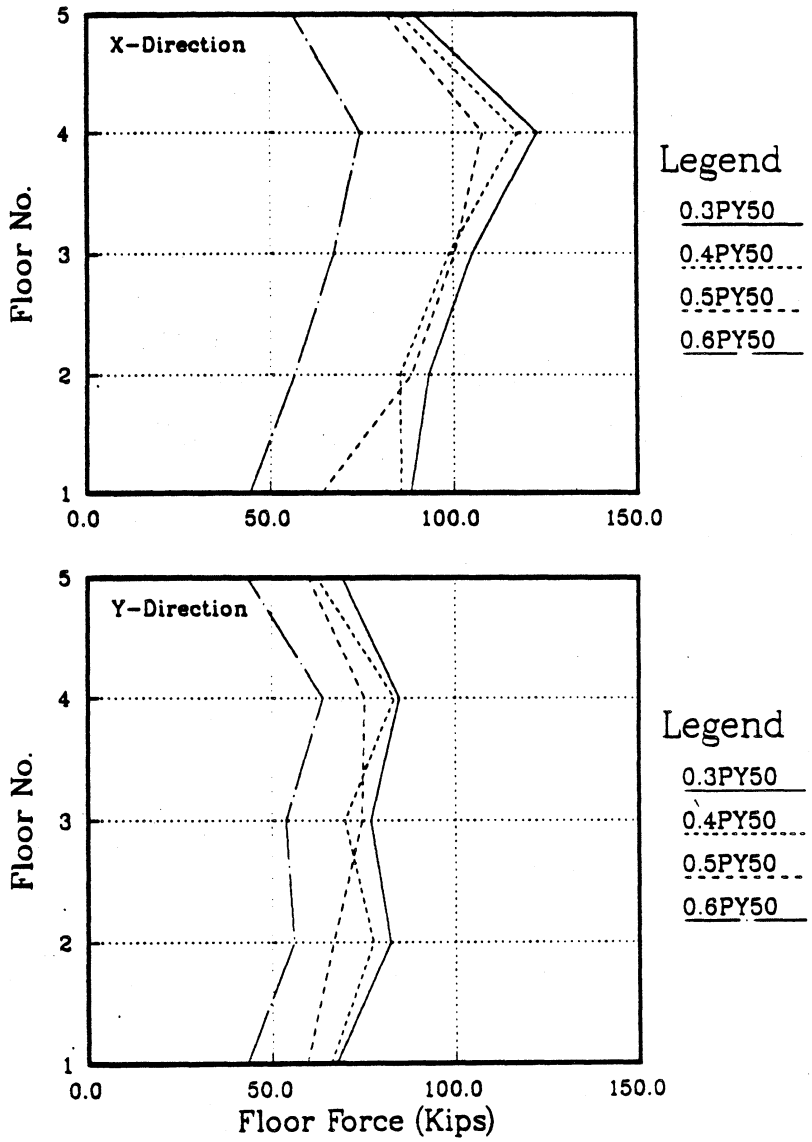

Figure 6.14: Comparison of Maximum Floor Force of Five Story Symmetrical Building Subjected to 0.5 g 1978 Miyagi-Ken-Oki Earthquake

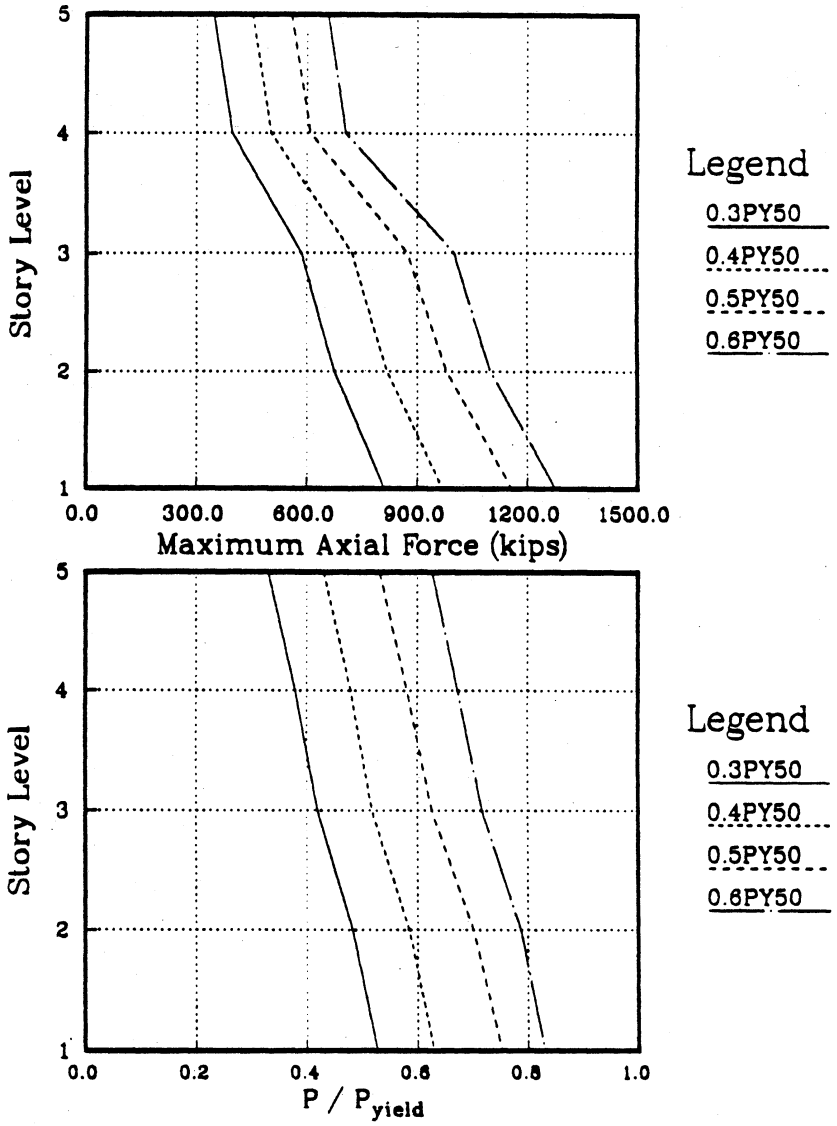

Figı Figure 6.15: Comparison of Maximum Column Axial Force of Five Story Symmetrical Building Subjected to 0.5 g 1978 Miyagi-Ken-Oki Earthquake

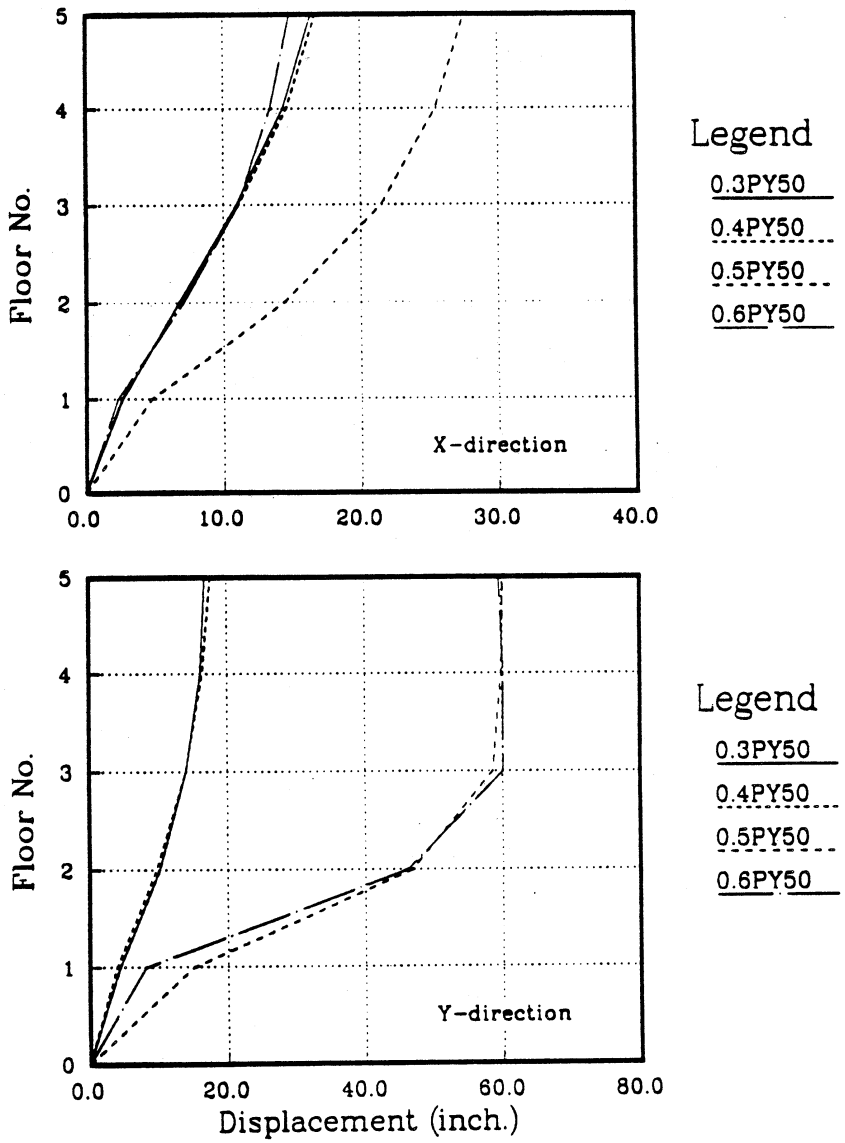

Figure 6.16: Comparison of Maximum Displacement of Five Story Symmetrical Building Subjected to 0.5 g 1978 Miyagi-Ken-Oki Earthquake

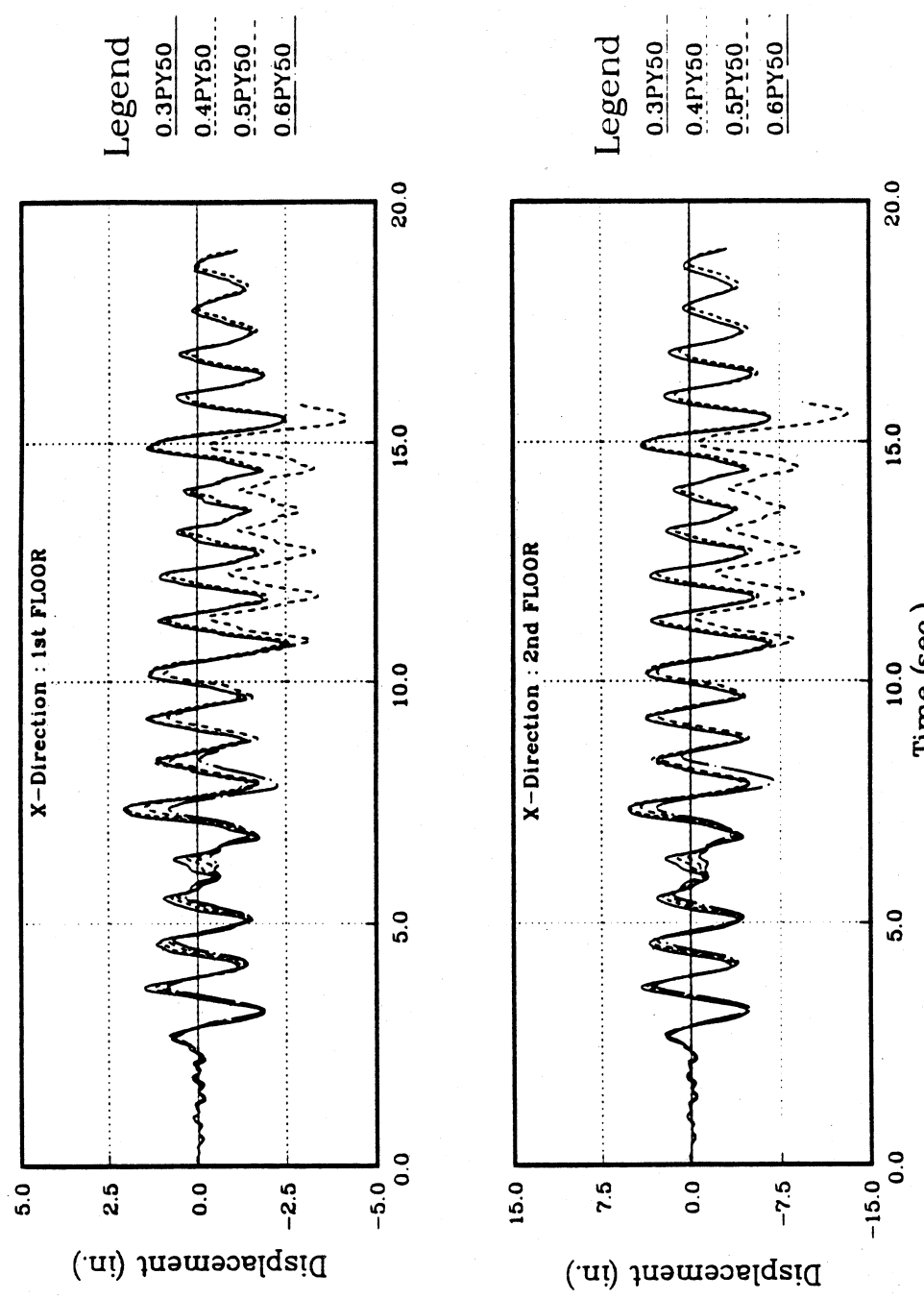

Figure 6.17: (a)1st and 2nd Floor Center of Mass Displacement Time History Response in the X-direction of Five Story Symmetrical Building Subjected to 0.5 g 1978 Miyagi-Ken-Oki Earthquake

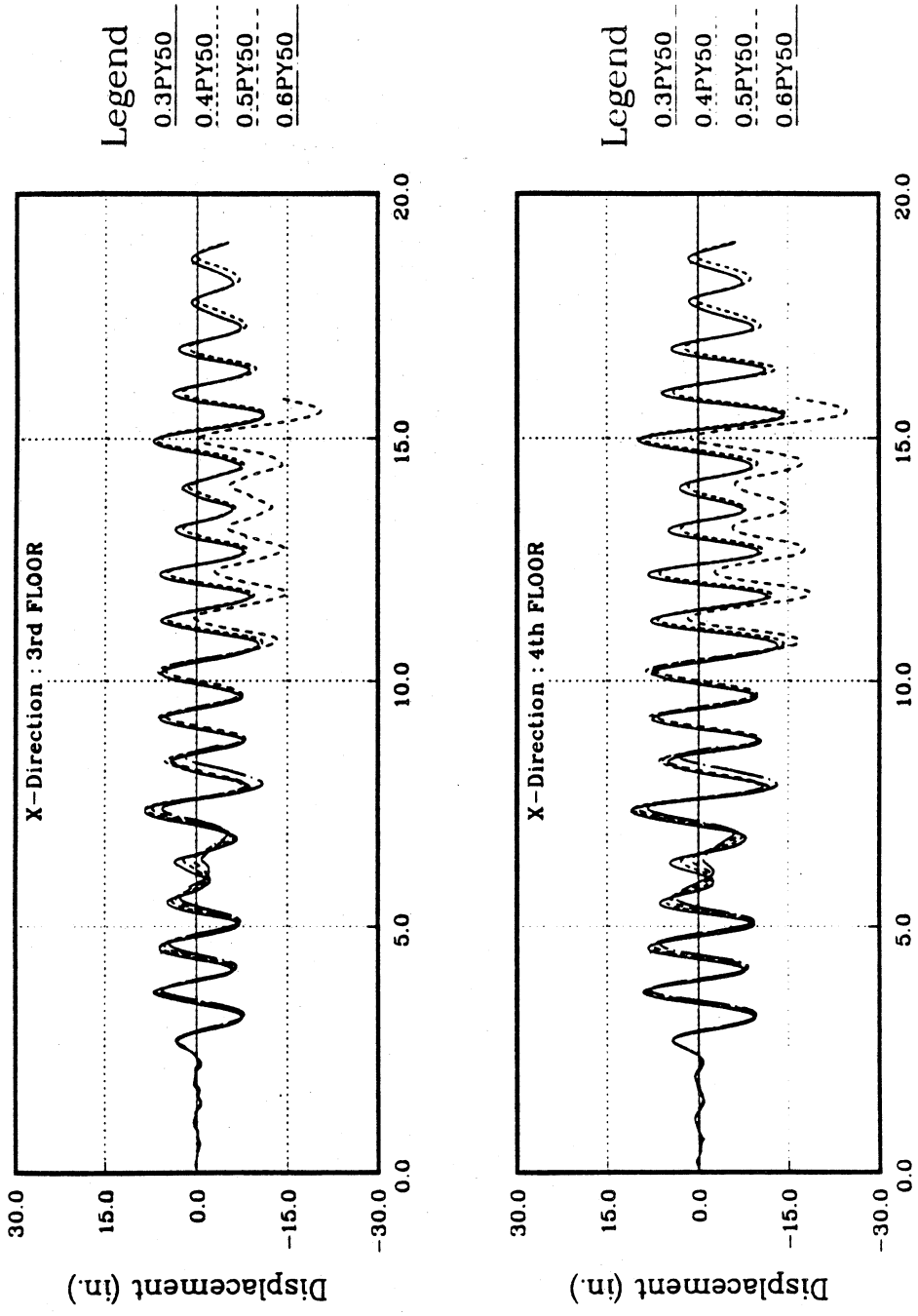

Figure 6.17: (b)3rd and 4th Floor Center of Mass Displacement Time History Response in the X-direction of Five Story Symmetrical Building Subjected to 0.5 g 1978 Miyagi-Ken-Oki Earthquake (Continue)

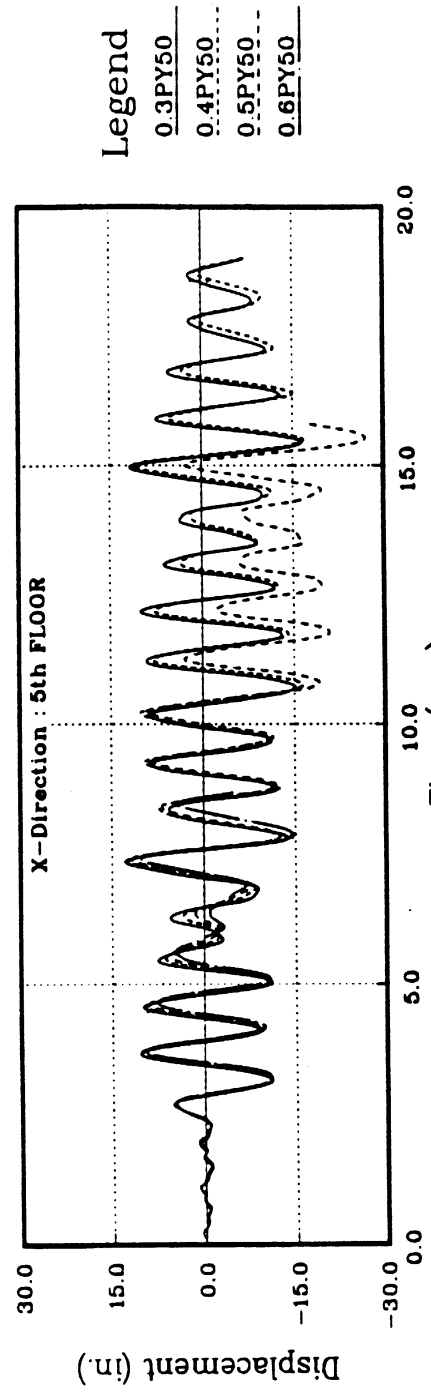

Figure 6.17: (c)5th Floor Center of Mass Displacement Time History Response in the X-direction of Five Story Symmetrical Building Subjected to 0.5 g 1978 Miyagi-Ken-Oki Earthquake (Continue)

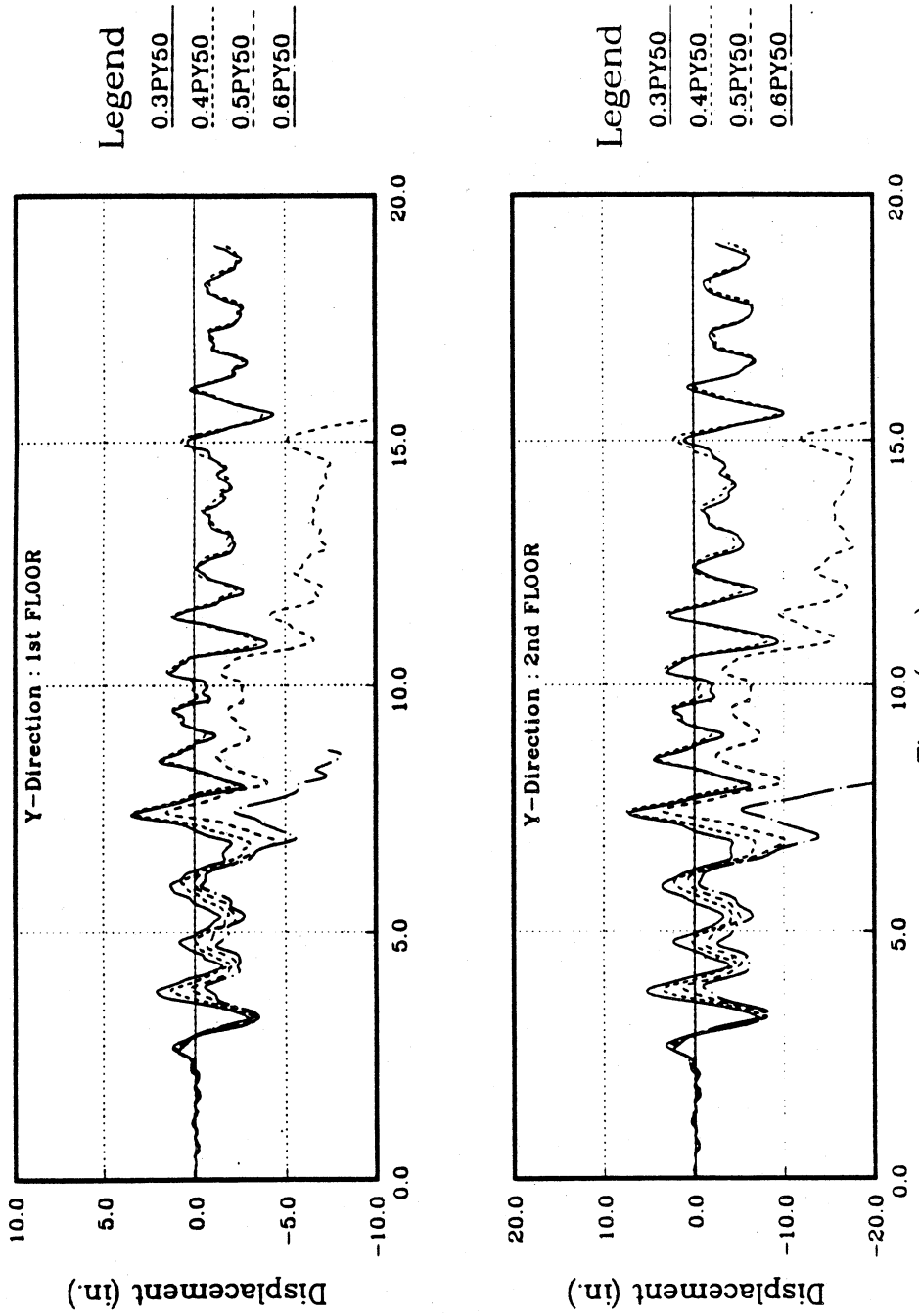

Figure 6.18: (a)1st and 2nd Floor Center of Mass Displacement Time History Response in the Y-direction of Five Story Symmetrical Building Subjected to 0.5 g 1978 Miyagi-Ken-Oki Earthquake

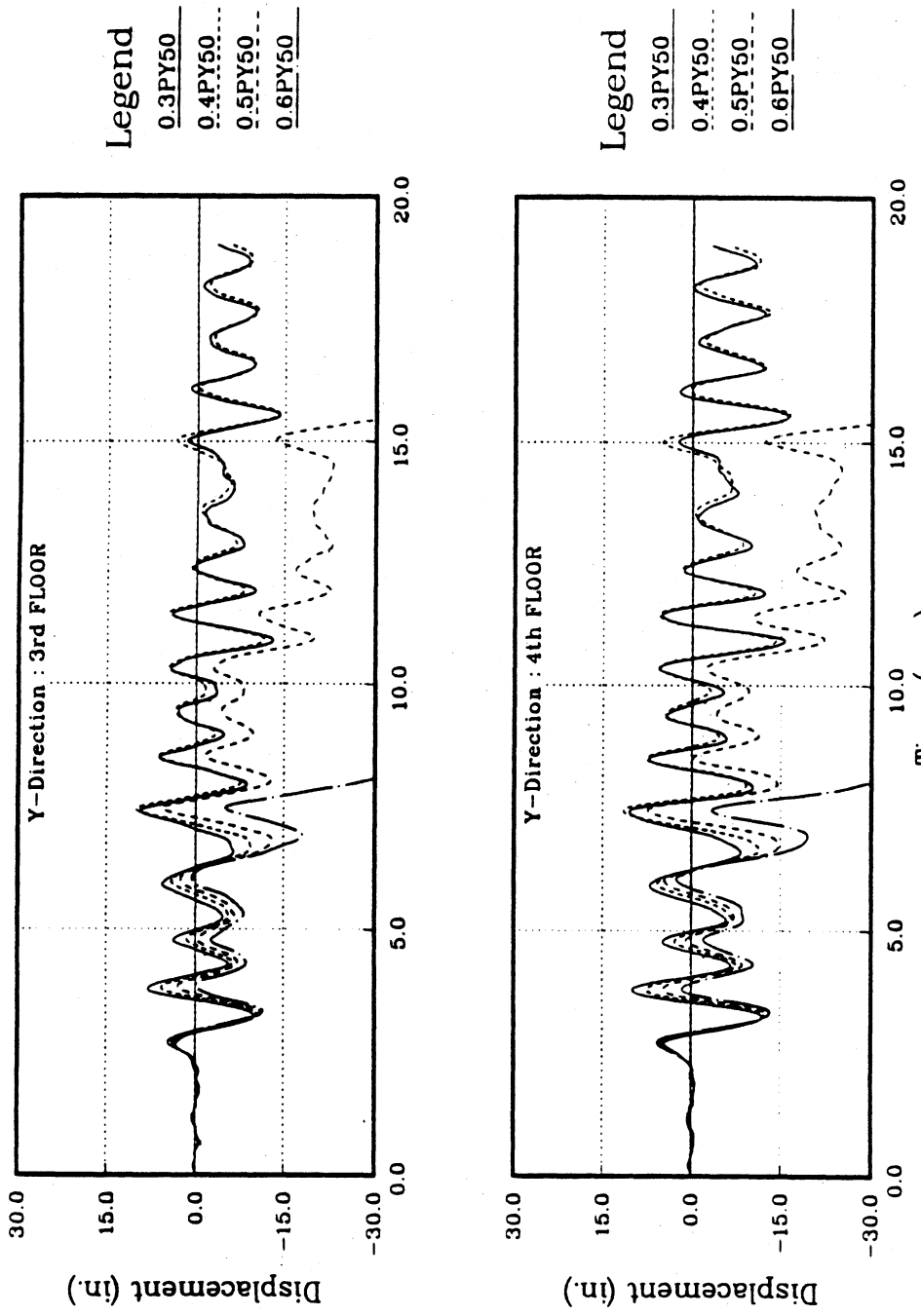

Figure 6.18: (b)3rd and 4th Floor Center of Mass Displacement Time History Response in the Y-direction of Five Story Symmetrical Building Subjected to 0.5 g 1978 Miyagi-Ken-Oki Earthquake (Continue)

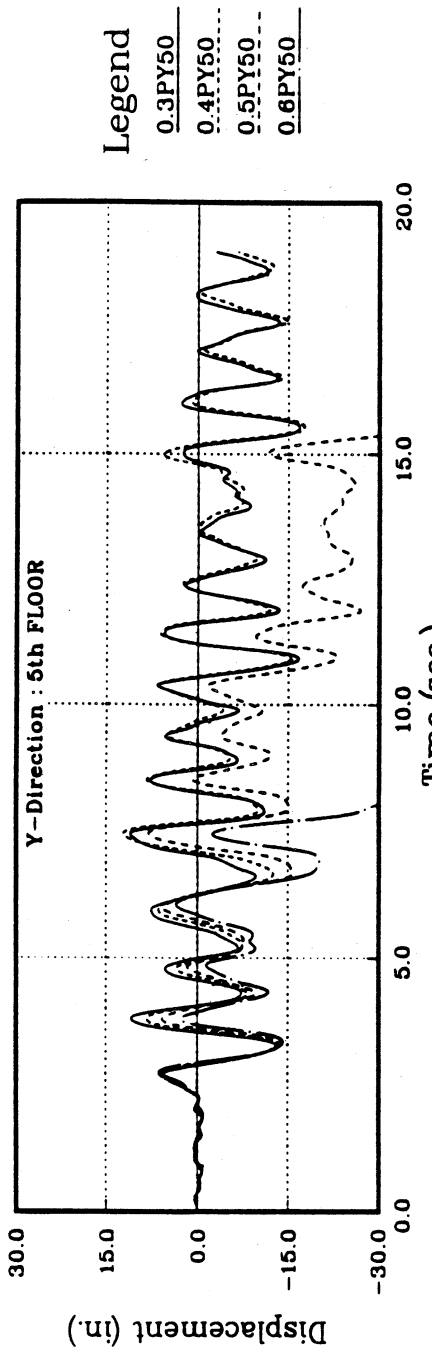

Figure 6.18: (c)5th Floor Center of Mass Displacement Time History Response in the Y-direction of Five Story Symmetrical Building Subjected to 0.5 g 1978 Miyagi-Ken-Oki Earthquake (Continue)

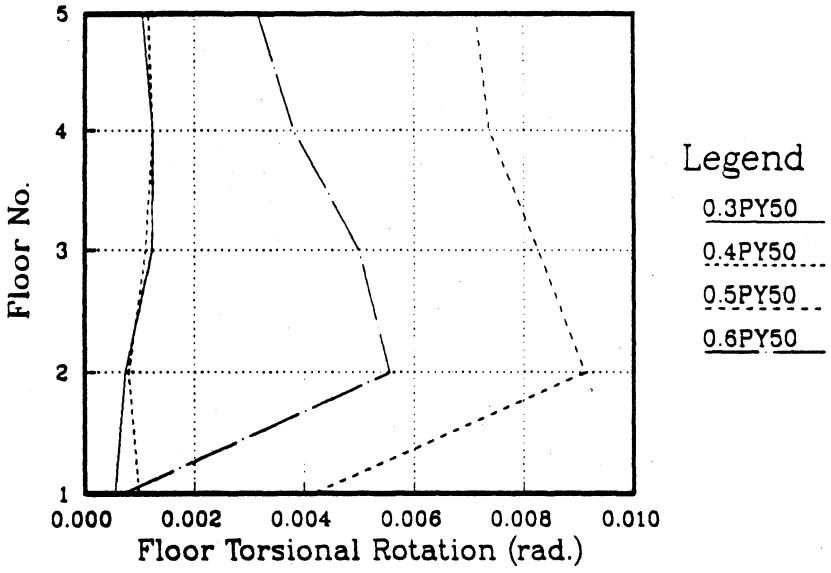

Figure 6.19: Envelope of Center of Mass Rotation of Five Story Symmetrical Building Subjected to 0.5 g 1978 Miyagi-Ken-Oki Earthquake

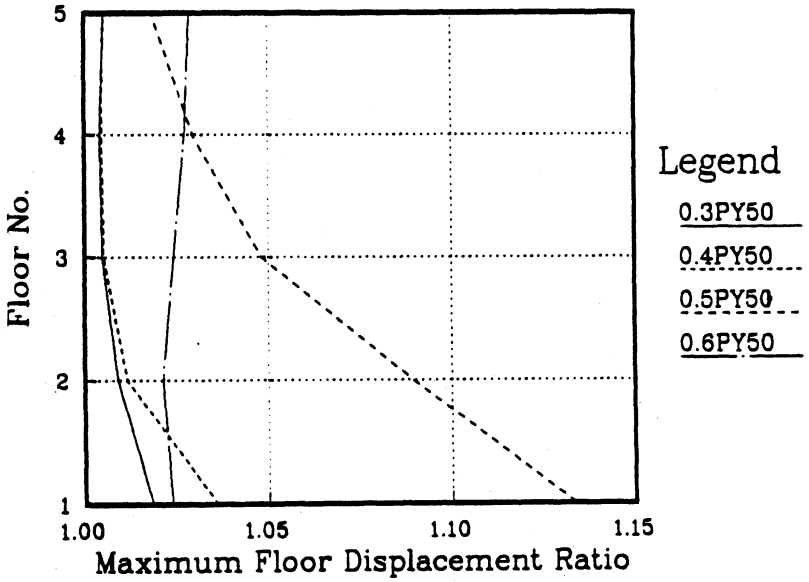

Figure 6.20: Maximum Ratio of Edge to Center of Mass Floor Displacement of Five Story Symmetrical Building Subjected to 0.5 g 1978 Miyagi-Ken-Oki Earthquake

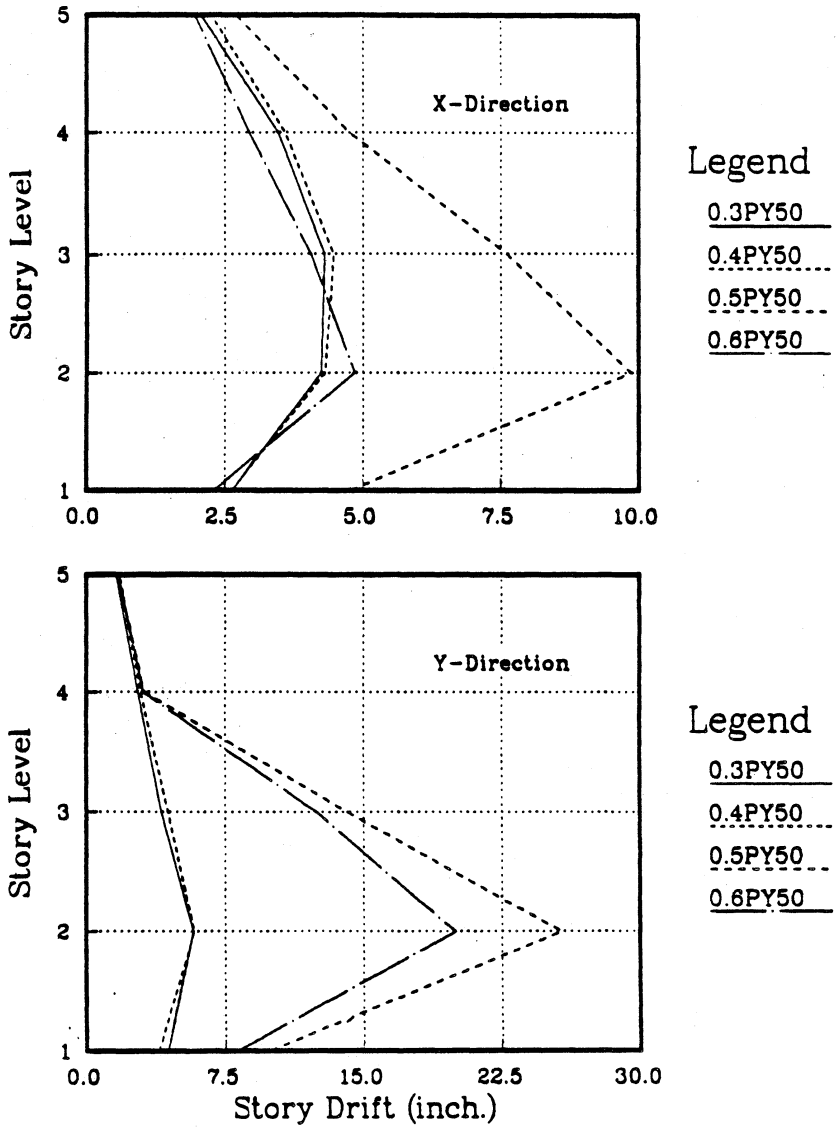

Figure 6.21: Comparison of Maximum Story Drift of Five Story Symmetrical Building Subjected to 0.5 g 1978 Miyagi-Ken-Oki Earthquake

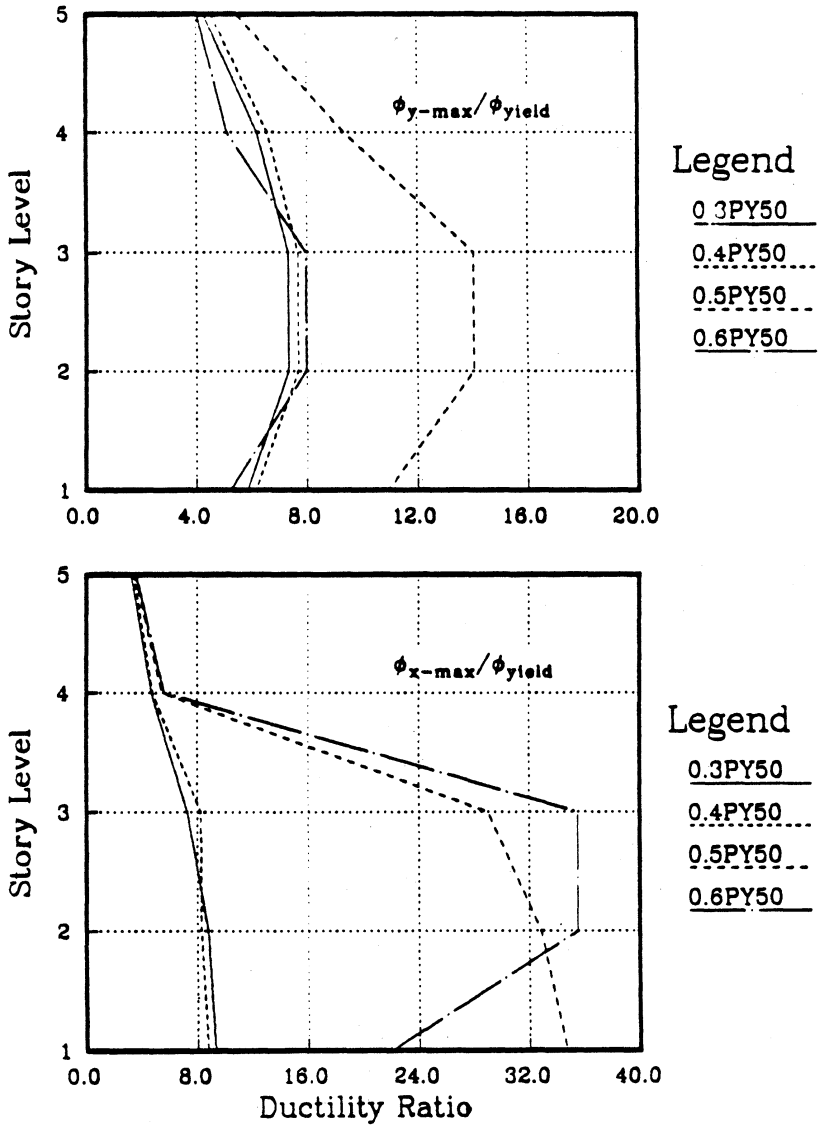

Figure 6.22: Envelope of Maximum Column Ductility Ratio of Five Story Symmetrical Building Subjected to 0.5 g 1978 Miyagi-Ken-Oki Earthquake

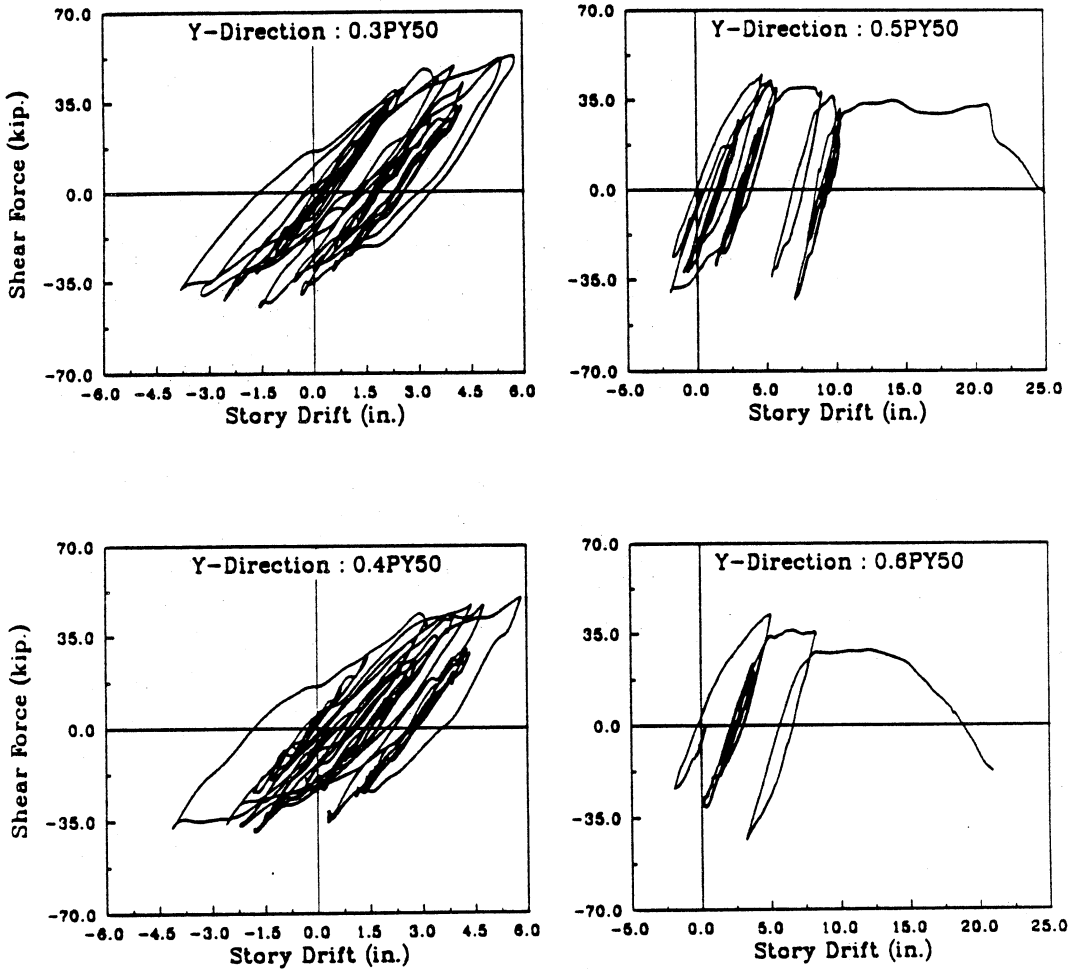

Figure 6.23: (a)Y-Direction Shear Force Hysteresis of Column 16 of Five Story Symmetrical Building Subjected to 0.5 g 1978 Miyagi-Ken-Oki Earthquake : 2nd Story

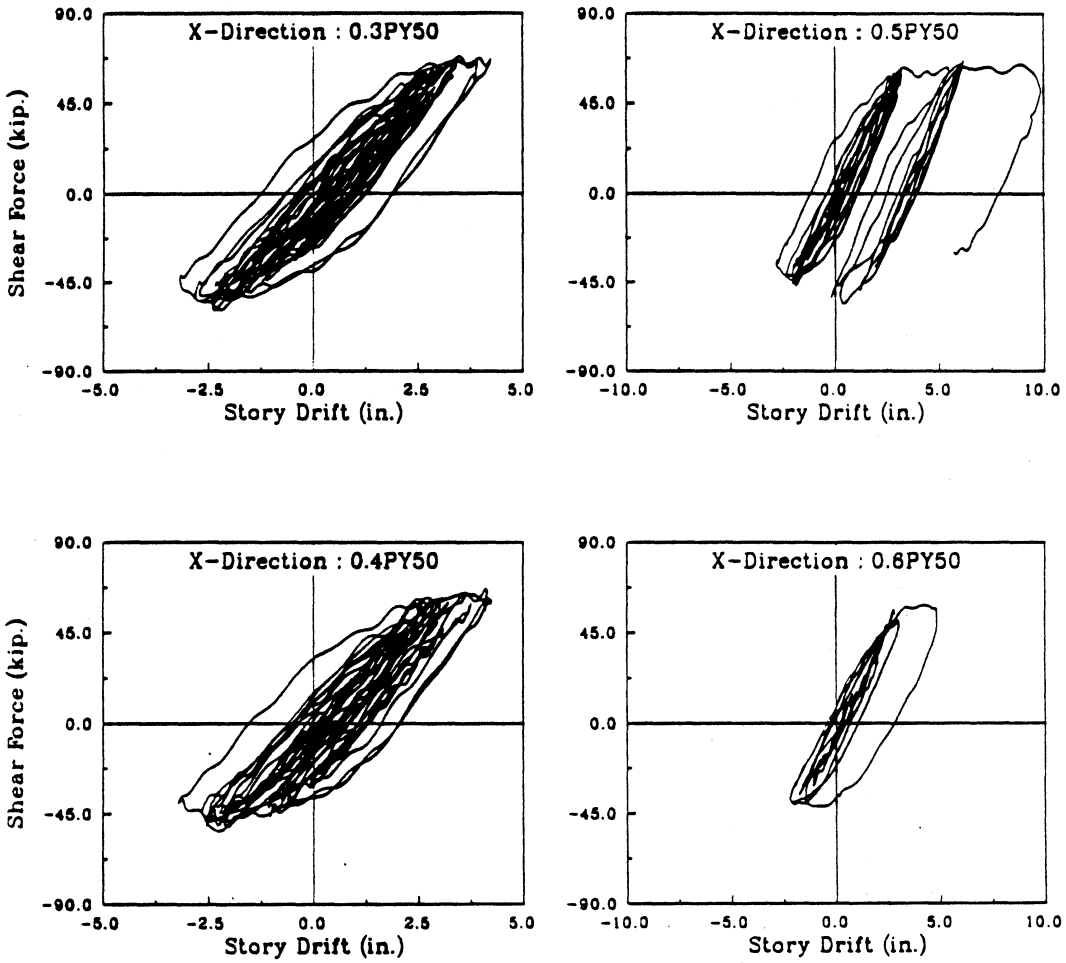

Figure 6.23: (b)X-Direction Shear Force Hysteresis of Column 16 of Five Story Symmetrical Building Subjected to 0.5 g 1978 Miyagi-Ken-Oki Earthquake : 2nd Story (Continue)

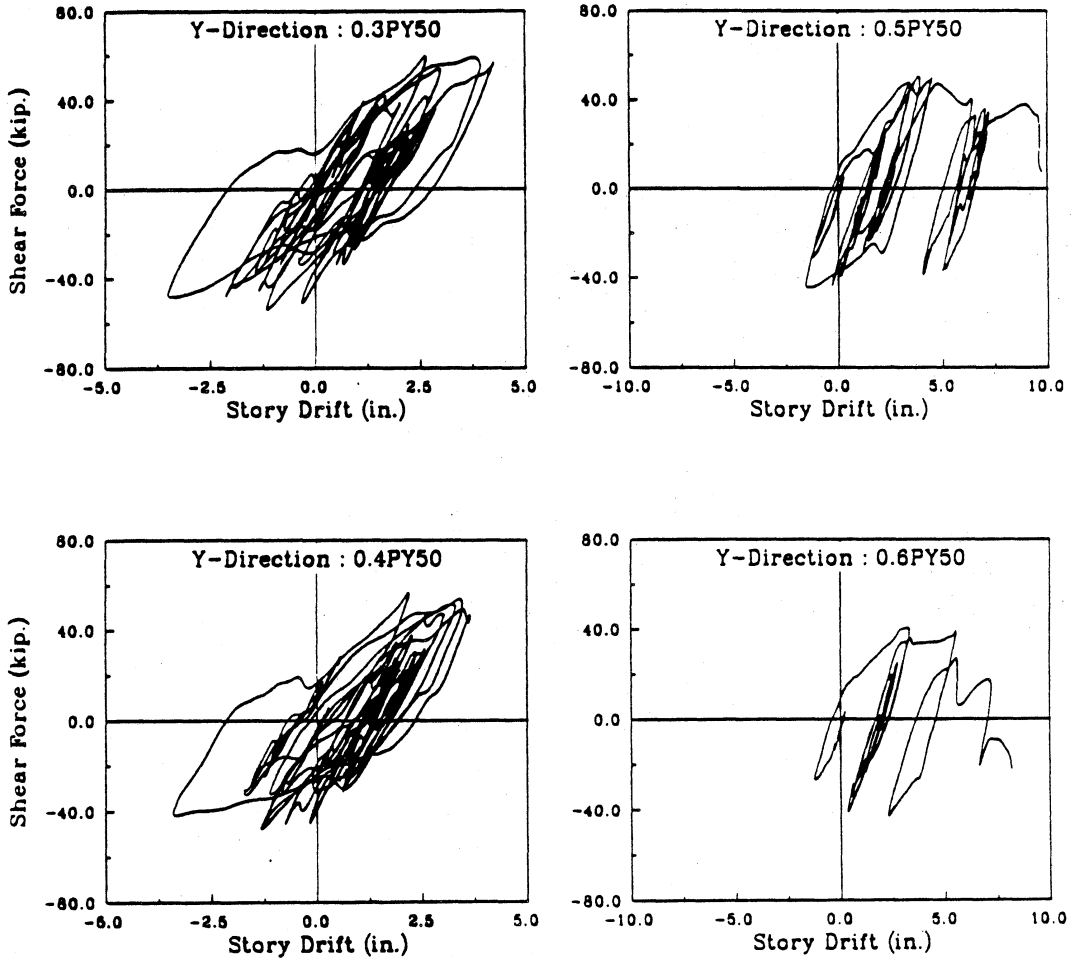

Figure 6.24: (a)Y-Direction Shear Force Hysteresis of Column 20 of Five Story Symmetrical Building Subjected to 0.5 g 1978 Miyagi-Ken-Oki Earthquake : 1st Story

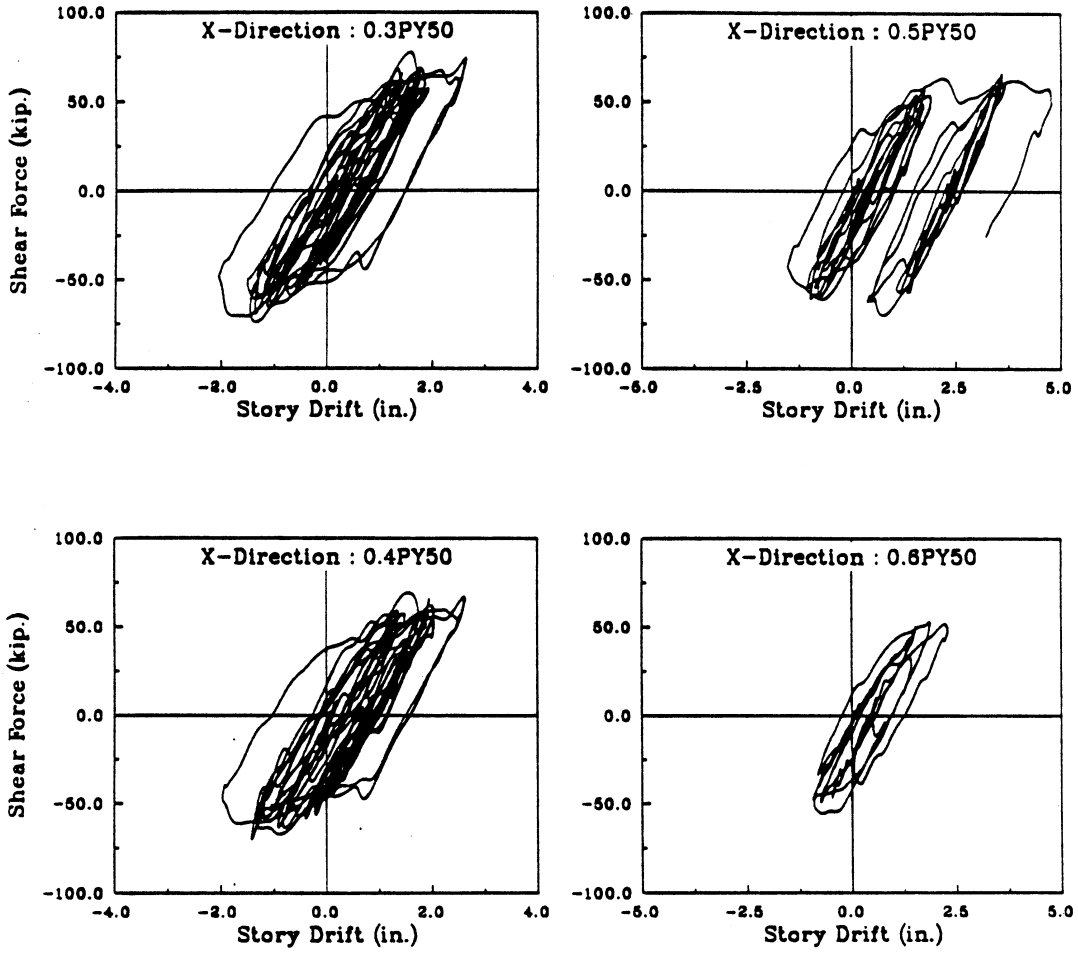

Figure 6.24: (b)X-Direction Shear Force Hysteresis of Column 20 of Five Story Symmetrical Building Subjected to 0.5 g 1978 Miyagi-Ken-Oki Earthquake : 1st Story (Continue)

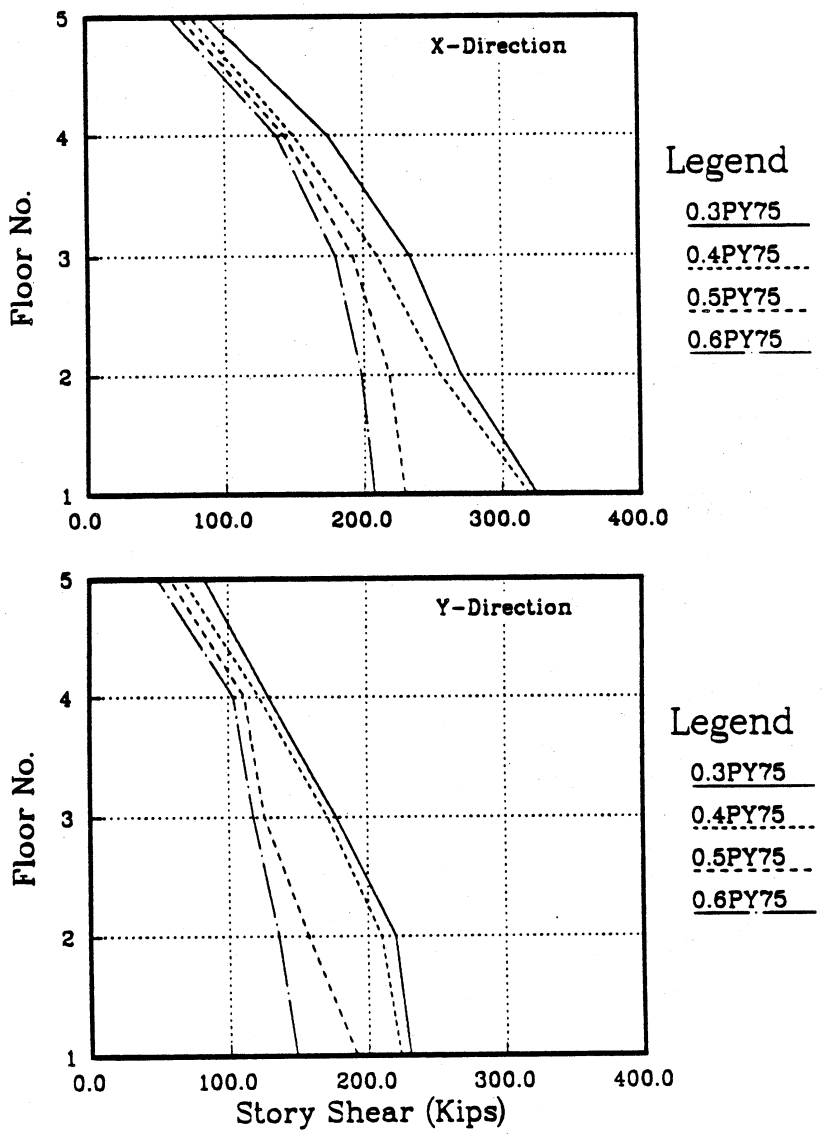

Figure 6.25: Comparison of Maximum Story Shear of Five Story Symmetrical Building Subjected to 0.75 g 1978 Miyagi-Ken-Oki Earthquake

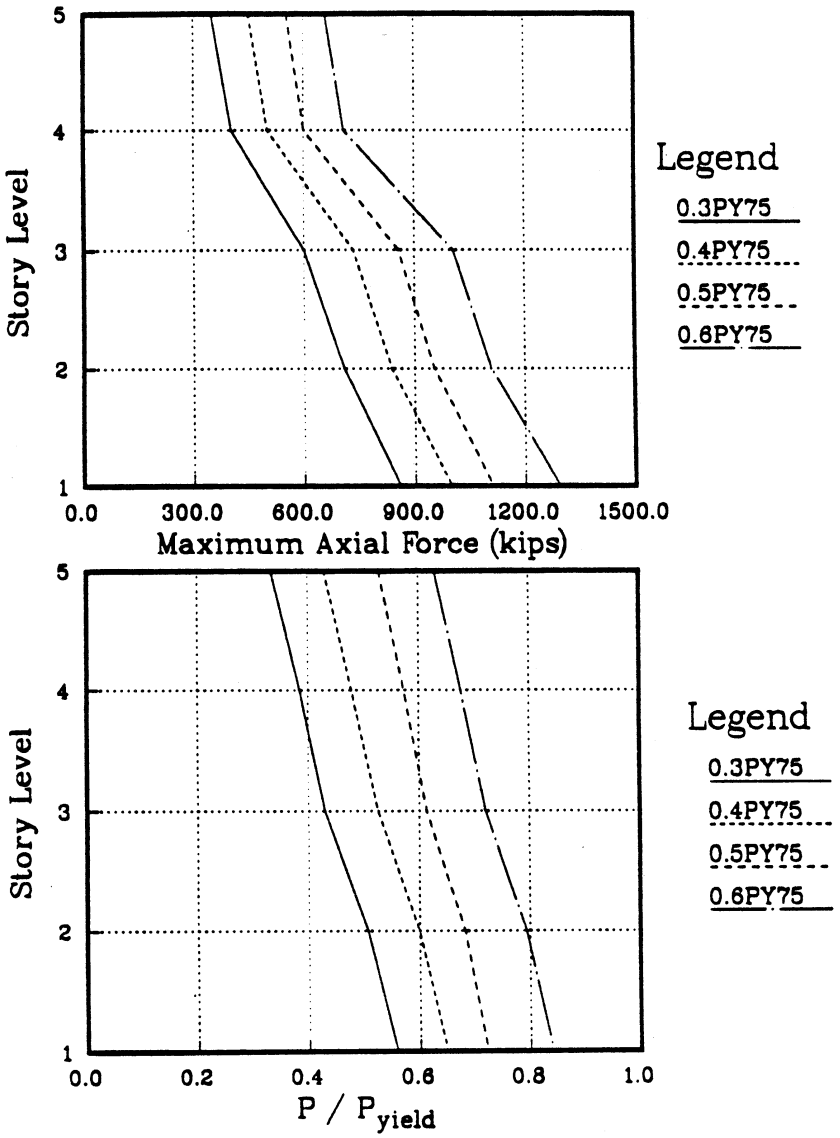

Figure 6.26: Comparison of Maximum Column Axial Force of Five Story Symmetrical Building Subjected to 0.75 g 1978 Miyagi-Ken-Oki Earthquake

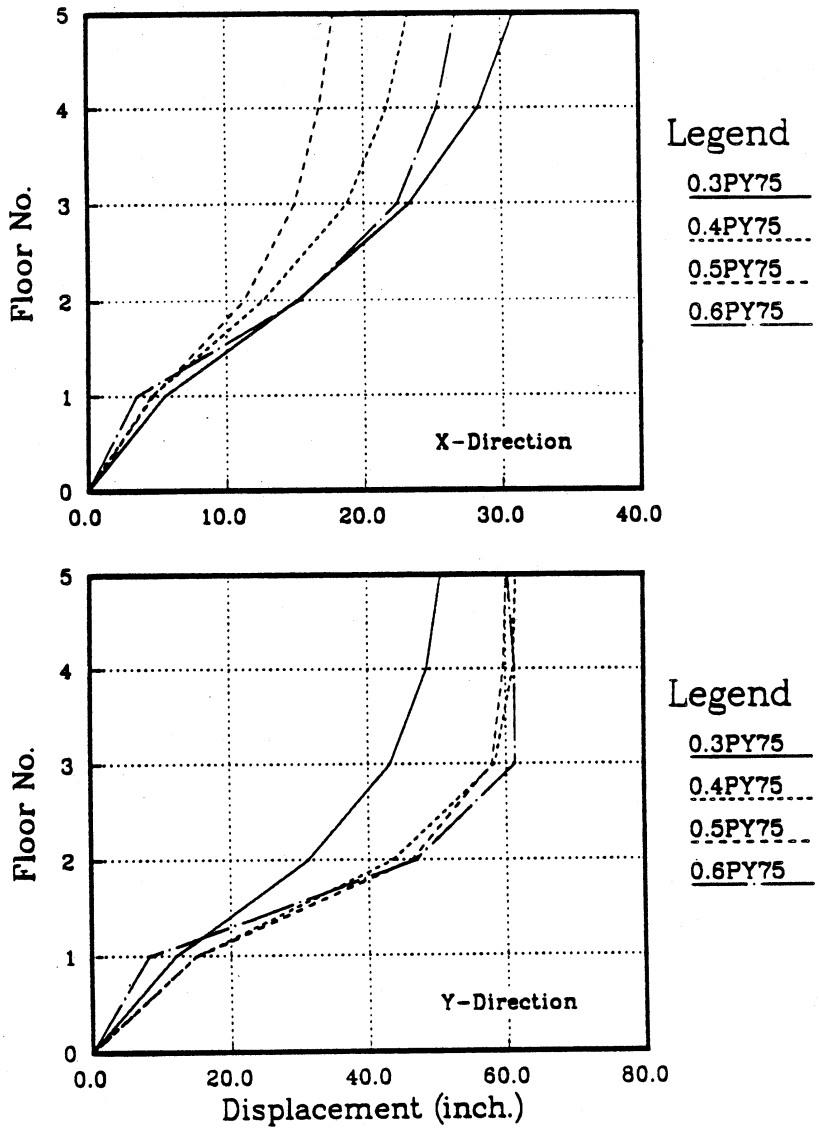

Figure 6.27: Comparison of Maximum Displacement of Five Story Symmetrical Building Subjected to 0.75 g 1978 Miyagi-Ken-Oki Earthquake

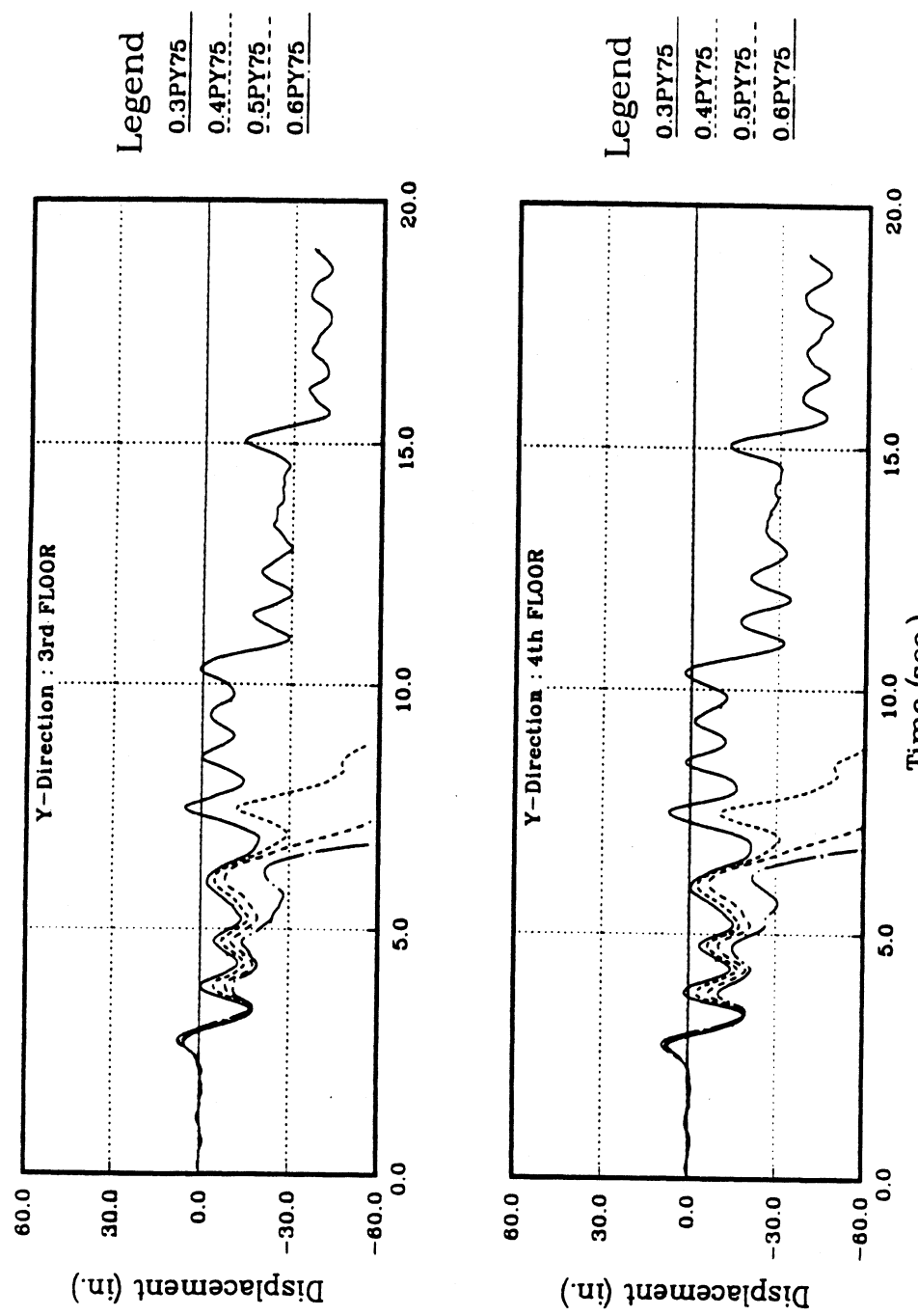

Figure 6.28: 3rd and 4th Floor Center of Mass Displacement Time History Response in the Y-direction of Five Story Symmetrical Building Subjected to 0.75 g 1978 Miyagi-Ken-Oki Earthquake

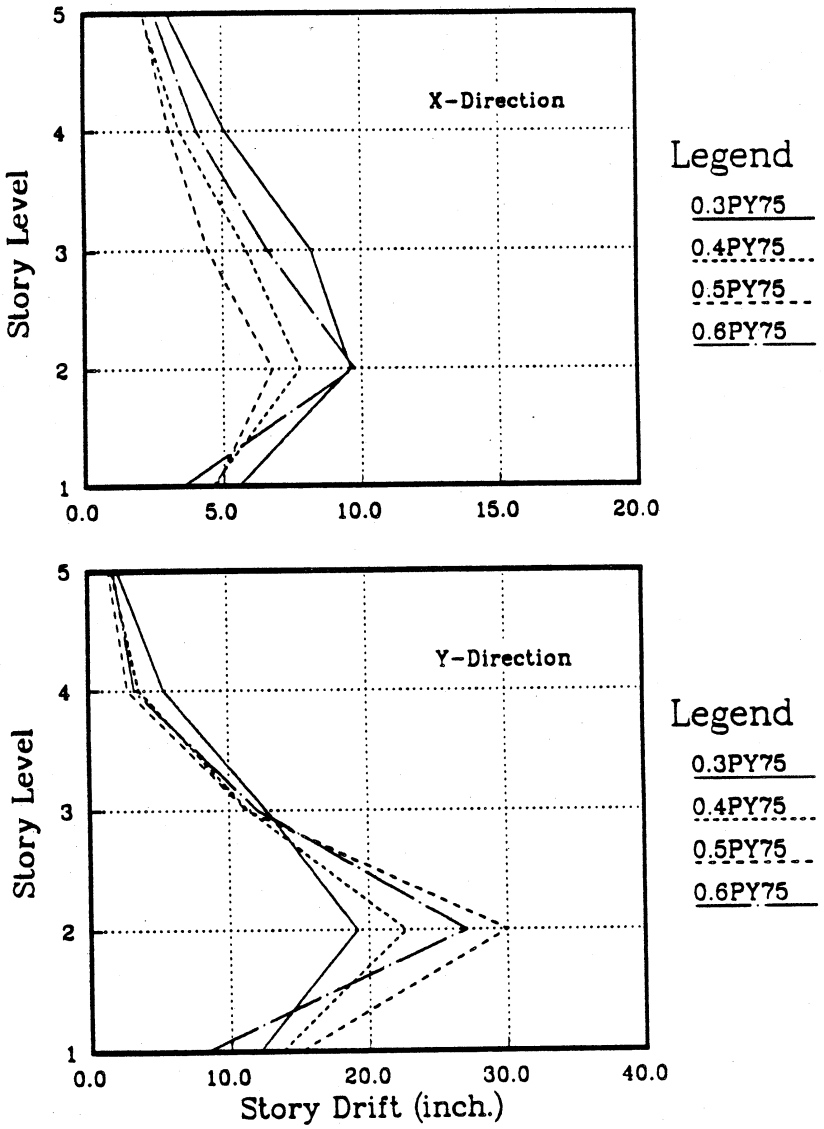

Figure 6.29: Comparison of Maximum Story Drift of Five Story Symmetrical Building Subjected to 0.75 g 1978 Miyagi-Ken-Oki Earthquake

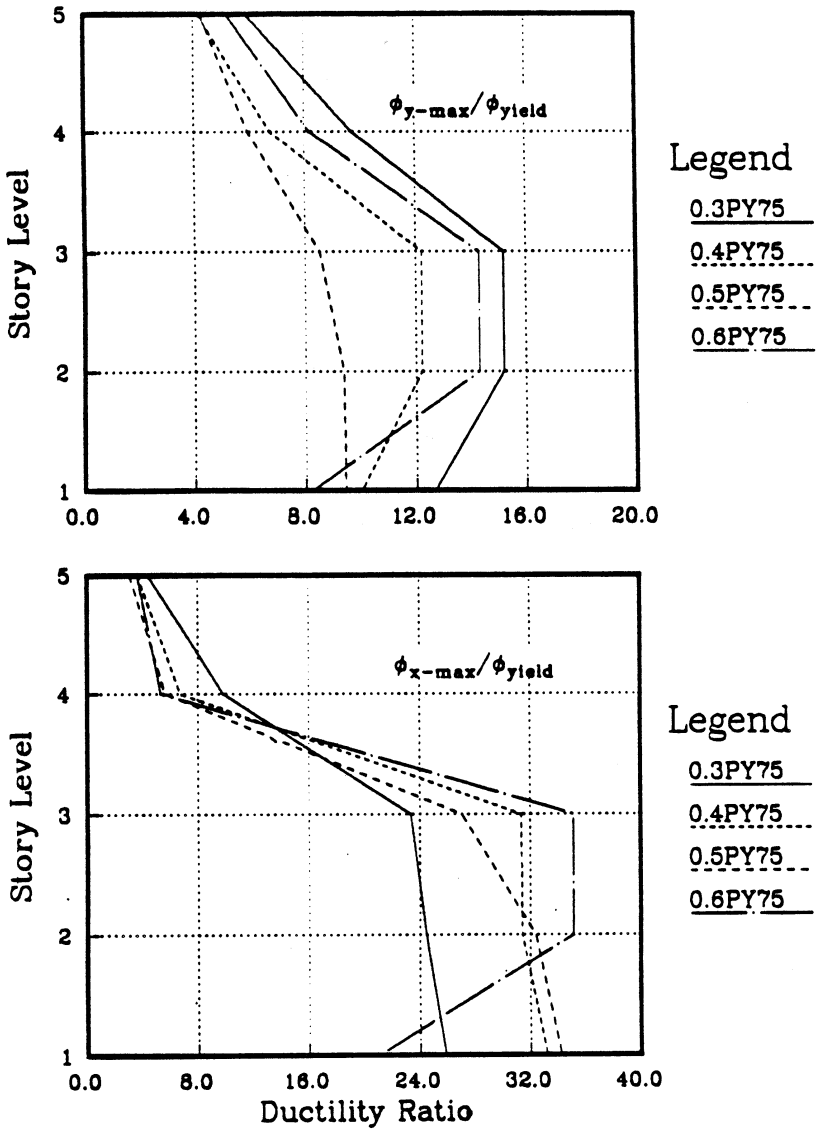

Figure 6.30: Envelope of Maximum Column Ductility Ratio of Five Story Symmetrical Building Subjected to 0.75 g 1978 Miyagi-Ken-Oki Earthquake

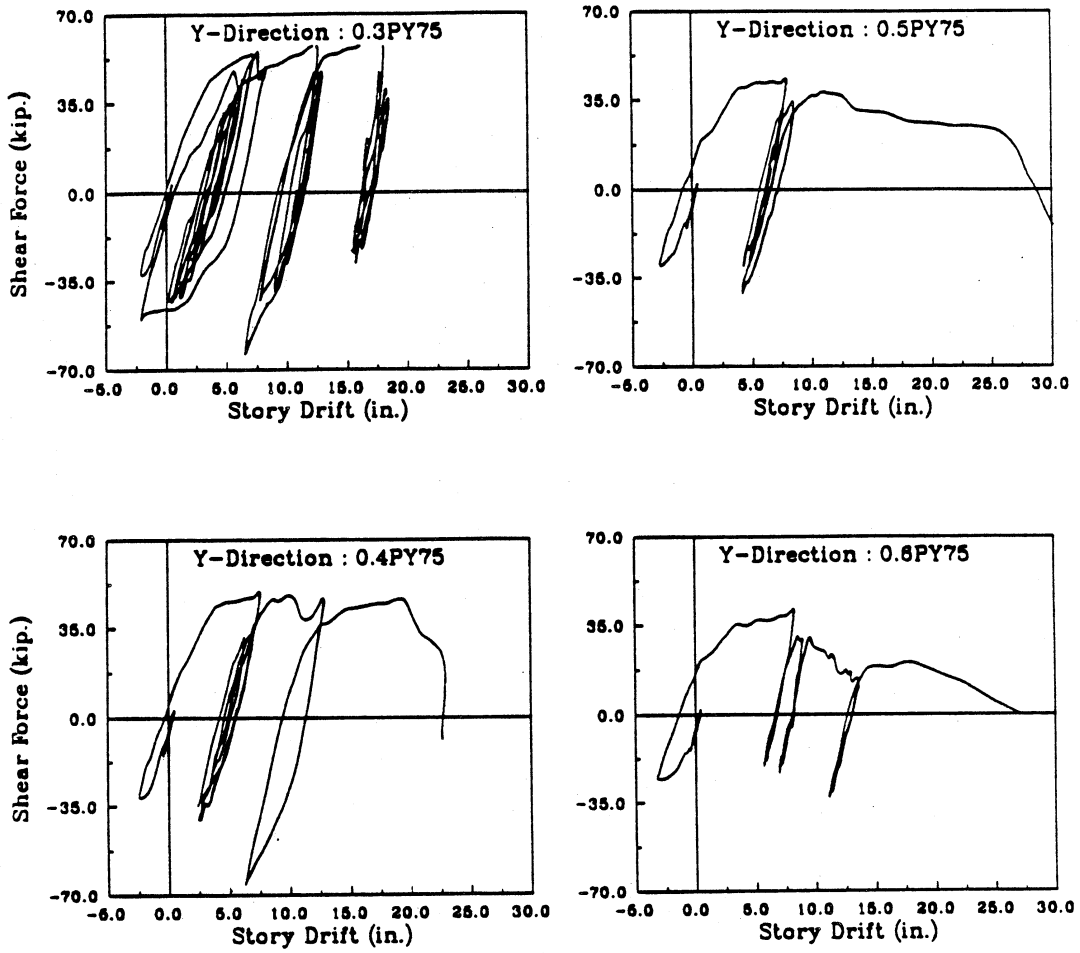

Figure 6.31: (a)Y-Direction Shear Force Hysteresis of Column 16 of Five Story Symmetrical Building Subjected to 0.75 g 1978 Miyagi-Ken-Oki Earthquake : 2nd Story

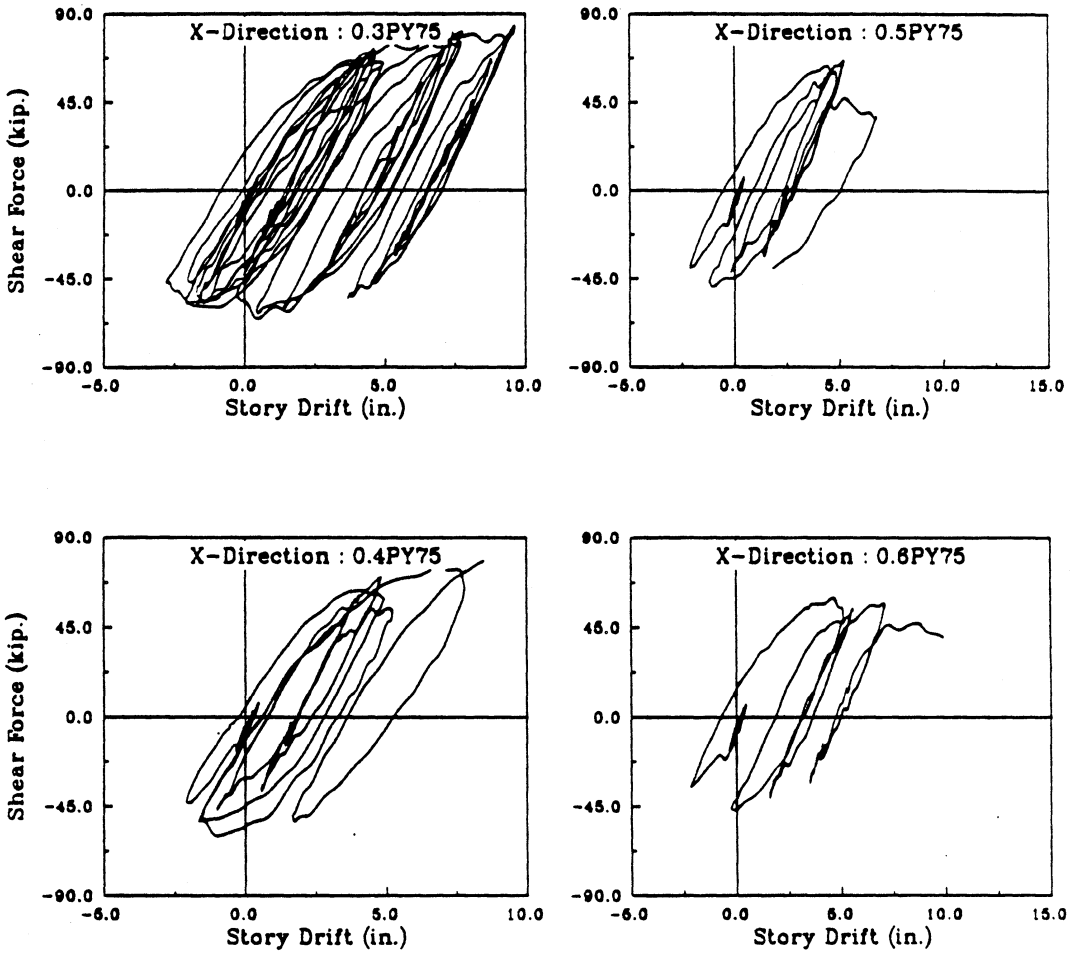

Figure 6.31: (b)X-Direction Shear Force Hysteresis of Column 16 of Five Story Symmetrical Building Subjected to 0.75 g 1978 Miyagi-Ken-Oki Earthquake : 2nd Story (Continue)

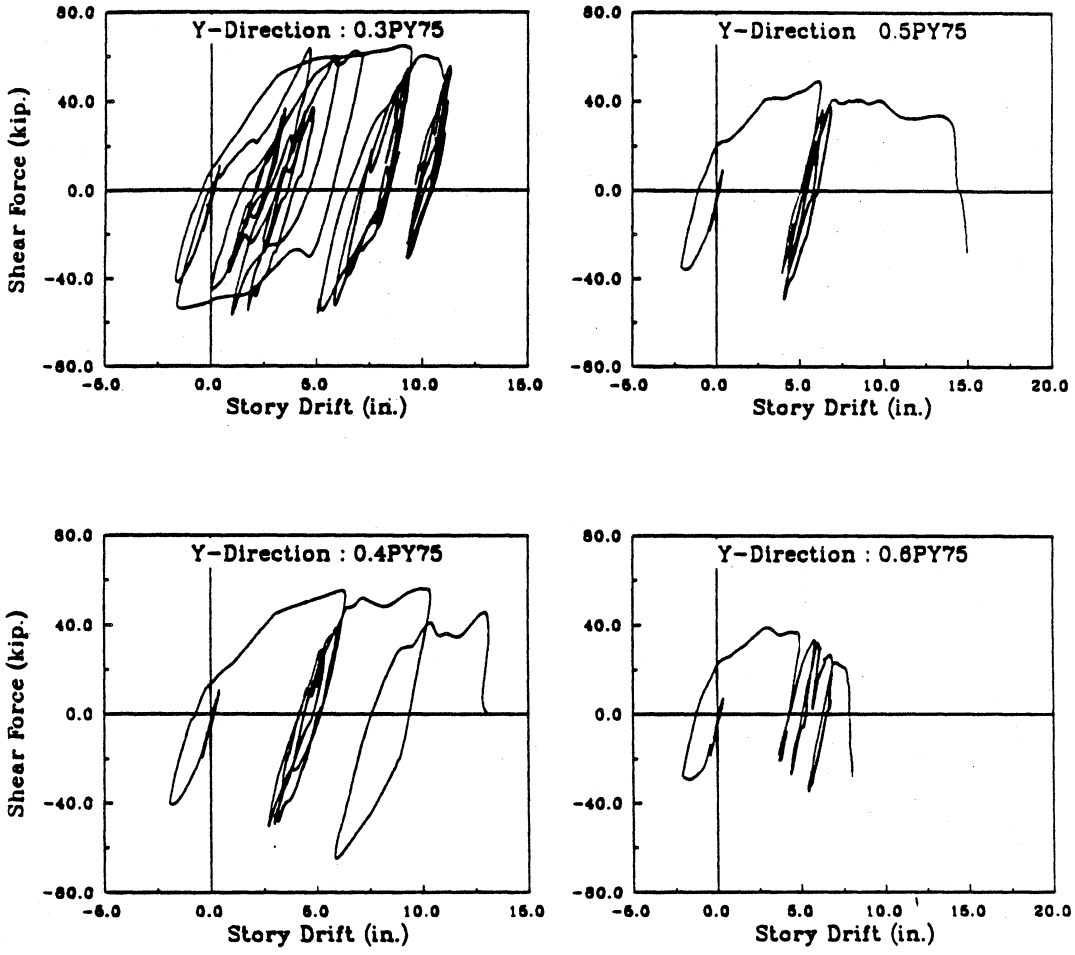

Figure 6.32: (a)Y-Direction Shear Force Hysteresis of Column 20 of Five Story Symmetrical Building Subjected to 0.75 g 1978 Miyagi-Ken-Oki Earthquake : 1st Story

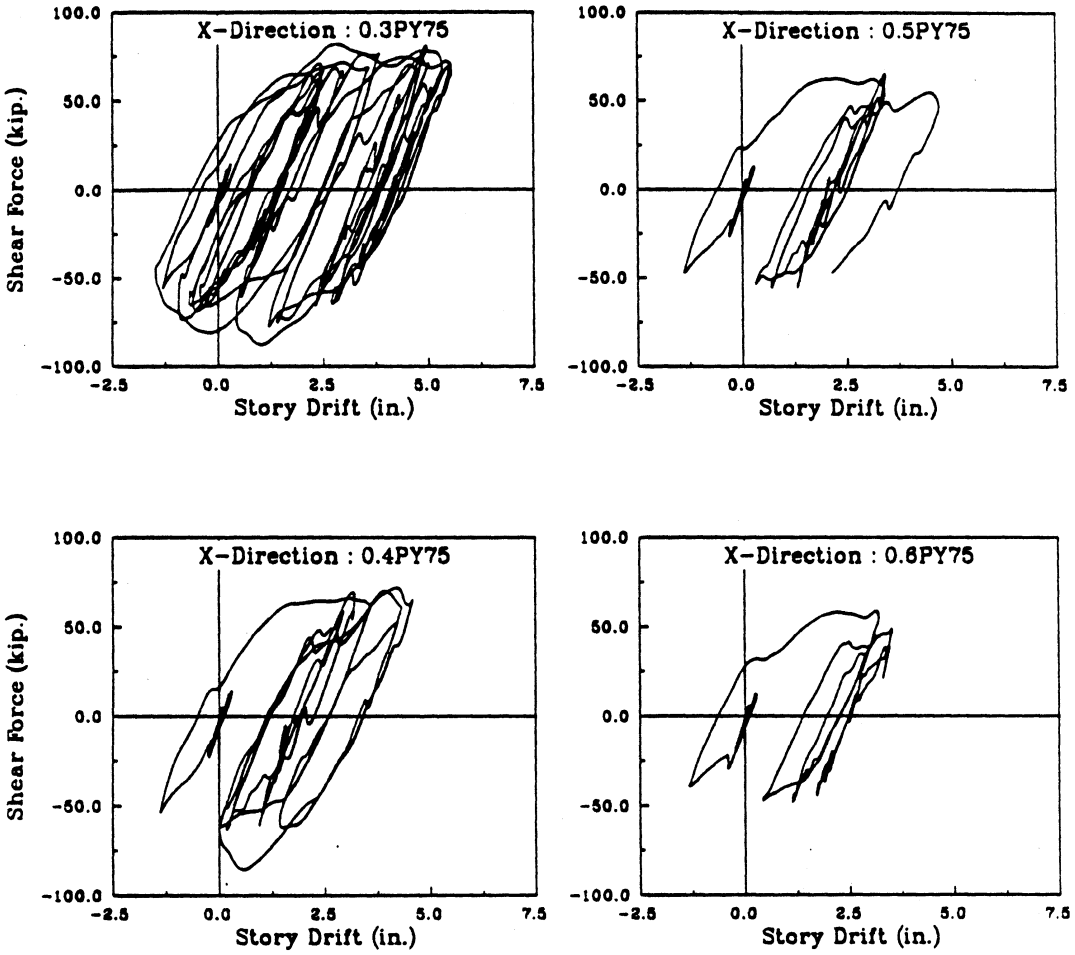

Figure 6.32: (b)X-Direction Shear Force Hysteresis of Column 20 of Five Story Symmetrical Building Subjected to 0.75 g 1978 Miyagi-Ken-Oki Earthquake : 1st Story (Continue)

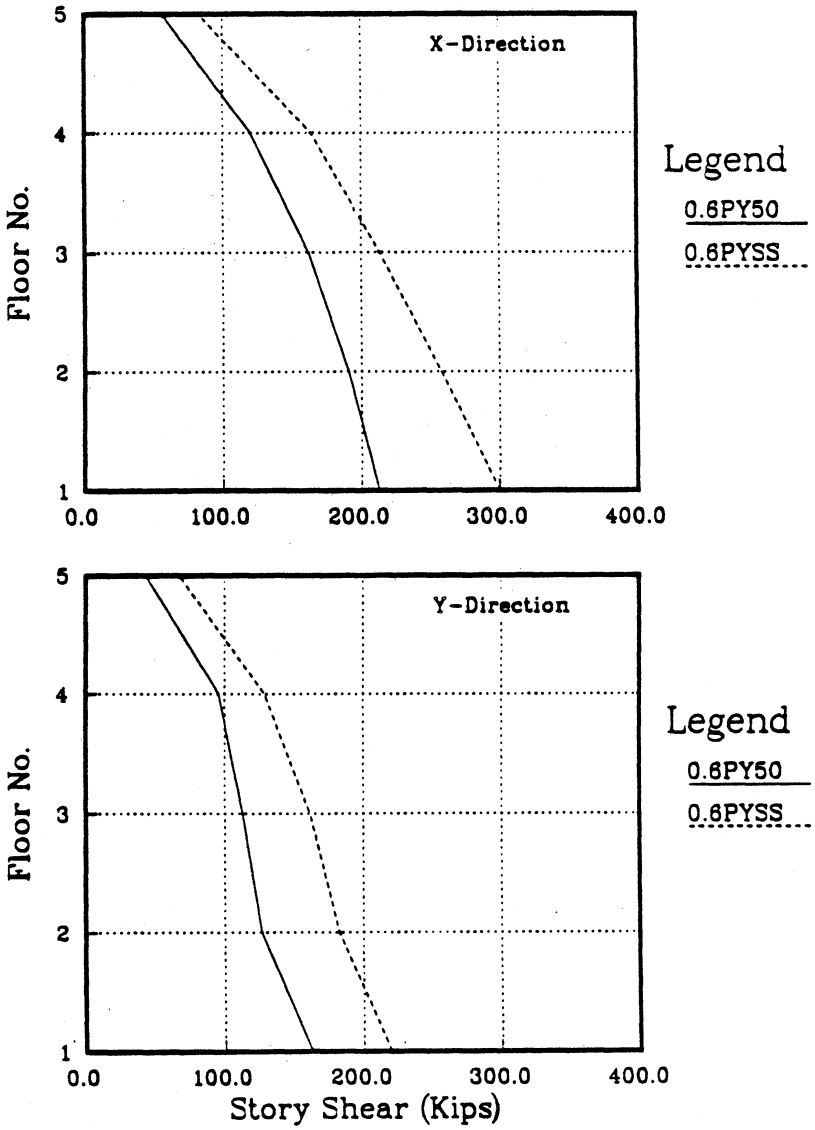

Figure 6.33: Comparison of Maximum Story Shear of Five Story Symmetrical Building Subjected to 0.5 g 1978 Miyagi-Ken-Oki Earthquake : Soft Story

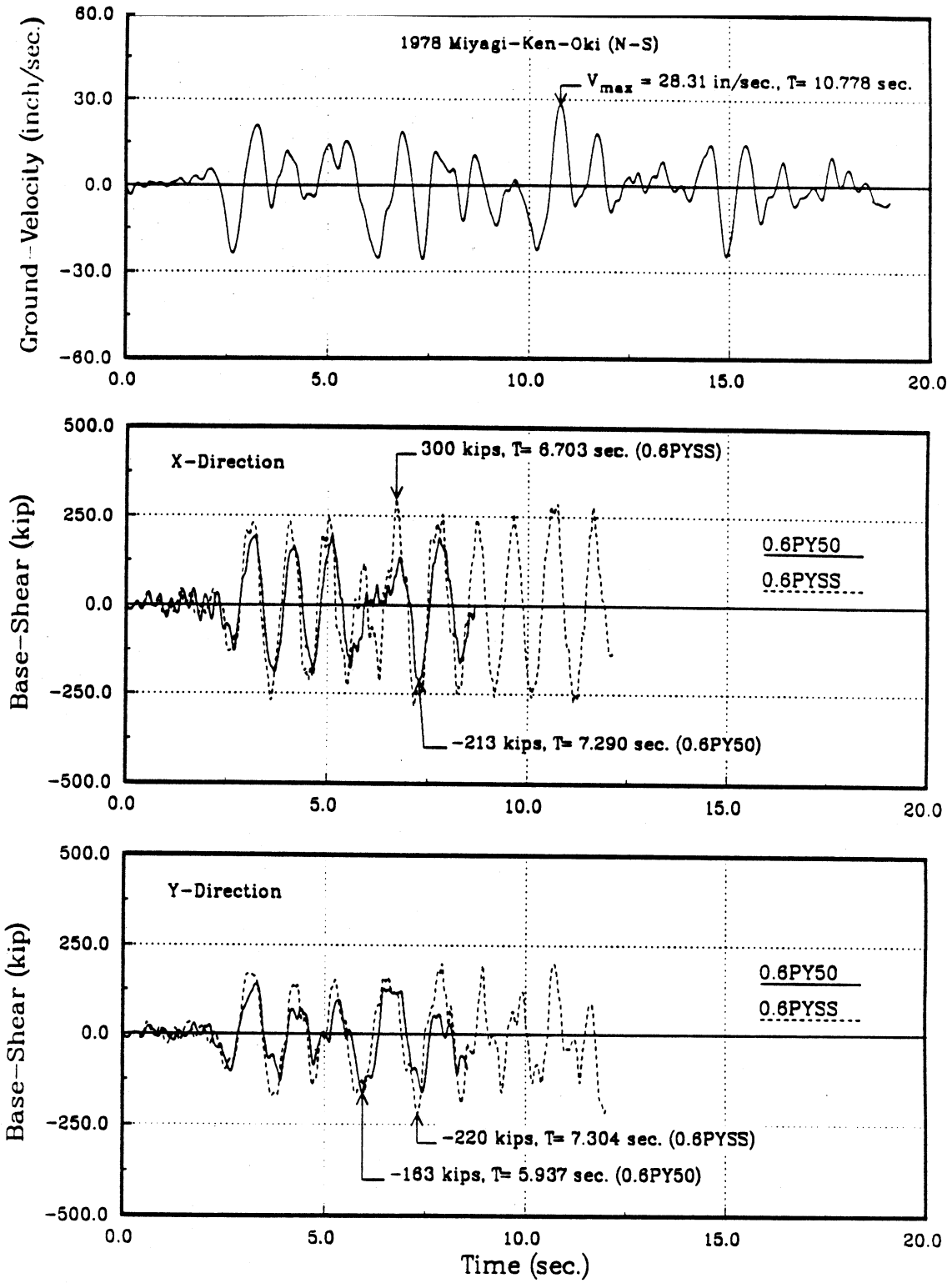

Figure 6.34: Input Ground Velocity and Base Shear Time History in the Principal Directions of Five Story Symmetrical Building Subjected to 0.5 g 1978 Miyagi-Ken-Oki Earthquake : Soft Story

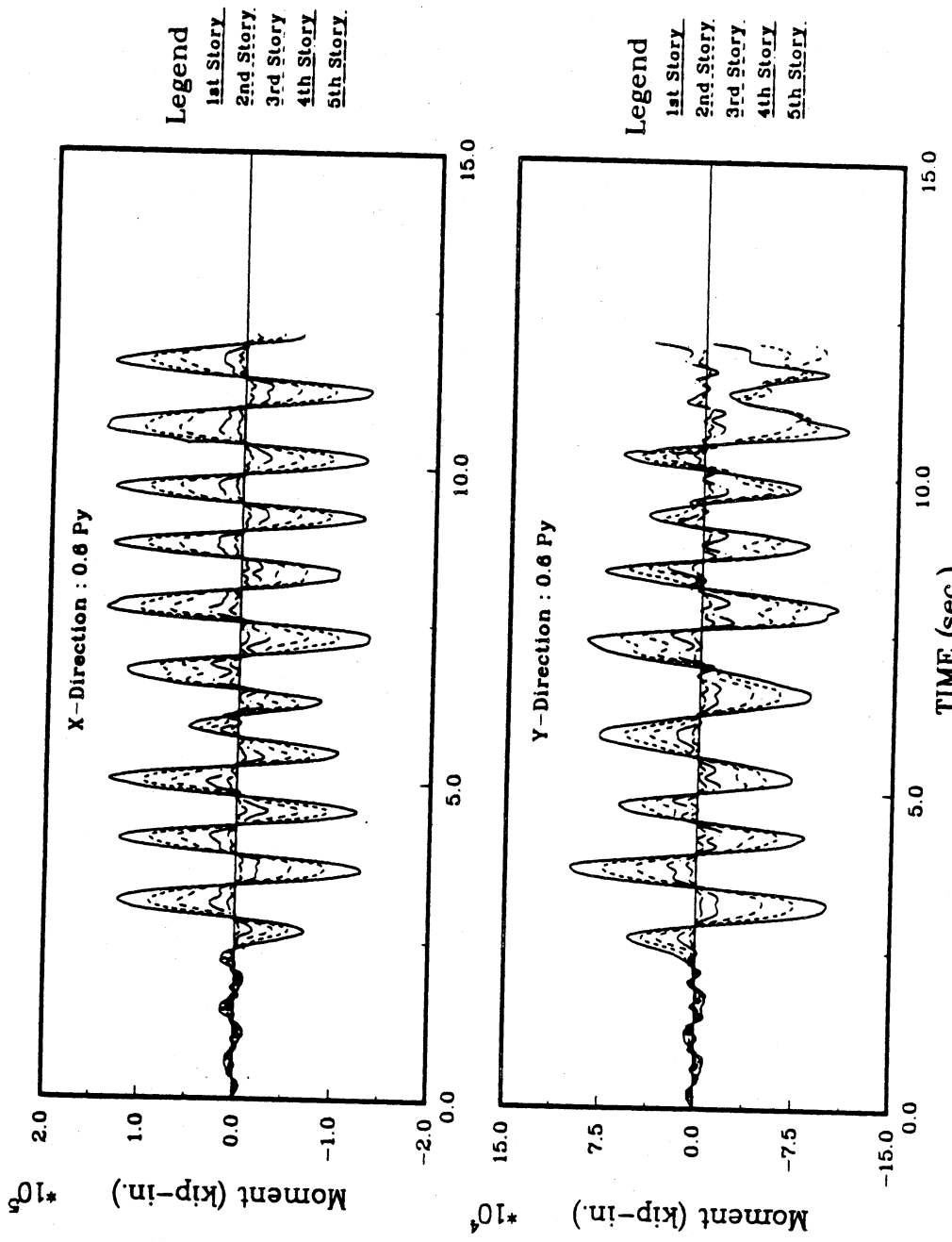

Figure 6.35: Overturning Moment Time History of Five Story Symmetrical Building Subjected to 0.5 g 1978 Miyagi-Ken-Oki Earthquake : Soft Story

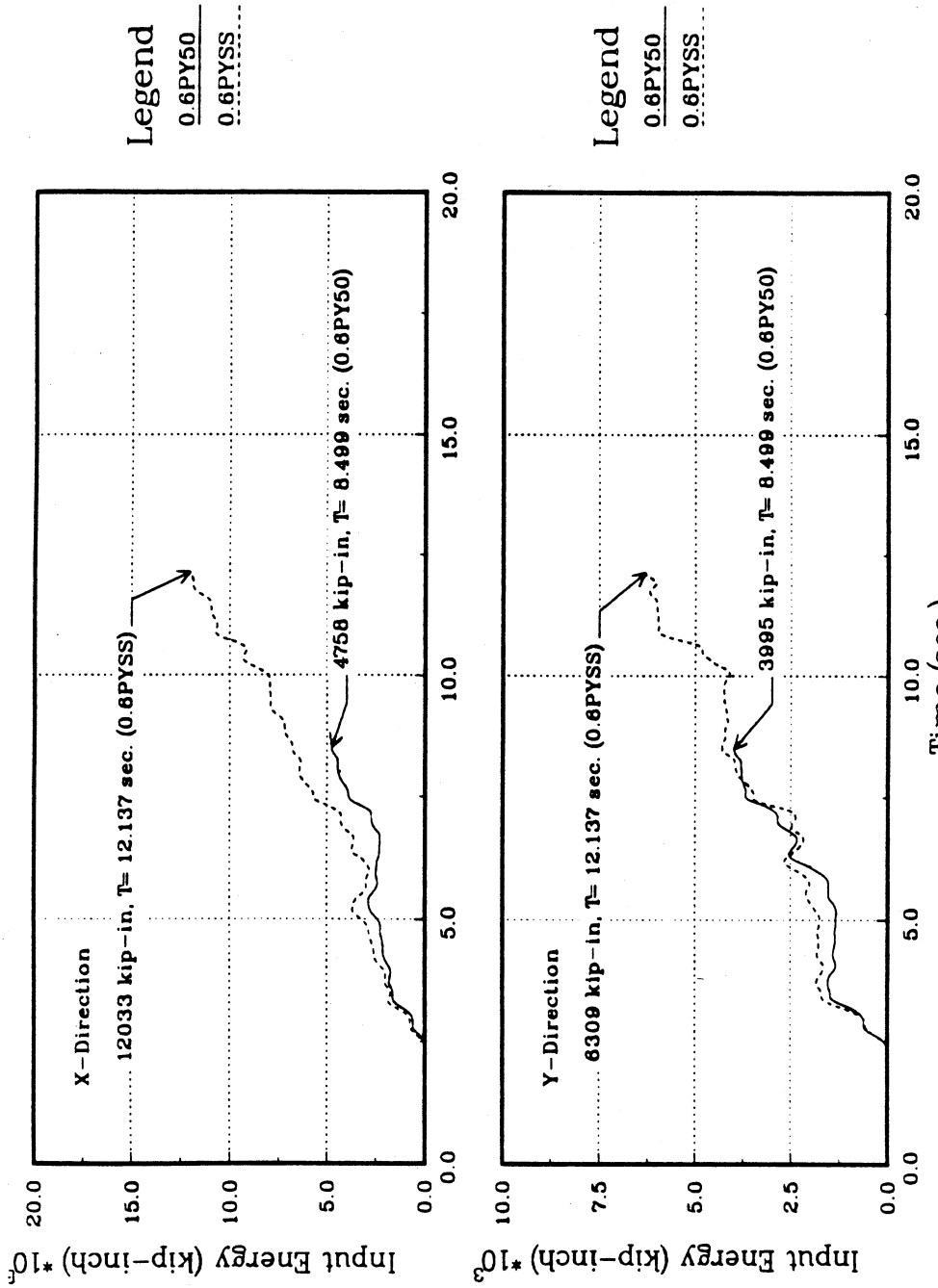

Figure 6.36: Absolute Input Energy Time History in the Principal Directions of Five Story Symmetrical Building Subjected to 0.5 g 1978 Miyagi-Ken-Oki Earthquake : Soft Story

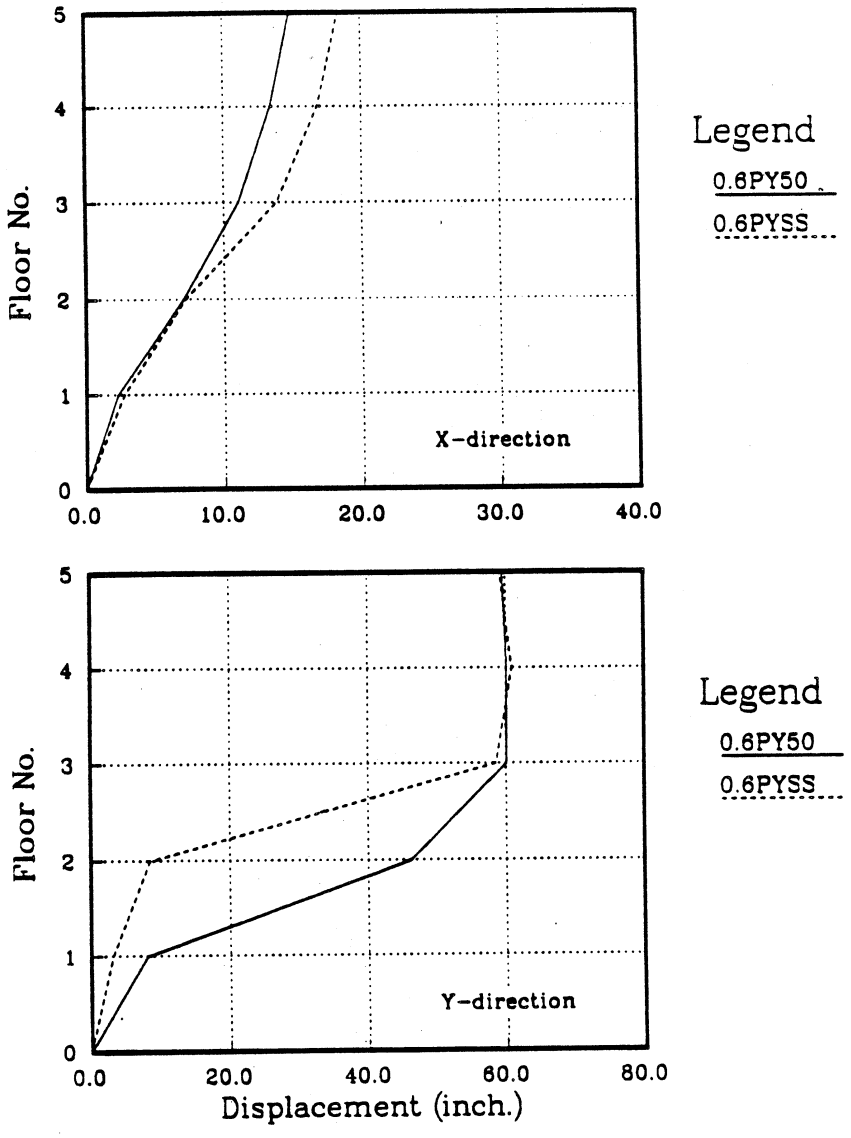

Figure 6.37: Comparison of Maximum Displacement of Five Story Symmetrical Building Subjected to 0.5 g 1978 Miyagi-Ken-Oki Earthquake : Soft Story

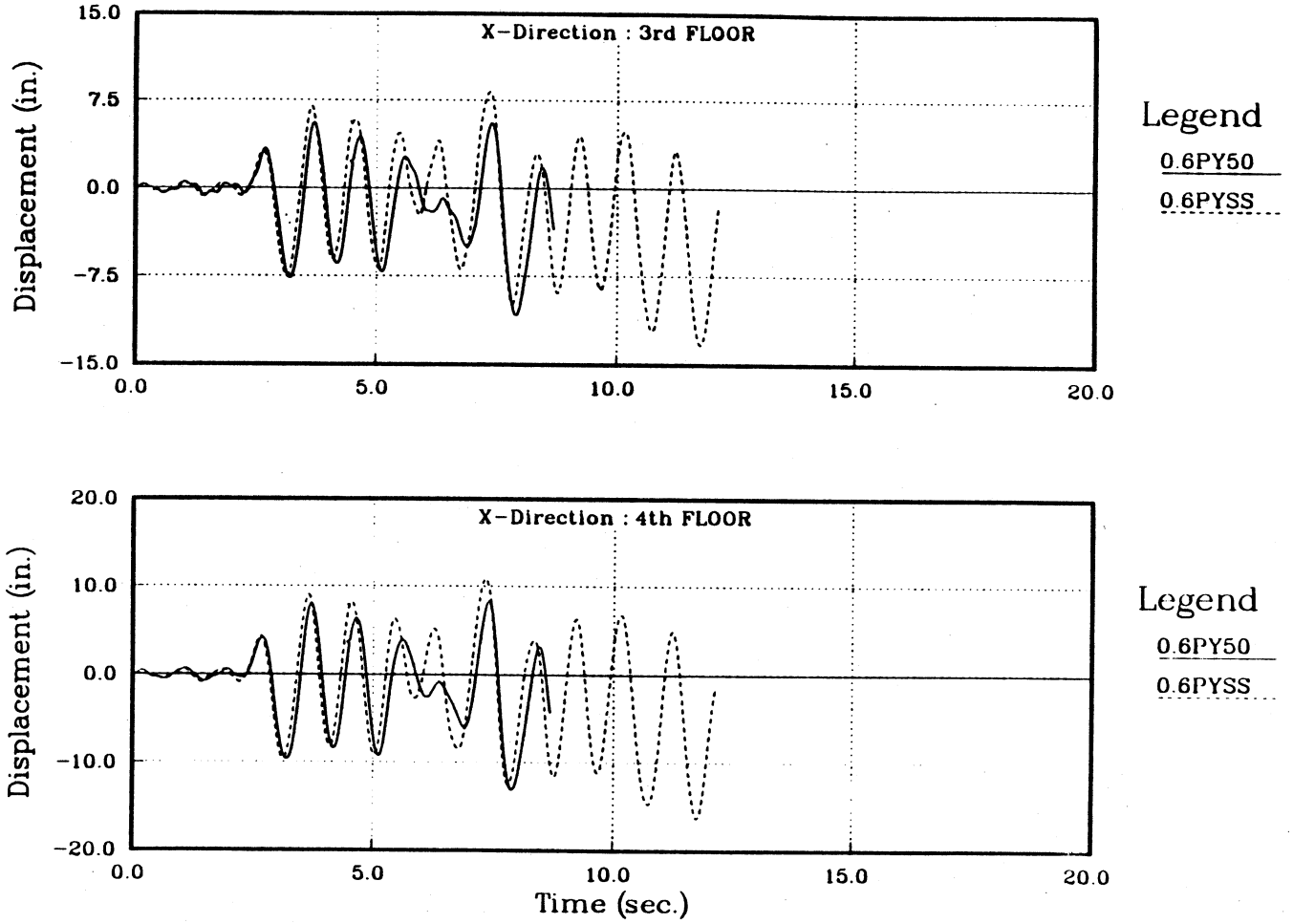

Figure 6.38: 3rd and 4th Floor Center of Mass Displacement Time History Response in the X-direction of Five Story Symmetrical Building Subjected to 0.5 g 1978 Miyagi-Ken-Oki Earthquake : Soft Story

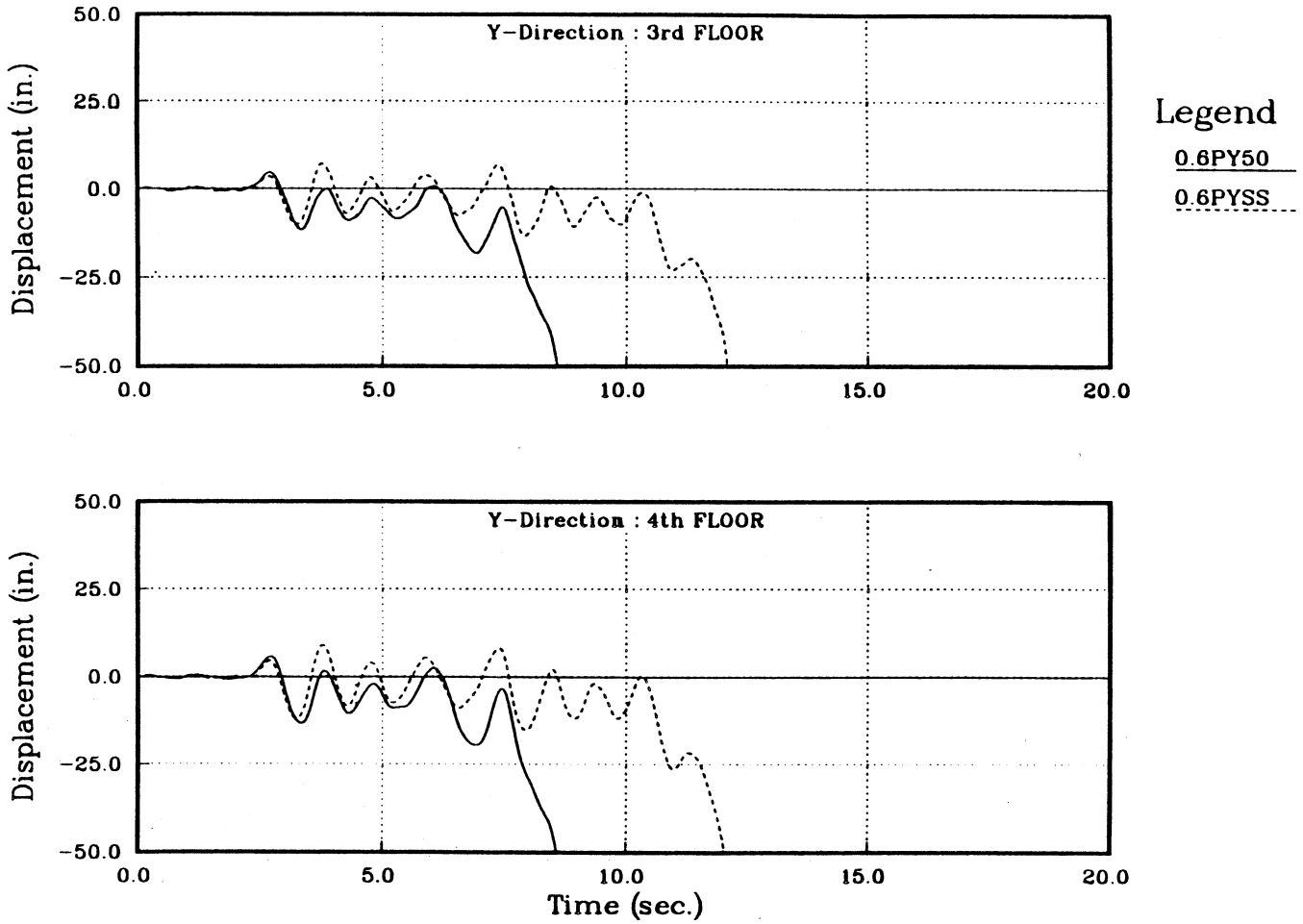

Figure 6.39: 3rd and 4th Floor Center of Mass Displacement Time History Response in the X-direction of Five Story Symmetrical Building Subjected to 0.5 g 1978 Miyagi-Ken-Oki Earthquake : Soft Story

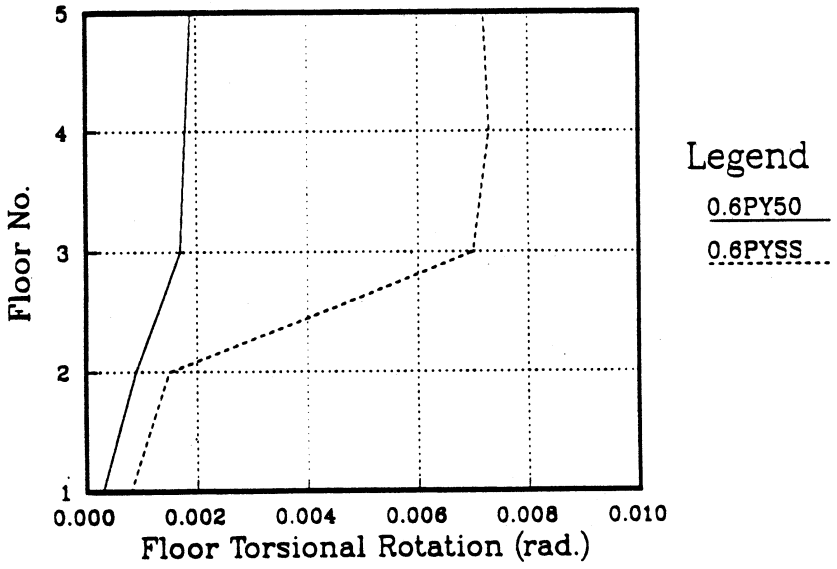

Figure 6.40: Envelope of Center of Mass Rotation of Five Story Symmetrical Building Subjected to 0.5 g 1978 Miyagi-Ken-Oki Earthquake : Soft Story

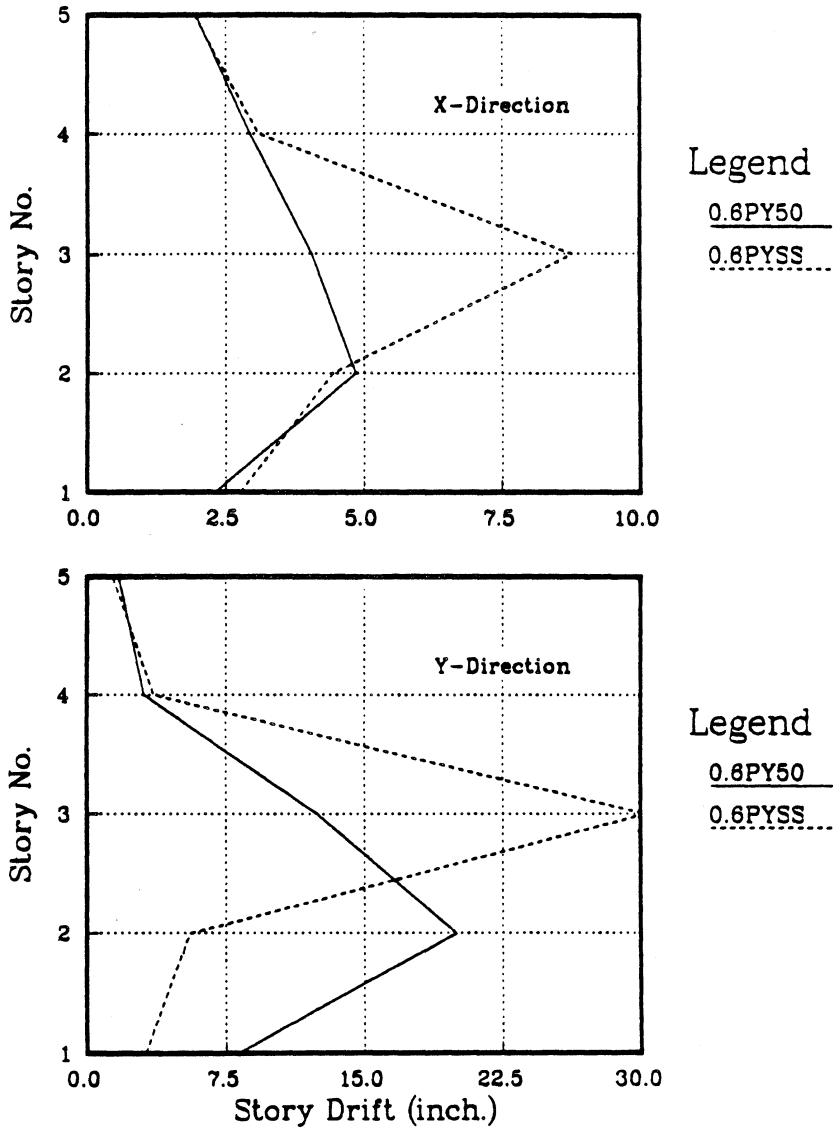

Figure 6.41: Comparison of Maximum Story Drift of Five Story Symmetrical Building Subjected to 0.5 g 1978 Miyagi-Ken-Oki Earthquake : Soft Story

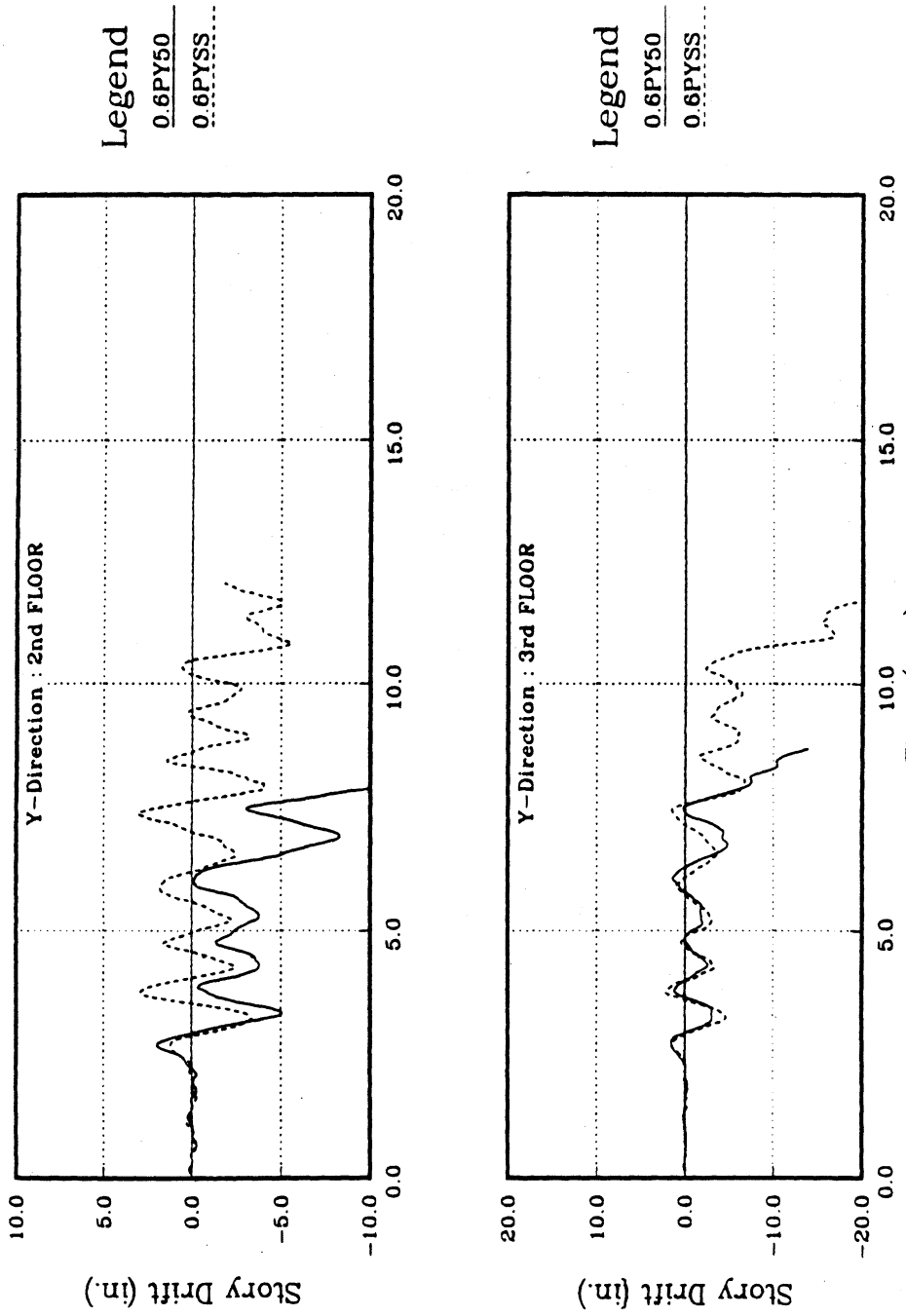

Figure 6.42: 3rd and 4th Floor Center of Mass Story Drift Time History Response in the Y-direction of Five Story Symmetrical Building Subjected to 0.5 g 1978 Miyagi-Ken-Oki Earthquake : Soft Story

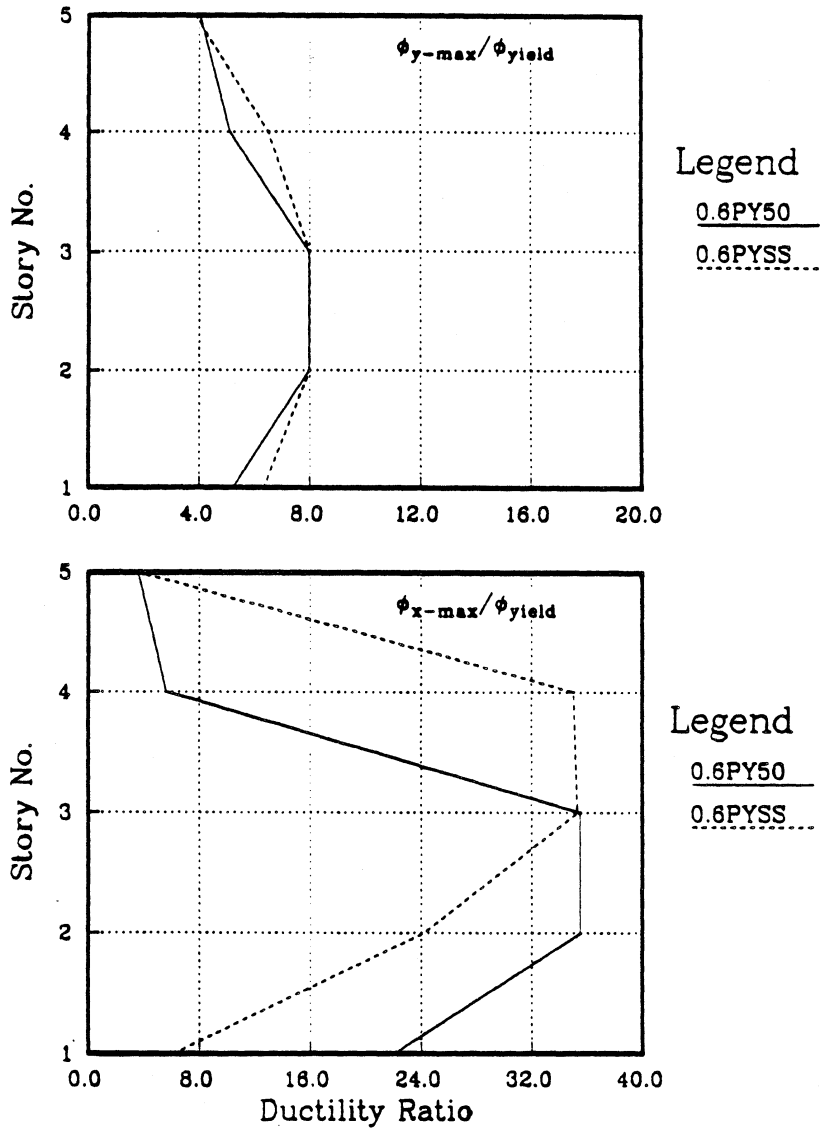

Figure 6.43: Envelope of Maximum Column Ductility Ratio of Five Story Symmetrical Building Subjected to 0.5 g 1978 Miyagi-Ken-Oki Earthquake : Soft Story

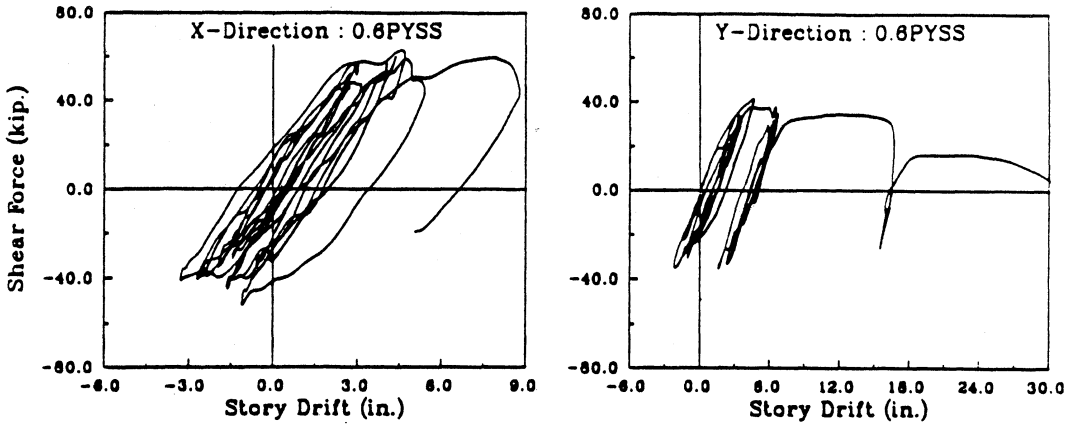

Figure 6.44: Shear Force Hysteresis of Column 12 of Five Story Symmetrical Building Subjected to 0.5 g 1978 Miyagi-Ken-Oki Earthquake : 3rd Story, 0.6PYSS

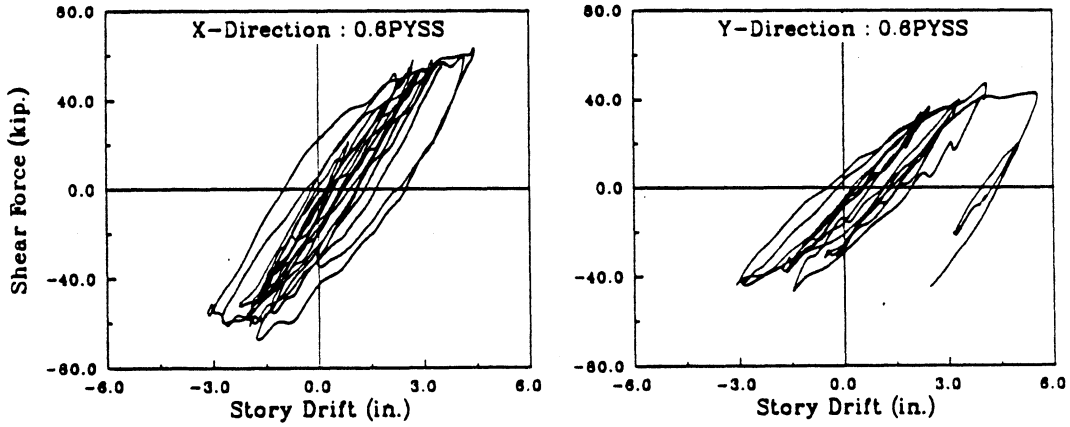

Figure 6.45: Shear Force Hysteresis of Column 16 of Five Story Symmetrical Building Subjected to 0.5 g 1978 Miyagi-Ken-Oki Earthquake : 2nd Story, 0.6PYSS

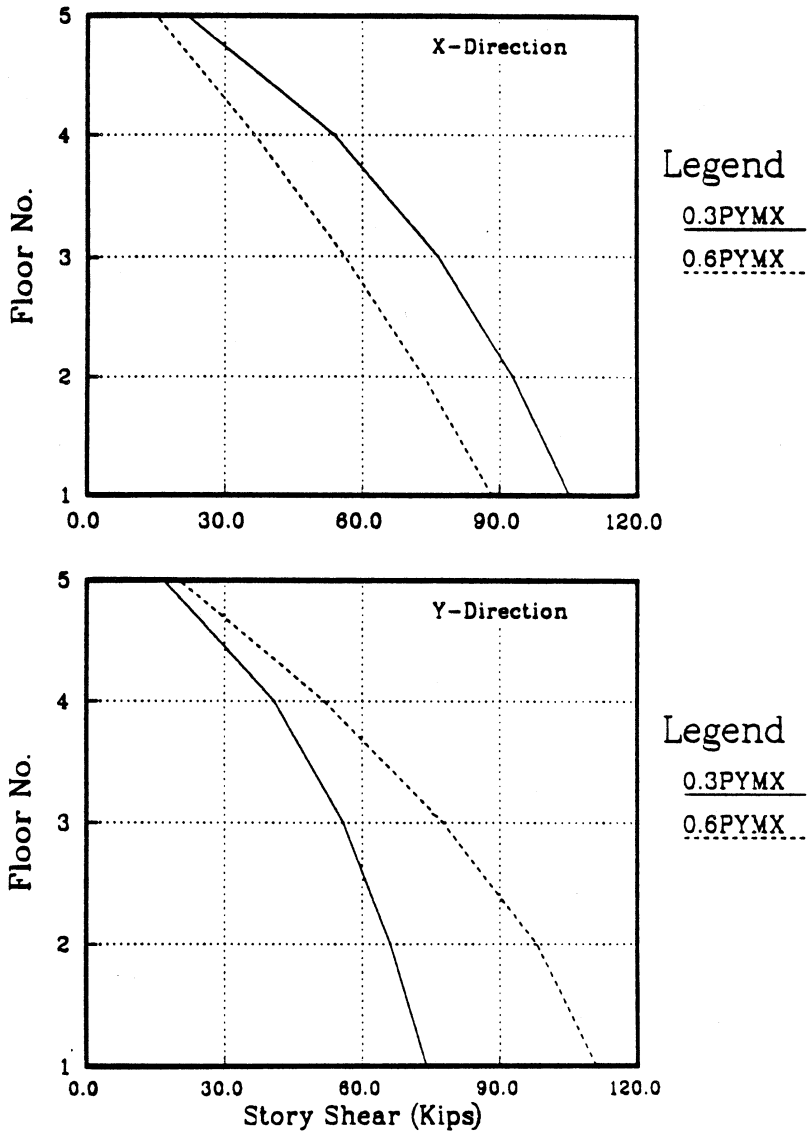

Figure 6.46: Comparison of Maximum Story Shear of Five Story Symmetrical Building Subjected to 1985 Mexico SCT Earthquake

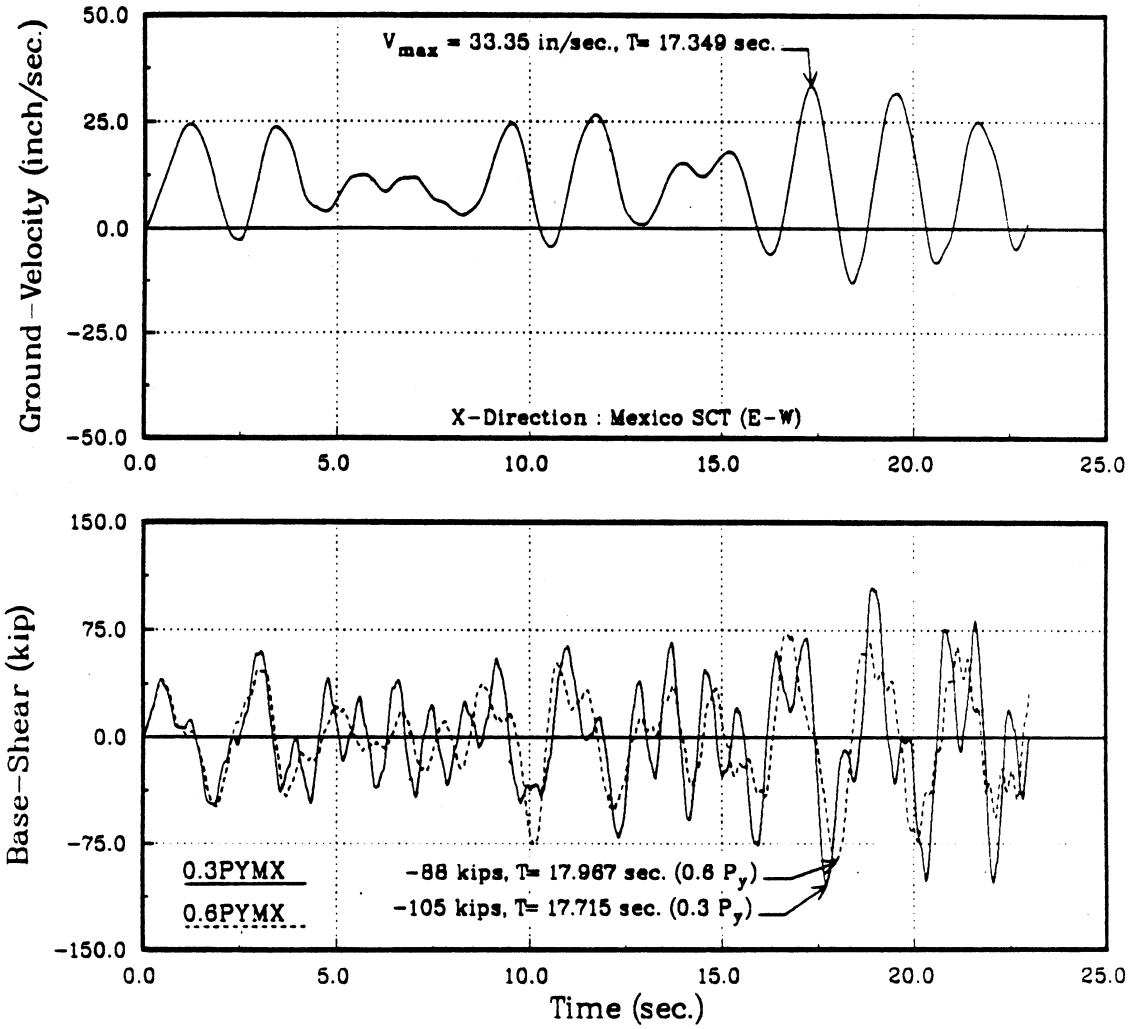

Figure 6.47: (a)X-Direction Input Ground Velocity and Base Shear Time History in the Principal Directions of Five Story Symmetrical Building Subjected to 1985 Mexico SCT Earthquake

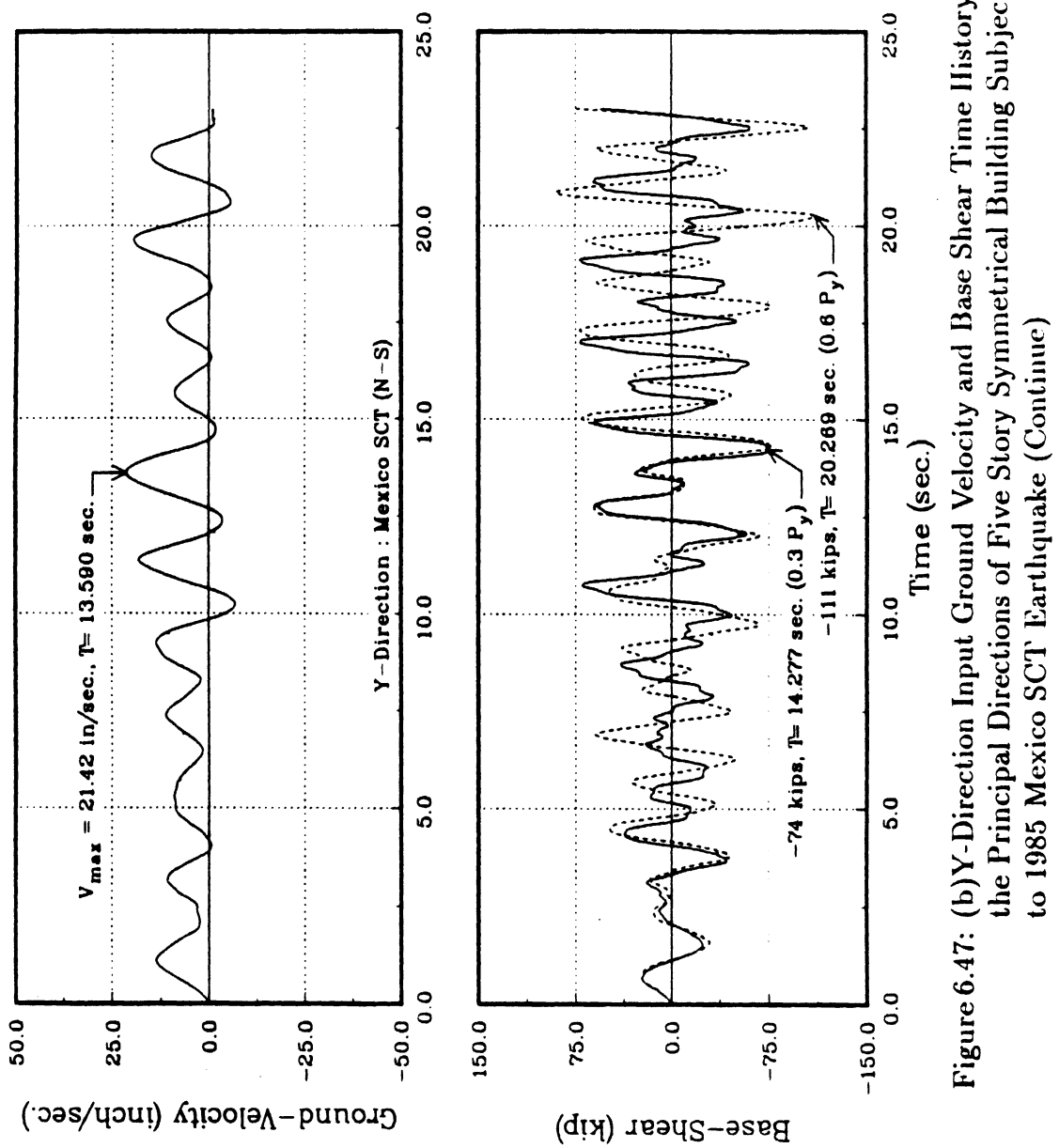

Figure 6.47: (b)Y-Direction Input Ground Velocity and Base Shear Time History in the Principal Directions of Five Story Symmetrical Building Subjected to 1985 Mexico SCT Earthquake (Continue)

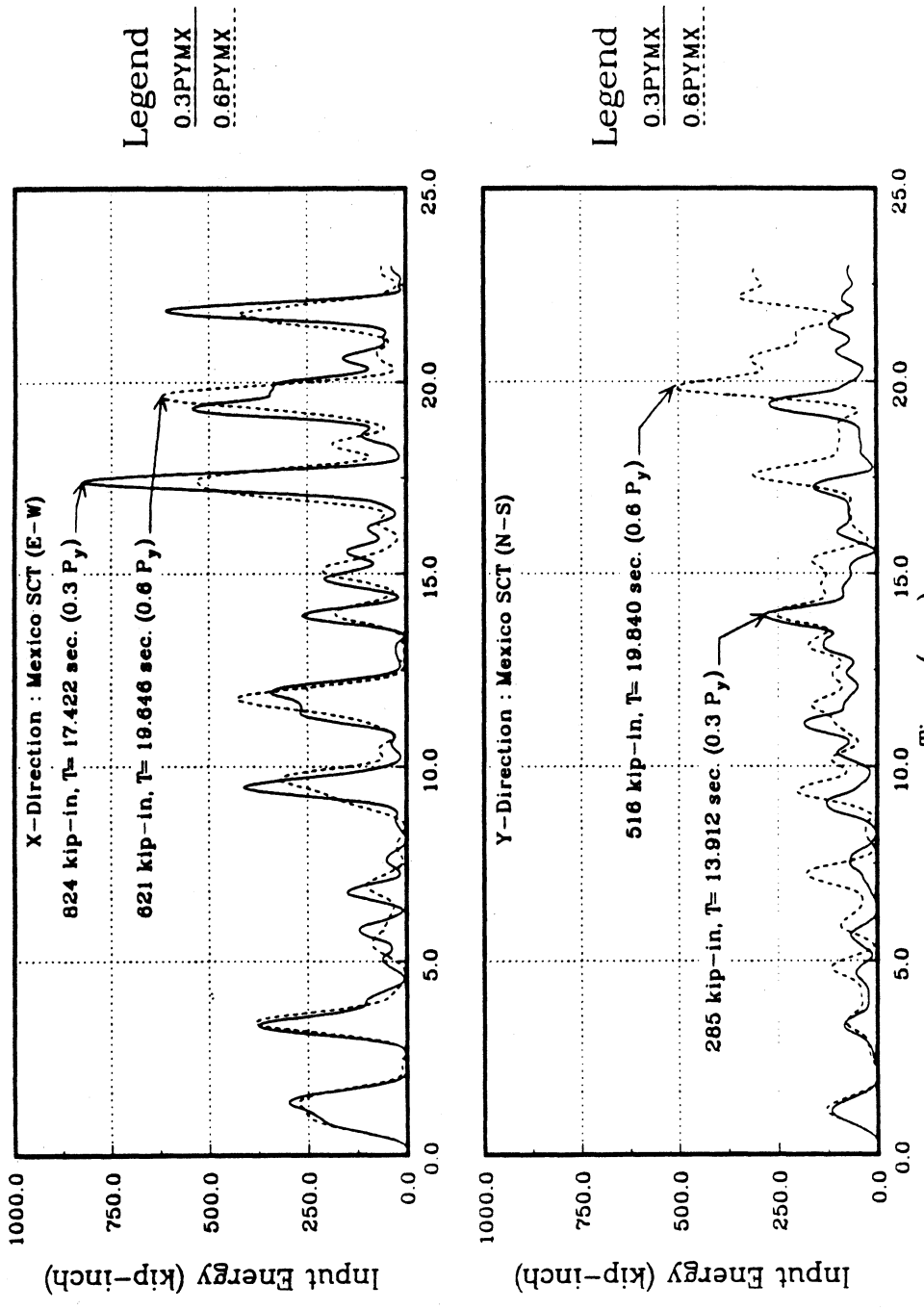

Figure 6.48: Absolute Input Energy Time History in the Principal Directions of Five Story Symmetrical Building Subjected to 1985 Mexico SCT Earthquake

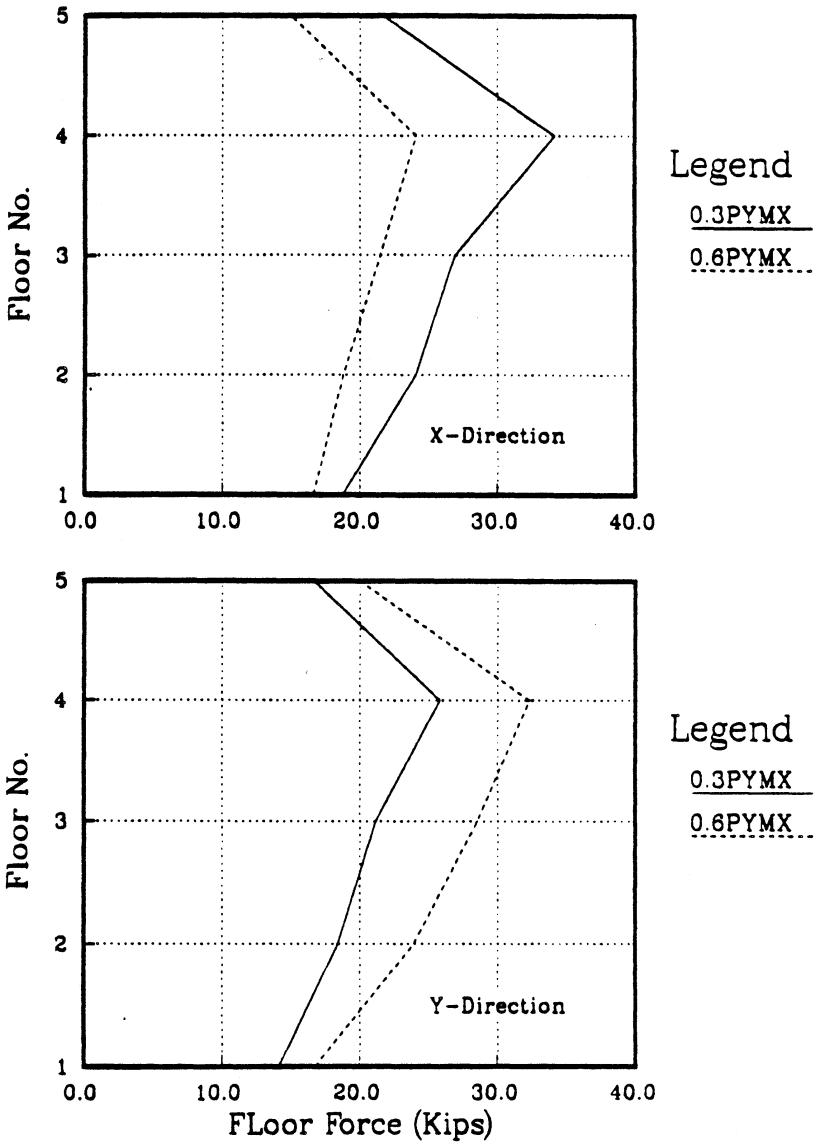

Figure 6.49: Comparison of Maximum Floor Force of Five Story Symmetrical Building Subjected to 1985 Mexico SCT Earthquake

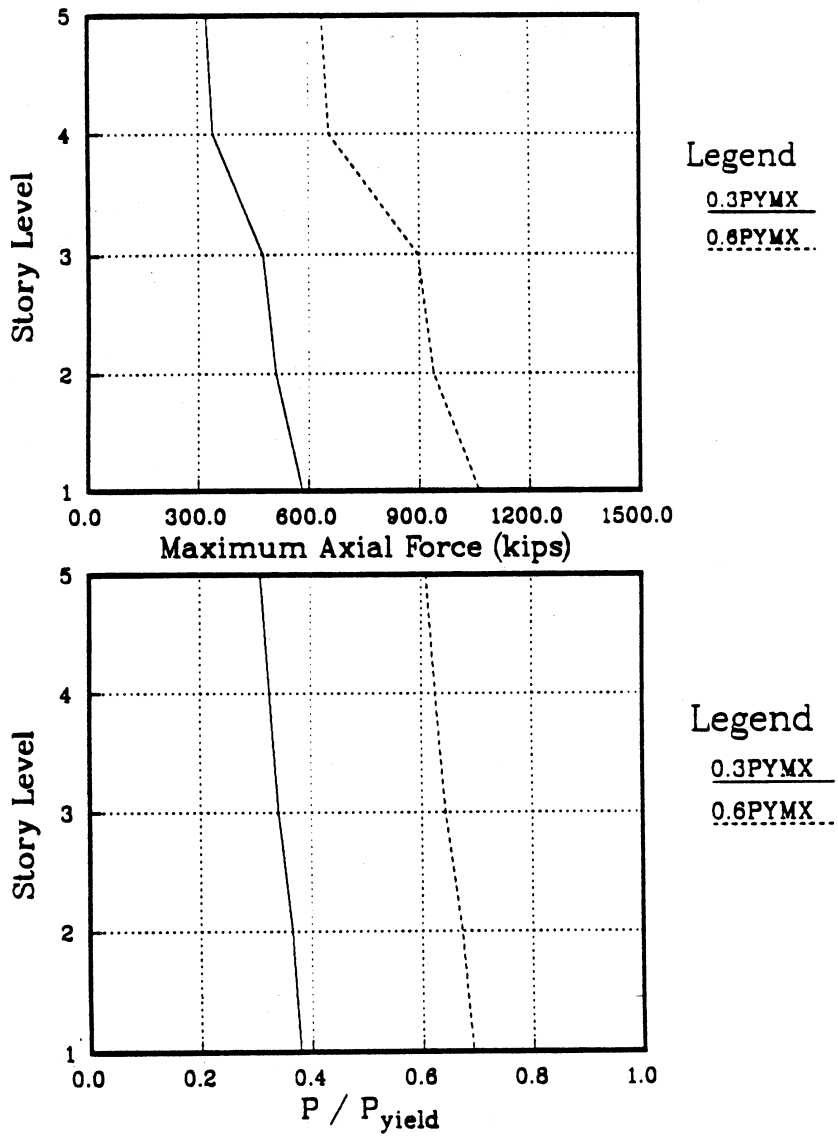

Figure 6.50: Comparison of Maximum Column Axial Force of Five Story Symmetrical Building Subjected to 1985 Mexico SCT Earthquake

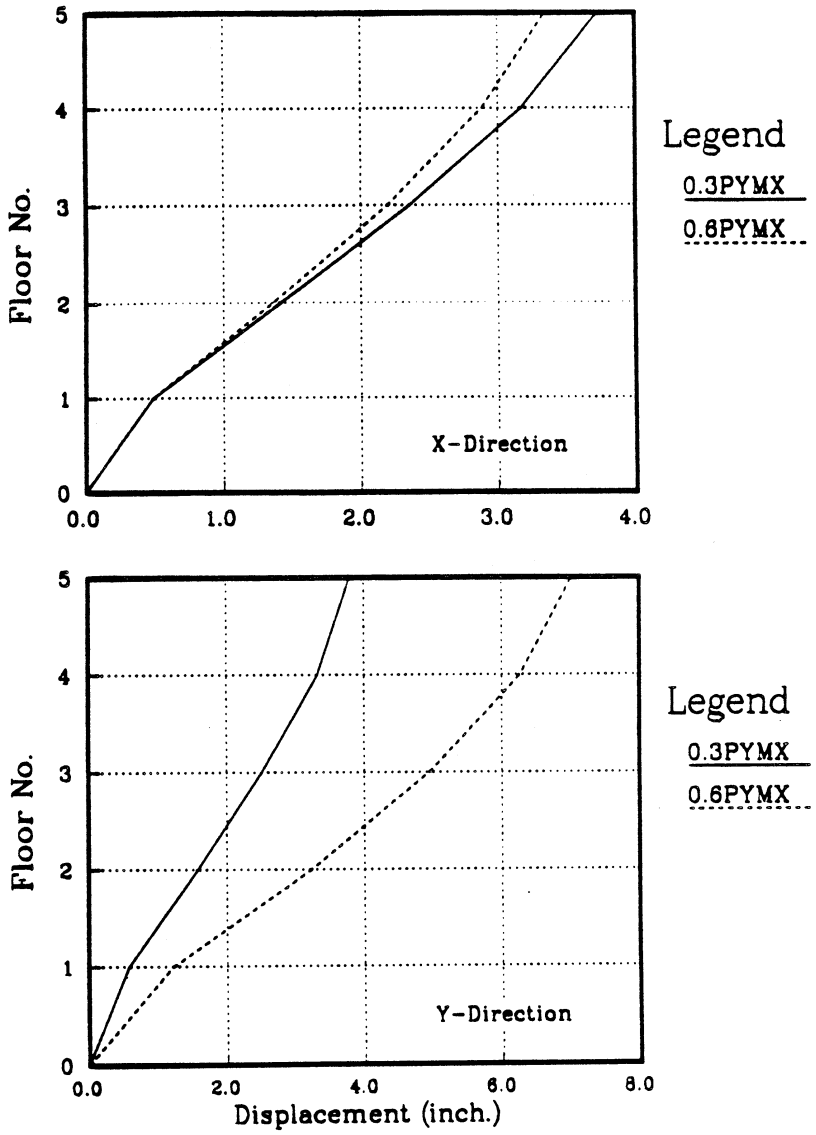

Figure 6.51: Comparison of Maximum Displacement of Five Story Symmetrical Building Subjected to 1985 Mexico SCT Earthquake

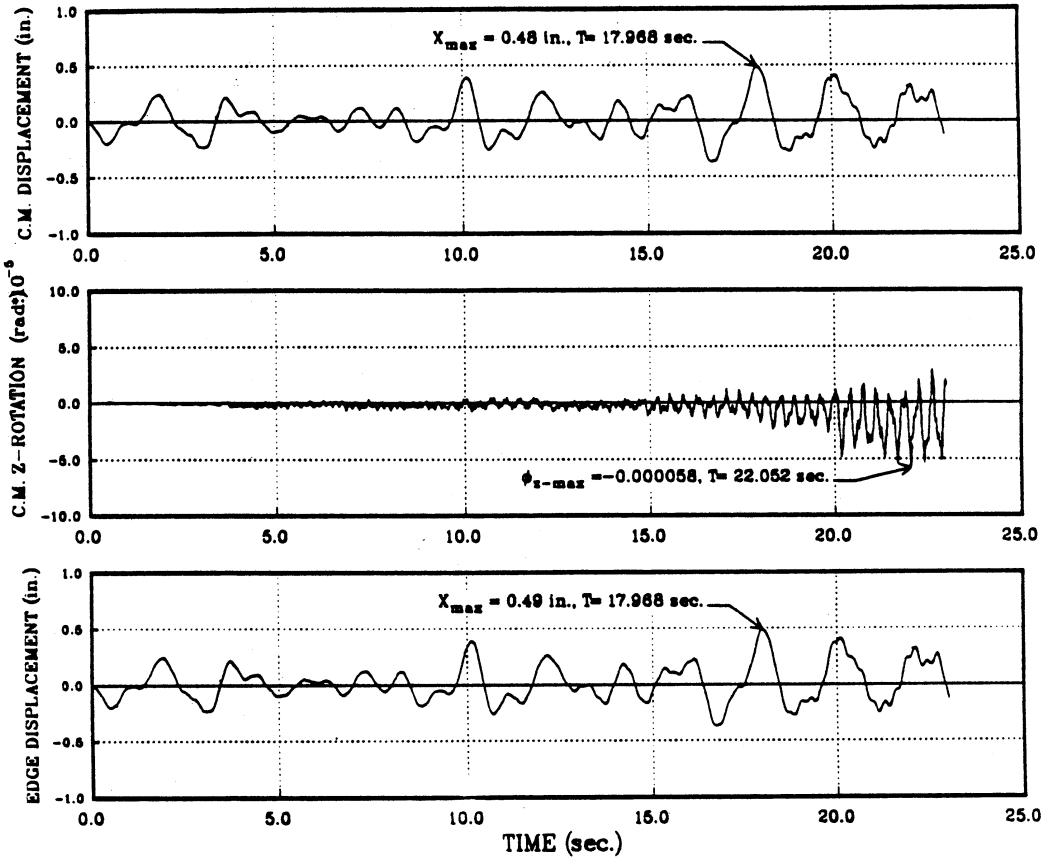

Figure 6.52: (a)1st Floor Center of Mass Displacement and Rotation, Edge Displacement Time History of Five Story Symmetrical Building Subjected to 1985 Mexico SCT Earthquake : $P = 0.6P_y$

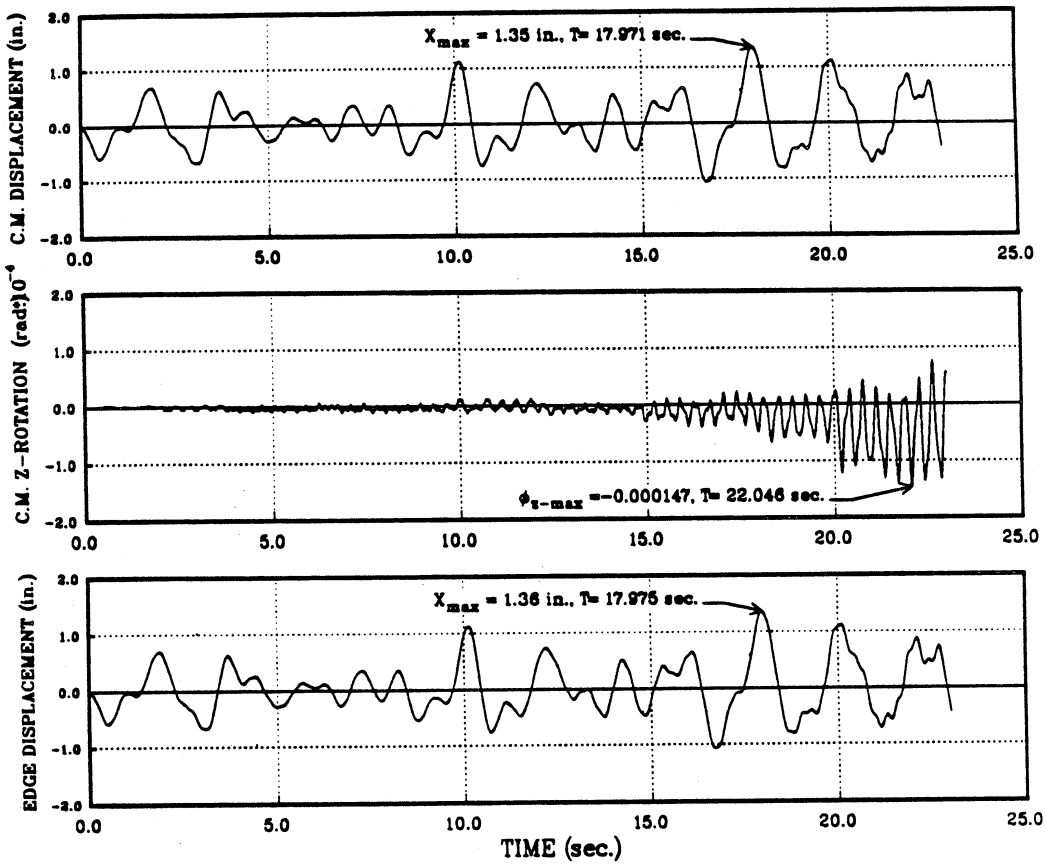

Figure 6.52: (b)2nd Floor Center of Mass Displacement and Rotation, Edge Displacement Time History of Five Story Symmetrical Building Subjected to 1985 Mexico SCT Earthquake : $P = 0.6P_y$ (Continue)

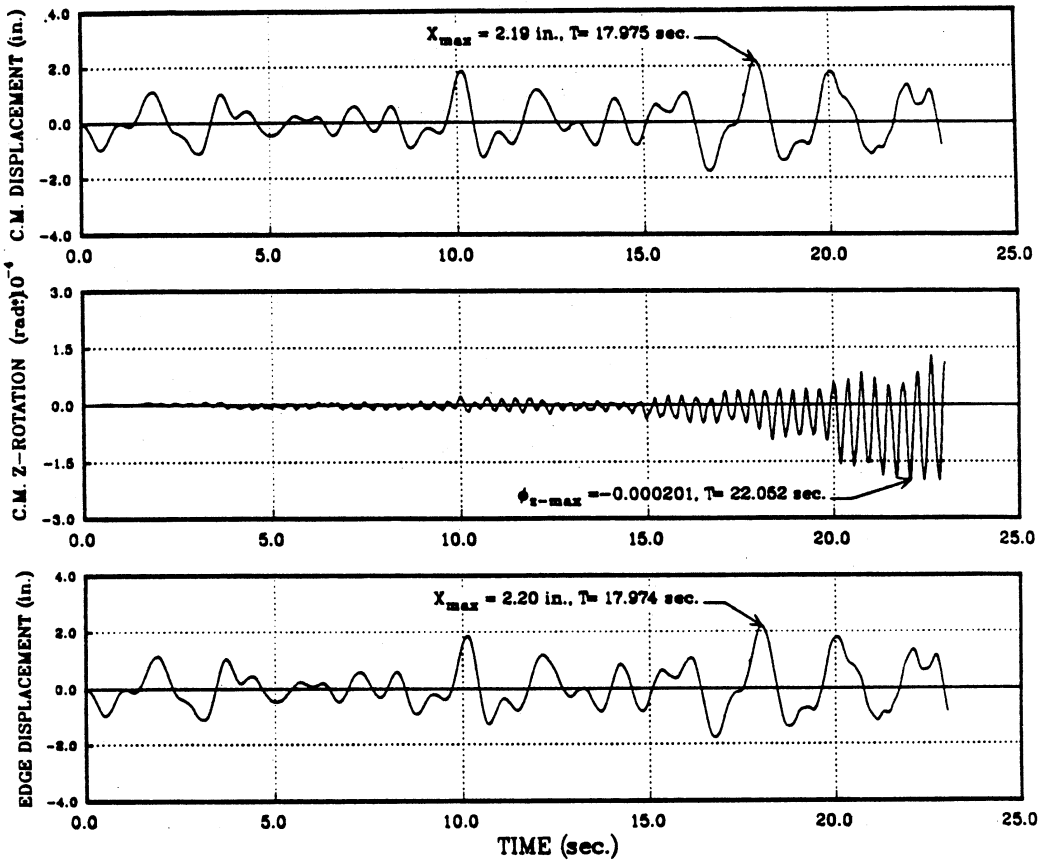

Figure 6.52: (c)3rd Floor Center of Mass Displacement and Rotation, Edge Displacement Time History of Five Story Symmetrical Building Subjected to 1985 Mexico SCT Earthquake : $P = 0.6P_y$ (Continue)

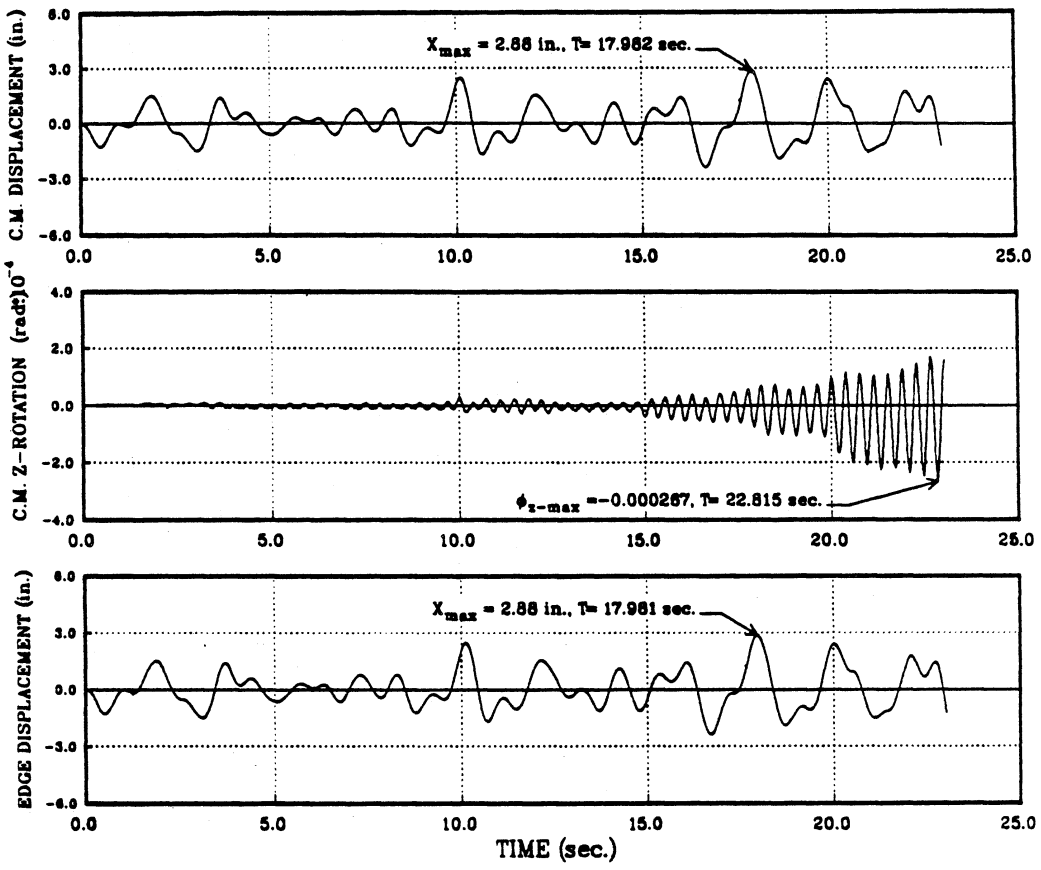

igure 6.52: (d)4th Floor Center of Mass Displacement and Rotation, Edge Displacement Time History of Five Story Symmetrical Building Subjected to 1985 Mexico SCT Earthquake : $P = 0.6P_y$ (Continue)

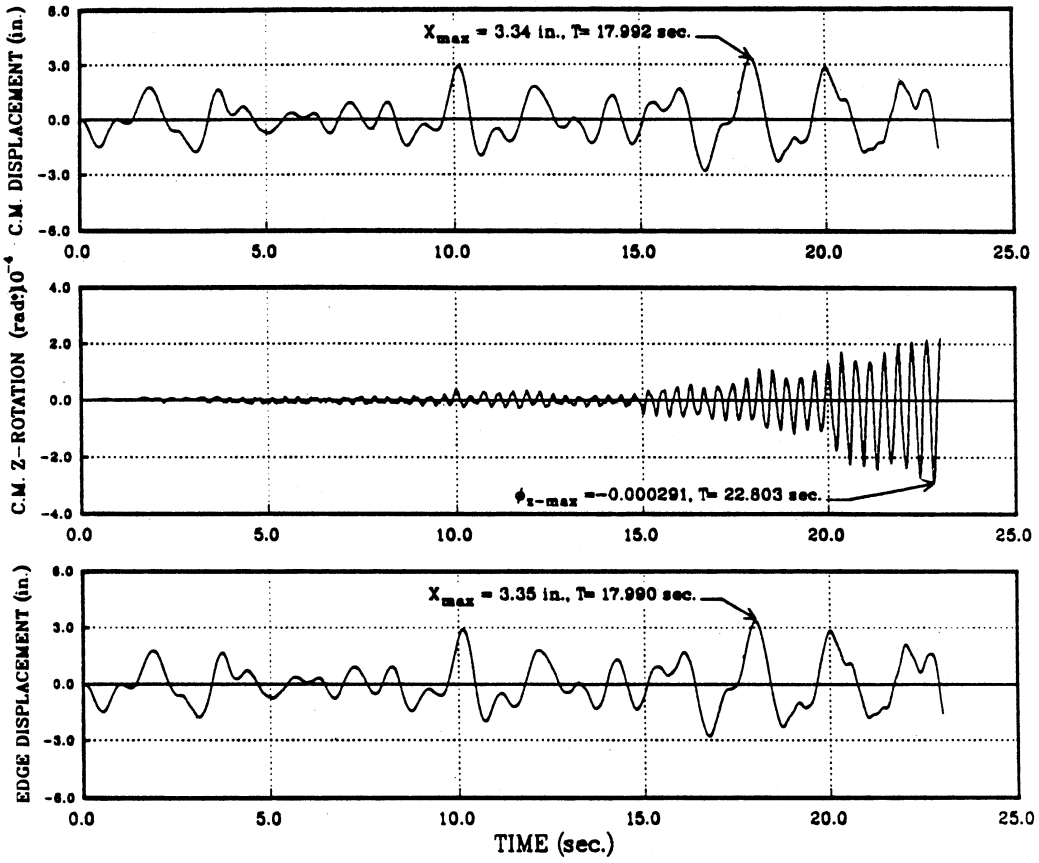

Figure 6.52: (e)5th Floor Center of Mass Displacement and Rotation, Edge Displacement Time History of Five Story Symmetrical Building Subjected to 1985 Mexico SCT Earthquake : $P = 0.6P_y$ (Continue)

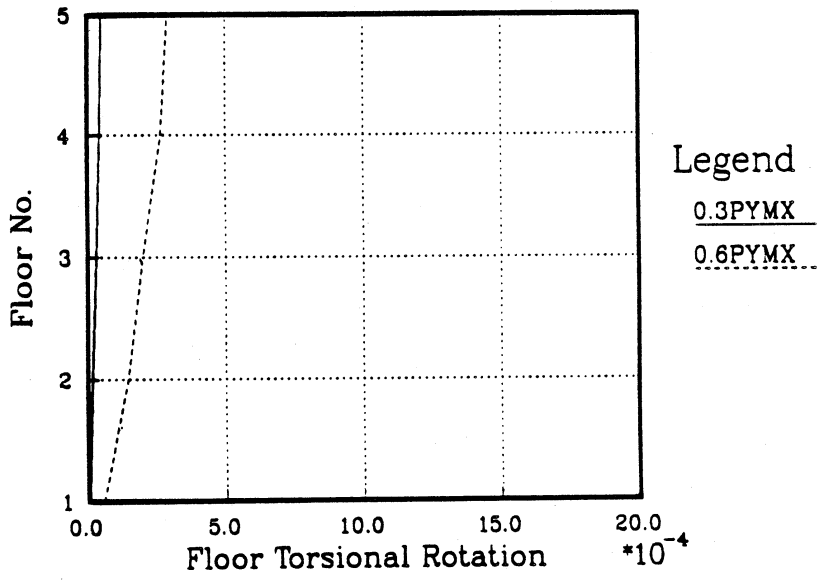

Figure 6.53: Envelope of Center of Mass Rotation of Five Story Symmetrical Building Subjected to 1985 Mexico SCT Earthquake

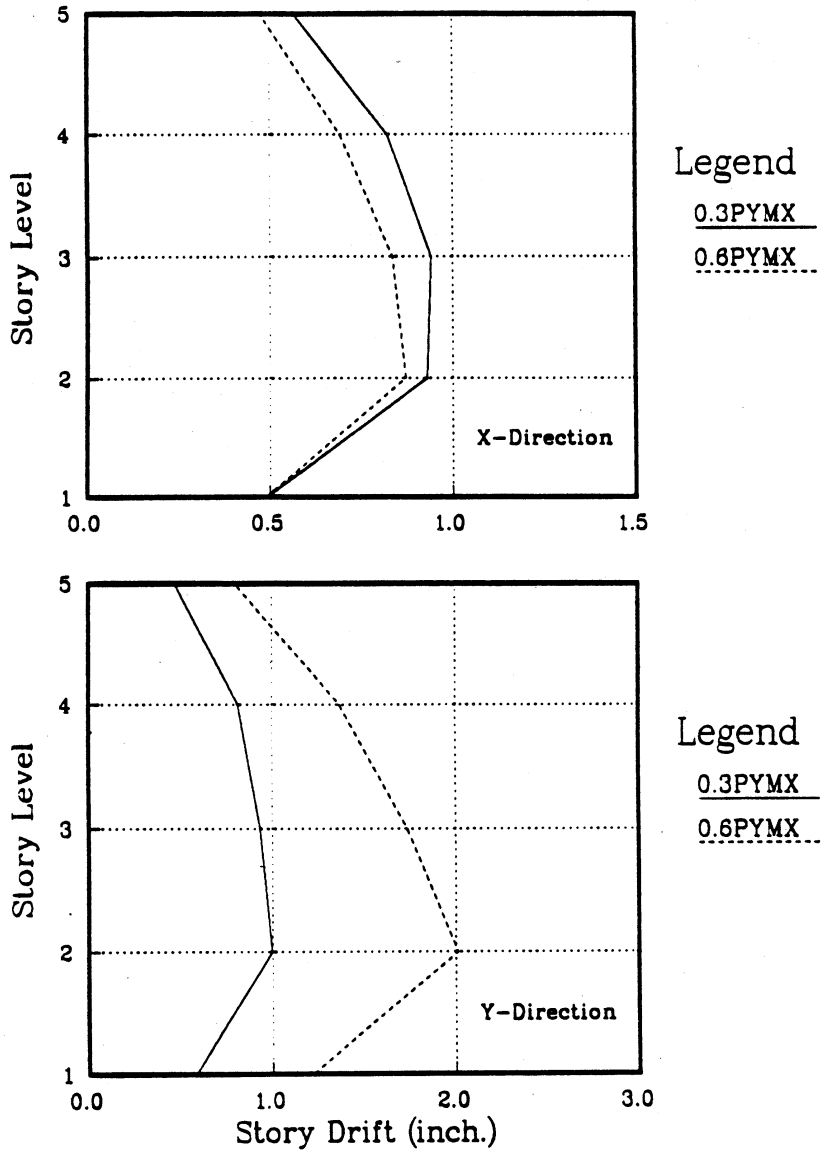

Figure 6.54: Comparison of Maximum Story Drift of Five Story Symmetrical Building Subjected to 1985 Mexico SCT Earthquake

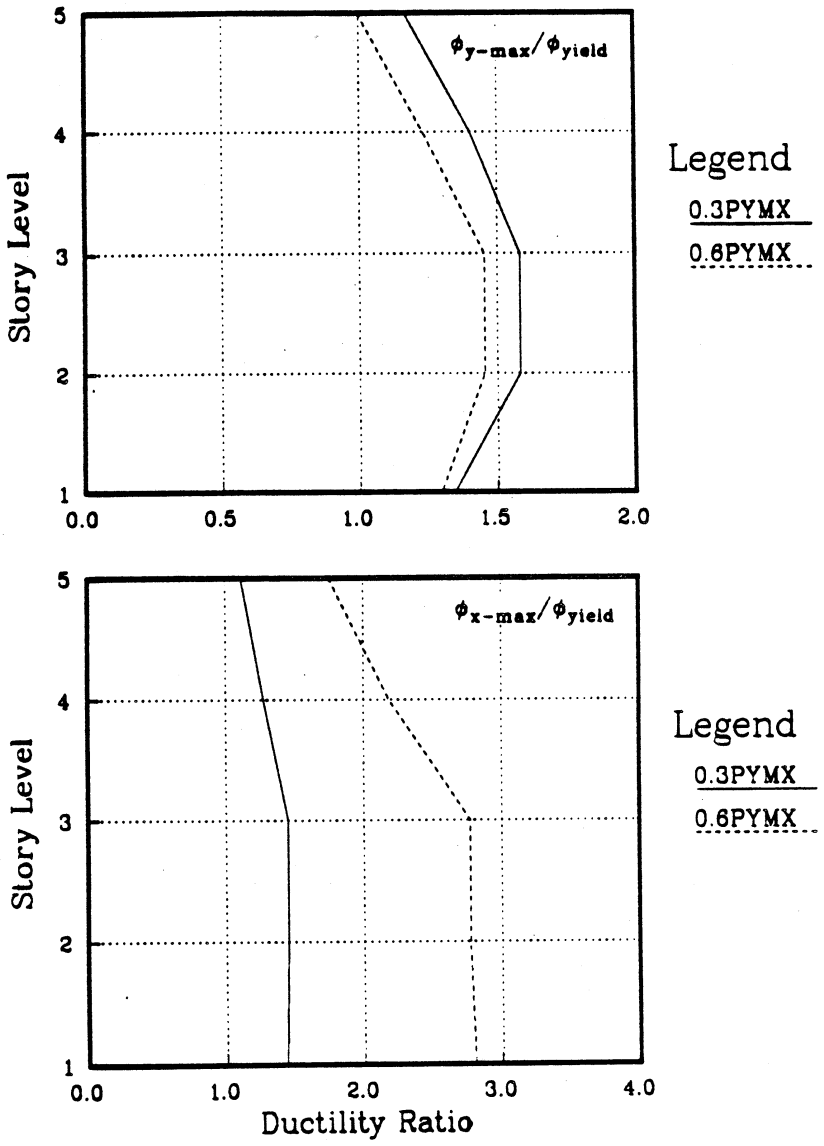

Figure 6.55: Envelope of Maximum Column Ductility Ratio of Five Story Symmetrical Building Subjected to 1985 Mexico SCT Earthquake

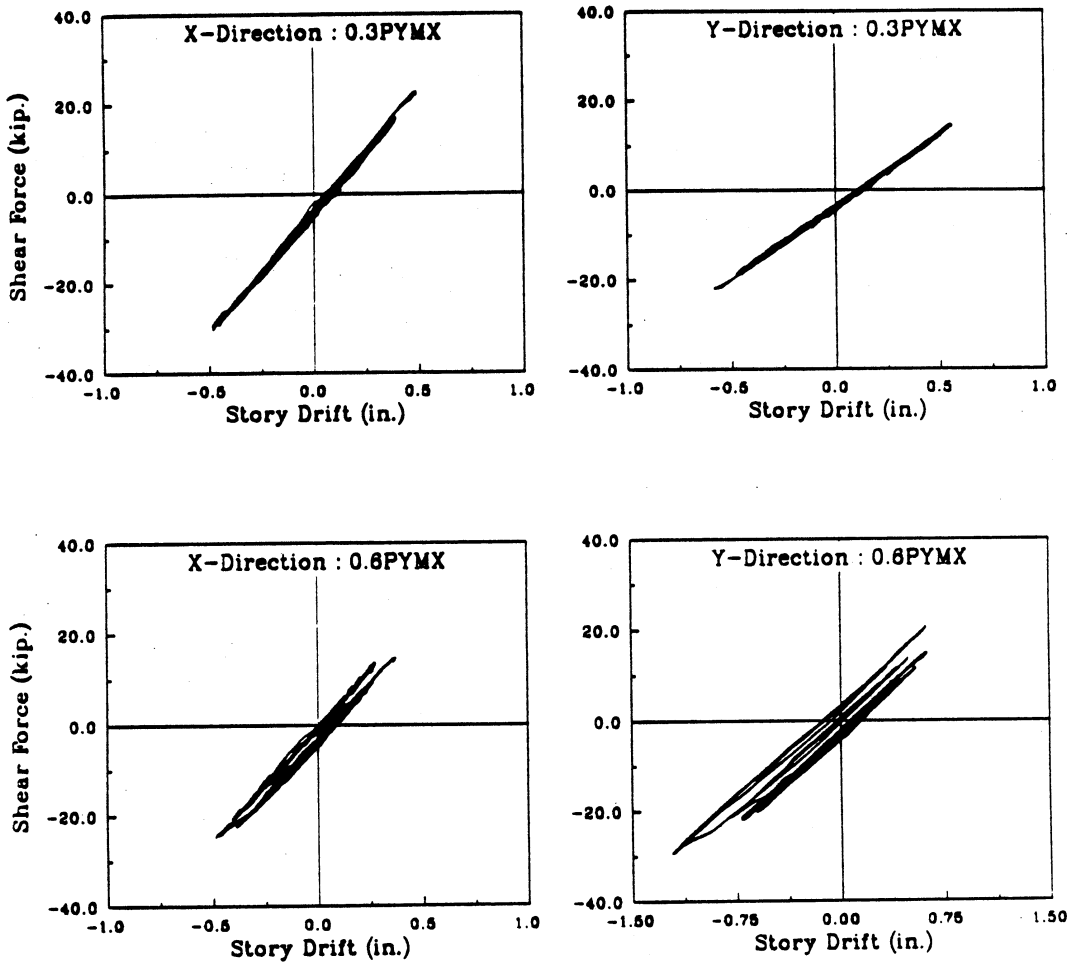

Figure 6.56: Shear Force Hysteresis of Column 20 of Five Story Symmetrical Building Subjected to 1985 Mexico SCT Earthquake : 1st Story

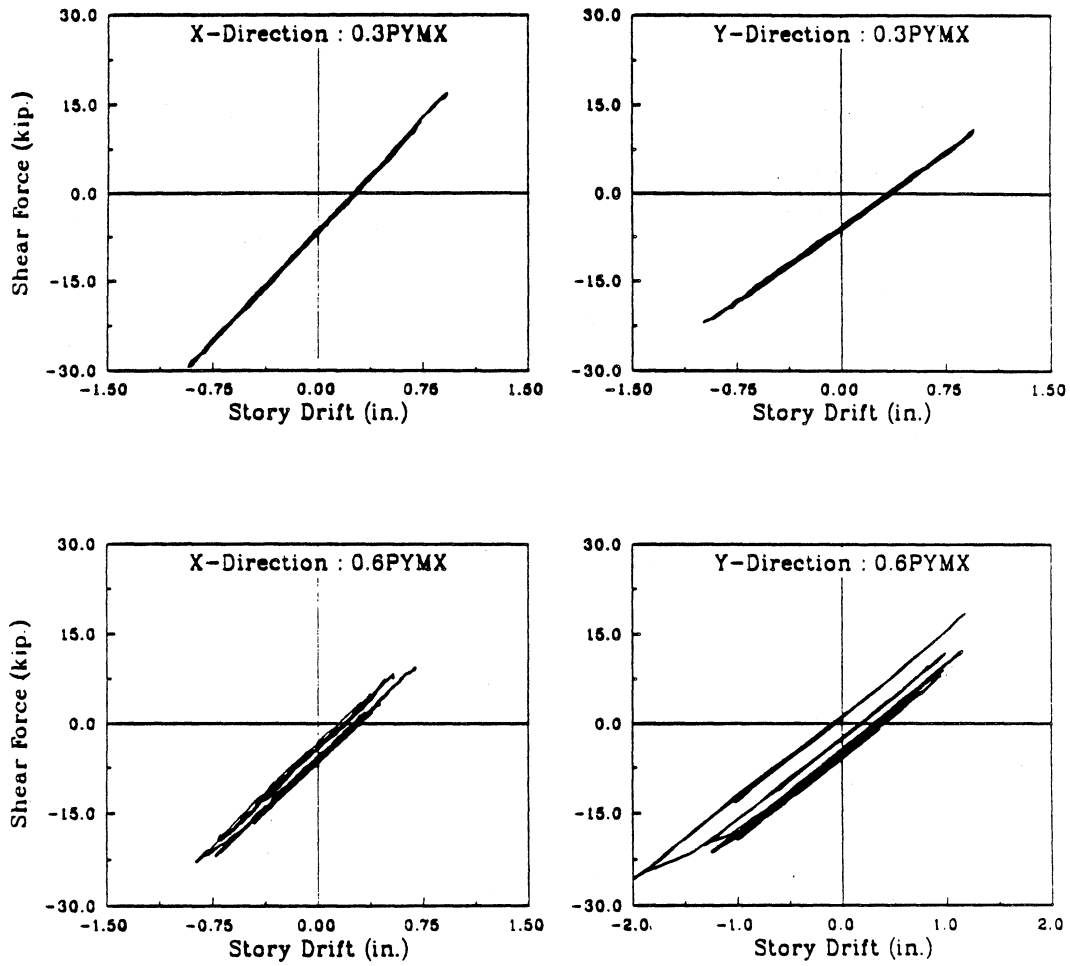

Figure 6.57: Shear Force Hysteresis of Column 16 of Five Story Symmetrical Building Subjected to 1985 Mexico SCT Earthquake : 2nd Story

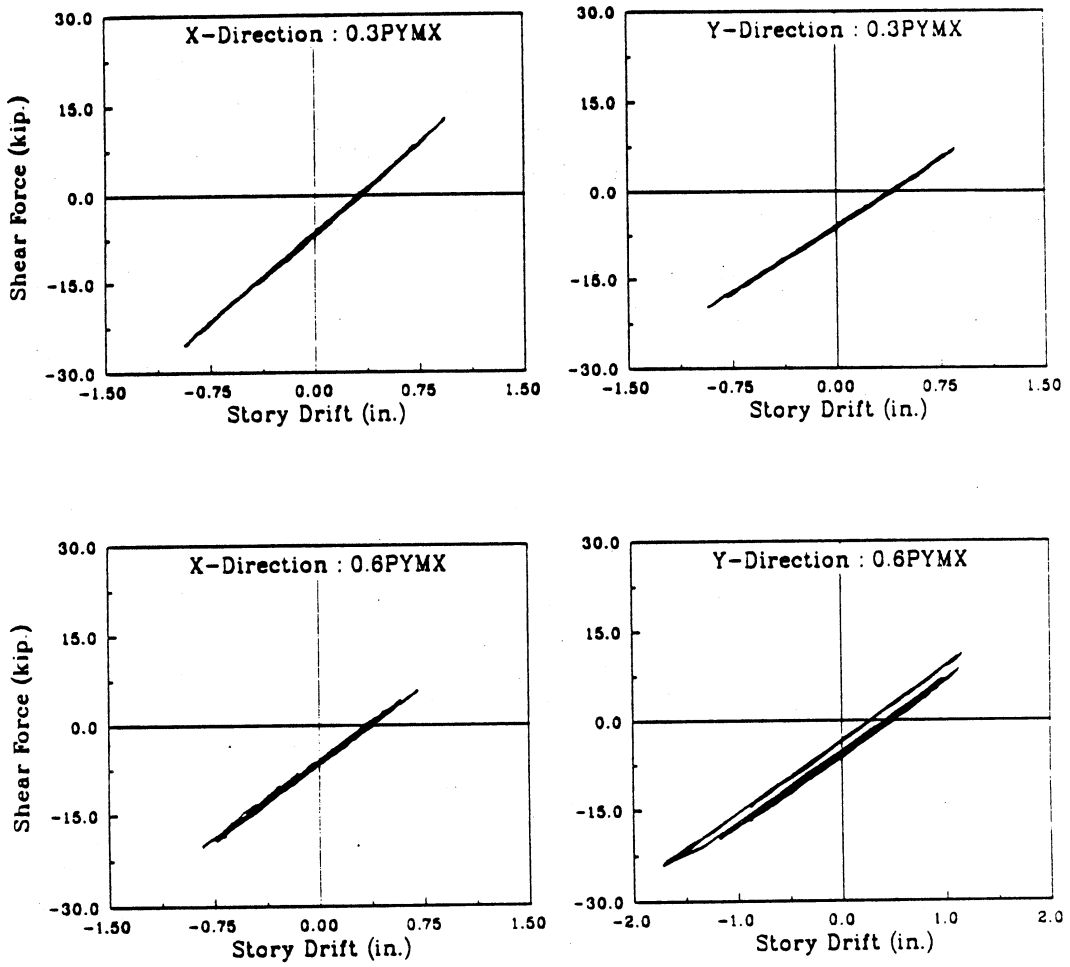

Figure 6.58: Shear Force Hysteresis of Column 12 of Five Story Symmetrical Building Subjected to 1985 Mexico SCT Earthquake : 3rd Story

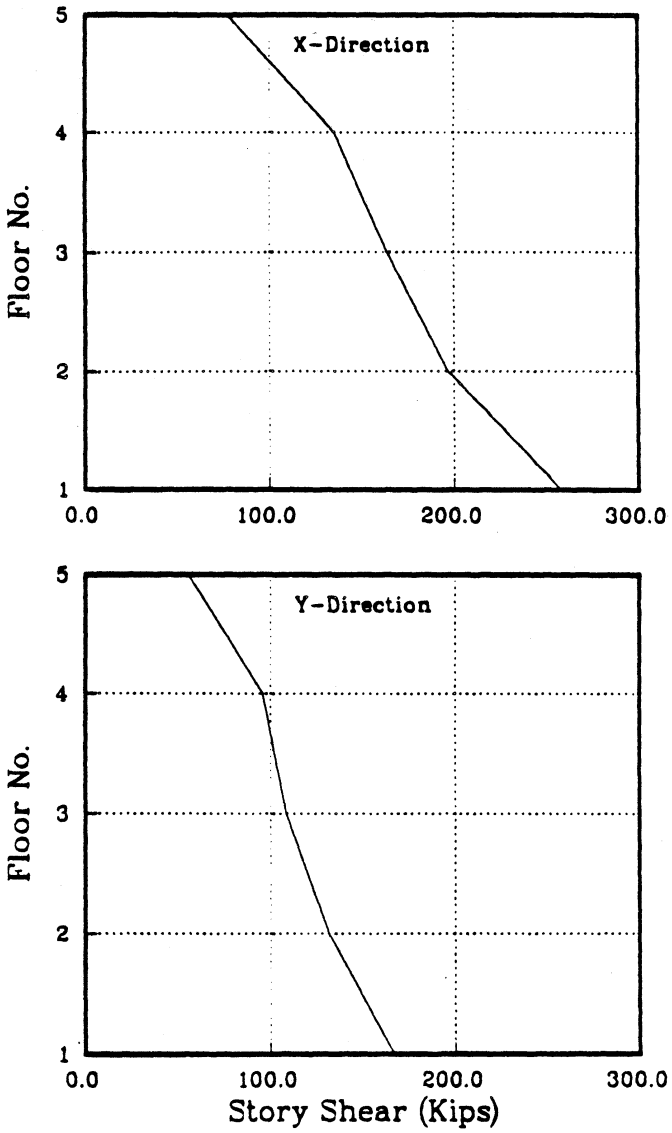

Figure 6.59: Comparison of Maximum Story Shear of Five Story Symmetrical Building Subjected to 0.68 g 1940 El Centro Earthquake

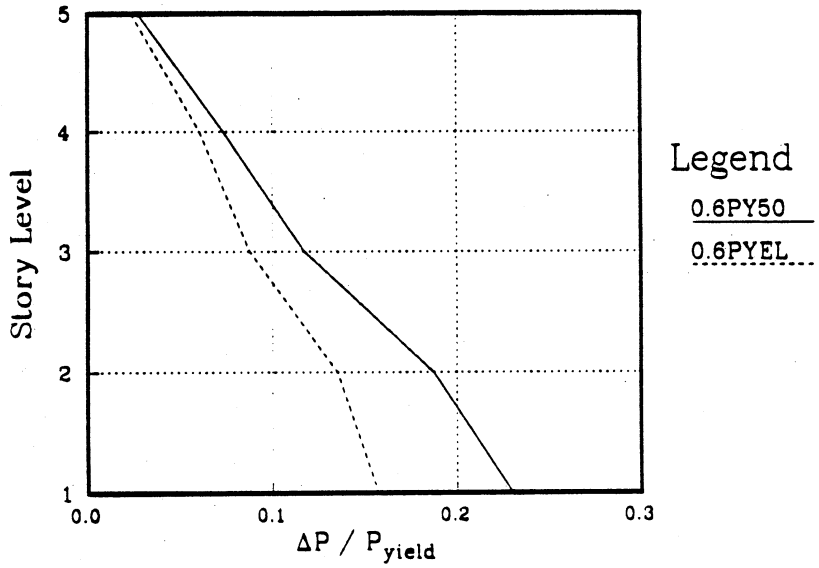

Figure 6.60: Maximum Increase of Column Axial Force of Five Story Symmetrical Building : Cases 0.6PY50 and 0.6PYEL

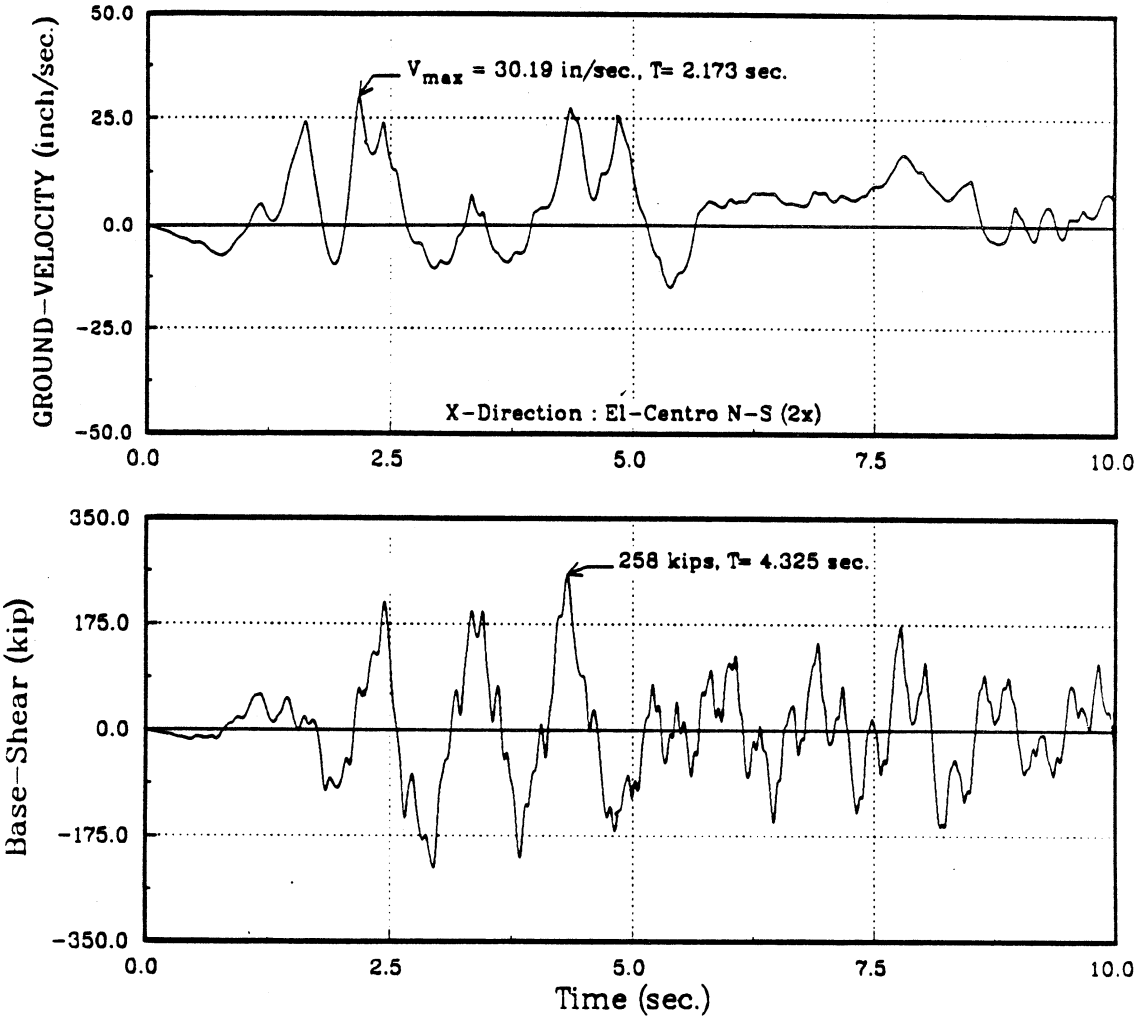

Figure 6.61: (a)X-Direction Input Ground Velocity and Base Shear Time History in the Principal Directions of Five Story Symmetrical Building Subjected to 0.68 g 1940 El Centro Earthquake

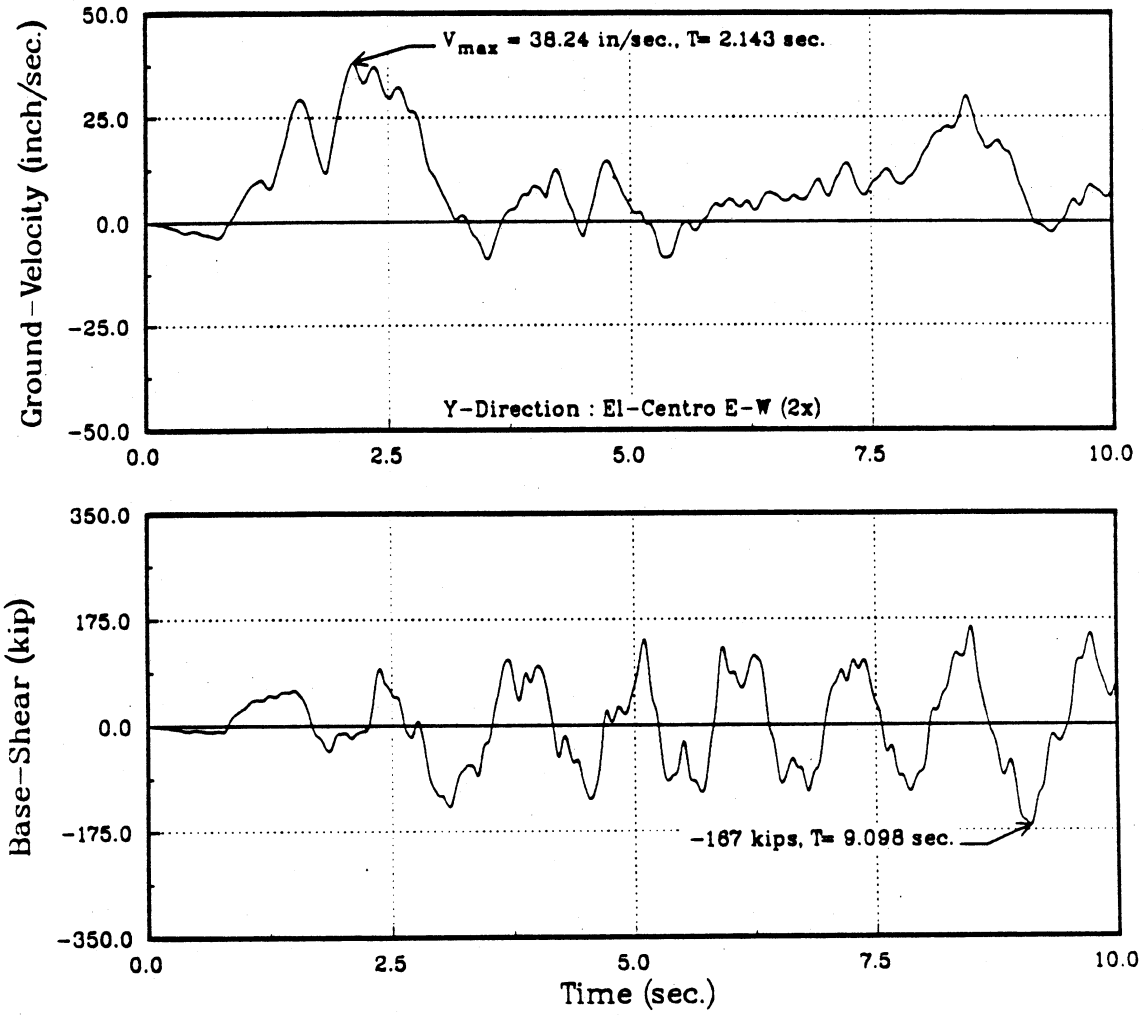

Figure 6.61: (b) Y-Direction Input Ground Velocity and Base Shear Time History in the Principal Directions of Five Story Symmetrical Building Subjected to 0.68 g 1940 El Centro Earthquake (Continue)

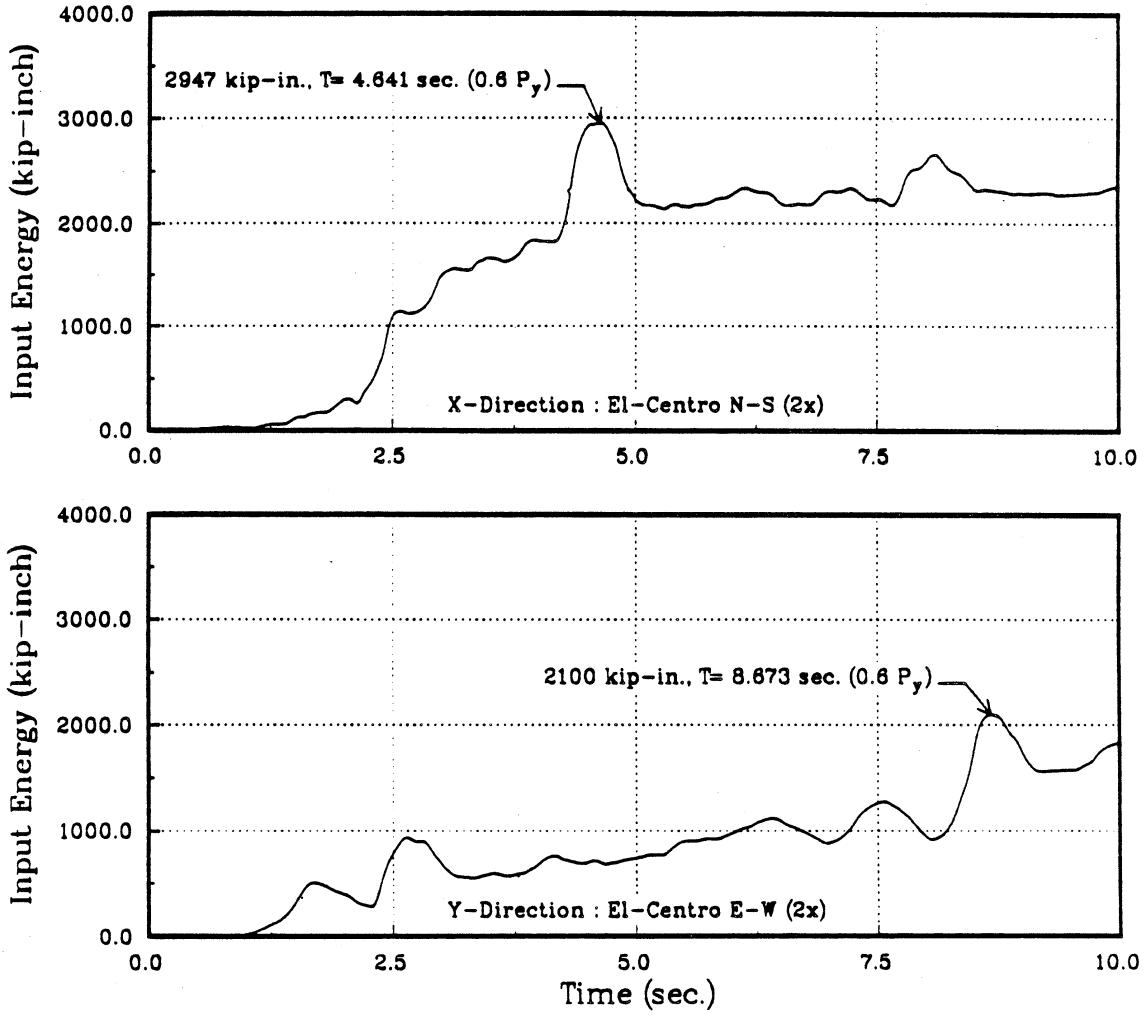

Figure 6.62: Absolute Input Energy Time History in the Principal Directions of Five Story Symmetrical Building Subjected to 0.68 g 1940 El Centro Earthquake

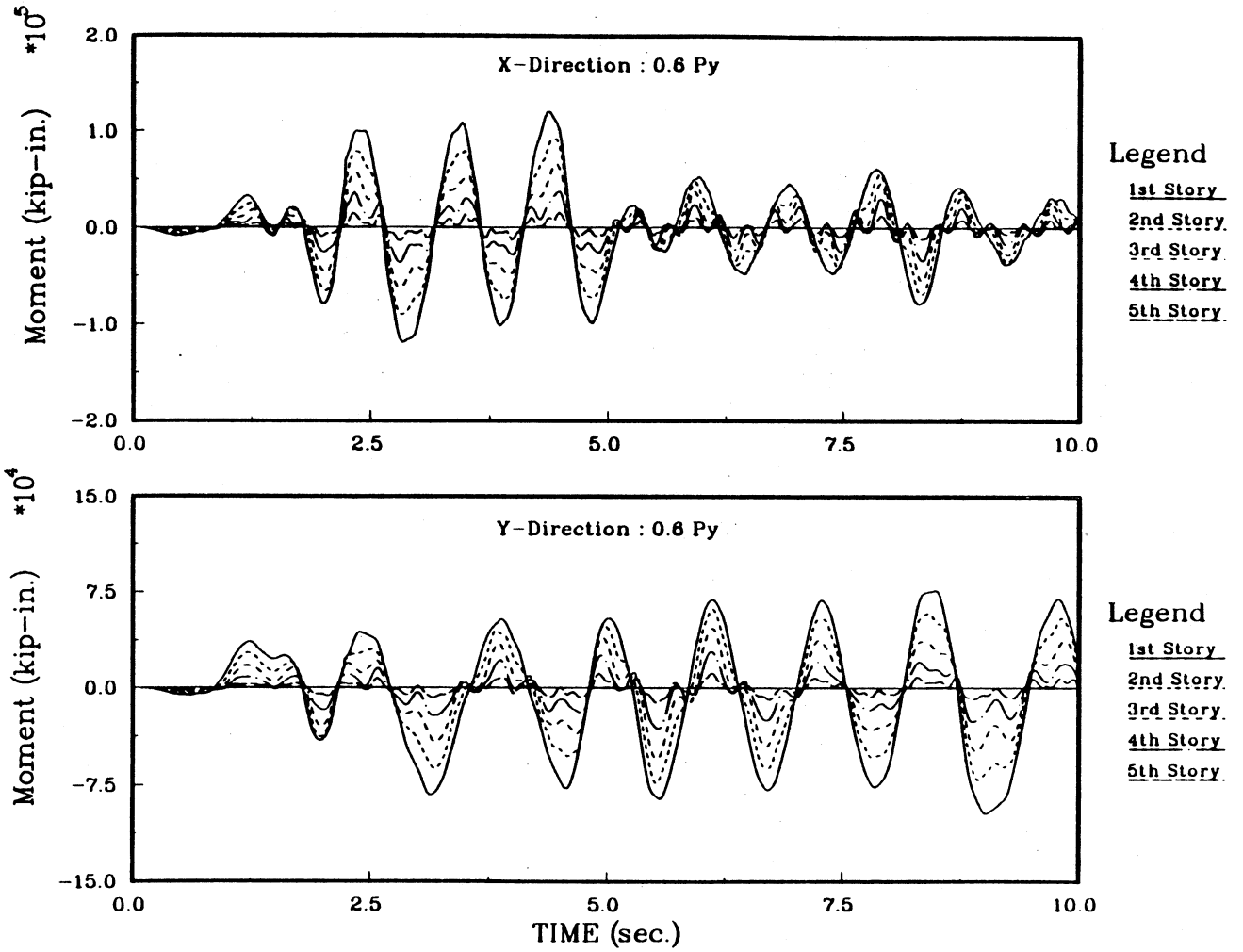

Figure 6.63: Overturning Moment Time History of Five Story Symmetrical Building Subjected to 0.68 g 1940 El Centro Earthquake

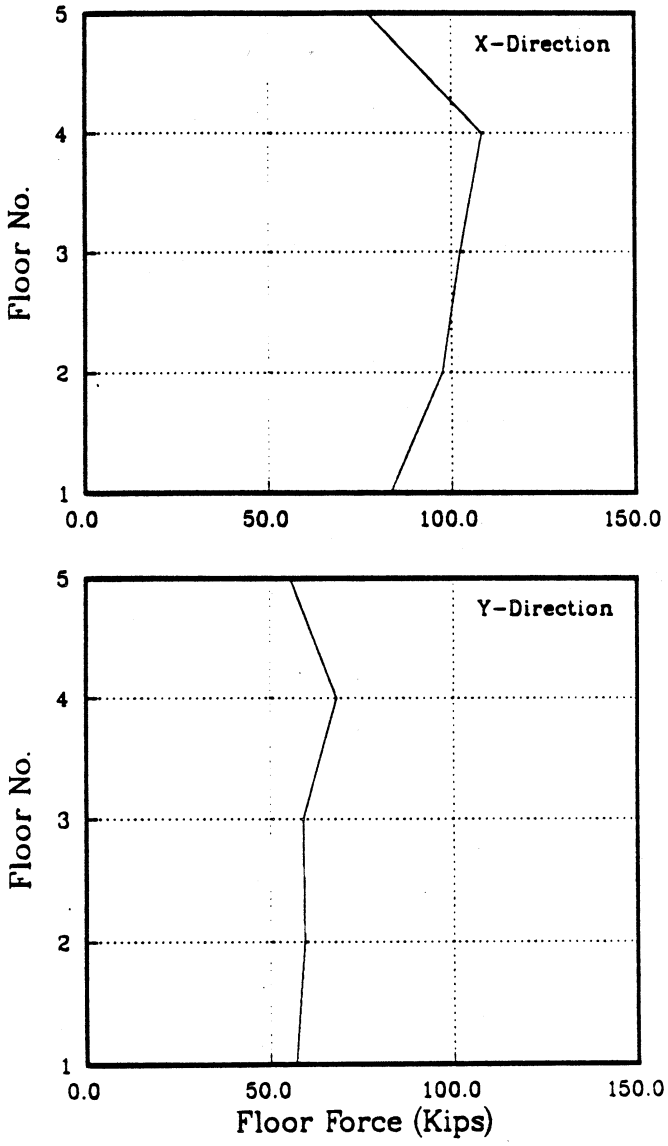

Figure 6.64: Comparison of Maximum Floor Force of Five Story Symmetrical Building Subjected to 0.68 g 1940 El Centro Earthquake

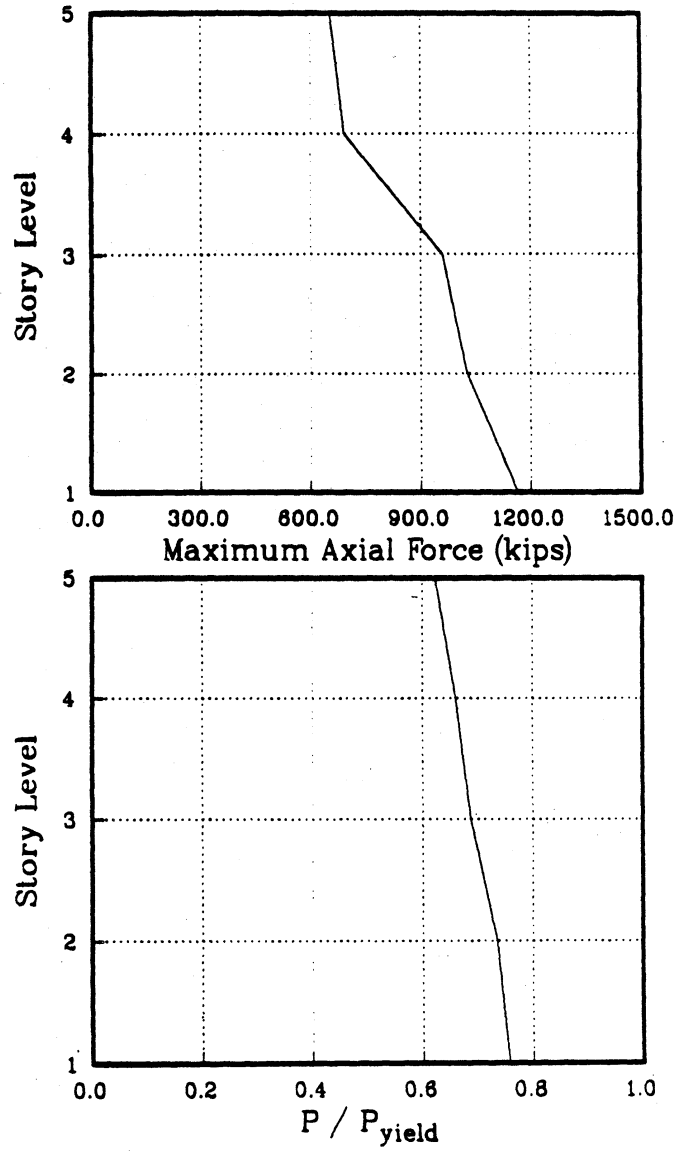

Figure 6.65: Comparison of Maximum Column Axial Force of Five Story Symmetrical Building Subjected to 0.68 g 1940 El Centro Earthquake

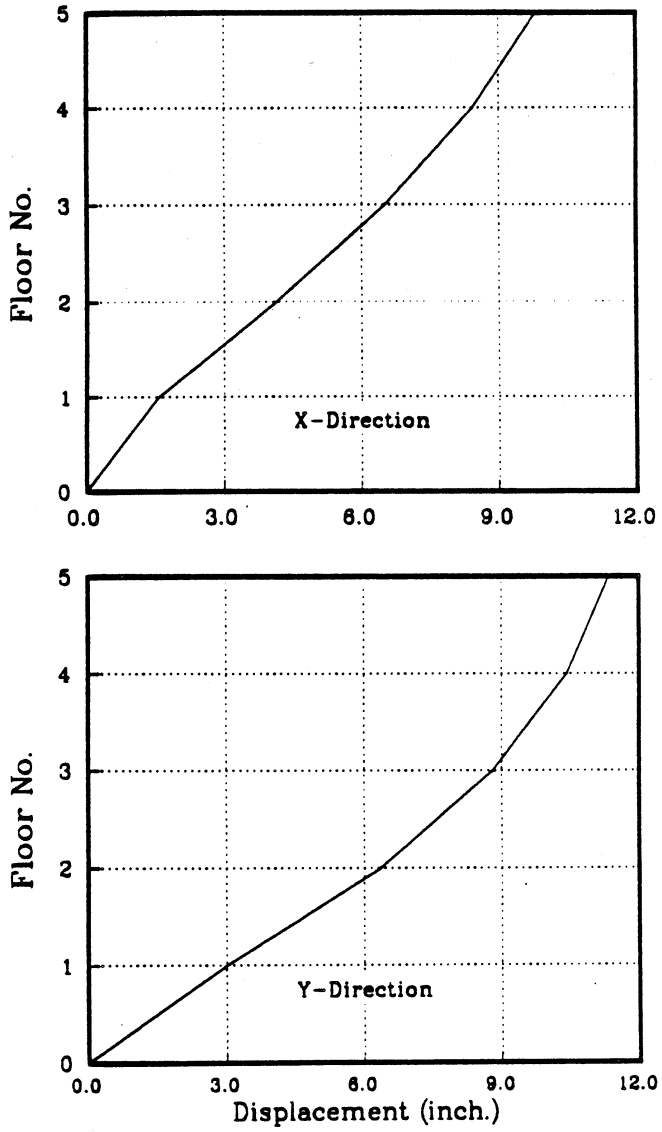

Figure 6.66: Comparison of Maximum Displacement of Five Story Symmetrical Building Subjected to 0.68 g 1940 El Centro Earthquake

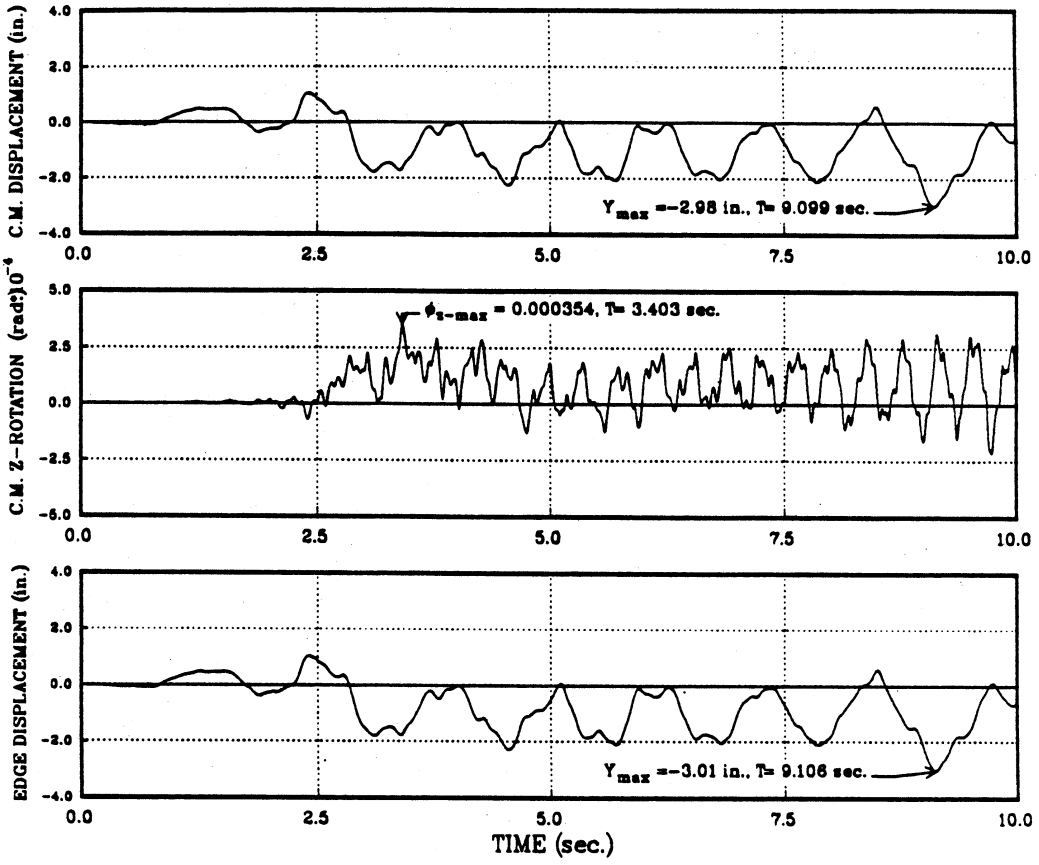

Figure 6.67: (a)1st Floor Center of Mass Displacement and Rotation, Edge Displacement Time History of Five Story Symmetrical Building Subjected to 0.68 g 1940 El Centro Earthquake : $P = 0.6P_y$

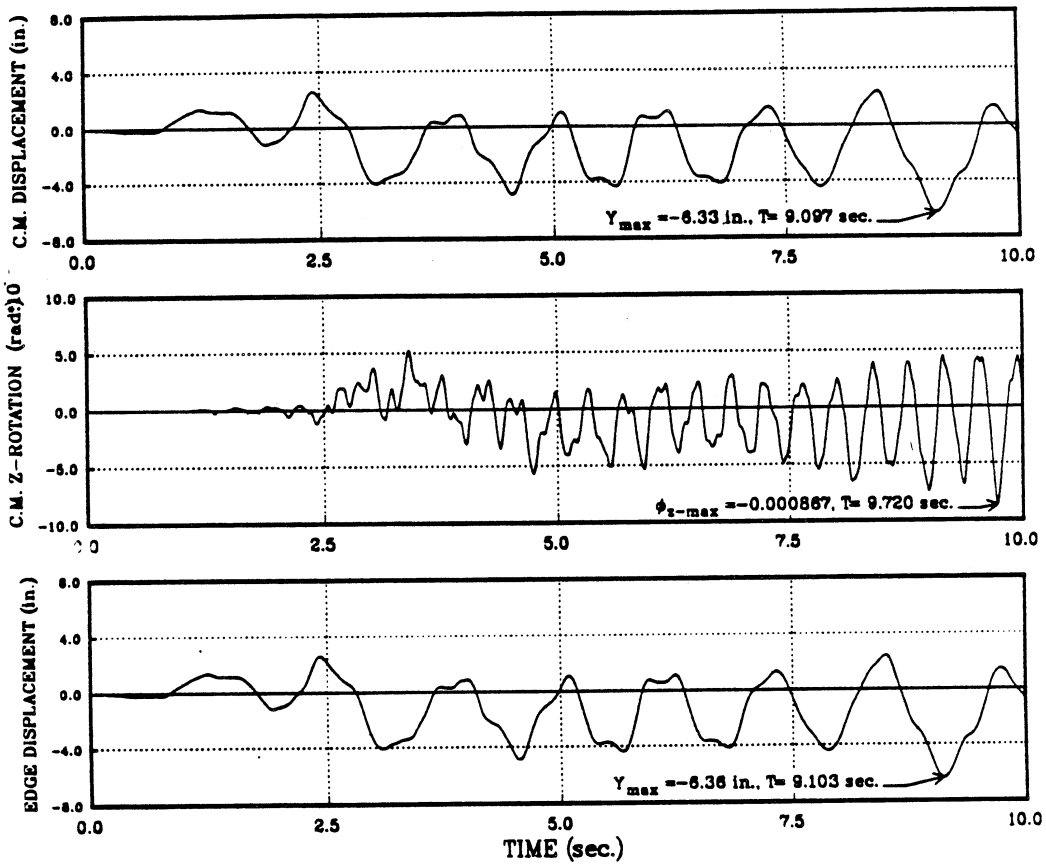

Figure 6.67: (b)2nd Floor Center of Mass Displacement and Rotation, Edge Displacement Time History of Five Story Symmetrical Building Subjected to 0.68 g 1940 El Centro Earthquake : $P = 0.6P_y$ (Continue)

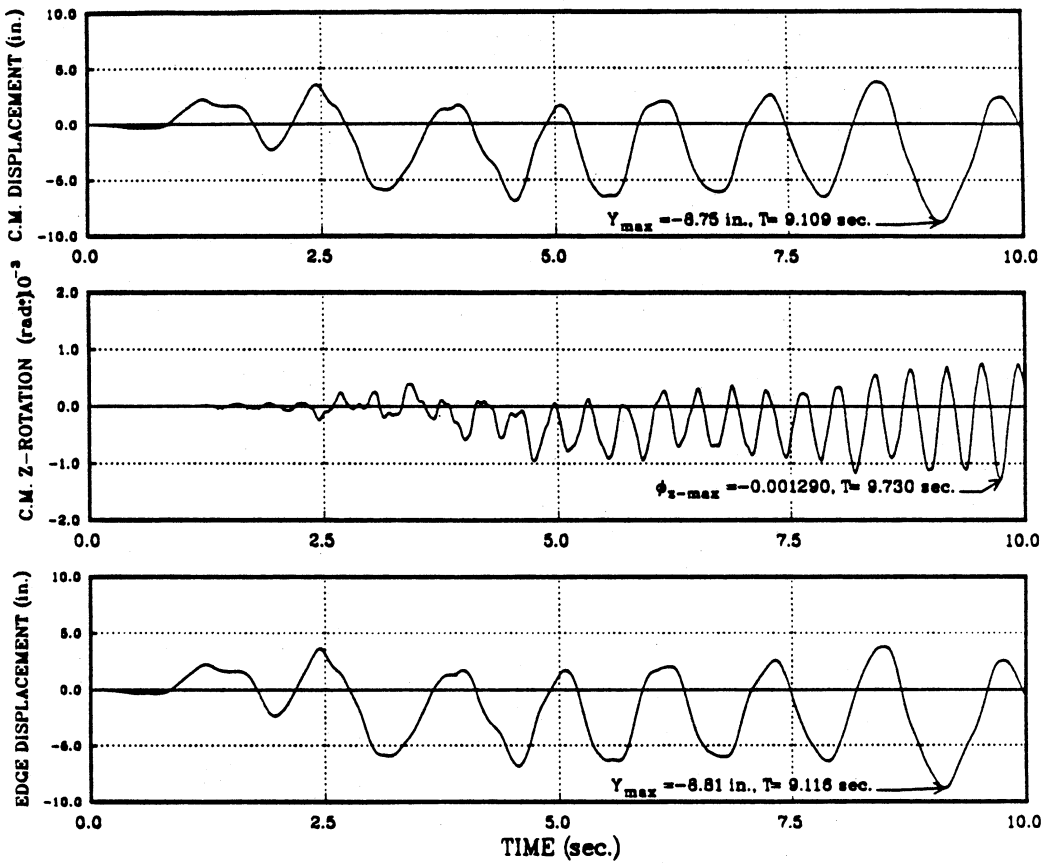

Figure 6.67: (c)3rd Floor Center of Mass Displacement and Rotation, Edge Displacement Time History of Five Story Symmetrical Building Subjected to 0.68 g 1940 El Centro Earthquake : $P = 0.6P_y$ (Continue)

placement Time History of Five Story Symmetrical Building Subjected to 0.68 g 1940 El Centro Earthquake : $P = 0.6P_y$ (Continue)

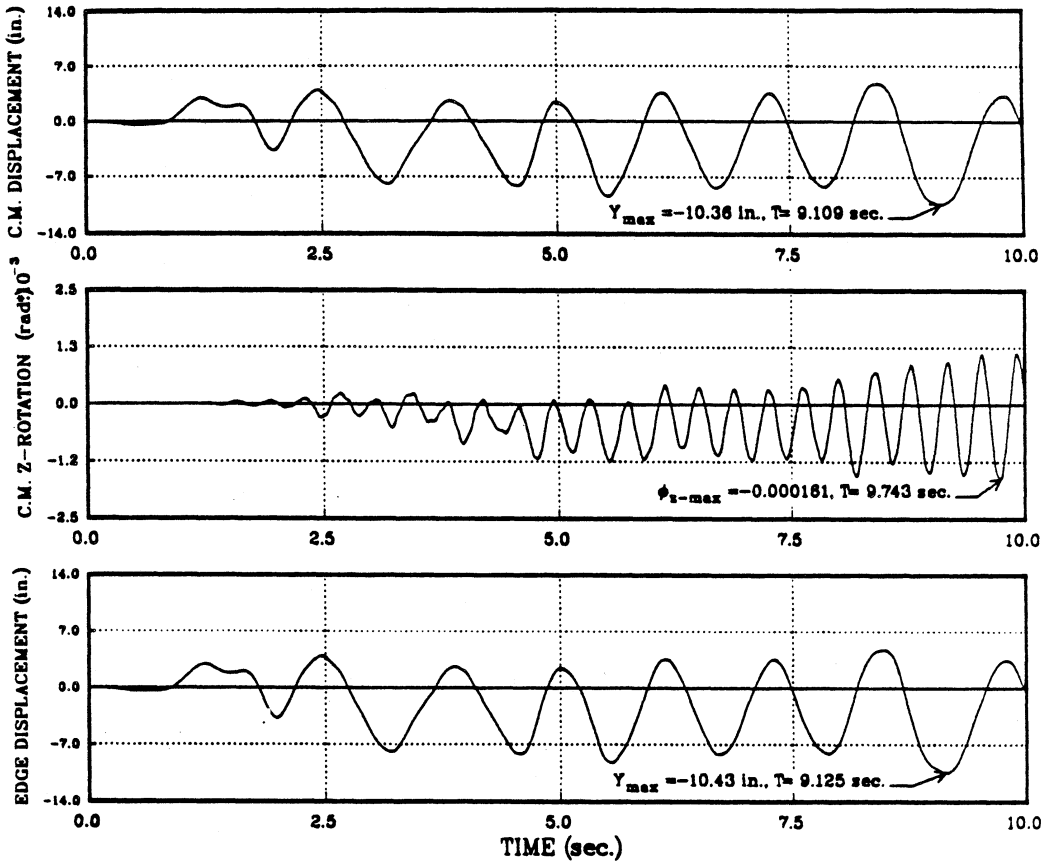

Figure 6.67: (d)4th Floor Center of Mass Displacement and Rotation, Edge Displacement Time History of Five Story Symmetrical Building Subjected to 0.68 g 1940 El Centro Earthquake : $P = 0.6P_y$ (Continue)

Figure 6.67: (d)4th Floor Center of Mass Displacement and Rotation, Edge Displacement Time History of Five Story Symmetrical Building Subjected to 0.68 g 1940 El Centro Earthquake : $P = 0.6P_y$ (Continue)

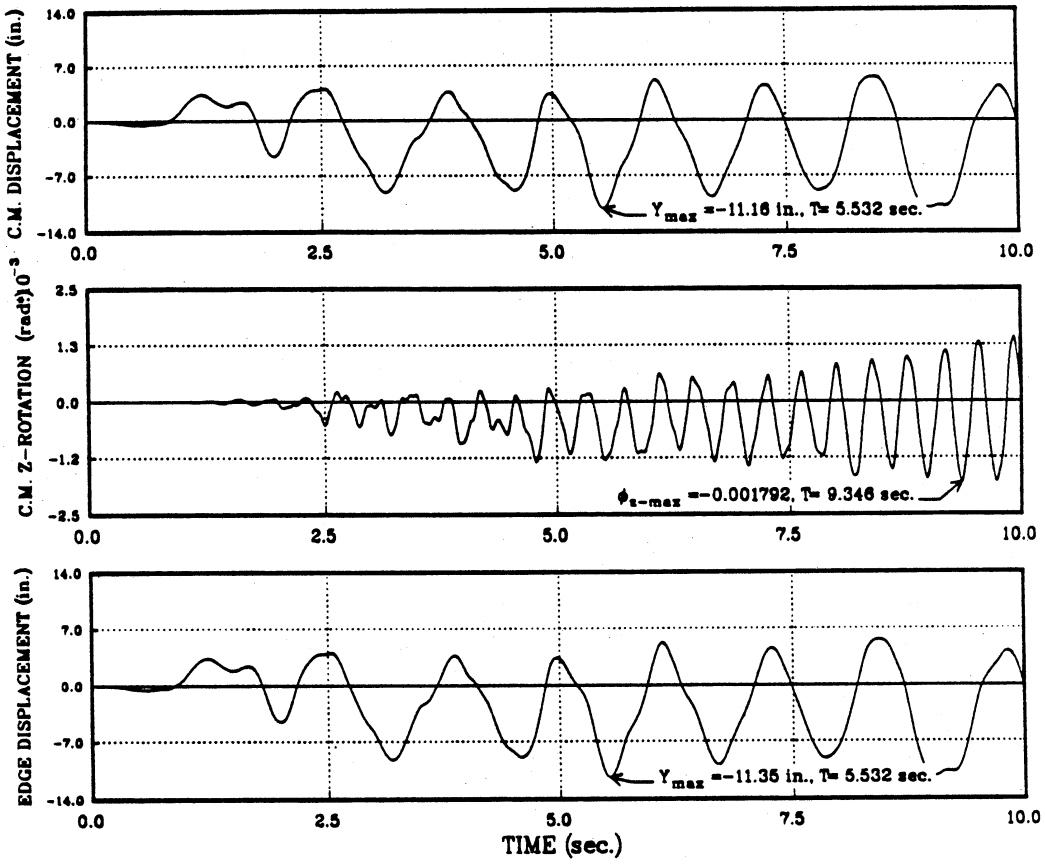

Figure 6.67: (e)5th Floor Center of Mass Displacement and Rotation, Edge Displacement Time History of Five Story Symmetrical Building Subjected to 0.68 g 1940 El Centro Earthquake : $P = 0.6P_y$ (Continue)

Figure 6.67: (e)5th Floor Center of Mass Displacement and Rotation, Edge Displacement Time History of Five Story Symmetrical Building Subjected to 0.68 g 1940 El Centro Earthquake : $P = 0.6P_y$ (Continue)

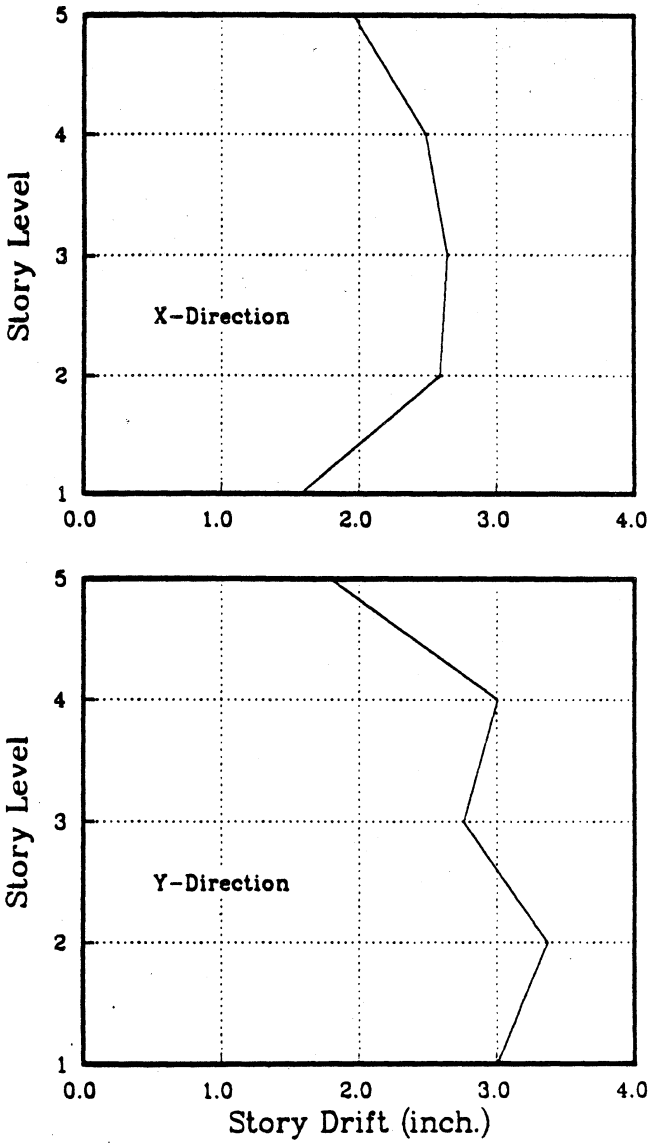

Figure 6.68: Comparison of Maximum Story Drift of Five Story Symmetrical Building Subjected to 0.68 g 1940 El Centro Earthquake

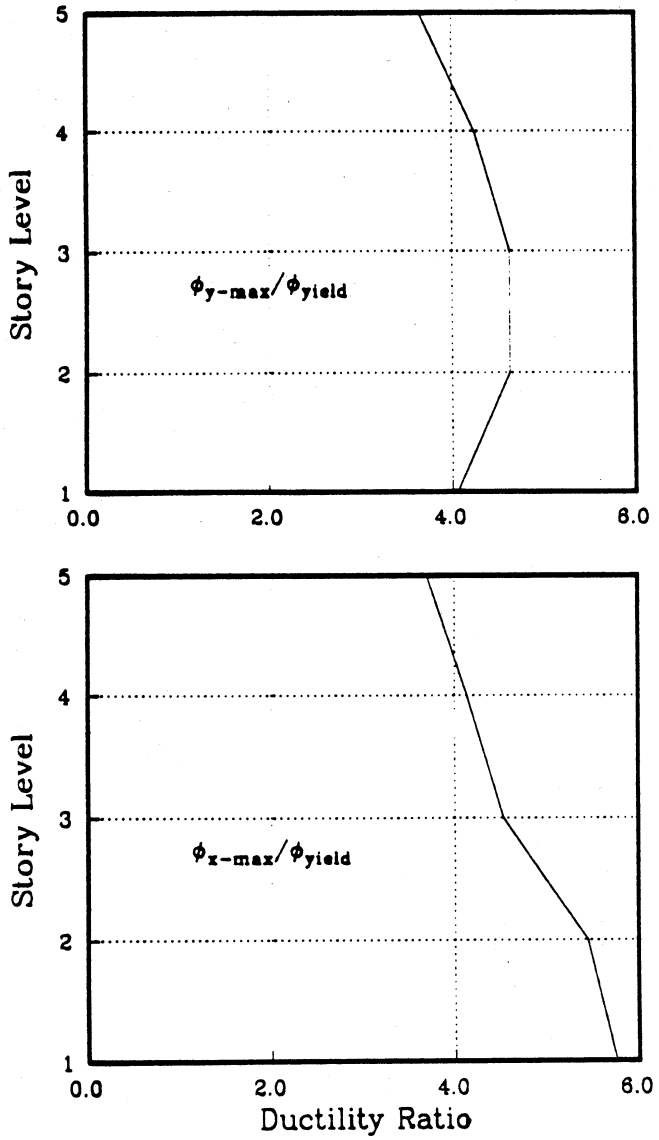

Figure 6.69: Envelope of Maximum Column Ductility Ratio of Five Story Symmetrical Building Subjected to 0.68 g 1940 El Centro Earthquake

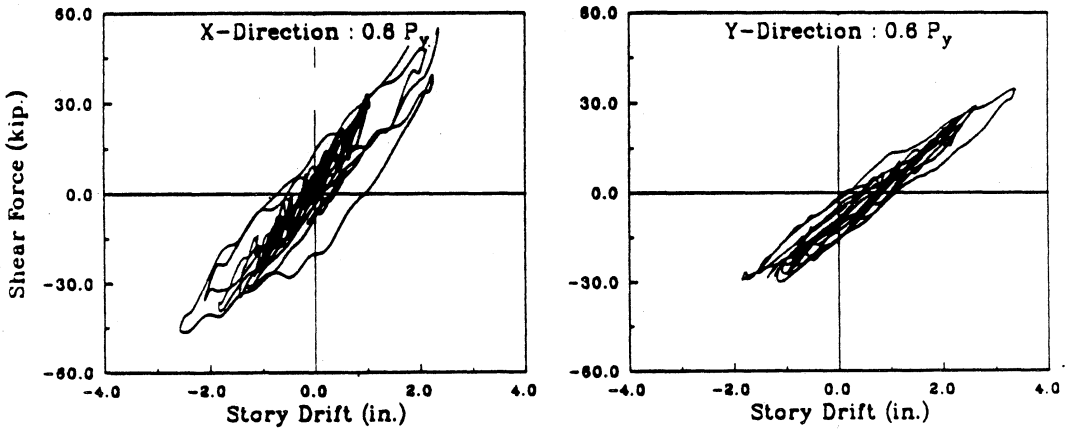

Figure 6.70: Shear Force Hysteresis of Column 16 of Five Story Symmetrical Building Subjected to 0.68 g 1940 El Centro Earthquake : 2nd Story

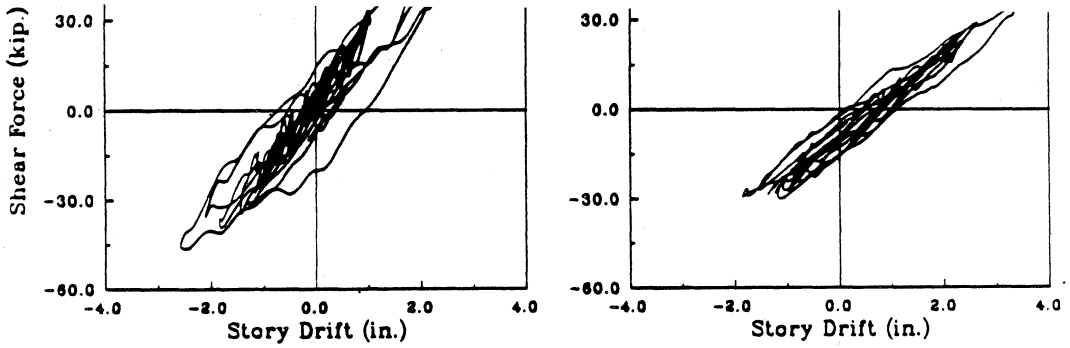

Figure 6.70: Shear Force Hysteresis of Column 16 of Five Story Symmetrical Building Subjected to 0.68 g 1940 El Centro Earthquake : 2nd Story

BIBLIOGRAPHY

BIBLIOGRAPHY

[1] Penzien, J., 'Dynamic Response of Elasto-Plastic Frames', Journal of the Structural Division, ASCE, Vol. 86, No. ST7, July 1960, pp. 81-94.

[2] Veletsos, A.S., and Newmark, N.M., 'Effect of Inelastic Behavior of the Response of Simple System to Earthquake Motions', Proceedings, 2nd World Conference on Earthquake Engineering, Japan, Vol. II, 1960, pp. 895-912.

[3] Jennings, P.C., 'Equivalent Viscous Damping for Yielding Structures', Journal of the Engineering Mechanics Division, ASCE, Vol. 94, No. EM1, February 1968, pp. 103-116.

[4] Kanaan, A.E., and Powell, G.H.,'General Purpose Program for Inelastic Dynamic Responses of Plane Structures', Earthquake Engineering Research Center, University of California, Berkeley, Report No. EERC 73-6, April, 1973.

[5] Powell, G.H., 'Drain-2D User's Guide', Earthquake Engineering Research Center, University of California, Berkeley, Report No. EERC 73-22, October, 1973.

[6] Tang, X., and Goel, S.C. 'DRAIN-2DM - Technical Notes and User's Guide', Research Report No. UMCE 88-1 Department of Civil Engineering, The University of Michigan, Ann Arbor, Michigan, January, 1988.

[7] Oughourlian, C.V., and Powell, G.H., 'ANSR-III, General Purpose Computer Program for Nonlinear Structural Analysis', Earthquake Engineering Research Center, University of California, Berkeley, Report No. EERC 82-21, November, 1982.

[8] Mallet, R.H., and Marcal, P.V., 'Finite Element Analysis of Nonlinear Structures', Journal of the Structural Division, ASCE, Vol. 94, No. ST9, September 1968, pp. 2081-2105.

[9] Yang, T.Y., and Saigal, S., 'A Simple Element for Static and Dynamic Response of Beams with Material and Geometrical Nonlinearities', International Journal for Numerical Methods in Engineering, Vol.20, No.5, May 1984, pp.851-867.

[10] Cichon, C., 'Large Displacement In-Plane Analysis of Elastic-Plastic Frames', Computer and Structures, Vol.19, No.5/6, 1984, pp.737-745.

[11] Holzer, S.M., and Somers, A.E., Jr., 'Nonlinear Model/Solution Process : Energy Approach', Journal of the Engineering Mechanics Division, ASCE, Vol. 103, No. EM4, August 1977, pp. 629-647.

[12] Kang, Y.J., and Scordelis, A.C., 'Nonlinear Analysis of Prestressed Concrete Frames', Journal of the Structural Division, ASCE, Vol. 106, No. ST2, February 1980, pp. 445-460.

[13] Rajasekaran, S., and Murray, D.W., 'Finite Element Solution of Inelastic Beam Equation', Journal of the Structural Division, ASCE, Vol. 99, No. ST6, June 1973, pp. 1025-1041.

[14] Jain, A.K., and Goel, S.C., 'Model for Steel Members Subjected to Cyclic Buckling and Cyclic End Moments and Buckling-User's Guide for EL9 and EL10 of DRAIN-2D', Report No. UMEE-78R6, Department of Civil Engineering, The University of Michigan, Ann Arbor, Michigan, December 1988.

[15] Kassimali, A., 'Large Deformation Analysis of Elastic-Plastic Frames', Journal of the Structural Division, ASCE, Vol. 109, No. 8, August 1983, pp. 1869-1886.

[16] Ueda.Y., Yamakawa, T., and Akamatsu, T., 'A New Theory on Elastic Plastic Analysis of Frames Structures', Technology Reports, Osaka University, Vol. 19, No. 875, March 1969, pp. 263-276.

[17] Inoue, K., and Ogawa, K., 'Nonlinear Analysis of Strain-Hardening Frames Subjected to Variable Repeated Loading', Technology Reports, Osaka University, Vol. 24, No. 1222, October 1974, pp. 763-781.

[18] Chen, P.F., and Powell, G.H., 'Generalized Plastic Hinge Concepts for 3D Beam-Column Elements', Earthquake Engineering Research Center, University of California, Berkeley, Report No. EERC 82-20, November, 1982.

[19] Clough, R.W., and Benuska, K.L., 'FHA Study of Seismic Design Criteria for High-Rise Buildings', HUD ST-3, August 1966.

[20] Saafan, S.A., 'Nonlinear Behavior of Structural Plane Frames', Journal of the Structural Division, ASCE, Vol. 89, No. ST4, August 1963, pp. 557-579.

[21] Galambos, T.V., and Van Kuren, R.C., 'Beam Column Experiments', Journal of the Structural Division, ASCE, Vol. 90, No. ST2, April 1964, pp. 223-256.

[22] Popov, E.P., Bertero, V.V., and Chandramouli, S., 'Hysteretic Behavior of Steel Columns', Earthquake Engineering Research Center, University of California, Berkeley, Report No. EERC 75-11, September, 1975.

[23] Ayre, R.S., 'Interconnection of Translational and Torsional Vibrations in Buildings', Bulletin of the Seismological Society of America, Vol. 28, No. 2, April 1938, pp. 89-130.

[24] Douglas, B.M., and Trabert, T.E., 'Coupled Torsional Dynamics Analysis of Multistory Buildings', Bulletin of the Seismological Society of America, Vol. 63, No. 3, June 1973, pp. 1025-1039.

[25] Hart, G.C., DiJulio, R.M., Jr., and Lew, M., 'Torsional Response of High-Rise Buildings', Journal of the Structural Division, ASCE, Vol. 101, No. ST2, February 1975, pp. 397-416.

[26] Housner, G.W., and Outinen, H., 'The effects of Torsional Oscillations on Earthquake Stresses', Bulletin of the Seismological Society of America, Vol. 48, No. 2, July 1958, pp. 221-229.

[27] Shepherd, R., and Donald, R.A.H, 'Seismic Response of Torsionally Unbalanced Buildings', Journal of Sound and Vibration, Vol.6, No. 1, 1967, pp. 20-37.

[28] Medearis, K., 'Coupled Bending and Torsional Oscillations of a Modern Skyscraper', Bulletin of the Seismological Society of America, Vol. 56, No. 4, August 1966, pp. 937-946.

[29] Douglas, B.M., and Trabert, T., 'Coupled Torsional Dynamic Analysis of a Multistory Building', Bulletin of the Seismological Society of America, Vol. 63, No. 3, June 1973, pp. 1025-1039.

[30] Shiga, T., 'Torsional Vibrations of Multi-Storied Buildings', Proceeding of the Third World Conference on Earthquake Engineering, Vol. 2, Auckland and Wellington, New Zealand, 1965, pp. 569-584.

[31] Kan, C.L., and Chopra, A.K., 'Coupled Lateral Torsional Response of Buildings to Ground Shaking', Earthquake Engineering Research Center, University of California, Berkeley, Report No. EERC 76-13, May, 1976.

[32] Hejal, R., and Chopra, A.K., 'Earthquake Response of Torsionally Coupled Frame Buildings', Journal of the Structural Division, ASCE, Vol. 115, No. 4, April 1989, pp. 834-867.

[33] Kan, C.L., and Chopra, A.K., 'Torsional Coupling and Earthquake Response of Simple Elastic and Inelastic Systems', Journal of the Structural Division, ASCE, Vol. 107, No. ST8, August 1981, pp. 1569-1588.

[34] Irvine, H.M., and Kountouris, G.E., 'Peak Ductility Demands in Simple Torsionally Unbalanced Buildings Models Subjected to Earthquake Excitation', Proceeding of the 7th World Conference on Earthquake Engineering, Part 4, Istanbul, Turkey, 1980, pp. 117-120.

[35] Syamal, P.K., and Pekau, O.A., 'Dynamic Response of Bilinear Asymmetric Structures', Journal of Earthquake Engineering and Structural Dynamics, No. 13, 1985, pp. 527-541.

[36] Tso, W.K., and Sadek, A.W., 'Inelastic Seismic Responses of Simple Eccentric Structures', Journal of Earthquake Engineering and Structural Dynamics, No. 13, 1985, pp. 255-269.

[37] Bozorgnia, Y., and Tso, W.K., 'Inelastic Earthquake Response of Asymmetric Structures', Journal of the Structural Division, ASCE, Vol. 112, No. 2, February 1986, pp. 383-400.

[38] Erdik, M.O., 'Torsional effects in Dynamically Excited Structures', Ph.D. Thesis, Rice University, Houston, Texas, 1975.

[39] Yamazaki, Y., 'Inelastic Torsional Response of Structures Subjected to Earthquake Ground Motions', Earthquake Engineering Research Center, University of California, Berkeley, Report No. EERC 80-07, April, 1980.

[40] Palazzo, B., and Fraternali, F., 'Seismic Ductility Demand in Buildings Irregular in Plan : A New Single Storey Nonlinear Model', Proceeding of the 9th World Conference on Earthquake Engineering, Part V, Tokyo-Kyoto, Japan, 1988, pp. 43-48.

[41] Sadek, A.W., and Tso, W.K., 'Strength Eccentricity Concept for Inelastic Analysis of Asymmetrical Structures', Journal of Engineering and Structures, No. 11, July 1989, pp. 189-194.

[42] Tso, W.K., and Ying, H., 'Additional Seismic Inelastic Deformation Caused by Structural Asymmetri', Journal of Earthquake Engineering and Structural Dynamics, No. 19, 1990, pp. 243-258.

[43] Goel, R.K., and Chopra, A.K., 'Inelastic Seismic Response of One Storey Asymmetric-Plan System : Effect of Stiffness and Strength Distribution', Journal of Earthquake Engineering and Structural Dynamics, No. 19, 1990, pp. 949-970.

[44] Chandler, A.M., and Duan, X.N., 'Evaluation of Factors Influencing the Inelastic Seismic Performance of Torsionally Asymmetric Buildings', Journal of Earthquake Engineering and Structural Dynamics, No. 20, 1991, pp. 87-95.

[45] Vignoli, A., and Berti, M., 'Nonlinear Earthquake Behavior of Spatial Frame Structures under the Influence of Bi-directional Ground Motions', Proceeding of the 9th World Conference on Earthquake Engineering, Part V, Tokyo-Kyoto, Japan, 1988, pp. 203-208.

[46] Sedarat, H., and Bertero, V.V., 'Effect of Torsion on The Linear and Nonlinear Seismic Response of Structures', Earthquake Engineering Research Center, University of California, Berkeley, Report No. EERC 90-12, September, 1990.

[47] Goel, S.C., 'P-Δ and Axial Column Deformation in Aseismic Frames', Journal of the Structural Division, ASCE, Vol. 95, No. ST8, August 1969, pp. 1693-1711

[48] Jennings, P.C., and Husid, R., 'Collapse of Yielding Structures During Earthquakes', Journal of the Engineering Mechanics Division, ASCE, Vol. 94, No. EM5, October 1968, pp. 1045-1064.

[49] Kunieda, H., 'On Dynamic Instability of Structures Subject to Dynamic Excitation - A Trial Regarding Prediction of Incipient Instability', Proceeding of the 9th World Conference on Earthquake Engineering, Part V, Tokyo-Kyoto, Japan, 1988, pp. 5-10.

[50] Okada, H., and Okada, T., 'The Study on The Collapse of Steel Structures Subjected to The Earthquake Ground Motion', Proceeding of the 9th World Conference on Earthquake Engineering, Part V, Tokyo-Kyoto, Japan, 1988, pp. 387-392.

[51] Sun, C.K., 'Gravity Effect on the Dynamic Stability of Inelastic Systems', Doctoral Dissertation, Department of Civil Engineering, The University of Michigan, Ann Arbor, MI, 1971

[52] Houbolt, J.C., 'A Recurrence Matrix Solution for the Dynamic Response of Elastic Aircraft', Journal of Aeronautical Science, Vol. 17, 1950, pp. 540-550.

[53] Wilson, E.L., and Bathe, K.J., 'Stability and Accuracy Analysis of Direct Integration Methods', Journal of Earthquake Engineering and Structural Dynamics, No. 1, 1973, pp. 283-291.

[54] Newmark, N.M., 'A method of Computation for Structural Dynamics', Journal of the Engineering Mechanics Division, ASCE, Vol. 85, No. EM3, July 1959, pp. 67-94.

[55] Hilber, H.M., Hughes, T.J.R., and Taylor, R.L., 'Improved Numerical Dissipation for Time Integration Algorithms in Structural Dynamics', Journal of Earthquake Engineering and Structural Dynamics, No. 5, 1977, pp. 283-292.

[56] Hibbitt, H.D., and Karlsson, B.I., 'Analysis of Pipe Whip', A.S.M.E. Pressure Vessels and Piping Conference, San Fransisco, California, June 25-29, 1979.

[57] Uang, C.M., and Bertero, V.V., 'Use of Energy as A Design Criterion in Earthquake-Resistant Design', Earthquake Engineering Research Center, University of California, Berkeley, Report No. EERC 88-18, November, 1988.

[58] Mosaddad, B., and Powell, G.H., 'Computational Models for Cyclic Plasticity, Rate Dependence, and Creep in Finite Element Analysis', Earthquake Engineering Research Center, University of California, Berkeley, Report No. EERC 82-26, November, 1982.

[59] Shield, R.T., and Ziegler, H., 'On Prager's Hardening Rule', ZAMP 9a, 1958, pp. 260-276.

[60] Ziegler, H., 'A Modification of Prager's Hardening Rule', Quaterly of Applied Mathematics, Vol. 17, 1959, pp. 55.

[61] Mroz, Z., 'On Description of Anisotropic Workhardening', Journal of Mechanical Physics and Solids, Vol. 15, 1967, pp. 163-175.

[62] Mroz, Z., 'An Attempt to Describe the Behavior of Metals under Cyclic Loads using a More General Workhardening Model', Acta Mechanica, Vol. 7, Nos. 2-3, 1969, pp. 199-212.

[63] Iwan, W.D., 'On a Class of Models for the Yielding Behavior of Continuous and Composite Systems', Journal of Applied Mechanics, Vol. 34, Transaction ASME Vol. 89, Series E, 1967, pp. 163.

[64] Dafalias, Y.F., and Popov, E.P., 'A Model of Nonlinearly Hardening Material for Complex Loading', Acta Mechanica, Vol. 21, 1975, pp. 173-192.

[65] Peterson, H., and Popov, E.P., 'Constitutive Relations for Generalized Loadings', Journal of the Engineering Mechanics Division, ASCE, Vol. 103, No. EM4, August 1977, pp. 611-627.

[66] Popov, E.P., and Peterson, H., 'Cyclic Metal Plasticity : Experiments and Theory', Journal of the Engineering Mechanics Division, ASCE, Vol. 104, No. EM6, December 1978, pp. 1371-1388.

[67] Hill, R., 'The Mathematical Theory of Plasticity', Oxford University Press, Oxford, England 1950.

[68] Hasegawa, A., Liyanage, K.L., Nishino, F., 'Spatial Instability and Nonlinear Finite Displacement Analysis of Thin-Walled Members and Frames', Journal of the Faculty of Engineering, University of Tokyo (B), Vol. 38, No. 4, 1986, pp. 19-78.

[69] Washizu, K., 'Variational Methods in Elasticity and Plasticity', Pergamon Press, Oxford, 1968.

[70] Belytschko, T., and Hsieh, B.J., 'Nonlinear Transient Finite Element Analysis with Convected Coordinates', International Journal for Numerical Methods in Engineering, Vol.7, No. 7, 1973, pp.255-271.

[71] Bathe, K.J., and Bolourchi, S., 'Large Displacement Analysis of Three-Dimensional Beam Structures', International Journal for Numerical Methods in Engineering, Vol.14, No. 7, 1979, pp.961-986.

[72] Derecho, A.T., Freskakis, G.N., and Fintel, M., 'A study of the Effect of the Frequency Characteristics of Ground Motions on Nonlinear Structural Response', Proceedings, International Symposium on Earthquake Structural Engineering, St. Louis, Missouri, August 1976, pp. 21-36.

[73] Wu, J., and Hanson, R.D. 'Inelastic Response of Stuctures with High Damping Subjected to Earthquakes', Research Report No. UMCE 87-9 Department of Civil Engineering, The University of Michigan, Ann Arbor, Michigan, November, 1987.

[74] AISC, "Specification for the Design, Fabrication and Erection of Steel Buildings, with Commentary", Manual of Steel Construction, American Institute of Steel Construction, Chicago, Illinois, 1980.

[75] "Uniform Building Code", (UBC), International Conference of Building Officials, 1988 Ed., Whitier, CA.